AD-786 562

MODEL ROTOR TEST DATA FOR VERIFICATION OF BLADE RESPONSE AND ROTOR PERFORMANCE CALCULATIONS

Charles F. Niebanck

United Aircraft Corporation

Prepared for:

Army Air Mobility Research and Development Laboratory

May 1974

DISTRIBUTED BY:

NTIS

National Technical Information Service
U. S. DEPARTMENT OF COMMERCE
5285 Port Royal Road, Springfield Va. 22151

DISCLAIMER NOTICE

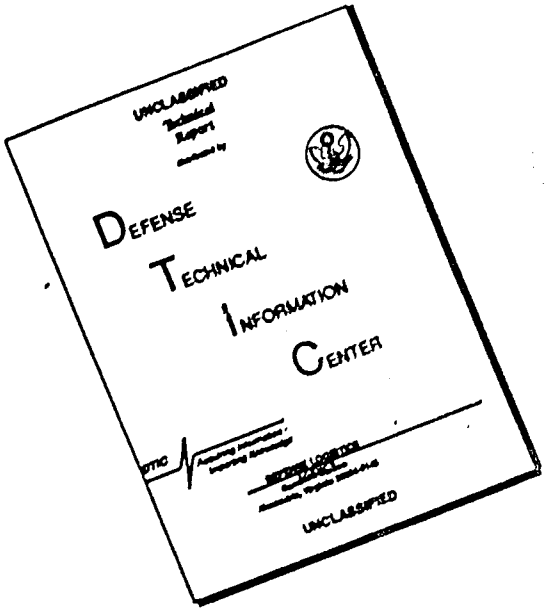

THIS DOCUMENT IS BEST QUALITY AVAILABLE. THE COPY FURNISHED TO DTIC CONTAINED A SIGNIFICANT NUMBER OF PAGES WHICH DO NOT REPRODUCE LEGIBLY.

EUSTIS DIRECTORATE POSITION STATEMENT

This report has been reviewed by the Eustis Directorate, U. S. Army Air Mobility Research and Development Laboratory and is considered technically sound.

This program was initiated to obtain data that would be useful in verifying aeroelastic computer mathematical models and to isolate areas where improvements to the mathematical models are needed in order to predict the rotor stability boundaries accurately.

The technical monitors for this contract were Mr. Patrick Cancro and Mr. Edward Austin, Technology Applications Division.

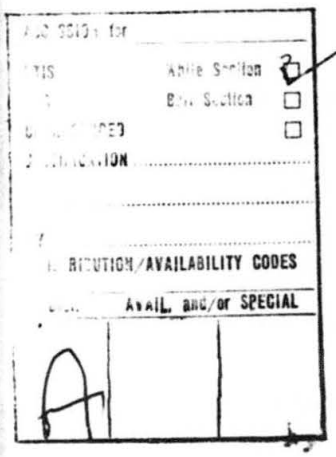

DISCLAIMERS

The findings in this report are not to be construed as an official Department of the Army position unless so designated by other authorized documents.

When Government drawings, specifications, or other data are used for any purpose other than in connection with a definitely related Government procurement operation, the United States Government thereby incurs no responsibility nor any obligation whatsoever; and the fact that the Government may have formulated, furnished, or in any way supplied the said drawings, specifications, or other data is not to be regarded by implication or otherwise as in any manner licensing the holder or any other person or corporation, or conveying any rights or permission, to manufacture, use, or sell any patented invention that may in any way be related thereto.

Trade names cited in this report do not constitute an official endorsement or approval of the use of such commercial hardware or software.

DISPOSITION INSTRUCTIONS

Destroy this report when no longer needed. Do not return it to the originator.

Unclassified

SECURITY CLASSIFICATION OF THIS PAGE (When Data Entered)

REPORT DOCUMENTATION PAGE		READ INSTRUCTIONS BEFORE COMPLETING FORM
1. REPORT NUMBER USAAMRDL-TR-74-29	2. GOVT ACCESSION NO.	3. RECIPIENT'S CATALOG NUMBER AD-786562
4. TITLE (and Subtitle) MODEL ROTOR TEST DATA FOR VERIFICATION OF BLADE RESPONSE AND ROTOR PERFORMANCE CALCULATIONS		5. TYPE OF REPORT & PERIOD COVERED Final
		6. PERFORMING ORG. REPORT NUMBER SER 50879
7. AUTHOR(s) Charles F. Niebanck		8. CONTRACT OR GRANT NUMBER(s) DAAJ02-72-C-0026
9. PERFORMING ORGANIZATION NAME AND ADDRESS United Aircraft Corporation Sikorsky Aircraft Division Stratford, Conn. 06497		10. PROGRAM ELEMENT, PROJECT, TASK AREA & WORK UNIT NUMBERS Project 1F263211D157
11. CONTROLLING OFFICE NAME AND ADDRESS Eustis Directorate U.S. Army Air Mobility R&D Laboratory Fort Eustis, Va. 23604		12. REPORT DATE May 1974 13. NUMBER OF PAGES 369
14. MONITORING AGENCY NAME & ADDRESS(If different from Controlling Office)		15. SECURITY CLASS. (of this report) Unclassified 15a. DECLASSIFICATION/DOWNGRADING SCHEDULE

16. DISTRIBUTION STATEMENT (of this Report)

Approved for public release; distribution unlimited.

17. DISTRIBUTION STATEMENT (of the abstract entered in Block 20, if different from Report)

18. SUPPLEMENTARY NOTES

Details of illustrations in this document may be better studied on microfiche

19. KEY WORDS (Continue on reverse side if necessary and identify by block number)

Rotor Blades
Rotors
Response
Wind Tunnel Models
Wind Tunnel Tests
Helicopter Rotors

Reproduced by
NATIONAL TECHNICAL
INFORMATION SERVICE
U S Department of Commerce
Springfield VA 22151

20. ABSTRACT (Continue on reverse side if necessary and identify by block number)

Dynamically scaled model helicopter rotor tests were carried out to collect data for the verification and improvement of helicopter rotor and blade response calculations.

Four fully articulated model rotor blade configurations were fabricated and tested. The configurations included variation in built-in twist, airfoil camber, and stiffness. The dynamically scaled configurations were based on

DD FORM 1 JAN 73 1473 EDITION OF 1 NOV 65 IS OBSOLETE

Unclassified

SECURITY CLASSIFICATION OF THIS PAGE (When Data Entered)

Block 20

H-34 rotor blades previously tested at full scale. The geometry, mass, and stiffness properties of the model blades are provided, along with two-dimensional aerodynamic test data for the blade airfoil sections. The rotor operating regime tested for the four configurations included lightly loaded and stalled conditions, variations in flapping trim, and rotor-wake interference conditions.

The complete body of rotor performance and blade response time history data is preserved in digital form on magnetic tapes. A computer program to sample the data tapes and perform the most common types of processing is also available for convenient future use.

SUMMARY

Dynamically scaled model helicopter rotor tests were carried out to collect data for the verification and improvement of helicopter rotor and blade response calculations.

Four fully articulated model rotor blade configurations were fabricated and tested. The configurations included variation in built-in twist, airfoil camber, and stiffness. The dynamically scaled configurations were based on H-34 rotor blades previously tested at full scale. The geometry, mass, and stiffness properties of the model blades are provided, along with two-dimensional aerodynamic test data for the blade airfoil sections. The rotor operating regime tested for the four configurations included lightly loaded and stalled conditions, variations in flapping trim, and rotor-wake interference conditions.

The complete body of rotor performance and blade response time history data is preserved in digital form on magnetic tapes. A computer program to sample the data tapes and perform the most common types of processing is also available for convenient future use.

Comparisons between model and full-scale performance and blade response data show qualitative and quantitative similarities. It is therefore concluded that full-scale rotor performance and blade response calculation methods can be verified or improved by correlating with model data.

Sample model test data are compared with blade response and rotor performance calculations. The model rotor provided more lift than could be expected from calculations employing static two-dimensional airfoil test data and the consideration of full-scale unsteady aerodynamics. The accuracy of the blade response and performance calculation method varied between the blade configurations. Good accuracy was obtained with the conventional amount of built-in twist.

Correlation of model results obtained herein with previous full-scale test data should be extended for further evaluation of the relationship between model and full-scale results.

Rotor performance and blade response calculations should generally include the effects of wake-induced inflow. The analytical representation of rotor blade excitation by wake vortices should be improved.

The analytical representation and data for considering unsteady aerodynamics in rotor performance and blade response calculations should be augmented to include characteristics of various symmetrical and unsymmetrical airfoils, other Reynolds number variations, and any appreciable effects of yawed flow.

PREFACE

This program was conducted for the Eustis Directorate, U. S. Army Air Mobility Research and Development Laboratory, under Contract DAAJ02-72-C-0026 (Project 1F263211D157). Technical monitors for the Government were Mr. Patrick Cancro and Mr. Edward Austin.

Mr. Edmond F. Kiely was Task Manager for this work at Sikorsky Aircraft. He also supervised the design, fabrication, and pretest checkout of model components. Mr. Charles F. Niebanck supervised the analytical calculations, performed their correlation with test data, and provided specifications for data reduction programs. Mr. Robert Murrill served as the Sikorsky test engineer during the pretest activities and the wind tunnel operations. Mr. Miles Waugh wrote the computer programs which stored the test data on tape, and which permit their retrieval for future use. Mr. John Corrigan used the Y-200 version of the Normal Modes Aeroelastic Analysis to provide the calculated blade response data. Technical supervision was provided by Dr. Raymond Carlson, Mr. Peter Arcidiacono, and Mr. Edward S. Carter.

This volume covers the testing and correlation with calculation for four model blades based on the H-34 rotor. Under this program, similar work was carried out for the more advanced Sikorsky IRB blade design. The data and results pertaining to this configuration are contained in a separate report and are provided with limited rights for the use of the Government only.

TABLE OF CONTENTS

Preceding page blank

LIST OF ILLUSTRATIONS

LIST OF TABLES

INTRODUCTION

Experimental data are required to verify and suggest means of improving mathematical analyses of helicopter rotor performance and blade response. The dynamically scaled model rotor is an excellent source of such data. Dynamically scaled model wind tunnel data for the verification of analytical calculations can be obtained rapidly for an extended range of accurately measured parameters at comparatively low cost and risk.

Dynamically scaled rotor models may also play an important direct role as a design tool for specific rotor systems. Application of dynamic models in this way requires some comparative model and full-scale data for an existing configuration, to evaluate the effects of parameters which are not simulated in the dynamic scale modeling process. A body of data of this type allows more confident extrapolation of the characteristics of new full-scale rotor designs from model test results.

The primary objective of the dynamically scaled model rotor test documented herein was the collection of data for the verification and improvement of helicopter rotor performance and blade response calculations. The four model rotor blade configurations fabricated and tested represented independent variations in twist, camber and stiffness. The configurations fabricated and tested included dynamically scaled fiber glass spar blade sets with 0 degrees and -8 degrees of built-in twist, a similar set with 0 degrees twist and a 20% chord, 5-degree deflection plain flap, and a fourth set with a three-times-scale stiffness aluminum spar. The dynamically scaled configurations were based on the H-34 blades tested at full scale in the programs documented by Reference 1, 2, and 3. Thus, the present data may also be useful for further establishing the relationship between full-scale and dynamically scaled rotor data.

A secondary objective of the program was the correlation of sample test data with calculated results from the Sikorsky-UARL Normal Modes Aeroelastic Analysis, to support an assessment and recommendations for improvement of that analysis.

Test data resulting from this program are appropriately sampled in this report for presentation and correlation with calculated and full-scale results. The complete body of rotor performance and blade response time history data are preserved in digital form on magnetic tapes. A computer program to sample the data tapes and perform the most usual processing is also supplied for convenient future use. The magnetic tapes are readable by using standard computer program routines. Additional processing modes which may be devised for analysis and correlation of the test data may be applied in the future by providing appropriate computer program modules.

MODEL DEFINITION

Data which describe the various H-34 model blade configurations, the corresponding rotor system, and the wind tunnel model supporting the rotor are supplied herein.

These data are required for input to rotor response calculation methods whose outputs will be compared to model test results.

The data are supplemented with descriptions of how the data were obtained. Where applicable, discussions of data verification and estimates of the data accuracy are also supplied.

GENERAL DESCRIPTION OF MODEL AND BLADE CONFIGURATIONS TESTED

The wind tunnel model with H-34 blades installed is shown mounted in the 18-foot test section of the United Aircraft Research Laboratories main wind tunnel in Figures 1 and 2. The compound helicopter model fuselage utilized for this test was identical to that used in the TRAC Telescoping Rotor test program (Reference 4). A six-component strain gage balance of appropriate capacity was installed. The 110-inch-diameter four-bladed fully articulated rotor is powered by a variable frequency electric motor. The control system provides independent collective pitch, longitudinal cyclic pitch, and lateral cyclic pitch. A slip ring installed below the swashplate transfers the blade strain gage signals and flap and lag potentiometer signals to the nonrotating system. The strain gage balance for measuring rotor forces and moments is mounted below the rotor transmission and supports the entire drive train and control system as well as the rotor. The grounded portion of the balance is supported in a soft damped gimbal frame which has been found effective in eliminating ground resonance type mechanical instabilities.

The model fuselage consists of a nonstructural fiber glass and aluminum outer shell mounted on a steel frame. Overall fuselage length is 123 inches and maximum diameter is 17.3 inches. The general arrangement is shown in Figure 3, where the side panels and nose cone have been removed from the model.

The four-bladed fully articulated model rotor head is of conventional design. The coincident flap and lag hinges are located at the 3-inch radial station corresponding to an offset ratio of .0545. Rotary viscous dampers equipped with 3:1 ratio mechanical linkages are provided for each lag hinge. A pitch flap coupling ratio of 0.0 was used. Pitch-lag coupling was measured to be approximately 0.8° for lag motions from 0° to 18° lag. Physical stops limited flapping motion from -7.5 to +21.0° and inplane motions from 7° lead to 18° lag.

Blade pitch control was achieved with an electromechanical swashplate control system. The system used three independent electric motors controlled from the rotor control console to provide pure collective and cyclic control inputs to the swashplate. Required mixing is accomplished

mechanically with three intermeshed differential gearsets. Mixed outputs are transferred to three conventionally positioned mechanical actuators by means of flexible shafts. The actuators transfer the rotary motion of the shafts into linear motion by means of a worm gear and jackscrew. Control angles are measured with geared potentiometers which effectively count the number of turns of the input electric motors. The impressed collective and cyclic pitch angles are displayed on three digital meters in the control console.

The rotor system is powered by a water-cooled variable frequency electric motor, nominally rated at 80 horsepower. Power is transmitted to the rotor shaft by a 5.25:1 reduction, two-stage gearbox. Gearbox lubrication and cooling are provided by an oil spray system.

The blades, rotor head, motor, gearbox, blade pitch control system, and instrumentation slipring comprise the internal model assembly. This portion of the model is metric. It is mounted on a six-component Task Mk. XIX strain gage balance for precision measurement of rotor forces and moments. The ground side of the balance is supported in a soft damped gimbal mount. The gimbal provides a pitch and roll freedom for the internal model about the axis formed by the intersection of the rotor shaft and balance centerlines. Spring restraint is provided between the gimbal (ground side of the balance) and the fuselage. Cantilever springs are used in the pitch direction and a torsion bar is used in the roll direction. Damping is provided by rotary viscous dampers with mechanical linkages to increase their effective output for small gimbal motions. One set of dampers was connected directly across the balance in the roll direction. It was demonstrated experimentally that this soft grounding of the balance did not affect the steady-state force and moment measurements. The gimbal mounting permitted the internal model assembly to respond to destabilizing forces by rotating at the gimbal axis rather than storing the energy as elastic deformations in the metric structure. The dampers dissipate the energy as the gimbal deflects, resulting in a stable system.

The wind tunnel model mounting strut system shown in Figures 1 and 2 was developed in conjunction with the gimbal mounting of the rotor to provide as nearly as possible a rigid support for the external fuselage. The stiff mount was effective in raising the primary natural frequencies of the model installation to values above those at which mechanical instabilities such as ground resonance were likely to occur.

Three of the model operating parameters (forward speed, rotor rpm, and fuselage angle of attack) were controlled from the wind tunnel facility control console. The remainder of the model controls were centralized in the model control console. The collective pitch and longitudinal and lateral cyclic pitch settings were independently controlled by three-position spring-centered toggle switches. The impressed blade pitch angles were displayed on digital meters immediately above the corresponding toggle switches.

The four model rotor blade configurations fabricated and tested represented independent variations in twist, camber and stiffness. The configurations

fabricated and tested included dynamically scaled fiber glass spar blade sets with 0 degrees and -8 degrees of built-in twist, a similar set with 0 degrees twist and a 20% chord, 5-degree deflection plain flap, and a fourth set with a three-times-scale stiffness aluminum spar. The dynamically scaled configurations were based on the H-34 blades tested at full scale in the programs documented by References 1, 2, and 3.

BLADE CONSTRUCTION

An exploded view showing typical construction details for the H-34 dynamically scaled blades is shown in Figure 4.

The internal load-carrying members of the blade are representative of full-scale construction, with a load-carrying D-tube spar at the leading edge. The trailing half of the blade is made up of individually attached fairing segments or pockets. The pockets are fastened to the spar, but not to each other.

BLADE STIFFNESS AND MASS DATA

Presentation of Blade Data

Inertia and chordwise center-of-gravity data for the H-34 model blade configurations are presented in Table I. The blade stiffness properties for the scale stiffness fiber glass and the three-times-scale stiffness aluminum spar configurations of the H-34 model blades are given in Tables II and III respectively. The actual distributions are represented by short constant property radial segments over the intervals given.

Derivation of Blade Data

The blade distributed mass data outboard of radial station 8.90 are determined by dividing the full-scale blade data by the appropriate power of the geometric scale factor, S_s which is 6.109 in this case. Thus, w is found by dividing corresponding full-scale data by S_s^2 and the moments of inertia by dividing full-scale data by S_s^4.

Blade mass properties inboard of radial station 8.90 are not scaled, and represent the properties of the actual components provided under the scope of this investigation.

Blade area moment of inertia and torsional constant data for the fiber glass blade properties outboard of radial station 8.90 are determined by dividing full-scale blade spar properties by S_s^4. These values were then adjusted in accordance with stiffness test results for the completed blade. When these values are used with the values of E and G given below the table, the resulting bending and twisting stiffness values EI_{flp}, EI_{chd}, and GJ for the fiber glass blades are one-fourth of those for a hypothetical model-scale replica of the full-scale blade spar.

Although the values of I_{flp}, I_{chd}, and J based on the actual crossectional area of the fiber glass-resin composite are not known precisely, the values derived as described above can be considered representative, because of

the thin-walled D-tube spar and pocket construction, which is similar to the actual blade.

Blade area moment of inertia and torsional constant data for the aluminum spar blade properties outboard of radial station 8.90 were based on values obtained by dividing full-scale blade spar values by the quantity $4S_s^4/3$. These values were then increased in accordance with stiffness test results for the completed blade, including the pockets. When these values are used with the values of E and G given, the resulting bending and twisting stiffness values EI_{flp}, EI_{chd}, and GJ obtained are approximately three-fourths of those for a hypothetical model-scale replica of the full-scale blade.

Inboard of station 8.90, the bending and twisting stiffness distributions are based on reasonable approximations of the actual cross-sections. The cross-sectional area contributions of the various components were weighted by the ratio of their elastic or shear moduli (E or G) to the reference values given in Tables II and III.

Verification of Blade Data

Blade bending stiffness is verified by applying a known weight to the blade tip at the feathering axis and measuring the resulting deflection at twelve locations. This test also verifies that the elastic axis and feathering axis are coincident within the accuracy of measurements. A photograph of the apparatus used in this test is provided in Figure 5.

Blade twisting stiffness is verified by applying a known torsional couple at the blade tip and optically measuring the torsional deflections at six spanwise stations.

Results of a set of such measurements for the three-times-scale stiffness aluminum spar blade and the scale stiffness fiber glass spar blades are shown in Figures 6, 7, 8 and 9. The test data are compared with nominal expected deflections which were calculated from beam theory for blade spar properties alone. Most of the discrepancy between the calculated and experimental values is believed to be due to stiffness contributions of the pockets. This deviation is considered acceptable.

Blade mass is verified by careful weighing of all significant components before assembly. Upon completion, the total blade weight and spanwise balance are checked.

EXPERIMENTAL DETERMINATION OF NONROTATING MODEL BLADE NATURAL FREQUENCIES

The nonrotating natural frequencies of each blade set were determined experimentally. The frequencies of both instrumented blades from each set were checked as were several of the noninstrumented blades. The blades were supported from an articulated model rotor hub which was attached to a rigid structure. A variable frequency air jet was used to excite the blade elastic motions. Strain gage outputs from the instrumented blade were recorded on a direct writing oscillograph for ease in determining maximum response, mode shape, and for measuring decay rate for

determination of structural damping coefficients. The natural frequencies of the noninstrumented blades were determined by visual observations of maximum blade excursions.

The test apparatus utilized for these determinations is shown in Figure 10. The rotor blades were mounted from sleeve-spindle assemblies identical to those used during the wind tunnel tests. The assembly was supported vertically from a model rotor hub. The rotor hub bearings provided a pin connection at the coincident flap and lag hinge axis. The lag dampers were disconnected, and blade pitch freedom was eliminated by grounding the pitch horn to the flapping pivot.

The variable frequency, variable amplitude air jet was obtained by connecting a function generator to a hydraulic servo controller. The associated servo valve was used to drive a shuttle valve which provided modulation to a "shop air" supply line. Excitation frequency was limited to 100 Hz where compressibility effects eliminated the modulation at the jet nozzle.

The experimentally determined nonrotating natural frequencies and critical damping coefficients derived from the strain gage decay records are listed in Table IV. The experimentally determined natural frequencies are compared to calculated values in Figures 11 and 12. Reasonable agreement is further verification that mass and stiffness distributions are as planned. Furthermore, lack of significant coupling between flapwise and torsional moments in the natural vibration test verifies the coincidence of the blade elastic axis and chordwise center-of-gravity position.

Accuracy of Blade Data

Blade mass and inertia properties are within ±5% of nominal values. Variations between individual blades are within ±2%, except for spanwise balance, which is held within ±.5%.

The various blade stiffness properties are within a tolerance of +10% to -3% of design values. Variations between individual blades are within ±3%.

FULL-SCALE EQUIVALENT STRESS FOR FIBER GLASS MODEL BLADES

The following relationships between the bending and twisting moments and stresses were obtained theoretically for the constant section part of the full-scale H-34 blades:

$$\sigma_F = \frac{M_{FSS}}{1.53}$$

$$\sigma_C = \frac{M_{CFS}}{4.72}$$

$$\sigma_T = \frac{M_{TFS}}{3.31}$$

At the .15 radius station, the relation between twisting moment and stress was similarly found to be

$$\sigma_{T.15R} = \frac{M_{TFS}}{5.93}$$

The stress-moment relations for a hypothetical aluminum spar replica model are found by multiplying the factors in the above equations by the scale factor cubed. With a scale factor of 6.11, the above relationships for the replica model are as follows:

$$\sigma_F = 149 \; M_{FRM}$$

$$\sigma_c = 48.4 \; M_{CRM}$$

$$\sigma_T = 69.0 \; M_{TRM}$$

$$\sigma_{T.15R} = 38.5 \; M_{TRM}$$

The fiber glass H-34 models have one-fourth the stiffness of a replica model. At a dynamically similar operating condition, the fiber glass blade loads will be one-fourth those of the replica model blade. Therefore, the following relationship is established between fiber glass model blade moments and full-scale equivalent stress, by multiplying the above factors by 4:

$$\sigma_{FFS} = 595 M_F$$

$$\sigma_{CFS} = 194 \; M_C$$

$$\sigma_{TFS} = 276 \; M_T$$

$$\sigma_{TFS.15R} = 154 \; M_T$$

ROTOR SYSTEM GEOMETRY, STIFFNESS AND DAMPING DATA

Remaining rotor system data required for input to the computer programs are presented in Table V. Supplementary discussion and estimated accuracy of these data are contained in the following paragraphs.

Geometric and dimensional accuracy of the blade data are as follows:

Blade Length	±.020 in.
Chord	±.018 in.
Local Twist	±.25 deg
Cumulative Twist	±.50 deg
Contour	±.007 in.
Shear Center Location	±.03 in.
Center-of-Gravity Location	±.03 in.
Location of Blade Hinges	±.010 in.

The pitch-flap coupling ratio of 0.0 occurs when blade pitch, flap, and lag are all zero.

The damper installation is identical to that used for the Reference 5 test, with the dampers operating through a 3 to 1 linkage. The orifices are opened wide at the 17.0 in.-lb-sec setting, minimizing the in-phase or spring part of the damper resistance. Tests of the dampers at the expected range of once-per-revolution frequency and motion showed that the coefficient is within ±20% of the nominal value, and that the apparent damper spring (in phase with displacement) moment is approximately 15% of the damper damping (out of phase with displacement) moment. This implies that the damper apparent spring constant is 200 in.-lb/rad or less at the once-per-revolution frequency range.

Linear dimensions defining the pitch control gometry are accurate to ±.01 in. Angular dimensions are accurate to ±.30 deg.

Although pitch control spring rate is not accurately known, and considerable azimuthal variation in its value occurs, it remains high enough so that blade root pitch deflections are negligible. The 21,000 in.-lb/rad value given in Table V was calculated for a blade pushrod at its furthest azimuth distance from one of the three actuators. It is estimated that blade torsional root stiffness may differ from this figure by ±10,000 in.-lb/rad. Variations are caused by simplifying approximations and the relative azimuthwise position of the push rods and actuators. Blade response observed during the Reference 5 test supports the conclusion that blade root pitch deflections are negligible.

AERODYNAMIC DATA

Hub Aerodynamic Drag

The aerodynamic drag of the four-bladed hub with blade cuffs installed was measured in a previous test program, reported in Reference 6. The measurements are expressed as an equivalent area in square feet. Multiplication of this equivalent area by dynamic pressure in pounds per square foot gives the aerodynamic drag in pounds.

The equivalent area varied between .28 square feet at a shaft angle of attack of 8 degrees and .25 square feet at a shaft angle of attack of -8 degrees. The accuracy of these data are ±5%.

The hub drag is subtracted from total rotor drag during data reduction. This provides rotor drag in terms of blade contributions only. This procedure is followed because no special attempt has been made to scale the hub configuration within the scope of this or previous programs.

Two-Dimensional Blade Section Steady Aerodynamic Coefficients

The two-dimensional blade section steady aerodynamic coefficients were obtained in the United Aircraft Research Laboratory Acoustic Tunnel. The test airfoils were made from untwisted aluminum spar model H-34 blade

sections. A steel spar was inserted through the leading-edge D-tube and bonded in place to provide reinforcement.

Aerodynamic load measurements of lift, drag and pitching moment were made with a strain gage balance. Tunnel velocity was calculated initially from the usual total and static pressure measurements.

A photograph of the wind tunnel and airfoil section installation appears in Figure 13.

The data reduction calculations incorporated balance axis interaction, corrections for airfoil deflection and weight, and conventional jet boundary corrections from Reference 7 for open-top-and-bottom wind tunnel test sections.

The test airfoils had a chord of 2.09 inches, and a span of 21.0 inches, which extended over the full width of the open-top-and-bottom test section. The height of the test section was 30.88 inches.

Presentation of Two-Dimensional Blade Section Steady Aerodynamic Coefficients

The H-34 model blade section aerodynamic coefficients for the standard NACA 0012 airfoil and the NACA 0012 airfoil with a 20% chord plain trailing edge flap deflected 5 degrees are tabulated in Tables VI through XV. Data are provided for five Mach numbers ranging from .10 to .56. Angles of attack cover ±180 degrees at the two lowest Mach numbers. Angle-of-attack ranges at the higher Mach numbers are adequate to cover the expected regime of operation of the one-half speed dynamically-scaled models.

The tabulated data are also plotted in Figures 14 and 15.

It should be noted that the data tabulated and plotted herein have been faired from a larger amount of test data. The number of angle of attack and coefficient values has been chosen to fit the Sikorsky Normal Modes Aeroelastic Analysis program input tables. The data values tabulated and plotted herein are the values provided to that computer program as steady aerodynamic data. In accordance with the assumptions used in that computer program, the unflapped airfoil is considered to be completely symmetrical, and data are provided for positive angles only.

Data Reduction for Two-Dimensional Blade Section Steady Aerodynamic Coefficients

This subsection documents the data reduction calculations for the two-dimensional blade section steady aerodynamic coefficients.

The structure of the raw data and the data reduction calculations themselves reflect the usual wind tunnel test procedure. A group of operating conditions referred to as a run were preceded and followed by wind-off measurements called start and end zeros, which provide zero airload balance readings to which wind-on readings are referred.

The smallest complete unit of useful data is, therefore, a wind tunnel run. The data reduction calculations described on the following pages were repeated for each wind tunnel run.

1. Calculation of Aerodynamic Loads and Geometric Angle of Attack.

The balance start and end zeros from a run were averaged from each of the three (lift, drag, and moment) balance outputs

$$G_{LO} = (G_{LS} + G_{LE})/2.0$$

$$G_{DO} = (G_{DS} + G_{DE})/2.0$$

$$G_{MO} = (G_{MS} + G_{ME})/2.0$$

For each of the test points in the run, the difference between wind-on balance output and average wind-off output for the run was taken. For test point i the calculations are:

$$V_{L(i)} = G_{L(i)} - G_{LO}$$

$$V_{D(i)} = G_{D(i)} - G_{DO}$$

$$V_{M(i)} = G_{M(i)} - G_{MO}$$

The balance outputs were converted into forces and moments for each test point through the following matrix multiplication:

$$\begin{Bmatrix} L_{R(i)} \\ D_{R(i)} \\ M_{R(i)} \end{Bmatrix} = [C_{mn}] \begin{Bmatrix} V_{L(i)} \\ V_{D(i)} \\ V_{M(i)} \end{Bmatrix}$$

The values of the elements of the C_{mn} matrix were determined experimentally. Sample values are:

$C_{11} = .0122$	$C_{12} = .0000202$	$C_{13} = .00023$
$C_{21} = .000085$	$C_{22} = .00473$	$C_{23} = .000137$
$C_{31} = .000105$	$C_{32} = .0000488$	$C_{33} = .00859$

The indicated angle of attack for each test point was determined from the transducer output in a manner analogous to the conversion of balance readings to force and moment:

$$G_{AO} = (G_{AS} + G_{AE})/2.0$$

$$V_{A(i)} = G_{A(i)} - G_{AO}$$

$$A_{(i)} = \frac{V_{A(i)}}{K_A} + \alpha_o$$

The angle α_o is the angle at which static zeros were taken. This angle was 0 or 180 for most of the runs.

The above calculations provide the aerodynamic lift and drag forces in the tunnel axis system, and the geometric angle of attack at the point where the airfoil is attached to the pitch drive mechanism.

Because of the flexibility of the model, its static unbalance, and the large angle-of-attack range to be tested, appropriate corrections to the measured pitching moment and angle of attack were applied.

The torsional deflection of the airfoil at the mid-span was calculated from engineering beam theory, and used as a correction to obtain the geometric angle of attack from the indicated angle of attack.

$$\alpha_{G(i)} = A_{(i)} + \theta_{(i)}$$

For the H-34 model blade sections,

$$\theta_{(i)} = 197 \times 10^{-4} \times M_{R(i)} \text{ deg}$$

The indicated lift and drag forces for each test point were resolved into normal and chordwise force components:

$$N_{(i)} = L_{R(i)} \cos \alpha_{G(i)} + D_{R(i)} \sin \alpha_{G(i)}$$

$$C_{(i)} = -L_{R(i)} \sin \alpha_{G(i)} + D_{R(i)} \cos \alpha_{G(i)}$$

The corrections applied to the indicated pitching moment included the following at each test point (i). The numerical coefficients given were obtained from engineering beam theory, and apply to the H-34 model two-dimensional sections:

(a) A moment due to the uniformly distributed chordwise force on an arm equal to the average normal deflection caused by the uniformly distributed normal force:

$$M_{NB(i)} = .00818\, C_{(i)} N_{(i)}$$

(b) A moment due to the uniformly distributed normal force acting on an arm equal to the average chordwise deflection caused by the uniformly distributed chordwise force:

$$M_{CB(i)} = -.000379\ C_{(i)}N_{(i)}$$

(c) A moment due to the chordwise component of model weight, acting through an arm equal to the average normal deflection caused by the uniformly distributed normal force:

$$M_{NW(i)} = .00818\ N_{(i)}\ W_M \sin \alpha_{G(i)}$$

(d) A moment caused by airfoil chordwise weight unbalance, which varies from its start and end zero value because of variation in angle of attack:

$$M_{UW(i)} = -W_M Y_{CG} \left[\cos \alpha_o - \cos \alpha_{G(i)}\right]$$

The chordwise unbalance was slightly nose-heavy for the H-34 model blade two-dimensional sections:

$$W_M Y_{CG} = 0.04185 \text{ in.-lb}$$

With this amount of unbalance, the term $M_{UW(i)}$ was negligible with respect to aerodynamic pitching moment.

The aerodynamic part of the pitching moment was found by subtracting the above-defined corrections from the total pitching moment measured by the balance:

$$M_{A(i)} = M_{R(i)} - M_{NB(i)} - M_{CB(i)} - M_{NW(i)} - M_{UW(i)}.$$

2. Calculation of Tunnel Mach Number, Density, Velocity, and Dynamic Pressure

The tunnel Mach number, density, velocity, and dynamic pressure were determined initially from the tunnel total pressure, test section total minus static pressure, and tunnel temperature. The customary compressible, isentropic, adiabatic flow and gas law relationships were used:

$$H\text{-}P = K_{MN}\ \Delta P$$

$$\frac{P}{H} = 1 - \frac{(H\text{-}P)}{H}$$

$$M = \left[\frac{\left(\frac{P}{H}\right)^{\frac{\gamma-1}{\gamma}} - 1}{\frac{\gamma-1}{2}}\right]^{\frac{1}{2}}$$

$$\frac{\rho}{\rho_o} = \left[1 + \frac{\gamma-1}{2} M^2\right]^{\frac{-1}{\gamma-1}}$$

$$\rho_o = \frac{H}{R_G\ (T_{SC} + 460)}$$

$$V = M\left[\frac{\gamma R_G(T_{SC} + 460)}{1 + \frac{\gamma-1}{2}M^2}\right]^{\frac{1}{2}}$$

$$q = \frac{\rho V^2}{2}$$

In evaluating the above quantities, the following values for γ and R were used:

$$\gamma = 1.4$$

$$R_G = 1722.\ \frac{^{\circ}F - SEC^2}{FT^2}$$

3. Calculation of Aerodynamic Coefficients

The uncorrected aerodynamic coefficients were calculated in the usual manner from the aerodynamic loads, model dimensions and dynamic pressures for each test point.

$$C_{l(i)} = \frac{L_{R(i)}}{q\ Sc}$$

$$C_{dR(i)} = \frac{D_{R(i)}}{q\ Sc}$$

$$C_{mR(i)} = \frac{M_{A(i)}}{q\ Sc^2}$$

In the above calculations, the model airfoil dimensions are expressed in feet, and the aerodynamic pitching moment in foot-pounds.

4. Jet Boundary Corrections

The following corrections from Reference 7 were applied to the angle of attack and the drag and moment coefficients. The corrections were theoretically derived in Reference 7 for the case of an airfoil in an infinitely long test section with an open top and bottom and in inviscid, incompressible flow.

$$\alpha_{(i)} = \alpha_{G(i)} - \frac{180.}{\pi}\left[\frac{c}{4h} + \frac{\pi}{24}\frac{c}{h}^2\right] C_{l(i)}$$

$$C_{d(i)} = C_{dR(i)} - \frac{1}{4.}\frac{c}{h}\left[C_{l(i)}\right]^2$$

$$C_{m(i)} = C_{mR(i)} - \frac{\pi^2}{96.}\left[\frac{c}{h}\right]^2 C_{l(i)}$$

5. Alternate Calculation of Tunnel Mach Number

The two-dimensional coefficient of lift versus angle-of-attack relationship obtained for the lowest Mach number tested by using the test results and the foregoing calculations is compared with similar data from References 8 and 9 in Figure 16.

Figure 16 indicates satisfactory agreement with these earlier sources, especially if the effects of Reynolds number and Mach number are considered in the comparison with the Reference 9 data.

Comparisons at higher Mach number, which were made in the same manner, were unsatisfactory, and the problem was finally attributed to an error in the total minus static pressure measurements (ΔP). As the indicated ΔP increased, the data reduction calculations gave progressively excessive values for the slope of coefficient of lift versus α and smaller than expected values for maximum C_L. In addition, there was an excessive indicated effect of Mach number on the coefficients of drag and moment. Since the data appeared satisfactory at the lowest Mach number tested, an alternate method was available for the determination of test section Mach number, from the observed ratio of lift to unstalled angle of attack, the Prandtl-Glauert relation, and the adiabatic, isentropic, compressible flow relationships.

Thus, if the slope $\frac{dC_L}{d\alpha}$ of the coefficient of lift versus α curve is known below stall at a low Mach number, the following expression for lift over α can be written:

$$\frac{L_{R(i)}}{\alpha_{G(i)}} = \left(\frac{dC_l}{d\alpha}\right)_{M=0} \left[\frac{eHSM_{(i)}^2}{2\sqrt{1-M_{(i)}^2}}\right] \left[1 + \frac{\gamma-1}{2} M_{(i)}\right]^{\frac{-\gamma}{\gamma-1}}$$

The lift over angle-of-attack ratio was extracted from the partially reduced data at each tunnel speed setting, incorporating an estimate of the small jet boundary correction in the value of α used. Then a plot of the right-hand side of the above expression was made against the value of the single varying parameter M. (The value of H was substantially constant for all the test points.) Finally, the above expression was solved graphically for the Mach number that existed at the tunnel speed setting, and the calculations of velocity and aerodynamic coefficients could proceed as before.

The above procedure for recalculating the tunnel Mach number uses well-established relationships, and its accuracy is consistent with the accuracy of the test data and its intended use. In addition to its effect on the coefficient of lift, the recalculation of velocity also improved the agreement of the coefficient of drag and the coefficient of moment data with the trends to be expected from previous data. The data in Figure 14 for the Mach number M = .33 agree well with the data from Reference 9 which is shown in Figure 16. The reduction of maximum lift coefficient due to the two higher Mach numbers in Figure 14 is somewhat greater than the proportionate decrease in full-scale data. These low values do not, however,

appreciably affect the half-scale speed blade response calculations performed under this program. At the two highest Mach numbers, angles of attack high enough to reach the maximum lift coefficients are rarely encountered.

Accuracy and Repeatability of Aerodynamic Data

The accuracy of the aerodynamic coefficient data is believed to be governed chiefly by the accuracy of the tunnel velocity measurement. The accuracy is estimated at 5%.

Many of the test points were repeated to give an indication of the repeatability of the data. The typical scatter band of measured points around the faired curves ranges from ±6% at M = .10 to ±3% at M = .56 for the lift data. The typical scatter band for the drag coefficients varies from ±.005 at M = .10 to ±.002 at M = .56. The scatter band for the moment data is typically ±.005 at M = .10, and reduces to about ±.001 at M = .56.

SUPPORT SYSTEM DATA

Natural Modes

The natural modes and frequencies of the support system were calculated from separate considerations of longitudinal, yaw-lateral, vertical, and shaft torsional motions of springs and masses representing the system.

The longitudinal, yaw-lateral, vertical, and shaft torsion equations considered 17, 26, 5, and 2 degrees of freedom respectively.

The undamped equations of motion of these spring-mass systems are of the following form:

$$[A][M]\{\ddot{\gamma}_m\} + \{\gamma_m\} = 0$$

The natural frequencies and modes are then obtained from the corresponding eigen problem in a routine manner.

$$\{[I] - \omega_n^2 [A][M]\}\{\gamma_m\} = 0$$

Calculation of Effective Mass, Stiffness, Damping, and Mechanical Compliance at the Rotor Head From Natural Modes

In order to simulate mechanical compliance at the rotor head for analytical purposes, the head and rotor support system was approximated as effective mass, stiffness, and damping values in the lateral and fore-aft directions in the plane of the rotor, and by similar quantities pertaining to vertical and shaft torsional motions. This approximation permits the correct compliance for steady-state sinusoidal forcing to be simulated if the effective values of mass, stiffness, and damping are allowed to vary with frequency. In the present case, the effective values were calculated for the range of four times rotor rotational frequency to be encountered during the model tests. This is expected to be the major forcing frequency on the rotor support and drive system during the model tests.

The method used to calculate these effective values uses the undamped natural modes and frequencies of vibration, normalized to unit deflection at the rotor head.

By applying the methods of Lagrange, the equations of motion for sinusoidal forcing of the damped linear system can be expressed in terms of the natural vibration modes. For convenience, the force is assumed to be of unit amplitude. To provide the desired effective properties in the various directions, the calculation is repeated with the loads and modes pertaining to those directions.

The equations of motion are of the following form:

$$\left[\gamma_m\right]^t \left[M\right]\left[\gamma_m\right]\left\{\ddot{q}_m\right\} + \left[\gamma_m\right]^t \left[K\right]\left\{\gamma_m\right\}\left\{\dot{q}_m\right\} + \left[\gamma_m\right]^t\left[D\right]\left[\gamma_m\right]\left\{\dot{q}_m\right\} = \left\{X_H^2\right\}\cos\omega_F T.$$

Because of orthogonality properties of the undamped, structural modes, and because the modes are normalized to have a unit value at the head, where the load is applied, the following equation is obtained:

$$\left[M_{Gi}\right]\left\{\ddot{q}_m\right\} + \left[M_{Gi}\ \omega_{ni}^2\right]\left\{q_m\right\} + \left[D_G\right]\left\{\dot{q}_m\right\} = \left\{I\right\}\cos\omega_F t$$

The elements of the generalized damping matrix, D_G, include the contributions of intentionally supplied viscous dampers and the structural damping naturally present, and are obtained from the following:

$$D_{Gij} = \sum_p C_{DP}\ \gamma_{Dpi}\ \gamma_{Dpj} \qquad i \neq j$$

$$D_{Gij} = \sum_p C_{Dp}\ (\gamma_{Dpi})^2 + 2\eta M_{Gi}\omega_{ni} \qquad i = j$$

where C_{Dp} is the coefficient of the pth viscous damper, γ_{Dpi} is the deflection of that damper in the ith mode, and η is an equivalent structural damping, expressed as a fraction of critical damping.

For sinusoidal forcing at constant amplitude, the solutions to the equations of motion are also sinusoidal. In other words, the response of the ith mode is the form

$$q_i = a_i\cos\omega_F t + b_i\sin\omega_F t$$

By equating sine and cosine terms in the equation of forced vibration, the following matrix equation for the a_i and b_i is obtained

$$\begin{bmatrix} M_{Gi}\ (\omega_{ni}^2-\omega_F^2) & \omega_F D_G \\ -\omega_F D_G & M_{Gi}(\omega_{ni}^2-\omega_F^2) \end{bmatrix} \begin{Bmatrix} a_i \\ b_i \end{Bmatrix} = \begin{Bmatrix} I \\ 0 \end{Bmatrix}$$

The above equation is solved by routine methods to obtain the a_i and b_i quantities.

The desired cosine and sine parts of the head mechanical compliance are obtained by summing the response of the individual modes:

$$X_{UR} = \Sigma_i \, a_i$$

$$X_{UI} = \Sigma_i \, b_i$$

An alternative expression for the above two quantities is the resultant amplitude and phase angle:

$$X_{UA} = \sqrt{X_{UR}^2 + X_{UI}^2}$$

$$\Phi_{UA} = \text{Arctan} \, (X_{UI}/X_{UR})$$

The kinetic energy of the system can be written as follows, because of the orthogonality of the modes:

$$T = \tfrac{1}{2} \sum_i M_{Gi} \, (a_i^2 + b_i^2) \omega_F^2$$

The effective mass at the rotor head, to be used in the analytical simulation, is taken to be that mass which will have the same kinetic energy due to the response under a unit force as the multimodal system:

$$\tfrac{1}{2} \, M_{EFF} \, X_{UA}^2 \, \omega_F^2 = T$$

or,

$$M_{EFF} = \frac{\sum_i M_{Gi} \, (a_i^2 + b_i^2)}{\Sigma_i \, a_i^2 + b_i^2}$$

The apparent stiffness and damping are set at those values which will cause the effective mass to have the same response to the vibratory force as the multimodal system.

$$K_{EFF} = \frac{X_{UR}}{(X_{UA})^2} + M_{EFF} \, \omega_F^2$$

$$C_{EFF} = \frac{\left[K_{EFF} - M_{EFF} \, \omega_F^2\right]}{X_{UR} \, \omega_F} X_{UI}$$

The above procedure is applied separately to obtain values for longitudinal, lateral, vertical, and torsional effective mass, stiffness, damping, and mechanical compliance. The resultant amplitude per unit force, phase of the amplitude response, and effective mass, stiffness, and damping are supplied on Figures 17 and 18.

Accuracy of Support System Compliance and Effective Property Data at the Rotor Head

Comparison of similar previous calculations with test results indicates variations of as much as 50% between calculated and test values. Nevertheless, the mechanical compliance of the model rotor support system is comparatively low, and even this variation is not expected to have any significant effect on blade stress or response.

MODEL TEST DATA

WIND TUNNEL FACILITY

The United Aircraft Research Laboratories main wind tunnel located in East Hartford, Connecticut, shown in Figure 19, was used for the model rotor tests documented herein. This tunnel is an atmospheric total pressure, single-return closed test section type. The low-speed test section which was utilized for the program is octagonal in shape, approximately 18 ft across the flats, and is capable of speeds of approximately 170 knots. Remotely controlled air exchangers located in the low-velocity portion of the circuit are employed to maintain tunnel stagnation temperatures at desired values. The large area of the exchangers insures that tunnel stagnation pressure is atmospheric. The tunnel fan is driven by a 9000-horsepower electric motor.

Wind tunnel velocity was measured with static pressure taps located in the side wall of the test section. Tunnel stagnation temperature was measured with a thermocouple located in the tunnel settling chamber.

MODEL INSTRUMENTATION AND CALIBRATION

Blade Strain Gages

Twelve strain gage bending bridges were installed on each instrumented blade. The bridges were arranged to measure flapwise moments at five radial stations, chordwise moments at five stations and torsional moments at two stations. The spanwise location and installation of the strain gages are shown in Figure 20.

All blade strain gage bridges were assembled with four active arm 350 ohm gages to provide maximum transducer output and optimum calculation of temperature, shear, and centrifugal effects. The flapwise and torsional gages were installed at the quarter-chord of the blade. The chordwise gages were installed at the flapwise neutral axis on the leading and trailing edge of the D spar. All bridge wiring was routed chordwise from the strain gages to the rear of the D spar and from there spanwise to solder tabs at the root end of the blade. Segmented trailing edge pockets were then installed on the spar encasing the wires. Thus, the instrumented blade airfoil contour was not disrupted except where the strain gage itself was installed.

The model blade strain gage bridges were calibrated in a fixture which provided cantilever restraint at the blade root end. Flapwise and chordwise forces and torsional moments are applied at the tip. A minimum of four discrete loads were applied in both the positive and negative directions. All results were referenced to a precision series resistance calibration value. The fixture shown in Figure 5 was also used for the strain gage calibration.

Blade Hinge Motions

Instrumented blade flap and lag motion were measured by using film potentiometers. A pinion and sector gear mechanically amplified the hinge motion, providing a high resolution output from the transducers. The flap and lag hinge motions were calibrated for each wind tunnel run by manually placing the blade on the lead-lag and flapping stops, and recording the transducer output at each position.

Model Internal Balance

Six components of rotor force and moment were measured on a Task Corporation MK XIX strain gage balance. The balance was calibrated by applying known pure forces and moments in the shaft axis system at the rotor head. A minimum of five discrete loadings were applied in both the positive and negative directions for each of the six coordinates.

Control Positions

Cyclic and collective pitch inputs were measured by potentiometers which were gear-driven by the electromechanical control actuating system.

Shaft Angle

Rotor shaft angle of attack was measured by the normal equipment provided for that purpose in the wind tunnel. The shaft angle is controlled by the pitching strut, which is attached to the aft part of the fuselage, as shown in Figures 1 and 2. The vertical position of this strut is remotely controllable from the tunnel console, causing the model to pitch about trunnions atop the two main struts visible in Figures 1 and 2 . The shaft angle readout on the tunnel console was calibrated by using an inclinometer. The shaft angle variation caused by the internal gimble deflection under the applied rotor airloads and gravity was investigated and found to be negligible.

Miscellaneous Model Instrumentation and Monitoring Equipment

Timing signals for defining rotor revolutions and azimuth positions were produced by a photoelectric device. Once-per-revolution and 72-per-revolution pulses were recorded.

Four accelerometers were used for monitoring internal model roll motions, gearbox vibration, and external fuselage yawing motions.

Motor and gearbox temperatures were monitored. Motor electrical power input, water and oil system pressure, and gearbox chip detector warnings were available.

Data Acquisition and Monitoring

The principal data recording device used for the test program was a

fourteen track FM tape recorder. The system used narrow band FM multiplex with standard subcarrier oscillators for IRIG channels 7 through 16, allowing ten channels of data to be recorded on each track. Three multiplexed direct record tracks were used, allowing all dynamic measurements to be recorded simultaneously, to provide proper time correlation of the signals. Additionally, one track was used for audio comments, one track for rotor azimuth reference, and one track for a 60-Hz standard time reference. All signal conditioning functions were accomplished using Sikorsky designed electronic modules.

Rotor forces and moments measured by the strain gage balance were displayed on-line, using a Sikorsky-developed Balance Axis Converter. In addition to containing the signal conditioning module for each of the bridges in the six component strain gage balance, the unit contains a small analog computer which performs the matrix manipulation to convert the measured strain gage element outputs to pure forces and moments in the shaft axis coordinate system at the rotor head. The unit utilizes third-order Butterworth filters to obtain steady readings from the vibratory signals. Resultant forces and moments in engineering units (pounds and foot-pounds) are displayed on six digital meters. A 70 mm camera was used to obtain a permanent record of the meter readings at each test point.

Critical transducers were monitored continuously during the test runs. The instrumented blade flap and lag motions were displayed on oscilloscopes. Any FM channel could be displayed on-line for study of amplitude, wave form, or signal quality. A four-trace oscilloscope synchronized to the instrumented blade 1-per-revolution signal was used for monitoring representative blade strain gage bridges.

An electronic flapping resolver was provided in the control console for on-line independent display of longitudinal and lateral tip path plane tilt. The unit responded to first-harmonic content of blade flapping motion only. The resolver was used continuously during the test runs in conjunction with the cyclic controls for trimming the rotor tip path plane either perpendicular to the rotor shaft (trimmed flapping) or at prescribed inclinations to the shaft.

WIND TUNNEL TEST PROCEDURE

Aerodynamic Tares

A series of wind tunnel runs were made without rotor blades to measure aerodynamic loadings on the rotor head and other aerodynamically loaded components of the metric part of the model. These loadings were deducted from the total rotor aerodynamic loads during the data reduction process. Thus the rotor performance results reported herein are due to the blades only. This procedure is followed because no special attempt has been made within the scope of this or previous programs to scale the hub configuration.

The aerodynamic tares were determined for the entire range of shaft angles and forward speeds planned for the test.

Typical Wind Tunnel Run Procedure

The typical wind tunnel run began with a series of calibration records. These records were taken with the rotor and tunnel turned off and are as follows:

1. A "ZCAL" or electrically zero output record was recorded for each transducer.

2. An "RCAL" or known electrical change from the electrical zero condition was recorded for each condition. The difference between the "RCAL" and "ZCAL" records was electrically equivalent to the transducer response to a certain amount of physical moment or hinge motion.

3. At least two "XCAL" records were taken. A low-lead record was taken with the blade manually placed on the lower flapping and lead stops. Then a high-lag record was taken with the blade held on the upper flapping and lag stops. These records were used to provide physical calibrations for the hinge motion transducers by using the known blade hinge positions on the physical motion stops.

4. Three or more "static zero" records were taken to obtain gravity tares for the rotor balance at various shaft angles.

5. The rotor was then started and brought up to an operating speed to be used during the run. Then a "dynamic zero" record was taken at zero lift in hover to provide a zero reference for the blade strain gages. It was more useful to consider this condition rather than a static condition as a moment reference, because of the fairly large steady drift in blade bending bridge output which occurs as the rotor is brought up to speed.

6. Dynamic zeros were repeated if more than one rotor speed was to be used during the run.

7. The tunnel was brought up to operating speed and the rotor controls were set to provide the desired operating condition. The balance axis converter was used to set the rotor at a preselected lift for some of the conditions. In others, the collective pitch was set to a desired value. In either case the cyclic pitch was varied to provide zero or some prescribed amount of first harmonic flapping at the hinge. The shaft angle was also set at a prescribed value. When the desired operating condition was reached, data was recorded.

8. When the data points in the run were complete, the dynamic, static, ZCAL, RCAL and XCAL records were repeated. These final zero and calibration records were used to check for transducer signal drifting, which was usually no more than a few percent of the full-scale reading.

9. After the data acquisition system was connected to each blade configuration, records were taken on tape as the blade was manually bent and twisted in the positive flapwise, chordwise and torsion directions. This provided an independent check on data signal polarity.

HELICOPTER MODEL TEST DATA REDUCTION PROCESS

Rotor Performance Parameters

The data reduction process for rotor performance consisted mainly of applying certain corrections to data recorded on line, performing some relatively simple conversions to coefficient form, and calculating some of the more common nondimensional rotor parameters.

The quantities recorded on-line for each operating condition included tunnel velocity in knots (V), rotor revolutions per minute (N), shaft (or fuselage) angle of attack in degrees (α_{fr}), tunnel stagnation temperature in degrees farenheit (T_{SC}), and the six balance axis converter outputs, X_{BAC}, Y_{BAC}, Z_{BAC}, L_{BAC}, M_{BAC}, N_{BAC}.

The rotor shaft load components due to blade aerodynamic forces were obtained from the balance axis converter readings by using the following equations.

$$X_s = (X_{BAC} - H_X - X_0)/N_{SFX}$$

$$Y_s = (Y_{BAC} - H_Y - Y_0)/N_{SFY}$$

$$Z_s = (Z_{BAC} - H_Z - Z_0)/N_{SFZ}$$

$$L_s = (L_{BAC} - H_L - L_0)/N_{SFL}$$

$$M_s = (M_{BAC} - H_M - M_0)/N_{SFM}$$

$$N_s = (N_{BAC} - H_N - N_0)/N_{SFN}$$

The quantities H_X through H_N in the above equations represent aerodynamic tares, and gravity tares due to changes in shaft angle of attack. The quantities X_0, Y_0, Z_0 and L_0, M_0, N_0 are the averages of balance axis converter readings taken at zero angle of attack static zero conditions before and after each wind tunnel run.

The control angles were corrected for the swashplate phase angle ψ_{SP}, which was 16.6 degrees.

$$A_{1s} = A_{1sR} \cos(\psi_{SP}) + B_{1sR} \sin(\psi_{SP})$$

$$B_{1s} = B_{1sR} \cos(\psi_{SP}) - A_{1sR} \sin(\psi_{SP})$$

The advance ratio is calculated from

$$\mu = \frac{V \times 1.688}{\Omega R}$$

The density is calculated by using the following equation for compressible, adiabatic flow:

$$\rho = \rho_o \left[1 + \frac{\gamma-1}{2} \left(\frac{V^2}{\gamma R T_{SC} - \left(\frac{\gamma-1}{2}\right) V^2} \right) \right]^{\frac{1}{\gamma-1}}$$

The rotor thrust coefficient is calculated from:

$$C_T = \frac{-Z_S}{\rho \pi \Omega^2 R^4}$$

The angle-of-attack tunnel wall correction is calculated by using an expression from Reference 10:

$$\Delta\alpha = -.55 \frac{\pi R^2}{A_T} \left(\frac{-C_T}{2\mu^2} \right)$$

$$\alpha_s = \alpha_{fr} + \Delta\alpha$$

The Z_s and X_s forces are resolved into the wind axis system:

$$L_R = -Z_S \cos \alpha_s + X_S \sin \alpha_s$$

$$D_R = -Z_S \sin \alpha_s - X_S \cos \alpha_s$$

The rotor force and moment coefficients are calculated from

$$\frac{C_L}{\sigma} = \frac{L_R}{F_n}$$

$$\frac{C_D}{\sigma} = \frac{D_R}{F_n}$$

$$\frac{C_Y}{\sigma} = \frac{Y_S}{F_n}$$

$$\frac{C_Q}{\sigma} = \frac{-N_S}{RF_n}$$

$$\frac{C_{RM}}{\sigma} = \frac{L_S}{RF_n}$$

$$\frac{C_{PM}}{\sigma} = \frac{M_S}{RF_n}$$

where

$$F_n = \rho \pi \Omega^2 R^4 \sigma$$

The rotor control angle of attack is

$$\alpha_c = \alpha_s - B_{1s}$$

The values of first-harmonic flapping components at the hinge were determined with the digital data processing program for operating conditions in which these quantities were not set equal to zero. This program will be discussed in a subsequent section of this report.

The blade tip Mach number at the 90° azimuth is determined from:

$$M_{1,90} = \frac{\Omega R + 1.688V}{\left[\gamma R T_{SC} - \frac{(\gamma-1)V^2}{2}\right]^{1/2}}$$

The values of V_s and $\Omega_s R$ are the simulated full-scale equivalent speeds. The conversion factor 2.0 between the actual and simulated speeds is appropriate to the 1/4 stiffness models.

$$V_s = 2.0 \times V$$

$$\Omega_s R = 2.0 \times \Omega R$$

Reduction of Blade Response Data

The blade response data on the FM multiplex analogue tapes which were recorded during the wind tunnel runs were converted to Sikorsky format digital tapes. The digital data were then placed temporarily on disc storage for computer-aided editing and quality checking. Upon completion of this task, the samples of blade response data were converted to engineering units and placed on standard FORTRAN readable tapes. One tape was written for each of the four blade configurations. The blade response data consist of response parameter values taken at 5° azimuth intervals over a forty-revolution record length. Rotor performance parameters for each of the operating conditions were also placed on the tape for each configuration.

A computer program was written to extract the blade response data from the final tapes and perform the most usual types of processing. The retrieval computer program and copies of the final data tapes are available from the Eustis Directorate of the U. S. Army Air Mobility Research and Development Laboratories.

Digital Conversion

Standard Sikorsky procedures and equipment were used to write digital tape records from the FM multiplex analogue tapes taken during the wind tunnel runs.

The digital records for each rotor operating condition and transducer consisted of values observed at azimuth intervals of 5 degrees, starting at zero azimuth as the instrumented blade passed over the tail of the model, and continuing for more than forty revolutions. The data were expressed in normalized computer units. All calibration and reference zero records were converted in the same manner, except that external timing pulses were used for calibration records during which the rotor was not turning. For records where the rotor was turning, the digital conversion intervals were governed by the once-per-revolution and the 72-per-revolution (every 5 degrees) pulses provided from the model. The normalized computer unit values on the Sikorsky digital tape were the equivalent of decimal integer values with a range from 0 to 512, because of the particular word length utilized.

Quality Checking and Editing of Blade Response Data

The blade response data were placed on temporary disc storage for editing and quality checking.

The basic quality check option calculated and printed out the maximum data value, minimum data value, average data value, and root-mean-square deviation from average of the data in a specified time history record from a certain transducer. These quantities were output in normalized computer units and in engineering units. Data discontinuties were found and counted by comparing actual and interpolated values, as discussed later. The number of data values in each record which reached the maximum and minimum value were also counted to give an indication as to how much data in a questionable record might be off scale. The quality check was carried out for specified groups of records and channels. The quality checking program also contained options for printout of sample time histories and frequency analyses, to investigate and diagnose any questionable data. The computerized quality checking was supplemented with inspection of the oscillograph records made when digital conversion took place.

The mathematical operations for the quality check options are discussed in the following paragraphs.

Conversion From Computer Units to Engineering Units

An average or individual data value in normalized computer units W_D is converted to engineering units by using the following transformation:

$$W_E = \frac{R_c W_D}{(W_R - W_Z)} - \frac{R_c W_o}{(W_R - W_Z)} - F_c$$

where

W_E is the desired value in engineering units.

R_c is the physical equivalent of the electrical difference between the "ZCAL" and "RCAL" records on the tape.

W_R is the average computer unit value in the "RCAL" records on the digital tape for the wind tunnel run.

W_Z is the average computer unit value in the "ZCAL" records on the digital tape for the wind tunnel run. W_0 is the average computer unit value in the zero reference records on the digital tape for the wind tunnel run. F_c is an arbitrary offset constant which is used when the physical reference condition is not at a zero data value, or when there is a need for a zero drift correction or the like.

The values R_c, W_R, W_Z, W_0 and F_c remain constant for a data time history segment. Different values are obtained for each transducer, of course. If postrun calibrations and zeros are invalidated by transducer failure, the prerun calibrations and zeros only are used.

Detection of Discontinuities

In order to check data for spiking caused by incipient instrumentation failure, data values X_J in the time history records are compared with values $\bar{X}_J$ interpolated from neighboring values:

$$\bar{X}_J = \frac{2}{3}(X_{J+1} + X_{J-1}) - \frac{1}{6}(X_{J+2} + X_{J-2})$$

A discontinuity is counted whenever

$$\left| X_J - \bar{X}_J \right| > \frac{R_c}{N_{FD}}$$

The value N_{FD} was set by trial and error by raising the value of N_{FD} when discontinuities were counted in an acceptable record. A value of 8 was found suitable for the blade bending and torsion data. A value of 16 was suitable for the hinge motions.

Frequency Analysis

The frequencies at which amplitude components are to be found are defined by a starting frequency, (F_S), an increment (ΔF_{RQ}), and the number of increments, $(N_{FI} + 1)$. Note that frequencies are expressed in cycles per revolution.

$$(F_{RQ})_j = F_s + (\Delta F_{RQ})(j-1) \qquad j = 1,2,3 \ldots (N_{FI} + 1)$$

The time history segment for frequency analysis begins with the start of the rotor revolution denoted by N_{FS}, counting from the beginning of the recorded sample.

The time history segment for frequency analysis ends with the end of the rotor revolution denoted by N_{FE}, counting from the beginning of the recorded sample.

The index k takes the values 1, 2, 3 ... K, and counts digital data values in the time history segment for frequency analysis, starting at azimuth zero of the N_{FS} revolution.

The integer K is the maximum value of k and is defined by

$$K = (1 + N_{FE} - N_{FS})N_{PRV} + 1$$

where N_{PRV} is the number of samples per rotor revolution (72). K refers to the first data value in the (N_{FE+1}) th revolution.

$(W_T)_k$ is the kth digital data value in the segment starting with the N_{FS}th revolution of the sample.

The amplitude components A_j, B_j and R_j desired are then given by the following expressions:

$$A_j = \frac{2}{N_{PRV}(1 + N_{FE} - N_{FS})}\left(\frac{R_c}{W_R - W_Z}\right)\left\{\left[\sum_{k=2,3,4}^{K-1}(W_T)_k \cos\left[(F_{RQ})_j\frac{2\pi(K-1)}{N_{PRV}}\right]\right] + \frac{(W_T)_1 + (W_T)_k \cos\left[(F_{RQ})_j \frac{2\pi(K-1)}{N_{PRV}}\right]}{2}\right\}$$

$$B_j = \frac{2}{N_{PRV}(1 + N_{FE} - N_{FS})}\left(\frac{R_c}{W_R - W_Z}\right)\left\{\left[\sum_{k=2,3,4}^{K-1}(W_T)_k \sin\left[(F_{RQ})_j\frac{2\pi(K-1)}{N_{PRV}}\right]\right] + \frac{(W_T)_k \sin\left[(F_{RQ})_j \frac{2\pi(K-1)}{N_{PRV}}\right]}{2}\right\}$$

$$R_j = (A_j^2 + B_j^2)^{\frac{1}{2}}$$

The above equations are numerically evaluated equivalents of

$$a(\omega_j) = \frac{1}{T}\int_{0=\psi}^{2T} W_E(\psi)\cos(\omega_j\psi)d\psi$$

$$b(\omega_j) = \frac{1}{T} \int_{0=\psi}^{2\pi} W_E(\psi) \sin(\omega_j \psi) \, d\psi$$

$$r(\omega_j) = \left[a^2(\omega_j) + b^2(\omega_j) \right]^{1/2}$$

Where ω_j is a frequency ratio with respect to rotational frequency Ω
W_E is time history data in engineering units, and ψ is the azimuth.

The accuracy of the numerical frequency analysis depends on the number of samples per revolution and on the length of the time history record if the frequencies to be analyzed are nonharmonic. For the 72-per-revolution sampling rate, nonharmonic frequencies beyond 15 cycles per revolution are not recommended. For the 40-revolution time history record length, frequencies below .15 per revolution are not recommended.

Generation of Final Data Tapes

When quality checking of the response data was complete, data samples for each condition number were specified and converted to engineering units as indicated on page 26. Forty revolutions of time history data for each operating condition were placed on the final tape.

The prerun and postrun calibration data were normally averaged in the conversion to engineering units. If a strain gage transducer failed during a wind tunnel run, only the prerun calibration data were used.

The electrically generated "ZCAL" and "RCAL" records were used to calibrate the strain gage transducer rate of change of engineering units with respect to computer units, as it appears in the equation on page 26. The physical zero reference for the strain gage bridge measurements of blade bending and twisting was the average transducer output during the zero lift hover condition. This physical zero condition avoided the substantial drift in bending and torsion bridge output which occurs as the rotor is brought up to operating rotational speed. In some cases the chordwise bending bridges displayed a moderate amount of zero drift during a wind tunnel run. This was compensated by adding appropriate F_c values for the operating conditions in the run.

Physically generated transducer signals were provided for the calibration of blade hinge motions, by manually placing the blade against the motion stops at the beginning and end of each run.

Data Retrieval and Display Program

The data retrieval and display program retrieves data from the final tapes according to operating condition, physical measurement channel, and rotor revolution.

Present processing options are direct time history sampling, frequency analysis, maximum and minimum values summary, average revolution, and harmonics.

The data retrieval and display program documentation and copies of the final data tapes are available from the Eustis Directorate of the U. S. Army Air Mobility Research and Development Laboratory.

The final data tapes are FORTRAN-readable to facilitate the provision of additional data processing modes that may be required in the future.

The users' instructions for the data retrieval program are presented under Appendix II. It is expected that these instructions will be used with the descriptions appearing in the next report section, "TEST DATA OBTAINED".

The data processing options are straightforward and require little additional explanation, since the data on tape is already in engineering units.

The frequency analysis option is identical to the similar quality check calculation described earlier on page 28, except that the terms $R_c/(W_R - W_Z)$ are not required to convert to engineering units.

TEST DATA OBTAINED

The reduced data tape for each blade configuration contains 19 rotor performance parameters and 40 revolutions of digital time history data for 14 blade response transducers for each rotor operating condition. Data is expressed in coefficient form or in engineering units.

The reduced data tapes for the dynamically scaled fiberglass blades contain 85 conditions each. The tape for the three-times-scale stiffness aluminum blade contains 93 conditions. The condition numbers refer to similar conditions on all four H-34 rotors, to facilitate comparative studies.

The various test conditions for each rotor configuration are listed in Table XVI with descriptive terms that indicate the purpose of each condition or series of conditions. Note that a particular phenomenon being explored, such as blade stall, does not necessarily occur at each condition of a series of conditions so designated. The conditions are generally numbered in the order in which they were taken during the wind tunnel runs.

The digital time history samples are provided in conventional computer language as discrete values which begin at the zero azimuth (blade over the tail) and proceed at 5-degree intervals for 40 rotor revolutions.

The number of unavoidable strain gage transducer failures was minimized by running the more lightly loaded conditions first. The conditions and transducer channels for which the strain gages were operative are given in Tables XVII through XX.

The time histories of blade response on the reduced data tapes are 40 revolution samples of the actual time histories. Noticeable amounts of nonharmonic motion are present in some of the test data. Flapwise and torsion response exhibited an apparently random nonharmonic response when rotor stall conditions were approached and exceeded. For example, the .65R flapwise bending and .20R torsion responses of the zero-degree twist dynamically scaled fiberglass spar blade contained variations of this type which were ±10 percent of the average half peak-to-peak amplitude, when operating at condition 7. In addition to the apparently random response, the chordwise strain gages and lead-lag motions contain excitations from the rotor drive system. Frequency analysis results for the .20R chordwise bending moment response in zero lift hover are given in Table XXI. These nonharmonic components (except for the small 7-per-revolution component) are effectively removed by the revolution-averaging procedure. If required, the unaveraged time history can be corrected for the drive system excitation by analyzing for the particular frequency components appearing in Table XXI, and then subtracting those results from the time history as recorded.

The reduced data tapes and a computer program to retrieve the data are available from the Eustis Directorate of the U. S. Army Air Mobility Research and Development Laboratory.

Rotor Performance Data

A complete listing of all performance data is provided for each of the four configurations in Tables XXII through XXV. Sample performance data are plotted in Figures 21 through 32. Comparisons are made between the performance of the four H-34 model rotors. Comparisons are also made between the performance of the H-34 model rotors and the corresponding full-scale results reported in References 2 and 3. Correlation with calculated results shown in these plots will be discussed in a subsequent part of this report.

Torque versus drag crossplots provided in Figure 21 show the comparative performance levels of the four model rotor configurations. The variations of torque versus drag for the various configurations fulfill qualitative expectations. The flapped airfoil blade is substantially better in its performance characteristics than the other two dynamically scaled blades. The three-times-scale stiffness aluminum blade performance becomes substantially worse than that of the dynamically scaled blades as the rotor reaches a stalled condition.

Sample comparisons of drag versus lift and torque versus lift for one shaft angle and advance ratio are provided in Figures 22 and 23. The model rotor data variations are qualitatively similar to the full-scale data, which was obtained from Reference 3. The quantitative variations between the model and the full-scale performance data can be attributed to Reynolds number effects.

Figures 24 through 27 display model rotor performance at various advance ratios and shaft angles included in the test program. The variations shown in these plots are, in general, qualitatively similar to the data from Reference 3. The intersection or close approach of the curves in Figures 24(a) for $\alpha_s = 2^o$ and $\alpha_s = 0^o$ at low lift was typical for the fiberglass spar dynamically scaled models with this small increment in shaft angle. The three-times-scale stiffness aluminum spar model did not exhibit this tendency. Figures 24 through 27 can be used to provide initial trim values of shaft angle and control position for blade response calculation correlation studies, when a desired rotor lift and drag is given. (Note that lift and cyclic pitch versus collective pitch for an advance ratio of $\mu = .5$ are presented in Figures 28 and 29 for comparison with full-scale data).

Figures 28, 29 and 30 compare model rotor performance parameter variation versus collective pitch with corresponding full-scale data from Reference 3 , and with calculated data. Plots of this type are of special interest for the comparison of model data with full-scale data and with calculated data.

The comparison between model and full-scale lift versus collective data shows that the model develops more lift beyond stall than would be expected from a comparison of full-scale and model airfoil two-dimensional steady-flow airfoil data. The model airfoil two-dimensional steady-flow maximum coefficient of lift shown in Figure 14 is about 60 percent of full-scale values. The model rotor lift shown for a collective pitch of 10 degrees in Figure 28 is, however, about 85 percent of the full-scale value. Plots of the drag, torque and cyclic pitch data against collective pitch display good qualitative and reasonable quantitative agreement.

The comparisons between model and full-scale results in Figures 22, 23, and 28 through 30 show that model and full-scale results are very similar qualitatively, and that the quantitative effects of Reynolds number and Mach numbers are milder than would be expected from a comparison of full-scale and model steady-flow two-dimensional airfoil data.

Figures 31 and 32 are included here to provide comparative test and calculated data for the remaining two model configurations. The comparatively small value of B_{1s} required for the flapped blade is attributed to aeroelastic twisting on the advancing part of the azimuth.

The significance of the calculated data shown on Figures 21 and 28 through 32 will be discussed under a subsequent part of this report.

Blade Response Sample Data

Figure 33 presents an example of the variation of the algebraic maximum and minimum bending and twisting response, as a function of rotor lift for the four blade configurations.

Bending response of the fiberglass spar dynamically scaled rotors is relatively similar. The untwisted aluminum spar three-times-scale stiffness blade has a much higher bending moment response. This is an indication that the bending displacement of this blade is much more than one-third as large as the dynamically scaled blade deflections.

Even at the moderate scale forward speed of 124 knots, the flapped blade has a much larger torsional moment than the other blades, except for stalled conditions. Thus the performance benefits of this blade would have to be considered as a trade-off against continuous high pushrod loadings.

Figure 34 presents sample time histories reproduced from Reference 1, along with model data from the present investigation, which was converted to equivalent full-scale stress by using the factors given on page 7 of this report.

The agreement between model and the full-scale bending response is quite good, considering the difference between operating conditions. The most notable difference in bending response is the high peaks in flapwise bending at .80R.

The model torsional response at the lower lift shown in Figure 34(c) has some similarities to the full-scale data. A stall-induced oscillation occurs on the model retreating blade at the higher lift condition shown. The retreating blade oscillation does not appear on the full-scale blade, presumably because of less stalling.

Sample average revolution time history data are presented in Figures 35 through 46. Blade bending and torsion response are presented for conditions at advance ratios of μ=.35, .40, and .50. Other blade response samples are presented and compared with calculated results under the report section dealing with the normal modes aeroelastic analysis. The conditions chosen for these samples include some of those for which the blades were expected to be close to or intersecting the rotor wake.

Flapwise bending moments response is presented in Figures 35 through 38. The flapwise bending response for the -8° twist blade is not consistently higher than the response for the dynamically scaled untwisted blade because of the moderately high lift coefficient. This trend is noticeable in the full-scale results presented in Figures 67 through 69 of Reference 2. The flapwise bending results for the untwisted 5-degree trailing-edge flap blade are very similar to those for the -8° twist blade, possibly because of a steady aeroelastic twist. The three-times-scale stiffness aluminum spar blade flapwise moments are much higher than those on the

dynamically scaled fiberglass spar blades, but with a similar wave form.

Chordwise bending moment response is sampled in Figures 39 through 42. Chordwise bending moment comparisons show the reduced response expected for the -8° twist blade, as compared to that for the 0° twist blade. The trends are again similar to the corresponding full-scale results presented in Figures 70 through 72 of Reference 2. The chordwise bending results for the trailing-edge flap blade are similar to the results for the -8° twist blade. The three-times-scale stiffness aluminum spar blade chordwise moments are much higher than the dynamically scaled fiberglass spar blade moments, and with a much different wave form.

Torsional moment response is sampled in Figures 43 through 46. The torsional response sample for the untwisted blade at $\mu = .35$ in Figures 43(a) shows an aggravated response in the azimuth region around $\psi = 340^{\circ}$, which may be due to the wake vortex passage frequency, which is approximately equal to the torsional natural frequency at this advance ratio. The torsional response in the azimuth region around $\psi = 340^{\circ}$ is much smaller at advance ratios of $\mu = .40$ and $\mu = .30$, as shown in Figures 43(b) and 81(a) respectively. At these advance ratios, the vortex passage frequency is respectively lower and higher than the blade torsional frequency

The torsional response of the three-times-scale stiffness aluminum spar blade shows a higher frequency which is approximately equal to the torsional natural frequency, and which is characteristic of a stall flutter response. A lower frequency is also present, and this may be due to wake vortex forcing or bending-torsion coupling.

NORMAL MODE AEROELASTIC ANALYSIS CALCULATIONS

GENERAL DESCRIPTION OF NORMAL MODES AEROELASTIC ANALYSIS

The normal mode aeroelastic analysis utilized in the work described herein is based on a step-by-step timewise integration of the elastic rotor blade equations of motion, which are documented in Reference 11. These equations of motion are expressed in terms of uncoupled flapwise bending, chordwise bending, and torsion natural vibration modes. The modes are calculated according to the methods presented in References 12 and 13. Articulated blade rigid body flap and lag hinge motions are also included as separate degrees of freedom.

When a steady-state rotor operating condition is being analyzed, the integration of the equations of motion proceeds in small but finite timewise steps from arbitrary starting values. After a number of rotor revolutions, the calculated blade motions typically become cyclic within a desired tolerance. At this point, time variations of blade bending and twisting loads or stresses are calculated from the blade response shapes. Rotor performance parameters are calculated by integrating blade local aerodynamic loadings over the rotor disc, in a manner similar to that used in Reference 14.

The rotor blade is represented analytically by up to 15 spanwise segments. The mass and elastic properties of each segment are defined by the local properties of the actual rotor blade.

Aerodynamic loading calculations for the blades consider the important effects of unsteady flow in the manner reported in Reference 15. The local aerodynamic lift and pitching moment coefficients at each segment and time step are determined by a table look-up procedure, with local angle of attack, nondimensional time rate of change of angle of attack, and nondimensional pitch acceleration as parameters. The table of unsteady aerodynamic coefficients was derived from oscillating airfoil test data presented in References 15 and 16. A table of static (steady flow) airfoil data is automatically used for angle of attack and speed regimes for which unsteady aerodynamic data are unavailable.

The calculated blade response cases presented herein utilized steady flow data for local blade drag coefficients.

As an option, inflow velocities which vary over the rotor disc may be utilized in the normal modes analysis. The variable velocity input replaces a basic uniform inflow velocity option which utilizes the classical momentum theory. A method for calculating inflow velocity due to a vortex wake with a prescribed helical geometry is presented in Reference 17. The method used herein is similar, but computational efficiency is improved by representing shed wake effects with modifications in the shapes of local lift curve shapes. A computer program to calculate inflow velocity distribution in this fashion is being provided to the Government under the provisions of Contract NAS 2-6463. The work of this contract is being per-

formed by Sikorsky Aircraft and the United Aircraft Research Laboratories for the National Aeronautics & Space Administration Ames Research Center.

The normal modes analysis has been extended to consider the motions of a rotor system with up to seven blades, attached to a rigid fuselage with six degrees of freedom. This modification is described in References 13, 18, and 19, and was provided to the Government under the provisions of Contract DAAJ02-71-C-0024.

COMPARISONS OF NORMAL MODES AEROELASTIC ANALYSIS CALCULATIONS WITH H-34 MODEL TEST RESULTS

Application of Analysis

For the purpose of comparison between model test and normal modes aeroelastic analysis calculations, the following parameters were considered as independent variables defining an analytical operating condition:

1. Forward velocity (V or V_s)
2. Rotational speed (ΩR or $\Omega_s R$)
3. Shaft Angle (α_s)
4. Lift coefficient - solidity ratio (C_L/σ)
5. First-harmonic flapping components at hinge (a_{1s} and b_{1s})

At each analytical condition, rotor control inputs (A_{1s}, B_{1s} and θ_c) or aerodynamic scaling factors were manipulated to produce a reasonable match between the analytical values of the above parameters and those existing at some test condition.

Choice of the above set of parameters caused the test and analytical blade motions to be geometrically similar with respect to the remote velocity. This similarity is expected to simplify the diagnosis of any shortcomings in the analysis.

The specific conditions chosen for correlation are given in Table XXVI. The condition numbers correspond to the experimental condition numbers listed in Tables XXII through XXV. The various unsteady airfoil data scaling and inflow calculations are discussed under the subheadings below.

Unsteady Airfoil Data and Associated Scaling Procedure

Aerodynamic loadings for the blades are calculated in the normal modes aeroelastic analysis by using a table look-up procedure at each local segment and time step of the numerical integration. The effects of unsteady flow are considered by the method presented in Reference 15. This method uses generalized data from a sinusoidally oscillating airfoil test. The normal force and pitching coefficients are made functions of angle of attack, α, nondimensional time rate of change of angle of attack, A, and nondimensional pitch acceleration, B. The parameters A and B, as they are used in the equation of motion, are defined by the following equations:

$$A = \frac{c\dot{\alpha}}{2U}$$

$$B = \left(\frac{c}{2U}\right)^2 \ddot{\theta}_e = \left(\frac{c}{2U}\right)^2 \ddot{\alpha}$$

The unsteady aerodynamic tables used herein were versions of the data used in Reference 15, with appropriate scaling factors applied to relate the data to various Mach numbers and model scale. Figures 47(a) and 47(b) are plotted from the unscaled tables and show the effects of typical values of the parameters A and B for an NACA 0012 airfoil chord of 2 feet and a Mach number of .20.

The version of the normal modes aeroelastic analysis used herein utilized steady-state aerodynamic coefficients for drag and for local blade conditions outside the angle-of-attack range of the unsteady aerodynamic coefficient tables.

As discussed in References 15 and 20, provision has been made in the normal modes analysis to scale the single set of unsteady aerodynamic normal force and pitching moment coefficients to various other Mach numbers.

The local value of the unsteady normal force coefficient $C_n(M, \alpha, A, B)$ on a blade segment at Mach number M is found from the tabulated data $C_{nt}(\alpha_T, A, B)$ by using the following transformation:

$$C_n(M,\alpha,A,B) = \frac{C_{nss}(M)}{C_{nsst}} C_{nt}\left(\alpha_T = \frac{\alpha_{snt}}{\alpha_{sn}(M)}\alpha, A, B\right)$$

The local value of the unsteady moment coefficient $C_m(M,\alpha, A, B)$ on a blade segment at Mach number M is found from the tabulated data $C_{mt}(\alpha_T, A, B)$ by using the following transformation:

$$C_m(M,\alpha,A,B) = C_{mt}\left(\alpha_T = \frac{\alpha_{smt}}{\alpha_{sm}(M)}\alpha, A, B\right)$$

where $\alpha_{sn}(M)$ and $\alpha_{sm}(M)$ are the respective angles of attack for normal force and pitching moment stall at Mach number M, and where α_{snt} and α_{smt} are the similar quantities for the tabulated data at A=B=0.

The original intent of these scaling procedures was the transformation of the one set of A=B=0 data for M=.2 and c=2ft., to match other steady-state two-dimensional data as closely as possible. It is assumed that this scaling procedure also applies satisfactorily to the tabulated unsteady data for which A≠0 and B≠0. In Reference 15 the scaling procedure was developed and used to account for the effects of varying Mach number.

In the present model case, the scaling procedures attempted to account for a large change in Reynolds number as well as Mach number. The use of the scaling transformations in this way for the model is considered to be an approximation, and reflects the lack of an unsteady aerodynamic coefficient tabulation at model scale for the normal modes aeroelastic analysis Y-200 program.

The transformations expressed in the above equations were used to scale the

existing unsteady data table for use with the model. The scaling parameter inputs for the normal modes analysis Y-200 program are given in Table XXVII. The special low Mach number values in Table XXVII allow the desired transformation to be carried out with the existing computer program. The Y-200 computer program identifies values given for M=0 in the input tables of $\alpha_{sn}(M)$ and $\alpha_{sm}(M)$ versus Mach number as the quantities α_{snt} and α_{smt}. Hence, machine interpolation in those tables will result in the desired values of $\alpha_{sn}(M)/\alpha_{snt}$ and $\alpha_{sm}(M)/\alpha_{smt}$ for all significant local velocities. The ratio $C_{nss}(M)/C_{nsst}$ is input directly as a function of Mach number, so no special treatment is required.

Because the unsteady aerodynamic data transformation to model scale is approximate, scaling parameters were considered as variables in the normal modes analysis calculations, and were changed as necessary to provide more useful comparisons between analytical results and the test data.

Comparison of initial normal modes aercelastic analysis calculations for the H-34 model blades with test results from the Reference 5 and 21 model tests indicated that a straightforward application of the scaling method resulted in rotor performance predictions that were far too pessimistic. Rotor performance parameters from the present test later confirmed this observation. This behavior was aggravated by calculated angle-of-attack ranges that exceeded the tabulated unsteady data angle-of-attack ranges.

In order to obtain more useful results with the existing Y-200 computer program and unsteady data tables, three different unsteady aerodynamic data scaling cases were utilized. The parameter of these scaling cases are given in Table XXVII. The use of each scaling case is shown in Table XXVI. The results of applying each scaling case to the tabulated data are shown in Figures 48 through 49. The aerodynamic coefficients for a 2-foot chord and a Mach number of .2, and for zero values of the parameters A and B are plotted on these figures from the data tables for the Y-200 program. Also shown in Figures 48 through 49 are the results of applying the three different scaling cases to the tabulated data for A=B=0, and the corresponding two-dimensional steady-state test data.

Scaling cases 1 and 2 were set up and utilized to avoid excessively pessimistic performance calculations, and to stay within the angle-of-attack range of the existing unsteady data tables. The transformed A=B=0 coefficient of lift curves for these cases compare reasonably well with previous steady-state data synthesized from model hover tests, and presented in Figure 11 of Reference 21. Scaling case 3 was developed to match the transformed A=B=0 data to the static two-dimensional data reasonably well with the existing procedures. This case was used to examine the effects of non-uniform inflow on the pessimistic performance predictions mentioned earlier.

Mach Number and Angle-of-Attack Boundaries for Unsteady Aerodynamic Utilization

Provision has been made in the Y-200 normal modes aeroelastic analysis computer program for user control of the Mach number and unscaled angle-of-attack (α) region over which unsteady aerodynamic coefficients are utilized.

This control is, of course, limited by the angle-of-attack range for which the unsteady aerodynamic data are tabulated. Outside the user defined Mach number and angle-of-attack region, the computer program automatically reverts to steady flow aerodynamic data tables. A transition region is also user defined, within which the computer program interpolates between the unsteady and steady flow aerodynamic coefficients.

The above described unsteady aerodynamic utilization boundaries for the normal modes aeroelastic analysis calculations described herein are given in Table XXVIII. If a blade segment angle of attack at a given local Mach number is less than the values on the boundary defined by CNREG1 versus Mach number, the local blade normal force coefficient is taken from the table of unsteady aerodynamic coefficients by the computer program. If the angle of attack is above CNREG2, the normal force coefficient is taken from the table of steady aerodynamics. If the angle of attack lies between the two boundaries, an interpolation between steady and unsteady data on the respective boundaries is used. In order to perform this interpolation, coefficient values are found at the Mach number on both the CNREG1(unsteady) and the CNREG2(steady) boundaries. The coefficient to be used is then found by interpolation with respect to angle of attack. The scaling techniques discussed under the previous subheading are, of course, utilized when finding the unsteady value on CNREG1. The coefficient of moment data is handled in an analogous manner, using the CMREG1 and CMREG2 boundaries also given in Table XXVIII. Plots of boundaries of the type discussed here are given in Figure 31 of Reference 15.

The unsteady data utilization boundaries for the flapped (δ_F=5°) blade were specially set to calculate the response of that blade with the existing computer program and set of symmetrical unsteady airfoil data. The calculations for the flapped airfoil used the unsymmetrical steady-state data whenever the local blade Mach number was greater than M=.28. This utilization boundary for the flapped blade is given in Table XXVIII. Use of this boundary allowed the effects of the unstalled coefficient of moment and lift due to camber to be considered in the calculation with the existing computer program and symmetrical unsteady data tables. On the retreating blade azimuth, unsteady aerodynamics with its effects on stall were considered. Figure 50 shows a sample of steady and unsteady data utilization regions for the flapped blade. This use of steady and unsteady data was expected to produce a reasonably good approximation of the proper airloads, since the area of steady-state stall for the blade extended from about ψ = 190° to ψ = 20°. Above steady-state stall angles of attack, comparisons of Figures 14(a) and 15(a) show the flapped and unflapped data to be similar, at least within the accuracy of the data scaling techniques discussed under the previous subheading.

Rotor Inflow Velocity Calculations

The basic inflow velocity option for the normal modes aeroelastic analysis Y-200 computer program is a uniform distribution whose nondimensionalized value (λ) is one of the input parameters. Upon completion of a calculation of blade response and rotor performance, the value of shaft angle (α_s) is obtained by the computer program from the following momentun relation:

$$\alpha_s = \text{ARCTAN}\left[\frac{\lambda}{\mu} - \frac{C_T}{2\mu\sqrt{\mu^2+\lambda^2}}\right]$$

In the present case, the value of α_s was considered to be an independent variable. The input values of λ consistant with the desired values of C_L, α_s, and μ were obtained from the following:

$$\lambda = \mu \sin \alpha_s - \frac{C_L}{2\mu}$$

As an option, the normal modes aeroelastic analysis Y-200 computer program can consider input values of rotor inflow velocity which vary over the rotor disc. The variable inflow velocities used herein were considered to be due to blade vortex wakes whose geometry was unaffected by their own induced velocity. This type of wake, which can be described as a prescribed or undistorted wake is formed by vortex elements which travel downstream from the rotor with constant relative velocity.

The transport velocity of the prescribed wake elements is assumed to be made up of a component V in the free-stream relative velocity direction and a momentum component

$$v = \frac{\Omega R C_L}{2\mu}$$

downwards normal to it.

The inflow velocities in the rotor disc are calculated by a method similar to that used in Reference 17. In the method used herein, computational efficiency is improved by considering only the trailing vortex effects in the computation of inflow velocity. Shed vortex effects are assumed to be sufficiently well represented by the use of unsteady aerodynamic data in the blade response calculations.

Figure 51 is a simplified diagram of one of the blades of a four-bladed rotor and the undistorted tip vortex segments in proximity to it as it passes through one revolution. The view is downward normal to the rotor disc. The rotor hub is passing the observer from left to right with constant velocity V. The straight line segments represent the blade at various azimuth positions. The curved lines represent tip vortices laid down by the blade tips. The vortex elements are moving normal to the plane of the paper. The induced velocity due to the vortex segments is upward on the convex side of each segment and downward on the concave side.

Samples of the azimuthal variation in inflow velocity due to the wake shown in Figures 51 are given in Figure 52 for various constant radii. The various positive and negative peaks in the calculated distribution do correlate, at least approximately with the radial and azimuthal positions of some of the blade-vortex intersections on Figure 51. The effects of variations in vortex strength with cyclic blade loading, and the effects of the vertical position of the vortex segments are also considered in the calculation of the induced velocity distribution. Vortex segments for all

four blades from four revolutions are represented in the induced velocity calculation as used herein.

Presentation and Discussion of Comparative Test and Calculated Data

Model rotor test data and corresponding data calculated with the normal modes aeroelastic analysis Y-200 computer programs are compared herein, with the objectives of finding out how well the analysis works, and of providing information and motivation for diagnosis of shortcomings. The extent of the comparisons and diagnostic data presented herein is necessarily limited, but is sufficient to support an assessment of the present status of the Y-200 computer program and some recommendations for its improvement.

The comparisons between calculated and test results for rotor performance and blade response should be extended in future work to include test data for a larger sample of the operating conditions obtained under this program. Future work should also relate the effects of a wider range of analytical assumptions and options to the correlation between calculated and test data.

Comparisons herein between theory and test are first carried out on the basis of the more important rotor performance parameters and selected one-half peak-to-peak blade bending moments for a relatively quick overview of the quality of correlation between analysis and test. These comparisons appear in Figures 53 through 58, and are summarized further in Tables XXIX through XXXIII.

The simplified comparisons of Figures 53 through 58 are necessary for a comprehensive judgment of the practical value of the analysis, but are not sufficient to fully evaluate a highly detailed mathematical model such as the normal modes aeroelastic analysis.

In contrast to more empirical methods, the normal modes aeroelastic analysis predicts the desired rotor design information by using a highly detailed mathematical simulation of the rotor blade and its environment to calculate a response time history. If the simulation is successful, the calculated and experimental time history will be more or less similar, and it can then be concluded that the analysis is producing a reliable prediction through its detailed consideration of many interacting factors.

In view of the above considerations, sample comparisons of calculated and average revolution test data are provided for each analytical condition in Figures 59 through 89. In addition to their use as a tool for evaluation of the analysis, the time history comparisons are required as a guide for detailed diagnosis of shortcomings.

Overview of Test and Calculated Data Correlation

In order to provide a useful comparison between test and calculation, the normal modes aeroelastic analysis was trimmed to essentially the same lift, shaft angle, first-harmonic flapping components, velocity, and rotational speed as the corresponding test condition. Choice of these parameters as independent variables prevented the test and analysis correlation from

being affected by different dynamic loadings due to different amounts of blade coning and flapping, and provided a similar geometrical relationship between the rotor and its wake for the variable inflow calculation.

The correlation between calculation and test at constant lift on the drag versus torque plots for each rotor are shown in Figures 21(a) through 21(c). The calculated and test data for rotor performance parameters and cyclic pitch required for trim versus collective pitch is presented in Figures 29 through 31. It should be noted that the uniform inflow calculated data presented in Figure 28(a) does not imply a continued predicted linear trend for rotor lift coefficient versus collective pitch. Additional uniform inflow cases would show a decreased slope for higher collective pitch, as indicated by the variable inflow calculated result shown.

Figures 53 through 58 and Tables XXIX through XXXIII have been prepared to provide an overview of blade bending moment correlation and a more intensive examination of performance correlation between calculation and test. Separate comparisons between theory and test values of rotor drag coefficient, torque coefficient, and control position are made at essentially the same lift, shaft angle, and first-harmonic flapping.

The comparisons between these quantities may be of secondary interest when comparing different rotor systems, but are more important for comparisons between theory and test. The solutions obtained from a highly detailed mathematical model like the normal modes aeroelastic analysis are the result of complicated interactions between many factors. In order to have confidence in the mathematical simulation, it must be verified that quantities such as control position and shaft angle are approximately correct. If a need for improvement of the analysis does become evident, comparisons of such quantities are required to diagnose the source of the inaccuracy.

On Figures 53 through 57, the four blade configurations are identified on the horizontal axis of the plots, in terms of the parameters varied, which are blade twist, flap deflection, and elastic stiffness. Figures 53 through 57 show the effects of blade configuration properties on rotor performance, control position, and one-half peak-to-peak blade bending moment amplitude. In addition, the effects of variable inflow are presented on Figures 54 and 55, and the effects of unsteady aerodynamic scaling assumptions are shown on Figure 54. Figure 58 shows the results of a further investigation of the effects of variable inflow for the zero degree twist dynamically scaled fiber glass spar blades. The horizontal scale has been extended on this plot to provide more clarity.

The quantitative data on the correlation between test and analysis has been further summarized in Tables XXIX through XXXIII. It should be noted that this further summarization is meaningful only for the few particular operating cases studied here.

Table XXIX presents the average, range, and (where applicable) the root-mean-square of the difference between calculated and test values of rotor drag and torque coefficients for the conditions analyzed. The significance of the differences between calculated and test values can be evaluated by

comparison to typical operating values such as -.010 for C_D/σ and .006 for C_Q/σ.

Table XXX presents the average and range of the fraction of test vibratory moment predicted by the analysis, for the conditions analyzed.

Tables XXXI and XXXII present a summary comparison of calculated and test increments in rotor drag and torque coefficients which are due to configuration changes.

Table XXXIII presents a summary comparison of calculated and test values of bending moment amplitudes for the various configurations, divided by the corresponding amplitudes for the zero-degree twist, zero-degree flap, dynamically scaled blade.

The information contained in Figures 53 through 58 and 21 supports the following observations:

Uniform Inflow Calculations

The magnitude and sign of deviations in rotor drag and torque between calculation and test for the uncambered blades were inconsistent but compensating. Predictions of the effects of configuration change on rotor performance were reasonably good for moderately loaded conditions, but became inconsistent for heavily stalled conditions. Performance prediction for the cambered blade was poor, as shown in Figure 21.

Calculation of rotor pitching moment for the moderately loaded out-of-flapping-trim condition was reasonably good, except for an over-prediction on the three-times-scale stiffness aluminum spar blade.

Prediction of control positions required for the uncambered blades was quite accurate, except for the heavily stalled operating conditions. The changes in control position required due to blade camber were poorly predicted, even at the lightly loaded conditions.

The correlation of calculated and test bending moment was notably better on the -8° twist blade than on the other blade configurations. On the untwisted blades, the use of uniform inflow resulted in a substantial underprediction of flapwise and chordwise bending moment amplitude.

The blade torsion moment analytical prediction was inconsistent in its agreement with the comparatively low test values existing at the moderately loaded conditions. There was a tendency to overpredict the higher torsion moments existing at the more heavily stalled operating conditions.

The qualitative effects of blade configuration change on blade flapwise and torsion moments were generally predicted by the analysis. The quantitative effects of blade twist were substantially overpredicted.

With the uniform inflow assumption, the effects of configuration change on chordwise bending moment amplitude were poorly predicted.

Variable Inflow Calculations and Aerodynamic Scaling

The variable inflow calculations utilized a prescribed geometry vortex wake, as previously described on pages 40 and 41. The effects of unsteady aerodynamic scaling assumptions are presented in combination with variable inflow. These scaling assumptions have been described on page 36.

Scaling assumption 3 matched the scaled unsteady aerodynamic table to the static aerodynamic data. This resulted in a pessimistic performance prediction and considerable error in control position, as shown on Figure 54. This was true even though variable inflow was included.

Use of scaling assumption 1 in conjunction with variable inflow produced the results shown in Figure 54 for the -8-degree twist blade, Figure 58 for the 0-degree twist blade, and Figure 55 for all four configurations.

The results shown in Figure 58 indicate that the assumption of a vortex core of size .3c is better than .6c, and .3c was used in the remaining calculations.

The use of variable inflow with scaling assumption 1 usually resulted in significant improvements in performance and control position correlation over that obtained with the uniform inflow assumption, except for the cambered blade. The rotor pitching moment coefficient correlation obtained for the untrimmed flapping condition 36 was usually more exact with the uniform inflow calculation than the variable inflow calculation. An exception to this trend was noted for the aluminum spar three-times-scale stiffness blade, as shown on Figure 54.

The use of variable inflow in the calculation improved flapwise bending moment correlation over that obtained with uniform inflow, but increased the tendency to overpredict torsional moments. Chordwise moment correlation was improved by variable inflow, but the magnitude was still generally underpredicted.

Discussion of Correlation Between Test and Calculated Time History Data

Sample comparisons of average revolution time histories and normal modes aeroelastic analysis results are provided in Figures 59 through 89. Examination of these figures supports the discussions to follow which supplement those given in the previous subsection. The independent parameters of the various operating conditions used for the correlation study are given in Table XXVI. A tabulation of all comparative test and calculated performance parameters is given in Tables XXXIV through XXXIX.

The discussions and observations which follow concern the effects on correlation between calculation and test of the inflow and aerodynamic scaling assumptions and the parameters of the four blade configurations.

Flapwise Bending Response

Flapwise bending time histories calculated for the zero twist blades have

some features which are similar to the test data, but which are substanially underpredicted with the uniform inflow calculations. For examples of this see Figures 59, 60, 63, 64, 65, 66 and 67. The underprediction of the relative peaks at azimuth angles of about 60 degrees and 300 degrees on the outboard part of the blade is a particularly important shortcoming.

The use of variable inflow in the calculation generally, but not always, improves flapwise bending correlation for the untwisted blades, but amplitudes are still generally underpredicted. Examples of flapwise bending correlation with variable inflow are given in Figures 60, 64, and 67.

The correlation of flapwise bending calculation and test time history is generally much better for the -8-degree twist blade than it is for the untwisted blades. This can be seen by comparing Figures 59 and 61 for the uniform inflow assumption and Figures 60 and 62 for the variable inflow assumption. As with the untwisted blades, the use of variable inflow instead of uniform inflow sometimes degrades the correlation.

The use of unsteady aerodynamic scaling case 1 instead of scaling case 3 improves flapwise bending correlation by a relatively small amount. (A discussion of these scaling cases is provided on page 36.) The effect of the scaling assumptions on flapwise bending correlation can be seen by comparing Figures 62(a) and 62(b).

The use of an assumed vortex core size of .6 chord in place of a .3 chord core size reduces the overall amplitude of the already underpredicted calculated flapwise bending response, as shown in Figures 67(b) and 67(c). It also reduces the higher frequency parts of the calculated response considerably.

Chordwise Bending Response

The calculated chordwise bending response is substantially underpredicted for the untwisted blades with the uniform inflow assumption. Some of the low frequency part of the inboard blade chordwise bending moment is predicted, but very little of the higher frequency response. Examples of this are given in Figures 68(a) and 68(e).

The use of variable inflow in the calculation improves the chordwise bending amplitude correlation with test data. The time history waveform correlation, however, is sometimes enhanced, and sometimes degraded. Examples of the effect of variable inflow can be seen by comparing Figures 69(a) and 68(g) or 69(b) and 68(i).

The correlation between calculated and test chordwise bending response is generally better for the -8-degree twist blade than for the untwisted blade configurations. The use of variable inflow usually improves correlation, but sometimes degrades it. Examples of the effects of variable inflow on correlation of chordwise bending response for the -8-degree twist blade can be seen by comparing Figures 71(b), and 71(c) with Figures 70(b) and 70(c) respectively.

The use of unsteady aerodynamic scaling case 1 instead of scaling case 3

improves chordwise bending correlation by a relatively small amount. (A discussion of the scaling cases is provided on page 36.) The effect of the scaling assumptions on chordwise bending correlation can be seen by comparing Figures 71(a) and 71(b).

The use of an assumed vortex core size of .6 chord in place of a .3 chord core size had little effect on the calculated chordwise bending response, as shown in Figures 76(b) and 76(c).

Effect of Trailing-Edge Flap on Bending Response

Figures 59 through 76 show that the test bending response for the flapped blade configuration resembles the response for the -8-degree twist configuration more than it resembles the response for the other untwisted blades. This is true for both the flapwise and the chordwise response, and can be attributed to an aeroelastically induced twist. This effect of the trailing edge flap does not appear in the calculated response plotted in the Figures cited above.

Blade Hinge Motions

Correlation between calculated and test hinge motions is considered good for most of the sample operating conditions. Examples from uniform inflow calculations are given in Figures 77 and 79. The amplitude and waveform correlations are distinctly better than those for the bending response. The constant offsets in the lag response are due to deviations between calculated and test values of rotor torque.

The use of the variable inflow assumption improves the hinge motion correlation in some cases, and degrades it in others. Examples of the effect of the variable inflow assumption on the hinge motion correlation are given in Figures 78 and 80.

Torsional Response

The use of the scaled unsteady full-scale aerodynamic data for the model calculations generally results in an overprediction of retreating blade torsional response. Examples of the correlation between calculated and test torsional response are shown in Figures 81, 83, 85 and 87 for the uniform inflow assumption. The use of the variable inflow assumption aggravates the tendency to overpredict the retreating blade torsional response, as shown in Figures 82, 84, 86 and 88.

Unsteady aerodynamic scaling case 3 results in increased blade stalling, and therefore greater overprediction of the stall-induced retreating blade oscillations than with scaling case 1. This is shown by comparing Figures 83(a) and 83(b).

The effects of variable inflow on the torsional response of the unstalled blade are shown in Figures 89(b) and 89(c), for the two vortex core sizes. The variable inflow distribution used resulted in an overprediction of torsional response. A change in vortex core size from .3 chord to .6 chord

had little effect on the torsional response caused by variable inflow.

Under moderate loading conditions, test data shows that the retreating blade torsional oscillation takes place at a frequency which is lower than the torsional natural frequency. This is shown for data from conditions 7 and 36 in Figures 81 and 83. The torsional vibration in condition 7 is at approximately 5 cycles per revolution, which is considerably lower than the torsional natural frequency of approximately 7.4 cycles per revolution for the dynamically scaled blades. The aluminum spar three-times-scale stiffness blade torsional response at conditions 7 and 36 is shown on Figures 87(a) and 87(b). The torsional response for this blade in the last azimuth quadrant exhibits the 5-cycle-per-revolution response, and another response at approximately 10 cycles per revolution. Both of these frequencies are lower than the torsional natural frequency, which is approximately 13 cycles per revolution for this blade.

The torsional oscillations predicted by the analysis are, in contrast, higher than the torsional natural frequency. The calculated frequency of these oscillations for the dynamically scaled blades is about 10 cycles per revolution, and is about 16 cycles per revolution for the aluminum spar three-times-scale stiffness blade. These frequencies also are calculated for the heavier blade loading conditions. At the heavier loading conditions, such as condition 71 or condition 82, the retreating blade test torsional oscillation frequency tends to be close to the torsional natural frequency. These data for condition 71 are presented in Figures 81(c), 83(c), 85(c), and 87(c). The retreating blade torsional response frequency is about 7.7 cycles per revolution for the untwisted dynamically scaled blade, which compares to a natural frequency of 7.4 cycles per revolution. The twisted dynamically scaled blade exhibits a response frequency of about 6.9 cycles per revolution. The aluminum spar three-times-scale stiffness blade has a test response frequency of about 12 cycles per revolution, which compares with the torsional natural frequency of 13 cycles per revolution.

The correlation between calculated and test torsional response for the flapped blade is shown in Figures 85 and 86. The torsion data for the flapped blade has a positive offset, because of the use of the zero lift hover condition as a reference for the strain gage instrumentation. As discussed earlier on page 22, this blade had a negative pitching moment at the zero condition, which is not known accurately, but is estimated to be about 5.0 inch-pounds.

The correlation between calculated and test torsional response for this blade reflects the use of symmetrical unsteady data on the retreating part of the azimuth, as explained on page 39. The flapped airfoil test data shows much less torsional response in this region than the other blades, because of the higher maximum lift coefficient available before stalling occurs. The calculated response in this region is similar to that for the unflapped, untwisted blade, since the same data is being used.

The variations in flapped blade torsional response which occur on the unstalled parts of the azimuth are underpredicted by the analysis.

ASSESSMENT OF NORMAL MODES AEROELASTIC ANALYSIS

Previous sections of this report present and discuss the correlation between test data generated under the present program and calculated data from the normal modes aeroelastic analysis.

These comparisons have shown that satisfactory predictions of rotor performance and blade response are possible when the blades have a conventional twist rate of -8 degrees and a symmetrical airfoil section.

For other applications, however, the comparisons demonstrate a need for the improvement of the calculation method itself, or the associated input data. In this section, evident reasons for lack of satisfactory correlation are presented, with the supporting diagnostic data. Suggested improvements which are expected to benefit the accuracy of the normal modes analysis are also presented.

Evaluation of Unsteady Aerodynamic Data and Associated Scaling Procedures

The current set of tabulated unsteady aerodynamic data for the Y-200 version of the normal modes aeroelastic analysis was obtained from oscillating NACA 0012 airfoil tests for a chord of 2 feet and a Mach number of .2.

These unsteady airfoil data are applied to other flow conditions by multiplying the tabulated coefficients and angles of attack by scaling factors, in the manner explained earlier on page 36.

The scaling procedure appears to work reasonably well for full-scale, symmetrical blade sections. The work of Reference 22 supports this contention. Figure 15 of Reference 22 shows excellent correlation of calculated and test variations of C_L/σ with tip path plane angle of attack. Except for a constant offset, the test values of C_L/σ beyond stall were obtained at the test values of collective pitch and tip path plane angle of attack.

The present investigation used dynamically scaled models of the rotors used for the Reference 22 correlation. Figures 48(a) through 48(e) show the full scale (M=.2, c=2 feet) and model two-dimensional static coefficient of lift versus angle of attack. The stall coefficient of lift and angle of attack is much lower for the model airfoil. Scaling case 3 matched the unsteady aerodynamic tables to the static data quite well.

Scaling case 3 was used for variable inflow calculations summarized in Figure 54. The excessively high collective pitch and torque coefficients calculated to reach the test values of lift and flapping indicated that the analysis was overpredicting the amount of blade stall. A much more favorable correlation was obtained for the twisted blade by using scaling case 1, which is shown in Figure 48. The improved correlation can be noted on Figure 54.

These results imply that the current scaling procedures cannot be applied without restriction. The errors involved in scaling to other full-scale

rotor blade sections from the .2 Mach number, 2-ft chord condition will probably be much smaller than the substantial discrepancy noted for the model. Nevertheless, additional unsteady airfoil data should be obtained for other Mach numbers, Reynolds numbers, and airfoil sections, so that the effects can be properly evaluated.

In the past few years, new rotor blade designs have been provided with cambered airfoils. Current scaling procedures available with the Y-200 version of the normal modes aeroelastic analysis cannot adequately represent the combined effects of a cambered airfoil and unsteady aerodynamics, since the tabulated unsteady aerodynamic data is for a symmetrical airfoil.

In the present investigation an attempt was made to simulate the effects of the 5-degree trailing-edge flap airfoil and unsteady aerodynamics by using the flapped airfoil steady-state aerodynamics data on the advancing blade azimuth and unsteady aerodynamic data on the retreating blade azimuth. This technique used the existing Y-200 program input provisions, as described on page 38. Useful performance predictions could not be obtained with this technique, as shown in Figures 53 through 57 and 21.

Comparison of the rotor performance versus collective pitch data for the -8-degree twist blade in Figures 29(a) through 29(d) with the similar data for the flapped blade in Figures 31(a) through 31(d) indicates that the substantial calculated performance discrepancy for the flapped blade is related to the underprediction of rotor lift at a given collective pitch. This is the result of using the symmetrical unsteady data on the retreating blade azimuth. This data does not reflect the higher lift coefficients available with the flapped airfoil. The requirement for lateral trim then, in turn, also prevents the development of the correct calculated lift on the advancing blade azimuth.

Examination of the various unsteady aerodynamic scaling cases for coefficient of lift and moment in Figures 48(a) through 49(e) indicates a limited potential for simulating new airfoil characteristics on advanced blade designs. For example, an abrupt stall of the type shown on Figure 48(c) cannot be represented. The moment coefficient scaling procedure consists of an angle-of-attack factor only, which provides an excessively steep moment stall, compared to the measured steady data shown, for example, on Figure 49(a). The coefficient of moment below stall for the scaled data at zero pitching velocity and acceleration is essentially zero, and therefore, the steady pitching moment coefficient effects of camber or shifts of aerodynamic center of pressure cannot be included.

Further generalization of the unsteady data would be accomplished by subtracting the tabulated zero pitching velocity and acceleration data from the remaining tabulated data. This would form a table of coefficient increments due to unsteady aerodynamics. This table could be modified in some prescribed manner to reflect Reynolds number, Mach number, and other effects as they are defined through future test and analysis.

In use, the proposed table of unsteady aerodynamic increments could be added to any particular set of steady aerodynamic characteristics, which

could also reflect various types of stall characteristics and the effects of blade camber, Mach number, and Reynolds number.

Further improvements in the mathematical model of blade airloads have been found advisable by other investigators in References 15, 20, and 22. These improvements include computationally simpler analytical definitions of unsteady airfoil behavior in place of the current tabular data.

Evaluation of Calculated Blade Bending Response

The quality of the correlation between normal modes aeroelastic analysis blade bending response calculated results and test data reported herein is similar to what has been published previously.

Most of the previously published comparisons have displayed results for blades with a conventional amount of built-in twist. The previous full-scale twisted blade correlation is similar in quality to that reported herein for the -8-degree twist model blade. Examples of blade bending correlation obtained earlier for twisted blades are shown in Figures 25 through 27 and 30 through 32 of Reference 1 , Figures 65 and 66 of Reference 15, Figures 58 and 61 of Reference 20, and Figure 53 of Reference 23. All of these twisted blade results show reasonably good correlation between calculated and test flapwise bending time history, and at least fair amplitude correlation for chordwise bending response.

Correlation of the normal modes aeroelastic analysis results with test data for an untwisted model blade was published in Reference 5.

The work of Reference 5 was concerned primarily with transient conditions, but the pretransient steady-state conditions are comparable to the results of the present investigation.

The results in Figure 19, page 123, of Reference 5 show a calculated underprediction of flapwise bending response for the uniform inflow assumption, similar to the quality of the untwisted blade correlation for the present investigation.

The chordwise bending response is also substantially underpredicted by the calculation for the untwisted blades, as shown in Figures 68, 69, 72, 73, 74, 75, and 76. A significant improvement in flapwise correlation is obtained by including variable inflow in the calculation for the untwisted blades, but the effect on the chordwise response is less prominent.

The quality of the correlation between calculated and test flap and lag hinge motion data is better than the bending response correlation, and is not strongly affected by blade twist. This can be seen by comparing Figures 77(g) and 77(h) to 21(a) and 21(b) respectively.

Figures 53 through 57 show that except for the blade with the trailing edge flap, the correlation of the calculated control positions with test data for the untwisted blades is about as good as it is for the twisted blades.

These observations about the correlation of calculated and test data provide motivation for more detailed investigations into the reasons for the lack of bending response correlation. The aspects of the calculation method which should be studied further in this regard are discussed in the following paragraphs.

It can be expected that the untwisted blade is more strongly affected by nonuniform inflow, and that, therefore, inaccuracies in the calculation of its inflow are more important. The untwisted blade tip is more highly loaded in the lift direction. This higher tip loading will cause the trailing vorticity to be more concentrated at the blade tip. This, in turn, causes higher tip inflow for the untwisted than for the twisted blade. Consideration of this inflow results in an induced angle-of-attack distribution which is aerodynamically equivalent to a certain amount of built-in twist. This results in load distribution components which tend to be more like those of the twisted blade. Consideration of variable inflow in the untwisted blade response calculations does make improvements of this type in the correlation with test data, as seen by comparing Figures 67(a), 67(b), and 67(c).

Thus, since additional improvement of the same type of flapwise bending response is still needed, more accurate calculations of wake-induced inflow are indicated, especially for the untwisted blade. A method for more accurate calculation of the blade wake geometry has been utilized and recommended, for example, in References 20 and 22.

The induced inflow velocity calculation utilizes the modified form of the Biot-Savart representation for a large number of straight-line vortex segments which make up the helical wake. This vortex theory states that the induced velocity is inversely proportional to the distance from the filament. Without modification, this idealization becomes inaccurate for sufficiently small distances from the vortex filament, since indefinitely large velocities are implied. Since rotor blades often pass very close to the wake vortices, indefinitely large inflow velocity impulses would appear in the calculation. These, in turn, would cause the calculation of unrealistically large load impulses. In order to avoid this theoretical shortcoming, and simulate the physical vortices, it is assumed that self-induced velocities are zero inside of an arbitrarily defined core radius around each vortex segment.

The effects of two different core size assumptions are shown in Figures 67(b), 76(b), 89(b), and 67(c), 76(c), 89(c). The assumption of a core radius .6 times blade chord produces too little flapwise blade response. The assumption of a core radius of .3 times blade chord provides more low-frequency response, but the higher frequency part of flapwise bending response is overpredicted. These results show that for this operating condition a significant part of the calculated blade flapwise response is due to vortex filaments passing closer to the blade than .6 times the chord. Therefore, the accuracy of the present lifting line theory with nearby vortices should be investigated, and a more refined theory used if it is justified.

The quantitative effects of limitations on the number of modes included in the normal modes aeroelastic analysis calculations should be investigated.

In addition to rigid blade flapping and lagging motions, the calculations use a limited number of orthogonal natural vibration modes as elastic degrees of freedom. These degrees of freedom are particularly easy to use in the numerical integration of the equations of motion.

As discussed in Reference 11, the solution of the equations of motion is expressed in terms of a summation of the modal motions. Furthermore, the elastic bending moments or stresses are calculated from a summation of modal curvatures, multiplied by the appropriate constants.

This formulation of the problem in terms of orthogonal modes is theoretically rigorous if enough modes are included in the solution. Up to four elastic flapwise and two elastic chordwise modes are permitted in the current version of the Y-200 program.

An increase in the number of modes will require more computer time to perform the calculations, because of the increase in the number of equations of motion, and because smaller azimuth step sizes are required with the higher frequency modes to be added. In addition, a larger number of spanwise segments are indicated, so that the more complicated higher frequency mode shapes, slopes, and curvatures can be adequately represented.

The comparisons between test and calculated data suggest that some loss of accuracy may be occurring because of approximations in the calculation of blade elastic response. As pointed out previously, the correlation of 0-degree twist blade hinge motions with test data is much better than the corresponding bending moment correlation. This suggests that blade aerodynamic blade loadings are calculated with reasonable accuracy, and that the elastic response to this loading is underpredicted. The improvement in flapwise correlation between the 0-degree twist and the -8-degree twist blade elastic moments may be due to greater compatibility between the -8-degree blade loading and the mode shapes.

Tables XL through XLV have been prepared to show samples of the contribution of each of the various flapwise and chordwise modes to the total bending moment. In each case, the contribution of the final mode added is significant, especially for the chordwise response. This implies that additional significant response could be obtained by including additional modes.

In contrast, the modal contributions to hinge motion become progressively smaller with each succeeding mode, as shown in Table XLVI.

The information in the above mentioned tables suggests that the position of the blades in space is determined with comparative accuracy by the calculation. The contributions of each additional mode to blade position does grow very small after the first few modes. This is in contrast to the contribution to blade curvature of each additional mode, which does not become negligible after the first few modes.

In view of the above, the consideration of an alternate method of calculating blade bending moments and stresses is suggested. The bending moment can also be calculated by a separate spanwise integration of the already calculated aerodynamic and inertial loadings. Table XLVII provides a sample summation of flapwise modal accelerations. Even though the component local acceleration and corresponding inertial loading contributions do not become negligible after the first few modes, it is at least plausible to expect better convergence of the spanwise integrals which form the shear and bending moments.

Evaluation of Calculated Blade Torsional Response

The correlation of calculated torsional response from the normal modes aeroelastic analysis with the corresponding test data showed that the calculation tended to overpredict retreating blade torsional oscillations. This effect is contrary to most of the previously published similar comparisons, which typically show an underprediction of torsional response by the calculation.

Previous comparisons of torsional response calculations and test data for full-scale blades appear in Figures 48 through 53 and 58 through 62 of Reference 15, and Figures 50, 53 through 57, 59, and 60 of Reference 20. Previous comparisons of torsional response calculations and Reference 5 model test data appear in Figures 62 through 64 of Reference 20.

The use of variable inflow tended to substantially aggravate the tendency of the analysis to overpredict retreating blade torsional response. This tendency was not apparent in the calculations shown in Figure 30 of Reference 15. Some tendency of the variable inflow to cause overprediction of torsional response is evident in a comparison between Figures 50 and 59 of Reference 20.

The reasons for the overprediction of torsional response by the calculation in the present investigation have not been definitely established. One difference between the present set of comparisons and the previous ones is the higher torsional natural frequency to rotational frequency ratio of the blades used in this investigation. Table XLVIII furnishes approximate sample values for the nondimensionalized pitching velocity and acceleration A and B, for the untwisted dynamically scaled blade. The values given for the variable inflow case shown exceed the unsteady aerodynamic data tabulated range of $A = \pm.04$ and $B = \pm.01$ by a small amount in this case. Nevertheless, a more comprehensive determination of how often the unsteady aerodynamic data table range is exceeded should be carried out. The effect on the blade torsional response calculation of these out-of-range points should of course, also be determined.

As pointed out earlier, the analysis also has a tendency to overpredict the retreating blade torsional response frequency. At the stall boundary the experimental data indicates a moderately large blade torsional response which is much lower than the torsional natural frequency. This was not predicted by the calculations with unsteady data utilized herein, and is believed to be caused by bending torsion coupling. The similar

lower frequency response appearing in Figure 30 of Reference 22 for steady aerodynamic data and zero moment coefficient supports this contention.

At the higher lift conditions, the experimental data shows the expected retreating blade response at slightly above the torsional natural frequency. The calculation predicts a response in the same region with a considerably higher frequency. This tendency has also been noted in the previous investigations of Reference 15 and 20. The predicted torsional frequency is about 35 percent higher than the experimental value for the fiber glass spar dynamically scaled blade and about 23 percent higher for the aluminum spar three-times-scale stiffness blade. These frequency ratios imply an effective stiffness 82 percent higher than the elastic stiffness for the fiber glass spar dynamically scaled blade and 51 percent higher for the aluminum spar three-times-scale stiffness blade. Thus, the apparent added stiffness is about twice as high in absolute terms for the three-times-scale stiffness aluminum spar blade. Since the apparent stiffness appears at relatively low torsional amplitude, it is probably not a result of exceeding the unsteady aerodynamic table range. Further investigation is required to establish the source of the apparent torsional stiffness.

The effect of variable inflow on torsional response with the two assumed vortex core radii is shown in Figure 89. For this unstalled case, the retreating blade torsional oscillations occur at approximately the torsional natural frequency. The current theory overpredicted the magnitude of the torsional oscillations, as it did for the stalled operating conditions.

The low-frequency torsional response of the trailing-edge flapped blade was underpredicted with the existing unsteady aerodynamic tables, while the high-frequency retreating blade torsional response was overpredicted. This was primarily due to the lack of proper unsteady aerodynamic data for the flapped airfoil, as discussed earlier.

CONCLUSIONS

1. Sample comparisons of model and full-scale test data show qualitative and quantitative similarities. Therefore, it is concluded that analytical methods for full-scale rotor performance and blade response can be verified or improved through correlation with model data.

2. The blade set with the 5-degree trailing-edge flap is observed to have substantially better performance than the unflapped blade sets. At an advance ratio of $\mu = .3$, at equal lift and propulsive force, rotor torque for the flapped blade set is typically about 80 percent of the torque for the blade set with -8 degrees of built-in twist.

3. Under stalled conditions, the aluminum spar three-times-scale stiffness blade set has less favorable performance than the other blade sets. At an advance ratio of $\mu = .3$, at equal lift and propulsive force, rotor torque for the aluminum spar three-times-scale stiffness blade set is typically about 110 percent of the torque for the similar fiber glass spar dynamically scaled blade set.

4. The bending moment amplitudes on the blade set with the 5-degree trailing-edge flap are similar in magnitude to those on the set with -8 degrees of built-in twist.

5. The torsional moment amplitudes on the blade set with the 5-degree trailing-edge flap are much higher than those on the unflapped blades, except at the more highly loaded conditions. At an advance ratio of $\mu = .3$, the torsional moments below stall on the flapped blade set are typically about two to three times the torsional moment on the unflapped blades. Blade stalling, however, causes the torsional moments on the unflapped blades to be higher at the more heavily loaded conditions.

6. The bending moment amplitudes on the aluminum spar three-times-scale stiffness blades are substantially higher than those on the fiber glass spar scale stiffness blades. At an advance ratio of $\mu = .3$, the bending moments on these blades are typically about two to three times those on the fiber glass spar scale stiffness blades.

7. Blade torsion moment amplitudes on the aluminum spar three-times-scale stiffness blades are similar to those on the other blades below stall. Above stall, at an advance ratio of $\mu = .3$, the aluminum spar three-times-scale stiffness blade torsional moments are typically about 25 percent to 50 percent greater than those on the fiber glass spar scale stiffness blades.

8. It appears that blade torsional vibration can be aggravated when wake vortex passage frequency relative to the blade is close to the torsional natural frequency. However, this effect is dependent on rotor blade configuration and loading condition.

9. In order to obtain reasonably good performance correlation between the

model rotor test data and the normal modes aeroelastic analysis, the existing full-scale unsteady aerodynamic data tables must be scaled to a steady-state maximum lift coefficient which is higher than the measured static two-dimensional model blade airfoil data.

10. Correlation between calculated rotor performance and test data is best for the -8-degree twist blade with the variable inflow assumption. With this assumption, deviations in drag and torque are on the order of 10 percent of typical operating values. The use of the uniform inflow assumption results in typical drag and torque deviations about twice as large. The deviations in drag and torque at a given condition are compensating, but inconsistent in sign for different conditions.

11. Correlation between calculated rotor performance and test data for the untwisted blades shows compensating deviations in drag and torque that are on the order of 20 to 30 percent of typical operating values. The use of variable inflow in the calculations does not consistently improve the accuracy of the drag and torque calculations.

12. Because of compensating deviations in drag and torque, correlation of rotor performance with test data on a drag versus torque plot at constant lift is good for all three blade configurations without flaps. Deviations in torque are smaller than 10 percent when correlation is made on this basis.

13. Increments in rotor drag and torque due to blade configuration are more accurately predicted than the absolute values. For the unflapped blade configurations, the average increment deviation is less than 5 percent of typical operating values for the twist variation and less than 20 percent for the stiffness variation.

14. Correlation between test and calculated performance for the blade with the trailing-edge flap is poor, because of overpredicted rotor torque at a given lift. This is attributed to the use of the existing symmetrical unsteady airfoil data. These data do not reflect the combined beneficial effects of unsteady aerodynamics and camber.

15. Correlation between test and calculated blade vibratory bending moment amplitudes is reasonably good for the -8-degree twist blade at moderate loadings when the variable inflow calculation is used. Under these conditions, the sample flapwise moment amplitude is overpredicted by 6 percent, the chordwise amplitude is overpredicted by 15 percent, and the torsional amplitude by 17 percent. Correlation is less favorable with higher loadings and the uniform inflow assumption.

16. For the untwisted blade configurations, correlation between test and calculated vibratory bending moment amplitudes is fair to poor with the variable inflow calculation, and poor with the uniform inflow assumption.

    With variable inflow, untwisted blade calculated flapwise moment amplitudes are typically about 80 percent of test values. Chordwise calcu-

lated moment amplitudes are typically 50 percent of test values. Torsional moments are typically 150 to 200 percent of test values.

With uniform inflow assumed, the calculated untwisted blade flapwise moment amplitude is typically 50 percent of the test value. The calculated chordwise moment amplitude is typically about 30 percent of the test value, and the calculated torsional moment about 120 percent of the test value.

17. The percentage change in flapwise bending moment amplitude due to twist is typically overpredicted by the calculation. The calculation predicts an increase in chordwise bending amplitude due to blade twist, instead of the decrease actually observed in the test data. The agreement of these bending moment ratios with test is improved by using variable inflow in the calculation. The percentage change in torsional moment due to twist is typically underpredicted with the uniform inflow assumption, and overpredicted with the variable inflow assumption.

18. The percentage change in bending moment amplitude due to the 5-degree trailing-edge flap is usually overpredicted with the uniform inflow assumption and underpredicted with the variable inflow assumption. The percentage change in torsional moment amplitude is typically underpredicted with both inflow assumptions.

19. The percentage change in bending moment amplitude due to the blade stiffness variation was typically underpredicted with the uniform inflow assumption and overpredicted with the variable inflow assumption. The percentage change in torsional moment due to the blade stiffness variation was typically overpredicted with both inflow assumptions.

20. Calculated moment amplitude is moderately sensitive to assumed wake vortex core sizes. Changing from an assumed radius of .3c to .6c lowered the flapwise moment amplitude by 30 percent.

RECOMMENDATIONS

1. Correlation of the model data with full-scale data should be continued for an extended range of operating conditions, to further evaluate the relationship of model and full-scale results. The correlation should include peak-to-peak and time histories of blade equivalent bending moment or stress, as well as rotor performance parameters.

2. Correlation of the model test data with calculated data should be continued for other operating conditions and analytical assumptions, to provide a more comprehensive evaluation of rotor performance and blade response calculations.

3. In general, rotor performance and blade response calculations should include consideration of wake-induced variable inflow.

4. The analytical representation of rotor blade excitation by the wake should be improved.

5. The analytical representation, data and associated scaling techniques for considering unsteady aerodynamics in rotor performance and blade response calculations should be augmented to include characteristics of other symmetrical and unsymmetrical airfoils, other Reynolds number variations, and any appreciable effects of yawed flow.

6. The two-dimensional model blade section aerodynamic data presented herein should be compared with similar data collected in a closed throat wind tunnel.

7. Alternate methods for calculating blade bending moment should be studied for possible incorporation in the normal modes aeroelastic analysis.

8. The adequacy of the modal representation of the rotor blade should be studied, with reference to the current limits on numbers of modes and radial blade segments.

LITERATURE CITED

1. Rabbott, J. P., Jr., Lizak, A. A., and Paglino, V. M., A PRESENTATION OF MEASURED AND CALCULATED FULL-SCALE ROTOR BLADE AERODYNAMIC AND STRUCTURAL LOADS, United Aircraft Corporation, Sikorsky Aircraft Division; USAAVLABS Technical Report 66-31, U. S. Army Aviation Materiel Laboratories, Fort Eustis, Virginia, July 1966, AD639981.

2. Paglino, V. M., and Logan, A. H., AN EXPERIMENTAL STUDY OF THE PERFORMANCE AND STRUCTURAL LOADS OF A FULL-SCALE ROTOR AT EXTREME OPERATING CONDITIONS, United Aircraft Corporation, Sikorsky Aircraft Division; USAAVLABS Technical Report 68-3, U. S. Army Aviation Materiel Laboratories, Fort Eustis, Virginia, July 1968, AD674187.

3. McCloud III, J. L., and Biggers, James C., and Stroub, Robert H., AN INVESTIGATION OF FULL-SCALE HELICOPTER ROTORS AT HIGH ADVANCE RATIOS AND ADVANCING TIP MACH NUMBERS, NASA TND-4632, National Aeronautics and Space Administration, Ames Research Center, Moffett Field, Californis, July 1968.

4. Fradenburgh, E. A., Murrill, R. J., and Kiely, E. F., DYNAMIC MODEL WIND TUNNEL TESTS OF A VARIABLE-DIAMETER, TELESCOPING-BLADE ROTOR SYSTEM (TRAC ROTOR), United Aircraft Corporation, Sikorsky Aircraft Division; USAAMRDL Technical Report 73-32, Eustis Directorate, U. S. Army Air Mobility Research and Development Laboratory, Fort Eustis, Virginia, July 1973.

5. Niebanck, C. F., and Bain, L. J., ROTOR AEROELASTIC STABILITY AND TRANSIENT CHARACTERISTICS, United Aircraft Corporation, Sikorsky Aircraft Division; USAAVLABS Technical Report 69-88, U. S. Army Aviation Materiel Laboratories, Fort Eustis, Virginia, February 1970, AD869035.

6. Linville, James C., AN EXPERIMENTAL INVESTIGATION OF THE EFFECTS OF ROTOR HEAD CONFIGURATION AND FUSELAGE YAW ON THE WAKE CHARACTERISTICS AND ROTOR PERFORMANCE OF A 1/8TH SCALE HELICOPTER, United Aircraft Corporation, Sikorsky Aircraft Division; USAAVLABS Technical Report 69-94, U. S. Army Aviation Materiel Laboratories, Fort Eustis, Virginia, February 1970, AD869390.

7. Pope, A., and Harper, J. J., LOW-SPEED WIND TUNNEL TESTING, New York, John Wiley and Sons, 1966.

8. Arcidiacono, P. J., ANALYTICAL AND EXPERIMENTAL INVESTIGATIONS OF THE AEROELASTIC CHARACTERISTICS OF HELICOPTER ROTORS OPERATING AT HIGH ADVANCE RATIOS, United Aircraft Research Laboratories Report B-110049-2, East Hartford, Connecticut, March 1963. (Available from the Eustis Directorate, U. S. Army Airmobility Research and Development Laboratories, Fort Eustis, Virginia)

9. Beavan, J. A., Sargent, R., North, R. J., and Burrows, P. M., MEASUREMENTS OF MAXIMUM LIFT ON 26 AEROFOIL SECTIONS AT HIGH MACH NUMBER, Ministry of Supply, Aeronautical Research Council, A. R. C. Technical Report R & M 2678 Her Majesty's Stationery Office, London, England, 1953.

10. Heyson, H. H., JET BOUNDARY CORRECTIONS FOR LIFTING ROTORS CENTERED IN RECTANGULAR WIND TUNNELS, NASA TR R-71, National Aeronautics and Space Administration, Langley Research Center, Langley Field, Virginia 1960.

11. Arcidiacono, P. J., PREDICTION OF ROTOR INSTABILITY AT HIGH FORWARD SPEEDS, VOLUME 1 - STEADY FLIGHT DIFFERENTIAL EQUATIONS OF MOTION FOR A FLEXIBLE HELICOPTER BLADE WITH CHORDWISE MASS UNBALANCE, Sikorsky Aircraft Division, United Aircraft Corporation; USAAVLABS Technical Report 68-18A, U. S. Army Aviation Materiel Laboratories, Fort Eustis, Virginia, February 1969, AD 685860.

12. Bergquist, R. R., DEVELOPMENT OF THE EQUATIONS OF MOTIONS ASSOCIATED WITH THE TRANSVERSE VIBRATIONS OF ROTOR BLADES, United Aircraft Corporation, Sikorsky Aircraft Division; Sikorsky Aircraft Report SER 50577, Stratford, Connecticut, February 1969. (Available from the Eustis Directorate, U. S. Army Airmobility Research and Development Laboratories, Fort Eustis, Virginia)

13. Bergquist, R. R., and Thomas, G. C., TECHNICAL MANUAL FOR NORMAL MODES AEROELASTIC COMPUTER PROGRAM, United Aircraft Corporation, Sikorsky Aircraft Division; Sikorsky Aircraft Report SER 50840, Stratford, Connecticut, July 1972.(Available from Eustis Directorate, U. S. Army Air Mobility Research and Development Laboratories, Fort Eustis, Virginia)

14. Tanner, W. H., CHARTS FOR ESTIMATING ROTARY WING PERFORMANCE IN HOVER AND AT HIGH FORWARD SPEEDS, United Aircraft Corporation, Sikorsky Aircraft Division; NASA Contractor Report CR-114, National Aeronautics and Space Administration, Washington, D. C., November 1964.

15. Arcidiacono, P. J., Carta, F. O., Cassellini, L. M., and Elman, H. L., INVESTIGATION OF HELICOPTER CONTROL LOADS INDUCED BY STALL FLUTTER, United Aircraft Corporation, Sikorsky Aircraft Division; USAAVLABS Technical Report 70-2, U. S. Army Aviation Materiel Laboratories, Fort Eustis, Virginia, March 1970, AD 869823.

16. Carta, F. O., and Niebanck, C. F., PREDICTION OF ROTOR INSTABILITY AT HIGH FORWARD SPEEDS, VOLUME III - STALL FLUTTER, United Aircraft Corporation, Sikorsky Aircraft Division; USAAVLABS Technical Report 68-18C, U. S. Army Aviation Materiel Laboratories, Fort Eustis, Virginia, February 1969, AD 687322.

17. Piziali, R. A., and DuWaldt, F. A., A METHOD FOR COMPUTING ROTARY WING AIRLOAD DISTRIBUTIONS IN FORWARD FLIGHT, TREC Technical Report 62-44, U. S. Army Aviation Materiel Laboratories, Fort Eustis, Virginia, November 1962.

18. Bergquist, R. F. and Thomas, G. C., USER'S MANUAL FOR NORMAL MODE BLADE AEROELASTIC COMPUTER PROGRAM, United Aircraft Corporation, Sikorsky Aircraft Division; Sikorsky Aircraft Report SER50839, Stratford, Connecticut, July 1972. (Available from the Eustis Directorate, U. S. Army Air Mobility Research and Development Laboratories, Fort Eustis, Virginia).

19. Bergquist, R. R., HELICOPTER GUST RESPONSE INCLUDING UNSTEADY AERODYNAMIC STALL EFFECTS, United Aircraft Corporation, Sikorsky Aircraft Division; USAAMRDL Technical Report 72-68, Eustis Directorate, U. S. Army Air Mobility Research and Development Laboratory, Fort Eustis, Virginia, May 1973, AD 763957.

20. Carta, F. O., Commerford, G. L., Carlson, R. G., and Blackwell, R. H., INVESTIGATION OF AIRFOIL DYNAMIC STALL AND ITS INFLUENCE ON HELICOPTER CONTROL LOADS, United Aircraft Corporation Research Laboratories; USAAMRDL Technical Report 72-51, Eustis Directorate, U. S. Army Air Mobility Research and Development Laboratory, Fort Eustis, Virginia, September 1972, AD 752917.

21. Rabbott, J. P., Jr., COMPARISON OF THEORETICAL AND EXPERIMENTAL MODEL HELICOPTER ROTOR PERFORMANCE IN FORWARD FLIGHT, United Aircraft Corporation, Sikorsky Aircraft Division; TCREC Technical Report 61-103, U. S. Army Transportation Research Command, Fort Eustis, Virginia, July 1961.

22. Bellinger, E. D., ANALYTICAL INVESTIGATION OF THE EFFECTS OF BLADE FLEXIBILITY, UNSTEADY AERODYNAMICS, AND VARIABLE INFLOW ON HELICOPTER ROTOR STALL CHARACTERISTICS, United Aircraft Corporation Research Laboratories; NASA CR-1769, National Aeronautics and Space Administration, Washington, D. C., September 1971.

23. Beno, E. A., CH-53A MAIN ROTOR AND STABILIZER VIBRATORY AIRLOADS AND FORCES, United Aircraft Division; Sikorsky Aircraft Report SER 65593, Contract NOw 63-0150-f, Department of the Navy, Naval Air Systems Command, Washington, D. C.

TABLE I. H-34 MODEL ROTOR BLADE INERTIA AND CENTER-OF-GRAVITY DATA

Δr (in.)	r_{in} (in.)	r_{out} (in.)	w (lb/in.)	I_θ (lb-sec^2 x10^{-3})	I_{mfl} (lb-sec^2 x10^{-3})	I_{mch} (lb-sec^2 x10^{-3})	Y_{CG} in.
.23	3.00	3.23	.147	.181	.0036	.177	.33
.52	3.23	3.75	.147				.33
.28	3.75	4.03	.475				.10
.20	4.03	4.23	.149				.33
.10	4.23	4.33	.162	.181	.0036	.177	.30
.17	4.33	4.50	.180	.334	.0801	.254	.27
.14	4.50	4.64	.273				.18
.14	4.64	4.78	.343	.334	.0801	.254	.14
.62	4.78	5.40	.343	.359	.0928	.266	.14
.17	5.40	5.57	.343	.178	.0892	.0892	0.0
.07	5.57	5.64	.295				
.27	5.64	5.91	.112				
.12	5.81	6.03	.169	.178	.0892	.0892	
.22	6.03	6.25	.169	.129	.0645	.0645	
.28	6.25	6.53	.048	.0354	.0177	.0177	
.54	6.53	7.07	.0822	.0392	.0193	.0199	
.56	7.07	7.63	.0588	.0206	.0111	.00955	
.65	7.63	8.28	.0414	.00924	.0042	.00504	
.125	8.28	8.405	.0176	.00351	.00037	.00314	
.495	8.405	8.900	.0081	.00293	.00025	.00268	
3.630	8.90	12.530	.0094	.0087	.00013	.0086	
.270	12.53	12.800	.0106	.0090	.00014	.0089	
40.135	12.80	52.935	.0121	.0116	.00018	.0114	
.72	52.935	53.655	.0202	.0224	.00034	.0221	
.18	53.655	53.835	.0178	.0224	.00034	.0221	
.32	53.835	54.155	.0276	.0224	.00034	.0221	
.845	54.155	55.000	.0044	.0058	.00009	.00571	0.0

NOTES:
1. Mass moments of inertia are with respect to the local chord line and an axis normal to it at the feathering axis.
2. Mass moments of inertia include parts at the root that flap, lag, and pitch with the blade. Parts that flap and lag but do not pitch are excluded.
3. The flapwise position of the blade center of gravity is on the chord line for all blade stations.

TABLE II. H-34 FIBER GLASS MODEL ROTOR BLADE STIFFNESS PROPERTIES

Δr (in.)	r_{in} (in.)	r_{out} (in.)	I_{flp} (in.^{4})	I_{chd} (in.^{4})	J (in.^{4})
.23	3.00	3.23	.466	2.68	2.37
.52	3.23	3.75	.578	3.54	
.28	3.75	4.03	1.870	5.32	
.30	4.03	4.33	.268	.268	
.45	4.33	4.78	1.600	1.600	2.37
.62	4.78	5.40	1.030	1.030	1.36
.63	5.40	6.03	.814	.814	1.36
.22	6.03	6.25	1.120	1.120	1.99
.28	6.25	6.53	.330	.359	.52
.54	6.53	7.07	.336	.332	.50
.56	7.07	7.63	.1907	.1497	.36
.65	7.63	8.28	.0711	.0712	.0440
.125	8.28	8.405	.003148	.02190	.00644
.495	8.405	8.900	.00196	.01730	.00393
3.630	8.900	12.530	.001236	.01240	.00340
.270	12.53	12.800	.001236	.01240	.00316
41.035	12.80	53.835	.001060	.01152	.00293
.320	53.835	54.155	.00057	.00625	.00174
.845	54.155	55.000	.00057	.00625	.00174

NOTE: The following values of E and G should be used with I_{flp}, I_{chd}, and J respectively to obtain the correct bending and twisting stiffnesses for the fiberglass model blade configurations.

$$E = 2.50 \times 10^6 \text{ lb/in}^2$$

$$G = 1.01 \times 10^6 \text{ lb/in}^2$$

The values of J for the segments between $r_{in} = 8.28$ and $r_{out} = 53.835$ have been corrected to reflect the stiffness test results for the fiberglass blades.

TABLE III. H-34 ALUMINUM MODEL ROTOR BLADE STIFFNESS PROPERTIES

Δr (in.)	r_{in} (in.)	r_{out} (in.)	I_{flp} (in.^{4})	I_{chd} (in.^{4})	J (in.^{4})
.23	3.00	3.23	.117	.670	.600
.52	3.23	3.75	.145	.885	
.28	3.75	4.03	.468	1.330	
.30	4.03	4.33	.0670	.0670	
.45	4.33	4.78	.400	.400	.600
.62	4.78	5.40	.258	.258	.344
.63	5.40	6.03	.204	.204	.344
.22	6.03	6.25	.280	.280	.503
.28	6.25	6.53	.0825	.0898	.132
.54	6.53	7.07	.0840	.0830	.127
.56	7.07	7.63	.0477	.0374	.0911
.65	7.63	8.28	.05456	.0574	.0367
.125	8.28	8.405	.002415	.0177	.00583
.495	8.405	8.90	.001504	.0140	.00356
3.630	8.90	12.53	.000948	.0100	.00308
.270	12.53	12.800	.000948	.0100	.00286
41.035	12.80	53.835	.000813	.00929	.00266
.320	53.835	54.100	.000437	.005041	.00145
.845	54.155	55.000	.000437	.005041	.00145

NOTE: The following values of E and G should be used with I_{flp}, I_{chd}, and J respectively to obtain the correct bending and twisting stiffnesses for the aluminum model blade configuration

$$E = 10.0 \times 10^6 \text{ lb/in.}^2$$

$$G = 4.00 \times 10^6 \text{ lb/in.}^2$$

The values of I_{flp}, I_{chd}, and J for the segments between $r_{in} = 8.28$ and $r_{out} = 53.835$ have been corrected to reflect the stiffness test results for the aluminum blade configurations.

TABLE IV. EXPERIMENTALLY DETERMINED NONROTATING BLADE NATURAL FREQUENCIES AND DAMPING

Blade Configuration			Blade Number	Natural Frequency						Damping			
θ_1 (deg)	δ_F (deg)	S_E		f_{BF1} (cps)	f_{BF2} (cps)	f_{BF3} (cps)	f_{EC1} (cps)	f_{EC2} (cps)	f_{T1} (cps)	ζ_{BF1} (%)	ζ_{BF2} (%)	ζ_{EC1} (%)	ζ_{T1} (%)
0	0	1	B4	8.1	25.2	52.0	29.0	87.0	77.0	-	-	-	-
0	0	1	B5	8.2	25.0	51.7	29.0	86.0	78.0	.48	-	1.3	-
-8	0	1	D4	8.3	25.5	52.5	29.0	85.0	78.3	.64	.64	1.1	3.3
-8	0	1	D5	8.0	24.5	50.0	29.5	85.0	-	.70	.64	1.1	-
0	5	1	C2	8.1	26.0	-	30.0	-	76.0	-	-	-	-
0	5	1	C4	8.0	25.0	52.0	28.3	86.6	80.0	1.10	1.20	6.60	6.6
0	5	1	C5	8.0	25.0	52.0	29.0	86.0	77.3	1.10	.80	1.20	5.9
0	0	3	A1	14.0	43.5	-	50.0	-	-	.45	.81	1.30	-
0	0	3	A4	14.3	44.1	-	49.5	-	-	-	-	-	-
0	0	3	A5	15.0	46.0	-	50.0	-	-	.48	2.0	.90	-

TABLE V. H-34 MODEL ROTOR BLADE MISCELLANEOUS DATA

Parameter or Description	Value	Units
Radius	55.0	in.
Blade Airfoil Chord outboard of 8.9" Radial Station	2.69	in.
Blade Shank Chord inboard of 8.9" Radial Station	1.19	in.
Blade Linear Twist from Center of Rotation to Tip		
Untwisted Blades	0.0	deg
Twisted Blade	-8.0	deg
Blade Shear Center Locations		
Beamwise with Respect to Feathering Axis	0.0	in.
Chordwise with Respect to Feathering Axis	0.0	in.
Location of Blade Hinges		
Radial Station of Coincident Flapping and Lead-Lag Hinge	3.0	in.
Feathering Bearing Outboard End Radial Station	5.60	in.
Feathering Bearing Inboard End Radial Stations (The feathering, flapping and lag bearing axes intersect at the same point)	4.64	in.
Location of Lead-Lag Damper		
Rotary Damper on Blade Lead-Lag Hinge		
Pitch Flap Coupling Ratio	0.0	
Damping Coefficient of Lead-Lag Damper (Expressed as a damping moment about the hinge)	17.0	in-lb-sec
Tabs or Flaps		
Flapped Blade Set plain flap deflection over the aft 20% of the airfoil chord	5.0	deg
Pitch Control Geometry		
At 0° collective and cyclic input:		
Distance aft along flapping hinge axis to pushrod upper end.	1.43	in.
Radius on swashplate of pushrod lower end	1.95	in.
Distance of plane of swashplate below plane of flapping hinges	6.31	in.
Angle on swashplate between pushrod lower end and plane of shaft and lead-lag axis	40.5	deg
Pitch Control Spring Rate	21,000.	in-lb/rad
Airfoil Section - NACA 0012		

TABLE VI. MODEL BLADE SECTION TWO-DIMENSIONAL AERODYNAMIC DATA (NACA 0012 Airfoil, δ_F = 0.0 deg, c = 2.69 in., M = .10, RN = .155 X 10^6)

α (deg)	C_l	α (deg)	C_d	α (deg)	C_m
0.0	.00	0.0	.0080	0.0	0.0
5.4	.45	1.0	.0084	4.0	.003
7.0	.59	2.5	.0103	8.0	.008
8.0	.675	4.0	.0150	8.6	.007
8.3	.71	6.5	.0295	9.0	.004
9.4	.74	8.5	.054	11.0	-.035
10.0	.73	10.0	.100	12.0	-.051
12.0	.71	11.5	.140	13.0	-.063
14.0	.68	12.5	.170	14.0	-.071
16.0	.67	14.0	.200	16.0	-.079
18.0	.67	29.0	.580	22.0	-.097
20.0	.69	45.0	1.150	24.0	-.106
23.0	.73	55.0	1.420	26.0	-.120
26.0	.81	63.0	1.600	32.0	-.177
33.0	1.00	70.0	1.730	41.0	-.250
39.0	1.07	75.0	1.800	55.0	-.325
45.0	1.06	80.0	1.850	72.0	-.395
50.0	1.03	85.0	1.880	90.0	-.460
60.0	.85	89.0	1.890	107.0	-.500
75.0	.50	93.0	1.880	117.0	-.513
92.0	0.00	100.0	1.850	125.0	-.510
120.0	-.72	105.0	1.80	133.0	-.495
130.0	-.89	112.0	1.71	140.0	-.465
137.0	-.94	120.0	1.55	147.0	-.420
143.0	-.94	130.0	1.28	155.0	-.360
148.0	-.90	145.0	0.75	158.0	-.290
156.0	-.70	150.0	.52	162.0	-.270
159.0	-.67	155.0	.40	165.0	-.275
163.0	-.66	160.0	.32	171.0	-.310
167.0	-.69	164.0	.28	173.0	-.290
171.0	-.75	170.0	.14	178.0	-.150
175.0	-.60	174.0	.06	180.0	0.0
180.0	0.00	180.0	.02		

TABLE VII. MODEL BLADE SECTION TWO-DIMENSIONAL AERODYNAMIC DATA (NACA 0012 Airfoil, δ_F = 0.0 deg, c = 2.69 in., M = .18, RN = .279 X 10^6)

α (deg)	C_l	α (deg)	C_d	α (deg)	C_m
0.0	0.0	0.0	.0080	0.0	0.0
8.4	.72	0.5	.0082	8.0	.012
8.8	.74	1.5	.0088	8.6	.012
9.3	.76	2.5	.0100	9.2	.008
9.8	.76	5.0	.0175	9.5	0.0
11.0	.72	7.5	.036	9.8	-.014
12.9	.68	10.2	.10	10.4	-.028
15.3	.65	10.7	.115	11.0	-.040
17.1	.64	11.8	.145	12.0	-.054
19.2	.645	13.0	.170	13.7	-.067
21.4	.67	15.0	.210	16.0	-.074
25.0	.745	19.0	.290	19.6	-.083
33.0	.97	30.0	.60	22.0	-.092
37.0	.99	41.0	1.00	24.0	-.110
41.0	.99	49.0	1.25	27.6	-.132
46.5	.965	56.0	1.40	32.0	-.176
52.0	.92	61.5	1.49	45.0	-.240
64.0	.70	68.0	1.57	58.0	-.314
79.5	.38	73.0	1.615	70.0	-.365
115.0	-.60	80.0	1.66	90.0	-.433
122.0	-.75	88.0	1.69	113.0	-.48
128.5	-.845	96.0	1.685	119.0	-.485
134.0	-.88	105.0	1.65	125.0	-.482
140.0	-.88	115.0	1.55	132.0	-.470
144.5	-.85	125.0	1.36	139.0	-.450
148.0	-.79	132.0	1.19	145.0	-.410
153.0	-.66	137.5	1.02	150.0	-.365
155.0	-.62	151.5	.49	156.0	-.295
159.0	-.60	155.0	.40	161.0	-.270
162.5	-.62	160.5	.30	163.5	-.266
167.5	-.67	165.5	.23	167.0	-.275
172.0	-.65	171.0	.11	170.0	-.295
175.0	-.58	174.5	.05	175.0	-.240
180.0	0.0	180.0	.015	180.0	0.0

TABLE VIII. MODEL BLADE SECTION TWO-DIMENSIONAL AERODYNAMIC DATA (NACA 0012 Airfoil, δ_F = 0.0 deg, c = 2.69 in., M = .33, RN = .512 X 10^6)

α (deg)	c_l	α (deg)	c_d	α (deg)	c_m
0.0	0.0	0.0	.0081	0.0	0.0
7.9	.715	.50	.0082	8.4	.015
8.5	.75	1.5	.0088	8.9	.014
8.9	.76	2.5	.010	9.3	.010
9.4	.75	3.5	.012	9.7	-.030
10.8	.63	7.5	.032	10.1	-.045
11.4	.60	8.4	.044	10.7	-.053
12.0	.575	9.0	.060	11.4	-.058
13.1	.56	9.6	.10	18.0	-.078
14.0	.56	9.8	.12	22.0	-.092
15.5	.565	10.5	.14	24.0	-.102
18.0	.59	11.5	.158	26.0	-.115
21.0	.635	14.0	.195	28.8	-.138
24.7	.710	20.0	.30	30.0	-.149
28.6	.80	30.0	.60		
32.0	.88				

TABLE IX. MODEL BLADE SECTION TWO-DIMENSIONAL AERODYNAMIC DATA (NACA 0012 Airfoil, δ_F = 0.0 deg, c = 2.69 in., M = .47, RN = .729 X 10^6)

α (deg)	c_l	α (deg)	c_d	α (deg)	c_m
0.0	0.0	0.0	.0080	0.0	0.0
5.7	.59	1.0	.0081	1.6	.002
6.0	.615	2.0	.0087	3.4	.006
6.5	.63	3.0	.010	5.2	.012
7.0	.635	5.5	.018	6.4	.018
7.6	.62	6.25	.0235	6.8	.018
9.0	.57	6.8	.030	7.2	.016
11.0	.535	7.2	.040	8.4	-.034
12.6	.53	7.7	.070	9.0	-.047
14.0	.53	8.0	.080	9.8	-.055
15.6	.54	8.6	.10	10.8	-.058
17.3	.56	9.5	.125	13.0	-.063
19.0	.567	11.0	.154	14.6	-.070
21.0	.557	12.5	.182	16.3	-.076
22.6	.525	14.5	.218	18.0	-.085
24.0	.475	16.5	.25	20.0	-.092
		20.25	.30	22.0	-.096
		22.5	.31	24.0	-.10
		25.0	.285	28.0	-.102

TABLE X. MODEL BLADE SECTION TWO-DIMENSIONAL AERODYNAMIC DATA (NACA 0012 Airfoil, δ_F = 0.0 deg, c = 2.69 in., M = .56, RN = .868 X 10^6)

α (deg)	C_l	α (deg)	C_d	α (deg)	C_m
0.0	0.0	0.0	.0080	0.0	0.0
3.6	.40	.50	.0081	1.4	.0010
4.0	.43	1.5	.0087	2.7	.0040
4.9	.455	2.0	.0094	4.5	.0090
5.7	.46	2.75	.011	5.2	.010
6.2	.455	3.5	.015	5.8	.010
7.4	.44	5.5	.04	6.5	.007
8.5	.435	7.75	.10	7.0	.002
10.7	.445	8.25	.112	7.4	-.004
13.1	.45	9.0	.128	8.0	-.020
14.6	.445	10.6	.148	8.8	-.040
16.2	.435	12.0	.16	9.5	-.050
17.6	.42	13.25	.175	10.3	-.056
19.0	.395	15.0	.187	11.3	-.060
19.6	.38	17.5	.20	13.1	-.062
		20.0	.20	16.0	-.066
				24.0	-.082

TABLE XI. MODEL BLADE SECTION TWO-DIMENSIONAL AERODYNAMIC DATA (NACA 0012 Airfoil, δ_F = 5.0 deg, c = 2.69 in., M = .10, RN = .155 X 10^6)

α (deg)	C_l	α (deg)	C_d	α (deg)	C_m
-180.0	.19	-180.0	.025	-180.0	.065
-176.0	.59	-176.0	.050	-175.0	.275
-170.0	.7[illegible]	-168.0	.21	-162.5	.236
-164.5	.59	-158.0	.34	-146.5	.392
-143.0	.91	-127.0	1.375	-137.0	.44
-136.0	.92	-109.5	1.72	-125.0	.47
-123.0	.75	- 93.5	1.855	-110.0	.465
- 62.0	-.77	- 84.0	1.835	- 85.0	.42
- 47.0	-.985	- 74.0	1.72	- 60.0	.31
- 39.0	-.995	- 59.0	1.43	- 30.0	.128
- 32.0	-.93	- 30.0	.56	- 26.0	.095
- 24.0	-.695	- 13.6	.17	- 20.0	.066
- 17.5	-.615	- 12.0	.145	- 12.0	.040
- 13.4	-.54	- 11.0	.11	- 10.3	-.040
- 11.6	-.585	- 10.5	.050	- 8.4	-.031
- 10.3	-.69	- 5.3	.014	- 5.3	-.030
- 8.0	-.575	- 2.25	.0066	- 1.4	-.042
0.0	.20	- 2.0	.0081	0.0	-.040
5.0	.64	0.0	.0090	3.0	-.020
7.8	.80	8.25	.058	8.0	-.011
8.9	.79	9.0	.120	10.0	-.081
11.1	.63	10.0	.153	18.0	-.103
14.2	.66	14.0	.220	24.0	-.135
17.6	.69	30.0	.70	30.0	-.185
32.0	1.03	52.0	1.40	60.0	-.360
36.5	1.08	68.0	1.715	85.0	-.450
45.0	1.07	82.5	1.85	110.0	-.495
61.0	.81	90.0	1.87	120.0	-.499
116.0	-.67	104.0	1.77	135.0	-.468
132.0	-.94	120.0	1.49	146.5	-.40
142.0	-.94	157.5	.34	154.0	-.30
158.5	-.64	163.5	.245	158.5	-.285
168.5	-.78	175.5	.035	171.5	-.315
180.0	.19	180.0	.025	180.0	.065

TABLE XII. MODEL BLADE SECTION TWO-DIMENSIONAL AERODYNAMIC DATA (NACA 0012 Airfoil, δ_F = 5.0 deg, c = 2.69 in., M = .18, RN = .279 X 10^6)

α (deg)	C_l	α (deg)	C_d	α (deg)	C_m
-180.0	.25	-180.0	.025	-180.0	.063
-177.0	.58	-175.0	.070	-175.0	.275
-172.5	.63	-169.5	.175	-165.0	.24
-164.0	.57	-158.0	.35	-159.5	.255
-141.0	.85	-138.5	1.00	-145.0	.375
-128.0	.74	-111.5	1.47	-130.0	.42
- 69.0	-.51	- 97.0	1.62	-110.0	.425
- 49.5	-.83	- 87.5	1.65	- 90.0	.38
- 40.0	-.88	- 82.0	1.635	- 60.0	.29
- 32.0	-.81	- 70.0	1.535	- 30.0	.118
- 23.0	-.605	- 55.0	1.30	- 22.0	.064
- 16.8	-.54	- 30.0	.52	- 18.0	.048
- 12.9	-.505	- 13.3	.150	- 14.5	.047
- 11.3	-.675	- 11.8	.118	- 13.0	.04
- 9.3	-.59	- 11.3	.047	- 12.2	.027
- 7.6	-.48	- 4.5	.0106	- 11.6	-.036
0.0	.23	- 2.8	.0085	- 10.8	-.040
5.4	.68	- 1.5	.0082	- 4.0	-.045
7.9	.82	0.0	.0090	0.0	-.038
8.6	.79	1.5	.0121	7.0	-.016
10.8	.62	8.3	.050	8.0	-.016
13.6	.64	9.4	.130	9.6	-.073
17.0	.64	10.5	.16	11.5	-.087
22.9	.735	30.0	.65	17.0	-.093
27.3	.89	49.0	1.15	23.0	-.12
33.5	.96	66.0	1.45	30.0	-.168
38.5	.965	84.0	1.595	60.0	-.313
44.0	.94	100.0	1.635	90.0	-.40
69.0	.61	110.5	1.56	110.0	-.423
128.0	-.745	137.0	1.00	130.0	-.41
141.0	-.85	155.5	.35	145.0	-.36
161.5	-.615	165.5	.20	159.0	-.245
173.0	-.745	173.0	.065	171.0	-.315
180.0	.25	180.0	.025	180.0	.063

TABLE XIII. MODEL BLADE SECTION TWO-DIMENSIONAL AERODYNAMIC DATA (NACA 0012 Airfoil, δ_F = 5.0 deg, c = 2.69 in., M = .33, RN = .512 X 10^6)

α (deg)	c_l	α (deg)	c_d	α (deg)	c_m
-30.0	-.725	-30.0	.50	-30.0	.106
-25.0	-.605	-17.5	.22	-22.0	.066
-22.0	-.55	-13.4	.16	-18.0	.05
-18.6	-.53	-12.3	.14	-16.0	.045
-15.0	-.485	-11.6	.125	-14.6	.043
-13.3	-.49	-11.3	.10	-12.4	.035
-11.7	-.545	-11.0	.06	-11.8	.022
-10.4	-.65	-10.8	.05	-11.1	-.022
- 9.2	-.59	- 9.5	.035	-10.7	-.030
- 8.2	-.53	- 4.5	.010	- 9.6	-.035
0.0	.22	- 3.5	.0088	- 8.0	-.037
5.2	.65	- 2.0	.0080	- 6.0	-.036
6.6	.745	- 1.0	.0082	0.0	-.028
8.1	.81	0.0	.0088	2.6	-.025
8.9	.70	6.3	.035	5.0	-.018
10.0	.62	7.5	.045	7.0	-.007
11.6	.60	8.3	.055	8.0	-.004
13.1	.62	8.5	.069	8.6	-.007
15.3	.605	8.8	.110	9.0	-.026
17.1	.625	9.3	.135	9.2	-.056
20.8	.68	10.0	.156	10.0	-.074
28.0	.815	12.0	.19	11.0	-.080
30.0	.85	16.8	.27	12.0	-.082
		30.0	.64	15.0	-.087
				19.0	-.103
				27.0	-.142
				30.0	-.15

TABLE XIV. MODEL BLADE SECTION TWO-DIMENSIONAL AERODYNAMIC DATA (NACA 0012 Airfoil, δ_F = 5.0 deg, c = 2.69 in., M = .46, RN = .713 X 10^6)

α (deg)	C_l	α (deg)	C_d	α (deg)	C_m
-30.0	-.71	-30.0	.60	-30.0	.126
-21.3	-.53	-23.5	.36	-22.0	.074
-17.9	-.49	-18.5	.23	-18.0	.053
-14.8	-.48	-15.0	.175	-15.0	.045
-11.6	-.51	-12.0	.142	-13.0	.043
-10.4	-.54	-11.3	.130	-11.6	.035
- 9.4	-.615	-10.5	.110	-10.6	.016
- 7.9	-.50	-10.3	.100	- 9.9	-.020
0.0	.25	- 9.0	.050	- 9.3	-.033
3.1	.545	- 7.9	.030	- 8.6	-.036
3.5	.55	- 5.0	.0115	- 5.0	-.03[illegible]
4.7	.51	- 4.0	.0094	0.0	-.027
6.1	.515	- 2.8	.0082	5.0	-.02[illegible]
7.0	.55	- 1.5	.0080	6.5	-.020
8.1	.58	- .60	.0084	7.0	-.050
9.7	.59	0.0	.0090	7.8	-.066
13.7	.585	5.0	.060	9.6	-.077
18.0	.55	6.0	.092	15.0	-.089
23.0	.48	6.8	.110	24.0	-.121
30.0	.38	8.0	.135	30.0	-.143
		10.0	.165		
		13.5	.210		
		17.5	.26		
		30.0	.45		

TABLE XV. MODEL BLADE SECTION TWO-DIMENSIONAL AERODYNAMIC DATA (NACA 0012 Airfoil, δ_F = 5.0 deg, c = 2.69 in., M = .50, RN = .868 X 10^6)

α (deg)	C_l	α (deg)	C_d	α (deg)	C_m
-20.0	-.50	-25.0	.370	-24.0	.104
-14.4	-.43	-12.5	.150	-16.3	.050
-12.8	-.43	-11.0	.130	-14.6	.044
-10.3	-.475	-10.0	.110	-12.0	.041
- 8.3	-.53	- 9.0	.070	-11.0	.036
- 7.9	-.51	- 6.0	.022	-10.0	.022
0.0	.27	- 3.8	.010	- 8.3	-.032
1.4	.405	- 3.0	.0088	- 6.0	-.030
1.9	.41	- 2.25	.0084	0.0	-.026
3.6	.36	- 1.4	.0090	6.4	-.026
4.8	.34	- .50	.0110	6.8	-.030
6.6	.355	0.0	.013	8.4	-.066
9.4	.41	1.0	.031	9.2	-.075
11.3	.415	2.0	.054	10.3	-.080
14.3	.40	4.0	.090	16.0	-.091
20.0	.325	6.0	.120	24.0	-.112
		8.5	.150		
		15.0	.215		
		25.0	.335		

TABLE XVI. CONDITION DESCRIPTIONS

Condition Numbers	Description
1, 14, 35	Parameter Variation Base Point
2, 3, 7, 15, 19-21	Collective Variation
4-6, 16-18, 36, 37, 50-53	Flapping Variation
8-13, 22-31, 38-45	Shaft Angle and Collective Variation
32-34, 46-49	Blade and Wake Intersection
54-61	Blade Resonance*
62-67	High μ
68-71, 76-90	Blade Stall
72-75	Blade Stall with Flapping Variation
91, 93	Hover, Zero Lift, $\Omega_s R$ = 700 FT/SEC
92	Hover, Zero Lift, $\Omega_s R$ = 400 FT/SEC

*Run for 3 x scale stiffness aluminum blades only.

TABLE XVII. BLADE CONFIGURATIONS, TRANSDUCERS, AND CONDITIONS WITH VALID BLADE RESPONSE DATA (Blade Configuration: θ_1 = 0 deg, δ_F = 0 deg, S_E = 1)

Transducer Number (Channel)	Description	Condition Numbers with Valid Data
1	Blade Flapping at Hinge (β), deg	1-53, 62-93
2	Blade Lagging at Hinge (ζ), deg	1-53, 62-93
3	.20R Flapwise Bending ($M_{BF.20R}$), in.-lb	1-53, 62-93
4	.35R Flapwise Bending ($M_{BF.35R}$), in.-lb	1-53, 62-93
5	.45R Flapwise Bending ($M_{BF.45R}$), in.-lb	1-53, 62-93
6	.65R Flapwise Bending ($M_{BF.65R}$), in.-lb	1-51, 62-93
7	.80R Flapwise Bending ($M_{BF.80R}$), in.-lb	1-51, 62-74, 93
8	.20R Chordwise Bending ($M_{BC.20R}$), in.-lb	1-53, 62-93
9	.35R Chordwise Bending ($M_{BC.35R}$), in.-lb	1-53, 62-93
10	.45R Chordwise Bending ($M_{BC.45R}$), in.-lb	1-45, 62-73, 92, 93
11	.65R Chordwise Bending ($M_{BC.65R}$), in.-lb	1-49, 62-93
12	.80R Chordwise Bending ($M_{BC.80R}$), in.lb	1-45, 62-93
13	.20R Torsion ($M_{T.20R}$), in.-lb	1-53, 62-93
14	.35R Torsion ($M_{T.35R}$), in.-lb	1-53, 62-93

TABLE XVIII. BLADE CONFIGURATIONS, TRANSDUCERS, AND CONDITIONS WITH VALID BLADE RESPONSE DATA (Blade Configuration: θ_1 = -8 deg, δ_F = 0 deg, S_E = -)

Transducer Number (Channel)	Description	Condition Numbers with Valid Data
1	Blade Flapping at Hinge (β), deg	1-53, 62-93
2	Blade Lagging at Hinge (ζ), deg	1-53, 62-93
3	.20R Flapwise Bending ($M_{BF.20R}$), in.-lb	1-53, 62-93
4	.35R Flapwise Bending ($M_{BF.35R}$), in.-lb	1-53, 62-93
5	.45R Flapwise Bending ($M_{BF.45R}$), in.-lb	1-53, 62-93
6	.65R Flapwise Bending ($M_{BF.65R}$), in.-lb	1-53, 62-93
7	.80R Flapwise Bending ($M_{BF.80R}$), in.-lb	1-53, 62-93
8	.20R Chordwise Bending ($M_{BC.20R}$), in.-lb	1-53, 62-93
9	.35R Chordwise Bending ($M_{BC.35R}$), in.-lb	1-53, 62-93
10	.45R Chordwise Bending ($M_{BC.45R}$), in.-lb	1-53, 62-93
11	.65R Chordwise Bending ($M_{BC.65R}$), in.-lb	1-53, 62-93
12	.80R Chordwise Bending ($M_{BC.80R}$), in.-lb	1-53, 62-93
13	.20R Torsion ($M_{T.20R}$), in.-lb	1-53, 62-93
14	.35R Torsion ($M_{T.35R}$), in.-lb	1-53, 62-66, 92, 93

TABLE XIX. BLADE CONFIGURATIONS, TRANSDUCERS, AND CONDITIONS WITH VALID BLADE RESPONSE DATA (Blade Configuration: θ_1 = 0 deg, δ_F = 5 deg, S_E = 1)

Transducer Number (Channel)	Description	Condition Numbers with Valid Data
1	Blade Flapping at Hinge (β), deg	1-53, 62-93
2	Blade Lagging at Hinge (ζ), deg	1-53, 62-93
3	.20R Flapwise Bending ($M_{BF.20R}$), in.-lb	1-53, 62-93
4	.35R Flapwise Bending ($M_{BF.35R}$), in.-lb	1-53, 62-93
5	.45R Flapwise Bending ($M_{BF.45R}$), in.-lb	1-53, 62-93
6	.65R Flapwise Bending ($M_{BF.65R}$), in.-lb	1-53, 62-93
7	.80R Flapwise Bending ($M_{BF.80R}$), in.-lb	1-53, 62-93
8	.20R Chordwise Bending ($M_{BC.20R}$), in.-lb	1-53, 62-93
9	.35R Chordwise Bending ($M_{BC.35R}$), in.-lb	1-53, 62-93
10	.45R Chordwise Bending ($M_{BC.45R}$), in.-lb	1-53, 62-93
11	.65R Chordwise Bending ($M_{BC.65R}$), in.-lb	1-53, 62-93
12	.80R Chordwise Bending ($M_{BC.80R}$), in.-lb	1-53, 62-64, 93
13	.20R Torsion ($M_{T.20R}$), in.-lb	1-53, 62-93
14	.35R Torsion ($M_{T.35R}$), in.-lb	1-53, 62-93

TABLE XX. BLADE CONFIGURATIONS, TRANSDUCERS, AND CONDITIONS WITH VALID BLADE RESPONSE DATA (Blade Configuration: θ_1 = 0 deg, δ_F = 5 deg, S_E = 1)

Transducer Number (Channel)	Description	Condition Number with Valid Data
1	Blade Flapping at Hinge (β), deg	1-93
2	Blade Lagging of Hinge (ζ), deg	1-93
3	.20R Flapwise Bending ($M_{BF.20R}$), in.-lb	1-93
4	.35R Flapwise Bending ($M_{BF.35R}$), in.-lb	1-93
5	.45R Flapwise Bending ($M_{BF.45R}$), in.-lb	1-93
6	.65R Flapwise Bending ($M_{BF.65R}$), in.-lb	1-93
7	.80R Flapwise Bending ($M_{BF.80R}$), in.-lb	1-93
8	.20R Chordwise Bending ($M_{BC.20R}$), in.-lb	1-93
9	.35R Chordwise Bending ($M_{BC.35R}$), in.-lb	1-93
10	.45R Chordwise Bending ($M_{BC.45R}$), in.-lb	1-93
11	.65R Chordwise Bending ($M_{BC.65R}$), in.-lb	1-93
12	.80R Chordwise Bending ($M_{BC.80R}$), in.-lb	1-93
13	.20R Torsion ($M_{T.20R}$), in.-lb	1-93
14	.35R Torsion ($M_{T.20R}$), in.-lb	1-93

TABLE XXI. ZERO LIFT HOVER DISCRETE FREQUENCY COMPONENTS IN CHORDWISE BENDING RESPONSE (M_{BC}.20R, Condition 93)

Frequency Ratio ω_{NH}/Ω	Blade Configuration θ_1=0 deg, δ_P=0 deg, S_E=1			Blade Configuration θ_1=-8 deg, δ_P=0 deg, S_E=1			Blade Configuration θ_1=0 deg, δ_P=-5 deg, S_E=1			Blade Configuration θ_1=0 deg, δ_P=0 deg, S_E=3		
	A_{NH} in.-lb	B_{NH} in.-lb	R_{NH} in.-lb	A_{NH} in.-lb	B_{NH} in.-lb	R_{NH} in.-lb	A_{NH} in.-lb	B_{NH} in.-lb	R_{NH} in.-lb	A_{NH} in.-lb	B_{NH} in.-lb	R_{NH} in.-lb
.39	.70	-.53	.88	1.09	-.02	1.09	.55	1.03	1.17	1.08	-.86	1.38
3.50	.56	1.14	1.27	1.31	.96	1.62	1.38	.87	1.63	-.49	.62	.79
5.25	-.21	1.10	1.11	-.26	1.24	1.27	.16	-1.17	1.18	3.81	.52	3.85
7.00	-.90	-.10	.91	-.32	-.12	.34	-.60	-.10	.61	-.13	.05	.14
10.50	-.24	-.31	.39	-.58	.08	.58	-.37	-.40	.55	1.18	-.67	1.35

TABLE XXII. H-34 MODEL BLADE PERFORMANCE DATA (Configuration: θ_1 = 0 deg, δ_F = 0 deg, S_E = 1)

CONDITION	VS	DENSITY	VU	M1.90	ALPHA S	ALPHA C	THETA C	A1S	B1S
1	124.0	699.7	0.294	0.407	0.0	-3.4	3.5	-2.1	3.4
2	124.0	699.7	0.294	0.407	0.1	-4.7	5.5	-2.8	4.8
3	124.0	699.7	0.294	0.407	-0.0	-2.1	1.5	-1.5	2.0
4	124.0	699.7	0.294	0.407	0.1	-1.9	3.5	-2.6	1.9
5	124.0	699.7	0.294	0.407	-0.0	-5.0	3.5	-1.9	5.0
6	124.0	699.7	0.294	0.407	0.0	-3.3	3.5	0.2	3.3
7	124.0	699.7	0.294	0.407	0.0	-6.2	7.6	-3.9	6.2
8	124.0	699.7	0.294	0.407	-2.1	-3.2	1.5	-1.2	1.1
9	124.0	699.7	0.294	0.407	-2.0	-5.1	3.5	-1.9	3.1
10	124.0	699.7	0.294	0.407	-1.9	-6.4	5.5	-2.6	4.5
11	124.0	699.7	0.294	0.407	2.0	-0.5	1.5	-1.9	2.5
12	124.0	699.7	0.294	0.407	2.1	-1.8	3.5	-2.3	3.9
13	124.0	699.7	0.294	0.407	2.1	-3.3	5.5	-3.1	5.4
14	165.0	699.7	0.394	0.434	-2.5	-6.2	3.9	-2.2	3.7
15	165.0	699.7	0.394	0.434	-2.4	-8.0	5.9	-3.0	5.5
16	165.0	699.7	0.394	0.434	-2.4	-4.8	3.9	-2.5	2.4
17	165.0	699.7	0.394	0.434	-2.5	-6.2	3.9	0.3	3.8
18	165.0	699.7	0.394	0.434	-2.5	-6.2	3.9	-4.4	3.7
19	165.0	699.7	0.394	0.434	-2.5	-8.3	6.3	-3.0	5.7
20	165.0	699.7	0.394	0.434	-2.5	-9.7	8.3	-4.0	7.2
21	165.0	699.7	0.394	0.434	-2.5	-11.2	10.3	-5.2	8.7
22	165.0	699.7	0.394	0.434	-0.4	-4.9	3.9	-2.6	4.5
23	165.0	699.7	0.394	0.434	-0.4	-6.6	5.9	-3.3	6.2
24	165.0	699.7	0.394	0.434	-0.5	-8.4	8.3	-4.4	7.9
25	165.0	699.7	0.394	0.434	-0.5	-9.8	10.3	-5.7	9.3
26	165.0	699.7	0.394	0.434	-4.5	-7.3	3.9	-1.7	2.8
27	165.0	699.7	0.394	0.434	-4.5	-5.7	1.9	-1.2	1.1
28	165.0	699.7	0.394	0.434	-4.5	-9.6	6.3	-2.8	5.1
29	165.0	699.7	0.394	0.434	-4.5	-11.2	8.3	-3.5	6.7
30	165.0	699.7	0.394	0.434	-4.5	-12.6	10.3	-4.7	8.1
31	165.0	699.7	0.394	0.434	-4.5	-13.9	12.3	-5.8	9.4
32	146.0	699.7	0.352	0.424	0.0	-5.4	6.3	-3.0	5.4
33	146.0	699.7	0.352	0.424	1.0	-5.7	7.6	-3.8	6.8
34	146.0	699.7	0.352	0.424	2.1	-5.2	8.0	-4.1	7.2
35	146.0	699.7	0.352	0.424	-5.0	-12.6	11.1	-4.9	7.6
36	146.0	699.7	0.352	0.424	-5.0	-8.1	8.5	-3.7	3.1
37	146.0	699.7	0.352	0.424	-5.0	-17.1	14.2	-5.8	12.1
38	165.0	699.7	0.394	0.434	-6.6	-9.5	5.6	-1.5	2.9
39	165.0	699.7	0.394	0.434	-6.6	-11.4	7.6	-2.4	4.8
40	165.0	699.7	0.394	0.434	-6.5	-12.9	9.6	-3.3	6.4
41	165.0	699.7	0.394	0.434	-6.5	-14.3	11.6	-4.3	7.8
42	208.0	699.7	0.502	0.462	-5.0	-11.0	8.0	-2.8	6.1
43	208.0	699.7	0.502	0.462	-5.0	-12.6	9.8	-3.6	7.7
44	208.0	699.7	0.502	0.462	-5.0	-14.6	12.4	-4.9	9.7
45	208.0	699.7	0.502	0.462	-4.9	-16.9	15.7	-6.7	12.0
46	208.0	699.7	0.502	0.462	0.0	-6.6	6.4	-3.2	6.7
47	208.0	699.7	0.502	0.462	1.1	-8.5	9.4	-4.9	9.6
48	208.0	699.7	0.502	0.462	2.1	-8.0	9.6	-5.3	10.1
49	208.0	699.7	0.502	0.462	3.0	-10.0	12.7	-7.2	13.0
50	208.0	699.7	0.502	0.462	1.0	-6.1	9.0	-5.3	7.1

TABLE XXII - Continued

CONDITION	VS	OMEGAS*	VU	M1*90	ALPHA S	ALPHA C	THETA C	A1S	B1S
51	208.0	699.7	0.502	0.462	1.0	-12.0	13.0	-6.6	13.0
52	208.0	699.7	0.502	0.462	1.0	-11.8	13.1	-2.5	12.8
53	208.0	699.7	0.502	0.462	1.0	-11.6	13.4	-9.3	12.6
62	194.0	529.3	0.61[illegible]	0.377	2.0	-0.7	1.6	-2.2	2.7
63	194.0	461.6	0.709	0.347	2.0	-2.1	2.8	-2.7	4.1
64	194.0	400.2	0.813	0.320	2.0	-7.5	7.5	-4.2	9.5
65	256.0	699.7	0.622	0.500	2.0	0.3	0.5	-1.9	1.7
66	294.0	699.7	0.709	0.523	2.0	-0.2	0.9	-2.1	2.3
67	300.0	618.1	0.819	0.491	2.0	-0.8	1.3	-2.5	2.8
68	124.0	699.7	0.299	0.407	0.0	-8.3	11.4	-5.4	8.3
69	124.0	699.7	0.299	0.407	0.1	-9.1	12.6	-6.1	9.2
70	124.0	699.7	0.299	0.407	0.1	-9.8	13.9	-6.8	9.9
71	124.0	699.7	0.299	0.407	0.1	-9.9	14.3	-7.2	10.0
72	124.0	699.7	0.299	0.407	0.1	-4.4	9.7	-4.8	4.5
73	124.0	699.7	0.299	0.407	0.1	-10.1	13.2	-6.4	10.2
74	124.0	699.7	0.299	0.407	0.1	-9.1	12.5	-1.8	9.1
75	124.0	699.7	0.299	0.407	0.1	-8.4	12.1	-10.0	8.4
76	124.0	699.7	0.299	0.407	-2.0	-7.2	7.6	-3.1	5.2
77	124.0	699.7	0.299	0.407	-2.0	-8.5	9.6	-4.1	6.5
78	124.0	699.7	0.299	0.407	-2.0	-9.9	11.6	-5.2	7.9
79	124.0	699.7	0.299	0.407	-1.9	-11.1	13.6	-6.5	9.1
80	124.0	699.7	0.299	0.407	-5.0	-9.7	7.6	-2.7	4.6
81	124.0	699.7	0.299	0.407	-5.0	-11.0	9.8	-3.5	6.0
82	124.0	699.7	0.299	0.407	-5.0	-13.8	14.[illegible]	-6.4	8.9
83	124.0	699.7	0.299	0.407	-5.0	-11.9	11.4	-4.4	6.9
84	124.0	699.7	0.299	0.407	2.0	-2.8	5.6	-2.8	4.8
85	124.0	699.7	0.299	0.407	2.0	-4.1	7.6	-3.8	6.1
86	124.0	699.7	0.299	0.407	2.0	-5.4	9.6	-4.8	7.4
87	124.0	699.7	0.299	0.407	5.0	0.5	4.3	-2.6	4.5
88	124.0	699.7	0.299	0.407	5.0	-0.6	5.7	-3.3	5.6
89	124.0	699.7	0.299	0.407	4.9	-1.9	7.7	-3.8	6.9
90	124.0	699.7	0.299	0.407	5.0	-3.2	9.6	-5.3	8.1
91	0.0	699.7	0.0	0.313	0.0	-0.0	0.0	0.7	0.0
92	0.0	400.2	0.0	0.179	0.0	-0.0	0.0	-0.1	0.0
93	0.0	700.0	0.0	0.313	0.0	0.0	0.0	0.1	0.0

TABLE XXII - Continued

CONDITION	SA1S	SB1S	CL/SIGMA	CD/SIGMA	CY/SIGMA	CG/SIGMA	CPM/SIGMA.	CRM/SIGMA	V	R*D
1	0.0	0.0	0.0494	0.00269	-0.00134	0.00222	-0.000854	0.000136	62.0	0.00236
2	0.0	0.0	0.0693	0.00173	-0.00235	0.00318	-0.000636	0.000228	62.0	0.00236
3	0.0	0.0	0.0246	0.00217	-0.00067	0.00162	-0.000530	0.000081	62.0	0.00236
4	1.9	0.0	0.0600	0.00374	-0.00210	0.00190	0.000681	0.000081	62.0	0.00236
5	-1.9	-0.2	0.0370	0.00019	-0.00109	0.00190	-0.001346	0.000154	62.0	0.00236
6	0.0	2.2	0.0494	0.00163	0.00026	0.00213	-0.000173	0.001349	62.0	0.00236
7	0.0	0.0	0.0820	-0.00049	-0.00378	0.00498	-0.000103	0.000244	62.0	0.00236
8	0.0	0.0	0.0097	0.00116	-0.00032	0.00156	0.000023	-0.000000	62.0	0.00236
9	0.0	0.0	0.0377	-0.00017	-0.00108	0.00234	-0.000183	0.000092	62.0	0.00236
10	0.0	0.0	0.0593	-0.00131	-0.00192	0.00335	-0.000205	0.000147	62.0	0.00236
11	0.0	0.0	0.0377	0.00265	-0.00110	0.00136	-0.000133	0.000038	62.0	0.00236
12	0.0	0.0	0.0609	0.00300	-0.00194	0.00196	-0.000081	0.000222	62.0	0.00236
13	0.0	0.0	0.0762	0.00264	-0.00279	0.00311	-0.000084	0.000314	62.0	0.00236
14	0.0	0.0	0.0260	0.00013	-0.00088	0.00241	-0.000091	0.000028	82.8	0.00231
15	0.0	0.0	0.0447	-0.00098	-0.00191	0.00344	-0.000226	0.000103	82.8	0.00231
16	2.0	0.1	0.0414	0.00129	-0.00157	0.00236	0.000918	0.000085	82.8	0.00231
17	-0.2	2.2	0.0253	0.00055	-0.00010	0.00241	-0.000271	0.001363	82.8	0.00231
18	0.2	-2.0	0.0275	0.00068	-0.00209	0.00246	-0.000349	-0.001044	82.8	0.00231
19	0.0	0.0	0.0466	-0.00065	-0.00208	0.00358	-0.000447	0.000176	82.8	0.00231
20	0.0	0.0	0.0617	-0.00208	-0.00329	0.00528	-0.000395	0.000195	82.8	0.00231
21	0.0	0.0	0.0717	-0.00357	-0.00475	0.00744	-0.000398	0.000195	82.8	0.00231
22	0.0	0.0	0.0393	0.00183	-0.00158	0.00238	-0.000759	0.000054	82.8	0.00231
23	0.0	0.0	0.0550	0.00133	-0.00253	0.00356	-0.000841	0.000167	82.8	0.00231
24	0.0	0.0	0.0686	0.00018	-0.00399	0.00562	-0.000788	0.000221	82.8	0.00231
25	0.0	0.0	0.0769	-0.00113	-0.00545	0.00779	-0.000735	0.000184	82.8	0.00231
26	0.0	0.0	0.0115	0.00061	-0.00044	0.00206	0.000066	0.000039	82.8	0.00231
27	0.0	0.0	-0.0085	0.00232	-0.00001	0.00126	0.000044	-0.000054	82.8	0.00231
28	0.0	0.0	0.0351	-0.00193	-0.00147	0.00352	-0.000073	0.000075	82.8	0.00231
29	0.0	0.0	0.0512	-0.00373	-0.00293	0.00479	-0.000020	0.000150	82.8	0.00231
30	0.0	0.0	0.0629	-0.00588	-0.00380	0.00690	0.000033	0.000169	82.8	0.00231
31	0.0	0.0	0.0727	-0.00761	-0.00500	0.00925	0.000217	0.000225	82.8	0.00231
32	0.0	0.0	0.0612	0.00173	-0.00243	0.00322	-0.000755	0.000164	73.0	0.00236
33	0.0	0.0	0.0701	0.00149	-0.00357	0.00429	-0.000571	0.000206	73.0	0.00236
34	0.0	0.0	0.0790	0.00222	-0.00429	0.00490	-0.000279	0.000342	73.0	0.00236
35	0.0	0.0	0.0700	-0.00730	-0.00380	0.00732	0.000011	0.000145	73.0	0.00236
36	3.4	0.3	0.0703	-0.00210	-0.00329	0.00470	0.001981	0.000071	73.0	0.00236
37	-3.4	-0.2	0.0712	-0.01328	-0.00397	0.01073	-0.001632	0.000292	73.0	0.00236
38	0.0	0.0	0.0085	0.00058	0.00009	0.00209	0.000192	-0.000111	82.8	0.00231
39	0.0	0.0	0.0281	-0.00250	-0.00069	0.00354	0.000096	-0.000074	82.8	0.00231
40	0.0	0.0	0.0464	-0.00511	-0.00155	0.00519	0.000131	-0.000036	82.8	0.00231
41	0.0	0.0	0.0588	-0.00737	-0.00284	0.00707	0.000205	0.000039	82.8	0.00231
42	0.0	0.0	0.0229	-0.00025	-0.00056	0.00351	-0.000234	-0.000115	104.0	0.00226
43	0.0	0.0	0.0369	-0.00164	-0.00135	0.00476	-0.000179	-0.000096	104.0	0.00226
44	0.0	0.0	0.0518	-0.00384	-0.00303	0.00746	-0.000123	-0.000019	104.0	0.00226
45	0.0	0.0	0.0660	-0.00675	-0.00505	0.01121	-0.000049	0.000058	104.0	0.00226
46	0.0	0.0	0.0415	0.00438	-0.00168	0.00308	-0.001757	-0.000058	104.0	0.00226
47	0.0	0.0	0.0637	0.00396	-0.00421	0.00573	-0.001778	0.000085	104.0	0.00226
48	0.0	0.0	0.0894	0.00477	-0.00497	0.00603	-0.001723	0.000112	104.0	0.00226
49	0.0	0.0	0.0835	0.00445	-0.00695	0.00960	-0.001877	0.000249	104.0	0.00226
50	3.5	0.2	0.0798	0.00822	-0.00569	0.00549	0.000102	0.000022	104.0	0.00226

TABLE XXII - Concluded

CONDITION	SAIS	SBIS	CL/SIGMA	CC/SIGMA	CY/SIGMA	CD/SIGMA	CPM/SIGMA	CRM/SIGMA	V	RHO
51	-0.9	-0.0	0.0739	0.00177	-0.00578	0.00934	-0.002459	0.000157	104.0	0.00226
52	-0.2	4.0	0.0774	0.00359	-0.00040	0.00972	-0.001942	0.002524	104.0	0.00226
53	0.0	-2.1	0.0783	0.00238	-0.00922	0.00977	-0.002213	-0.001132	104.0	0.00226
62	0.0	0.0	0.0113	0.00473	-0.00030	0.00146	-0.001175	0.000060	97.0	0.00228
63	0.0	0.0	0.0149	0.00620	-0.00060	0.00149	-0.001407	0.000122	97.0	0.00228
64	0.0	0.0	0.0184	0.01028	-0.00160	0.00257	-0.002205	-0.000070	97.0	0.00228
65	0.0	0.0	0.0053	0.00383	-0.00009	0.00145	-0.000982	0.000034	129.0	0.00226
66	0.0	0.0	0.0072	0.00428	-0.00021	0.00149	-0.001626	0.000075	147.0	0.00221
67	0.0	0.0	0.0092	0.00837	-0.00026	0.00159	-0.003137	0.000096	150.0	0.00221
68	0.0	0.0	0.0915	-0.00306	-0.00529	0.00848	0.000342	0.000433	62.0	0.00238
69	0.0	0.0	0.0959	-0.00456	-0.00604	0.00990	0.000549	0.000415	62.0	0.00238
70	0.0	0.0	0.0984	-0.00540	-0.00621	0.01135	0.000719	0.000542	62.0	0.00238
71	0.0	0.0	0.0996	-0.00575	-0.00654	0.01185	0.000962	0.000488	62.0	0.00238
72	3.5	0.3	0.0954	0.00579	-0.00529	0.00648	0.001002	0.000324	62.0	0.00238
73	-0.9	0.0	0.0957	-0.00366	-0.00579	0.01062	-0.001014	0.000415	62.0	0.00238
74	-0.2	4.1	0.0954	-0.00168	0.00139	0.00999	-0.000097	0.002546	62.0	0.00238
75	0.3	-3.8	0.0959	-0.00345	-0.01306	0.00926	-0.000127	-0.001626	62.0	0.00238
76	0.0	0.0	0.0696	-0.00220	-0.00270	0.00418	-0.000176	0.000189	62.0	0.00238
77	0.0	0.0	0.0812	-0.00384	-0.00386	0.00614	-0.000006	0.000262	62.0	0.00238
78	0.0	0.0	0.0887	-0.00559	-0.00503	0.00846	0.000146	0.000353	62.0	0.00238
79	0.0	0.0	0.0953	-0.00706	-0.00629	0.01083	0.000298	0.000353	62.0	0.00238
80	0.0	0.0	0.0563	-0.00477	-0.00189	0.00420	0.000049	0.000141	62.0	0.00238
81	0.0	0.0	0.0737	-0.00711	-0.00289	0.00602	0.000255	0.000269	62.0	0.00238
82	0.0	0.0	0.0911	-0.01176	-0.00573	0.01144	0.000571	0.000360	62.0	0.00238
83	0.0	0.0	0.0811	-0.00877	-0.00369	0.00785	0.000466	0.000360	62.0	0.00238
84	0.0	0.0	0.0713	0.00240	-0.00262	0.00263	-0.000051	0.000279	62.0	0.00238
85	0.0	0.0	0.0649	0.00174	-0.00396	0.00445	0.000083	0.000279	62.0	0.00238
86	0.0	0.0	0.0925	0.00060	-0.00521	0.00654	0.000253	0.000443	62.0	0.00238
87	0.0	0.0	0.0737	0.00627	-0.00294	0.00156	0.000058	0.000356	62.0	0.00238
88	0.0	0.0	0.0821	0.00619	-0.00370	0.00256	0.000101	0.000447	62.0	0.00238
89	0.0	0.0	0.0932	0.00554	-0.00502	0.00466	0.000273	0.000461	62.0	0.00238
90	0.0	0.0	0.0994	0.00516	-0.00602	0.00657	0.000552	0.000497	62.0	0.00238
91	0.0	0.0	-0.0017	-0.00038	-0.00008	0.00132	0.000151	0.0	0.0	0.00239
92	0.0	0.0	-0.0006	-0.00031	0.00025	0.00125	0.000296	0.000055	0.0	0.00239
93	0.0	0.0	0.0005	-0.00050	0.00013	0.00128	0.000311	0.000027	0.0	0.00237

TABLE XXIII. H-34 MODEL BLADE PERFORMANCE DATA (Configuration: θ_1 = -8 deg, δ_F = 0 deg, S_E = 1)

CONDITION	VS	OMEGAS*R	MU	M1.90	ALPHA S	ALPHA C	THETA C	A1S	B1S
1	124.0	699.7	0.299	0.407	0.0	-2.9	3.5	-1.2	2.9
2	124.0	699.7	0.299	0.407	0.1	-4.2	5.5	-1.9	4.3
3	124.0	699.7	0.299	0.407	-0.0	-0.9	1.5	-0.3	0.9
4	124.0	699.7	0.299	0.407	0.1	-1.3	3.5	-1.3	1.4
5	124.0	699.7	0.299	0.407	-0.0	-4.3	3.5	-0.8	4.3
6	124.0	699.7	0.299	0.407	0.0	-2.8	3.5	1.1	2.8
7	124.0	699.7	0.299	0.407	0.0	-5.5	7.3	-2.5	5.5
8	124.0	699.7	0.299	0.407	-2.1	-2.6	1.5	0.1	0.5
9	124.0	699.7	0.299	0.407	-2.0	-4.3	3.5	-0.8	2.3
10	124.0	699.7	0.299	0.407	-1.9	-5.7	5.5	-1.6	3.8
11	124.0	699.7	0.299	0.407	2.0	0.2	1.5	-0.6	1.8
12	124.0	699.7	0.299	0.407	2.1	-1.2	3.5	-1.3	3.3
13	124.0	699.7	0.299	0.407	2.1	-2.8	5.5	-2.1	4.9
14	165.6	699.7	0.399	0.434	-2.5	-5.1	3.8	-0.6	2.6
15	165.6	699.7	0.399	0.434	-2.4	-6.9	5.8	-1.3	4.5
16	165.6	699.7	0.399	0.434	-2.4	-4.0	3.8	-0.9	1.6
17	165.6	699.7	0.399	0.434	-2.5	-4.8	3.8	1.8	2.3
18	165.6	699.7	0.399	0.434	-2.5	-5.3	3.8	-2.6	2.8
19	165.6	699.7	0.399	0.434	-2.5	-6.8	5.7	-1.3	4.3
20	165.6	699.7	0.399	0.434	-2.5	-8.6	7.7	-2.2	6.1
21	165.6	699.7	0.399	0.434	-2.5	-10.0	9.7	-3.1	7.5
22	165.6	699.7	0.399	0.434	-0.4	-3.9	3.8	-0.9	3.5
23	165.6	699.7	0.399	0.434	-0.4	-5.6	5.8	-1.7	5.2
24	165.6	699.7	0.399	0.434	-0.5	-7.2	7.7	-2.6	6.7
25	165.6	699.7	0.399	0.434	-0.5	-8.7	9.7	-3.6	8.2
26	165.6	699.7	0.399	0.434	-4.5	-6.4	3.8	-0.1	1.9
27	165.6	699.7	0.399	0.434	-4.5	-4.6	1.8	0.6	0.1
28	165.6	699.7	0.399	0.434	-4.6	-8.4	5.7	-0.8	3.8
29	165.6	699.7	0.399	0.434	-4.5	-10.0	7.7	-1.7	5.5
30	165.6	699.7	0.399	0.434	-4.5	-11.4	9.7	-2.7	6.9
31	165.6	699.7	0.399	0.434	-4.5	-12.7	11.7	-3.8	8.2
32	146.8	699.7	0.352	0.420	0.6	-4.6	5.4	-1.9	4.6
33	146.8	699.7	0.352	0.420	1.0	-4.6	6.4	-2.4	5.6
34	146.8	699.7	0.352	0.420	2.1	-4.1	6.9	-2.8	6.2
35	146.8	699.7	0.352	0.420	-5.0	-11.3	9.8	-2.8	6.3
36	146.8	699.7	0.352	0.420	-5.0	-7.2	7.3	-2.3	2.2
37	146.8	699.7	0.352	0.420	-5.0	-15.4	12.5	-3.8	10.4
38	165.6	699.7	0.399	0.434	-6.6	-8.7	5.3	-0.4	2.1
39	165.6	699.7	0.399	0.434	-6.5	-10.5	7.3	-1.4	4.0
40	165.6	699.7	0.399	0.434	-6.5	-12.0	9.3	-2.2	5.5
41	165.6	699.7	0.399	0.434	-6.5	-13.4	11.3	-3.3	6.9
42	208.0	699.7	0.502	0.467	-5.0	-8.7	6.8	-0.6	3.7
43	208.0	699.7	0.502	0.467	-5.0	-10.6	8.5	-1.5	5.6
44	208.0	699.7	0.502	0.467	-5.0	-12.7	10.9	-2.7	7.7
45	208.0	699.7	0.502	0.467	-4.9	-14.7	13.7	-4.3	9.8
46	208.0	699.7	0.502	0.467	0.0	-5.8	4.9	-5.8	5.8
47	208.0	699.7	0.502	0.467	1.1	-6.4	7.9	-2.5	7.5
48	208.0	699.7	0.502	0.467	2.1	-5.8	7.9	-2.7	7.9
49	208.0	699.7	0.502	0.467	3.0	-7.1	10.2	-4.2	10.1
50	208.0	699.7	0.502	0.467	1.0	-4.1	7.4	-2.9	5.1

TABLE XXIII - Continued

CONDITION	VS	OMEGAS*R	MU	M1.90	ALPHA S	ALPHA C	THETA C	A1S	B1S
51	206.0	699.7	0.502	0.467	1.0	-10.7	12.4	-4.5	11.7
52	208.0	699.7	0.502	0.467	1.0	-9.8	11.7	-0.2	10.8
53	208.0	699.7	0.502	0.467	1.0	-9.3	11.3	-6.2	10.3
62	194.0	529.8	0.618	0.381	2.0	2.1	-0.6	0.5	-0.1
63	194.0	461.6	0.709	0.350	2.0	1.5	-0.2	0.6	0.5
64	194.0	400.2	0.818	0.323	2.0	-4.4	4.5	0.1	6.4
65	258.0	699.7	0.622	0.502	2.0	3.8	-1.9	1.1	-1.8
66	294.0	699.7	0.709	0.530	2.0	4.4	-2.4	1.7	-2.4
67	300.0	618.1	0.819	0.496	2.0	7.3	-4.9	2.5	-5.3
68	124.0	699.7	0.299	0.407	0.0	-7.5	10.1	-4.1	7.5
69	124.0	699.7	0.299	0.407	0.1	-8.3	11.2	-4.7	8.3
70	124.0	699.7	0.299	0.407	0.1	-9.0	12.3	-5.2	9.1
71	124.0	699.7	0.299	0.407	0.1	-9.4	12.9	-5.5	9.5
72	124.0	699.7	0.299	0.407	0.1	-4.1	5.8	-3.7	4.2
73	124.0	699.7	0.299	0.407	0.1	-9.3	11.8	-4.9	9.4
74	124.0	699.7	0.299	0.407	0.1	-8.4	11.4	-0.7	8.5
75	124.0	699.7	0.299	0.407	0.1	-7.8	10.7	-8.3	7.9
76	124.0	699.7	0.299	0.407	-2.0	-7.1	7.3	-2.2	5.1
77	124.0	699.7	0.299	0.407	-2.0	-8.5	9.3	-3.2	6.5
78	124.0	699.7	0.299	0.407	-2.0	-9.8	11.3	-4.4	7.8
79	124.0	699.7	0.299	0.407	-1.9	-11.3	13.3	-5.5	9.3
80	124.0	699.7	0.299	0.407	-5.1	-9.0	6.7	-1.6	4.0
81	124.0	699.7	0.299	0.407	-5.0	-10.5	9.0	-2.6	5.5
82	124.0	699.7	0.299	0.407	-5.0	-13.4	13.2	-5.0	8.4
83	124.0	699.7	0.299	0.407	-5.0	-11.4	10.3	-3.1	6.4
84	124.0	699.7	0.299	0.407	2.0	-2.8	5.3	-2.1	4.8
85	124.0	699.7	0.299	0.407	2.0	-4.0	7.3	-3.0	6.0
86	124.0	699.7	0.299	0.407	2.1	-5.3	9.3	-4.0	7.4
87	124.0	699.7	0.299	0.407	5.0	0.8	3.7	-1.7	4.2
88	124.0	699.7	0.299	0.407	5.0	-0.0	4.9	-2.3	5.0
89	124.0	699.7	0.299	0.407	4.9	-1.5	6.8	-3.2	6.4
90	124.0	699.7	0.299	0.407	5.0	-3.3	9.4	-4.5	8.3
91	0.0	699.7	0.0	0.313	0.0	-0.3	0.0	-0.1	0.3
92	0.0	400.2	0.0	0.179	0.0	0.3	0.0	0.2	-0.3
93	0.0	699.7	0.0	0.313	0.0	-0.5	0.0	0.2	0.5

TABLE XXIII - Continued

CONDITION	SAIS	SAIS	CL/SIGMA	CD/SIGMA	CY/SIGMA	CQ/SIGMA	CPM/SIGMA	CRM/SIGMA	V	RHO
1	0.0	0.0	0.0488	0.00280	-0.00109	0.00218	-0.001124	0.000044	62.0	0.00235
2	0.0	0.0	0.0691	0.00175	-0.00169	0.00324	-0.001047	0.000118	62.0	0.00235
3	0.0	0.0	0.0196	0.00278	-0.00025	0.00154	-0.007490	0.000007	62.0	0.00235
4	1.9	0.2	0.0596	0.00399	-0.00135	0.00200	0.000159	0.000062	62.0	0.00235
5	-1.8	-0.1	0.0374	0.00097	-0.00059	0.00227	-0.001703	0.000062	62.0	0.00235
6	-0.0	2.1	0.0486	0.00198	0.00068	0.00218	-0.000629	0.001225	62.0	0.00235
7	0.0	0.0	0.0622	0.00002	-0.00244	0.00467	-0.000552	0.000226	62.0	0.00235
8	0.0	0.0	0.0078	0.00166	0.00001	0.00156	-0.000328	-0.000013	62.0	0.00235
9	0.0	0.0	0.0372	0.00004	-0.00058	0.00225	-0.000473	0.000037	62.0	0.00235
10	0.0	0.0	0.0592	-0.00088	-0.00134	0.00327	-0.000433	0.000073	62.0	0.00235
11	0.0	0.0	0.0268	0.00305	-0.00077	0.00142	-0.000355	0.000093	62.0	0.00235
12	0.0	0.0	0.0601	0.00322	-0.00127	0.00197	-0.000426	0.000186	62.0	0.00235
13	0.0	0.0	0.0768	0.00267	-0.00212	0.00317	-0.000386	0.000223	62.0	0.00235
14	0.0	0.0	0.0272	0.00098	-0.00065	0.00223	-0.000242	-0.000028	82.8	0.00230
15	0.0	0.0	0.0446	-0.00012	-0.00114	0.00322	-0.000390	0.000028	82.8	0.00230
16	1.9	-0.1	0.0413	0.00181	-0.00068	0.00223	0.000614	-0.000028	82.8	0.00230
17	-0.0	2.1	0.0724	0.00161	0.00033	0.00209	-0.000308	0.001142	82.8	0.00230
18	0.2	-1.9	0.0272	0.00138	-0.00132	0.00228	-0.000400	-0.001085	82.8	0.00230
19	0.0	0.0	0.0453	0.00036	-0.00114	0.00312	-0.000434	0.000026	82.8	0.00230
20	0.0	0.0	0.0606	-0.00110	-0.00192	0.00454	-0.000526	0.000083	82.8	0.00230
21	0.0	0.0	0.0720	-0.00274	-0.00287	0.00647	-0.000429	0.000196	82.8	0.00230
22	0.0	0.0	0.0407	0.00241	-0.00089	0.00220	-0.000558	0.000017	82.8	0.00230
23	0.0	0.0	0.0572	0.00159	-0.00167	0.00333	-0.000668	0.000074	82.8	0.00230
24	0.0	0.0	0.0686	0.00044	-0.00244	0.00469	-0.000627	0.000128	82.8	0.00230
25	0.0	0.0	0.0794	-0.00096	-0.00357	0.00692	-0.000549	0.000128	82.8	0.00230
26	0.0	0.0	0.0107	0.00060	-0.00001	0.00193	0.000334	-0.000074	82.8	0.00230
27	0.0	0.0	-0.0074	0.00234	0.00068	0.00127	0.000356	-0.000074	82.8	0.00230
28	0.0	0.0	0.0316	-0.00104	-0.00052	0.00296	0.000226	-0.000019	82.8	0.00230
29	0.0	0.0	0.0503	-0.00305	-0.00122	0.00429	0.000154	0.000018	82.8	0.00230
30	0.0	0.0	0.0034	-0.00494	-0.00199	0.00594	0.000232	0.000094	82.8	0.00230
31	0.0	0.0	0.0739	-0.00719	-0.00329	0.00834	0.000367	0.000151	82.8	0.00230
32	0.0	0.0	0.0627	0.00219	-0.00170	0.00320	-0.000847	0.000064	73.0	0.00230
33	0.0	0.0	0.0727	0.00253	-0.00218	0.00387	-0.000747	0.000144	73.0	0.00230
34	0.0	0.0	0.0796	0.00328	-0.00284	0.00440	-0.000707	0.000171	73.0	0.00230
35	0.0	0.0	0.0709	-0.00683	-0.00216	0.00631	0.000268	0.000158	73.0	0.00230
36	3.5	0.4	0.0715	-0.00206	-0.00199	0.00438	0.002193	0.000082	73.0	0.00230
37	-3.5	-0.3	0.0713	-0.01247	-0.00259	0.00928	-0.001610	0.000252	73.0	0.00230
38	0.0	0.0	0.0127	0.00024	0.00009	0.00219	0.000372	-0.000065	82.8	0.00230
39	0.0	0.0	0.0344	-0.00269	-0.00052	0.00365	0.000375	-0.000046	82.8	0.00230
40	0.0	0.0	0.0522	-0.00525	-0.00121	0.00521	0.000378	0.000011	82.8	0.00230
41	0.0	0.0	0.0654	-0.00781	-0.00225	0.00729	0.000475	0.000068	82.8	0.00230
42	0.0	0.0	0.0209	0.00073	0.00006	0.00275	0.000329	-0.000047	104.0	0.00229
43	0.0	0.0	0.0365	-0.00065	-0.00055	0.00393	0.000312	-0.000028	104.0	0.00229
44	0.0	0.0	0.0507	-0.00269	-0.00154	0.00592	0.000296	0.000009	104.0	0.00229
45	0.0	0.0	0.0653	-0.00545	-0.00307	0.00920	0.000375	0.000066	104.0	0.00229
46	0.0	0.0	0.0404	0.00416	-0.00096	0.00246	-0.000767	0.000009	104.0	0.00229
47	0.0	0.0	0.0622	0.00372	-0.00249	0.00470	-0.000917	0.000074	104.0	0.00229
48	0.0	0.0	0.0764	0.00424	-0.00269	0.00485	-0.000844	0.000138	104.0	0.00229
49	0.0	0.0	0.0810	0.00433	-0.00424	0.00718	-0.000510	0.000175	104.0	0.00229
50	3.5	0.3	0.0767	0.00736	-0.00352	0.00451	0.000839	0.000088	104.0	0.00229

TABLE XXIII - Concluded

CONDITION	SAIS	SAIS	CL/SIGMA	CD/SIGMA	CY/SIGMA	CG/SIGMA	CPM/SIGMA	CRM/SIGMA	V	RHO
51	-0.8	0.1	0.0768	0.00125	-0.00396	0.00906	-0.001547	0.000259	104.0	0.00229
52	-0.2	4.0	0.0772	0.00296	0.00161	0.00859	-0.001070	0.002307	104.0	0.00229
53	0.2	-1.9	0.0773	0.00267	-0.00691	0.00792	-0.001067	-0.000879	104.0	0.00229
62	0.0	0.0	0.0115	0.00645	-0.00060	0.00129	-0.001030	0.000059	97.0	0.00229
63	0.0	0.0	0.0147	0.00800	-0.00060	0.00127	-0.001313	0.000122	97.0	0.00229
64	0.0	0.0	0.0195	0.01317	-0.00079	0.00154	-0.002839	-0.000012	97.0	0.00229
65	0.0	0.0	0.0053	0.00425	-0.00044	0.00136	-0.000910	0.000073	129.0	0.00225
66	0.0	0.0	0.0090	0.00719	-0.00065	0.00118	-0.001234	0.000151	147.0	0.00224
67	0.0	0.0	0.0122	0.01110	-0.00049	0.00083	-0.001634	0.000421	150.0	0.00222
68	0.0	0.0	0.0929	-0.00215	-0.00416	0.00767	-0.000060	0.000308	62.0	0.00235
69	0.0	0.0	0.0988	-0.00343	-0.00477	0.00906	0.000035	0.000365	62.0	0.00235
70	0.0	0.0	0.1003	-0.00457	-0.00477	0.01035	0.000185	0.000457	62.0	0.00235
71	0.0	0.0	0.1014	-0.00503	-0.00519	0.01109	0.000373	0.000494	62.0	0.00235
72	3.4	0.3	0.0967	0.00646	-0.00409	0.00615	0.000388	0.000272	62.0	0.00235
73	-0.7	-0.1	0.0969	-0.00230	-0.00469	0.00979	-0.001621	0.000383	62.0	0.00235
74	0.0	3.9	0.0971	-0.00022	0.00234	0.00956	-0.000898	0.002414	62.0	0.00235
75	0.2	-3.6	0.0973	-0.00145	-0.01145	0.00850	-0.001088	-0.001666	62.0	0.00235
76	0.0	0.0	0.0745	-0.00248	-0.00214	0.00452	-0.000105	0.000210	62.0	0.00235
77	0.0	0.0	0.0861	-0.00432	-0.00332	0.00659	-0.000028	0.000247	62.0	0.00235
78	0.0	0.0	0.0926	-0.00599	-0.00459	0.00899	0.000196	0.000339	62.0	0.00235
79	0.0	0.0	0.0972	-0.00812	-0.00527	0.01139	0.000181	0.000431	62.0	0.00235
80	0.0	0.0	0.0556	-0.00390	-0.00132	0.00393	0.000091	0.000162	62.0	0.00235
81	0.0	0.0	0.0747	-0.00667	-0.00225	0.00573	0.000168	0.000180	62.0	0.00235
82	0.0	0.0	0.0913	-0.01154	-0.00471	0.01086	0.000300	0.000272	62.0	0.00235
83	0.0	0.0	0.0624	-0.00817	-0.00285	0.00726	0.000229	0.000291	62.0	0.00235
84	0.0	0.0	0.0754	0.00242	-0.00206	0.00298	-0.000115	0.000154	62.0	0.00235
85	0.0	0.0	0.0879	0.00168	-0.00325	0.00478	0.000128	0.000264	62.0	0.00235
86	0.0	0.0	0.0962	0.00053	-0.00410	0.00686	0.000334	0.000357	62.0	0.00235
87	0.0	0.0	0.0746	0.00624	-0.00205	0.00176	0.000097	0.000342	62.0	0.00235
88	0.0	0.0	0.0838	0.00627	-0.00281	0.00260	0.000248	0.000305	62.0	0.00235
89	0.0	0.0	0.0934	0.00562	-0.00399	0.00430	0.000289	0.000300	62.0	0.00235
90	0.0	0.0	0.1022	0.00426	-0.00517	0.00712	0.000551	0.000411	62.0	0.00235
91	0.0	0.0	0.0002	-0.00034	-0.00008	0.00138	0.000215	0.000037	0.0	0.00236
92	0.0	0.0	0.0006	0.00991	0.0	0.00154	-0.003678	0.000225	0.0	0.00236
93	0.0	0.0	0.0001	-0.00221	0.00013	0.00133	0.001640	0.000101	0.0	0.00236

TABLE XXIV. H-34 MODEL BLADE PERFORMANCE DATA (Configuration: θ_1 = 0 deg, δ_F = 5 deg, S_E = 1)

CONDITION	VS	OMEGAS*R	MU	M1.90	ALPHA S	ALPHA C	THETA C	A1S	B1S
1	124.0	699.7	0.299	0.407	0.0	-1.4	1.7	-1.5	1.4
2	124.0	699.7	0.299	0.407	0.1	-2.8	3.7	-2.3	2.8
3	124.0	699.7	0.299	0.407	-0.0	0.6	-0.3	-0.9	-0.7
4	124.0	699.7	0.299	0.407	0.1	0.1	1.7	-1.9	-0.0
5	124.0	699.7	0.299	0.407	-0.0	-2.5	1.7	-1.1	2.5
6	124.0	699.7	0.299	0.407	0.0	-1.3	1.7	0.8	1.3
7	124.0	699.7	0.299	0.407	0.0	-3.6	5.0	-2.7	3.6
8	124.0	699.7	0.299	0.407	-2.1	-1.1	-0.3	-0.6	-1.0
9	124.0	699.7	0.299	0.407	-2.0	-1.3	1.7	-1.4	0.9
10	124.0	699.7	0.299	0.407	-1.9	-4.3	3.7	-1.9	2.4
11	124.0	699.7	0.299	0.407	2.0	2.0	-0.3	-1.0	-0.0
12	124.0	699.7	0.299	0.407	2.1	0.2	1.7	-1.8	1.9
13	124.0	699.7	0.299	0.407	2.1	-1.2	3.7	-2.4	3.3
14	165.0	699.7	0.399	0.434	-2.5	-3.0	2.7	-1.1	0.6
15	165.0	699.7	0.399	0.434	-2.4	-5.2	4.7	-1.9	2.8
16	165.0	699.7	0.399	0.434	-2.4	-2.2	2.7	-1.7	-0.2
17	165.0	699.7	0.399	0.434	-2.5	-2.9	2.7	1.3	0.5
18	165.0	699.7	0.399	0.434	-2.5	-3.0	2.7	-3.4	0.6
19	165.0	699.7	0.399	0.434	-2.5	-4.8	4.3	-1.7	2.3
20	165.0	699.7	0.399	0.434	-2.5	-6.6	6.3	-2.5	4.1
21	165.0	699.7	0.399	0.434	-2.5	-8.1	8.3	-3.6	5.6
22	165.0	699.7	0.399	0.434	-0.4	-2.3	2.7	-1.7	1.8
23	165.0	699.7	0.399	0.434	-0.4	-4.0	4.7	-2.3	3.6
24	165.0	699.7	0.399	0.434	-0.5	-5.3	6.3	-3.0	4.8
25	165.0	699.7	0.399	0.434	-0.5	-6.8	8.3	-3.9	6.4
26	165.0	699.7	0.399	0.434	-4.5	-4.5	2.7	-1.0	-0.0
27	165.0	699.7	0.399	0.434	-4.5	-2.7	0.7	-0.5	-1.8
28	165.0	699.7	0.399	0.434	-4.6	-6.1	4.3	-1.2	1.5
29	165.0	699.7	0.399	0.434	-4.5	-7.9	6.3	-2.2	3.3
30	165.0	699.7	0.399	0.434	-4.5	-9.5	8.3	-3.0	5.0
31	165.0	699.7	0.399	0.434	-4.5	-10.9	10.3	-4.0	6.4
32	146.0	699.7	0.352	0.420	0.0	-2.5	3.7	-2.0	2.6
33	146.0	699.7	0.352	0.420	1.0	-2.3	4.3	-2.3	3.4
34	146.0	699.7	0.352	0.420	2.1	-1.7	4.4	-2.5	3.8
35	146.0	699.7	0.352	0.420	-5.0	-9.3	7.9	-2.8	4.3
36	146.0	699.7	0.352	0.420	-5.0	-4.6	5.3	-2.3	-0.4
37	146.0	699.7	0.352	0.420	-5.0	-13.7	10.4	-3.1	8.8
38	165.0	699.7	0.399	0.434	-6.6	-5.8	3.0	-0.4	-0.8
39	165.0	699.7	0.399	0.434	-6.6	-7.6	5.0	-1.0	1.1
40	165.0	699.7	0.399	0.434	-6.5	-9.5	7.0	-1.8	3.0
41	165.0	699.7	0.399	0.434	-6.5	-11.0	9.0	-2.7	4.5
42	208.0	699.7	0.502	0.462	-5.0	-6.3	5.6	-0.8	1.3
43	208.0	699.7	0.502	0.462	-5.0	-8.1	7.6	-1.5	3.2
44	208.0	699.7	0.502	0.462	-5.0	-10.3	9.6	-2.5	5.3
45	208.0	699.7	0.502	0.462	-4.9	-12.6	12.7	-4.2	7.6
46	208.0	699.7	0.502	0.462	0.0	-2.1	3.6	-1.4	2.1
47	208.0	699.7	0.502	0.462	1.1	-3.8	6.1	-2.3	4.8
48	208.0	699.7	0.502	0.462	2.1	-3.3	6.1	-2.6	5.3
49	208.0	699.7	0.502	0.462	3.0	-4.5	8.3	-3.6	7.4
50	208.0	699.7	0.502	0.462	1.0	-1.1	5.3	-2.6	2.0

TABLE XXIV - Continued

CONDITION	VS	OMEGASQR	MU	M1,90	ALPHA S	ALPHA C	THETA C	A1S	B1S
51	200.0	699.7	0.502	0.462	1.0	-7.9	10.4	-3.8	8.9
52	200.0	699.7	0.502	0.462	1.0	-6.7	9.4	0.8	7.7
53	200.0	699.7	0.502	0.462	1.0	-6.5	9.3	-5.7	7.4
62	194.0	529.6	0.61[illegible]	0.379	2.0	4.1	-2.6	-0.8	-2.1
63	194.0	461.6	0.709	0.349	2.0	2.9	-2.4	-1.2	-0.9
64	194.0	460.2	0.815	0.322	2.0	-2.4	1.5	-2.1	4.4
65	250.0	699.7	0.622	0.502	2.0	8.2	-3.1	0.8	-6.2
66	294.0	699.7	0.709	0.530	2.0	10.7	-4.5	1.6	-8.7
67	300.0	618.1	0.819	0.496	2.0	11.1	-5.8	1.5	-9.1
68	124.0	699.7	0.299	0.407	0.1	-4.5	7.1	-3.3	4.6
69	124.0	699.7	0.299	0.407	0.1	-5.1	7.9	-3.7	5.2
70	124.0	699.7	0.299	0.407	0.1	-5.8	8.9	-4.2	5.8
71	124.0	699.7	0.299	0.407	0.1	-6.2	9.5	-4.4	6.2
72	124.0	699.7	0.299	0.407	0.1	-0.9	5.5	-3.2	1.0
73	124.0	699.7	0.299	0.407	0.1	-6.7	8.9	-4.0	6.7
74	124.0	699.7	0.299	0.407	0.1	-5.2	8.0	0.7	5.3
75	124.0	699.7	0.299	0.407	0.1	-4.7	7.3	-7.4	4.8
76	124.0	699.7	0.299	0.407	-2.0	-4.8	5.0	-2.1	2.8
77	124.0	699.7	0.299	0.407	-2.0	-6.1	7.0	-2.9	4.2
78	124.0	699.7	0.299	0.407	-1.9	-7.5	9.0	-3.8	5.5
79	124.0	699.7	0.299	0.407	-1.9	-8.7	11.0	-5.0	6.8
80	124.0	699.7	0.299	0.407	-5.0	-7.1	5.1	-1.6	2.1
81	124.0	699.7	0.299	0.407	-5.0	-8.4	7.0	-2.2	3.4
82	124.0	699.7	0.299	0.407	-5.0	-10.3	9.9	-3.7	5.4
83	124.0	699.7	0.299	0.407	-5.0	-9.3	8.1	-2.8	4.3
84	124.0	699.7	0.299	0.407	2.0	-0.5	3.0	-1.8	2.5
85	124.0	699.7	0.299	0.407	2.0	-2.1	5.0	-2.5	4.1
86	124.0	699.7	0.299	0.407	2.1	-3.2	7.0	-3.5	5.3
87	124.0	699.7	0.299	0.407	5.0	2.8	1.6	-1.7	2.2
88	124.0	699.7	0.299	0.407	5.0	2.0	2.6	-2.0	3.0
89	124.0	699.7	0.299	0.407	5.0	1.0	3.9	-2.6	4.0
90	124.0	699.7	0.299	0.407	5.0	-0.4	6.0	-3.3	5.4
91	0.0	699.7	0.0	0.313	0.0	-0.5	-2.0	-0.1	0.5
92	0.0	460.2	0.0	0.179	0.0	0.8	-2.0	0.2	-0.8
93	0.0	699.7	0.0	0.313	0.0	0.3	-2.0	0.3	-0.3

TABLE XXIV - Continued

CONDITION	SAIS	SBIS	CL/SIGMA	CD/SIGMA	CY/SIGMA	CQ/SIGMA	CPH/SIGMA	CRH/SIGMA	V	RHO
1	0.0	0.0	0.0500	0.00233	-0.00114	0.00200	-0.000951	0.000201	62.0	0.00235
2	0.0	0.0	0.0714	0.00155	-0.00216	0.00293	-0.000876	0.000220	62.0	0.00235
3	0.0	0.0	0.0196	0.00201	-0.00046	0.00140	-0.000375	0.000053	62.0	0.00235
4	1.0	0.2	0.0620	0.00344	-0.00173	0.00172	0.000551	0.000127	62.0	0.00235
5	-1.9	-0.2	0.0317	0.00022	-0.00072	0.00200	-0.001391	0.000164	62.0	0.00235
6	-0.1	2.2	0.0497	0.00126	0.00056	0.00200	-0.000280	0.001305	62.0	0.00235
7	0.0	0.0	0.0022	-0.00017	-0.00258	0.00371	-0.000130	0.000273	62.0	0.00235
8	0.0	0.0	0.0061	0.00007	-0.00020	0.00147	-0.000018	0.000009	62.0	0.00235
9	0.0	0.0	0.0322	-0.00021	-0.00062	0.00198	-0.000036	0.000138	62.0	0.00235
10	0.0	0.0	0.0584	-0.00135	-0.00164	0.00309	-0.000183	0.000194	62.0	0.00235
11	0.0	0.0	0.0300	0.00178	-0.00073	0.00119	-0.000014	0.000084	62.0	0.00235
12	0.0	0.0	0.0615	0.00233	-0.00166	0.00174	-0.000068	0.000195	62.0	0.00235
13	0.0	0.0	0.0021	0.00230	-0.00242	0.00267	0.000025	0.000325	62.0	0.00235
14	0.0	0.0	0.0270	-0.00057	-0.00067	0.00223	0.000102	0.000113	82.0	0.00230
15	0.0	0.0	0.0499	-0.00211	-0.00145	0.00346	-0.000086	0.000170	82.0	0.00230
16	1.0	0.1	0.0454	0.00024	-0.00119	0.00228	0.000919	0.0	82.0	0.00230
17	0.0	2.3	0.0208	-0.00003	0.00046	0.00223	-0.000028	0.001362	82.0	0.00230
18	0.3	-1.9	0.0285	-0.00020	-0.00162	0.00228	-0.000140	-0.001060	82.0	0.00230
19	0.0	0.0	0.0483	-0.00085	-0.00118	0.00318	-0.000309	0.000160	82.0	0.00230
20	0.0	0.0	0.0620	-0.00222	-0.00214	0.00441	-0.000516	0.000206	82.0	0.00230
21	0.0	0.0	0.0743	-0.00379	-0.00344	0.00630	-0.000477	0.000225	82.0	0.00230
22	0.0	0.0	0.0447	0.00146	-0.00128	0.00230	-0.000647	0.000045	82.0	0.00230
23	0.0	0.0	0.0621	0.00074	-0.00215	0.00339	-0.000778	0.000216	82.0	0.00230
24	0.0	0.0	0.0716	-0.00012	-0.00293	0.00466	-0.000796	0.000232	82.0	0.00230
25	0.0	0.0	0.0824	-0.00142	-0.00414	0.00660	-0.000795	0.000209	82.0	0.00230
26	0.0	0.0	0.0140	-0.00020	-0.00031	0.00205	0.000124	-0.000008	82.0	0.00230
27	0.0	0.0	-0.0031	0.00169	0.00012	0.00132	0.000144	-0.000121	82.0	0.00230
28	0.0	0.0	0.0275	-0.00135	-0.00048	0.00278	-0.000214	0.000085	82.0	0.00230
29	0.0	0.0	0.0520	-0.00367	-0.00152	0.00430	-0.000062	0.000123	82.0	0.00230
30	0.0	0.0	0.0672	-0.00551	-0.00256	0.00590	-0.000193	0.000198	82.0	0.00230
31	0.0	0.0	0.0773	-0.00768	-0.00386	0.00813	-0.000117	0.000236	82.0	0.00230
32	0.0	0.0	0.0623	0.00008	-0.00197	0.00288	-0.000151	0.000215	73.0	0.00230
33	0.0	0.0	0.0719	0.00040	-0.00245	0.00313	-0.000093	0.000296	73.0	0.00230
34	0.0	0.0	0.0795	0.00131	-0.00293	0.00318	0.000153	0.000341	73.0	0.00230
35	0.0	0.0	0.0711	-0.00779	-0.00251	0.00557	0.000283	0.000234	73.0	0.00230
36	3.0	0.4	0.0709	-0.00269	-0.00234	0.00378	0.002437	0.000196	73.0	0.00230
37	-3.0	-0.2	0.0700	-0.01332	-0.00234	0.00822	-0.001568	0.000305	73.0	0.00230
38	0.0	0.0	0.0043	-0.00010	0.00000	0.00167	0.000624	0.000060	82.0	0.00230
39	0.0	0.0	0.0219	-0.00268	-0.00034	0.00281	0.000473	0.000049	82.0	0.00230
40	0.0	0.0	0.0430	-0.00589	-0.00112	0.00451	0.000530	0.000162	82.0	0.00230
41	0.0	0.0	0.0620	-0.00871	-0.00208	0.00626	0.000549	0.000181	82.0	0.00230
42	0.0	0.0	0.0213	0.00000	-0.00038	0.00295	-0.000628	0.000068	104.0	0.00224
43	0.0	0.0	0.0354	-0.00073	-0.00091	0.00411	-0.000706	0.000106	104.0	0.00224
44	0.0	0.0	0.0522	-0.00275	-0.00189	0.00590	-0.000725	0.000145	104.0	0.00224
45	0.0	0.0	0.0669	-0.00538	-0.00393	0.00920	-0.000570	0.000184	104.0	0.00224
46	0.0	0.0	0.0418	0.00486	-0.00134	0.00252	-0.002028	-0.000010	104.0	0.00224
47	0.0	0.0	0.0627	0.00464	-0.00281	0.00412	-0.002106	0.000230	104.0	0.00224
48	0.0	0.0	0.0682	0.00547	-0.00349	0.00428	-0.002164	0.000219	104.0	0.00224
49	0.0	0.0	0.0820	0.00545	-0.00486	0.00642	-0.002162	0.000357	104.0	0.00224
50	3.0	0.3	0.0780	0.00933	-0.00422	0.00359	-0.000361	0.000187	104.0	0.00224

TABLE XXIV - Concluded

CONDITION	BAIS	SSIS	CL/SIGMA	CD/SIGMA	CY/SIGMA	CG/SIGMA	CPM/SIGMA	CRM/SIGMA	V	RHO
51	-0.8	0.1	0.0784	0.00273	-0.00439	0.00814	-0.002839	0.000400	104.0	0.00224
52	-0.3	4.1	0.0774	0.00480	0.00128	0.00741	-0.002394	0.002646	104.0	0.00224
53	0.3	-1.9	0.0786	0.00416	-0.00741	0.00707	-0.002491	-0.000800	104.0	0.00224
62	0.0	0.0	0.0127	0.00491	-0.00061	0.00131	-0.001294	0.000144	97.0	0.00227
63	0.0	0.0	0.0142	0.00617	-0.00060	0.00150	-0.001300	0.000145	97.0	0.00227
64	0.0	0.0	0.0196	0.00621	-0.00107	0.00185	-0.002540	0.000076	97.0	0.00227
65	0.0	0.0	0.0066	0.00398	-0.00071	0.00137	-0.000922	0.000141	129.0	0.00225
66	0.0	0.0	0.0085	0.00557	-0.00083	0.00104	-0.000860	0.000142	147.0	0.00224
67	0.0	0.0	0.0140	0.00787	-0.00072	0.00039	-0.001021	0.000259	150.0	0.00221
68	0.0	0.0	0.0943	-0.00353	-0.00385	0.00565	0.000965	0.000319	62.0	0.00235
69	0.0	0.0	0.0975	-0.00429	-0.00436	0.00658	0.001062	0.000356	62.0	0.00235
70	0.0	0.0	0.1011	-0.00529	-0.00495	0.00778	0.001104	0.000412	62.0	0.00235
71	0.0	0.0	0.1019	-0.00581	-0.00504	0.00857	0.001090	0.000467	62.0	0.00235
72	3.7	0.2	0.0963	0.00590	-0.00419	0.00404	0.001333	0.000153	62.0	0.00235
73	-1.0	0.0	0.0981	-0.00336	-0.00436	0.00778	-0.001067	0.000449	62.0	0.00235
74	-0.1	4.2	0.0966	-0.00066	0.00294	0.00686	-0.000174	0.002558	62.0	0.00235
75	0.3	-3.9	0.0970	-0.00143	-0.01089	0.00584	-0.000355	-0.001697	62.0	0.00235
76	0.0	0.0	0.0701	-0.00415	-0.00214	0.00379	0.000567	0.000256	62.0	0.00235
77	0.0	0.0	0.0874	-0.00563	-0.00316	0.00531	0.000627	0.000330	62.0	0.00235
78	0.0	0.0	0.0961	-0.00717	-0.00452	0.00767	0.000761	0.000404	62.0	0.00235
79	0.0	0.0	0.1024	-0.00889	-0.00579	0.01017	0.000914	0.000515	62.0	0.00235
80	0.0	0.0	0.0569	-0.00629	-0.00141	0.00385	0.000771	0.000245	62.0	0.00235
81	0.0	0.0	0.0750	-0.00836	-0.00217	0.00524	0.000831	0.000375	62.0	0.00235
82	0.0	0.0	0.0918	-0.01155	-0.00395	0.00829	0.000891	0.000375	62.0	0.00235
83	0.0	0.0	0.0832	-0.00974	-0.00277	0.00630	0.000674	0.000338	62.0	0.00235
84	0.0	0.0	0.0721	0.00125	-0.00198	0.00225	0.000350	0.000237	62.0	0.00235
85	0.0	0.0	0.0883	0.00076	-0.00283	0.00350	0.000391	0.000348	62.0	0.00235
86	0.0	0.0	0.1002	-0.00004	-0.00453	0.00572	0.000674	0.000367	62.0	0.00235
87	0.0	0.0	0.0748	0.00547	-0.00231	0.00098	0.000475	0.000296	62.0	0.00235
88	0.0	0.0	0.0845	0.00592	-0.00265	0.00149	0.000498	0.000352	62.0	0.00235
89	0.0	0.0	0.0937	0.00577	-0.00366	0.00255	0.000579	0.000366	62.0	0.00235
90	0.0	0.0	0.1032	0.00509	-0.00459	0.00459	0.000657	0.000551	62.0	0.00235
91	0.0	0.0	-0.0001	-0.00116	0.0	0.00129	0.000543	-0.000009	0.0	0.00236
92	0.0	0.0	0.0055	-0.00029	0.00026	0.00169	0.000183	-0.000028	0.0	0.00236
93	0.0	0.0	-0.0007	-0.00027	-0.00008	0.00124	0.000186	0.000018	0.0	0.00236

TABLE XXV. H-34 MODEL BLADE PERFORMANCE DATA (Configuration: θ_1 = 0 deg, δ_F = 0 deg, S_E = 3)

CONDITION	VS	OMEGAS*R	MU	M1,90	ALPHA S	ALPHA C	THETA C	A1S	B1S
1	124.0	699.7	0.299	0.407	0.0	-3.3	3.6	-2.3	3.4
2	124.0	699.7	0.299	0.407	0.1	-4.8	5.6	-2.9	4.8
3	124.0	699.7	0.299	0.407	-0.0	-1.8	1.6	-1.4	1.7
4	124.0	699.7	0.299	0.407	0.1	-1.8	3.6	-2.4	1.9
5	124.0	699.7	0.299	0.407	-0.0	-5.0	3.6	-2.0	5.0
6	124.0	699.7	0.299	0.407	0.0	-3.5	3.6	0.1	3.5
7	124.0	699.7	0.299	0.407	0.0	-8.3	8.3	-4.4	6.3
8	124.0	699.7	0.299	0.407	-2.1	-3.4	1.6	-1.1	1.3
9	124.0	699.7	0.299	0.407	-2.0	-5.0	3.6	-2.0	3.0
10	124.0	699.7	0.299	0.407	-1.9	-6.4	5.6	-2.8	4.4
11	124.0	699.7	0.299	0.407	2.0	-0.4	1.6	-1.8	2.4
12	124.0	699.7	0.299	0.407	2.1	-1.8	3.6	-2.5	3.9
13	124.0	699.7	0.299	0.407	2.1	-3.1	5.6	-3.5	5.2
14	165.0	699.7	0.399	0.439	-2.5	-6.1	4.0	-2.1	3.7
15	165.0	699.7	0.399	0.439	-2.4	-7.9	6.0	-3.0	5.5
16	165.0	699.7	0.399	0.439	-2.4	-4.9	4.0	-2.5	2.5
17	165.0	699.7	0.399	0.439	-2.5	-6.2	4.0	0.1	3.8
18	165.0	699.7	0.399	0.439	-2.5	-8.3	4.2	-4.4	3.8
19	165.0	699.7	0.399	0.439	-2.5	-8.0	6.2	-3.1	5.5
20	165.0	699.7	0.399	0.439	-2.5	-9.5	6.2	-4.1	7.0
21	165.0	699.7	0.399	0.439	-2.5	-10.7	10.2	-5.2	8.2
22	165.0	699.7	0.399	0.439	-0.4	-4.8	4.0	-2.6	4.3
23	165.0	699.7	0.399	0.439	-0.4	-6.5	6.0	-3.5	6.0
24	165.0	699.7	0.399	0.439	-0.5	-8.2	8.2	-4.3	7.5
25	165.0	699.7	0.399	0.439	-0.5	-9.4	10.2	-5.7	8.9
26	165.0	699.7	0.399	0.439	-4.5	-7.3	4.0	-1.7	2.8
27	165.0	699.7	0.399	0.439	-4.5	-5.7	2.0	-1.1	1.2
28	165.0	699.7	0.399	0.439	-4.6	-9.5	8.7	-2.6	4.9
29	165.0	699.7	0.399	0.439	-4.5	-11.0	8.7	-3.4	6.5
30	165.0	699.7	0.399	0.439	-4.5	-12.3	10.7	-4.4	7.8
31	165.0	699.7	0.399	0.439	-4.5	-13.6	12.7	-5.7	9.1
32	146.0	699.7	0.352	0.424	0.0	-5.3	6.1	-3.0	5.3
33	146.0	699.7	0.352	0.424	1.0	-5.2	7.3	-3.7	6.3
34	146.0	699.7	0.352	0.424	2.0	-4.7	7.8	-4.3	6.8
35	146.0	699.7	0.352	0.424	-5.0	-12.1	10.8	-4.3	7.1
36	146.0	699.7	0.352	0.424	-5.0	-7.8	8.3	-3.9	2.9
37	146.0	699.7	0.352	0.424	-5.0	-10.5	13.5	-5.4	11.6
38	165.0	699.7	0.399	0.439	-6.6	-11.8	7.1	-2.2	5.2
39	165.0	699.7	0.399	0.439	-6.5	-13.2	9.1	-3.1	6.7
40	165.0	699.7	0.399	0.439	-6.5	-14.6	11.1	-4.3	8.1
41	165.0	699.7	0.399	0.439	-6.5	-15.8	13.1	-5.4	9.3
42	203.0	699.7	0.502	0.471	-5.0	-11.2	7.3	-2.6	6.2
43	203.0	699.7	0.502	0.471	-5.0	-13.3	9.7	-3.7	8.4
44	203.0	699.7	0.502	0.471	-5.0	-15.4	12.5	-5.2	10.5
45	203.0	699.7	0.502	0.471	-4.9	-17.3	15.6	-6.9	12.4
46	203.0	699.7	0.502	0.471	0.0	-7.0	6.0	-3.2	7.1
47	203.0	699.7	0.502	0.471	0.2	-10.3	10.3	-5.5	10.5
48	203.0	699.7	0.502	0.471	2.1	-8.1	9.0	-5.2	10.2
49	203.0	699.7	0.502	0.471	3.0	-9.6	11.8	-7.2	12.6
50	203.0	699.7	0.502	0.471	1.0	-6.3	8.5	-5.2	7.3

Reproduced from best available copy.

TABLE XXV - Continued

CONDITION	VS	OMEGAS&R	MU	M1.90	ALPHA S	ALPHA C	THETA C	A1S	B1S
51	208.0	699.7	0.502	0.471	1.0	-12.2	12.5	-6.7	13.2
52	208.0	699.7	0.502	0.471	1.0	-12.0	12.8	-2.9	13.0
53	208.0	699.7	0.502	0.471	1.0	-11.3	12.7	-9.1	12.3
54	120.0	479.9	0.422	0.385	-4.9	-16.2	16.3	-8.3	11.3
55	120.0	499.5	0.414	0.310	-4.9	-15.5	15.0	-7.2	10.6
56	120.0	500.0	0.405	0.314	-4.9	-14.7	13.7	-6.3	9.8
57	120.0	500.6	0.397	0.319	-4.9	-13.9	12.7	-5.6	9.0
58	120.0	620.0	0.327	0.368	-4.9	-9.7	6.8	-2.5	4.9
59	120.0	699.6	0.322	0.372	-4.9	-9.3	6.5	-2.4	4.5
60	120.0	640.1	0.316	0.377	-4.9	-9.2	6.2	-2.2	4.3
61	120.0	649.7	0.312	0.382	-4.9	-8.9	6.0	-2.2	4.0
62	194.0	529.4	0.618	0.377	2.0	-0.5	0.9	-2.1	2.5
63	194.0	451.6	0.709	0.347	2.0	-3.0	3.0	-2.7	5.0
64	194.0	400.2	0.818	0.320	2.0	-10.4	9.3	-4.4	12.4
65	258.0	699.7	0.622	0.500	2.0	1.0	-0.6	-1.7	1.0
66	294.0	699.7	0.709	0.523	2.0	-0.1	-0.1	-2.2	2.1
67	300.0	618.1	0.819	0.431	2.0	-1.6	1.5	-2.7	3.8
68	124.0	649.7	0.299	0.407	0.1	-8.8	12.0	-6.1	8.8
69	124.0	649.7	0.299	0.407	0.1	-9.5	13.3	-7.0	9.6
70	124.0	649.7	0.299	0.407	0.1	-10.3	14.7	-8.0	10.4
71	124.0	699.7	0.299	0.407	0.1	-10.6	15.5	-8.4	10.7
72	124.0	699.7	0.299	0.407	0.1	-4.8	9.9	-5.2	4.9
73	124.0	699.7	0.299	0.407	0.1	-10.8	14.1	-7.3	10.9
74	124.0	699.7	0.299	0.407	0.1	-9.8	13.2	-2.6	9.8
75	124.0	699.7	0.299	0.407	0.1	-9.1	13.2	-10.9	9.2
76	124.0	649.7	0.299	0.407	-2.0	-8.9	9.1	-4.0	6.9
77	124.0	699.7	0.299	0.407	-2.0	-10.0	11.1	-5.3	8.0
78	124.0	649.7	0.299	0.407	-1.9	-11.5	13.1	-6.3	9.5
79	124.0	699.7	0.299	0.407	-1.9	-12.1	15.1	-7.8	10.2
80	124.0	699.7	0.299	0.407	-5.0	-10.1	7.2	-2.5	5.0
81	124.0	699.7	0.299	0.407	-5.0	-11.9	10.4	-4.1	6.9
82	124.0	699.7	0.299	0.407	-4.9	-15.0	16.1	-7.9	10.1
83	124.0	699.7	0.299	0.407	-5.0	-13.2	12.6	-5.6	8.3
84	124.0	699.7	0.299	0.407	2.0	-4.2	7.1	-3.8	6.3
85	124.0	699.7	0.299	0.407	2.0	-5.5	9.1	-4.8	7.5
86	124.0	699.7	0.299	0.407	2.1	-6.7	11.1	-5.9	8.8
87	124.0	649.7	0.299	0.407	5.0	-0.0	4.2	-2.8	5.0
88	124.0	699.7	0.299	0.407	5.0	-1.2	6.0	-3.7	6.2
89	124.0	699.7	0.299	0.407	5.0	-2.8	8.4	-4.9	7.7
90	124.0	699.7	0.299	0.407	5.0	-4.5	11.3	-6.5	9.5
91	0.0	699.7	0.0	0.333	0.0	-0.2	0.0	-0.2	0.2
92	0.0	479.9	0.0	0.215	0.0	0.2	0.0	-0.2	-0.2
93	0.0	699.7	0.0	0.313	0.0	-0.0	0.0	0.0	0.0

TABLE XXV - Continued

CONDITION	SAIS	SBIS	CL/SIGMA	CD/SIGMA	CY/SIGMA	CB/SIGMA	CPM/SIGMA	CRM/SIGMA	V	RHO
1	0.0	0.0	0.0479	0.00225	-0.00141	0.00206	-0.000714	0.000143	62.0	0.00239
2	0.0	0.0	0.0662	0.00126	-0.00224	0.00319	-0.000689	0.000270	62.0	0.00239
3	0.0	0.0	0.0194	0.00218	-0.00089	0.00142	-0.000555	0.000089	62.0	0.00239
4	2.0	0.1	0.0589	0.00386	-0.00183	0.00187	0.000470	0.000143	62.0	0.00239
5	-1.8	-0.1	0.0365	0.00058	-0.00099	0.00224	-0.001576	0.000143	62.0	0.00239
6	-0.1	2.1	0.0471	0.00187	0.00026	0.00206	-0.000570	0.001306	62.0	0.00239
7	0.0	0.0	0.0804	-0.00084	-0.00415	0.00619	-0.000327	0.000304	62.0	0.00239
8	0.0	0.0	0.0080	0.00191	-0.00024	0.00140	-0.000538	0.000045	62.0	0.00239
9	0.0	0.0	0.0305	0.00070	-0.00099	0.00217	-0.000622	0.000100	62.0	0.00239
10	0.0	0.0	0.0575	-0.00046	-0.00190	0.00317	-0.000669	0.000154	62.0	0.00239
11	0.0	0.0	0.0305	0.00362	-0.00125	0.00121	-0.000697	0.000264	62.0	0.00239
12	0.0	0.0	0.0577	0.00386	-0.00217	0.00180	-0.000690	0.000301	62.0	0.00239
13	0.0	0.0	0.0734	0.00333	-0.00350	0.00335	-0.000646	0.000319	62.0	0.00239
14	0.0	0.0	0.0255	0.00129	-0.00110	0.00215	-0.000623	0.000200	82.8	0.00238
15	0.0	0.0	0.0428	0.00009	-0.00194	0.00315	-0.000725	0.000200	82.8	0.00238
16	1.9	0.1	0.0367	0.00221	-0.00161	0.00211	0.000303	0.000182	82.8	0.00238
17	-0.2	2.1	0.0241	0.00159	-0.00010	0.00215	-0.000784	0.001306	82.8	0.00238
18	0.1	-1.9	0.0262	0.00144	-0.00211	0.00224	-0.000795	-0.000857	82.8	0.00238
19	0.0	0.0	0.0443	0.00048	-0.00185	0.00329	-0.000825	0.000160	82.8	0.00238
20	0.0	0.0	0.0568	-0.00128	-0.00319	0.00521	-0.000836	0.000217	82.8	0.00238
21	0.0	0.0	0.0661	-0.00282	-0.00444	0.00726	-0.000628	0.000308	82.8	0.00238
22	0.0	0.0	0.0390	0.00273	-0.00153	0.00217	-0.000877	0.000226	82.8	0.00238
23	0.0	0.0	0.0527	0.00158	-0.00270	0.00354	-0.000979	0.000226	82.8	0.00238
24	0.0	0.0	0.0656	0.00062	-0.00403	0.00568	-0.000499	0.000315	82.8	0.00238
25	0.0	0.0	0.0752	-0.00153	-0.00529	0.00791	-0.000838	0.000388	82.8	0.00238
26	0.0	0.0	0.0090	0.00066	-0.00026	0.00181	-0.000024	0.000102	82.8	0.00238
27	0.0	0.0	-0.0073	0.00224	0.00007	0.00109	0.000002	0.000047	82.8	0.00238
28	0.0	0.0	0.0314	-0.00249	0.00016	0.00314	0.000420	0.000036	82.8	0.00238
29	0.0	0.0	0.0469	-0.00436	-0.00193	0.00459	0.000467	0.000091	82.8	0.00238
30	0.0	0.0	0.0581	-0.00647	-0.00319	0.00678	0.000587	0.000218	82.8	0.00238
31	0.0	0.0	0.0696	-0.00894	-0.00477	0.00933	0.000725	0.000273	82.8	0.00238
32	0.0	0.0	0.0600	0.00083	-0.00231	0.00318	-0.000615	0.000171	73.0	0.00239
33	0.0	0.0	0.0703	0.00047	-0.00327	0.00447	-0.000385	0.000285	73.0	0.00239
34	0.0	0.0	0.0775	0.00157	-0.00433	0.00525	-0.000551	0.000438	73.0	0.00239
35	0.0	0.0	0.0600	-0.00673	-0.00359	0.00732	-0.000256	0.000298	73.0	0.00239
36	3.5	0.1	0.0650	-0.00178	-0.00342	0.00505	0.001612	0.000043	73.0	0.00239
37	-3.5	-0.2	0.0671	-0.01207	-0.00392	0.01028	-0.002236	0.000371	73.0	0.00239
38	0.0	0.0	0.0289	-0.00284	-0.00081	0.00349	0.000278	0.000086	82.8	0.00232
39	0.0	0.0	0.0452	-0.00513	-0.00184	0.00504	0.000265	0.000086	82.8	0.00232
40	0.0	0.0	0.0572	-0.00794	-0.00322	0.00752	0.000255	0.000142	82.8	0.00232
41	0.0	0.0	0.0657	-0.01000	-0.00442	0.00991	0.000413	0.000217	82.8	0.00232
42	0.0	0.0	0.0215	0.00019	-0.00067	0.00315	-0.000030	-0.000028	104.0	0.00231
43	0.0	0.0	0.0255	-0.00144	-0.00168	0.00499	-0.000249	-0.000047	104.0	0.00231
44	0.0	0.0	0.0504	-0.00376	-0.00378	0.00805	-0.000166	0.000085	104.0	0.00231
45	0.0	0.0	0.0634	-0.00659	-0.00551	0.01191	-0.000045	0.000330	104.0	0.00231
46	0.0	0.0	0.0400	0.00375	-0.00212	0.00330	-0.001408	0.000047	104.0	0.00231
47	0.0	0.0	0.0620	0.00423	-0.00472	0.00721	-0.002246	0.000108	104.0	0.00231
48	0.0	0.0	0.0666	0.00593	-0.00499	0.00638	-0.002256	0.000232	104.0	0.00231
49	0.0	0.0	0.0422	0.00474	-0.00719	0.00996	-0.002322	0.000291	104.0	0.00231
50	3.5	0.3	0.0770	0.00859	-0.00579	0.00608	-0.003560	0.000238	104.0	0.00231

TABLE XXV - Concluded

CONDITION	SAIS	SBIS	CL/SIGMA	CD/SIGMA	CY/SIGMA	CQ/SIGMA	CPM/SIGMA	CRM/SIGMA	V	RHO
51	-0.9	-0.1	0.0704	0.00216	-0.00630	0.00999	-0.002741	0.000295	104.0	0.00231
52	-0.3	4.0	0.0754	0.00339	-0.00095	0.01070	-0.002054	0.002518	104.0	0.00231
53	0.3	-1.9	0.0769	0.00273	-0.00959	0.01023	-0.002084	-0.000798	104.0	0.00231
54	0.0	0.0	0.0766	-0.00937	-0.00724	0.01463	-0.000544	0.000298	60.0	0.00232
55	0.0	0.0	0.0741	-0.00862	-0.00626	0.01292	-0.000438	0.000363	60.0	0.00232
56	0.0	0.0	0.0702	-0.00762	-0.00533	0.01119	-0.000414	0.000348	60.0	0.00232
57	0.0	0.0	0.0684	-0.00686	-0.00497	0.01007	-0.000322	0.000370	60.0	0.00232
58	0.0	0.0	0.0469	-0.00268	-0.00161	0.00383	-0.000451	0.000202	60.0	0.00232
59	0.0	0.0	0.0458	-0.00248	-0.00156	0.00365	-0.000387	0.000173	60.0	0.00232
60	0.0	0.0	0.0440	-0.00254	-0.00141	0.00348	-0.000369	0.000212	60.0	0.00232
61	0.0	0.0	0.0427	-0.00233	-0.00137	0.00338	-0.000288	0.000162	60.0	0.00232
62	0.0	0.0	0.0135	0.00401	-0.00047	0.00116	-0.000646	0.000146	97.0	0.00222
63	0.0	0.0	0.0163	0.00554	-0.00082	0.00142	-0.001209	0.000148	97.0	0.00222
64	0.0	0.0	0.0236	0.01110	-0.00273	0.00323	-0.002491	0.000137	97.0	0.00222
65	0.0	0.0	0.0062	0.00386	-0.00009	0.00124	-0.001046	0.000144	129.0	0.00221
66	0.0	0.0	0.0092	0.00414	-0.00031	0.00128	-0.000167	0.000087	147.0	0.00216
67	0.0	0.0	0.0112	0.00880	-0.00027	0.00131	-0.003665	0.000111	150.0	0.00215
68	0.0	0.0	0.0949	-0.00486	-0.00620	0.01099	0.000178	0.000472	62.0	0.00232
69	0.0	0.0	0.0961	-0.00644	-0.00680	0.01286	0.000443	0.000491	62.0	0.00232
70	0.0	0.0	0.1020	-0.00835	-0.00757	0.01496	0.000708	0.000547	62.0	0.00232
71	0.0	0.0	0.1039	-0.00950	-0.00774	0.01622	0.001067	0.000565	62.0	0.00232
72	3.5	0.2	0.0981	0.00612	-0.00603	0.00856	0.000052	0.000341	62.0	0.00232
73	-0.9	0.0	0.0983	-0.00421	-0.00663	0.01407	-0.002074	0.000584	62.0	0.00232
74	-0.1	4.1	0.0983	-0.00152	0.00074	0.01319	-0.001211	0.002644	62.0	0.00232
75	0.3	-1.9	0.0960	-0.00363	-0.01391	0.01253	-0.001301	-0.001621	62.0	0.00232
76	0.0	0.0	0.0762	-0.00397	-0.00405	0.00700	-0.000455	0.000334	62.0	0.00232
77	0.0	0.0	0.0871	-0.00610	-0.00533	0.00962	-0.000283	0.000371	62.0	0.00232
78	0.0	0.0	0.0935	-0.00797	-0.00628	0.01228	-0.000073	0.000483	62.0	0.00232
79	0.0	0.0	0.0985	-0.01014	-0.00756	0.01522	0.000154	0.000483	62.0	0.00232
80	0.0	0.0	0.0573	-0.00461	-0.00177	0.00426	-0.000104	0.000192	62.0	0.00232
81	0.0	0.0	0.0761	-0.00857	-0.00374	0.00814	0.000124	0.000379	62.0	0.00232
82	0.0	0.0	0.0938	-0.01508	-0.00708	0.01608	0.000502	0.000509	62.0	0.00232
83	0.0	0.0	0.0836	-0.01111	-0.00528	0.01090	0.000206	0.000379	62.0	0.00232
84	0.0	0.0	0.0822	0.00122	-0.00406	0.00517	-0.000010	0.000277	62.0	0.00232
85	0.0	0.0	0.0914	-0.00026	-0.00517	0.00765	0.000105	0.000408	62.0	0.00232
86	0.0	0.0	0.0969	-0.00190	-0.00603	0.01012	0.000240	0.000464	62.0	0.00232
87	0.0	0.0	0.0760	0.00590	-0.00319	0.00230	0.000075	0.000318	62.0	0.00232
88	0.0	0.0	0.0862	0.00515	-0.00439	0.00431	0.000266	0.000393	62.0	0.00232
89	0.0	0.0	0.0958	0.00346	-0.00558	0.00702	0.000421	0.000482	62.0	0.00232
90	0.0	0.0	0.1050	0.00199	-0.00703	0.01080	0.000574	0.000575	62.0	0.00232
91	0.0	0.0	0.0008	-0.00029	0.0	0.00107	0.000158	-0.000041	0.0	0.00264
92	0.0	0.0	0.0	-0.00047	0.0	0.00129	0.000285	-0.000020	0.0	0.00233
93	0.0	0.0	0.0062	-0.00053	-0.00004	0.00118	0.000231	0.0	0.0	0.00240

TABLE XXVI. H-34 MODEL NORMAL MODES AEROELASTIC ANALYSIS CASES FOR CORRELATION WITH TEST DATA

Cond. No.	Case No.	Nominal Independent Operating Parameters									Unsteady Aerodynamic Scaling Case	Inflow Assumption	Vortex Core Size r_{vc}/c
		Vs (kn)											
1	1.1	124.	.30	0.0	.049	0.0	0.0	0.0	0.0	1.0	1	Uniform	-
1	1.2	124.	.30	0.0	.049	0.0	0.0	0.0	0.0	1.0	1	Variable	.3
1	1.3	124.	.30	0.0	.049	0.0	0.0	0.0	0.0	1.0	1	Variable	.6
7	7.1	124.	.30	0.0	.081	0.0	0.0	0.0	0.0	1.0	1	Uniform	-
7	7.2	124.	.30	0.0	.081	0.0	0.0	-8.0	0.0	1.0	1	Uniform	-
7	7.3	124.	.30	0.0	.081	0.0	0.0	0.0	5.0	1.0	1	Uniform	-
7	7.4	124.	.30	0.0	.081	0.0	0.0	0.0	0.0	3.0	1	Uniform	-
36	36.1	146.	.35	-5.0	.070	-3.6	0.0	0.0	0.0	1.0	1	Uniform	-
36	36.2	146.	.35	-5.0	.070	-3.6	0.0	-8.0	0.0	1.0	1	Uniform	-
36	36.3	146.	.35	-5.0	.070	-3.6	0.0	0.0	5.0	1.0	1	Uniform	-
36	36.4	146.	.35	-5.0	.070	-3.6	0.0	0.0	0.0	3.0	1	Uniform	-
36	36.5	146.	.35	-5.0	.070	-3.6	0.0	0.0	0.0	1.0	3	Variable	.3
36	36.6	146.	.35	-5.0	.070	-3.6	0.0	-8.0	0.0	1.0	3	Variable	.3
36	36.7	146.	.35	-5.0	.070	-3.6	0.0	0.0	5.0	1.0	3	Variable	.3
36	36.8	146.	.35	-5.0	.070	-3.6	0.0	0.0	0.0	3.0	3	Variable	.3
36	36.9	146.	.35	-5.0	.070	-3.6	0.0	-8.0	0.0	1.0	1	Variable	.3
71	71.1	124.	.30	0.0	.100	0.0	0.0	0.0	0.0	1.0	2	Uniform	-
71	71.2	124.	.30	0.0	.100	0.0	0.0	-8.0	0.0	1.0	2	Uniform	-
71	71.3	124.	.30	0.0	.100	0.0	0.0	0.0	5.0	1.0	2	Uniform	-
71	71.4	124.	.30	0.0	.100	0.0	0.0	0.0	0.0	3.0	2	Uniform	-
71	71.5	124.	.30	0.0	.100	0.0	0.0	0.0	0.0	1.0	1	Variable	.3
71	71.6	124.	.30	0.0	.100	0.0	0.0	-8.0	0.0	1.0	1	Variable	.3
71	71.7	124.	.30	0.0	.100	0.0	0.0	0.0	5.0	1.0	1	Variable	.3
71	71.8	124.	.30	0.0	.100	0.0	0.0	0.0	0.0	3.0	1	Variable	.3

TABLE XXVI - Concluded

Cond. No.	Case No.	Nominal Independent Operating Parameters						Blade Configuration			Unsteady Aerodynamic Scaling Case	Inflow Assumption	Vortex Core Size
		Vs (kn)	μ	α_s (deg)	C_L/σ	a_{1s} (deg)	b_{1s} (deg)	θ_1 (deg)	δ_F (deg)	C_{T_c}			r_{vc}/c
80	80.1	124.	.30	-5.0	.058	0.0	0.0	0	0	1.0	1	Uniform	.3
80	80.2	124.	.30	-5.0	.058	0.0	0.0	-8	0	1.0	1	Uniform	.3
80	80.3	124.	.30	-5.0	.058	0.0	0.0	0	5	1.0	1	Uniform	.3
80	80.4	124.	.30	-5.0	.058	0.0	0.0	0	0	3.0	1	Uniform	.3
82	82.1	124.	.30	-5.0	.093	0.0	0.0	0	0	1.0	1	Uniform	.3
82	82.2	124.	.30	-5.0	.093	0.0	0.0	-8	0	1.0	1	Uniform	.3
82	82.3	124.	.30	-5.0	.093	0.0	0.0	0	5	1.0	1	Uniform	.3
82	82.4	124.	.30	-5.0	.093	0.0	0.0	0	0	3.0	1	Uniform	.3

TABLE XXVII. H-34 MODEL UNSTEADY TWO-DIMENSIONAL AERODYNAMIC SCALING DATA

Scaling Case No.	Mach. No.	$\alpha_{sn}(M)$ (deg)	$C_{nss}(M)/C_{nsst}$	$\alpha_{sm}(M)$ (deg)
1	0.0	10.0	.779	13.5
1	.00001	8.6	.779	9.2
1	.10	8.6	.779	9.2
1	.18	8.4	.800	9.5
1	.33	7.8	.800	9.5
1	.47	5.8	.632	7.6
1	.56	3.5	.421	7.2
2	0.0	10.0	.850	13.5
2	.00001	8.6	.850	9.2
2	.10	8.6	.850	9.2
2	.18	8.4	.874	9.5
2	.33	7.8	.874	9.5
2	.47	5.8	.690	7.6
2	.56	3.5	.460	7.2
3	0.0	10.0	.614	13.5
3	.00001	7.5	.614	10.3
3	.10	7.5	.614	10.3
3	.18	7.4	.648	10.1
3	.33	7.4	.634	9.5
3	.47	5.2	.535	8.0
3	.56	3.5	.391	7.6

TABLE XXVIII. UTILIZATION BOUNDARIES FOR UNSTEADY AERODYNAMIC COEFFICIENTS

Application	Mach No.	Upper Angle of Attack Limit for Unsteady C_n α = CNREG1	Lower Angle of Attack Limit for Steady C_n α = CNREG2	Upper Angle of Attack Limit for Unsteady C_m α = CMREG1	Lower Angle of Attack Limit for Steady C_m α = CMREG2
$\delta_F = 0$	0.0	24.1	27.0	24.3	27.0
$\delta_F = 0$	.2	24.1	27.0	24.3	27.0
$\delta_F = 0$	.3	25.2	28.1	23.3	26.0
$\delta_F = 0$	.31	6.1	6.0	10.6	11.6
$\delta_F = 0$	.5	2.0	2.0	10.4	10.4
$\delta_F = 0$	.51	0.0	0.0	0.0	0.0
$\delta_F = 5^o$	0.0	24.1	27.0	24.3	27.0
$\delta_F = 5^o$	.2	24.1	27.0	24.3	27.0
$\delta_F = 5^o$	.27	25.2	28.1	23.3	26.0
$\delta_F = 5^o$	.28	0.0	0.0	0.0	0.0

TABLE XXIX. SUMMARY OF CORRELATION BETWEEN CALCULATED AND TEST ROTOR PERFORMANCE

Configuration			Inflow Assumption	Condition Numbers Summarized	Calculated Values Minus Test Values					
					Rotor Drag Coefficient			Rotor Torque Coefficient		
θ_1 (deg)	δ_F (deg)	S_L			Average	Root-Mean-Square	Range	Average	Root-Mean-Square	Range
0	0	1	Uniform	1,7,36,71,80,82	-.00104	.00181	-.00276, .00164	.00002	.00138	-.00290, .00133
0	0	1	Variable	1,36,71	-.00153		-.00251, .00036	.00092		-.00290, .00307
-8	0	1	Uniform	7,36,71,80,82	-.00092	.00159	-.00243, .00114	-.00015	.00139	-.00282, .00103
-8	0	1	Variable	36,71	-.00029		-.00085, .00027	.00038		.00008, .0068
0	5	1	Uniform	7,36,71,80,82	-.00102	.00188	-.00273, .00064	.00039	.00431	-.00109, .00604
0	5	1	Variable	36,71	-.00115		-.00233, .00003	.00555		.00535, .00574
0	0	3	Uniform	7,36,71,80,82	.00055	.00209	-.00235, .0050	-.00185	.00322	-.00656, .000510
0	0	3	Variable	36,71	.00010		-.00307, .00326	-.00026		-.00339, .00297

TABLE XXX. SUMMARY OF CORRELATION BETWEEN CALCULATED AND TEST BLADE VIBRATORY MOMENT AMPLITUDE

Configuration			Inflow Assumption	Condition Numbers Summarized	Calculated Vibratory Moment Divided by Test Vibratory Moment					
					Flapwise $M_{BF,65R}$		Chordwise $M_{BC,65R}$		Torsion $M_{T,20R}$	
θ_1 (deg)	δ_F (deg)	S_E			Average	Range	Average	Range	Average	Range
0	0	1	Uniform	1,7,36,71,80,82	.50	.27, .85	.29	.22, .36	1.16	.63, 1.85
0	0	1	Variable	1,36,71	.76	.69, .88	.62	.43, .80	1.51	1.27, 1.87
-8	0	1	Uniform	7,36,71,80,82	.95	.88, 1.06	.65	.51, .81	1.23	.39, 1.69
-8	0	1	Variable	36,71	1.00	.94, 1.06	.85	.56, 1.15	1.54	1.17, 1.91
0	5	1	Uniform	7,36,71,80,82	.61	.43, .87	.54	.39, .64	1.19	.63, 1.93
0	5	1	Variable	36,71	.79	.46, 1.11	.67	.54, .79	1.34	.88, 1.79
0	0	3	Uniform	7,36,71,80,82	.49	.31, .64	.27	.16, .39	.90	.90, 2.54
0	0	3	Variable	36,71	.94	.86, 1.02	.56	.51, .69	2.51	1.96, 3.05

TABLE XXXI. SUMMARY OF CORRELATION BETWEEN CALCULATED AND TEST INCREMENT IN ROTOR DRAG COEFFICIENT DUE TO BLADE CONFIGURATION CHANGE

CONFIGURATION			INFLOW ASSUMPTION	CONDITION NUMBERS SUMMARIZED	TEST INCREMENTS (TEST VALUES FOR EACH CONFIGURATION MINUS TEST VALUES FOR CONFIGURATION WITH $\theta_1 = 0$, $\delta_F = 0$, $S_E = 1$)			CALCULATED INCREMENTS (CALCULATED VALUES FOR EACH CONFIGURATION MINUS CALCULATED VALUES FOR CONFIGURATION WITH $\theta_1 = 0$, $\delta_F = 0$, $S_E = 1$)		
θ_1 (deg)	δ_F (deg)	S_E			AVERAGE	ROOT-MEAN SQUARE	RANGE	AVERAGE	ROOT-MEAN SQUARE	RANGE
-8	0	1	Uniform	7,36,71,80,82	.00045	.00044	.00004, .00078	.00024	.00053	-.00065, .00066
-8	0	1	Variable	36, 71	.00038		.00004, .00072	.00050		.00037, .00063
0	5	1	Uniform	7,36,71,80,82	-.00033	.00070	-.00152, .00030	-.00064	.00089	-.00167, .00028
0	5	1	Variable	36, 71	-.00033		-.00059, -.00006	-.00043		-.00039 - .00047
0	0	3	Uniform	7,36,71,80,82	-.00138	.00223	-.00375, .00032	-.00120	.00028	-.00039, .00039
0	0	3	Variable	36,71	-.00172		-.00375, .00032	-.00058		-.00085, -.00030

TABLE XXXII. SUMMARY OF CORRELATION BETWEEN CALCULATED AND TEST INCREMENT IN ROTOR TORQUE COEFFICIENT DUE TO BLADE CONFIGURATION CHANGE

CONFIGURATION			INFLOW ASSUMPTION	CONDITION NUMBERS SUMMARIZED	TEST INCREMENTS (TEST VALUES FOR EACH CONFIGURATION MINUS TEST VALUES FOR CONFIGURATION WITH $\theta_1 = 0$, $\delta_F = 0$, $S_E = 1$)			CALCULATED INCREMENTS (CALCULATED VALUES FOR EACH CONFIGURATION MINUS CALCULATED VALUES FOR CONFIGURATION WITH $\theta_1 = 0$, $\delta_F = 0$, $S_E = 1$)		
θ_1 (deg)	δ_F (deg)	S_E			AVERAGE	ROOT-MEAN SQUARE	RANGE	AVERAGE	ROOT-MEAN SQUARE	RANGE
-8	0	1	Uniform	7,36,71,80,82	-.00052	.00055	-.00076, -.00027	-.00064	.00063	-.00078, -.00055
-8	0	1	Variable	36, 71	-.00054		-.00076, -.00032	-.00039		-.00040, -.00038
0	5	1	Uniform	7,36,71,80,82	-.00179	.00214	-.00328, -.00032	.00207	.00259	.00034, .00497
0	5	1	Variable	36, 71	-.00210		-.00328, -.00092	.00205		.00175, .00235
0	0	3	Uniform	7,36,71,80,82	.00213	.00290	.00006, .00464	.00023	.00042	-.00030, .00068
0	0	3	Variable	36, 71	.00236		.00035, .00437	.00071		.00015, .00126

TABLE XXXIII. SUMMARY OF CORRELATION BETWEEN CALCULATED AND TEST RATIOS OF VIBRATORY MOMENT AMPLITUDES DUE TO CONFIGURATION CHANGE

CONFIGURATION			INFLOW ASSUMPTION	CONDITION NUMBERS SUMMARIZED	MOMENT CHANNEL	TEST MOMENT RATIO (TEST VALUE FOR EACH CONFIGURATION DIVIDED BY TEST VALUE FOR CONFIGURATION WITH $\theta_1 = 0$, $\delta_F = 0$, $S_E = 1$)		CALCULATED MOMENT RATIO (CALCULATED VALUE FOR EACH CONFIGURATION DIVIDED BY CALCULATED VALUE FOR CONFIGURATION WITH $\theta_1 = 0$, $\delta_F = 0$, $S_E = 1$)	
θ_1 (deg)	δ_F (deg)	S_E				AVERAGE	RANGE	AVERAGE	RANGE
-8	0	1	Uniform	7,36,71,80,82	Flapwise $M_{BF.65R}$	1.11	1.01, 1.20	2.14	1.11, 3.06
					Chordwise $M_{BC.65R}$	.73	.62, .82	1.54	1.36, 1.70
					Torsion $M_{T.20R}$	.94	.32, 2.29	.68	.46, .83
-8	0	1	Variable	36,71	Flapwise $M_{BF.65R}$	1.13	1.06, 1.20	1.44	1.13, 1.74
					Chordwise $M_{BC.65R}$	.71	.62, .79	1.03	1.03, 1.03
					Torsion $M_{T.20R}$	.59	.44, .75	1.24	1.12, 1.36
0	5	1	Uniform	7,36,71,80,82	Flapwise $M_{BF.65R}$	.97	.85, 1.13	1.11	.72, 1.29
					Chordwise $M_{BC.65R}$	.67	.56, .76	1.18	.96, 1.47
					Torsion $M_{T.20R}$	2.21	.68, 7.43	1.41	.79, 3.30
0	5	1	Variable	36, 71	Flapwise $M_{BF.65R}$	.99	.85, 1.13	.91	.74, 1.08
					Chordwise $M_{BC.65R}$	.66	.56, .76	.75	.56, .94
					Torsion $M_{T.20R}$	1.02	.68, 1.37	.90	.84, .95
0	0	3	Uniform	7,36,71,80,82	Flapwise $M_{BF.65R}$	2.26	2.06, 2.60	2.11	1.24, 2.50
					Chordwise $M_{BC.65R}$	1.79	1.42, 2.34	1.53	1.19, 2.00
					Torsion $M_{T.20R}$	1.17	.90, 1.60	1.59	.71, 2.33
0	0	3	Variable	36, 71	Flapwise $M_{BF.65R}$	2.21	2.09, 2.33	2.64	2.43, 2.84
					Chordwise $M_{BC.65R}$	1.67	1.59, 1.75	1.89	1.02, 2.76
					Torsion $M_{T.20R}$	1.07	.90, 1.24	1.93	1.91, 1.95

TABLE XXXIV. TEST AND CALCULATED ROTOR PERFORMANCE (Condition 1, θ_1 = 0 deg, δ_F = 0 deg, S_E = 1)

Parameter	Test Values	Calculated Values		
		Uniform Inflow	Variable Inflow	
			r_{vc} = 0.3c	r_{vc} = 0.6c
VS	124.0	124.0	124.0	124.0
OMEGA*R	699.7	700.0	700.0	700.0
MU	0.299	0.300	0.300	0.300
M1.90	0.407	0.407	0.407	0.407
ALPHA S	0.0	0.0	0.0	0.0
ALPHA C	-3.4	-3.3	-3.8	-3.8
THETA C	3.5	4.4	4.7	4.7
A1S	-2.1	-1.2	-1.6	-1.6
B1S	3.4	3.3	3.8	3.8
SA1S	0.0	0.1	0.1	0.0
SB1S	0.0	0.1	0.0	0.0
CL/SIGMA	0.0494	0.0470	0.0500	0.0500
CD/SIGMA	0.00269	-0.00007	0.00018	0.00030
CY/SIGMA	-0.00134	-0.00038	-0.00066	-0.00065
CQ/SIGMA	0.00222	0.00210	0.00220	0.00230
CPM/SIGMA	-0.000854	0.000054	0.000016	-0.000080
CRM/SIGMA	0.000156	0.000178	0.000072	0.000180
V	62.0	62.0	62.0	62.0
RHO	0.00236	0.00238	0.00238	0.00238

TABLE XXXV. TEST AND CALCULATED ROTOR PERFORMANCE (Condition 7)

Parameter	Configuration: θ_1 = 0 deg, δ_F = 0 deg, S_E = 1		Configuration: θ_1 = -8 deg, δ_F = 0 deg, S_E = 1		Configuration: θ_1 = 0 deg, δ_F = 5 deg, S_E = 1		Configuration: θ_1 = 0 deg, δ_F = 0 deg, S_E = 3	
	Test Values	Uniform Inflow Calculation	Test Values	Uniform Inflow Calculation	Test Values	Uniform Inflow Calculation	Test Values	Uniform Inflow Calculation
VS	124.0	124.0	124.0	124.0	124.0	124.0	124.0	124.0
OMEGA*R	699.7	700.0	699.7	700.0	699.7	700.0	699.7	700.0
MU	0.299	0.300	0.299	0.300	0.299	0.300	0.299	0.300
M1.90	0.407	0.407	0.407	0.407	0.407	0.407	0.407	0.407
ALPHA S	0.0	0.0	0.0	0.0	0.0	0.0	0.0	0.0
ALPHA C	-6.2	-7.0	-5.5	-6.7	-3.6	-6.3	-6.3	-6.5
THETA C	7.6	8.8	7.3	8.6	5.0	9.2	8.3	8.5
A1S	-3.9	-3.4	-2.5	-1.7	-2.7	-3.6	-4.4	-3.8
B1S	6.2	7.0	5.5	6.7	3.6	6.3	6.3	6.5
SA1S	0.0	-0.1	0.0	0.0	0.0	-0.1	0.0	0.0
SB1S	0.0	0.2	0.0	0.0	0.0	0.0	0.0	-0.1
CL/SIGMA	0.0826	0.0809	0.0822	0.0824	0.0822	0.0918	0.0804	0.0828
CD/SIGMA	-0.00049	-0.00309	0.00002	-0.00243	-0.00017	-0.00390	-0.00084	-0.00319
CY/SIGMA	-0.00376	-0.00159	-0.00244	-0.00014	-0.00258	-0.00192	-0.00415	-0.00237
CQ/SIGMA	0.00498	0.00651	0.00467	0.00570	0.00374	0.00822	0.00649	0.00670
CPM/SIGMA	-0.000103	-0.000187	-0.000552	-0.000207	-0.000130	-0.000177	-0.000327	0.000197
CRM/SIGMA	0.000244	0.000330	0.000226	0.000342	0.000273	0.000122	0.000304	0.000094
V	62.0	62.0	62.0	62.0	62.0	62.0	62.0	62.0
RHO	0.00236	0.00238	0.00235	0.00238	0.00235	0.00238	0.00239	0.00238

TABLE XXXVI. TEST AND CALCULATED ROTOR PERFORMANCE (Condition 36)

Parameter	Configuration: θ_1 = 0 deg, δ_F = 0 deg, S_E = 1			Configuration: θ_1 = -8deg, δ_F = 0 deg, S_E = 1			
	Test Values	Uniform Inflow Calculation Scaling Case 1	Variable Inflow Calculation Scaling Case 3	Test Values	Uniform Inflow Calculation Scaling Case 1	Variable Inflow Calculation Scaling Case 3	Variable Inflow Calculation Scaling Case 1
VS	146.0	145.6	146.0	146.0	146.0	146.0	146.0
OMEGA*R	699.7	700.0	700.0	699.7	700.0	700.0	700.0
MU	0.352	0.350	0.351	0.352	0.351	0.351	0.351
M1,90	0.424	0.424	0.424	0.420	0.424	0.424	0.424
ALPHA S	-5.0	-5.0	-5.0	-5.0	-5.0	-5.0	-5.0
ALPHA C	-8.1	-7.5	-11.6	-7.2	-7.4	-10.5	-8.4
THETA C	8.5	8.0	11.0	7.3	7.8	11.0	8.8
A1S	-3.7	-2.7	-3.7	-2.3	-0.5	-2.0	-1.3
B1S	3.1	2.5	5.6	2.2	2.4	5.5	3.4
SA1S	3.4	4.2	3.6	3.5	4.0	3.6	3.6
SB1S	0.3	-0.1	0.3	0.4	0.0	0.3	-0.2
CL/SIGMA	0.0703	0.0691	0.0679	0.0715	0.0695	0.0715	0.0689
CD/SIGMA	-0.00210	-0.00250	-0.00455	-0.00206	-0.00211	-0.00418	-0.00291
CY/SIGMA	-0.00329	-0.00186	-0.00214	-0.00199	0.00027	-0.00052	-0.00044
CQ/SIGMA	0.00470	0.00507	0.00777	0.00438	0.00452	0.00739	0.00506
CPM/SIGMA	0.001981	0.002287	0.001898	0.002193	0.001932	0.001673	0.001677
CRM/SIGMA	0.000071	0.000102	0.000381	0.000082	0.000445	0.000562	0.000199
V	73.0	72.8	73.0	73.0	72.8	72.8	73.0
RHO	0.00236	0.00238	0.00238	0.00230	0.00238	0.00238	0.00238

TABLE XXXVI - Concluded

Parameter	Configuration: θ_1=0 deg, δ_F=5 deg, S_E=1			Configuration: θ_1=0 deg, δ_F=0 deg, S_E=3		
	Test Values	Uniform Inflow Calculation Scaling Case 3	Variable Inflow Calculation Scaling Case 3	Test Values	Uniform Inflow Calculation Scaling Case 1	Variable Inflow Calculation Scaling Case 3
VS	146.0	146.0	146.0	146.0	146.0	146.0
OMEGA*R	699.7	700.0	700.0	699.7	700.0	700.0
MU	0.352	0.351	0.351	0.352	0.350	0.350
M1.90	0.420	0.424	0.424	0.424	0.424	0.424
ALPHA S	-5.0	-5.0	-5.0	-5.0	-5.0	-5.0
ALPHA C	-4.6	-6.4	-9.5	-7.6	-7.4	-10.0
THETA C	5.3	8.3	11.2	8.3	7.9	10.5
A1S	-2.3	-2.7	-4.2	-3.9	-3.0	-4.2
B1S	-0.4	1.4	4.5	2.9	2.4	5.0
SA1S	3.6	4.2	3.8	3.5	4.2	3.5
SB1S	0.4	-0.2	0.1	0.1	-0.2	0.1
CL/SIGMA	0.0709	0.0689	0.0691	0.0690	0.0697	0.0679
CD/SIGMA	-0.00269	-0.00294	-0.00502	-0.00178	-0.00273	-0.00485
CY/SIGMA	-0.00234	-0.00193	-0.00288	-0.00342	-0.00208	-0.00275
CQ/SIGMA	0.00378	0.00632	0.00952	0.00505	0.00533	0.00792
CPM/SIGMA	0.002437	0.002106	0.001970	0.001612	0.002059	0.002052
CRM/SIGMA	0.000196	0.000117	0.000065	0.000043	0.000061	0.000158
V	73.0	73.0	73.0	73.0	73.0	73.0
RHO	0.00230	0.00238	0.00238	0.00239	0.00238	0.00238

TABLE XXXVII. TEST AND CALCULATED ROTOR PERFORMANCE (Condition 71)

Parameter	Configuration: θ_1=0 deg, δ_F=0 deg, S_E=1			Configuration: θ_1=-8 deg, δ_F=0 deg, S_E=1		
	Test Values	Uniform Inflow Calculation	Variable Inflow Calculation	Test Values	Uniform Inflow Calculation	Variable Inflow Calculation
VS	124.0	124.0	124.0	124.0	124.0	124.0
OMEGA*R	699.7	700.0	700.0	699.7	700.0	700.0
MU	0.299	0.300	0.300	0.299	0.300	0.300
M1.90	0.407	0.407	0.407	0.407	0.407	0.407
ALPHA S	0.1	0.0	0.0	0.1	0.0	0.0
ALPHA C	-9.9	-9.0	-10.6	-9.4	-8.9	-10.2
THETA C	14.3	11.6	14.3	12.9	11.3	14.3
A1S	-7.2	-5.4	-7.3	-5.5	-3.3	-5.8
B1S	10.0	9.0	10.6	9.5	8.9	10.2
SA1S	0.0	0.2	0.0	0.0	0.1	0.1
SB1S	0.0	0.1	0.3	0.0	0.1	-0.4
CL/SIGMA	0.0996	0.1023	0.0996	0.1014	0.1028	0.1039
CD/SIGMA	-0.00575	-0.00411	-0.00539	-0.00503	-0.00389	-0.00476
CY/SIGMA	-0.00654	-0.00259	-0.00335	-0.00519	-0.00030	-0.00260
CQ/SIGMA	0.01185	0.00895	0.01157	0.01109	0.00827	0.01117
CPM/SIGMA	0.000962	0.000061	0.000062	0.000373	0.000206	-0.000115
CRM/SIGMA	0.000488	0.000532	0.000257	0.000494	0.000644	0.000377
V	62.0	62.0	63.0	62.0	62.0	62.0
RHO	0.00238	0.00238	0.00238	0.00235	0.00238	0.00238

TABLE XXXVII - Concluded

Parameter	Configuration: θ_1=0 deg, δ_F=5 deg, S_E=1			Configuration: θ_1=0 deg, δ_F =0 deg, S_E=1		
	Test Values	Uniform Inflow Calculation	Variable Inflow Calculation	Test Values	Uniform Inflow Calculation	Variable Inflow Calculation
VS	124.0	124.0	124.0	124.0	124.0	124.0
OMEGA*R	699.7	700.0	700.0	699.7	700.0	700.0
MU	0.299	0.300	0.300	0.299	0.300	0.300
M1.90	0.407	0.407	0.407	0.407	0.407	0.407
ALPHA S	0.1	0.0	0.0	0.1	-0.2	0.0
ALPHA C	-6.2	-8.8	-9.7	-10.6	-8.4	-9.5
THETA C	9.5	12.6	14.6	15.5	10.9	13.5
A1S	-4.4	-5.7	-7.8	-8.4	-5.1	-7.8
B1S	6.2	8.8	9.7	10.7	8.2	9.5
SA1S	0.0	0.1	0.0	0.0	0.2	0.0
SB1S	0.0	0.2	0.1	0.0	0.1	-0.1
CL/SIGMA	0.1019	0.1036	0.0991	0.1039	0.0956	0.1024
CD/SIGMA	-0.00561	-0.00502	-0.00578	-0.00950	-0.00450	-0.00624
CY/SIGMA	-0.00504	-0.00201	-0.00388	-0.00774	-0.00258	-0.00509
CQ/SIGMA	0.00857	0.01226	0.01392	0.01622	0.00966	0.01283
CPM/SIGMA	0.001090	0.000383	0.000219	0.001067	0.001318	0.000910
CRM/SIGMA	0.000407	0.000628	0.000285	0.000565	0.000045	-0.000395
V	62.0	62.0	62.0	62.0	62.0	62.0
RHO	0.00235	0.00238	0.00238	0.00232	0.00238	0.00238

TABLE XXXVIII. TEST AND CALCULATED ROTOR PERFORMANCE (Condition 80)

Parameter	Configuration: θ_1 = 0 deg, δ_p = 0 deg, S_E = 1		Configuration: θ_1 = -8 deg, δ_p = 0 deg, S_E = 1		Configuration: θ_1 = 0 deg δ_p = 5 deg, S_E = 1		Configuration: θ_1 = 0 deg, δ_p = 0 deg, S_E = 3	
	Test Values	Uniform Inflow Calculations	Test Values	Uniform Inflow Calculations	Test Values	Uniform Inflow Calculations	Test Values	Uniform Inflow Calculations
VS	124.0	123.8	124.0	124.0	124.0	123.8	124.0	123.8
OMEGA*R	699.7	700.0	699.7	700.0	699.7	700.0	699.7	700.0
MU	0.299	0.298	0.299	0.300	0.299	0.298	0.299	0.298
M1.90	0.407	0.407	0.407	0.407	0.407	0.407	0.407	0.407
ALPHA S	-5.0	-5.0	-5.1	-5.0	-5.0	-5.0	-5.0	-5.1
ALPHA C	-9.7	-9.6	-9.0	-9.6	-7.1	-8.8	-10.1	-9.5
THETA C	7.6	7.6	6.7	7.5	5.1	7.7	7.2	7.2
A1S	-2.7	-2.3	-1.6	-0.9	-1.6	-2.1	-2.5	-2.1
B1S	4.6	4.6	4.0	4.6	2.1	3.8	5.0	4.4
SA1S	0.0	0.1	0.0	0.0	0.0	0.0	0.0	0.0
SB1S	0.0	-0.1	0.0	-0.2	0.0	0.0	0.0	0.0
CL/SIGMA	0.0563	0.0586	0.0556	0.0585	0.0559	0.0548	0.0573	0.0544
CD/SIGMA	-0.00477	-0.00593	-0.00399	-0.00533	-0.00629	-0.00565	-0.00461	-0.00554
CY/SIGMA	-0.00169	-0.00097	-0.00132	-0.00012	-0.00141	-0.00087	-0.00177	-0.00077
CQ/SIGMA	0.00420	0.00460	0.00393	0.00404	0.00385	0.00494	0.00426	0.00419
CPM/SIGMA	0.000049	0.000041	0.000091	-0.000053	0.000771	-0.000147	-0.000104	-0.000109
CRM/SIGMA	0.000141	0.000051	0.000102	0.000246	0.000245	0.000034	0.000192	0.000039
V	62.0	61.9	62.0	62.0	62.0	61.9	62.0	61.9
RHO	0.00238	0.00238	0.00235	0.00238	0.00235	0.00238	0.00232	0.00238

TABLE XXXIX. TEST AND CALCULATED ROTOR PERFORMANCE (Condition 82)

Parameter	Configuration: θ_1 = 0 deg, δ_F = 0 deg, S_E = 1		Configuration: θ_1 = -8 deg, δ_F = 0 deg, S_E = 1		Configuration: θ_1 = 0 deg, δ_F = 5 deg, S_E = 1		Configuration: θ_1 = 0 deg, δ_F = 0 deg, S_E = 3	
	Test Values	Uniform Inflow Calculation	Test Values	Uniform Inflow Calculation	Test Values	Uniform Inflow Calculation	Test Values	Uniform Inflow Calculation
VS	124.0	124.0	124.0	124.0	124.0	124.0	124.0	124.0
OMEGA*R	699.7	700.0	699.7	700.0	699.7	700.0	699.7	700.0
MU	0.299	0.300	0.299	0.300	0.299	0.300	0.299	0.300
M1*90	0.407	0.407	0.407	0.407	0.407	0.407	0.407	0.407
ALPHA S	-5.0	-5.0	-5.0	-4.9	-5.0	-5.0	-4.9	-4.9
ALPHA C	-13.8	-14.6	-13.4	-14.9	-10.3	-14.2	-15.0	-13.5
THETA C	14.3	14.0	13.2	13.7	9.9	14.3	16.1	13.1
A1S	-6.4	-6.5	-5.0	-4.5	-3.7	-6.3	-7.9	-6.0
B1S	8.9	9.6	8.4	10.0	5.4	9.2	10.1	8.6
SA1S	0.0	0.2	0.0	-0.4	0.0	-0.1	0.0	0.3
SB1S	0.0	0.0	0.0	0.2	0.0	0.1	0.0	0.2
CL/SIGMA	0.0911	0.0933	0.0919	0.0949	0.0918	0.0899	0.0938	0.0940
CD/SIGMA	-0.01170	-0.01282	-0.01154	-0.01347	-0.01155	-0.01336	-0.01508	-0.01309
CY/SIGMA	-0.00573	-0.00293	-0.00471	-0.00057	-0.00395	-0.00215	-0.00708	-0.00353
CQ/SIGMA	0.01144	0.01245	0.01086	0.01167	0.00829	0.01433	0.01608	0.01267
CPM/SIGMA	0.000571	-0.000030	0.000300	-0.000371	0.000891	-0.000316	0.000502	0.000329
CRM/SIGMA	0.000360	0.000279	0.000272	0.000409	0.000375	-0.000077	0.000509	-0.000114
V	62.0	62.0	62.0	62.0	62.0	62.0	62.0	62.0
RHO	0.00236	0.00238	0.00235	0.00238	0.00235	0.00238	0.00232	0.00238

TABLE XL. SUMMATION OF MODAL CONTRIBUTIONS TO FLAPWISE MOMENT RESPONSE AT .20R (Condition 7, ψ = 30 deg, Uniform Inflow, θ_1 = 0 deg, δ_F = 0 deg, S_E = 1)

Bending Mode Number	Modal Amplitude	Modal Curvature	Curvature Contribution	Summations	
				Curvature	Moment (in.-lb)
i	q_{wi}	γ''_{wi} (.20R)	$q_{wi}\gamma''_{wi}$	$\sum q_{wi}\gamma''_{wi}$	$\frac{EI}{R}\sum_i q_{wi}\gamma''_{wi}$
1	.009171	10.63	.09748	.09748	5.36
2	-.001459	-54.82	.07998	.1775	9.76
3	.0001520	91.02	.01384	.1913	10.5
4	-.0003857	-114.3	.04409	.2354	12.9

TABLE XLI. SUMMATION OF MODAL CONTRIBUTIONS TO CHORDWISE MOMENT RESPONSE AT .20R (Condition 7, ψ = 50 deg, Uniform Inflow, θ_1 = 0 deg, δ_F = 0 deg, S_E = 1)

Bending Mode Number	Modal Amplitude	Modal Curvature	Curvature Contribution	Summations	
				Curvature	Moment (in.-lb)
j	q_{vj}	γ''_{vj} (.20R)	$q_{vj}\gamma''_{vj}$	$\sum q_{vj}\gamma''_{vj}$	$\frac{EI}{R}\sum_j q_{vj}\gamma''_{vj}$
1	-.001412	7.89	-.01114	-.01114	6.24
2	.0003062	-45.89	-.01405	-.02519	14.10

TABLE XLII. SUMMATION OF MODAL CONTRIBUTIONS TO FLAPWISE MOMENT RESPONSE AT .65R (Condition 7, ψ = 120 deg, Uniform Inflow, θ_1 = 0 deg, δ_F = 0 deg, S_E = 1)

Bending Mode Number	Modal Amplitude	Modal Curvature (.65R)	Curvature Contribution	Summations	
				Curvature	Moment (in.-lb)
i	q_{wi}	γ''_{wi}	$q_{wi}\gamma''_{wi}$	$\sum q_{wi}\gamma''_{wi}$	$\frac{EI}{R}\sum_i q_{wi}\gamma''_{wi}$
1	.001978	11.24	.02223	.02223	1.07
2	-.001073	30.51	-.03274	-.0105	-.503
3	.0001941	10.84	.002104	-.0084	-.403
4	-.00004348	-110.81	.004818	-.00358	-.172

TABLE XLIII. SUMMATION OF MODAL CONTRIBUTIONS TO FLAPWISE MOMENT RESPONSE AT .65R (Condition 7, ψ = 280 deg, Uniform Inflow, θ_1 = 0 deg, δ_F = 0 deg, S_E = 1)

Bending Mode Number	Modal Amplitude	Modal Curvature (.65R)	Curvature Contribution	Summations	
				Curvature	Moment (in.-lb)
i	q_{wi}	γ''_{wi}	$q_{wi}\gamma''_{wi}$	$\sum q_{wi}\gamma''_{wi}$	$\frac{EI}{R}\sum_i q_{wi}\gamma''_{wi}$
1	.009089	11.24	.1022	.1022	4.90
2	-.0003008	30.51	-.009177	.0930	4.46
3	-.00008789	10.84	-.0009527	.0920	4.41
4	-.0001682	-110.81	+.01864	.1106	5.31

TABLE XLIV. SUMMATION OF MODAL CONTRIBUTIONS TO FLAPWISE MOMENT RESPONSE AT .65R (Condition 7, ψ = 120 deg, Uniform Inflow, θ_1 = -8 deg, δ_F = 0 deg, S_E = 1)

Bending Mode Number	Modal Amplitude	Modal Curvature (.65R)	Curvature Contribution	Summations Curvature	Summations Moment (in.-lb)
i	q_{wi}	γ''_{wi}	$q_{wi}\gamma''_{wi}$	$\sum q_{wi}\gamma''_{wi}$	$\frac{EI}{R}\sum q_{wi}\gamma''_{wi}$
1	-.01059	11.24	-.1190	-.1190	-5.71
2	-.001702	30.51	-.0519	-.1709	-8.20
3	.0004925	10.84	.0053	-.1656	-7.94
4	-.0001437	-110.81	.0159	-.1497	-7.18

TABLE XLV. SUMMATION OF MODAL CONTRIBUTIONS TO FLAPWISE MOMENT RESPONSE AT .65R (Condition 7, ψ = 280 deg, Uniform Inflow, θ_1 = -8 deg, δ_F = 0 deg, S_E = 1)

Bending Mode Number	Modal Amplitude	Modal Curvature (.65R)	Curvature Contribution	Summation Curvature	Summation Moment (in.-lb)
i	q_{wi}	γ''_{wi}	$q_{wi}\gamma''_{wi}$	$\sum q_{wi}\gamma''_{wi}$	$\frac{EI}{R}\sum q_{wi}\gamma''_{wi}$
1	.009286	11.24	.1044	.1044	5.011
2	-.000321	30.51	-.0098	.0945	4.54
3	.0000004421	10.84	.0000	.0945	4.54
4	-.0001095	-110.81	.0121	.1067	5.12

TABLE XLVI. SUMMATION OF MODAL CONTRIBUTIONS TO FLAPPING RESPONSE AT HINGE (Condition 7, ψ = 90 deg, Uniform Inflow, θ_1 = 0 deg, δ_F = 0 deg, S_E = 1)

Bending Mode Number	Modal Amplitude	Modal Slope	Flapping Contribution	Summation (Radians)
i	q_{wi}	γ'_{wi}	$q_{wi}\gamma'_{wi}$	$\sum_i q_{wi}\gamma'_{wi}$
0	.1024	1.00	.1024	.1024
1	.002532	-2.39	-.00605	.0963
2	-.0002080	4.16	-.000865	.0955
3	.00008204	-3.16	-.0002592	.0952
4	.00001312	2.16	.0000283	.0952

TABLE XLVII. SUMMATION OF MODAL CONTRIBUTIONS TO FLAPWISE ACCELERATION RESPONSE AT .65R (Condition 7, ψ = 120 deg, Uniform Inflow, θ_1 = 0 deg, δ_F = 0 deg, S_E = 1)

Bending Mode Number	Modal Acceleration	Mode Shape (.65R)	Acceleration Contribution	Summations of Acceleration	
				Nondimensional	Dimensional
i	q_{wi}	γ_{wi}	$q_{wi}\gamma_{wi}$	$\sum_i q_{wi}\gamma_{wi}$	$R\Omega^2\sum q_{wi}\gamma_{wi}$ ft/sec^2
0	-.02163	.618	-.01337	-.01337	-357
1	.00594	-.330	-.00196	-.01533	-410
2	.00388	-.630	-.00244	-.01777	-485
3	-.00430	-.140	.000602	-.01717	-459
4	-.00883	.690	-.00609	-.02326	-621

TABLE XLVIII. APPROXIMATE VALUES OF CALCULATED STALL FLUTTER PARAMETERS
(θ_1 = 0 deg, δ_F = 0 deg, S_E = 1)

Item Inflow Assumption	Condition 7 Uniform	Condition 71 Uniform	Condition 71 Variable
Azimuth, ψ, deg	340	355	15
Torsional Moment Amplitude $M_{T.20R}$, in.-lb	6.03	10.6	14.9
Blade .8R Torsional Deflection Amplitude, θ_e, rad	.0521	.0917	.129
Blade .8R Pitching Velocity Amplitude, $\dot{\alpha}$, rad/sec	39.8	70.0	98.5
Blade .8R Pitching Acceleration Amplitude, $\ddot{\alpha}$, rad/sec	30.4×10^3	53.5×10^3	75.1×10^3
Blade Element .8R Relative Velocity, U, ft/sec	233	253	283
Nondimensional Pitching Velocity, A	.0192	.0338	.0475
Nondimensional Pitching Acceleration, B	.00700	.0105	.0118

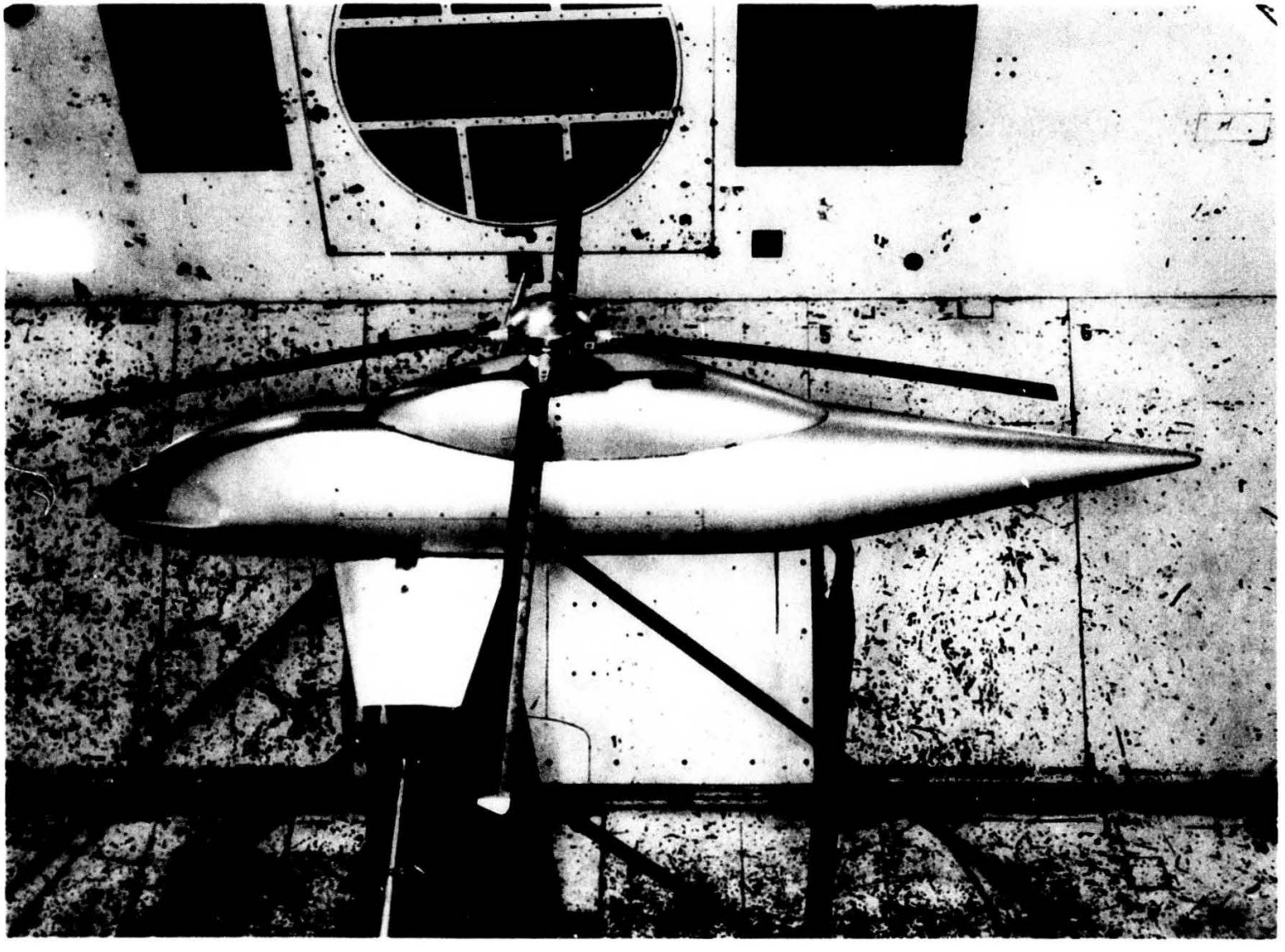

Figure 1. Helicopter Model With H-34 Model Blades.

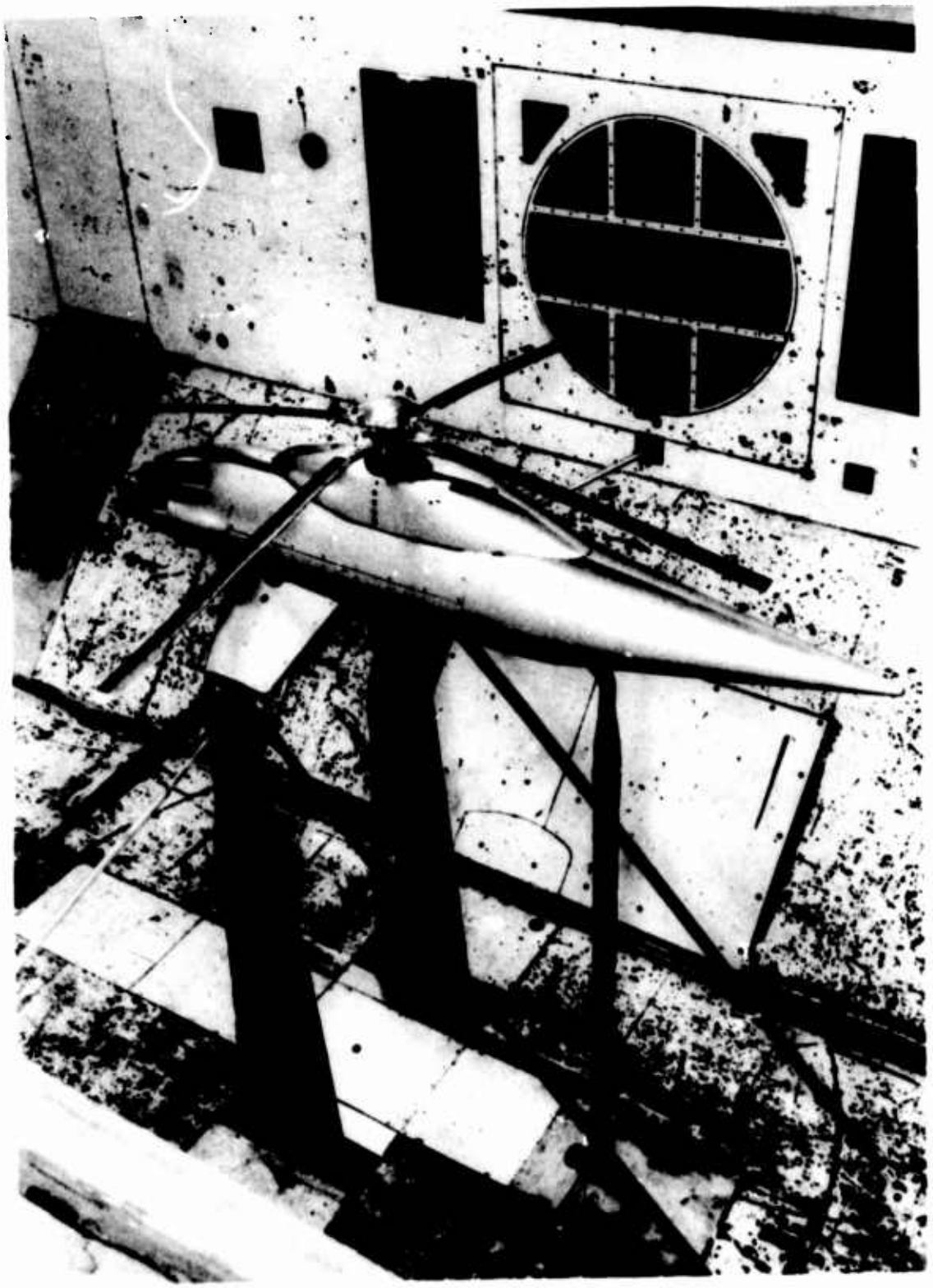

Figure 2. Helicopter Model Wind Tunnel Installation.

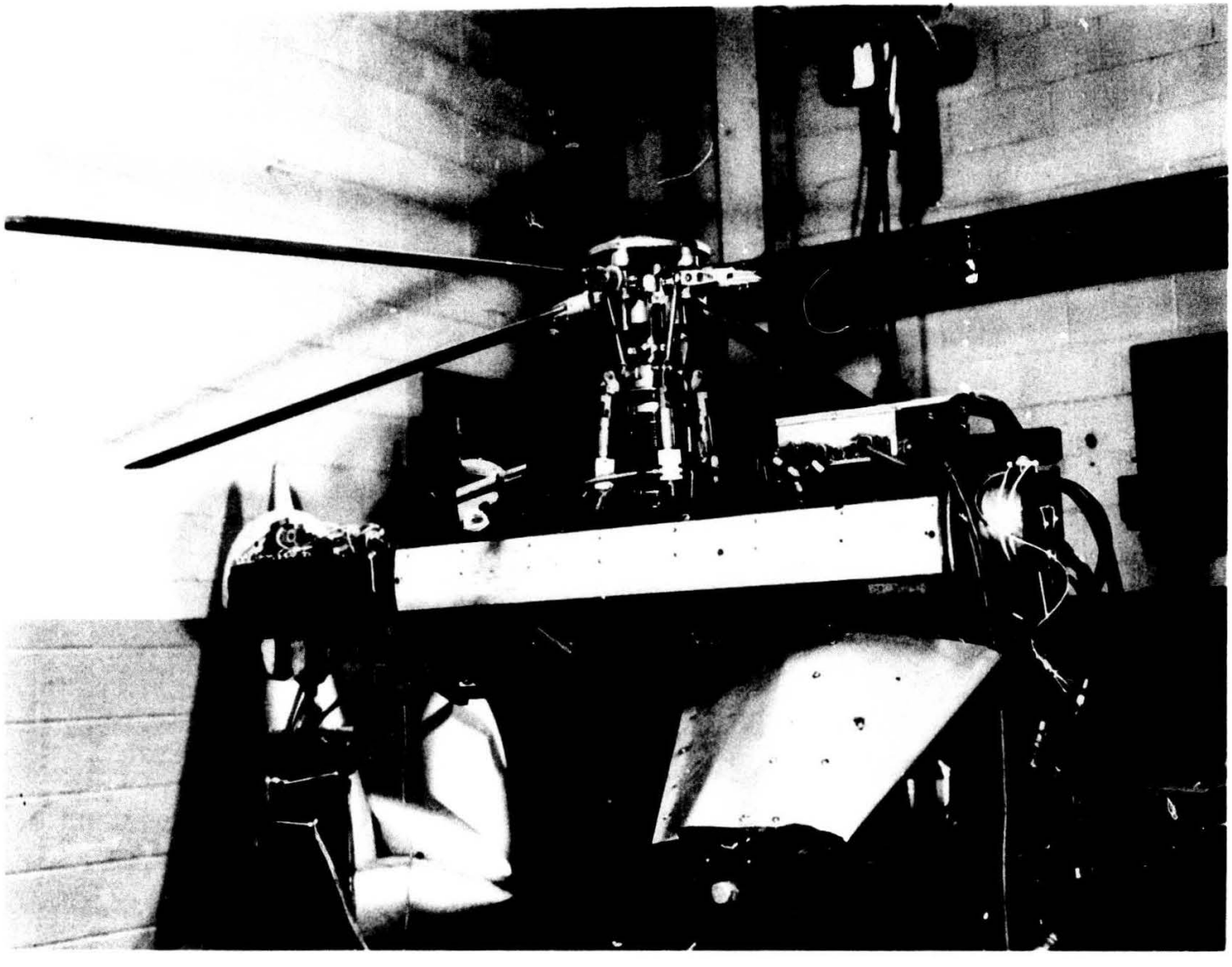

Figure 3. Internal Details of Helicopter Model.

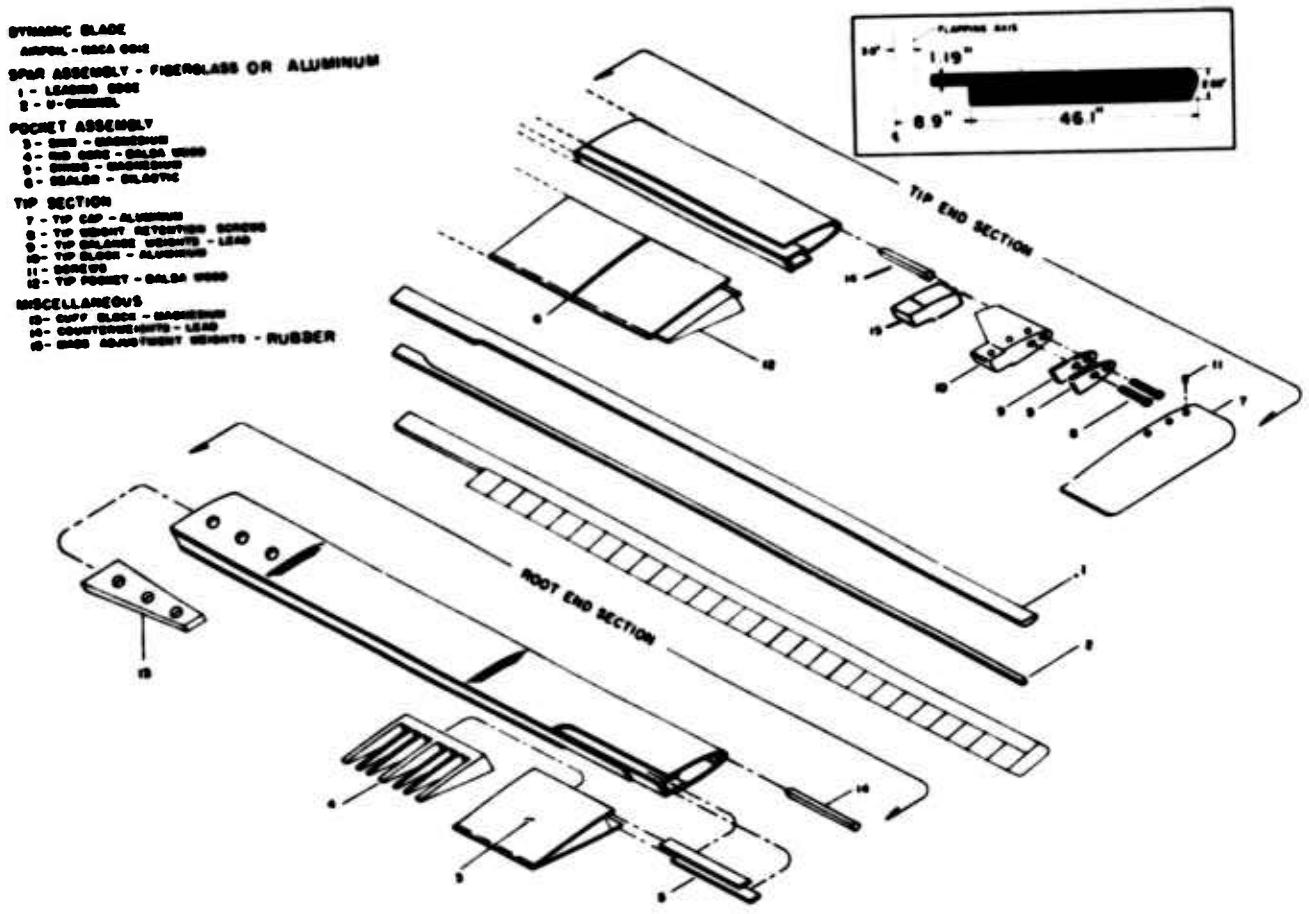

Figure 4. Dynamically Scaled Blade-Exploded View.

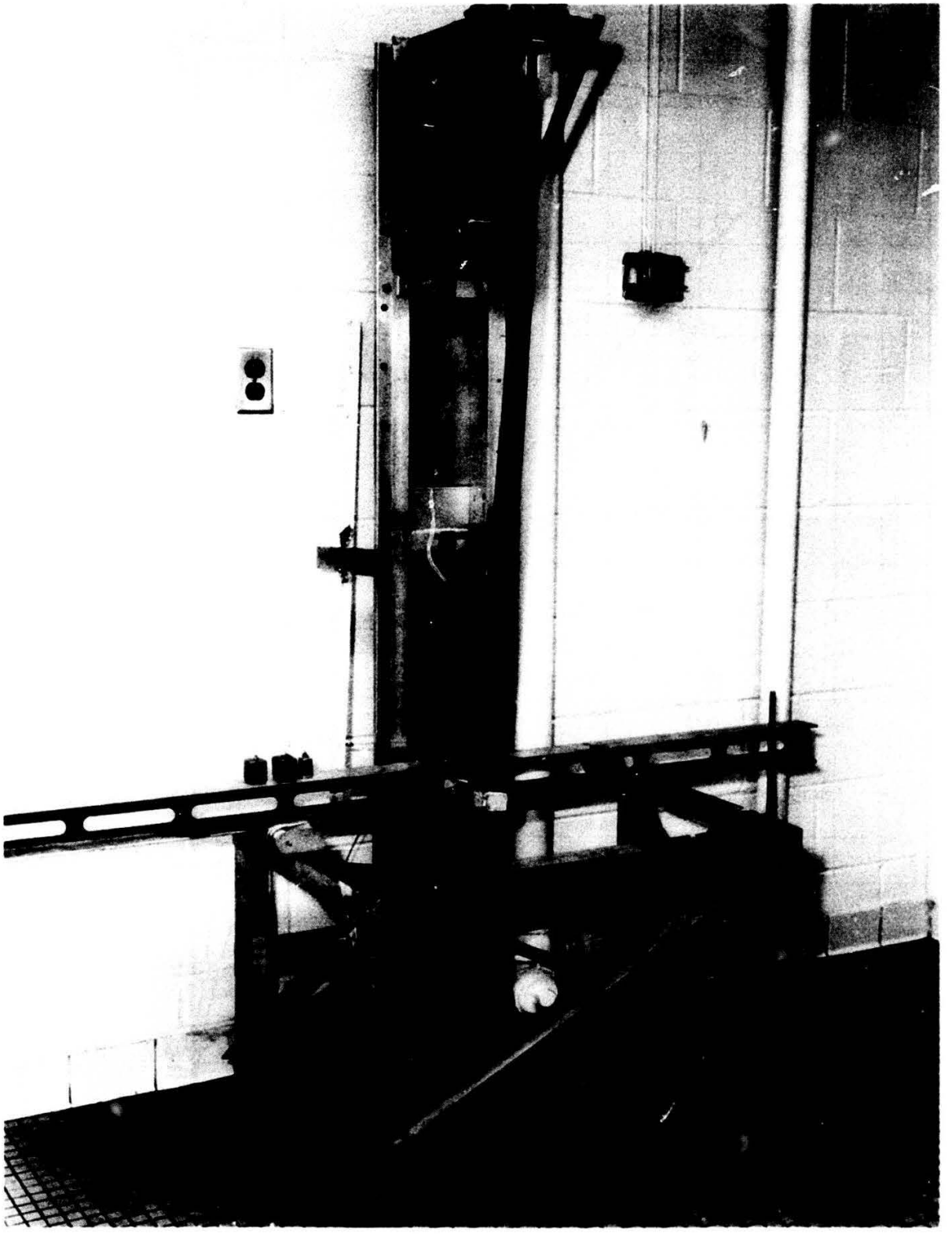

Figure 5. Blade Deflection Test and Calibration Stand.

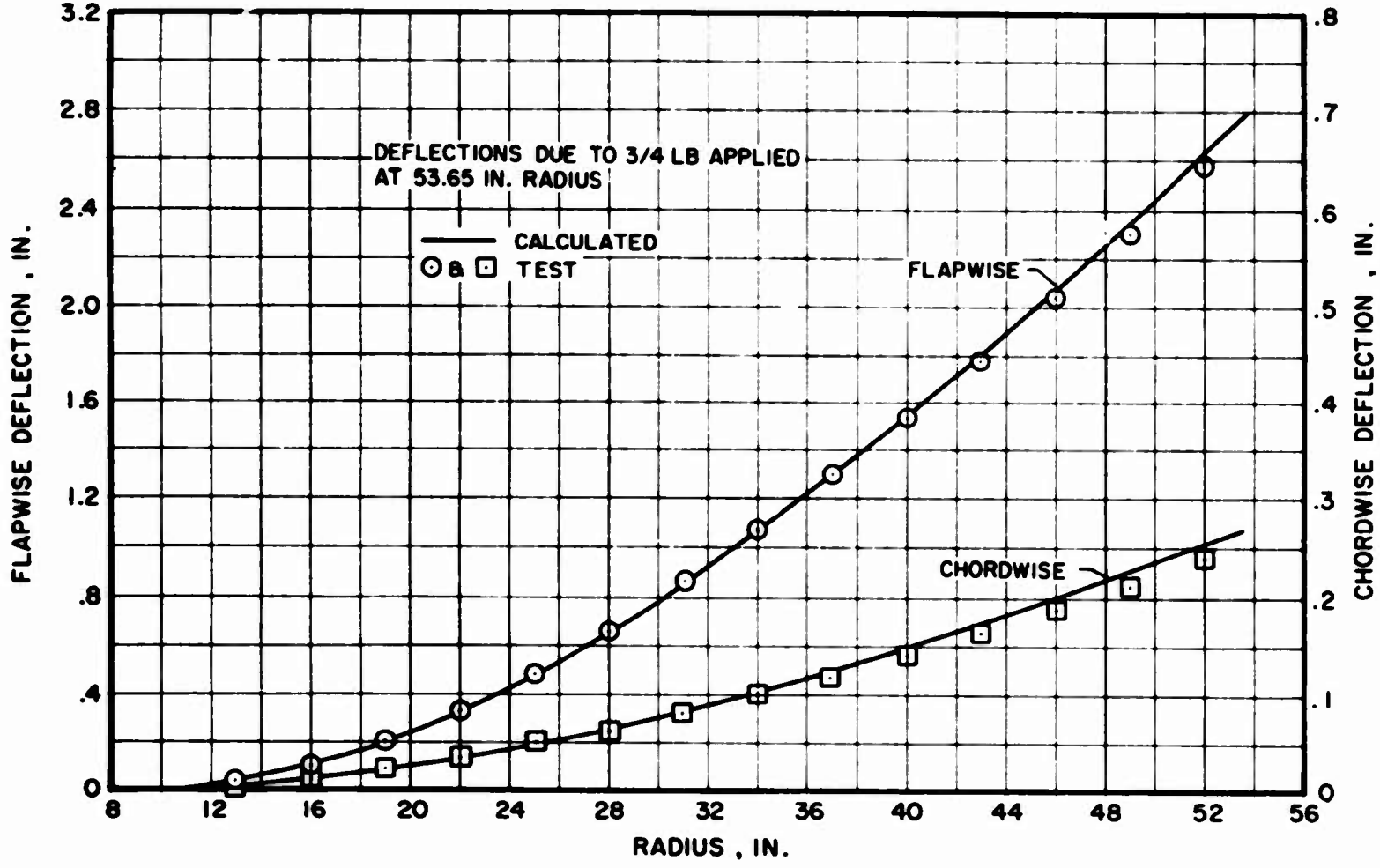

Figure 6. H-34 Model Rotor Blade Flapwise and Chordwise Deflections, Blade Clamped at 6.25-Inch Radius, Three-Times-Scale Stiffness Aluminum Spar.

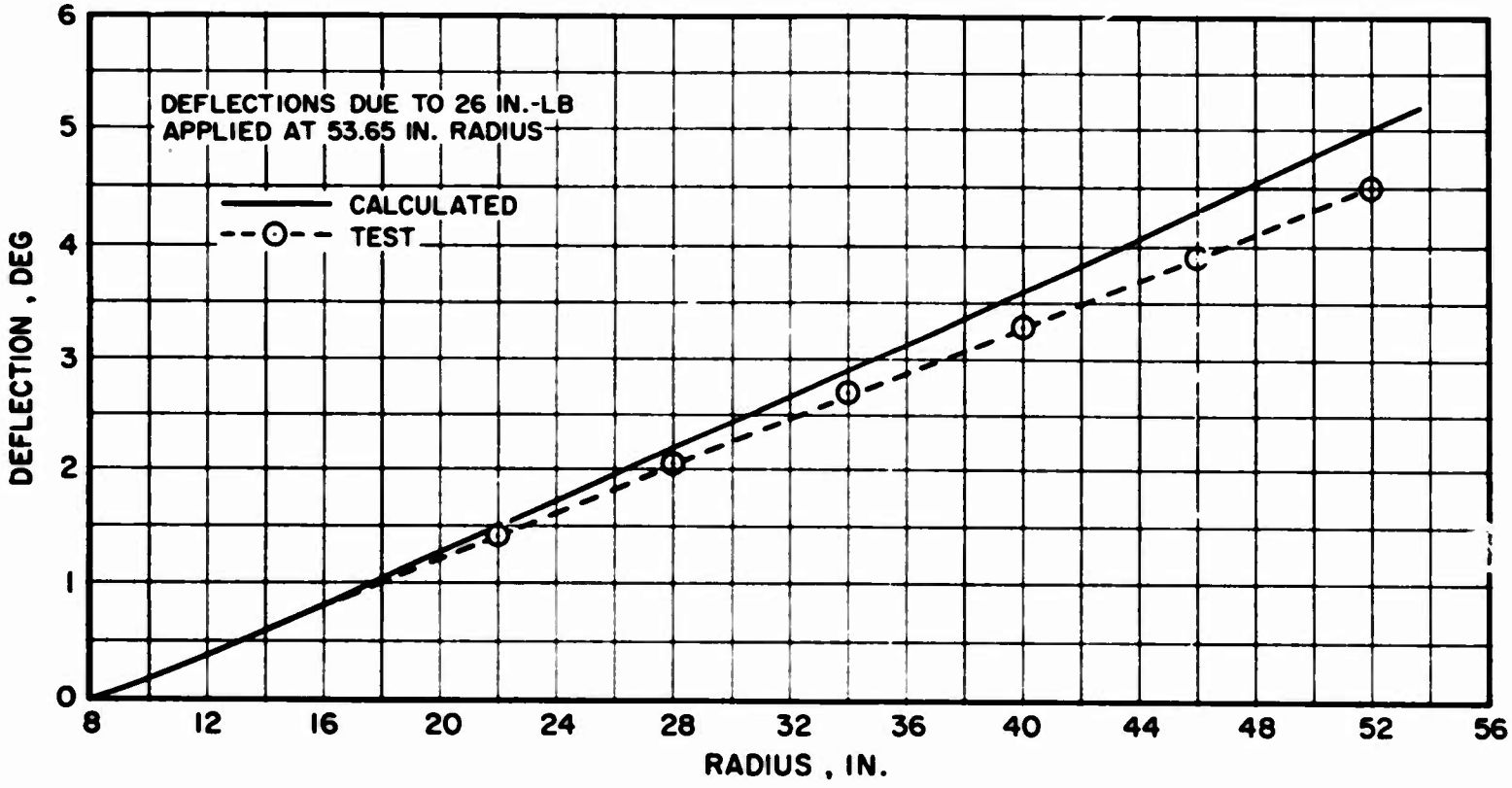

Figure 7. H-34 Model Rotor Blade Torsional Deflections, Blade Clamped at 6.25-Inch Radius, Three-Times-Scale Stiffness Aluminum Spar.

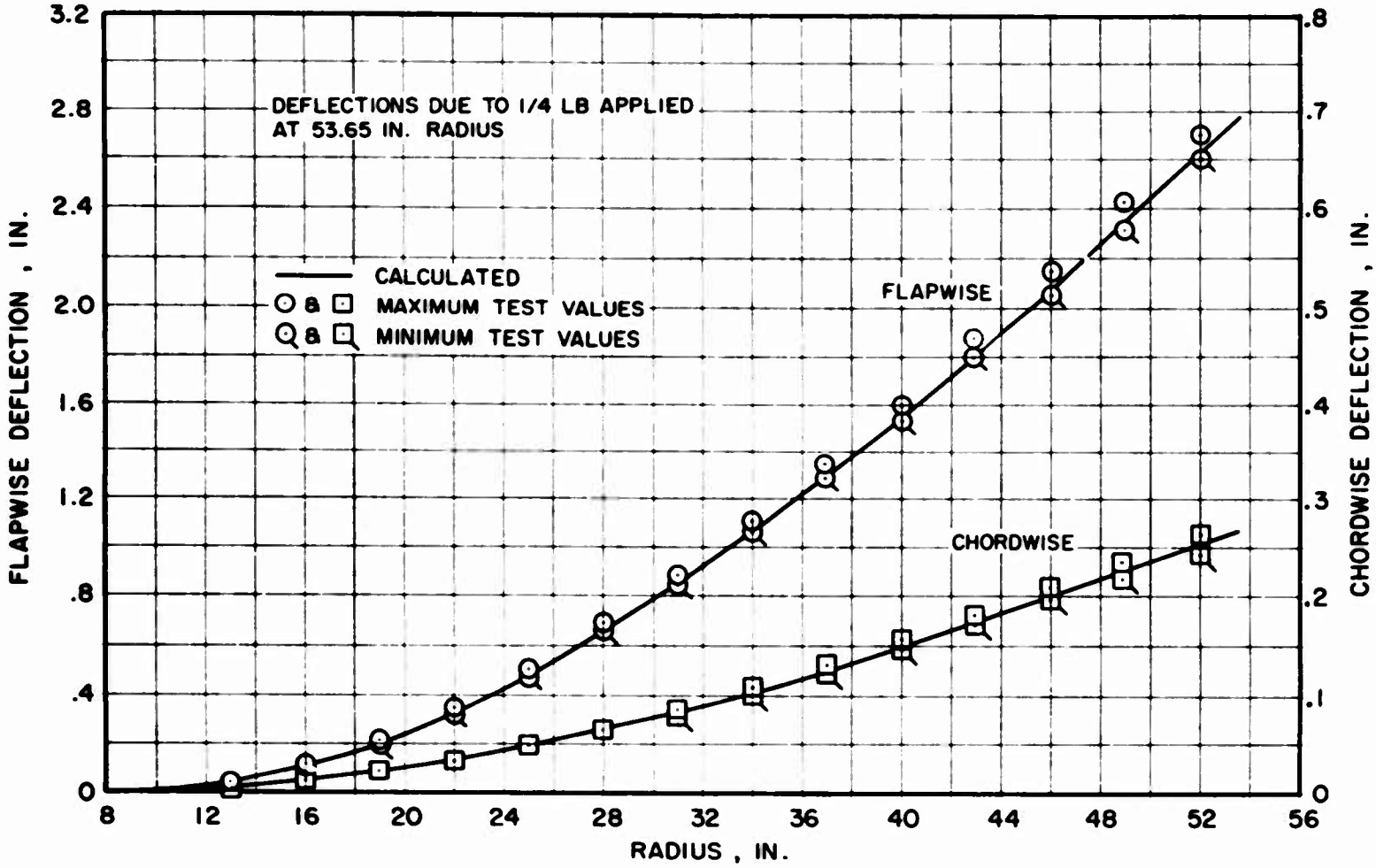

Figure 8. H-34 Model Rotor Blade Flapwise and Chordwise Deflections, Blade Clamped at 6.25-Inch Radius, Scale Stiffness Fiber Glass Spar.

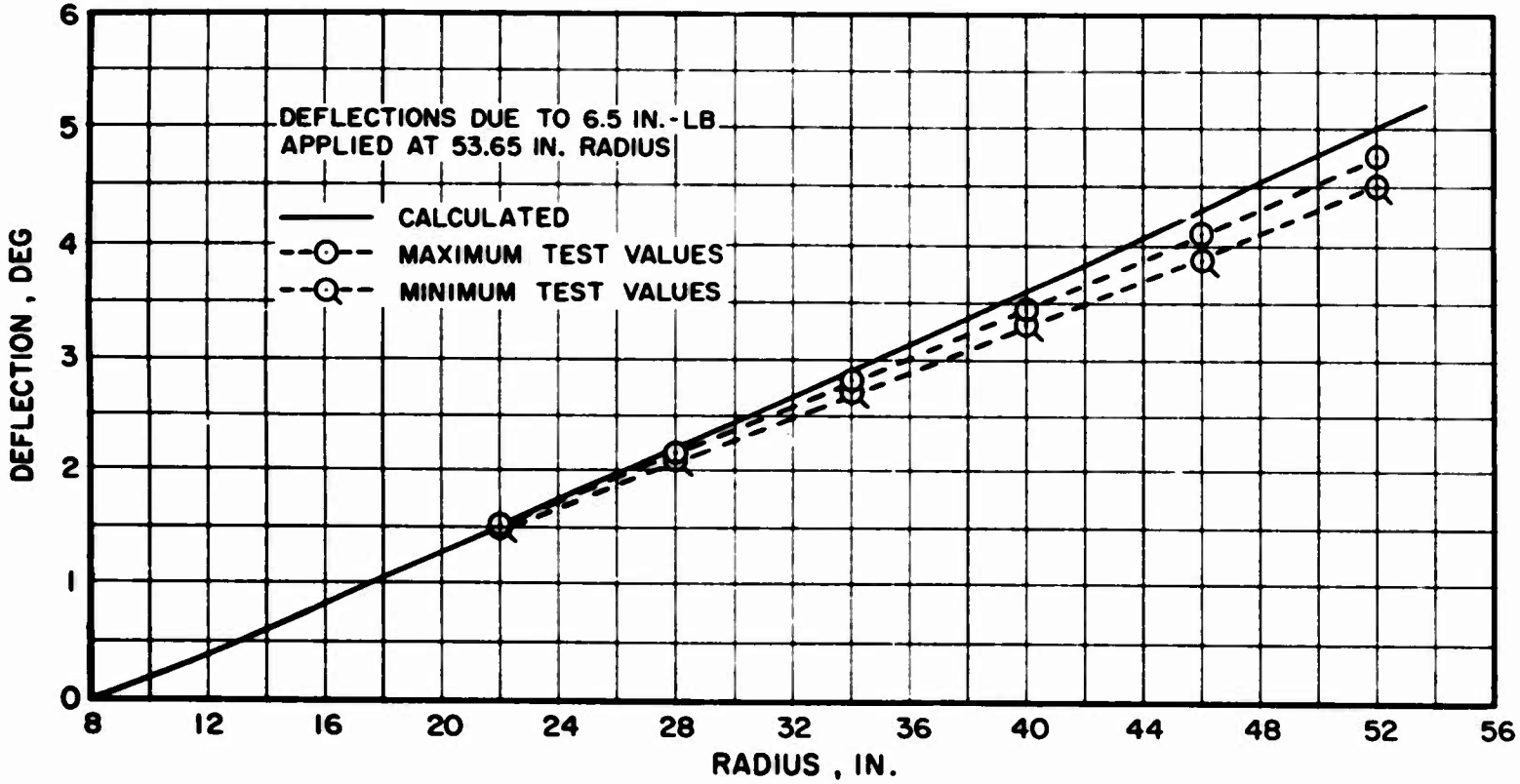

Figure 9. H-34 Model Rotor Blade Torsional Deflections, Blade Clamped at 6.25-Inch Radius, Scale Stiffness Fiber Glass Spar.

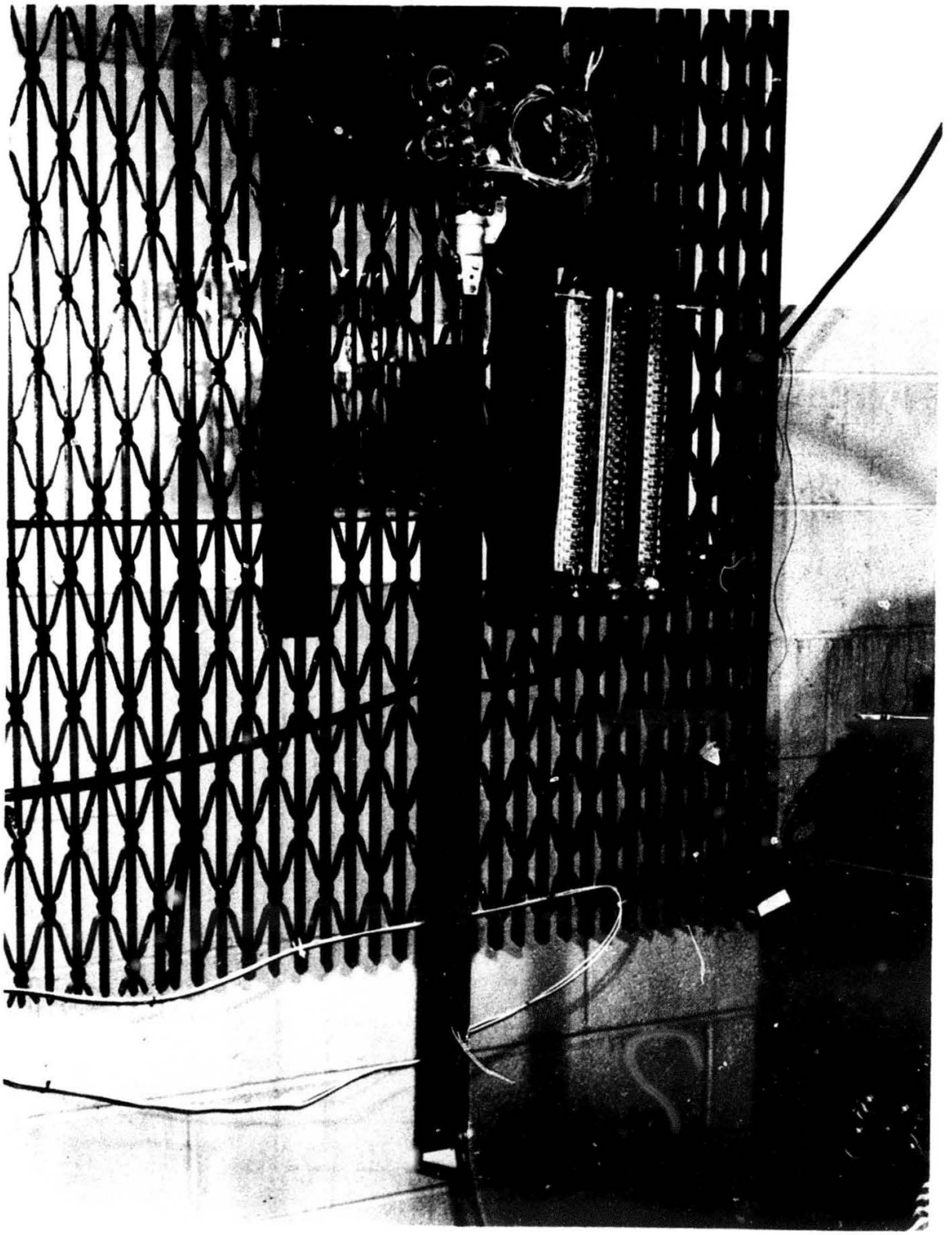

Figure 10. Blade Natural Frequency Test Setup.

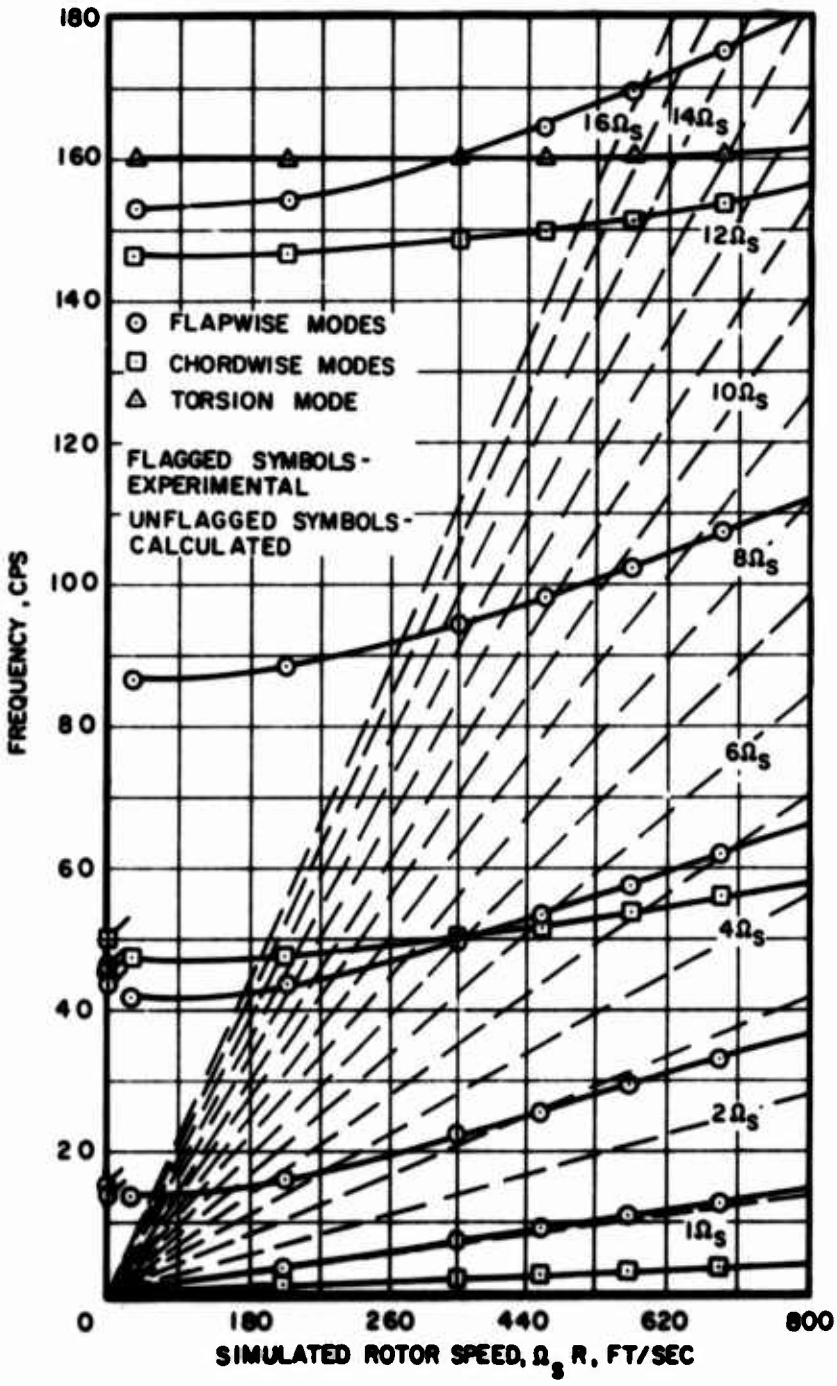

Figure 11. Natural Frequencies Versus Rotational Tip Speed for Three-Times-Scale Stiffness Aluminum Spar H-34 Model Blades.

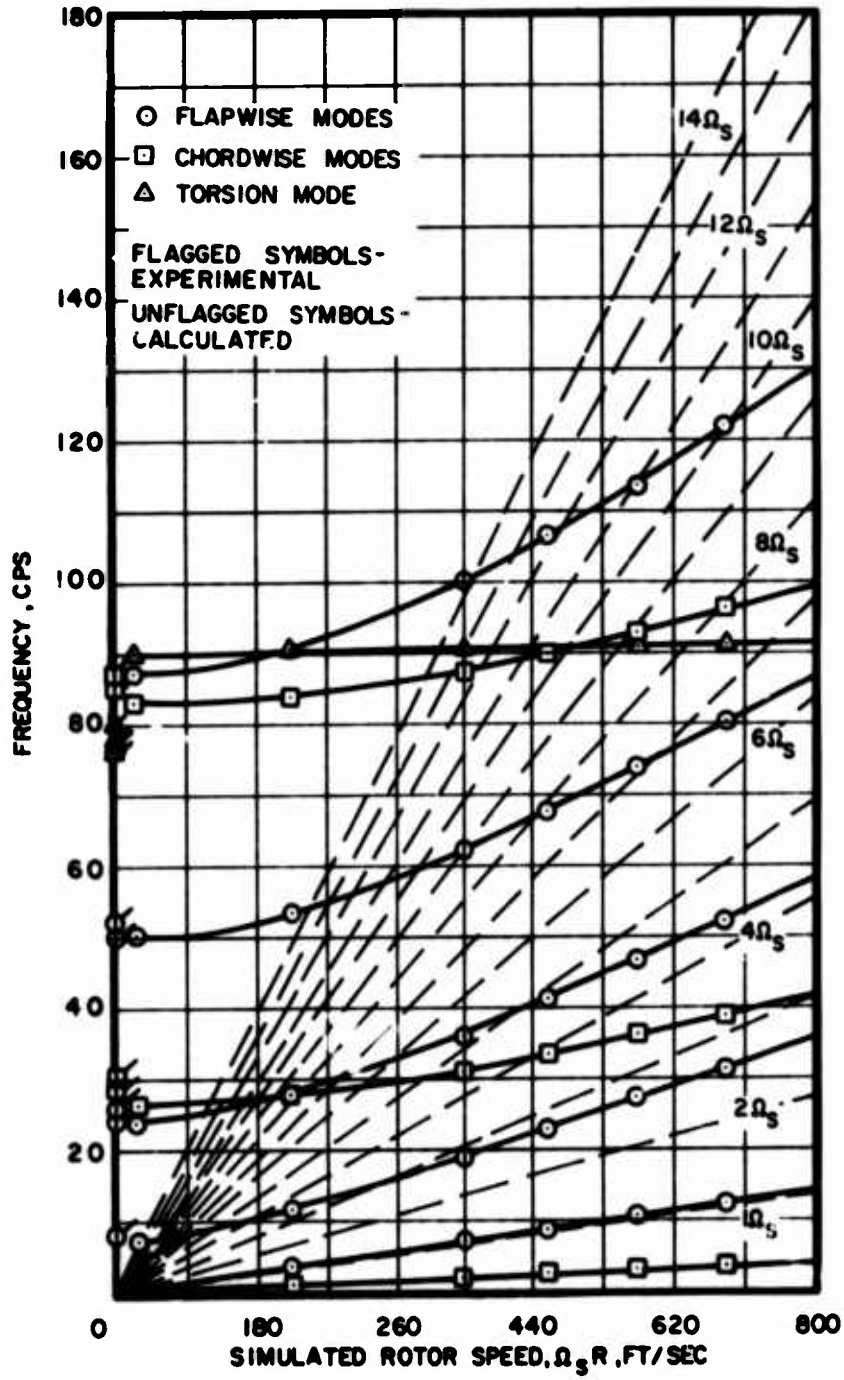

Figure 12. Natural Frequencies Versus Rotational Tip Speed for Dynamically Scaled Fiber Glass H-34 Model Blades.

Figure 13. Two-Dimensional Blade Section Wind Tunnel Test Setup.

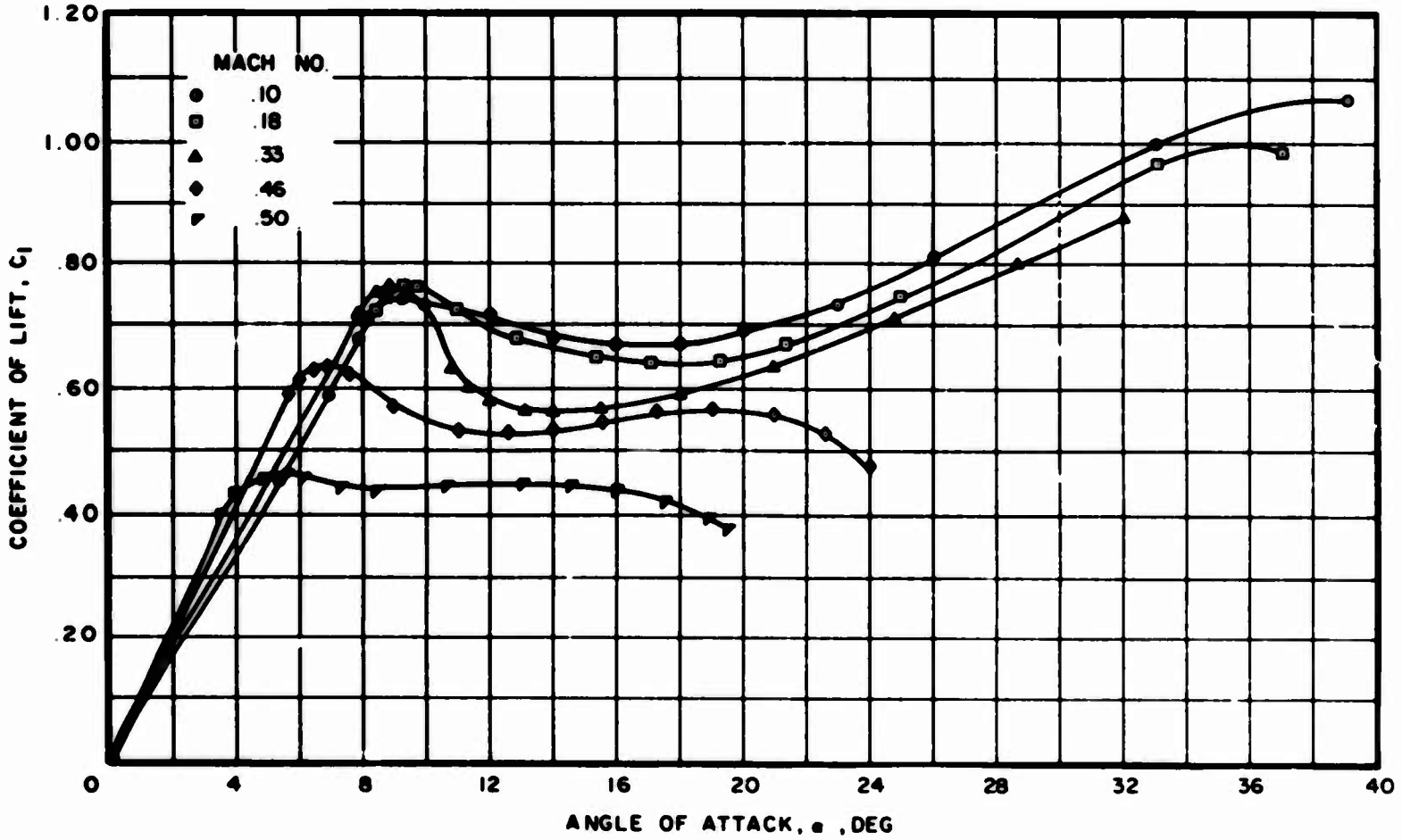

(a) Coefficient of Lift $0 < \alpha < 40^{\circ}$

Figure 14. Two-Dimensional Aerodynamic Coefficients for the Symmetrical 2.69-Inch Chord Airfoil Section.

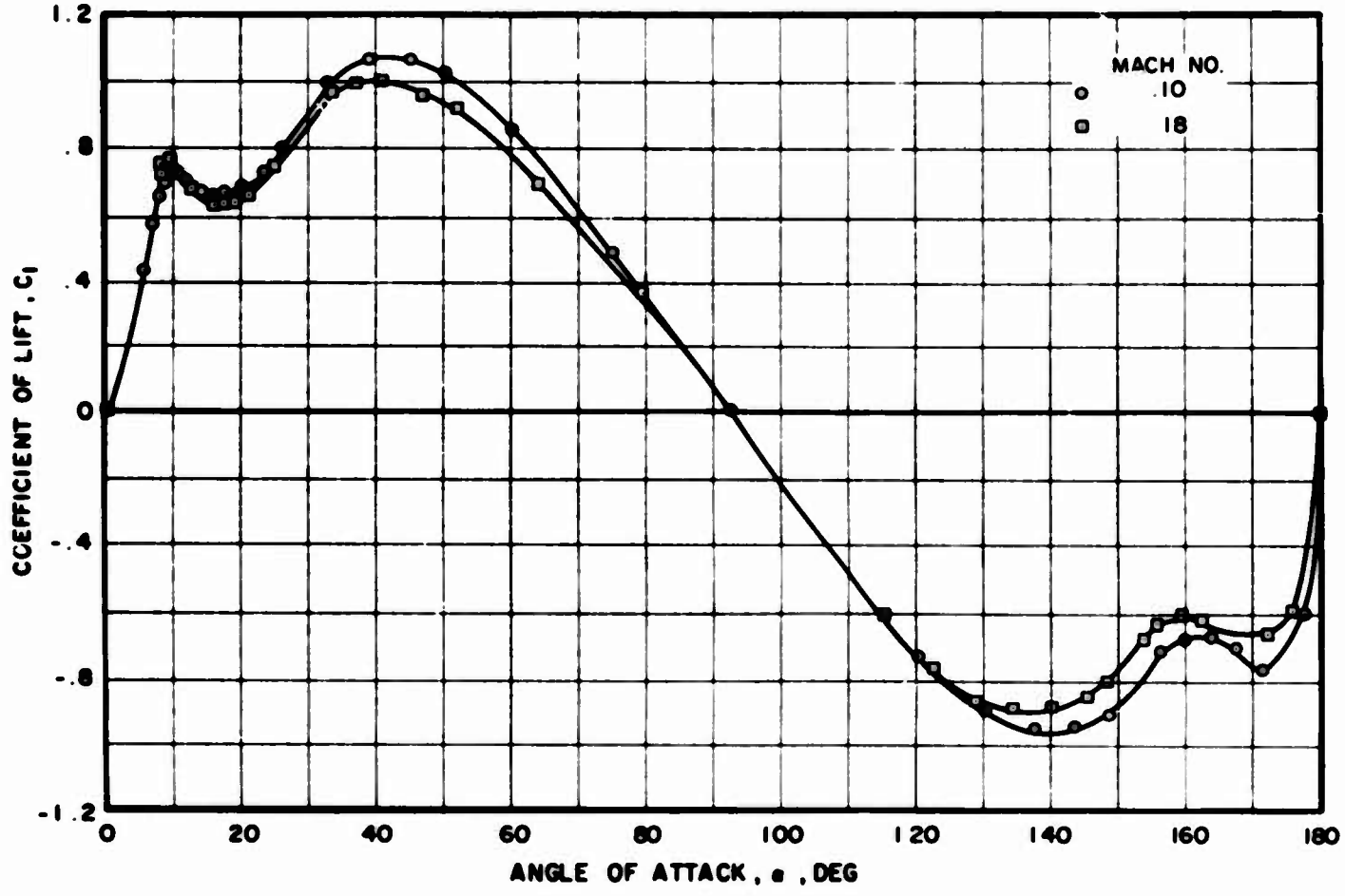

(b) Coefficient of Lift $0 < \alpha < 180^{\circ}$

Figure 14. Continued.

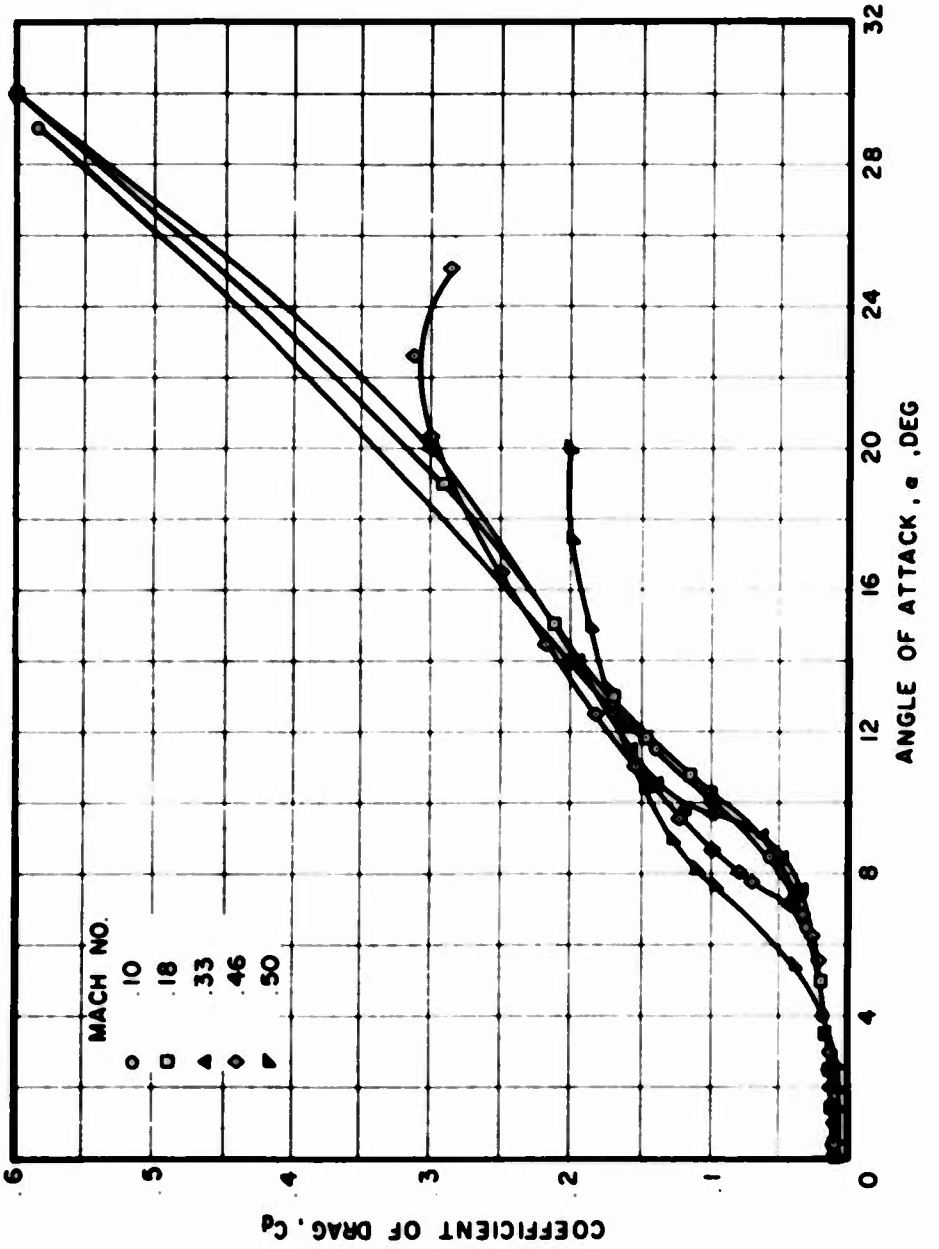

(c) Coefficient of Drag $0 < \alpha < 30^{\circ}$

Figure 14. Continued.

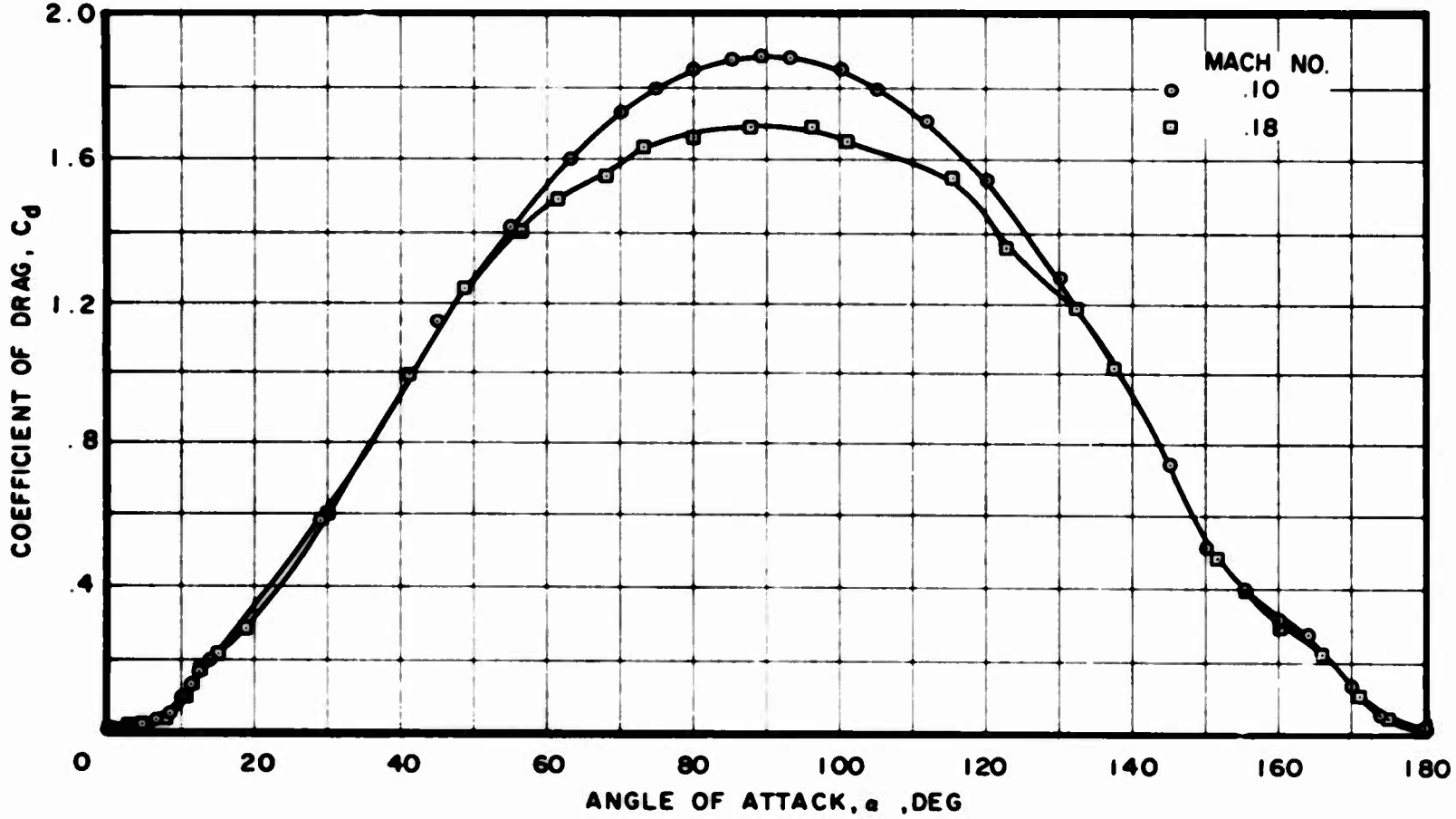

(d) Coefficient of Drag $0 < \alpha < 180^{\circ}$

Figure 14. Continued.

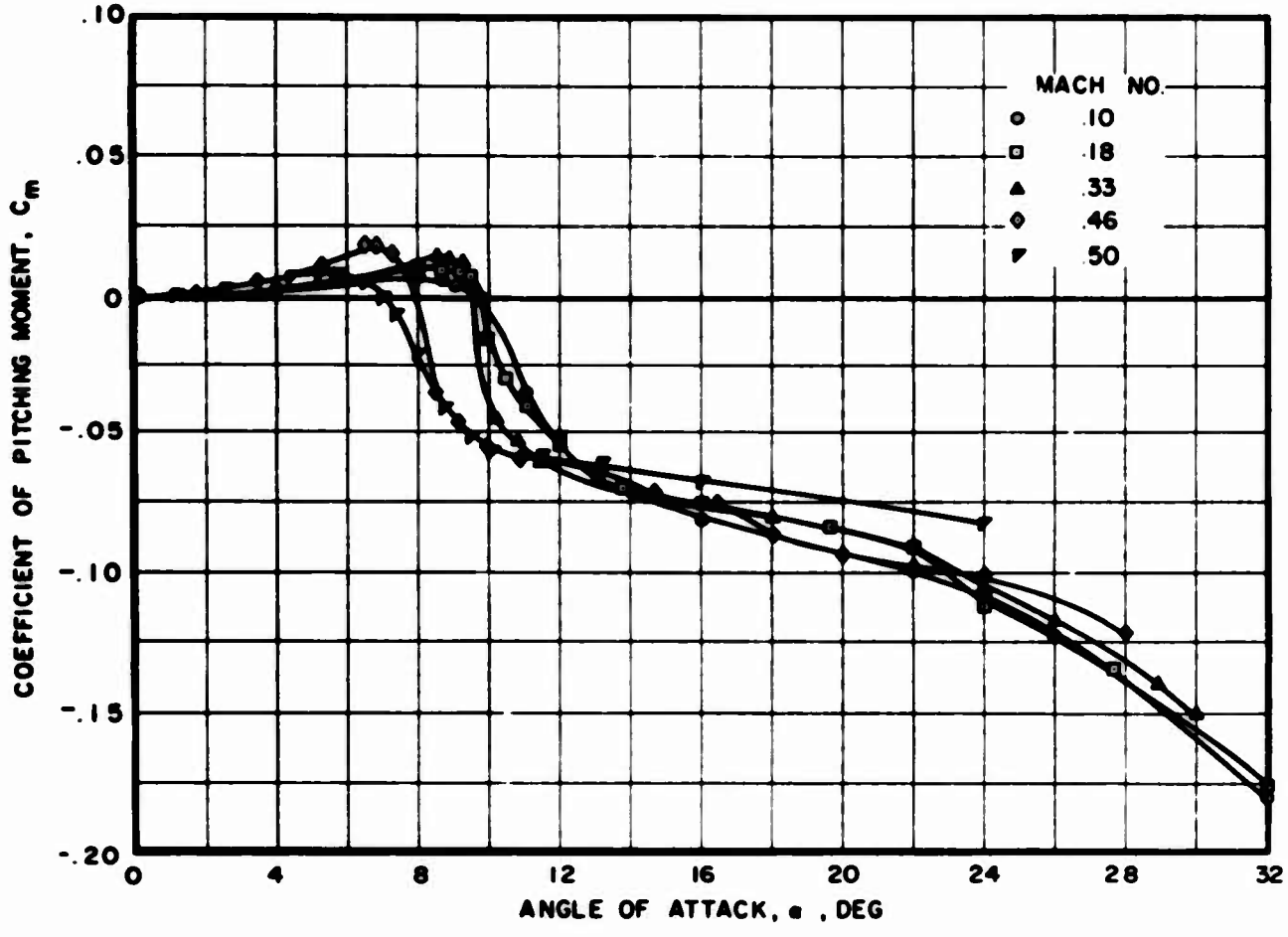

(e) Coefficient of Pitching Moment $0 < \alpha < 32^{\circ}$

Figure 14. Continued.

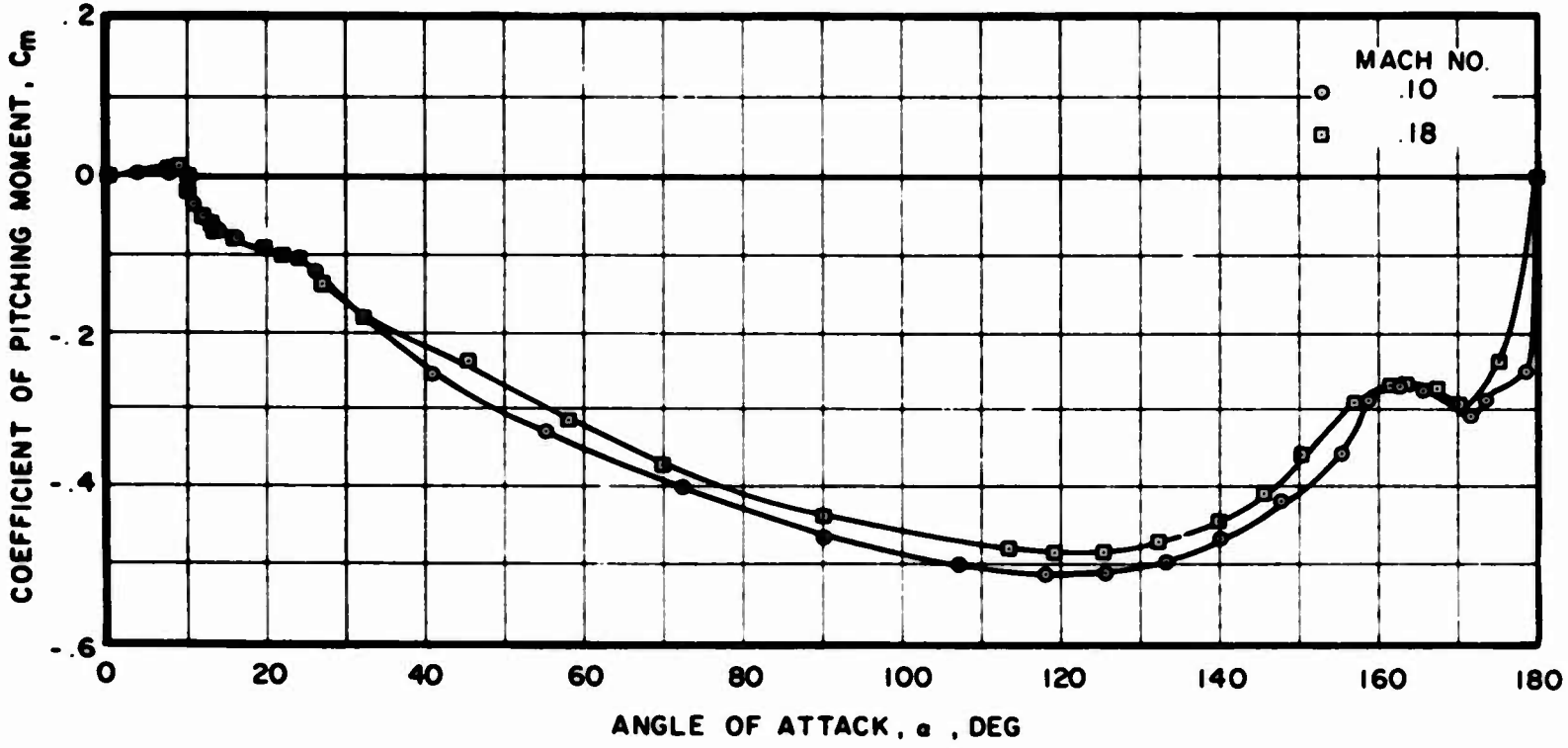

(f) Coefficient of Pitching Moment $0 < \alpha < 180^{\circ}$

Figure 14. Concluded.

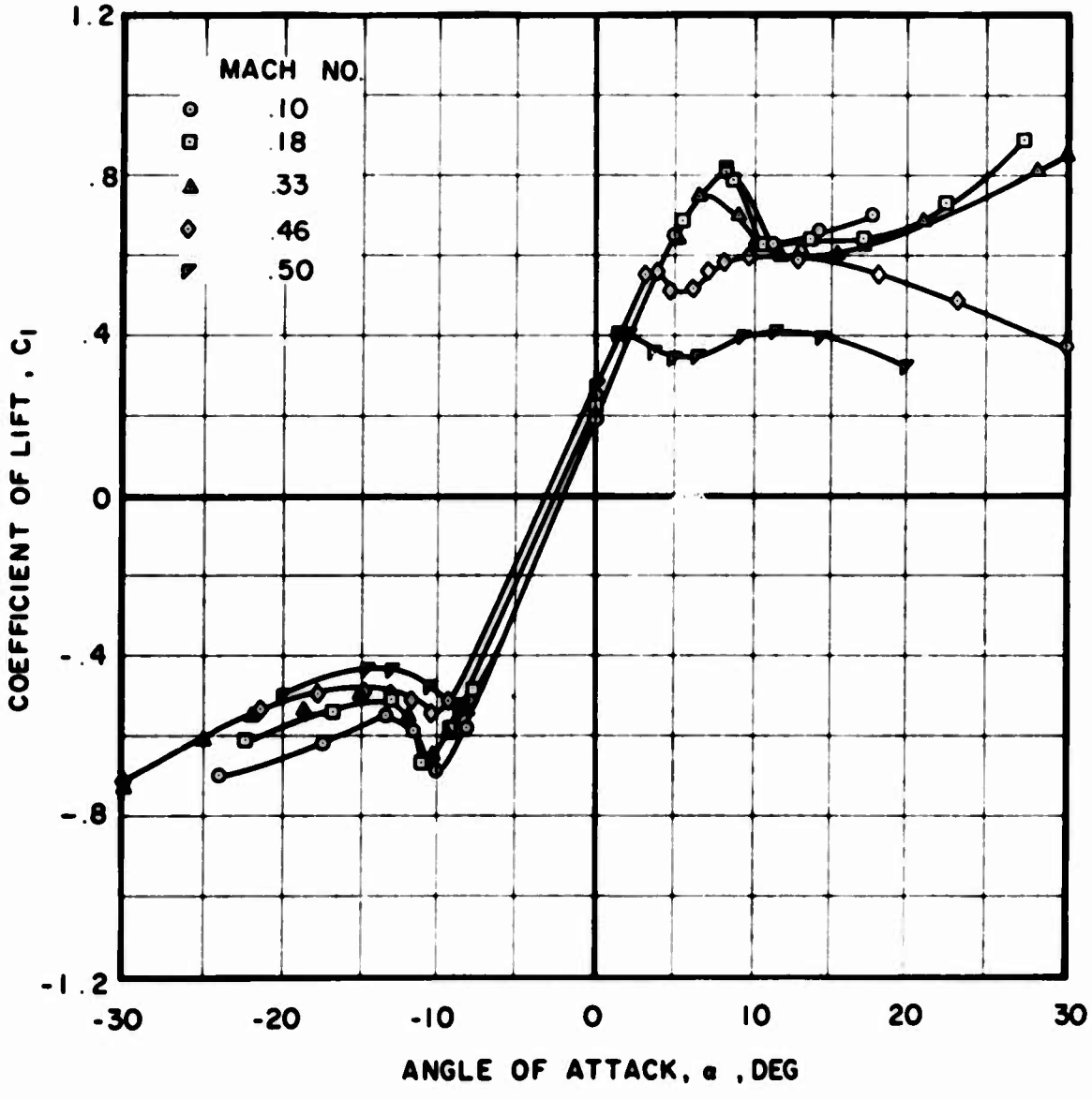

(a) Coefficient of Lift $-30^{\circ} < \alpha < 30^{\circ}$

Figure 15. Two-Dimensional Aerodynamic Coefficients for the 2.69-Inch Chord Flapped Airfoil Section.

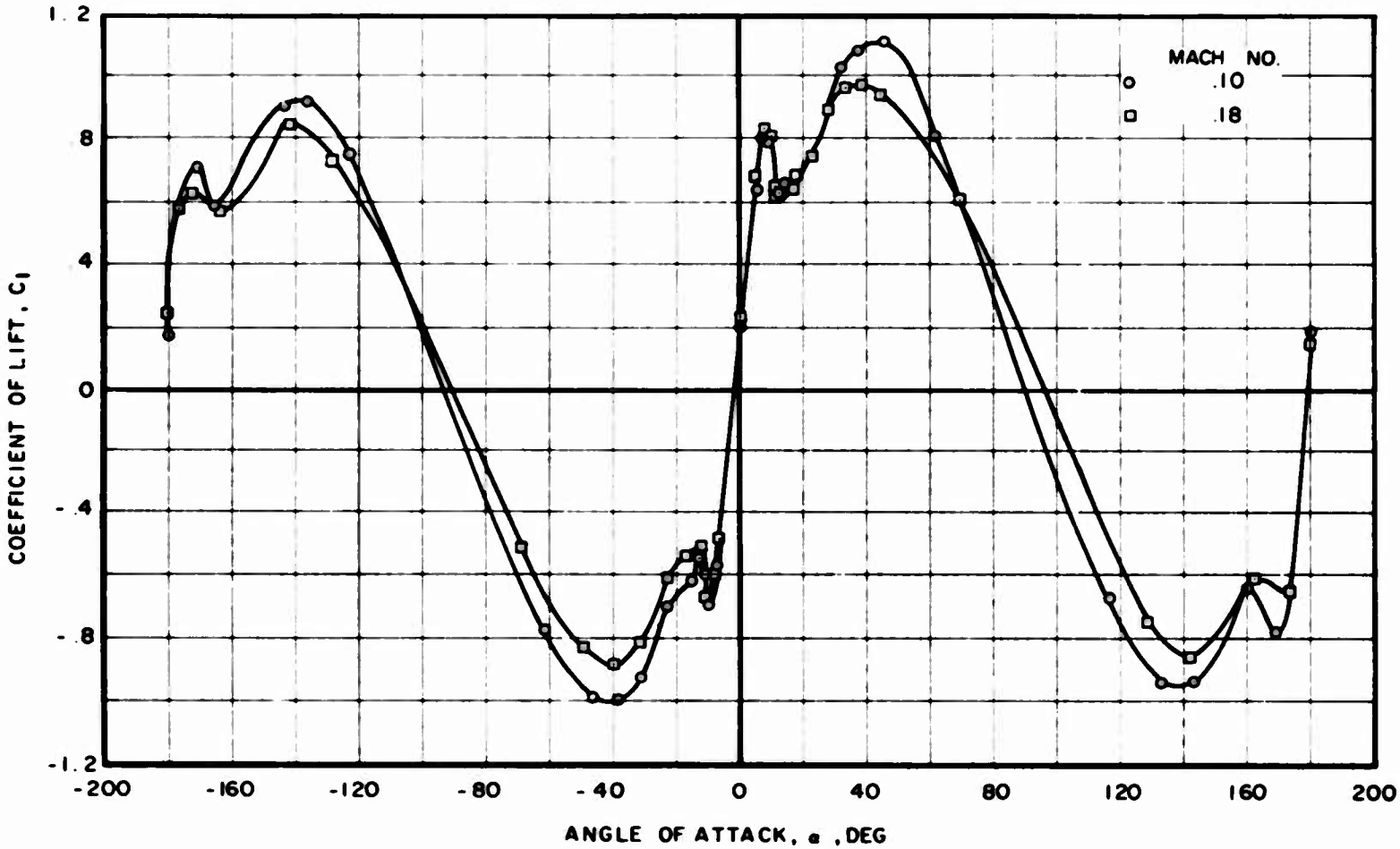

(b) Coefficient of Lift $-180^{\circ} < \alpha < 180^{\circ}$

Figure 15. Continued.

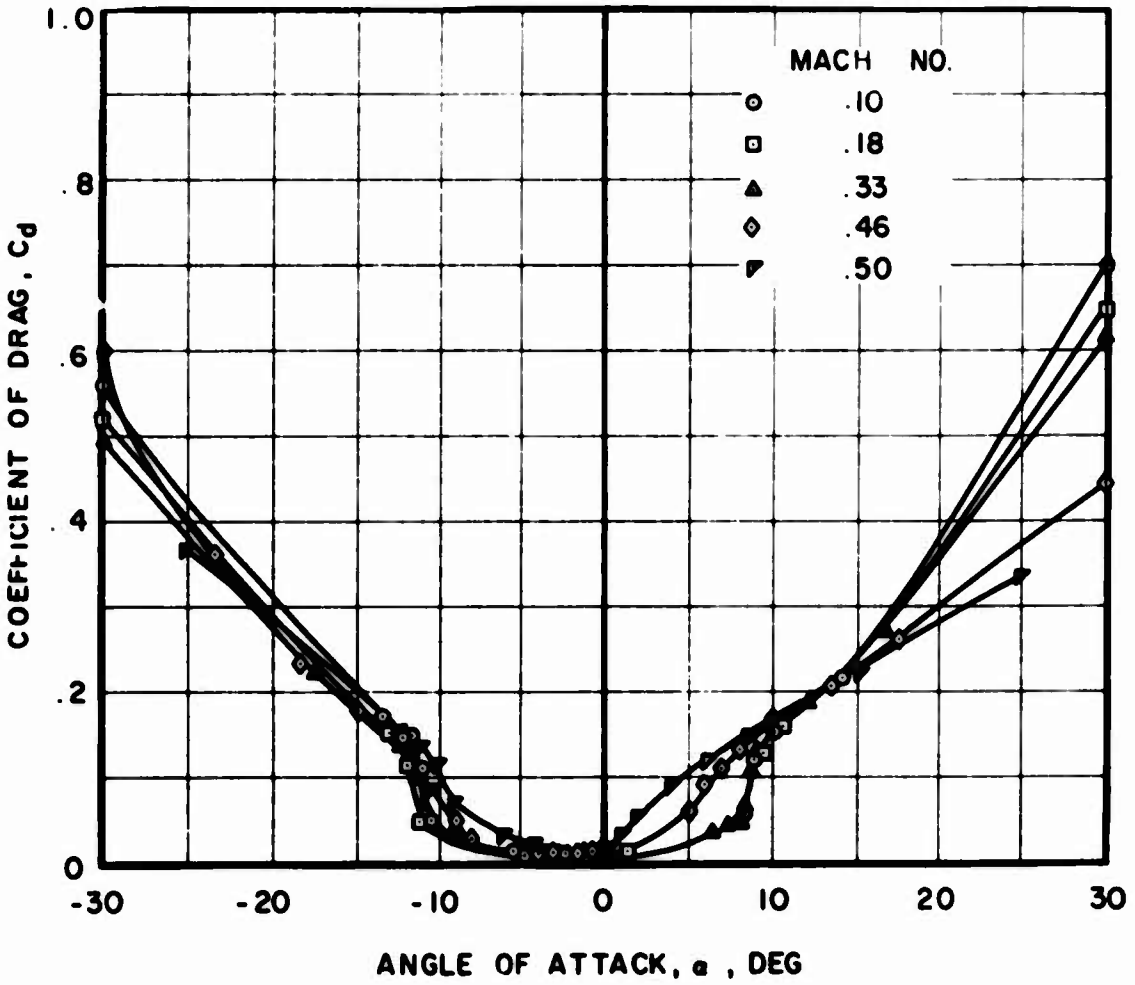

(c) Coefficient of Drag $-30^{\circ} < \alpha < 30^{\circ}$

Figure 15. Continued.

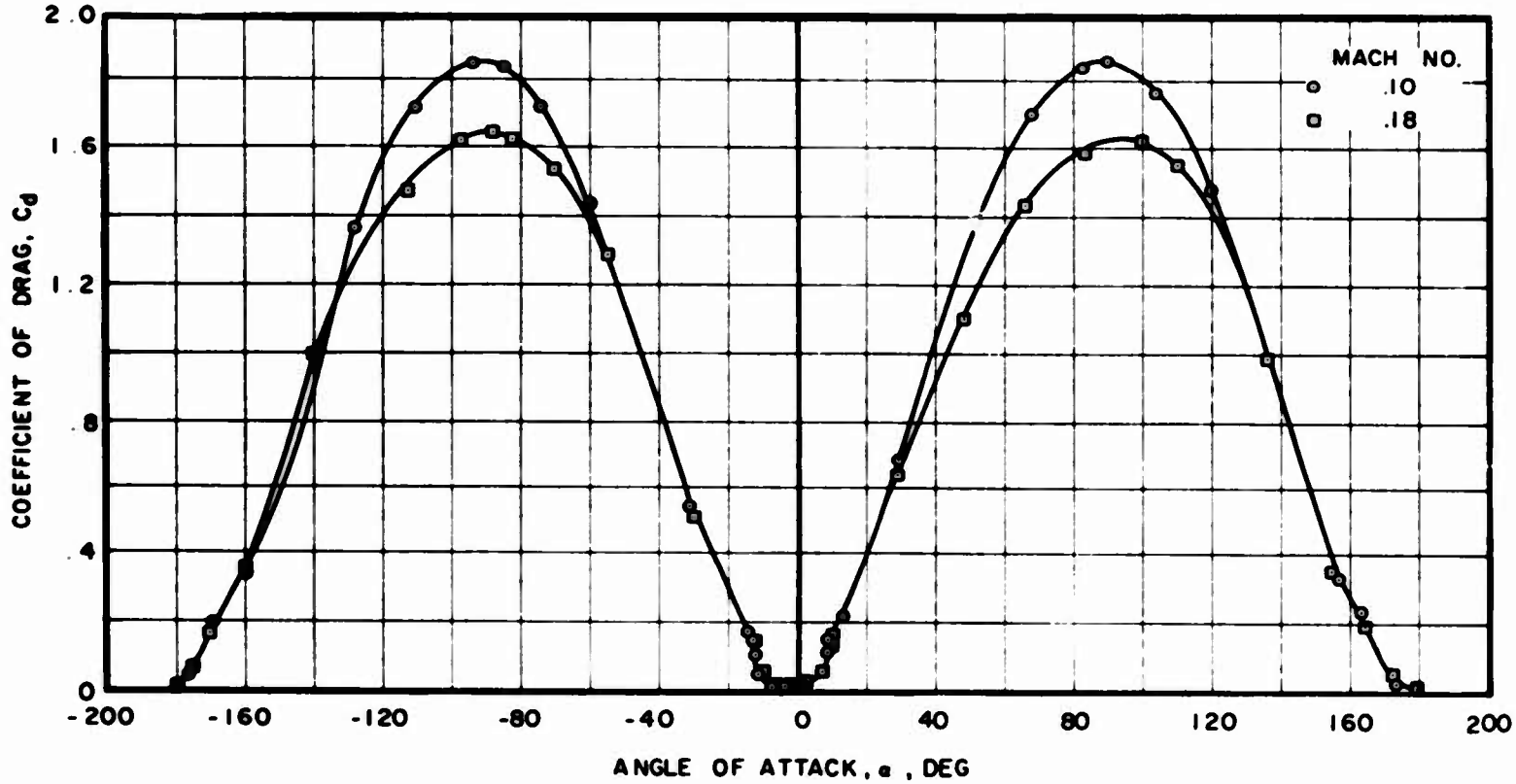

(d) Coefficient of Drag $-180^{\circ} < \alpha < 180^{\circ}$

Figure 15. Continued.

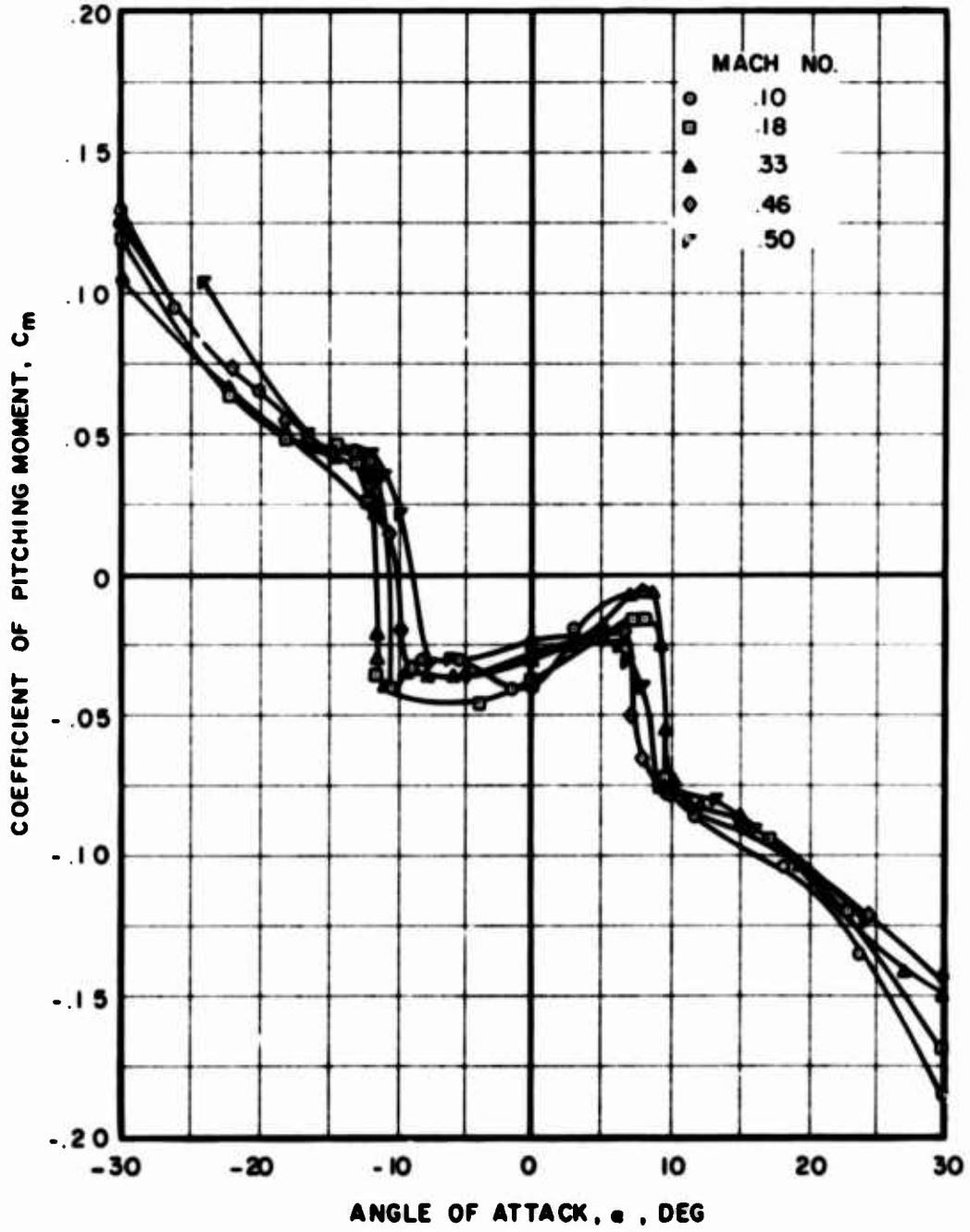

(e) Coefficient of Pitching Moment, $-30^{\circ} < \alpha < 30^{\circ}$

Figure 15. Continued.

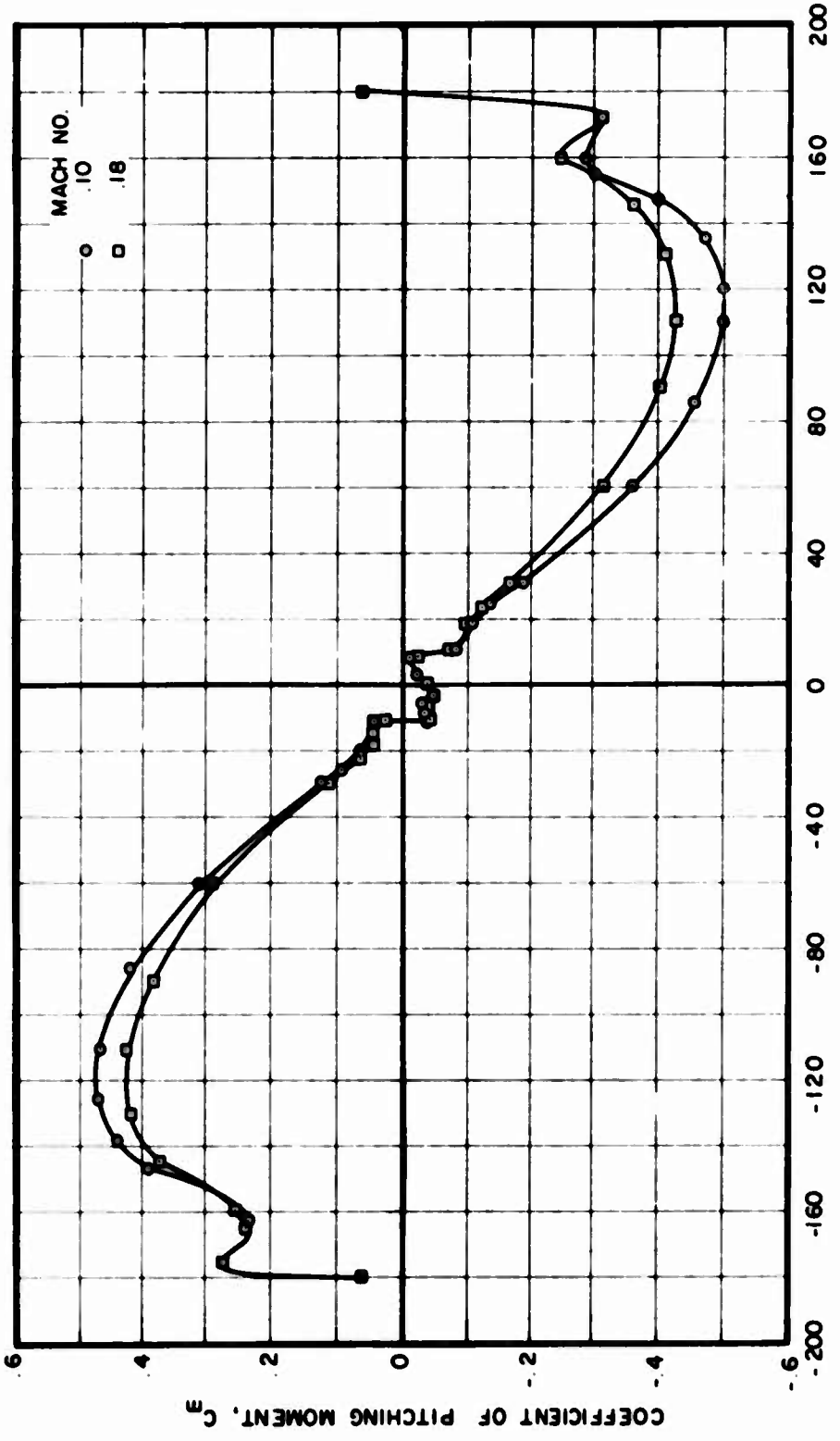

(f) Coefficient of Pitching Moment, $-180^{\circ} < \alpha < 180^{\circ}$

Figure 15. Concluded.

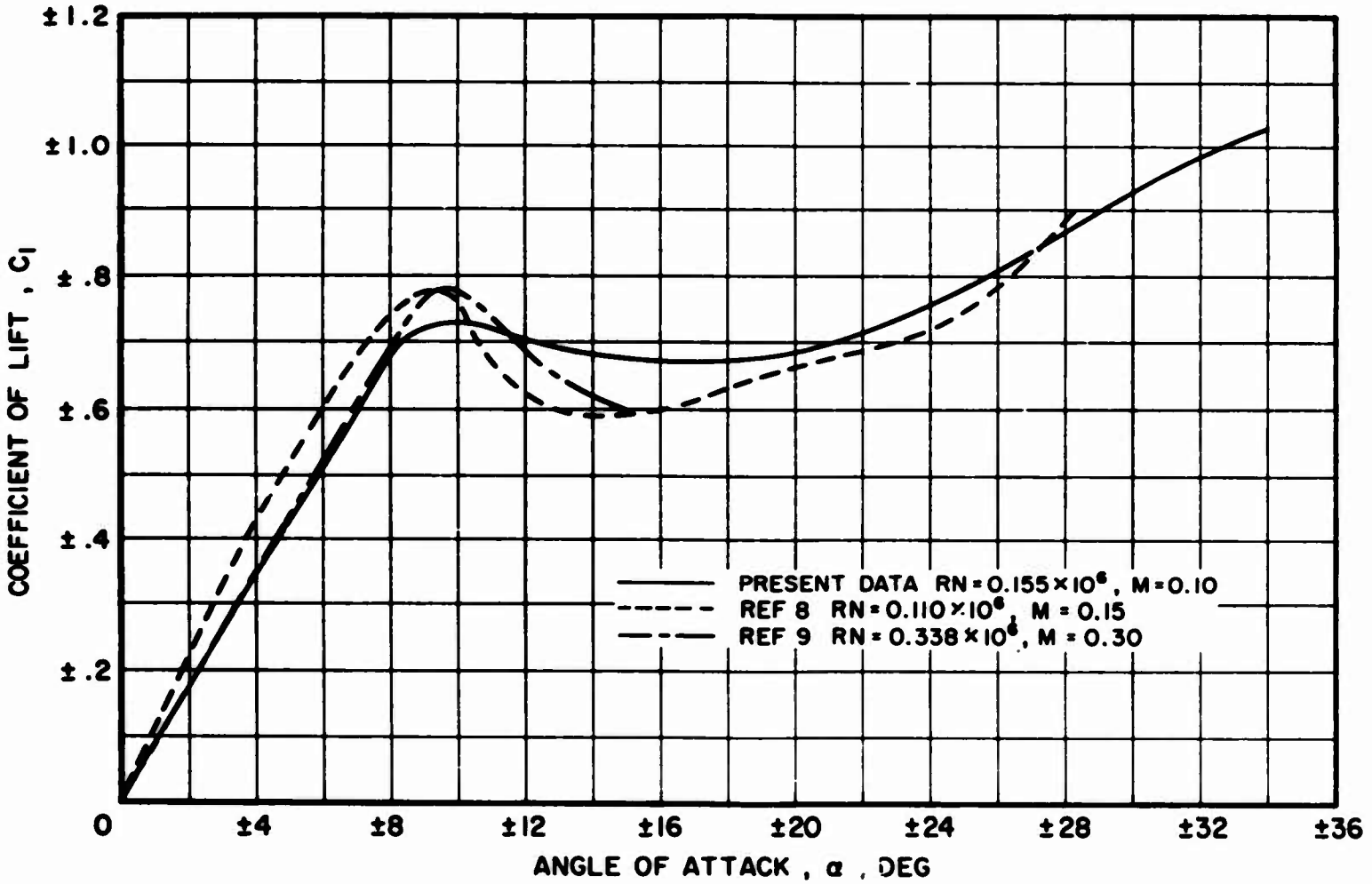

Figure 16. Comparison of Low Reynolds Number Two-Dimensional Airfoil Test Data.

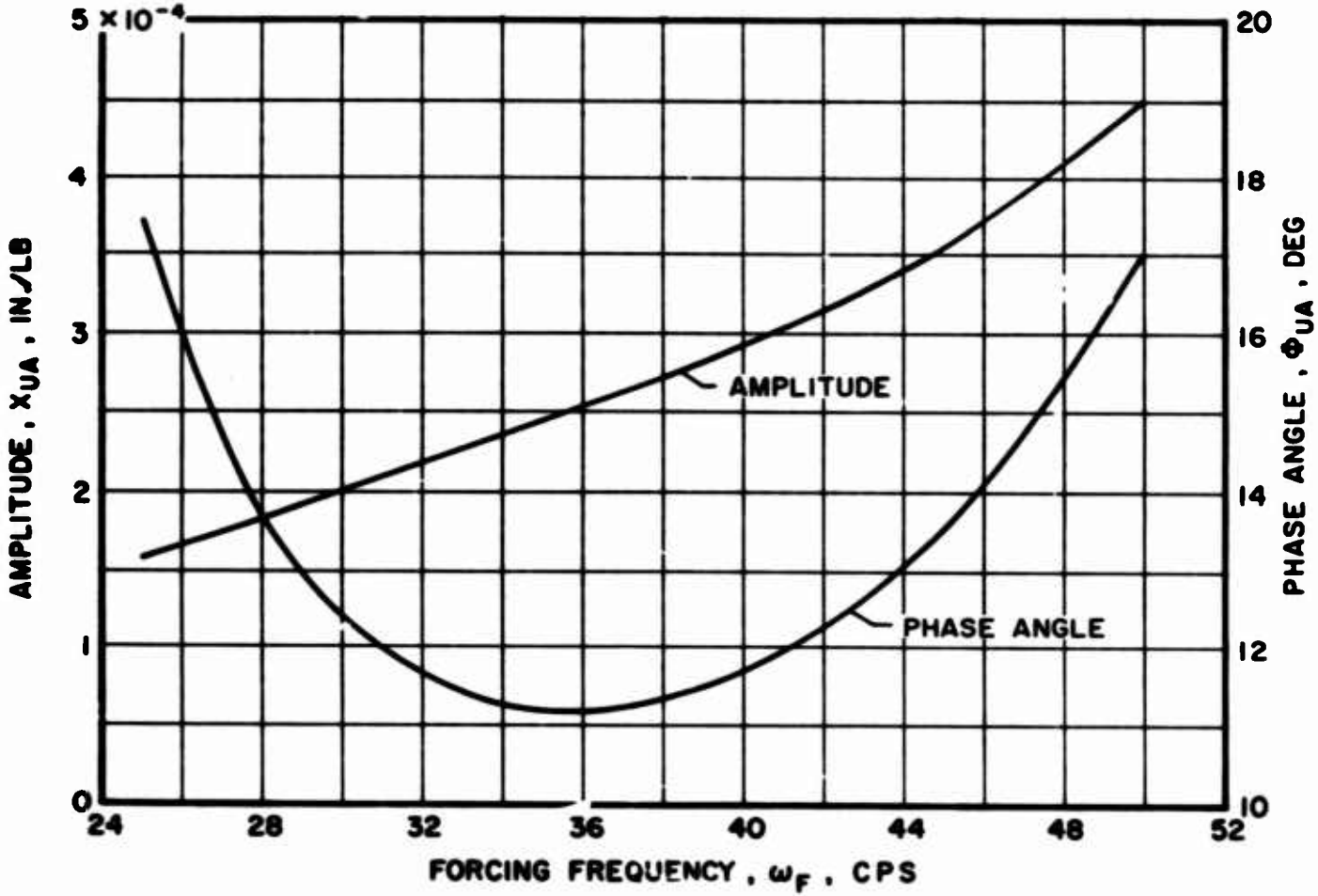

(a) Longitudinal Response

Figure 17. Calculated Rotor Hub Response to Vibratory Loadings.

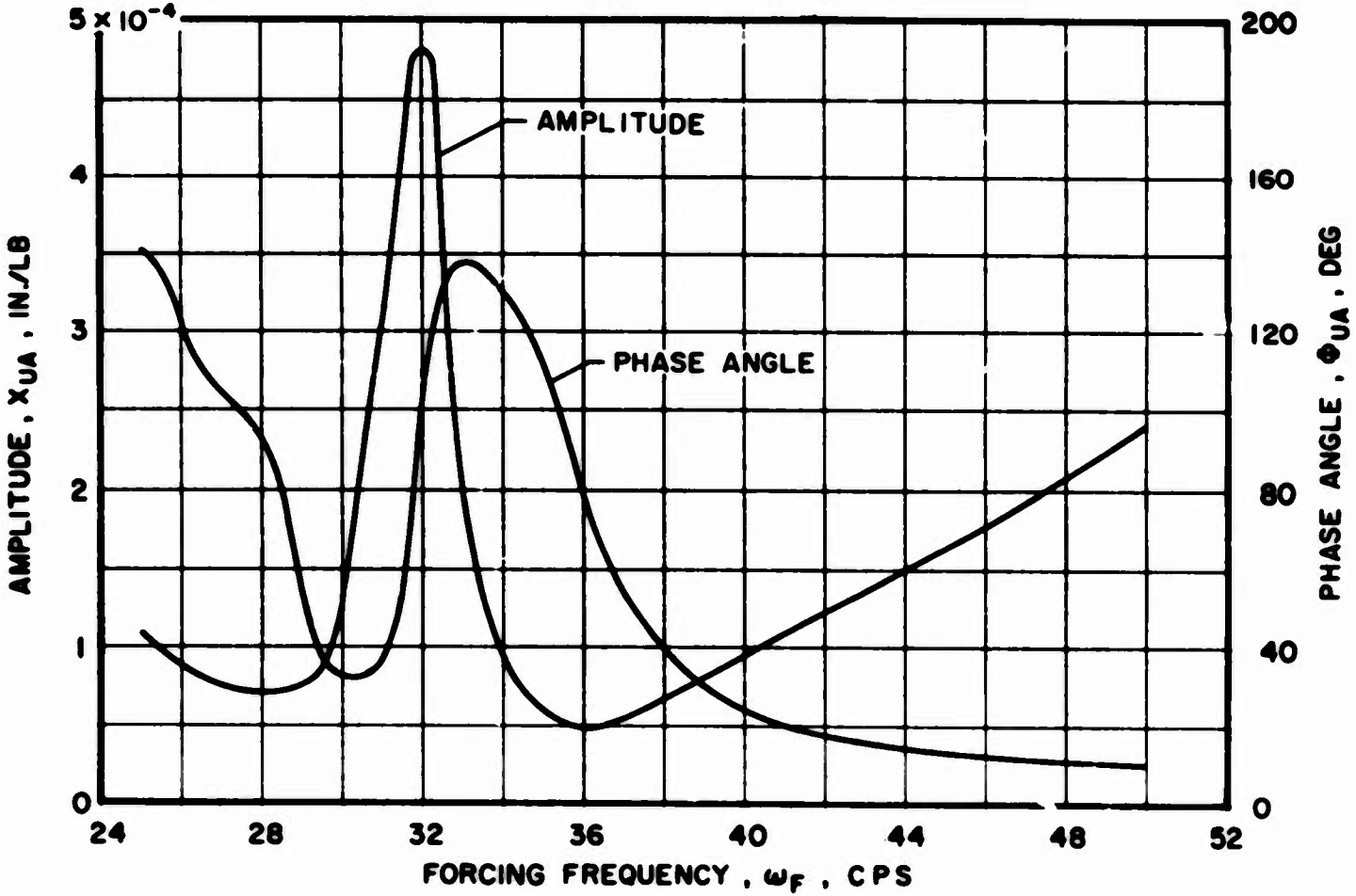

(b) Lateral Response

Figure 17. Continued.

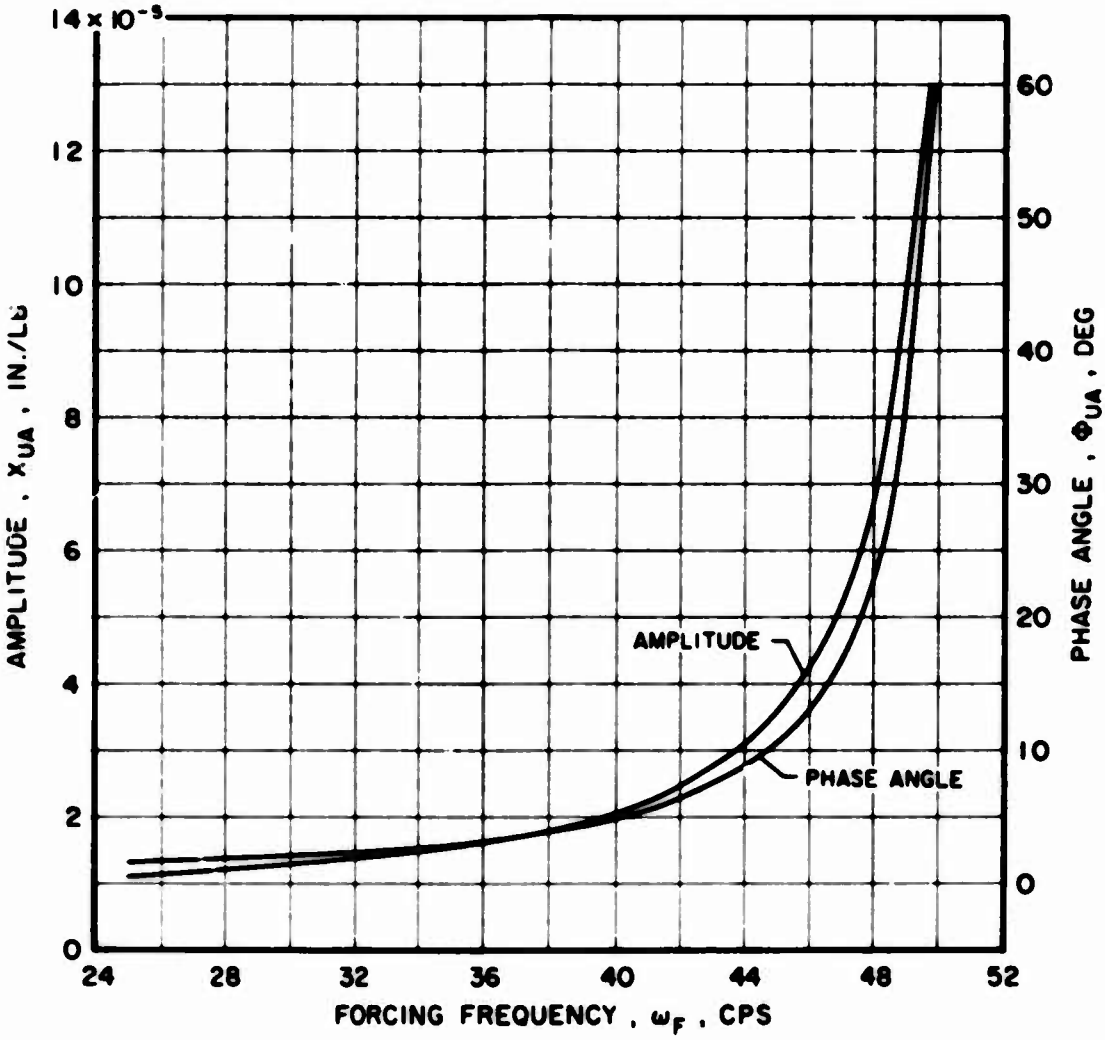

(c) Vertical Response

Figure 17. Continued.

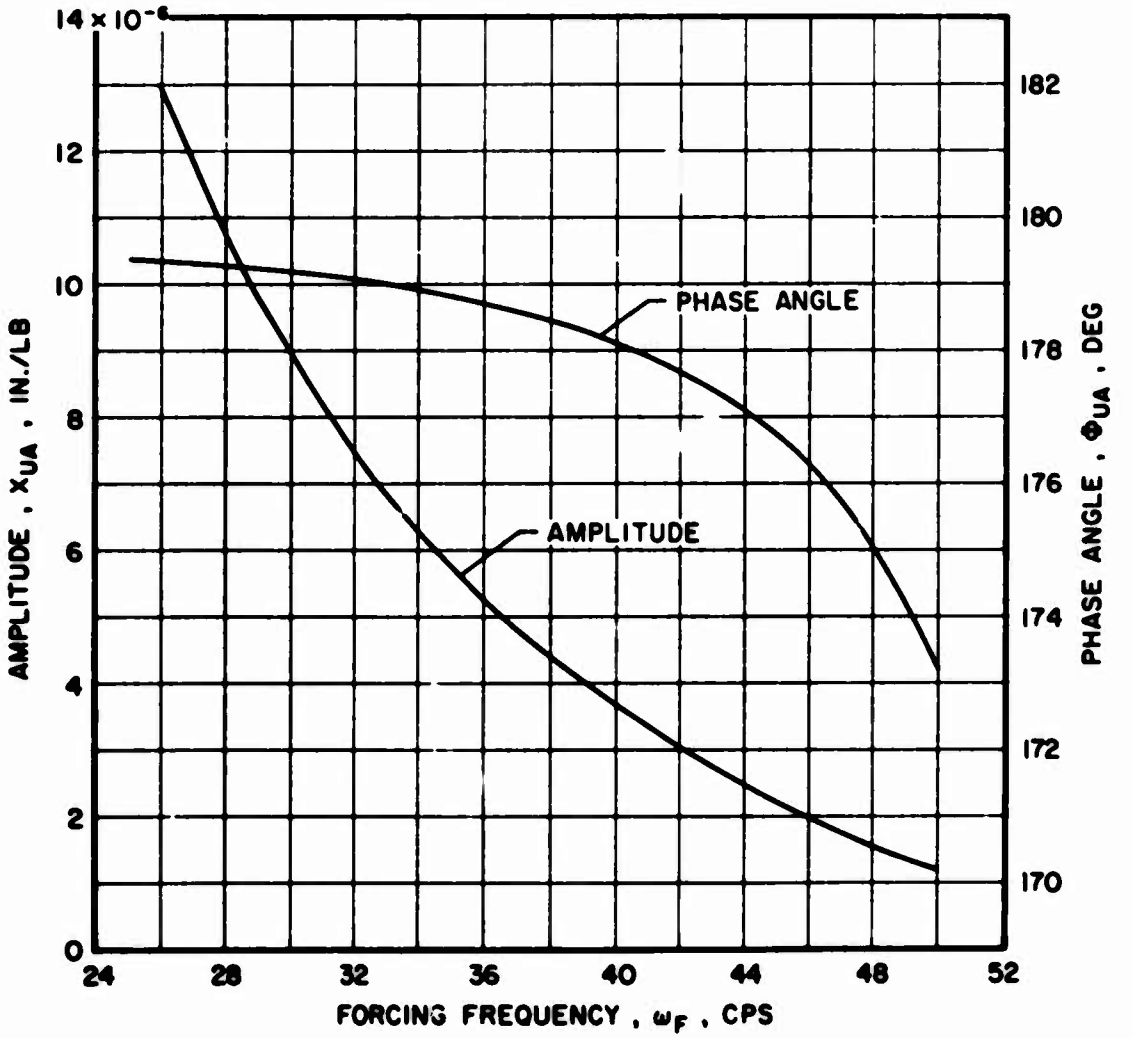

(d) Torsional Response

Figure 17. Concluded.

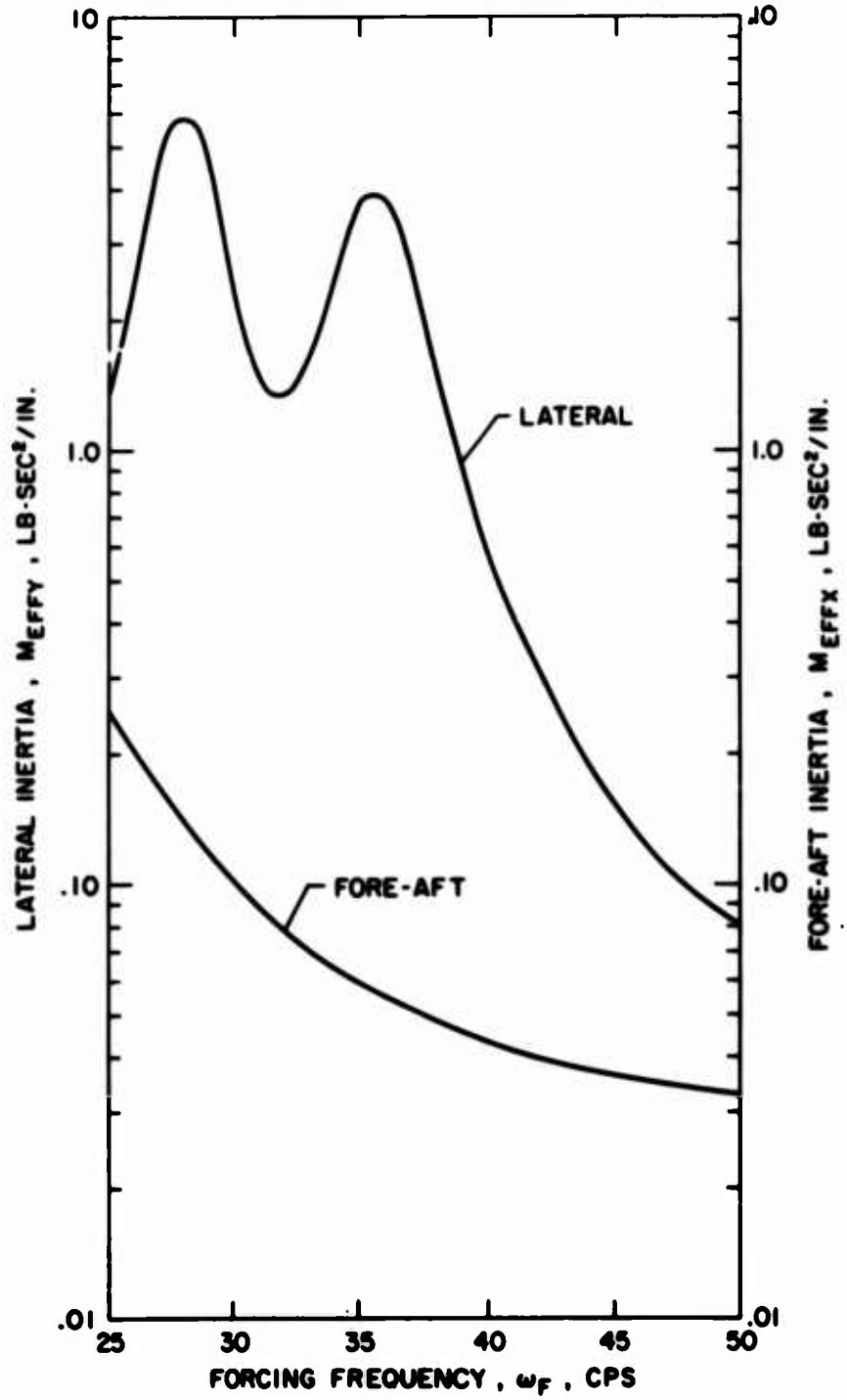

(a) Effective In-Plane Inertia

Figure 18. Calculated Effective Dynamic Properties at the Rotor Hub.

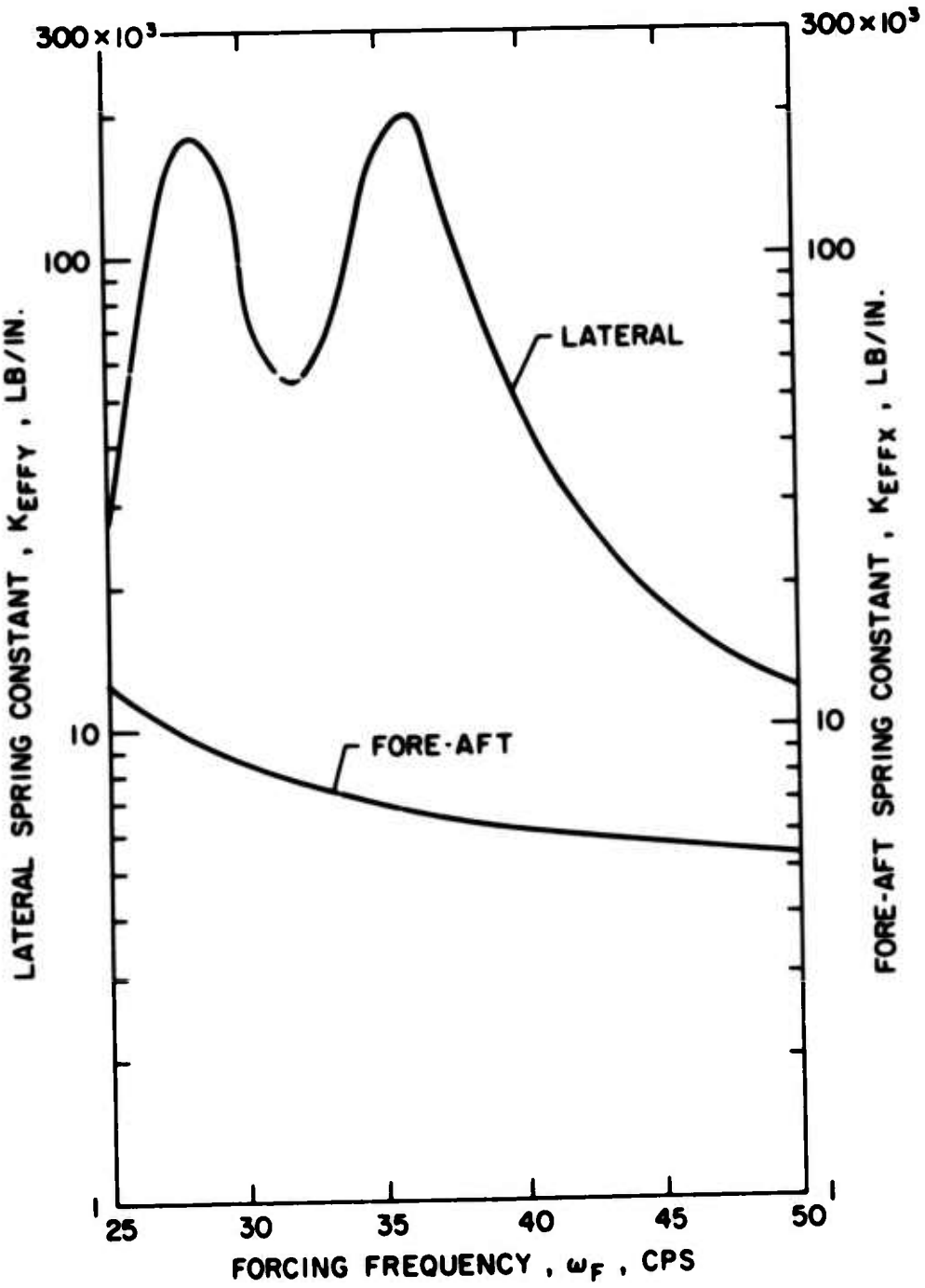

(b) Effective In-Plane Spring Rate

Figure 18. Continued.

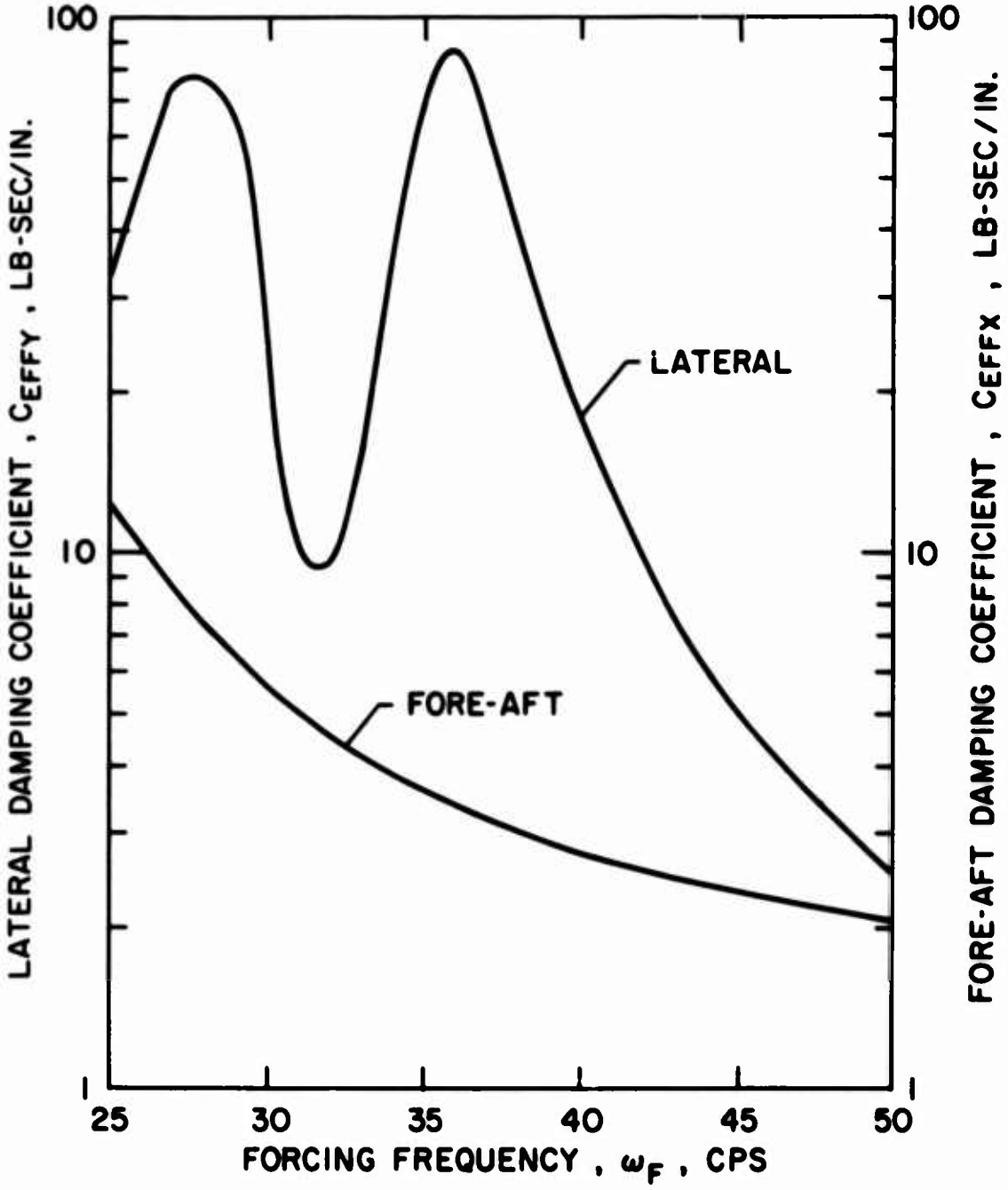

(c) Effective In-Plane Damping

Figure 18. Continued.

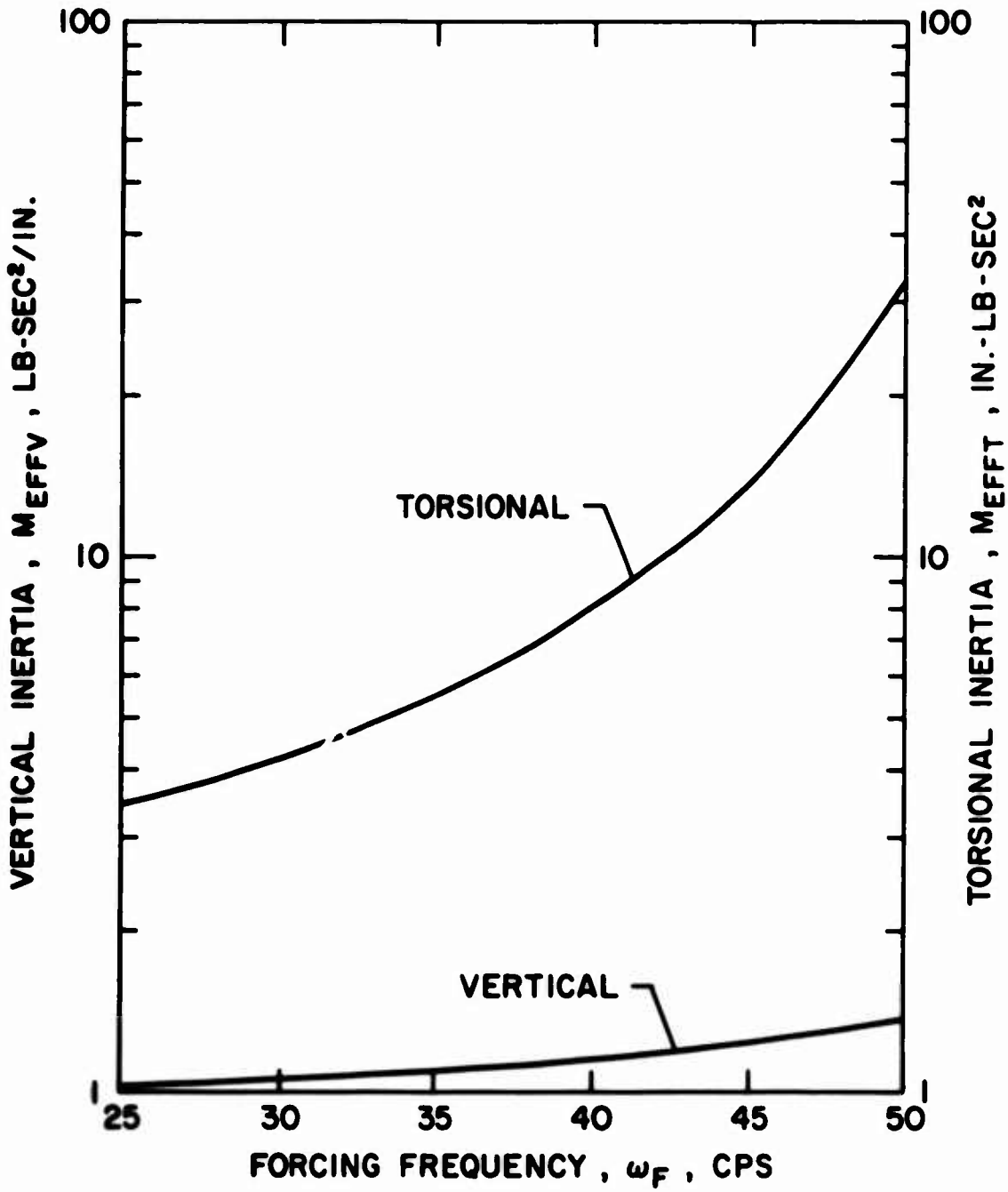

(d) Effective Vertical and Torsional Inertia

Figure 18. Continued.

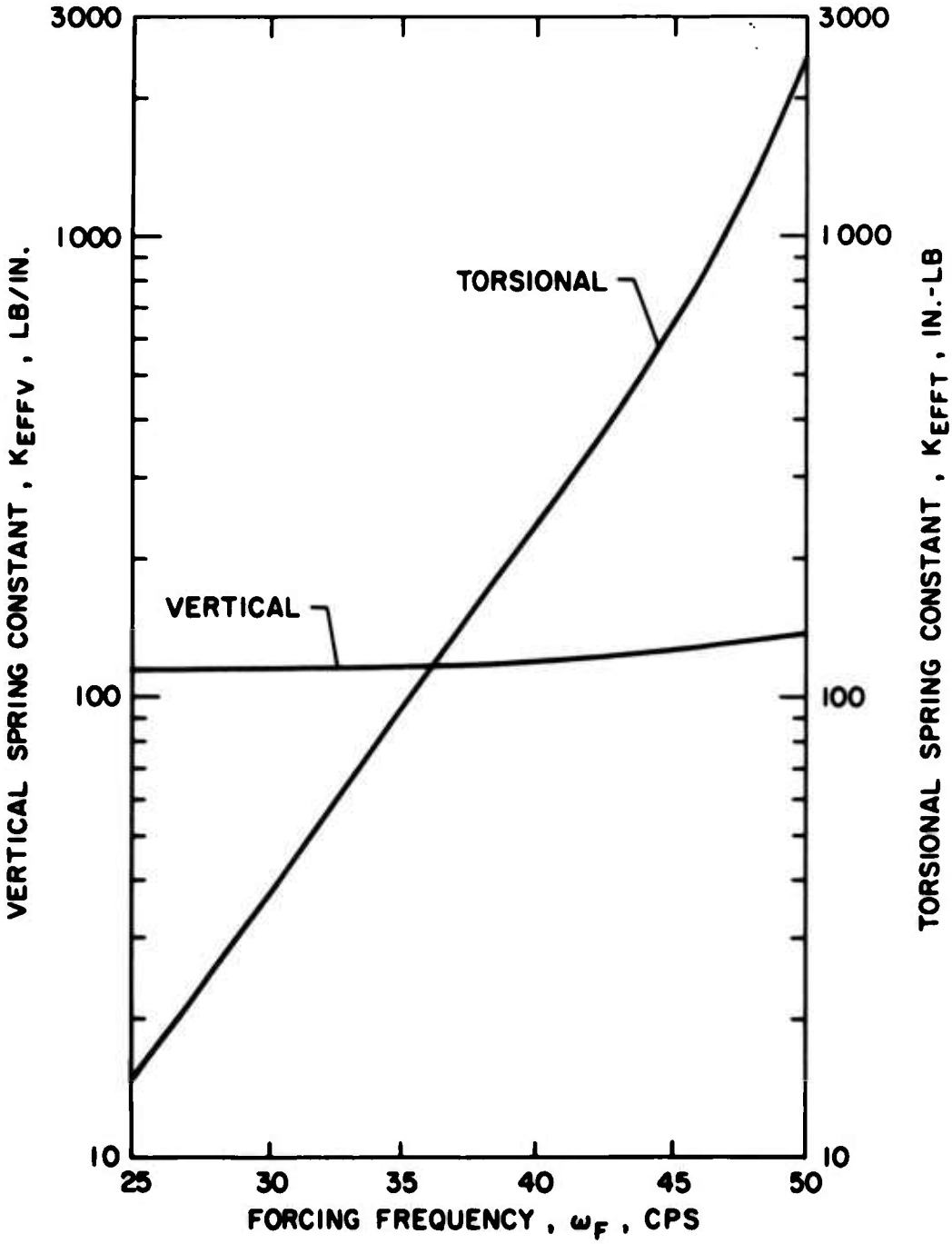

(e) Effective Vertical and Torsional Spring Rate

Figure 18. Continued.

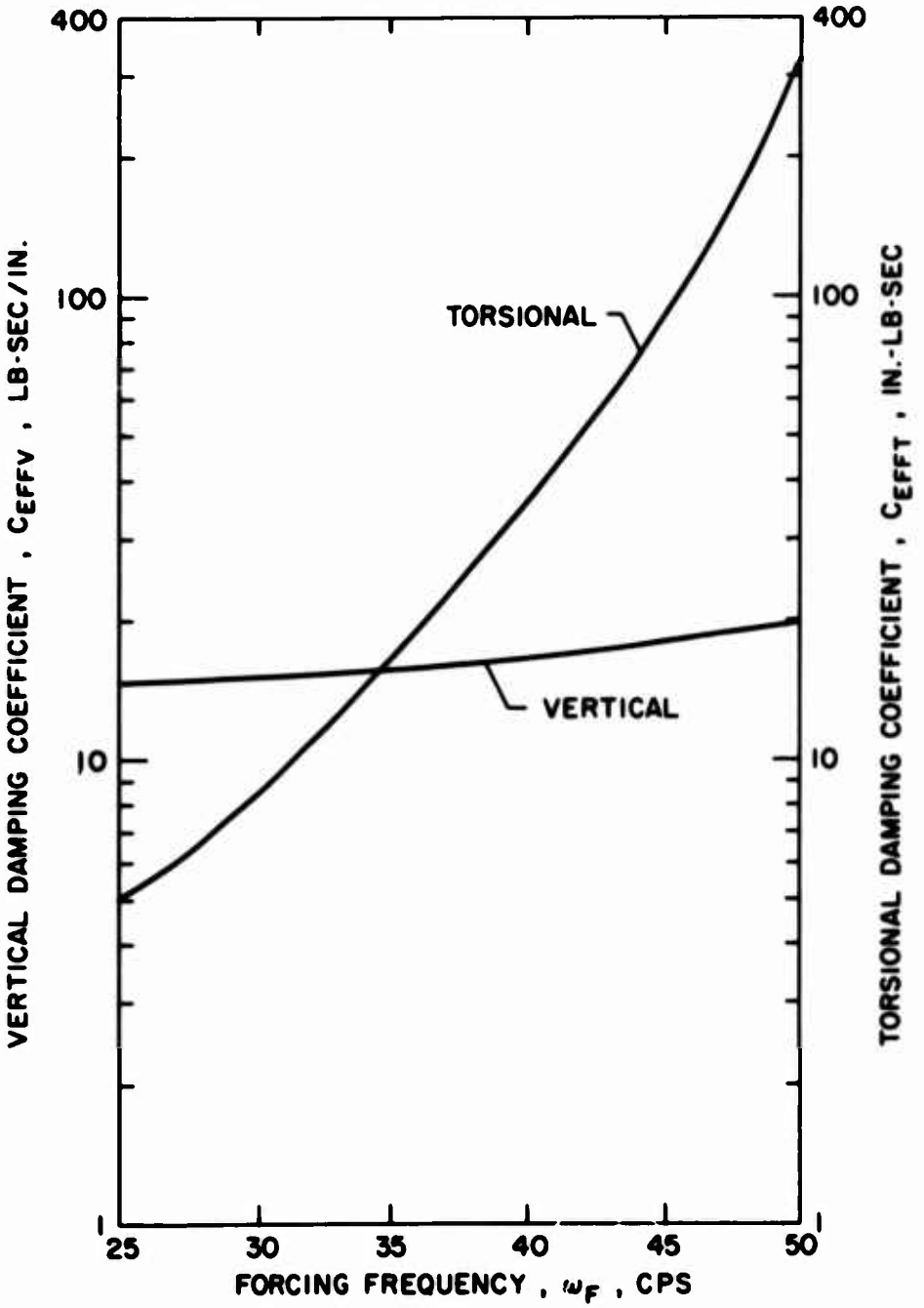

(f) Effective Vertical and Torsional Damping

Figure 18. Concluded.

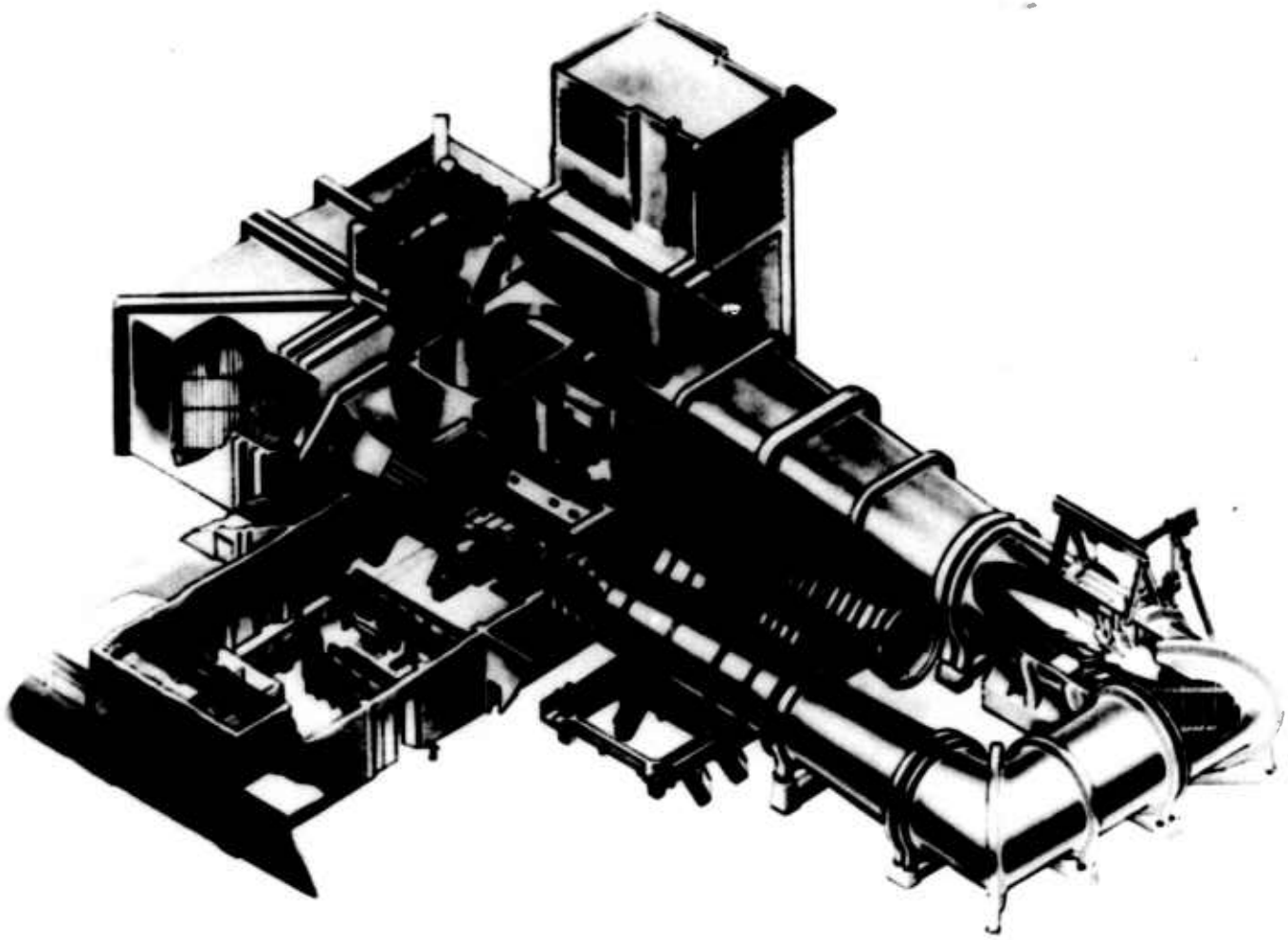

Figure 19. United Aircraft Subsonic Wind Tunnel.

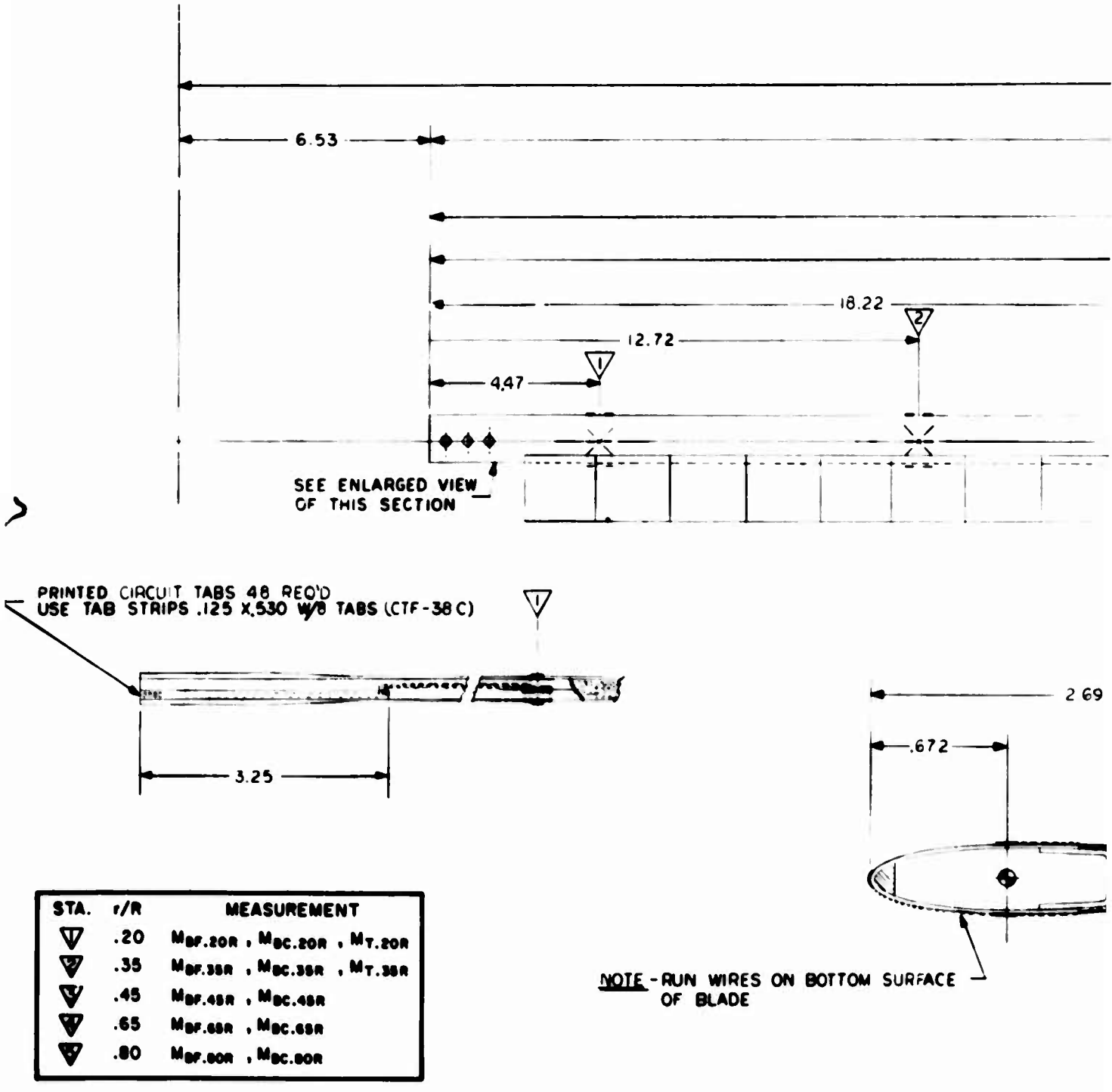

STA.	r/R	MEASUREMENT
▽	.20	$M_{BF.20R}$, $M_{BC.20R}$, $M_{T.20R}$
▽	.35	$M_{BF.35R}$, $M_{BC.35R}$, $M_{T.35R}$
▽	.45	$M_{BF.45R}$, $M_{BC.45R}$
▽	.65	$M_{BF.65R}$, $M_{BC.65R}$
▽	.80	$M_{BF.80R}$, $M_{BC.80R}$

Figure 20. H-34 Model Blade Instrumentation.

Preceding page blank

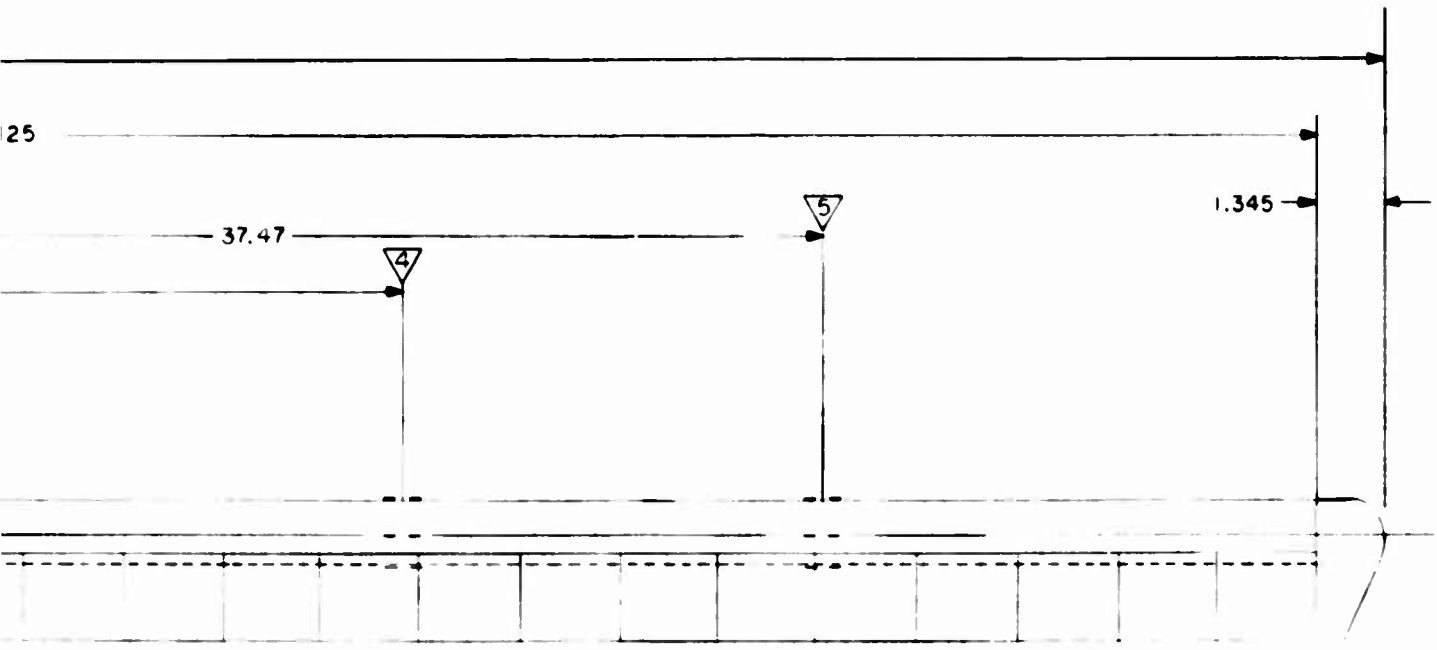

>

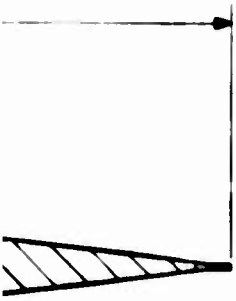

MEASUREMENT	TYPE OF GAGE ALUMINUM SPAR	FIBER GLASS SPAR
FLAPWISE	EA13-125-BZ-350	
CHORDWISE	EA13-125-BZ-350	
TORSION	EA13-120-NC-350	

L-BALSA CORE-MODIFY AS REQ'D

(005 DIA.) NYLCLAD COATED WIRE

!

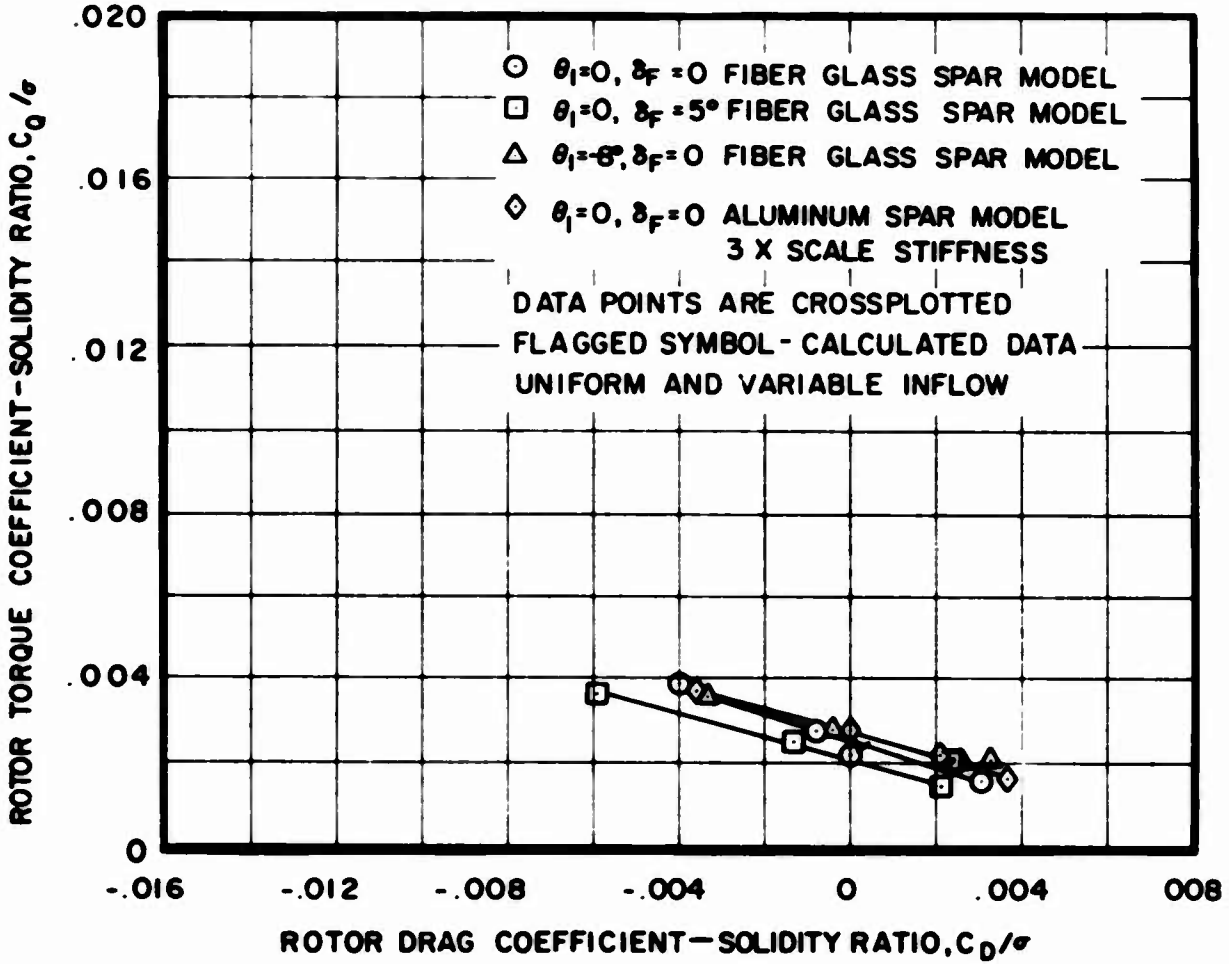

(a) $C_L/\sigma = 0.050$

Figure 21. Torque vs. Drag Performance and Correlation for Model Rotor Configurations; V_s = 124 kn, μ = 0.3, $a_{1s} = b_{1s}$ = 0 deg.

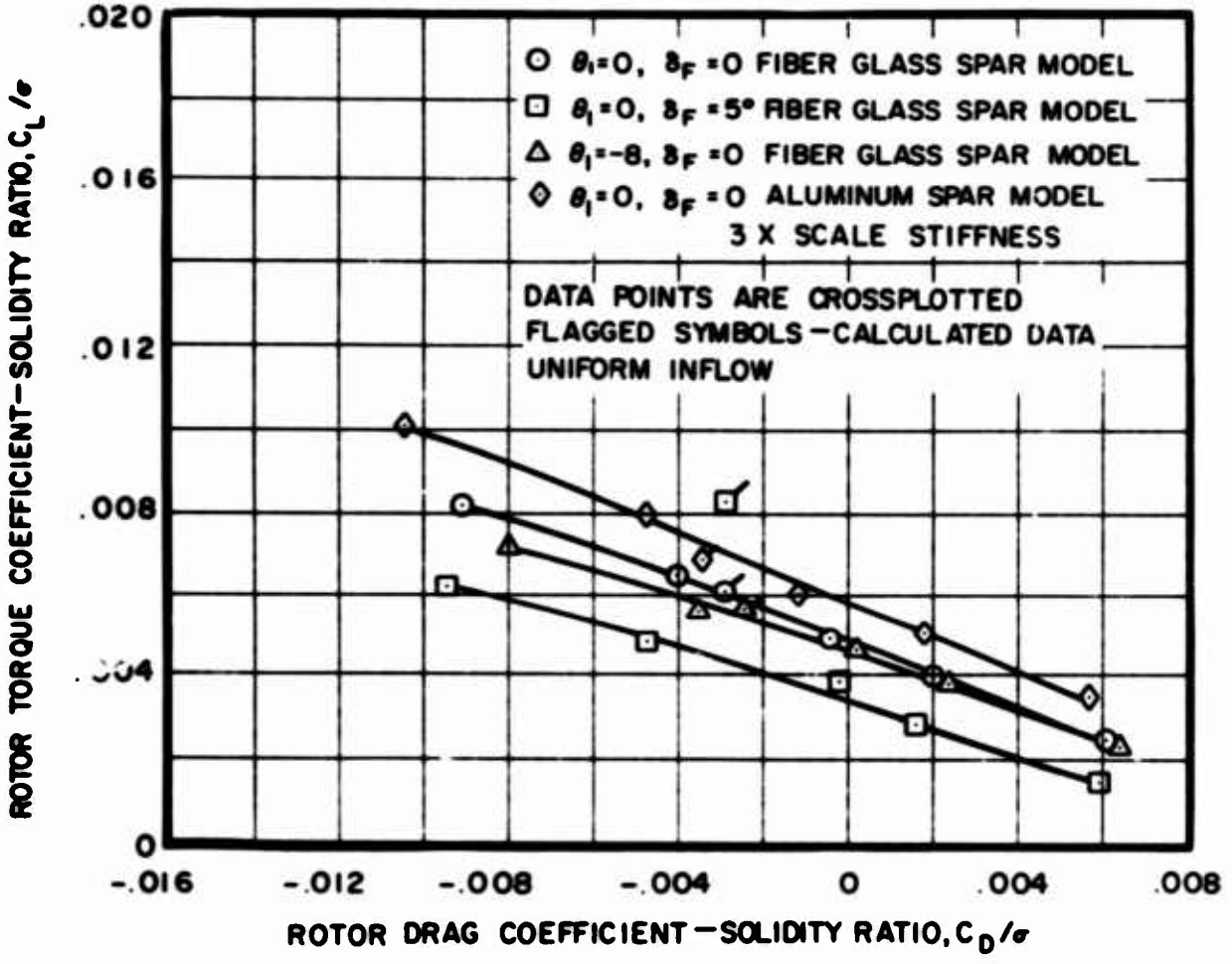

(b) C_L/σ = 0.082

Figure 21. Continued.

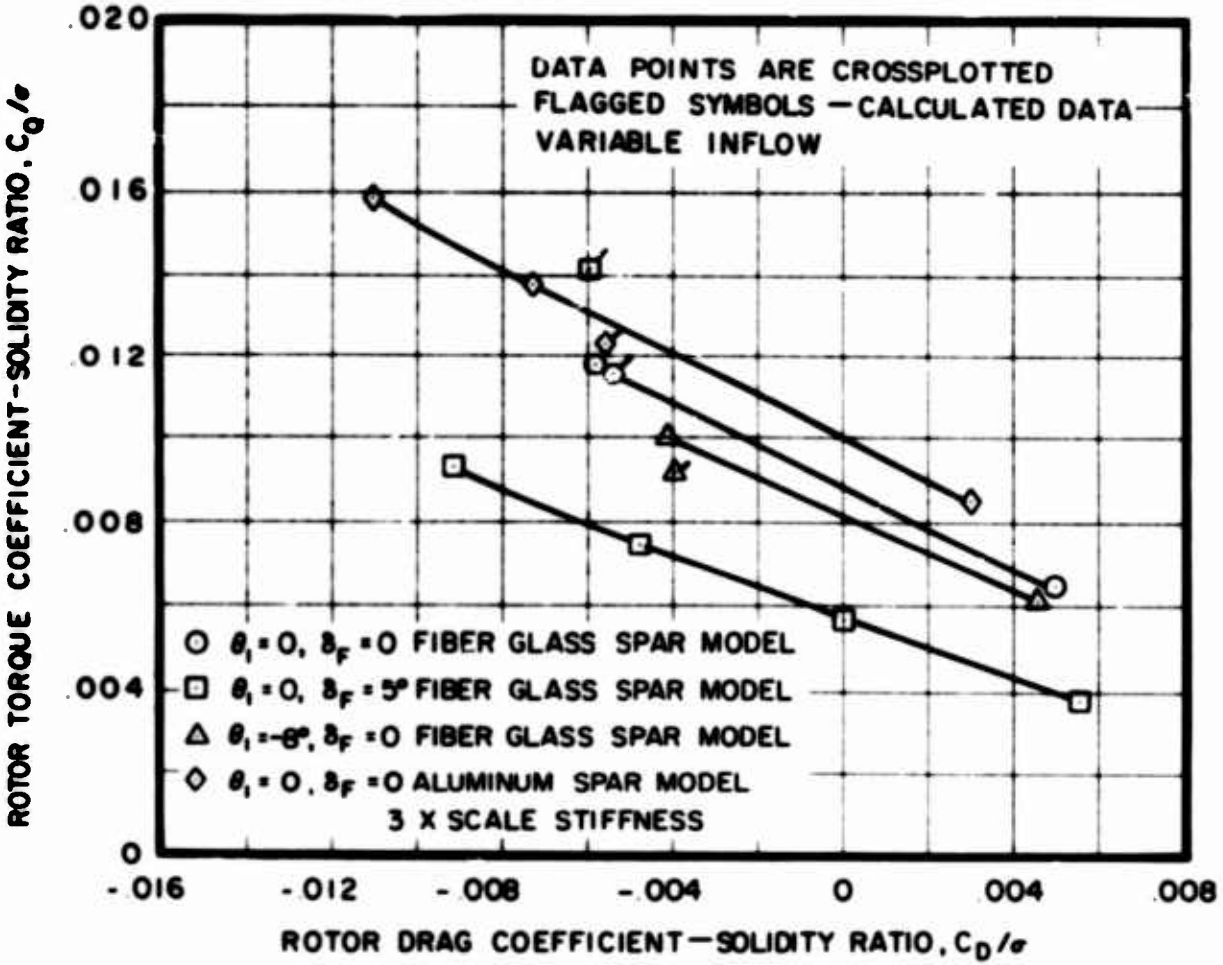

(c) $C_L/\sigma = 0.100$

Figure 21. Concluded.

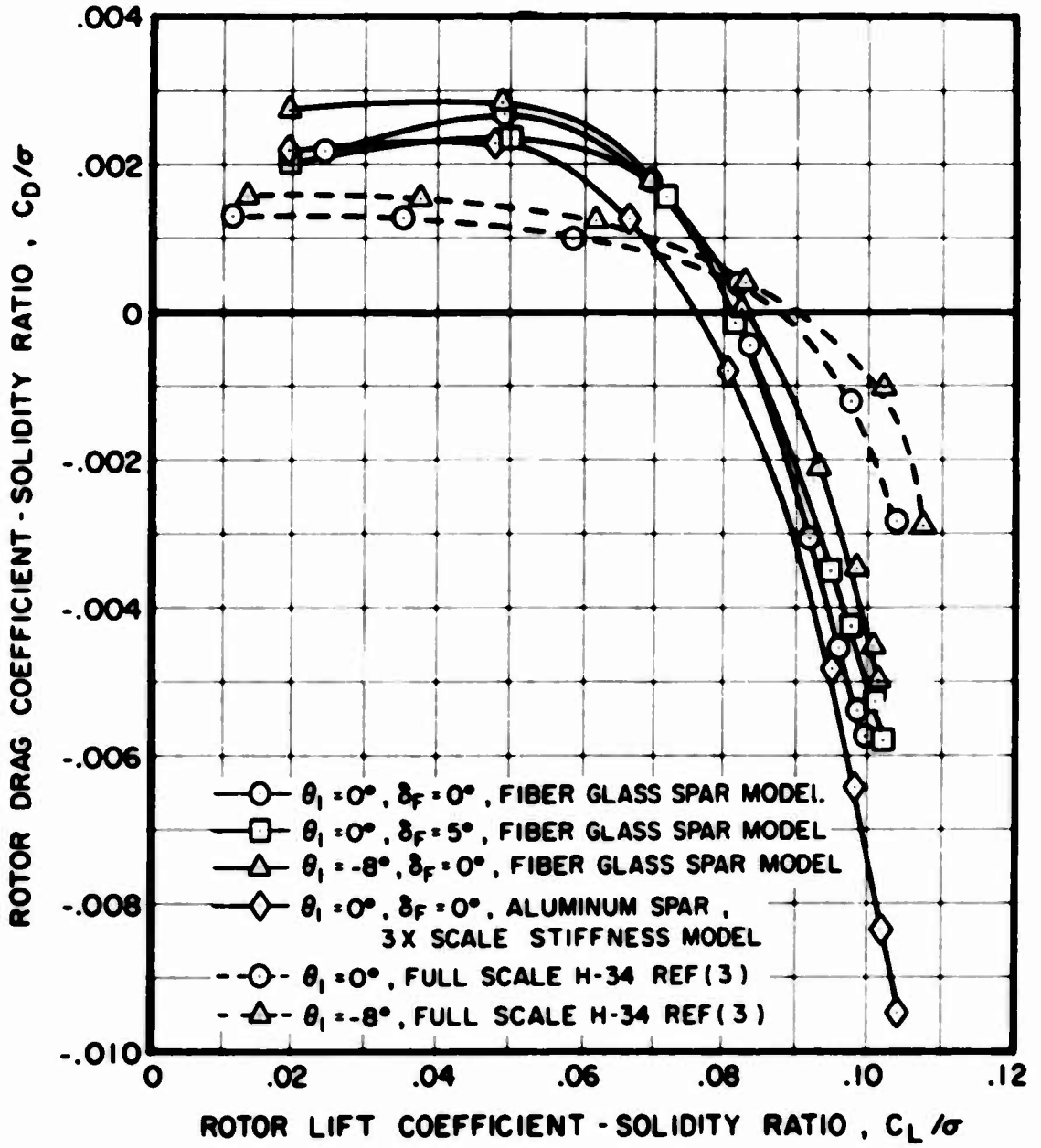

Figure 22. Drag vs. Lift Performance for Model Rotor Configurations; V_s = 124 kn, μ = 0.3, $a_{1s} = b_{1s}$ = 0 deg, a_s = 0 deg.

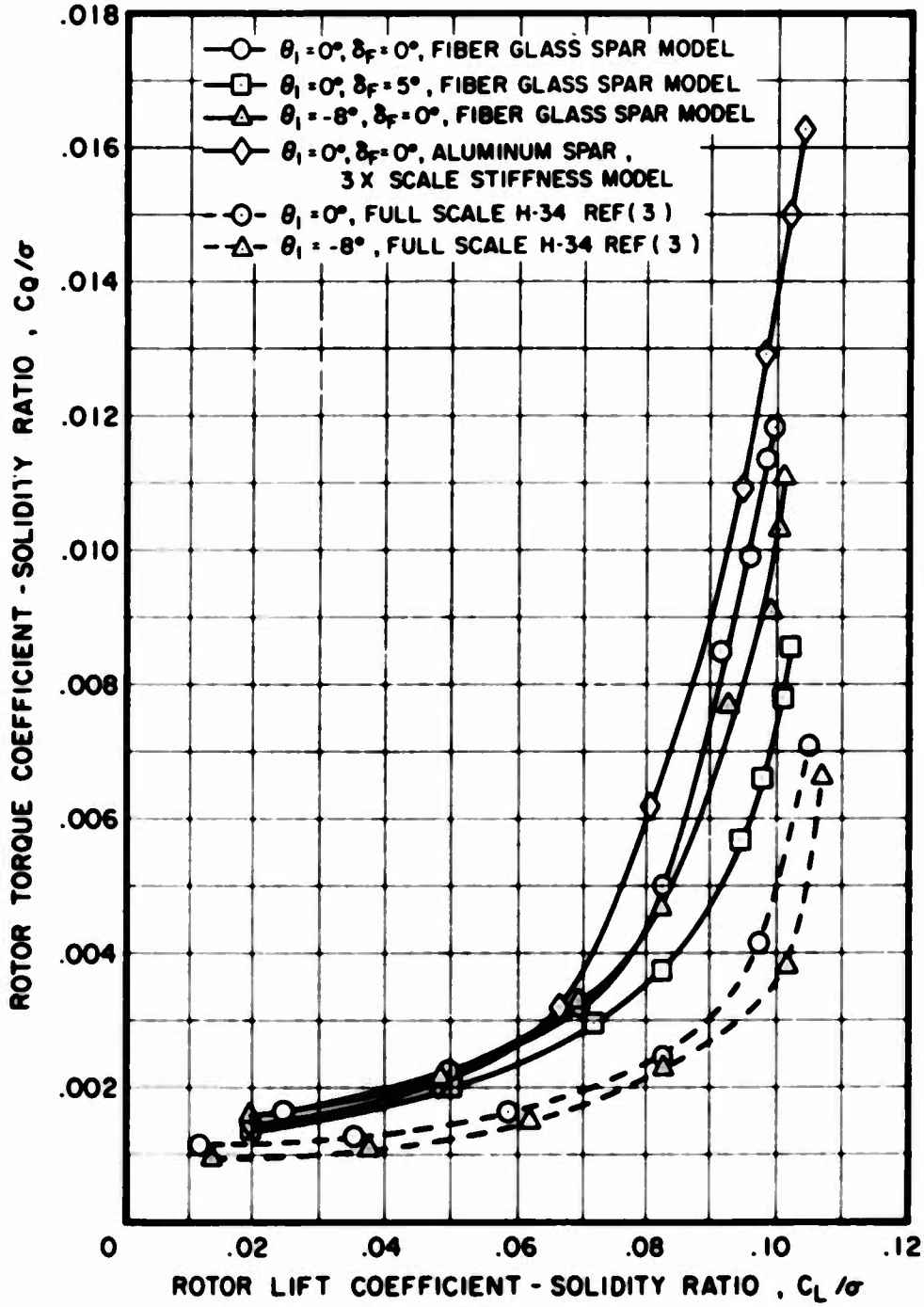

Figure 23. Torque vs. Lift Performance for Model Rotor Configurations; V_s = 124 kn, μ = 0.3, a_{1s} = b_{1s} = 0 deg, α_s = 0 deg.

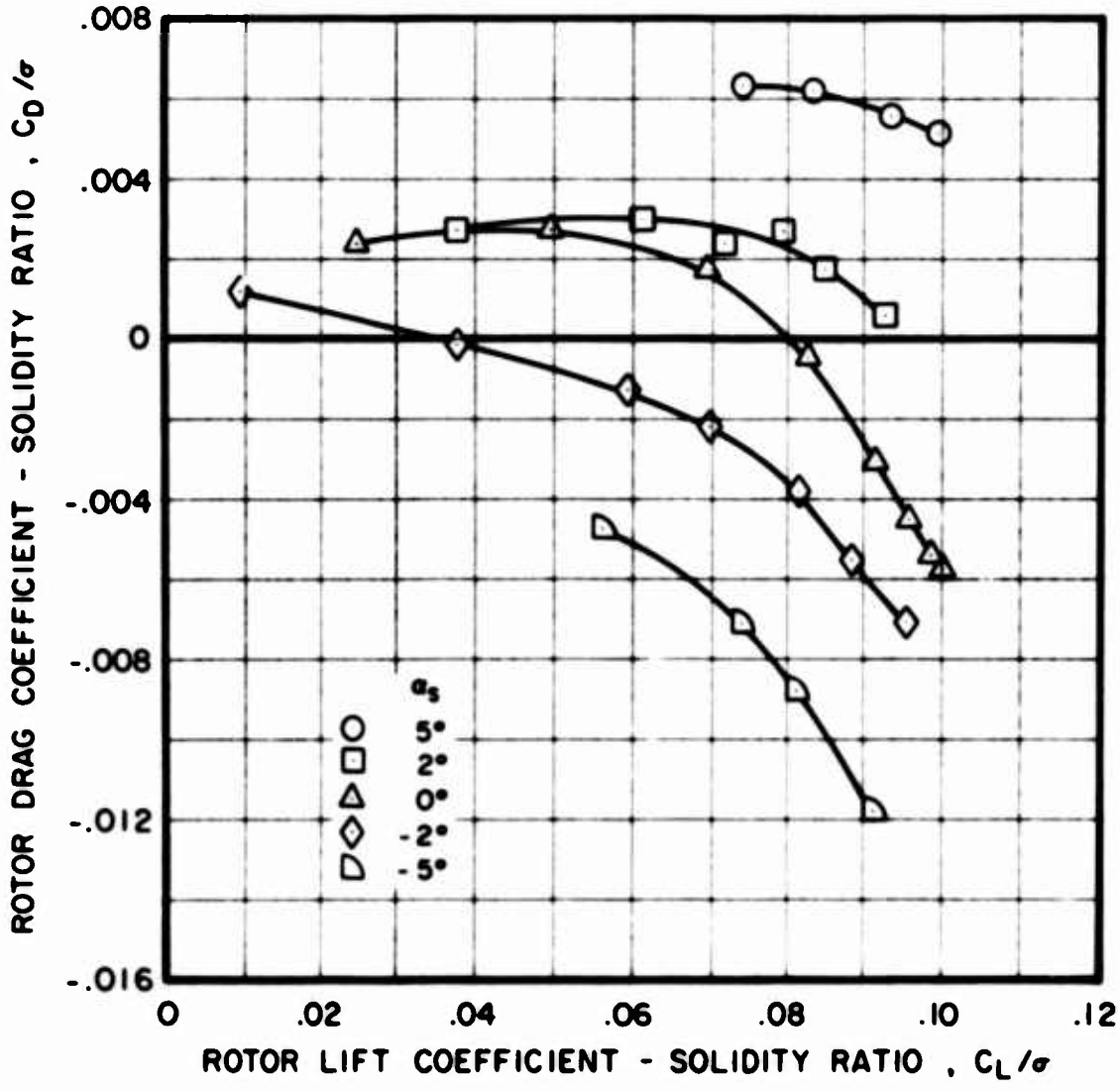

(a) $\mu = 0.3$, $V_s = 124$ kn

Figure 24. Drag vs. Lift Performance of Model Rotor at Various Advance Ratios; $\theta_1 = 0$ deg, $\delta_F = 0$ deg, $S_E = 1$, $a_{1s} = b_{1s} = 0$ deg.

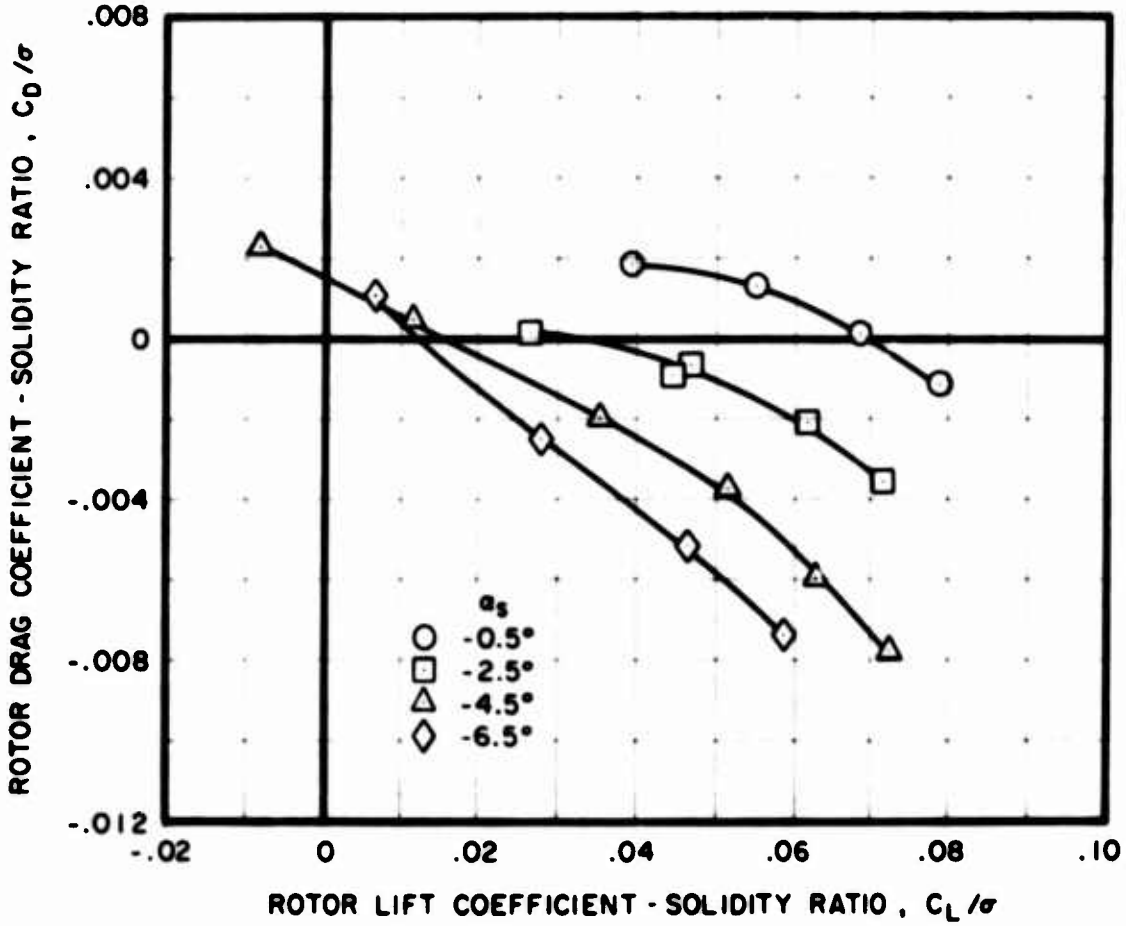

(b) $\mu = 0.4$, $V_s = 166$ kn

Figure 24. Continued.

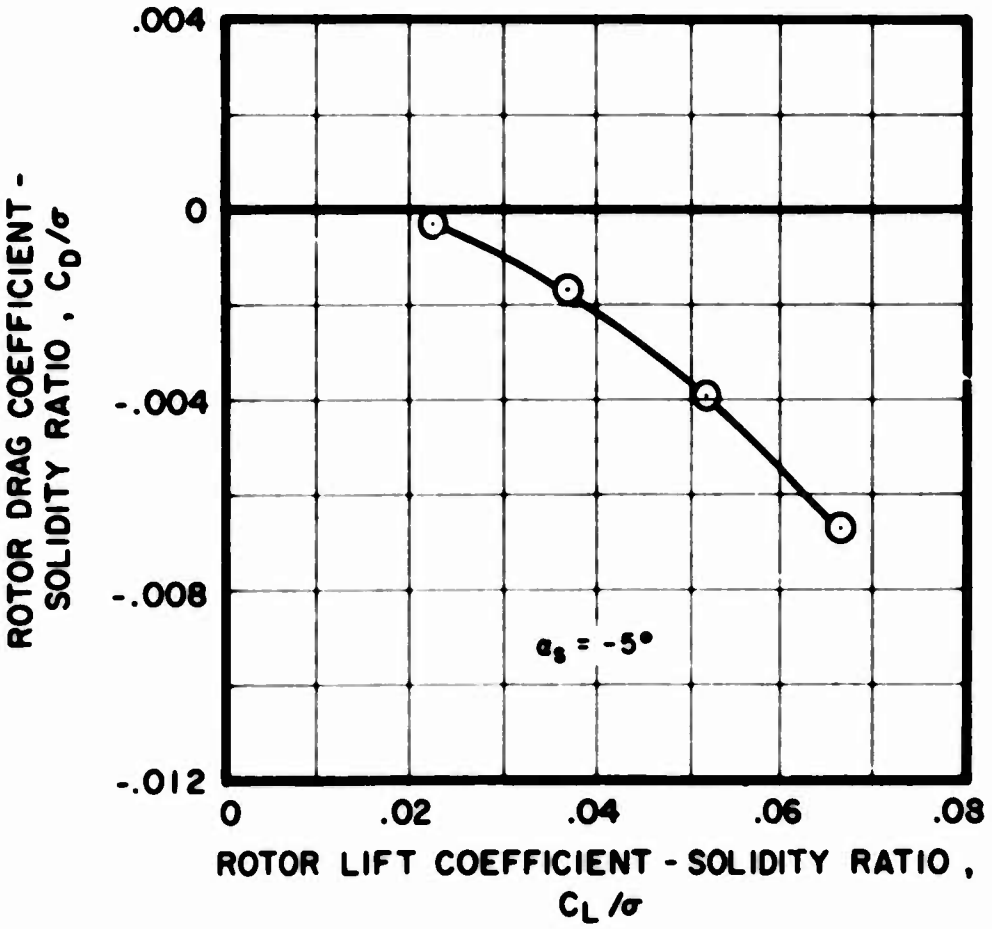

(c) $\mu = 0.5$, $V_s = 208$ kn

Figure 24. Concluded.

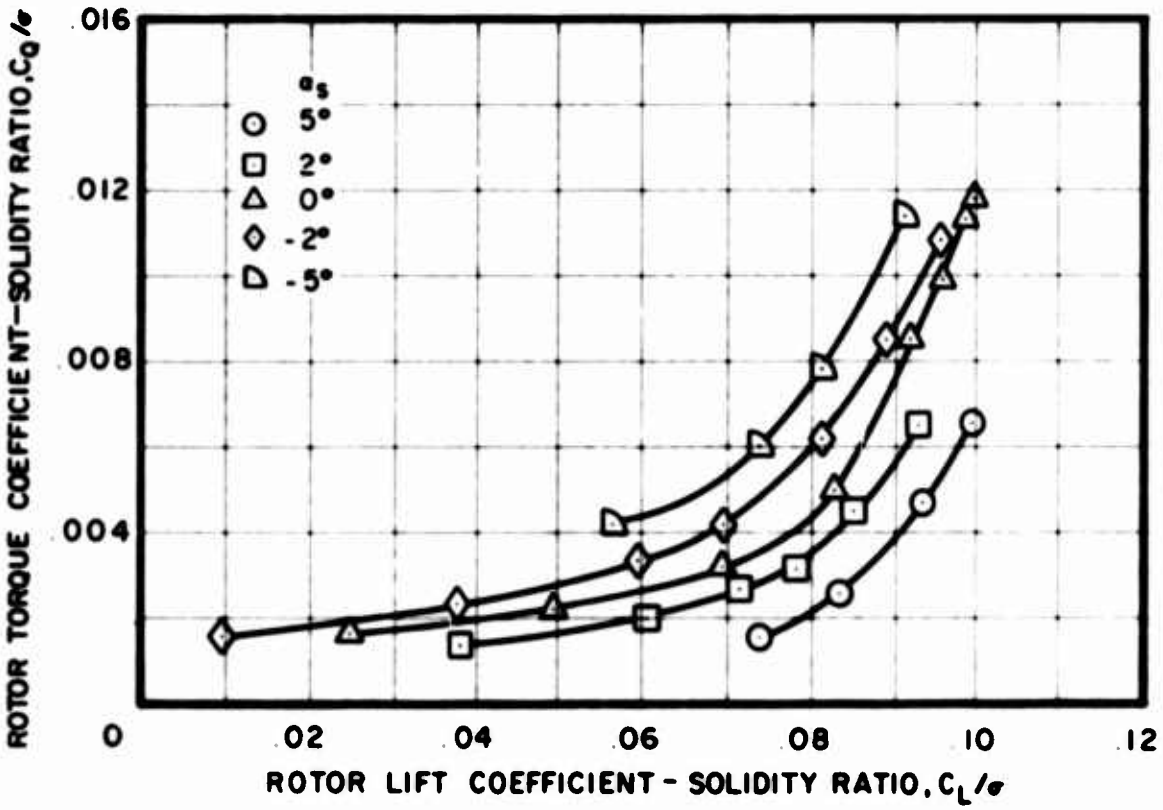

(a) $\mu = 0.3$, $V_s = 124$ kn

Figure 25. Torque vs. Lift Performance of Model Rotor at Various Advance Ratios; $\theta_1 = 0$ deg, $\delta_F = 0$ deg, $S_E = 1$, $a_{1s} = b_{1s} = 0$ deg.

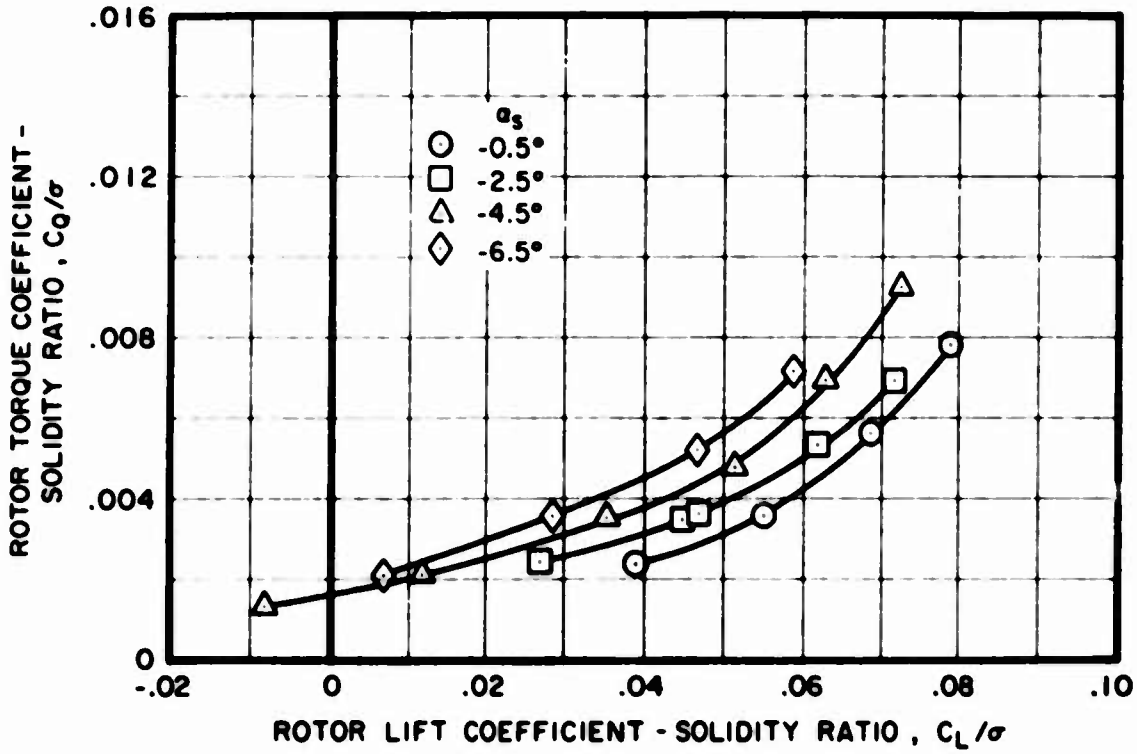

(b) $\mu = 0.4$, $V_s = 166$ kn

Figure 25. Continued.

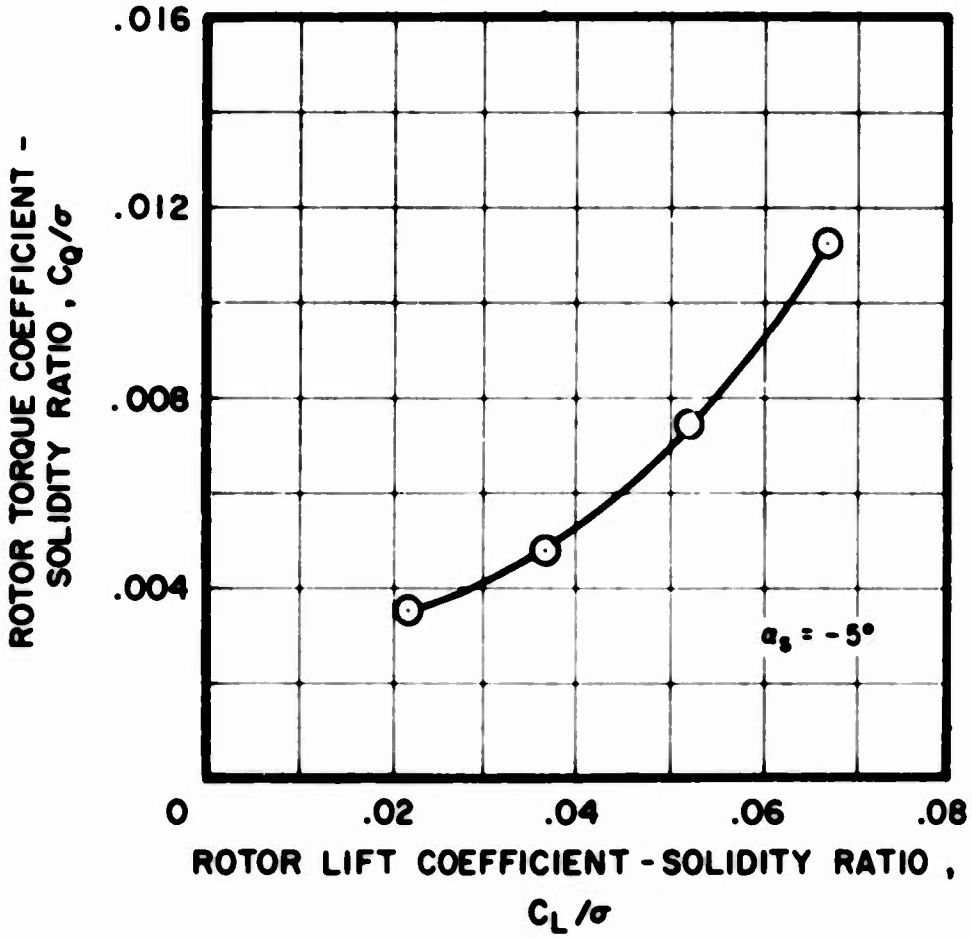

(c) $\mu = 0.5$, $V_s = 208$ kn

Figure 25. Concluded.

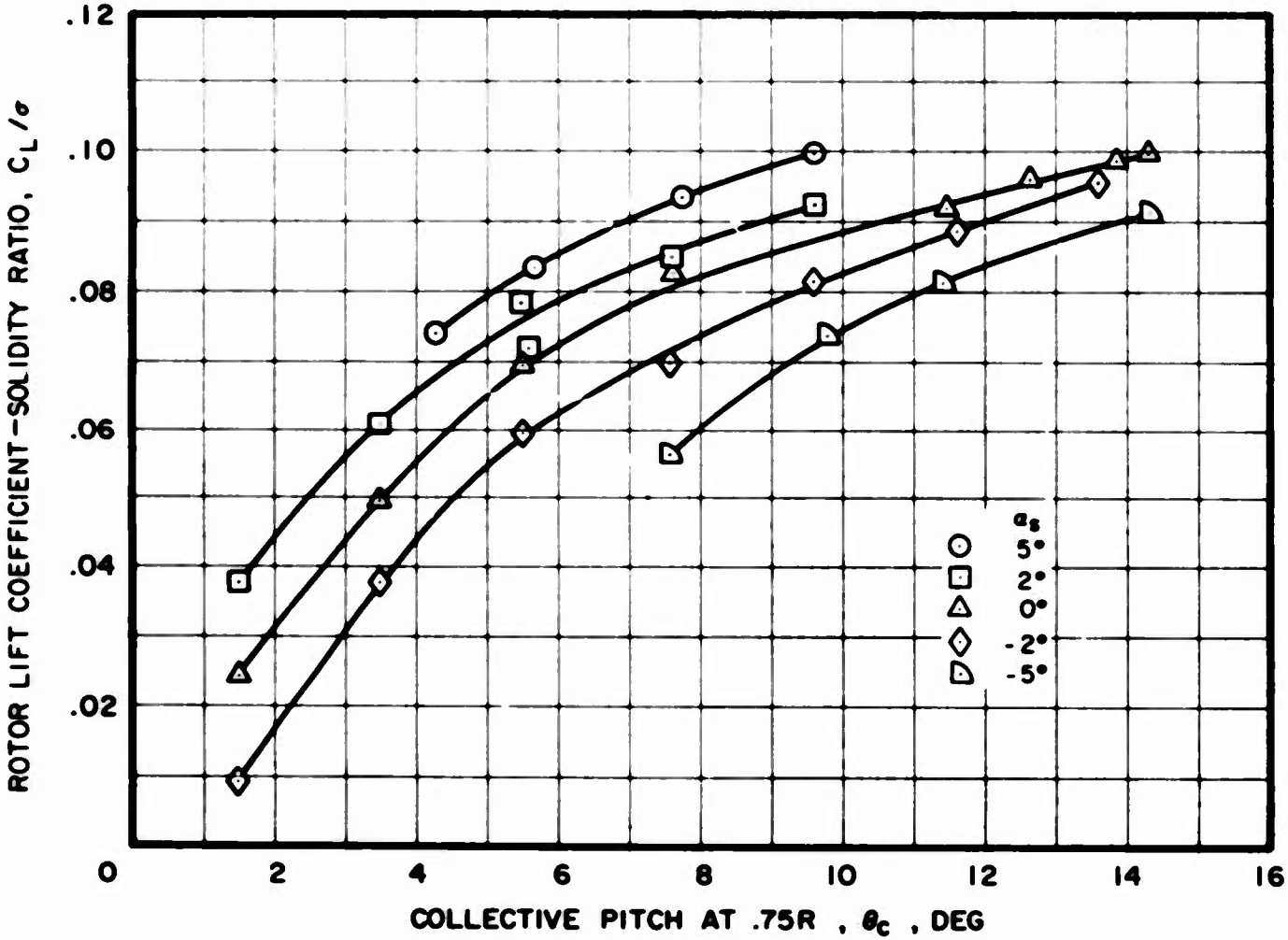

(a) $\mu = 0.3$, $V_s = 124$ kn

Figure 26. Lift vs. Collective Pitch Performance of Model Rotor at Various Advance Ratios; $\theta_1 = 0$ deg, $\delta_F = 0$ deg, $S_E = 1$, $a_{1s} = b_{1s} = 0$ deg.

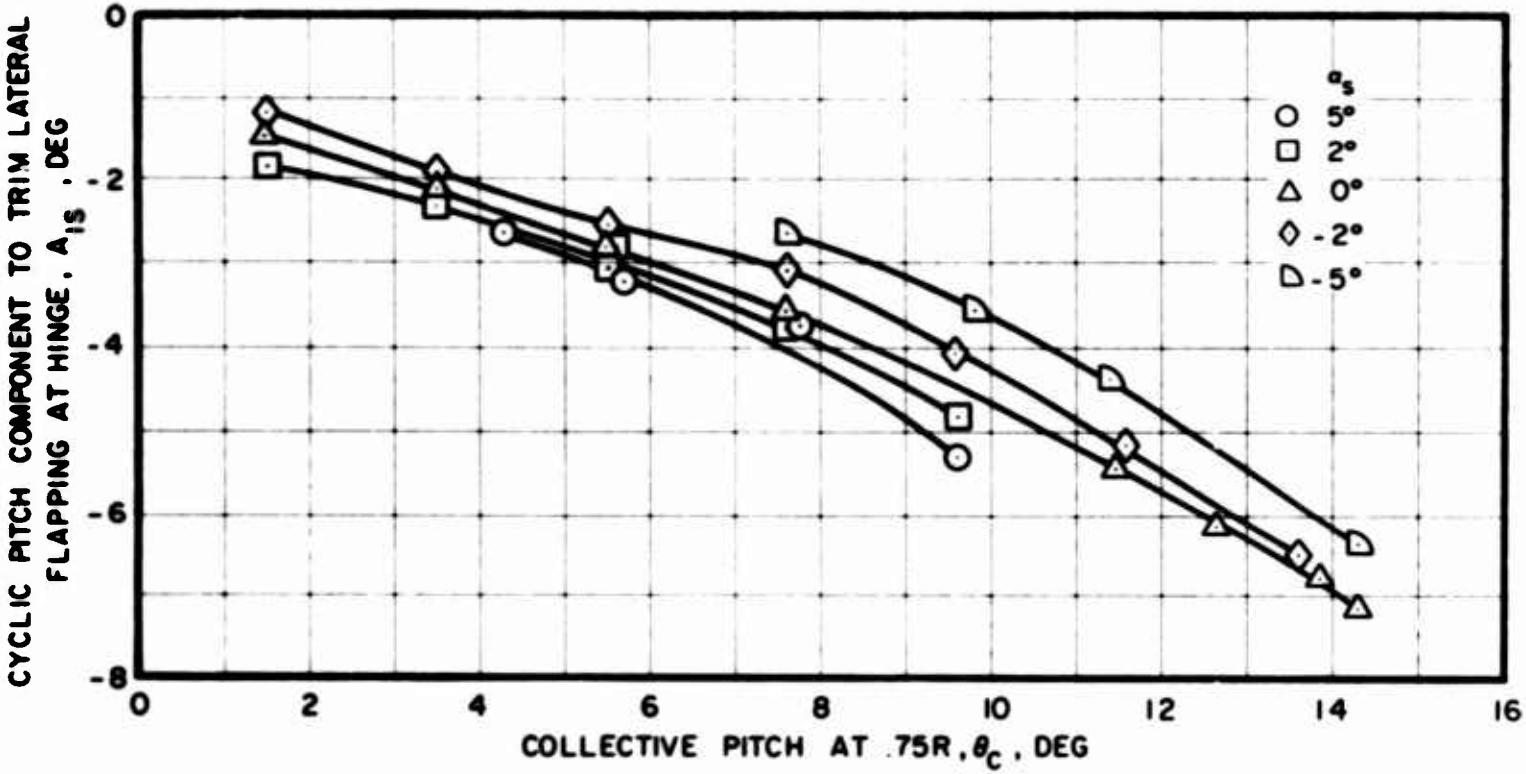

(a) A_{1s}; $\mu = 0.3$, $V_s = 124$ kn

Figure 27. Cyclic Pitch to Trim Flapping vs. Collective Pitch at Various Advance Ratios; $\theta_1 = 0$ deg, $\delta_F = 0$ deg, $S_E = 1$, $a_{1s} = b_{1s} = 0$ deg.

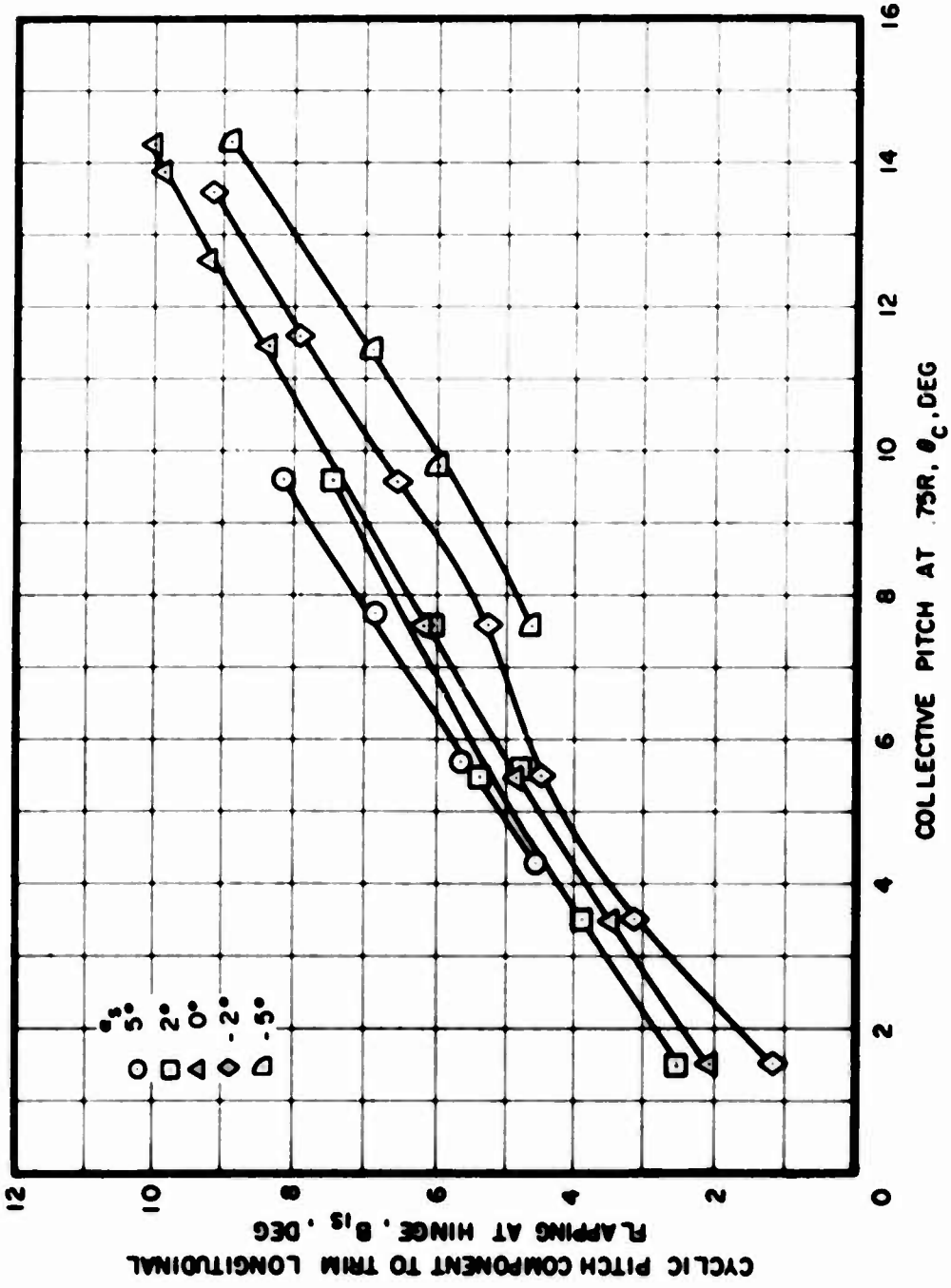

(b) B_{1s}; $\mu = 0.3$, $V_s = 124$ kn

Figure 27. Continued.

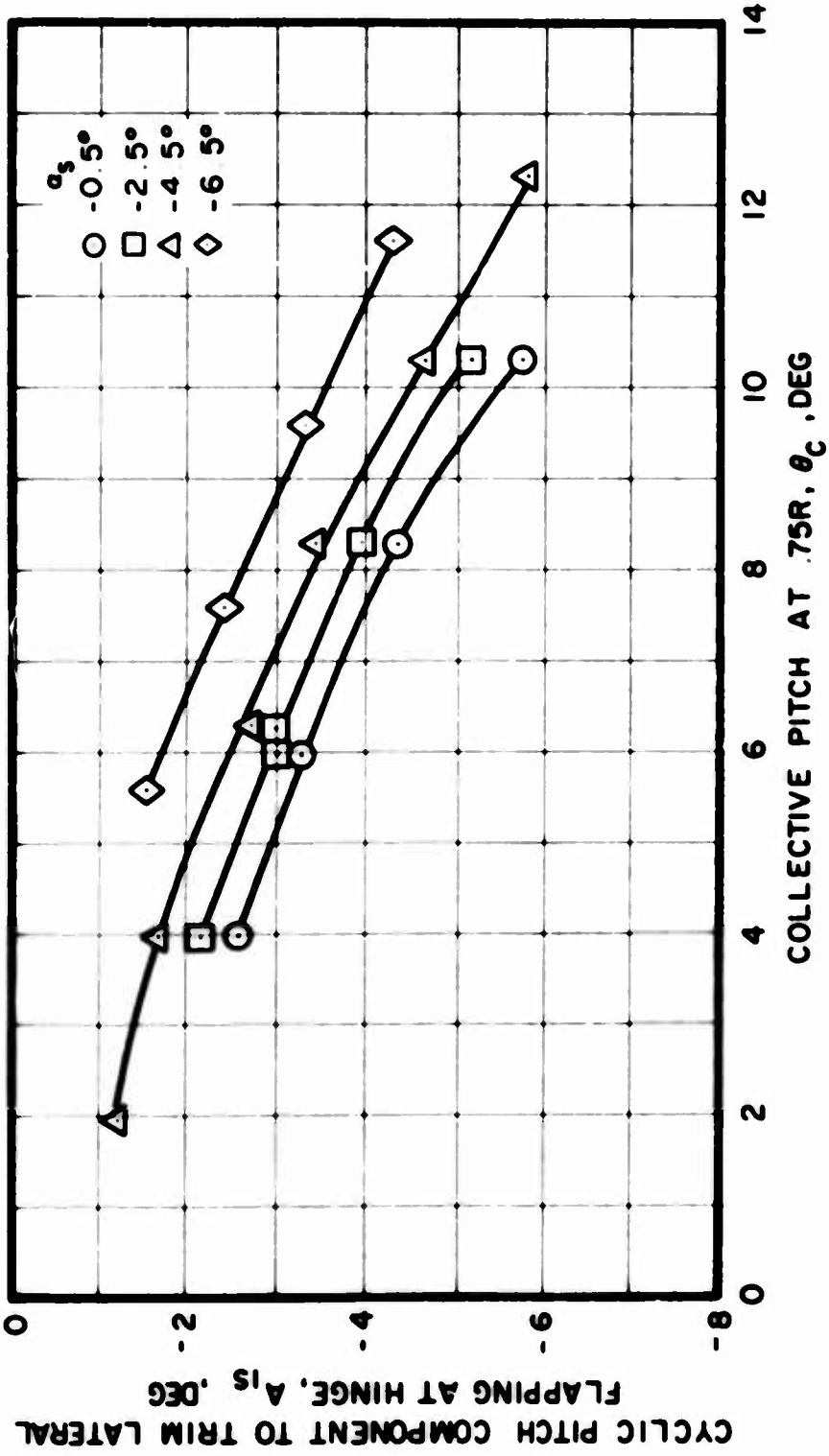

(c) A_{1s}; $\mu = 0.4$, $V_s = 124$ kn

Figure 27. Continued.

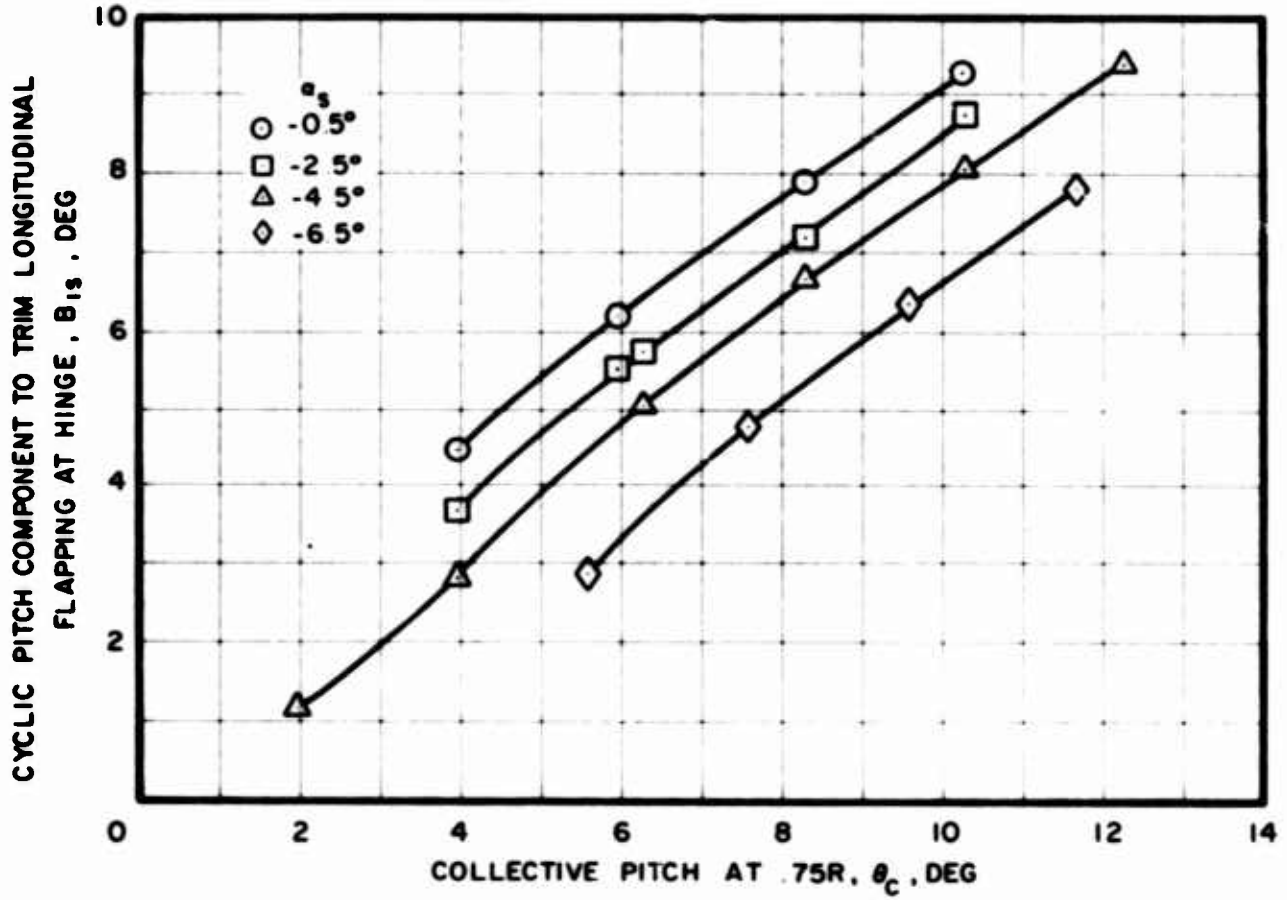

(d) B_{1s}; $\mu = 0.4$, $V_s = 166$ kn

Figure 27. Concluded.

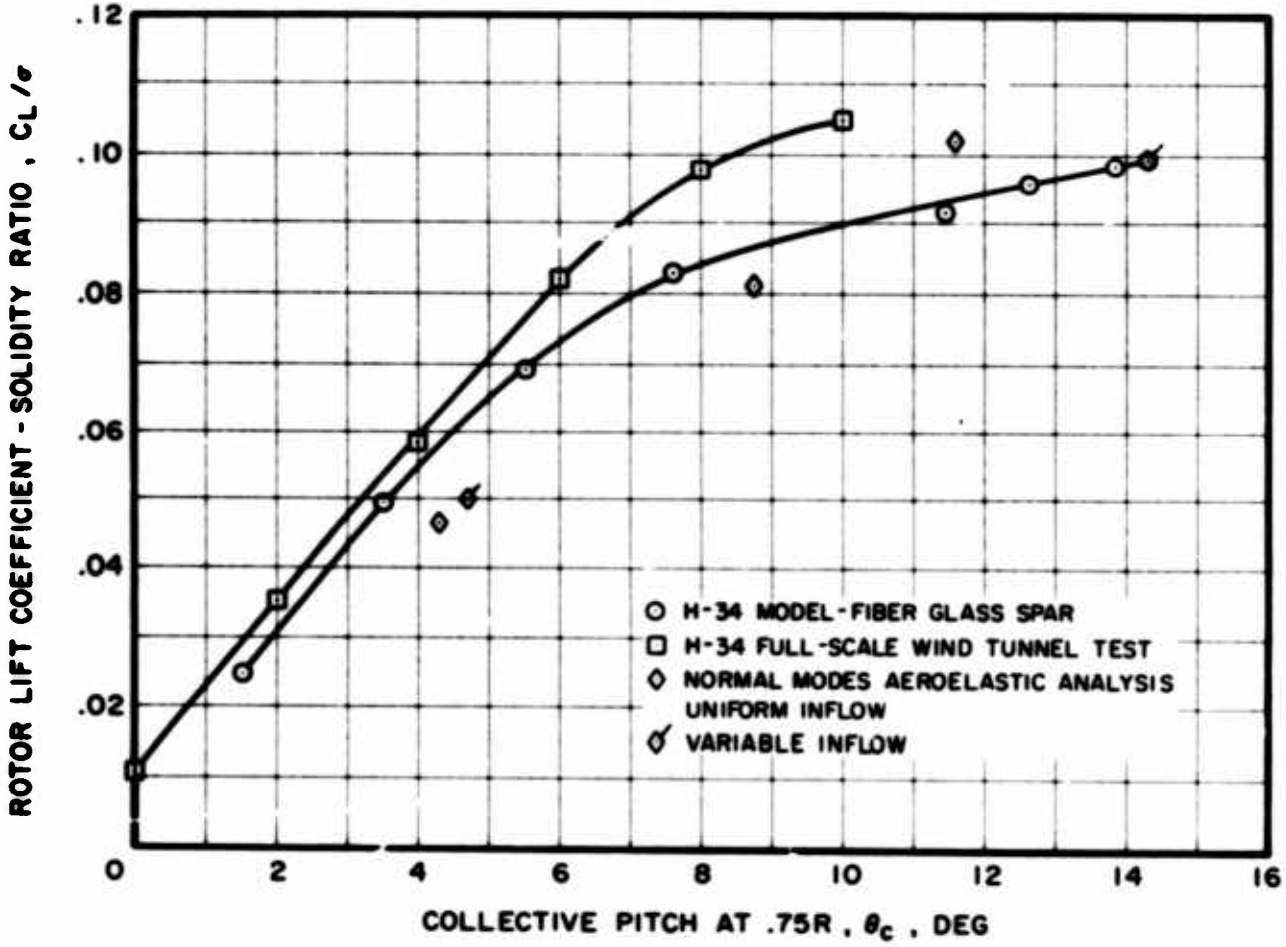

(a) Rotor Lift Coefficient-Solidity Ratio.

Figure 28. Presentation and Correlation of Model Rotor Performance vs. Collective Pitch; V_s = 124 kn, θ_1 = 0 deg, δ_F = 0 deg, S_E = 1, α_s = 0 deg, μ = 0.3.

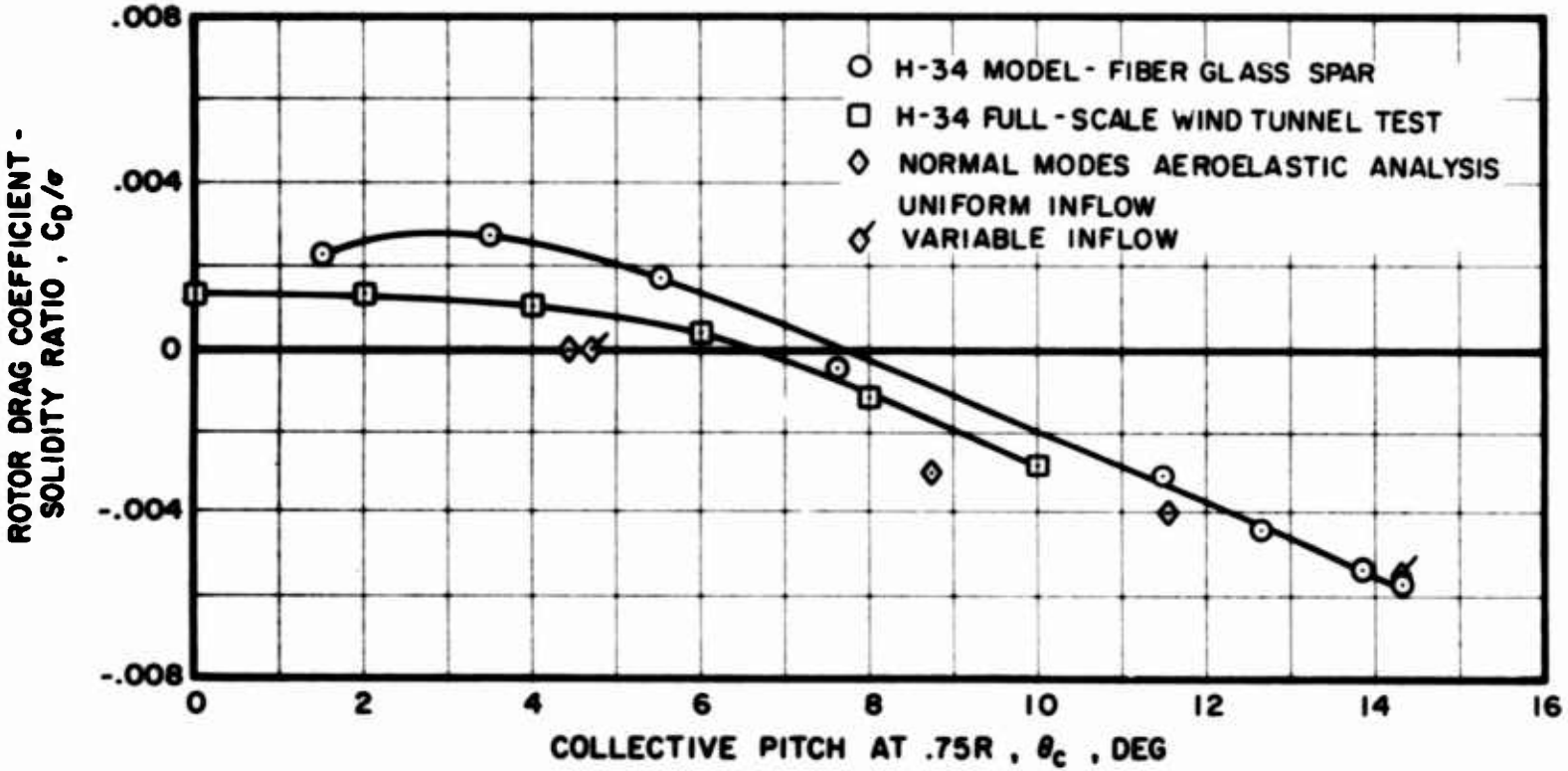

(b) Rotor Drag Coefficient-Solidity Ratio

Figure 28. Continued.

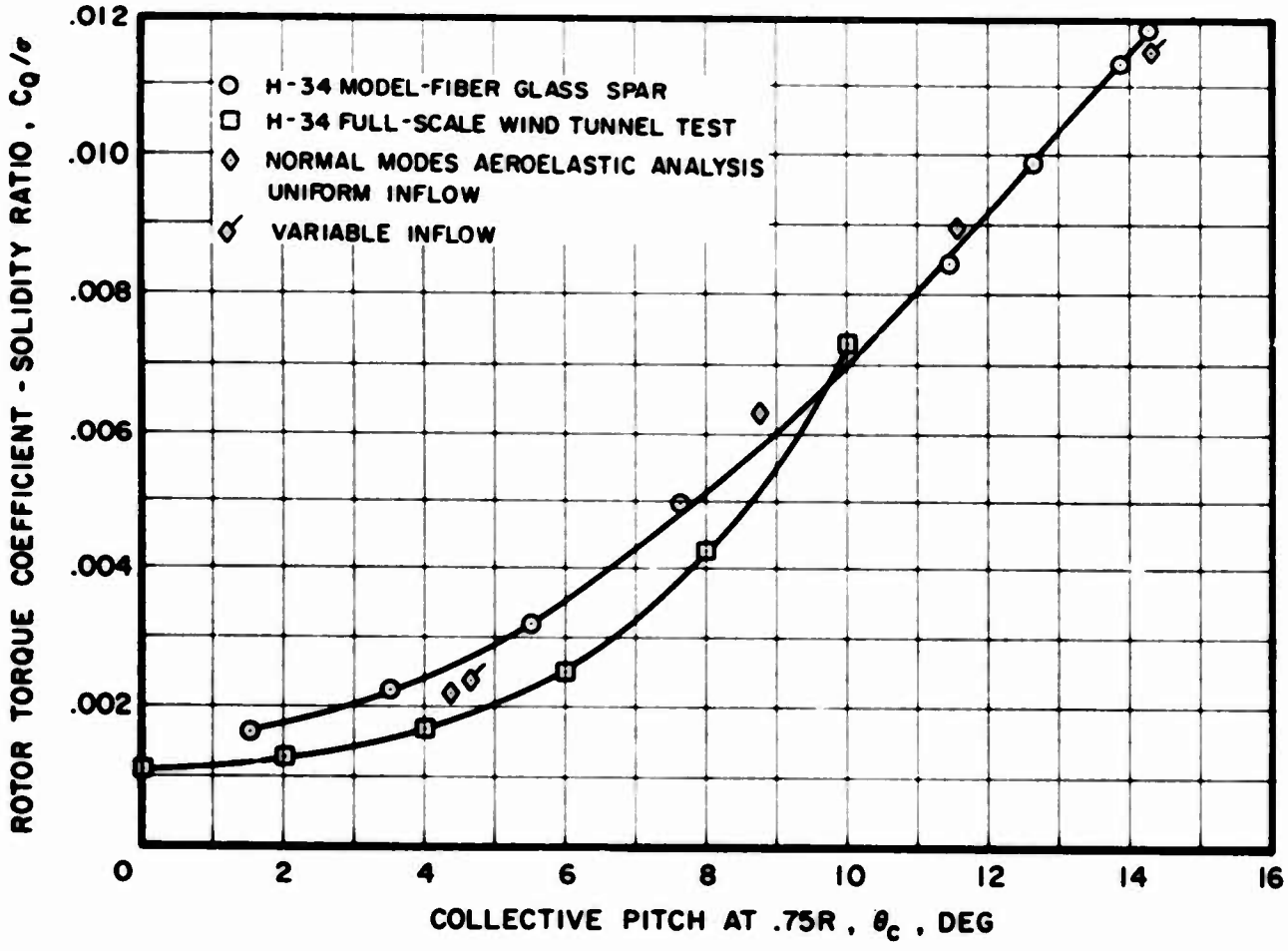

(c) Rotor Torque Coefficient-Solidity Ratio

Figure 28. Continued.

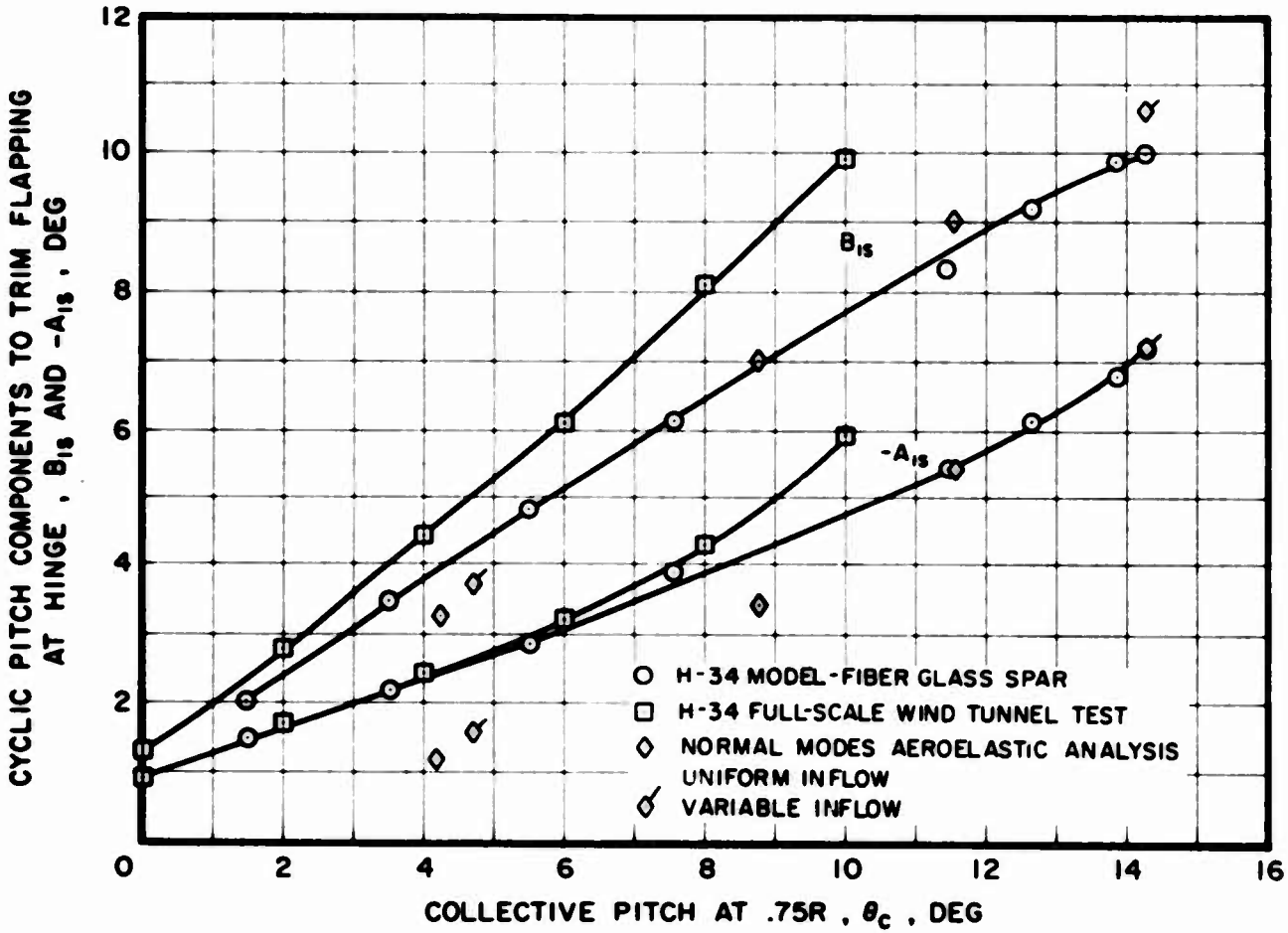

(d) Cyclic Pitch to Trim Flapping

Figure 28. Concluded.

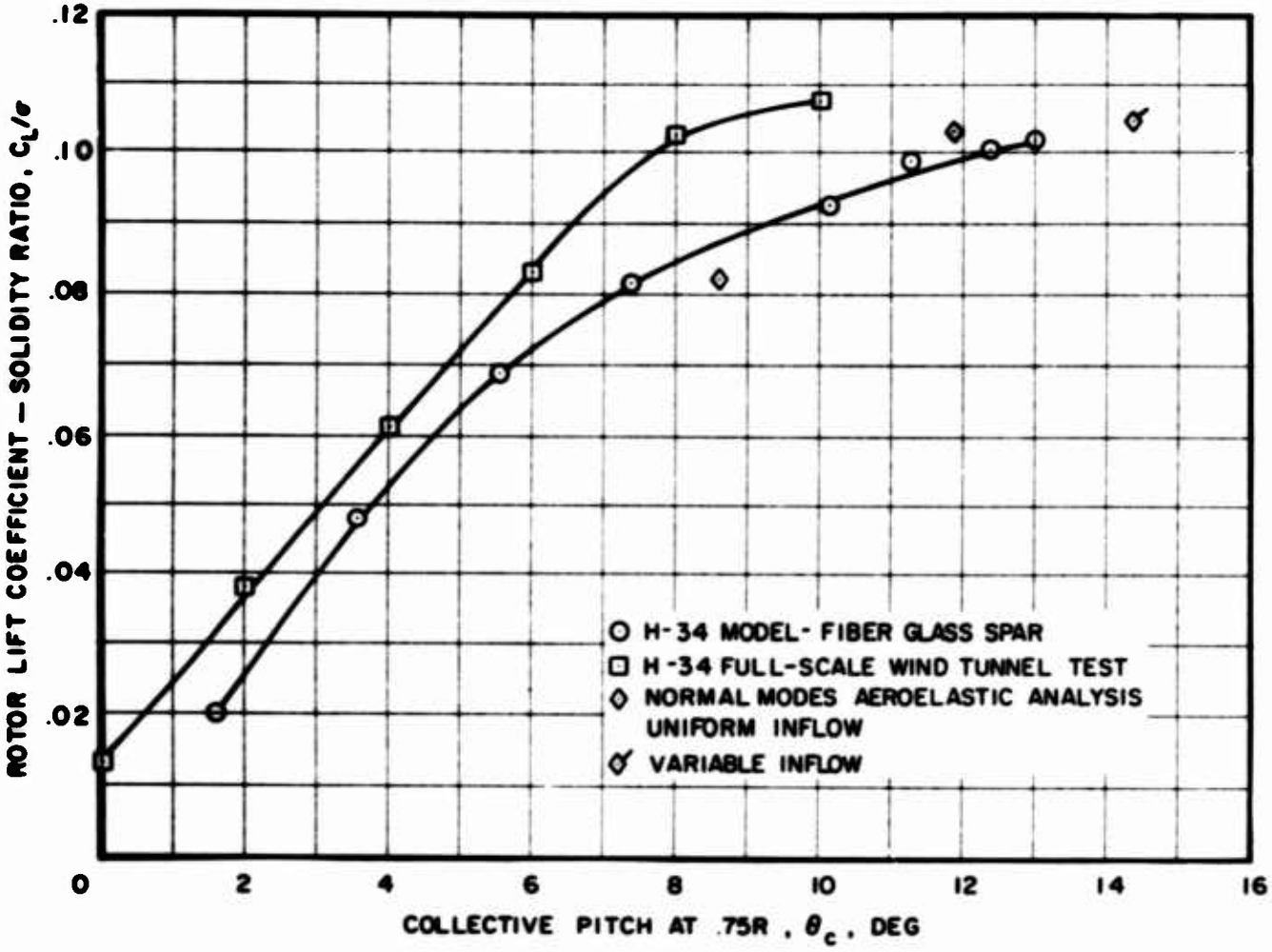

(a) Rotor Lift Coefficient-Solidity Ratio

Figure 29. Presentation and Correlation of Model Rotor Performance vs. Collective Pitch; V_s = 124 kn, θ_1 = -8 deg, δ_F = 0 deg, S_E = 1, α_s = 0 deg, μ = 0.3.

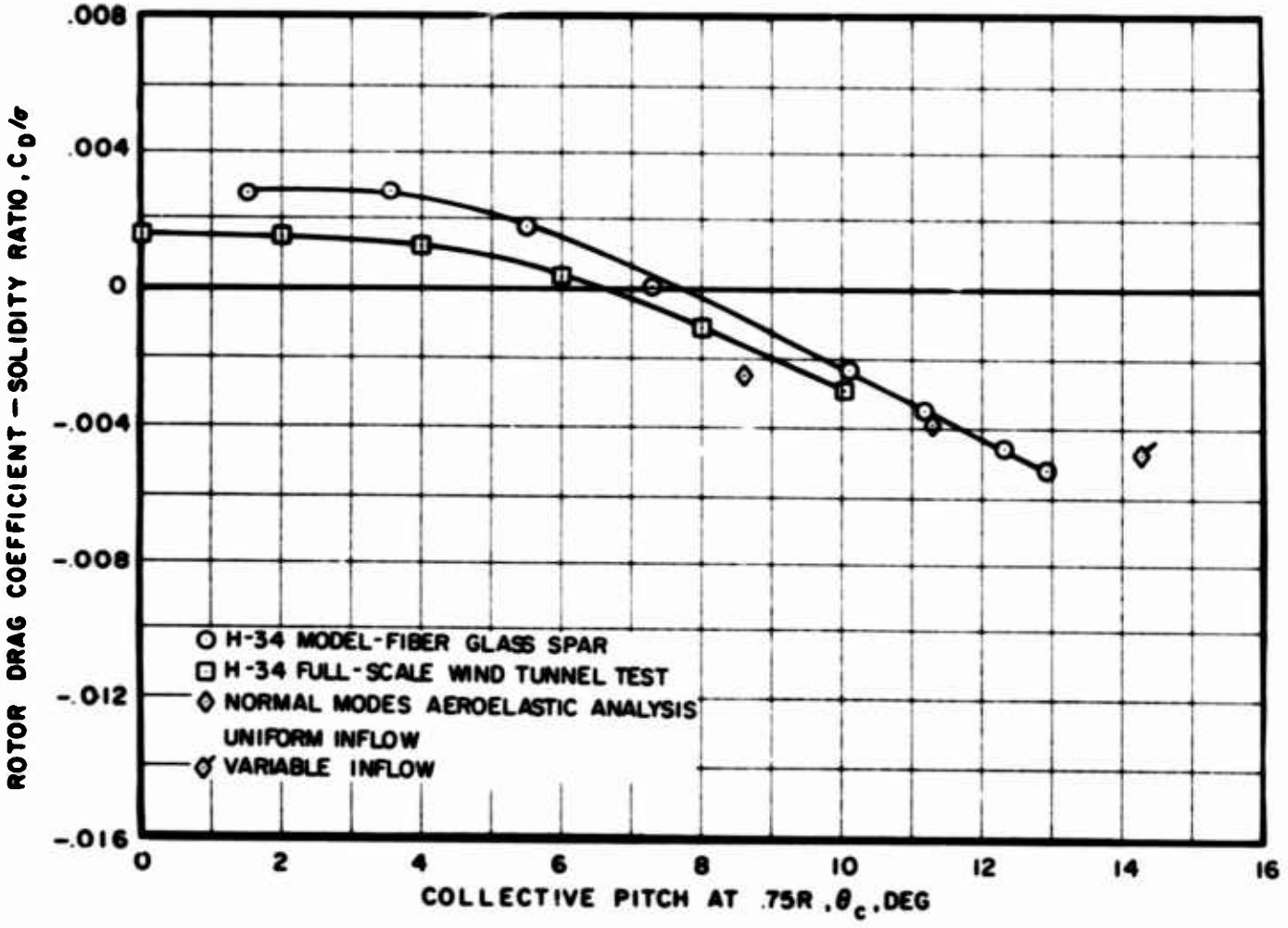

(b) Rotor Drag Coefficient-Solidity Ratio

Figure 29. Continued.

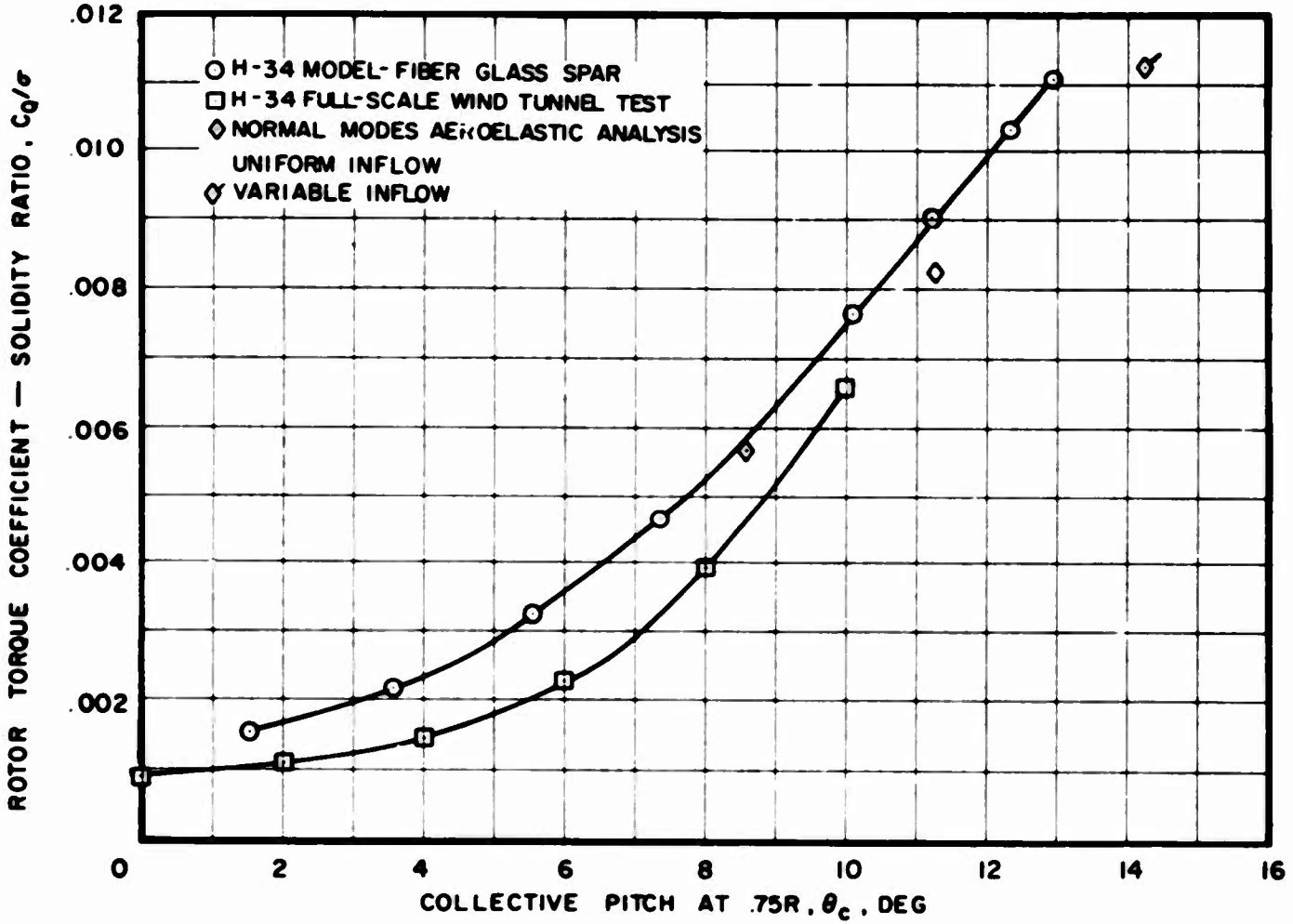

(c) Rotor Torque Coefficient Solidity Ratio

Figure 29. Continued.

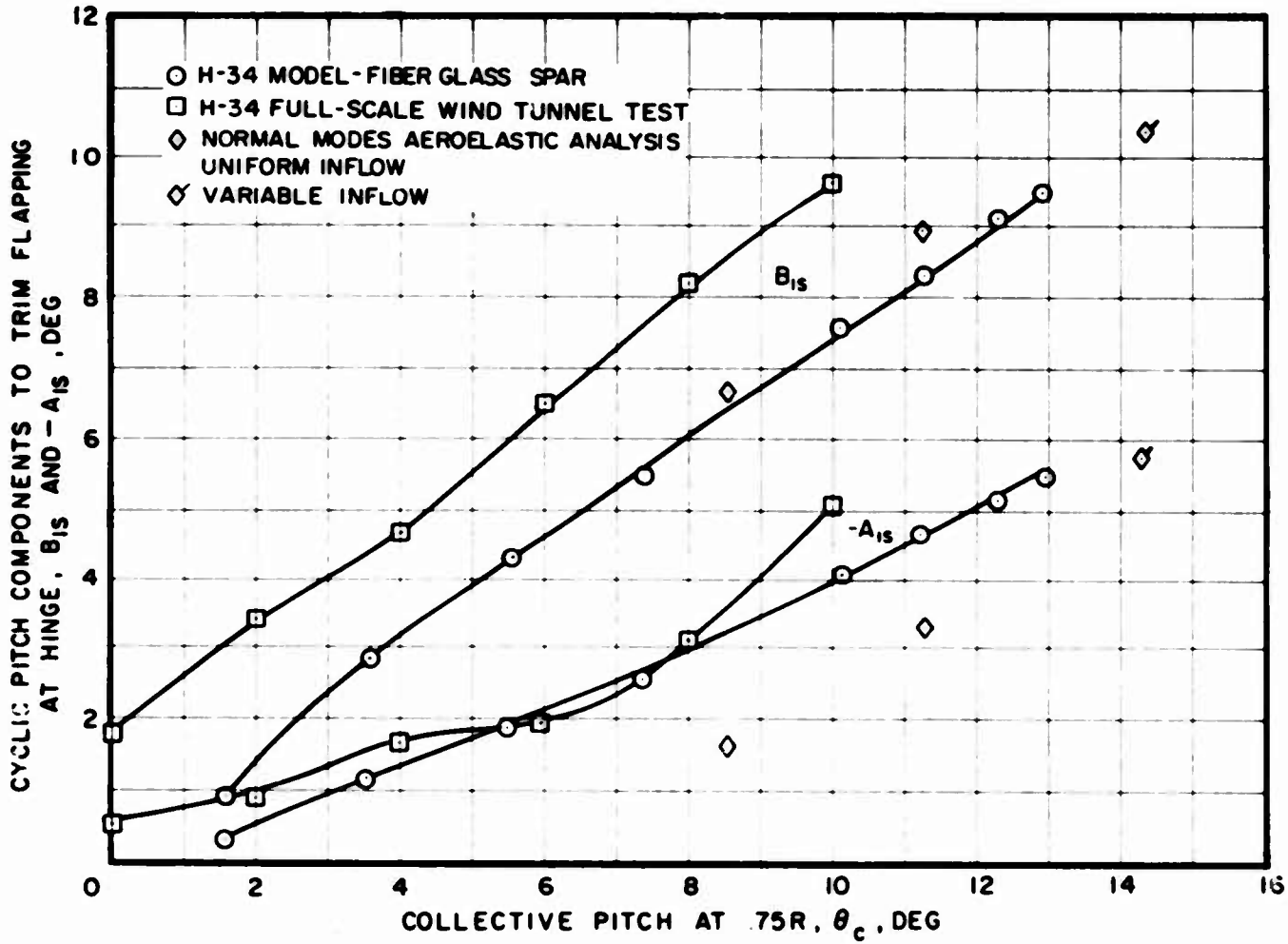

(d) Cyclic Pitch to Trim Flapping

Figure 29. Concluded.

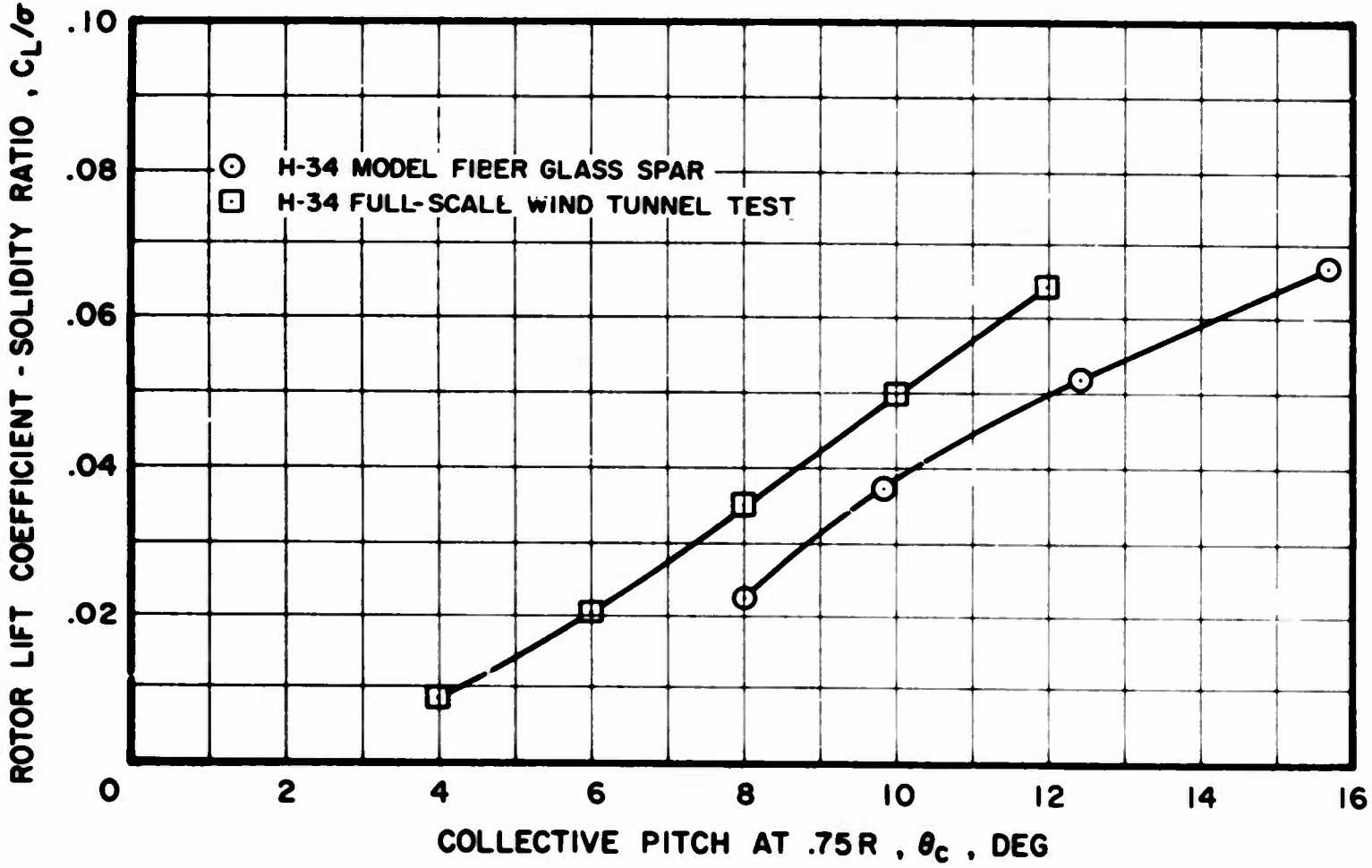

(a) Rotor Lift Coefficient-Solidity Ratio

Figure 30. Presentation and Correlation of Model Rotor Performance vs. Collective Pitch; V_s = 208 kn, θ_1 = 0 deg, δ_F = 0 deg, S_E = 1, α_s = 5 deg, μ = 0.5.

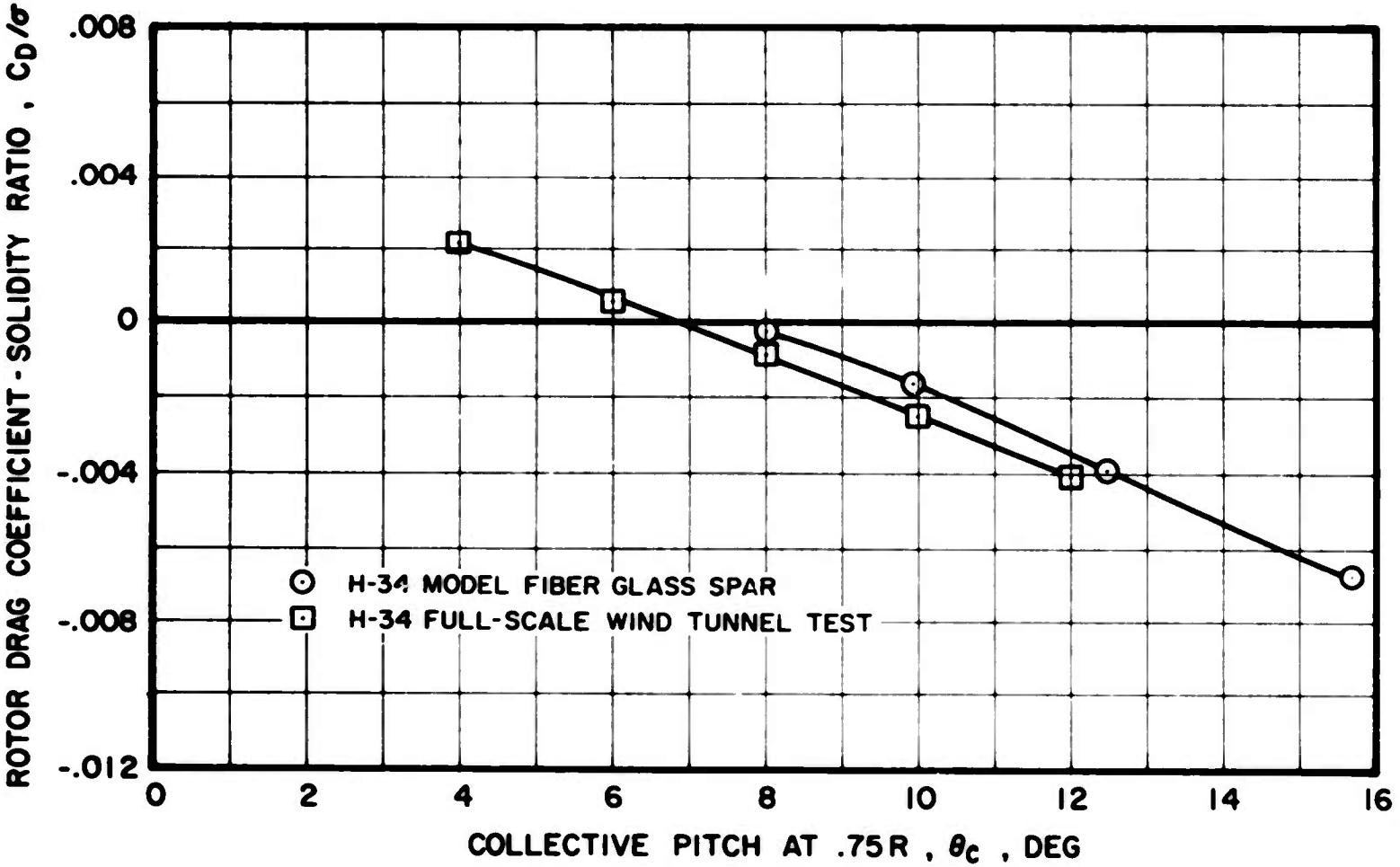

(b) Rotor Drag Coefficient-Solidity Ratio

Figure 30. Continued.

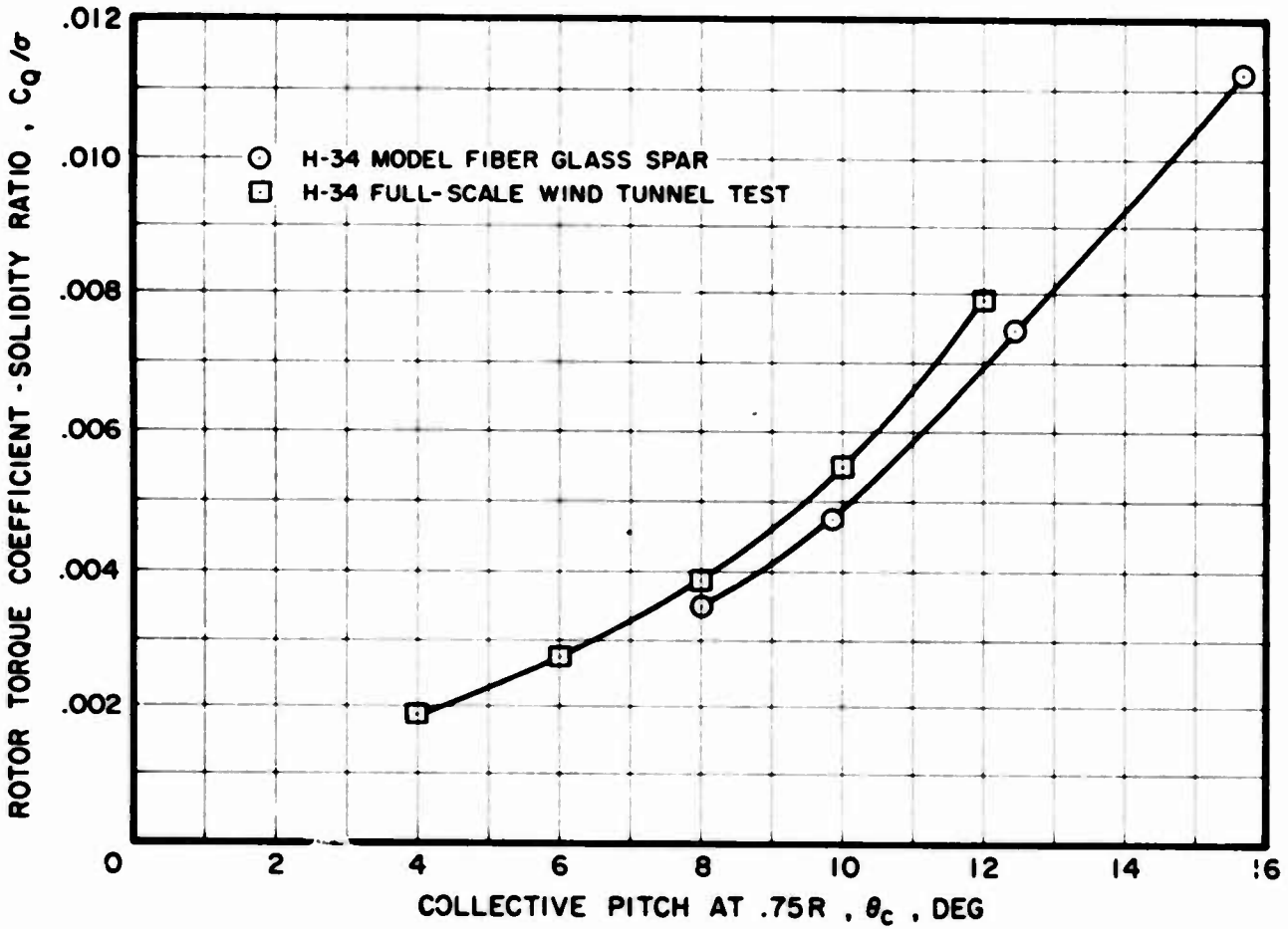

(c) Rotor Torque Coefficient-Solidity Ratio

Figure 30. Continued.

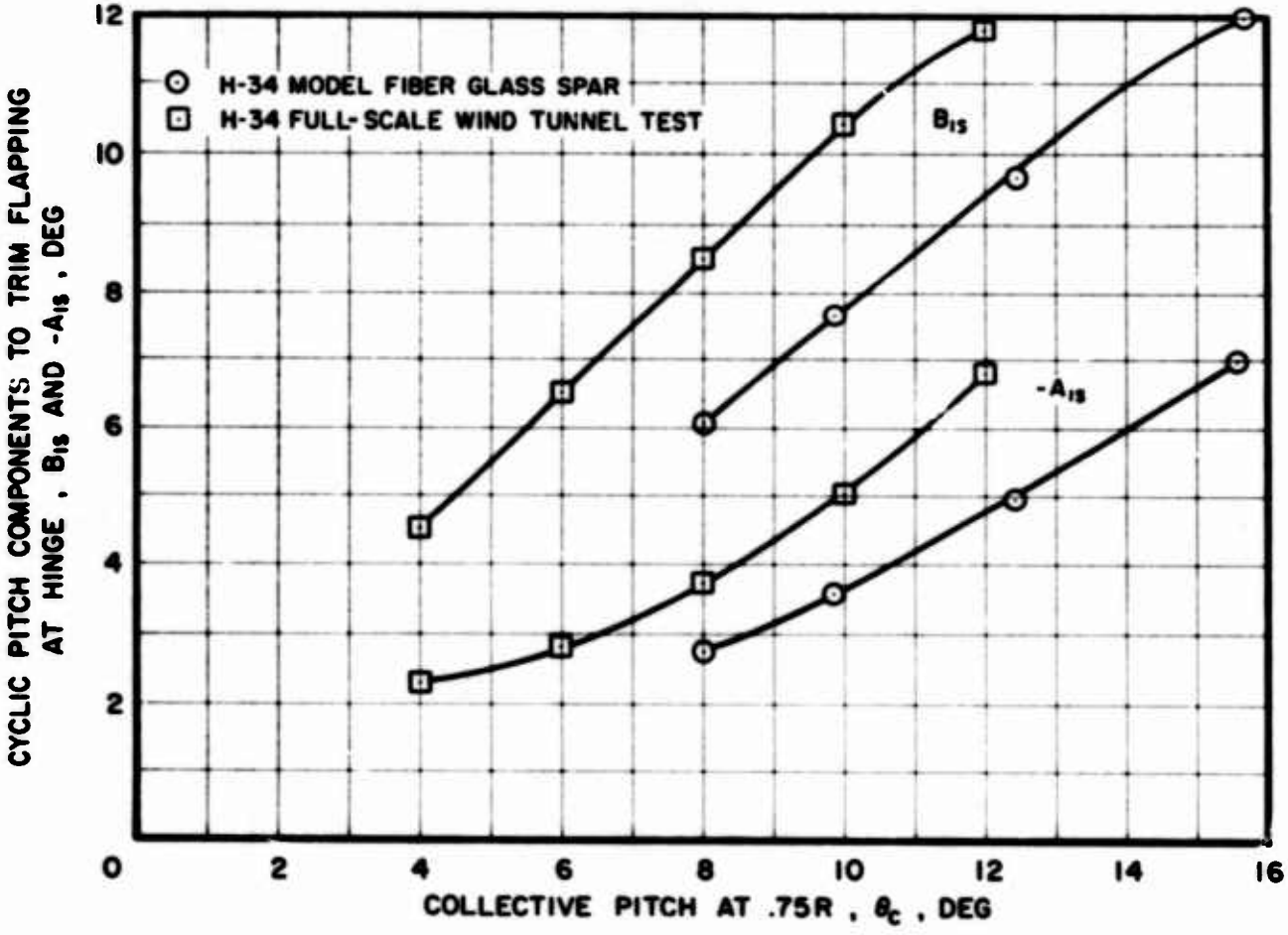

(d) Cyclic Pitch to Trim Flapping

Figure 30. Concluded.

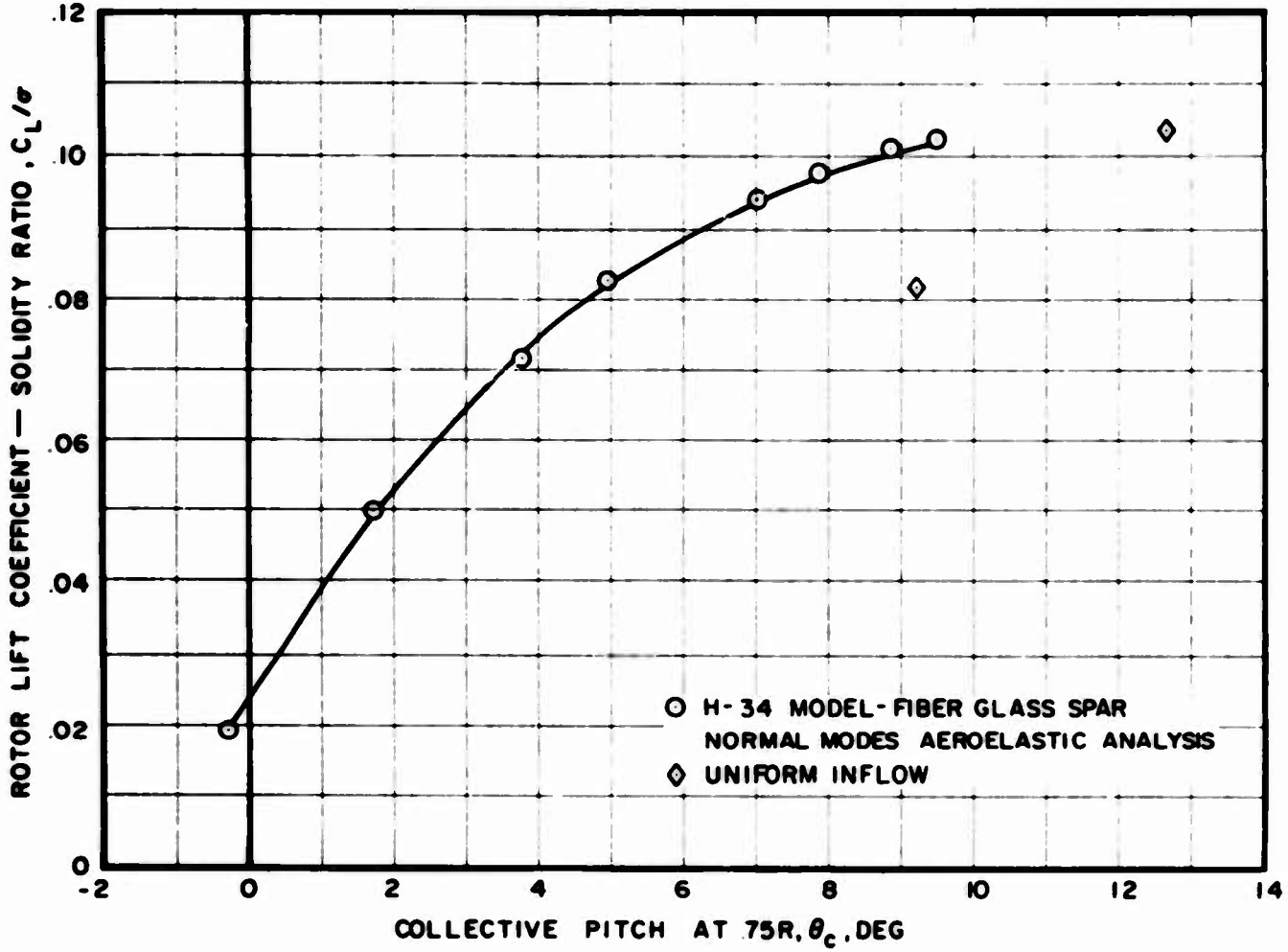

(a) Rotor Lift Coefficient-Solidity Ratio

Figure 31. Presentation and Correlation of Model Rotor Performance vs. Collective Pitch; V_s = 124 kn, θ_1 = 0 deg, δ_F = 5 deg, S_E = 1, α_s = 0 deg, μ = 0.3.

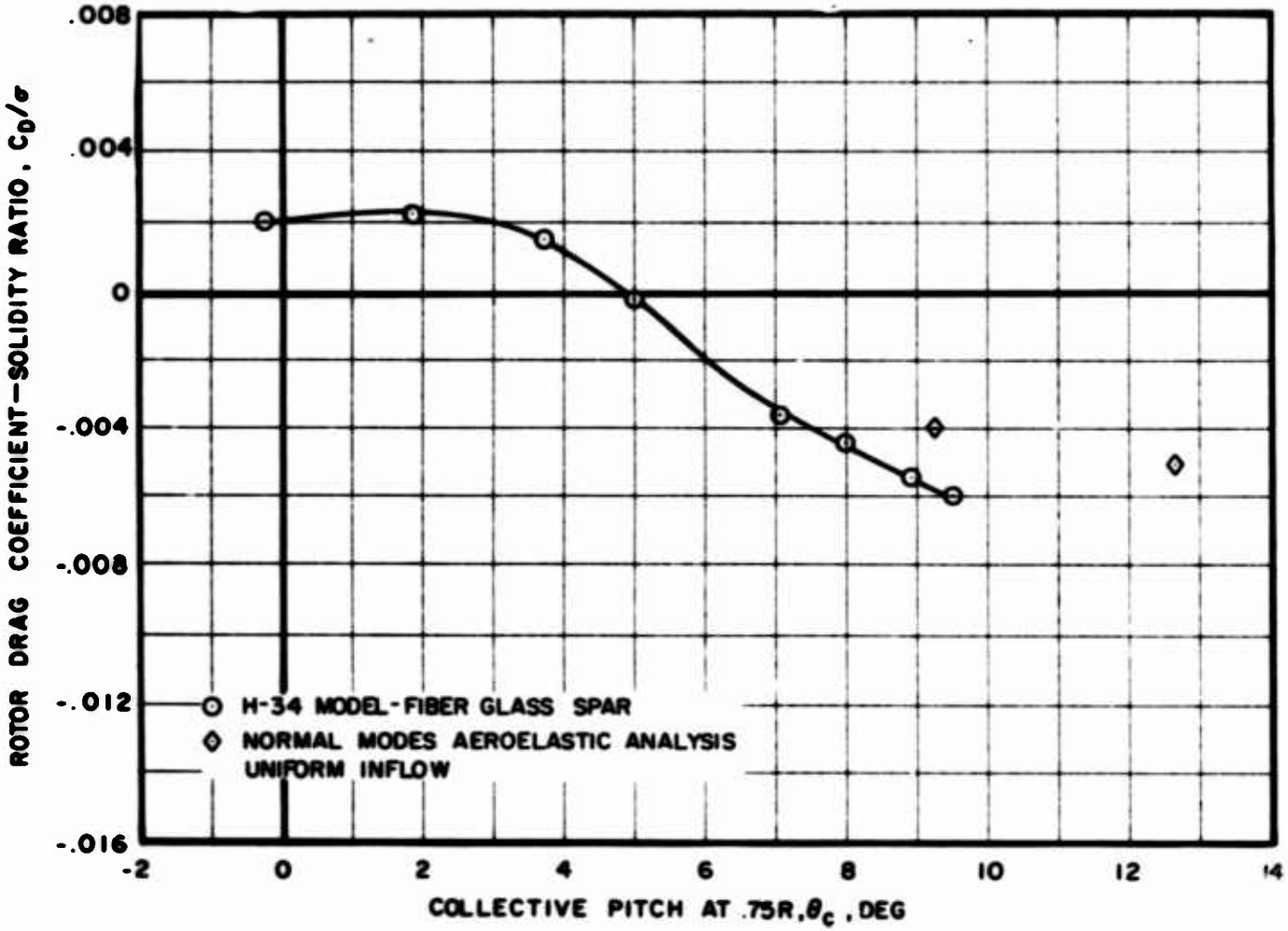

(b) Rotor Drag Coefficient-Solidity Ratio

Figure 31. Continued.

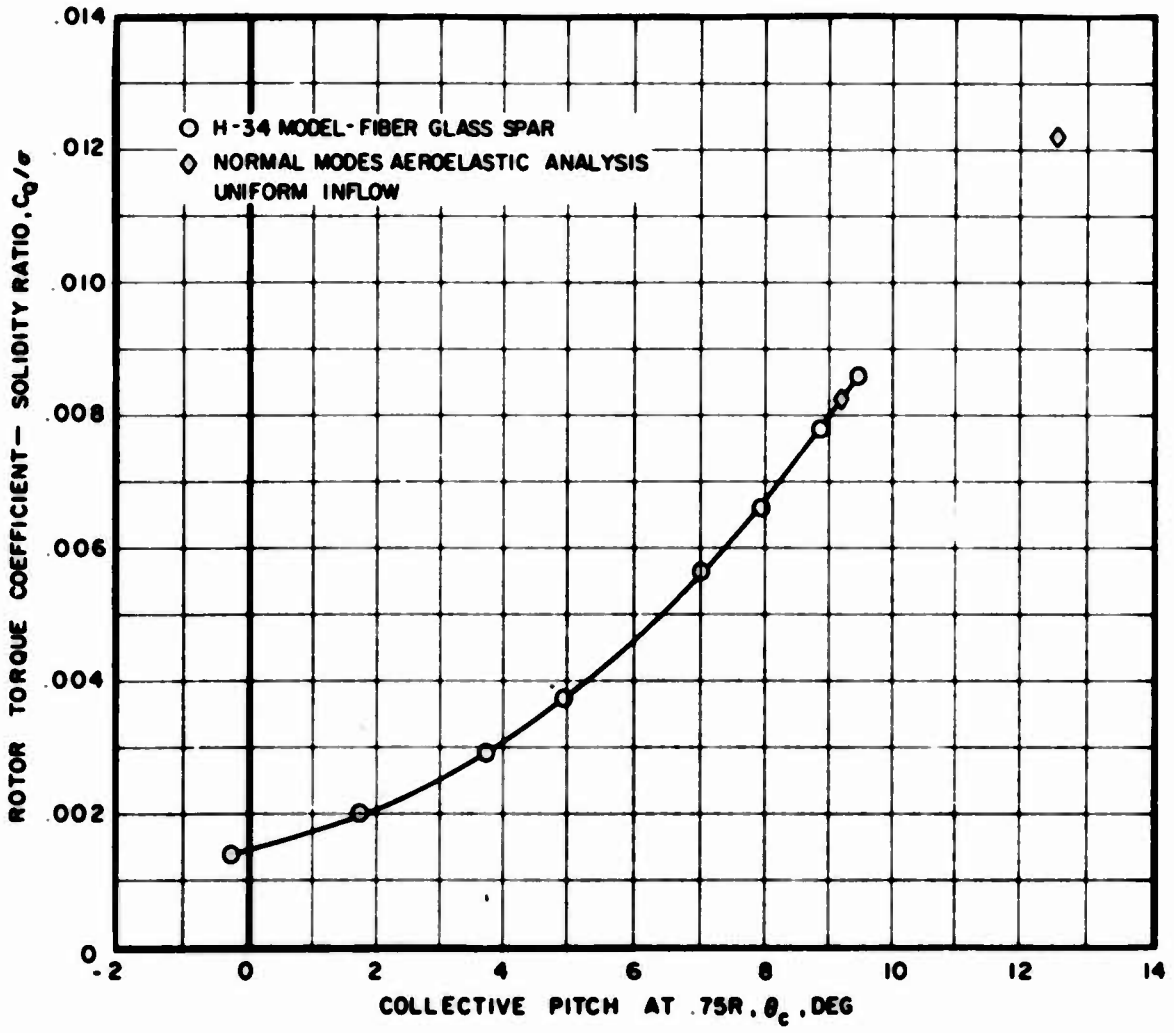

(c) Rotor Torque Coefficient-Solidity Ratio

Figure 31. Continued.

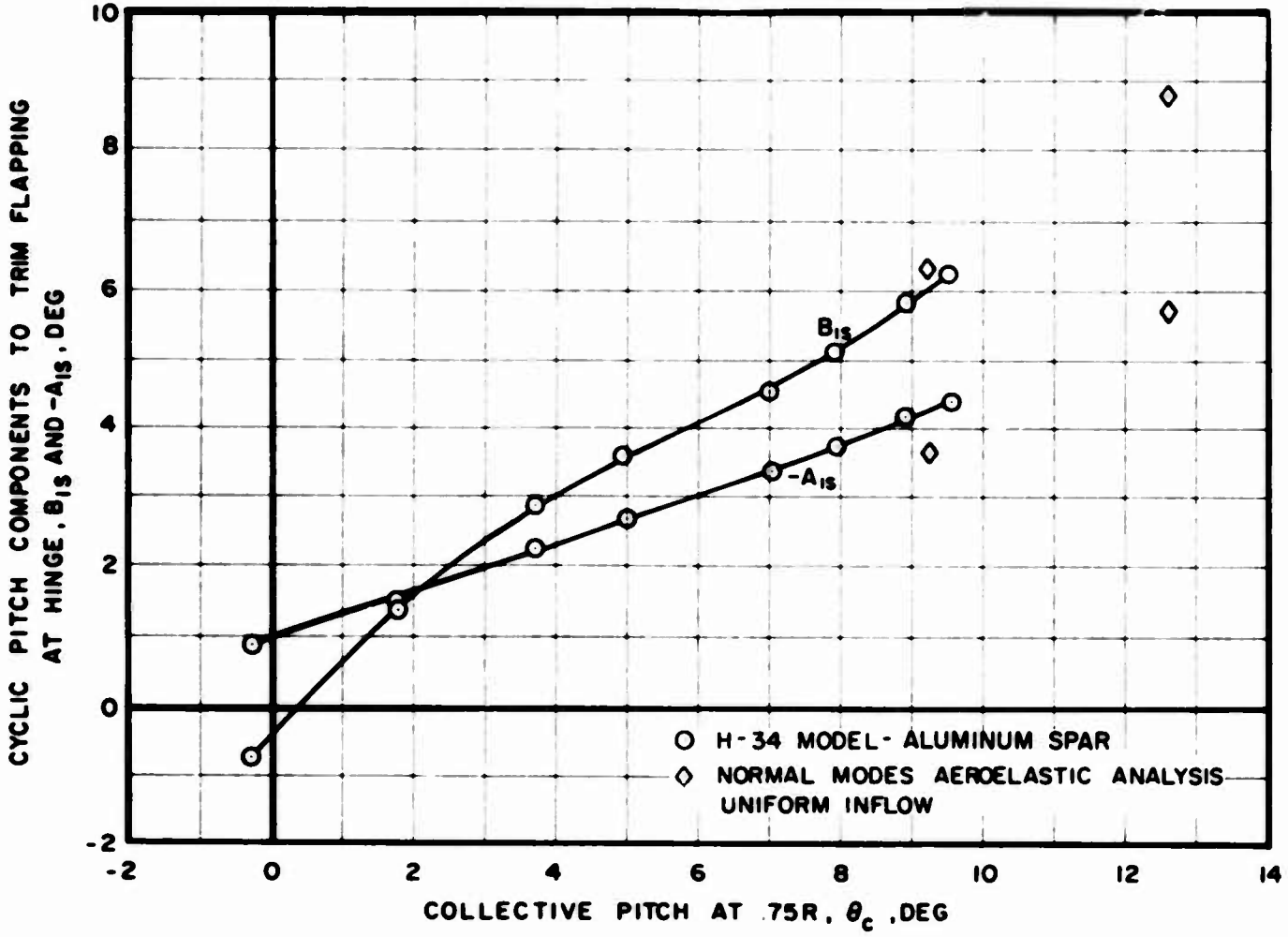

(c) Cyclic Pitch to Trim Flapping

Figure 31. Concluded.

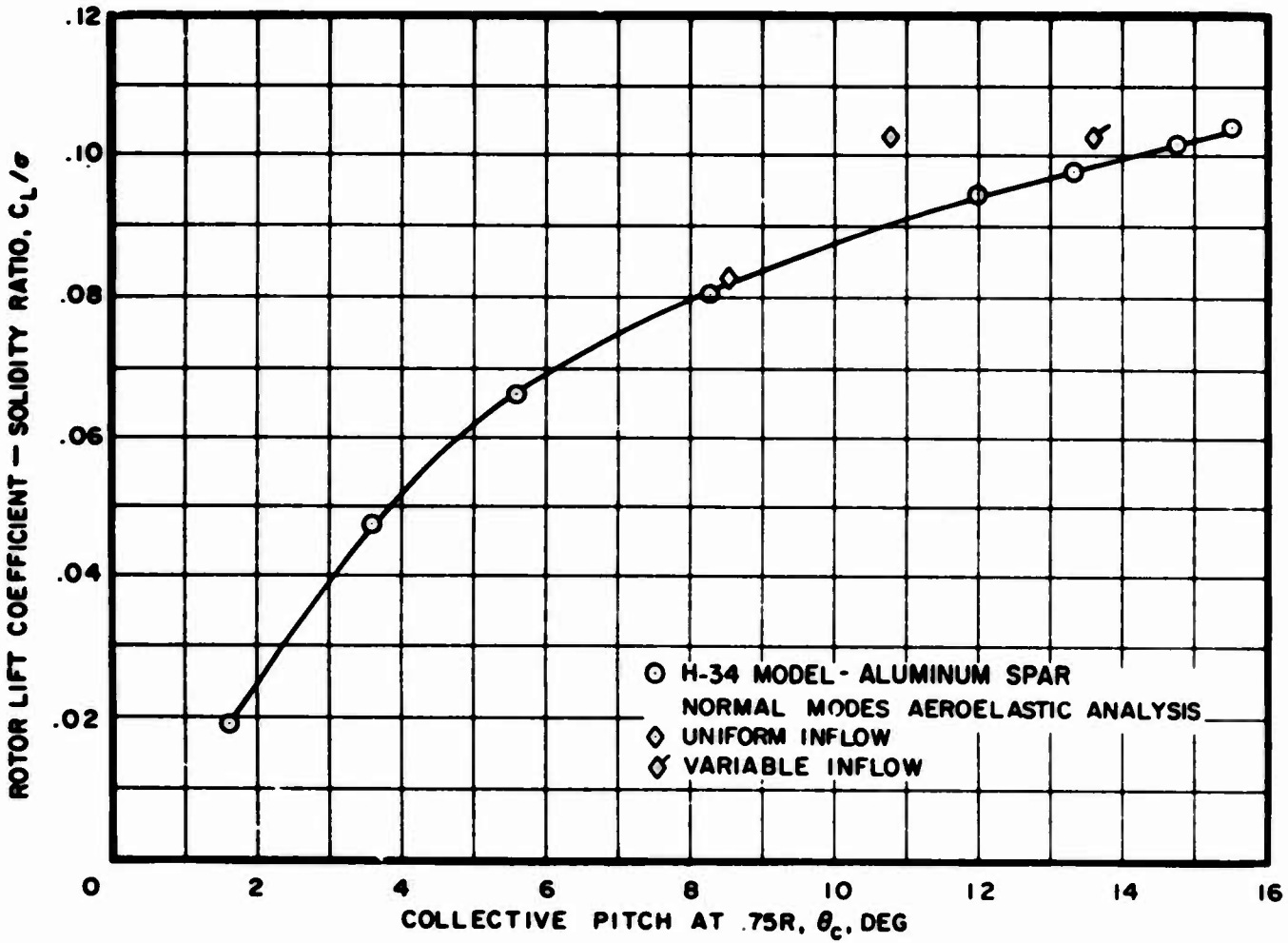

(a) Rotor Lift Coefficient - Solidity Ratio

Figure 32. Presentation and Correlation of Model Rotor Performance vs. Collective Pitch; V_s = 124 kn, θ_1 = 0 deg, δ_F = 0 deg, S_E = 3, α_s = 0 deg, μ = 0.3.

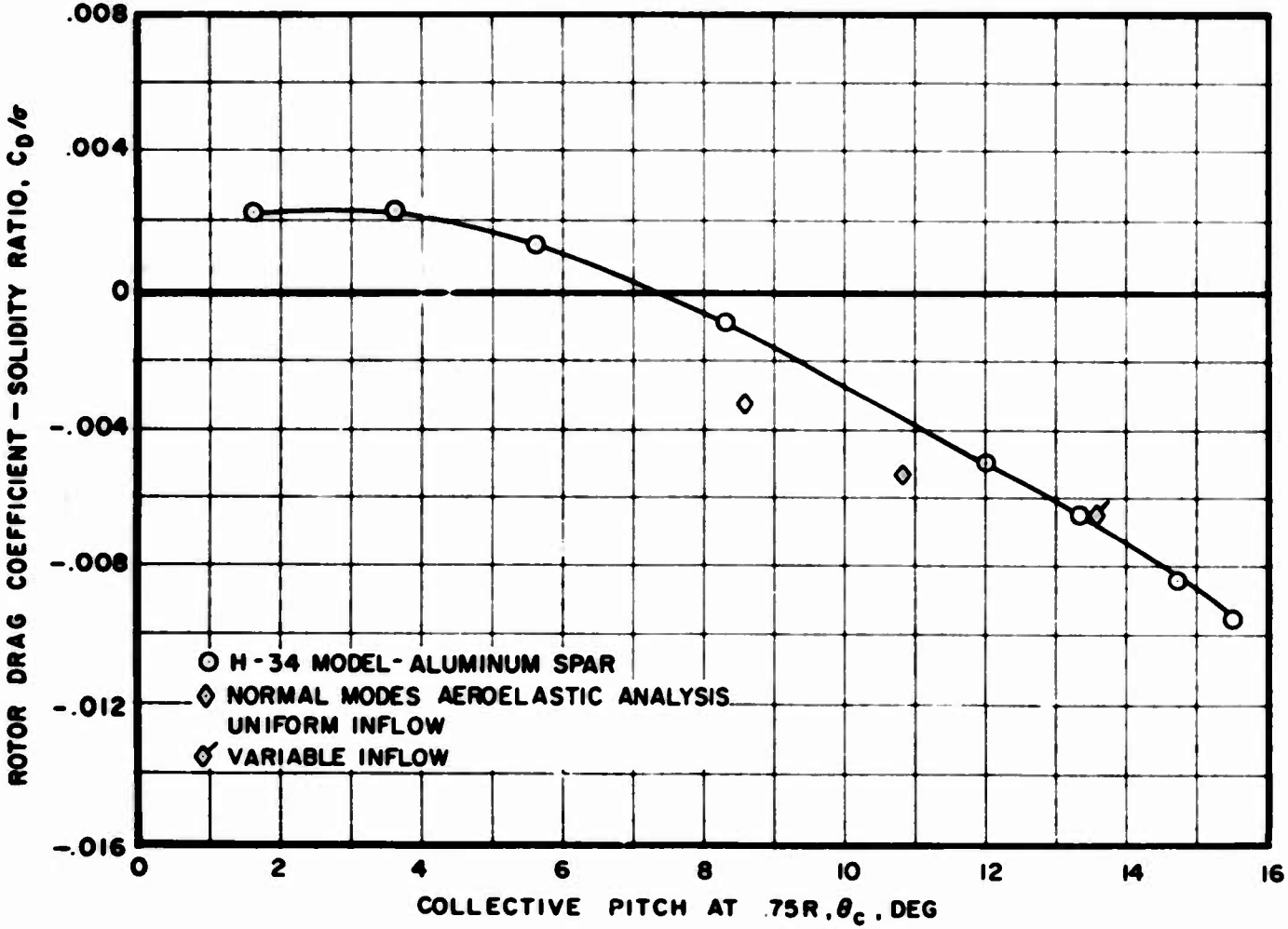

(b) Rotor Drag Coefficient - Solidity Ratio

Figure 32. Continued.

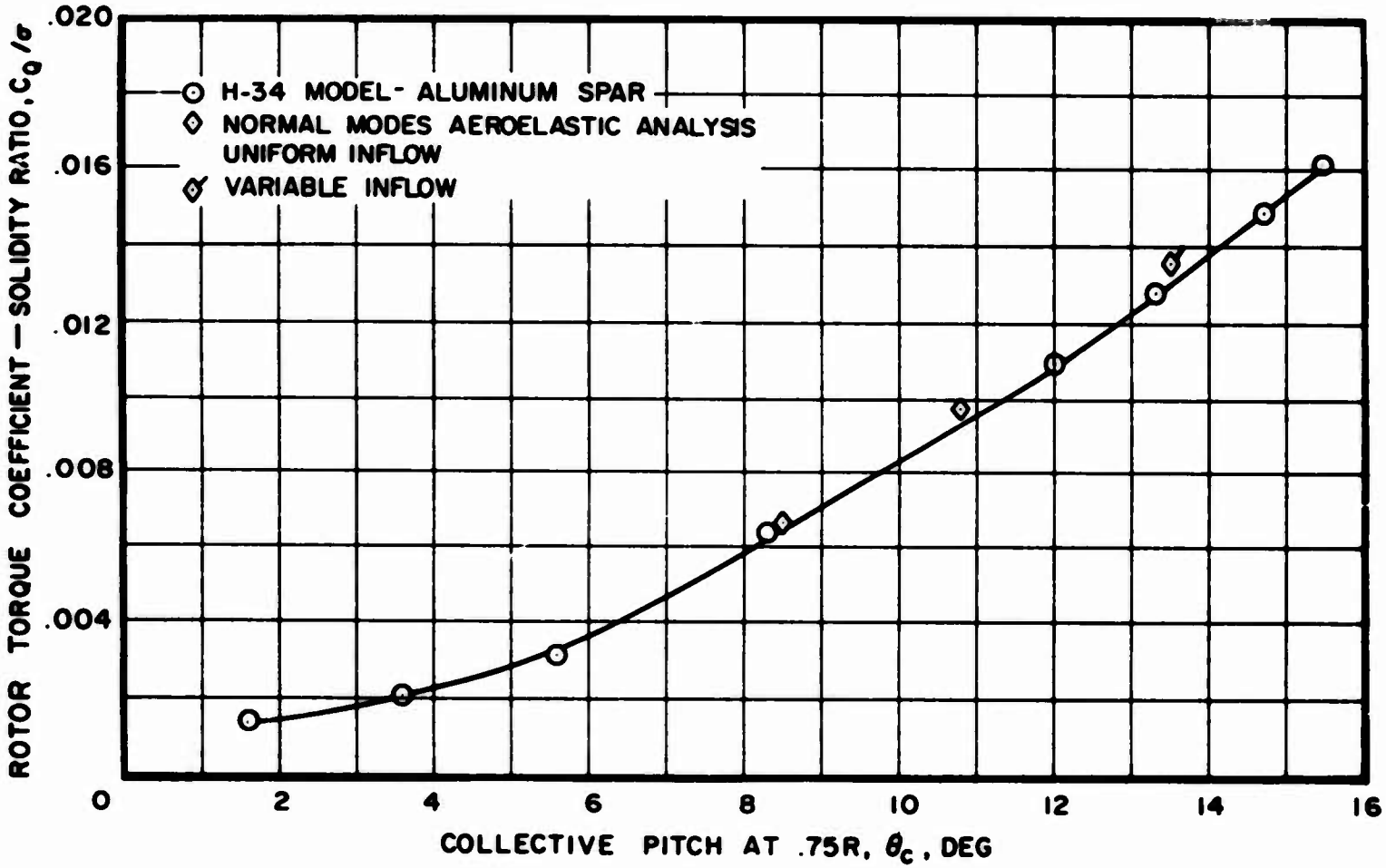

(c) Rotor Torque Coefficient - Solidity Ratio

Figure 32. Continued.

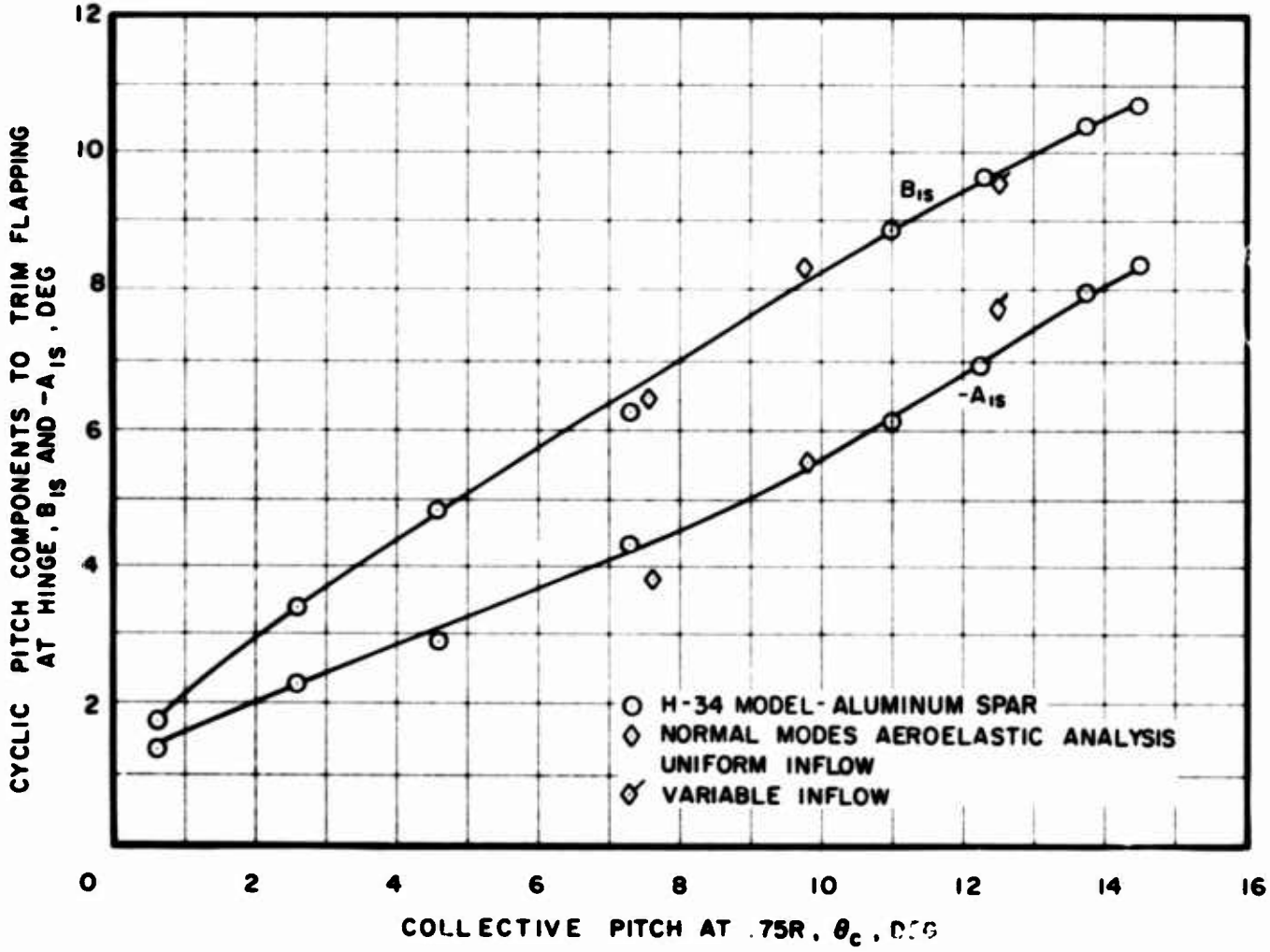

(d) Cyclic Pitch to Trim Flapping

Figure 32. Concluded.

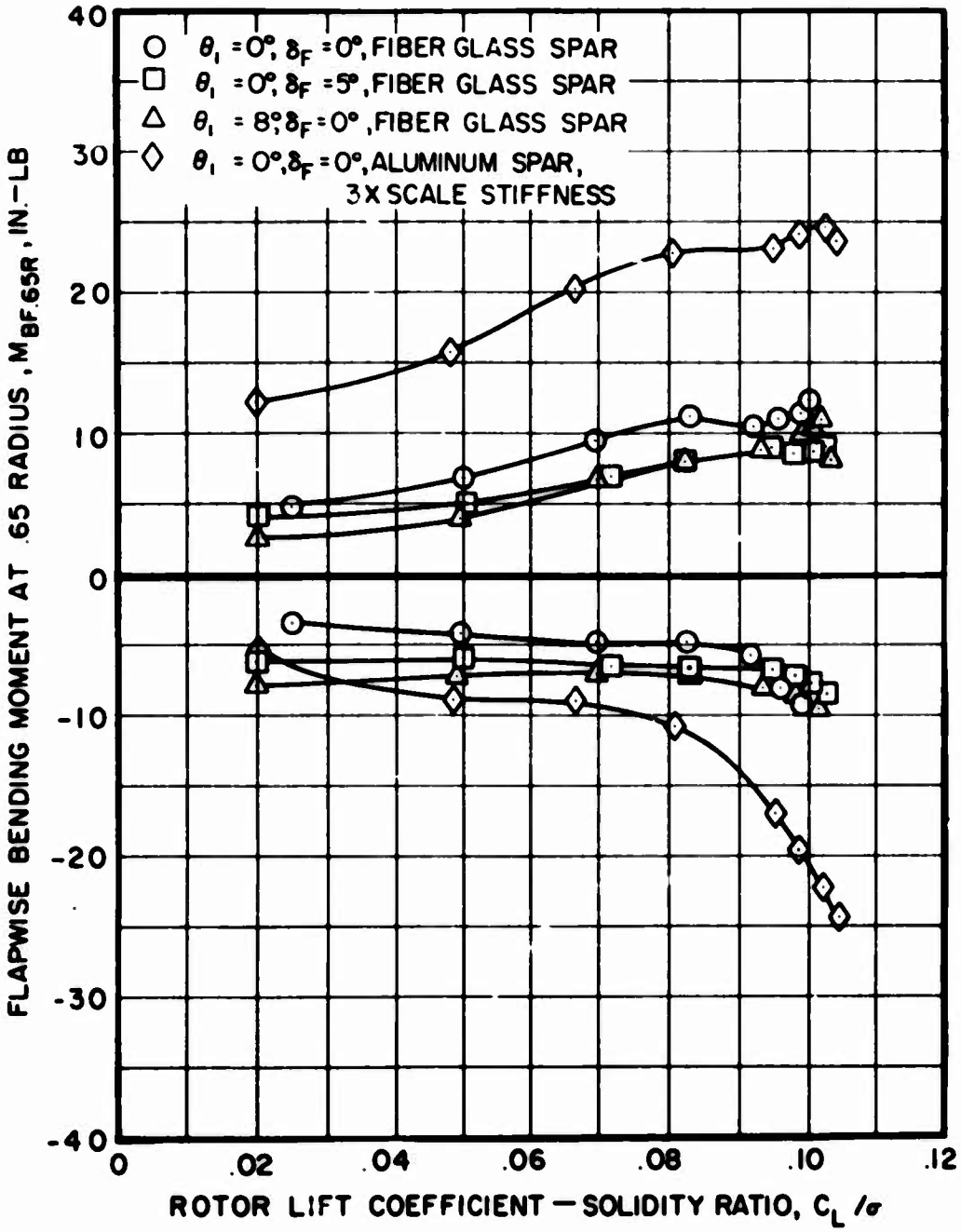

(a) Flapwise Bending Moment

Figure 33. Range of Blade Response vs. Lift Coefficient-Solidity Ratio for Model Blade Configurations; V_s = 124 kn, μ = 0.3, α_s = 0 deg, $a_{1s} = b_{1s}$ = 0 deg.

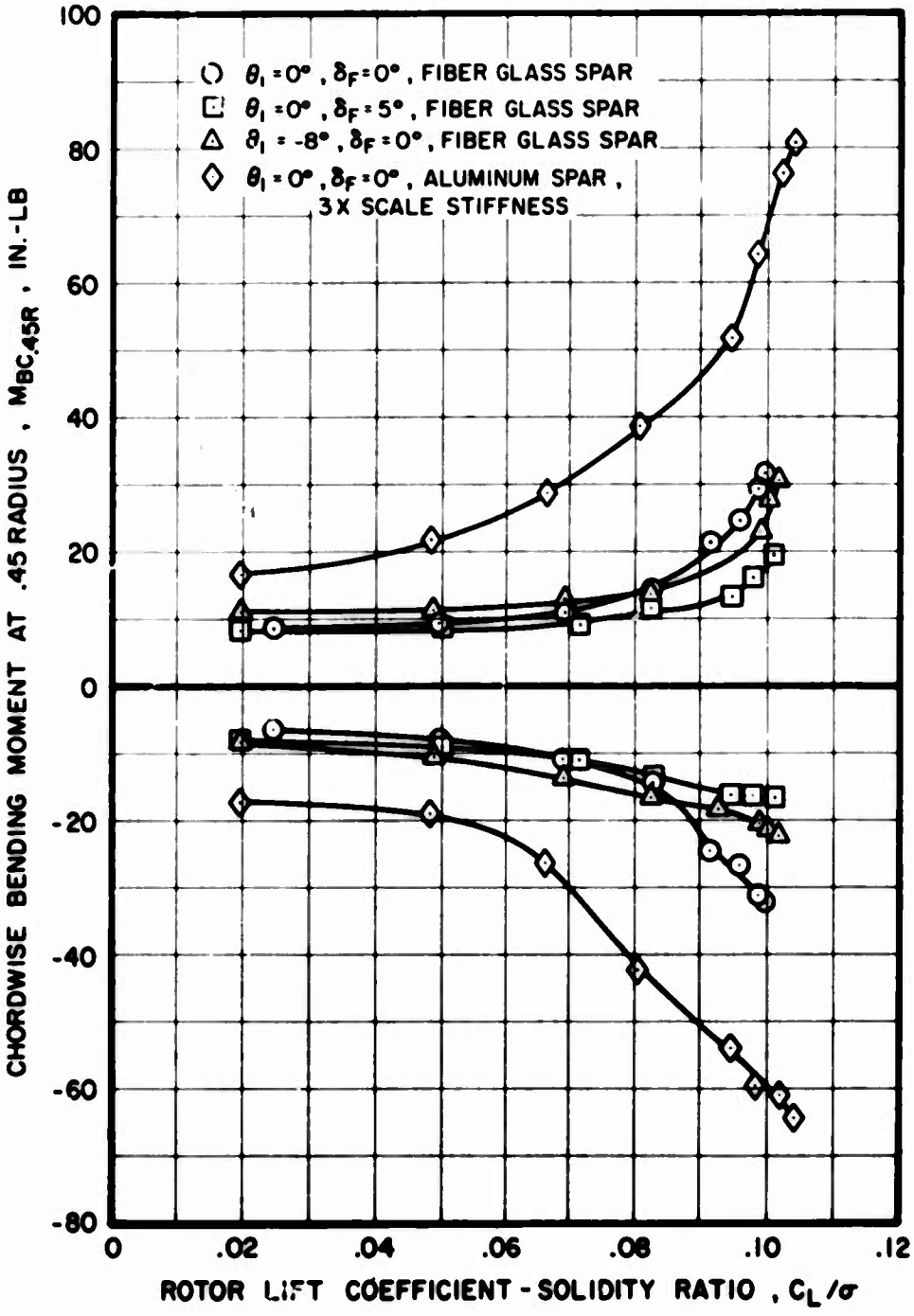

(b) Chordwise Bending Moment

Figure 33. Continued.

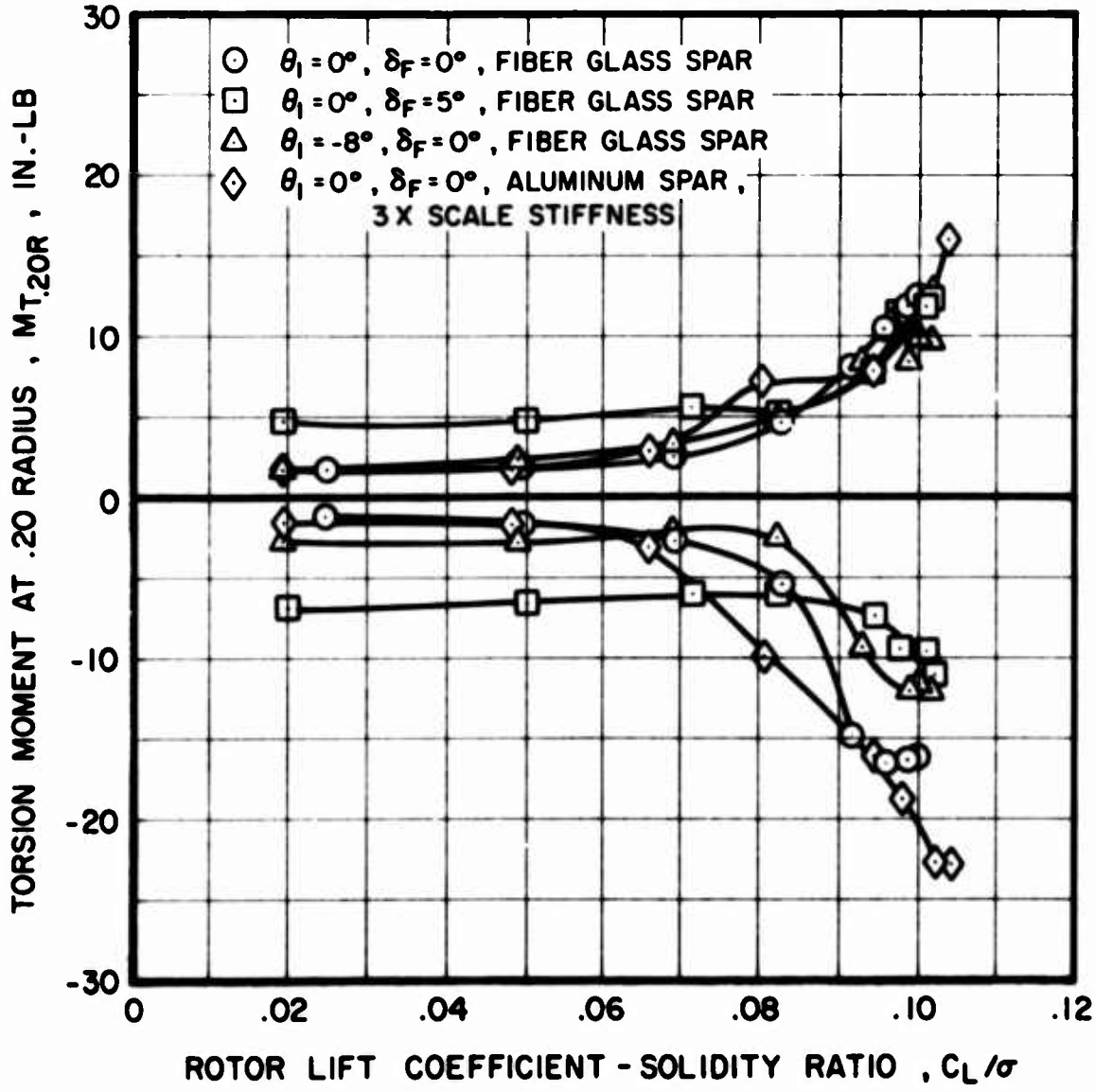

(c) Torsional Moment

Figure 33. Concluded.

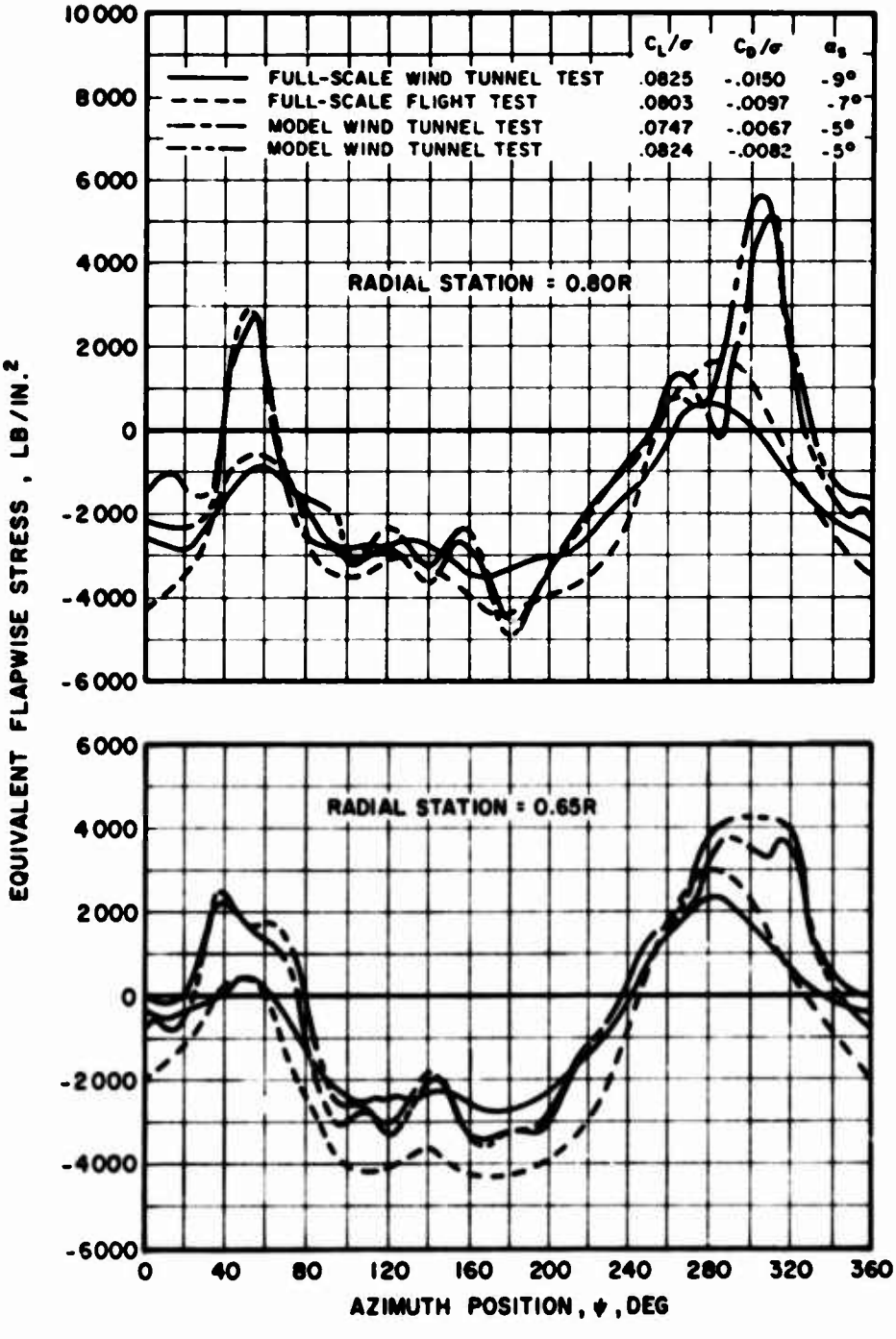

(a) Flapwise Stress

Figure 34. Comparison of Full-Scale Flight Test, Full-Scale Wind Tunnel Test, and Dynamically Scaled Model Test Blade Response Time History Data; V_s = 120 kn, μ = 0.3, θ_1 = -8 deg.

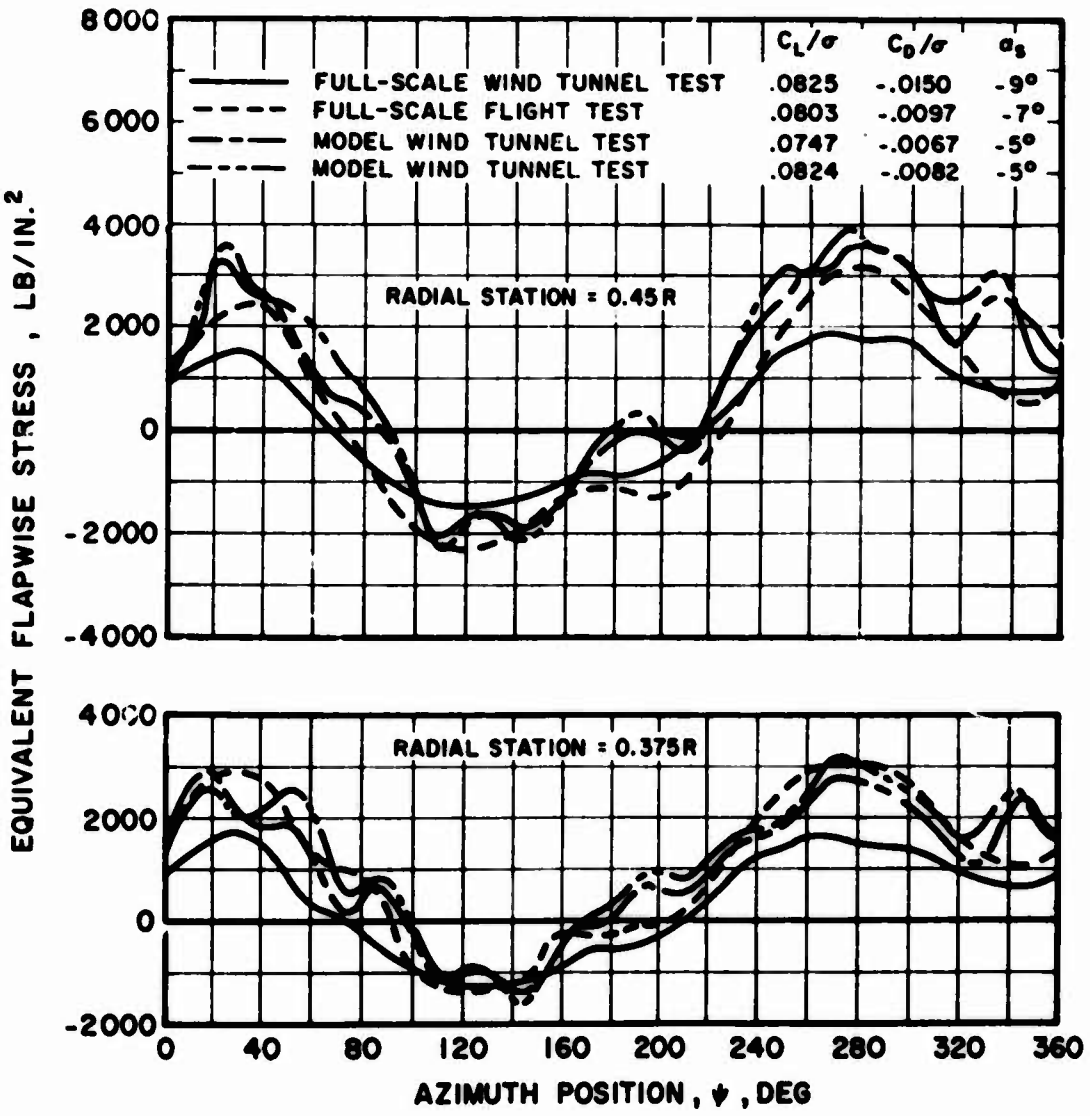

(a) CONTINUED.

Figure 34. Continued.

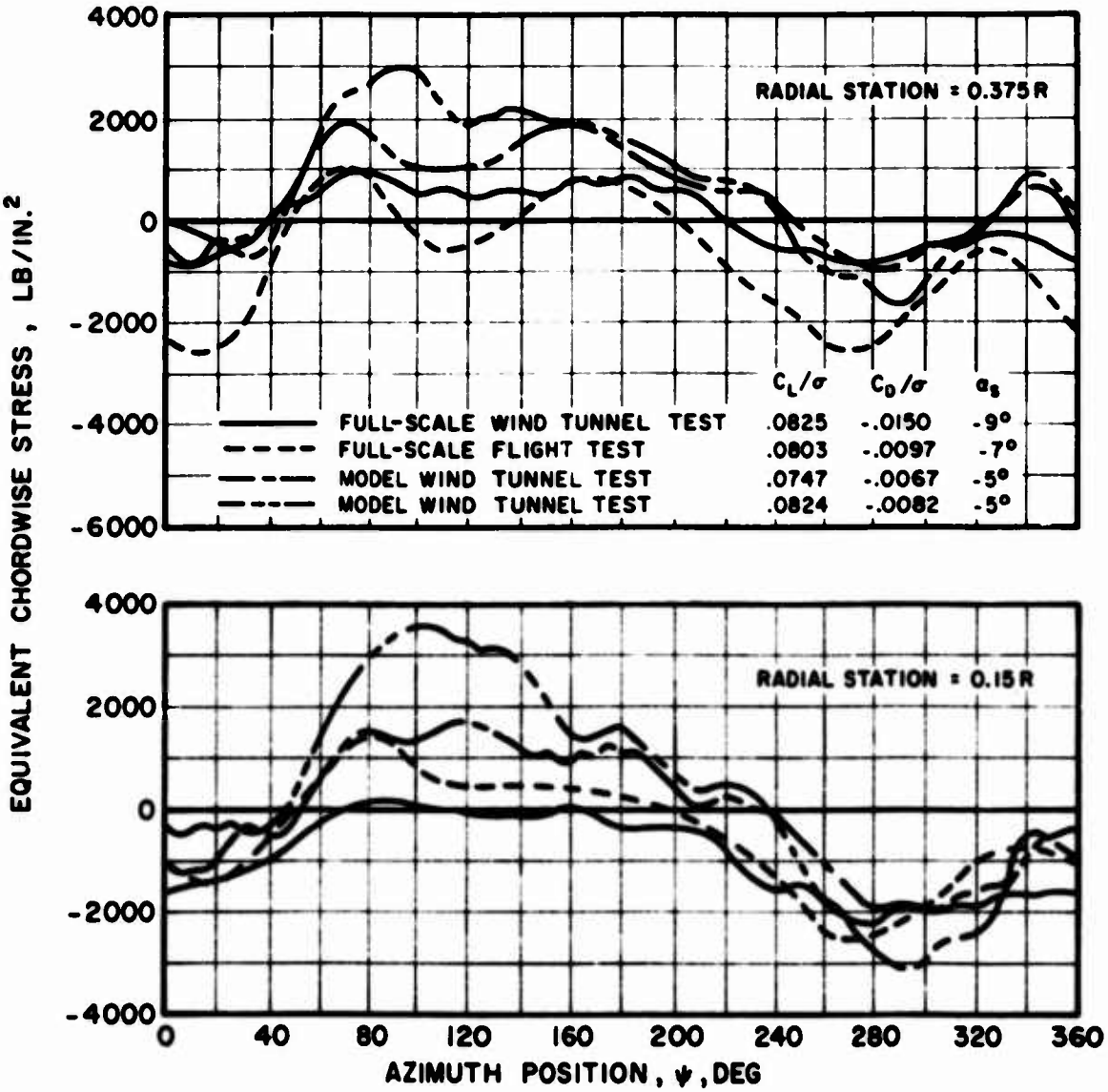

(b) Chordwise Stress

Figure 34. Continued.

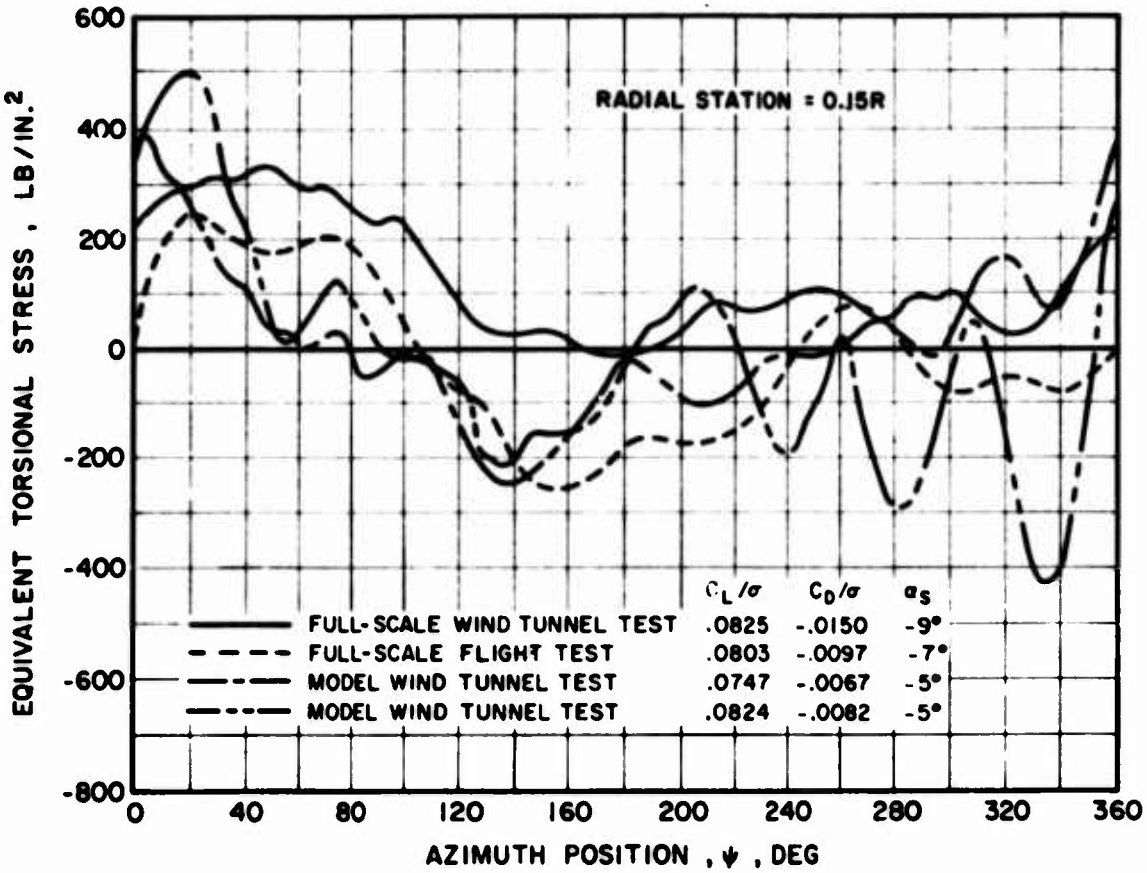

(c) Torsion Stress

Figure 34. Concluded.

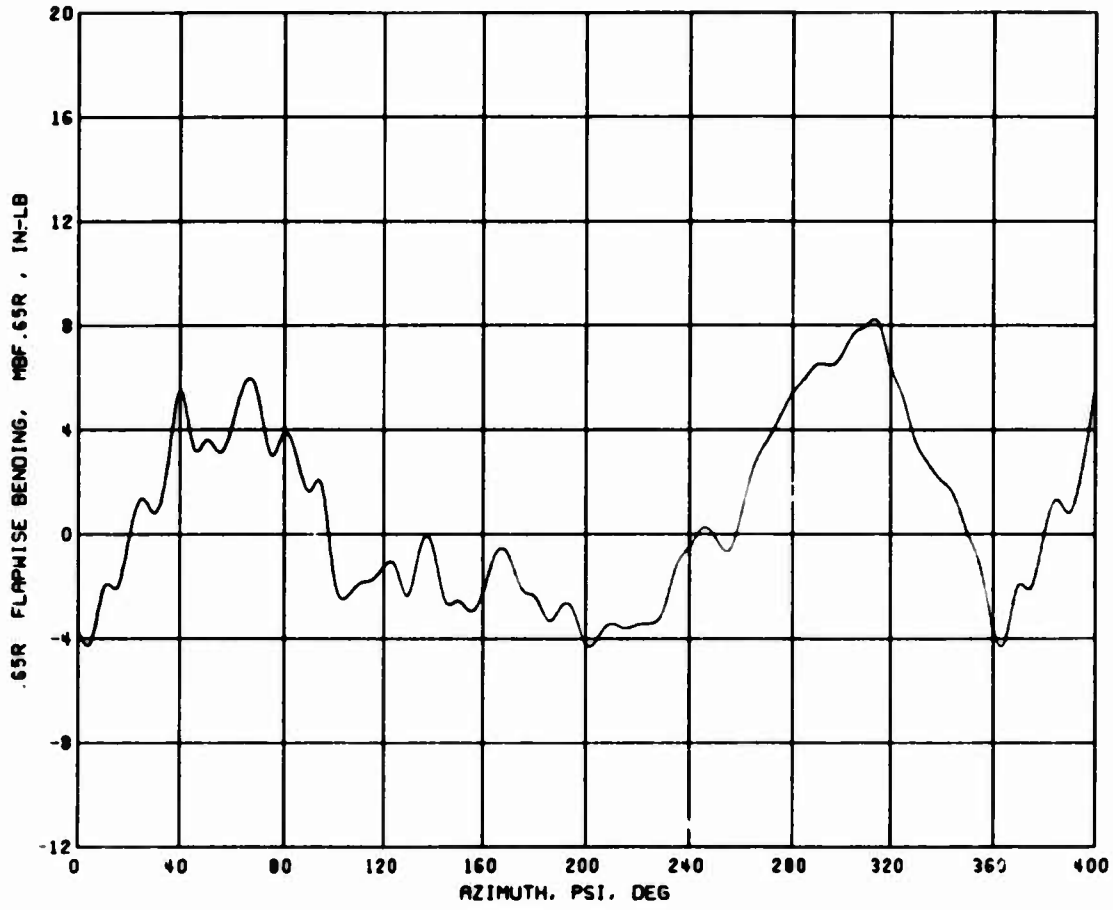

(a) Condition 34, $\mu = 0.352$, $C_L/\sigma = 0.0790$, $C_D/\sigma = 0.00222$

Figure 35. Average Revolution Time History Data; .65R Flapwise Bending, $\theta_1 = 0$ deg, $\delta_F = 0$ deg, $S_E = 1$.

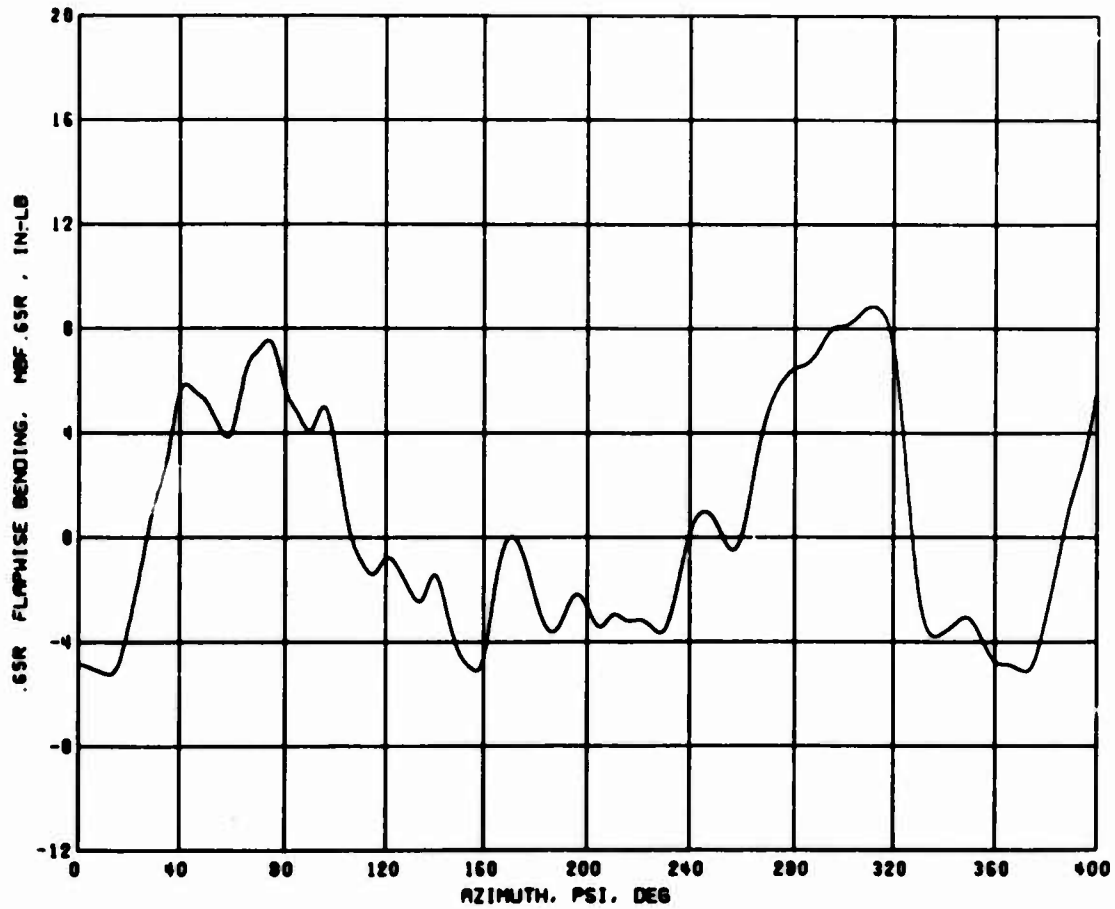

(b) Condition 25, $\mu = 0.40$, $C_L/\sigma = 0.0789$, $C_D/\sigma = -0.00113$

Figure 35. Continued.

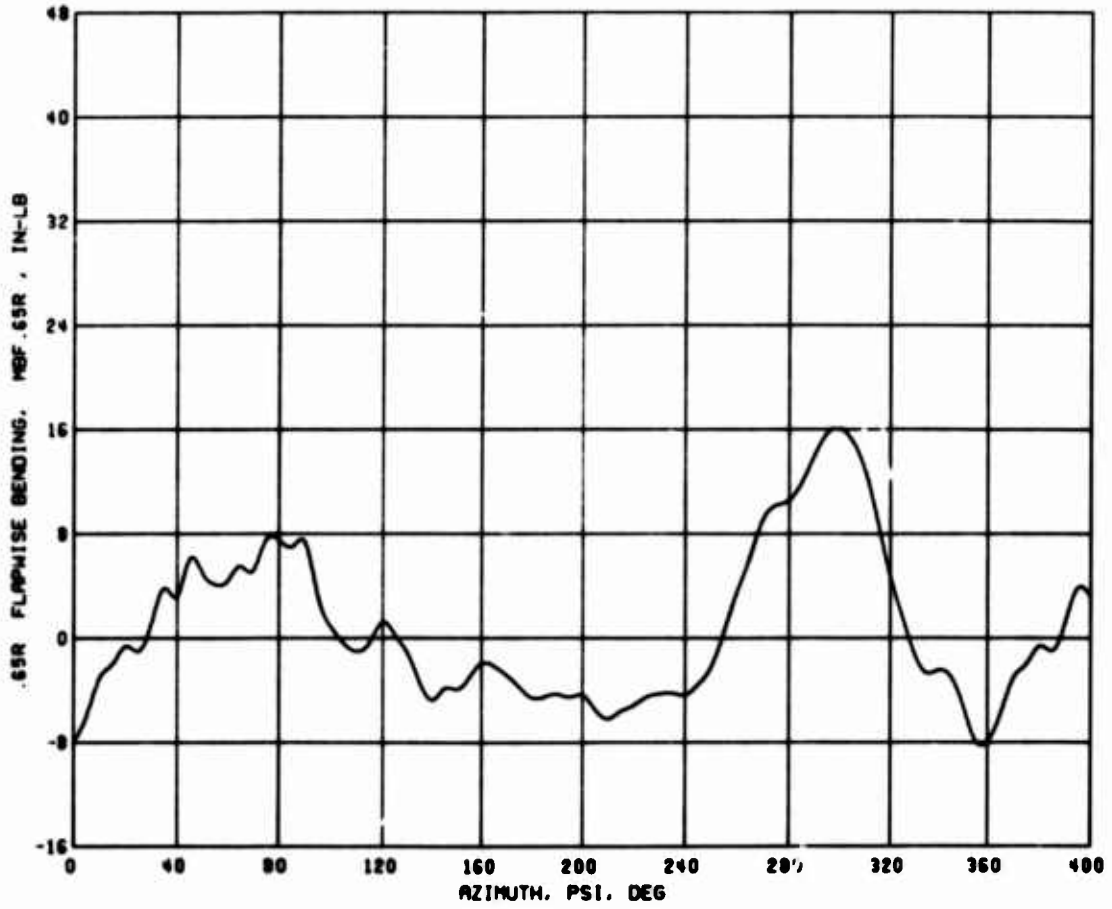

(c) Condition 49, $\mu = 0.50$, $C_L/\sigma = 0.0835$, $C_D/\sigma = 0.00445$

Figure 36. Concluded.

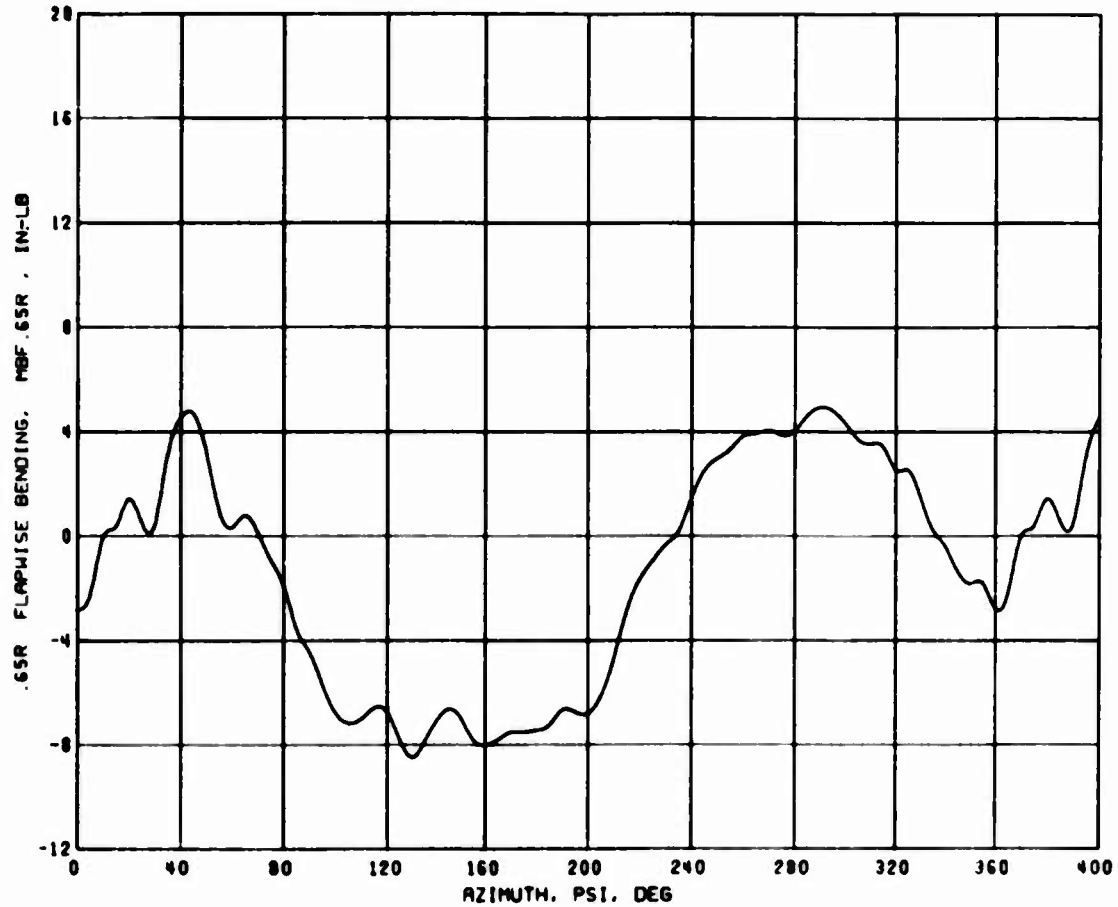

(a) Condition 34, $\mu = 0.352$, $C_L/\sigma = 0.0796$, $C_D/\sigma = 0.00328$

Figure 36. Average Revolution Time History Data; .65R Flapwise Bending, $\theta_1 = -8$ deg, $\delta_F = 0$ deg, $S_E = 1$.

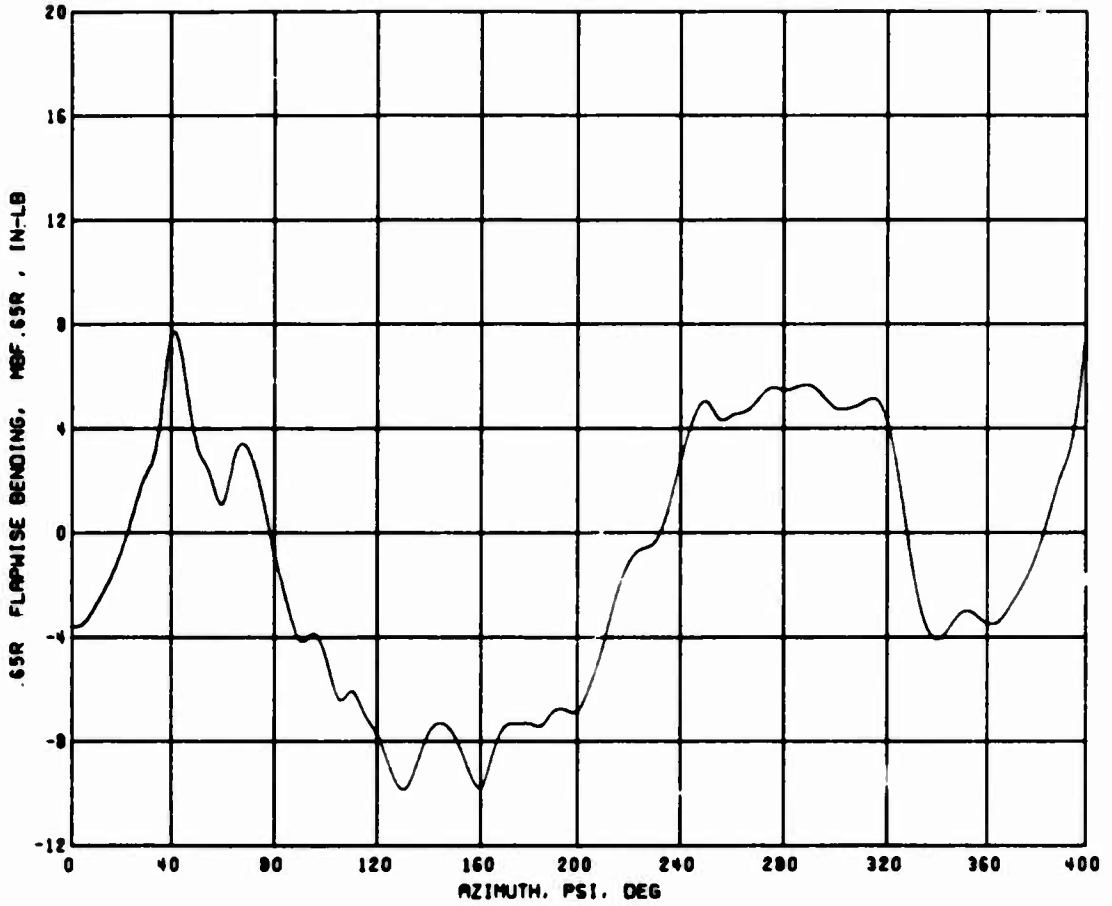

(b) Condition 25, $\mu = 0.399$, $C_L/\sigma = 0.0794$, $C_D/\sigma = -0.00096$

Figure 36. Continued.

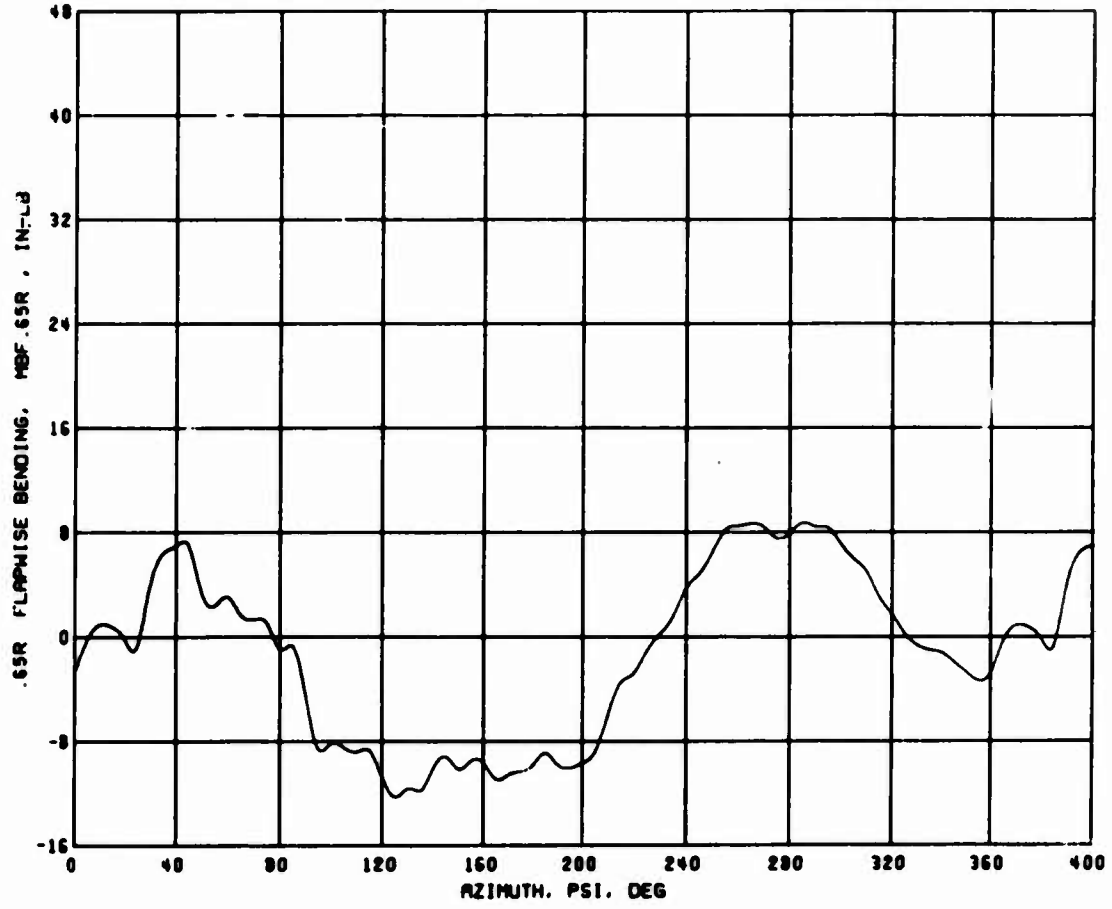

(c) Condition 49, $\mu = 0.502$, $C_L/\sigma = 0.0810$, $C_D/\sigma = 0.00433$

Figure 36. Concluded.

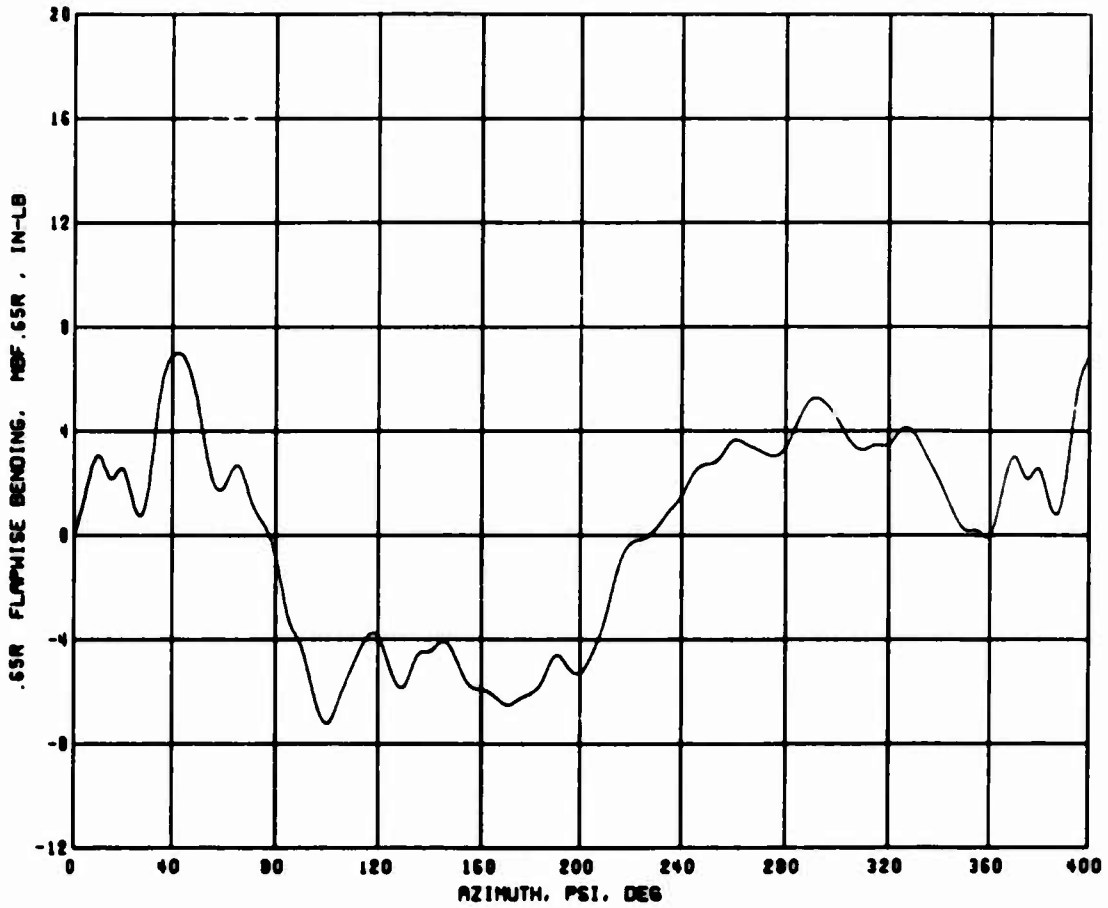

(a) Condition 34, $\mu = 0.352$, $C_L/\sigma = 0.0795$, $C_D/\sigma = 0.00131$

Figure 37. Average Revolution Time History Data; .65R Flapwise Bending, $\theta_1 = 0$ deg, $\delta_F = 5$ deg, $S_E = 1$.

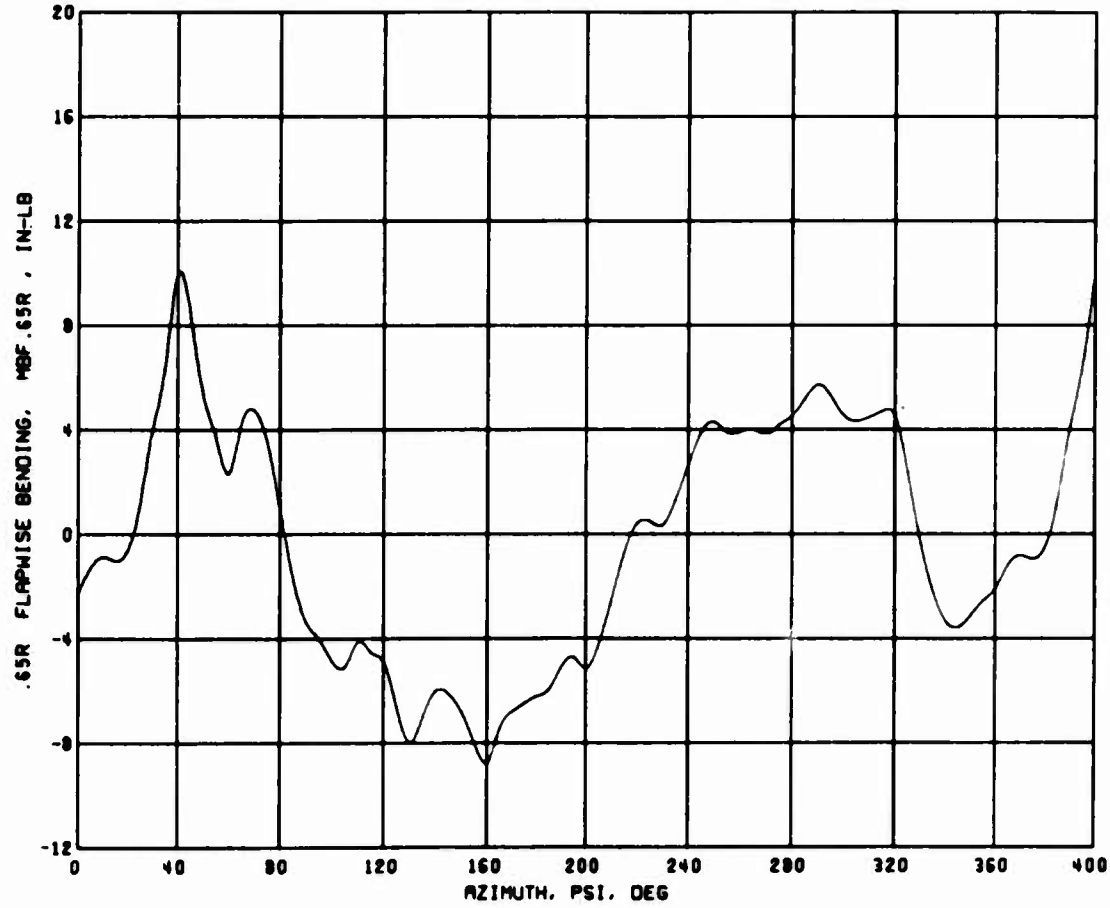

(b) Condition 25, $\mu = 0.399$, $C_L/\sigma = 0.0824$, $C_D/\sigma = -0.00142$

Figure 37. Continued.

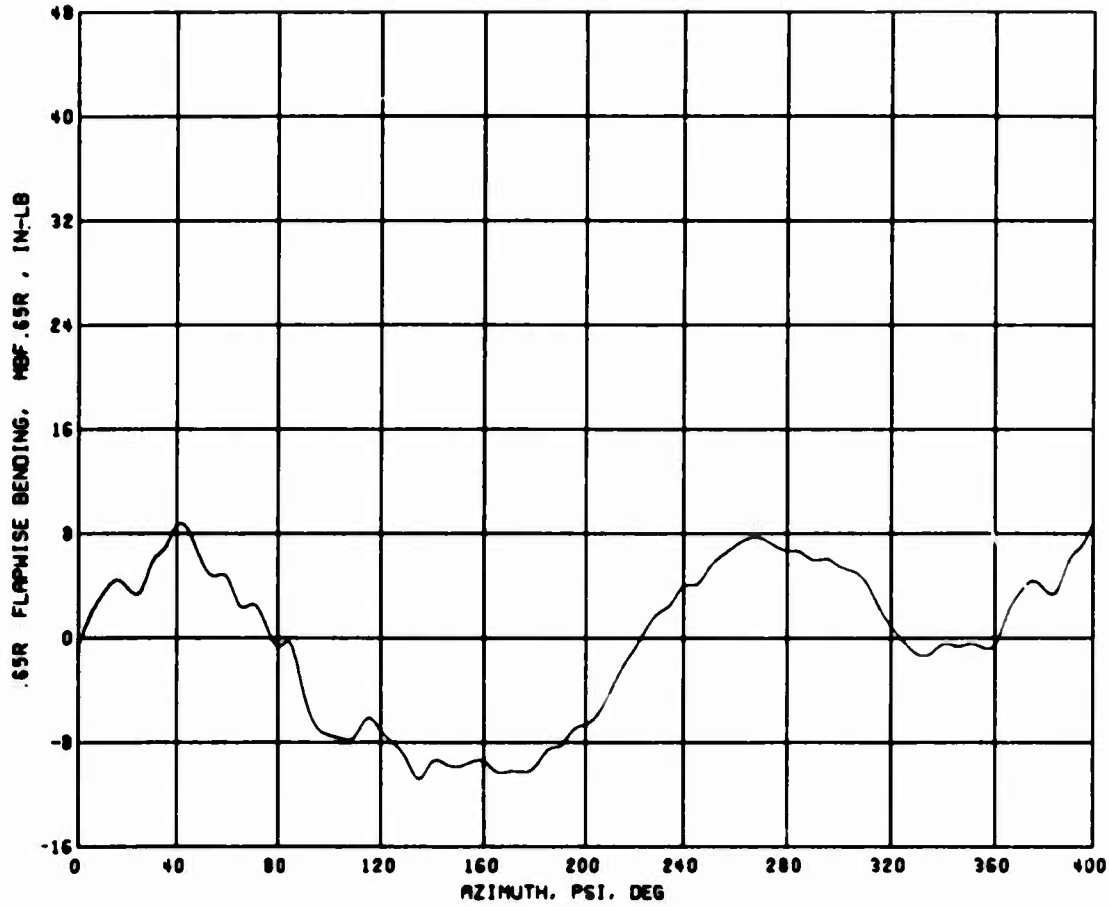

(c) Condition 49, $\mu = 0.502$, $C_L/\sigma = 0.0826$, $C_D/\sigma = 0.00545$

Figure 37. Concluded.

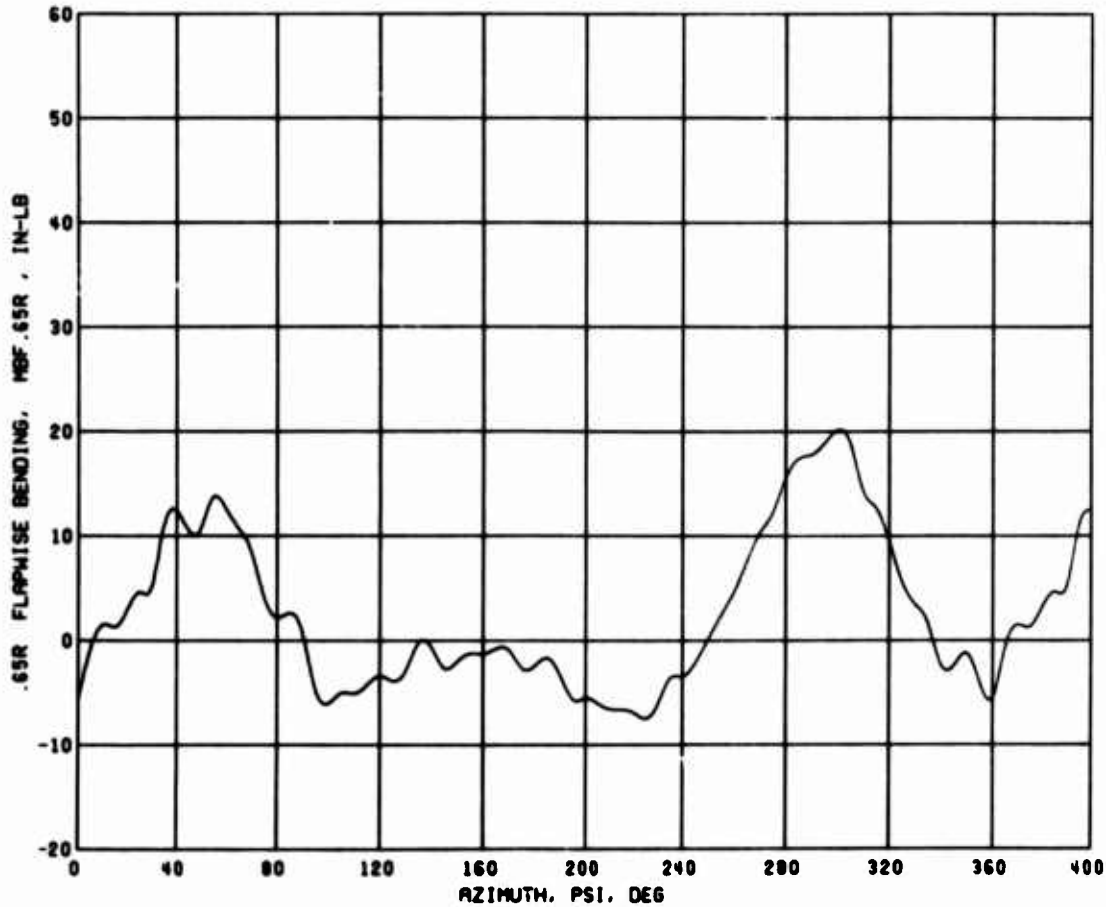

(a) Condition 34, $\mu = 0.352$, $C_L/\sigma = 0.0775$, $C_D/\sigma = 0.00157$

Figure 38. Average Revolution Time History Data; .65R Flapwise Bending, $\theta_1 = 0$ deg, $\delta_F = 0$ deg, $S_E = 3$.

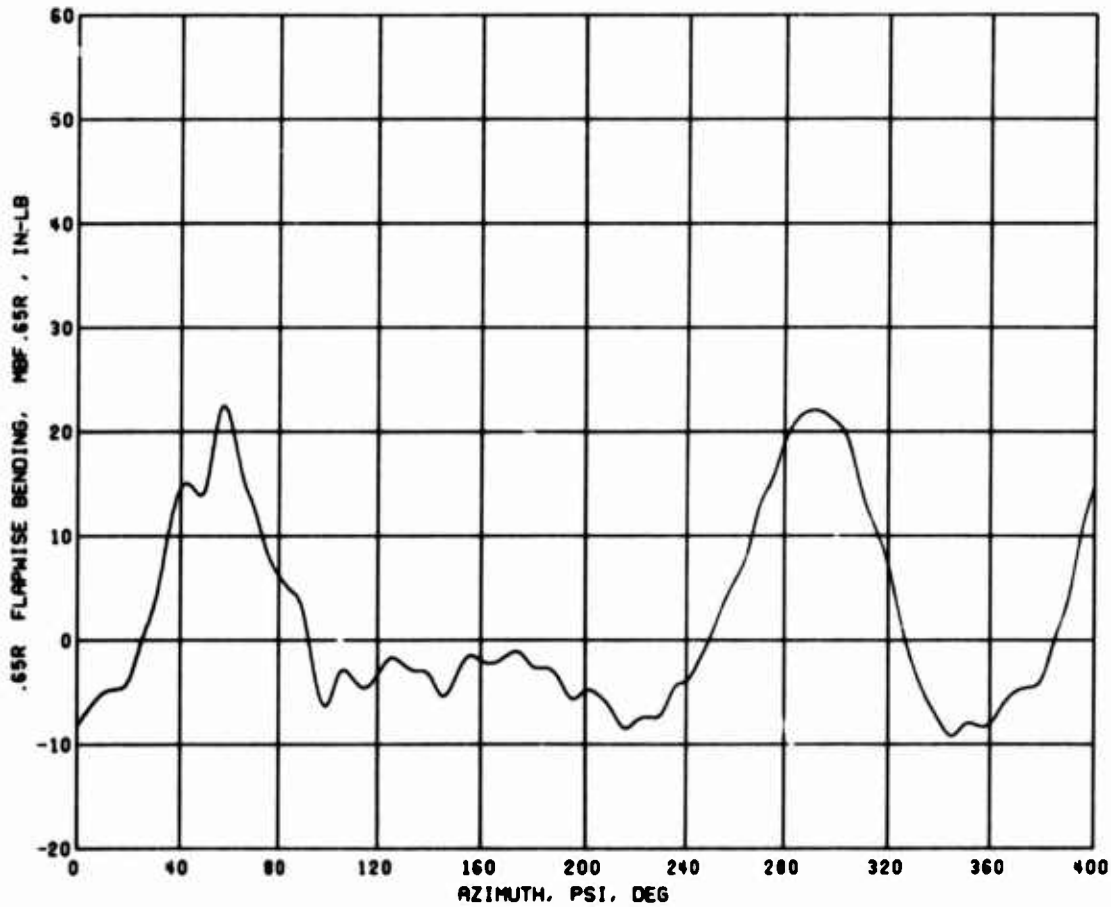

(b) Condition 25, μ = 0.399, C_L/σ = 0.0752, C_D/σ = -0.00153

Figure 38. Continued.

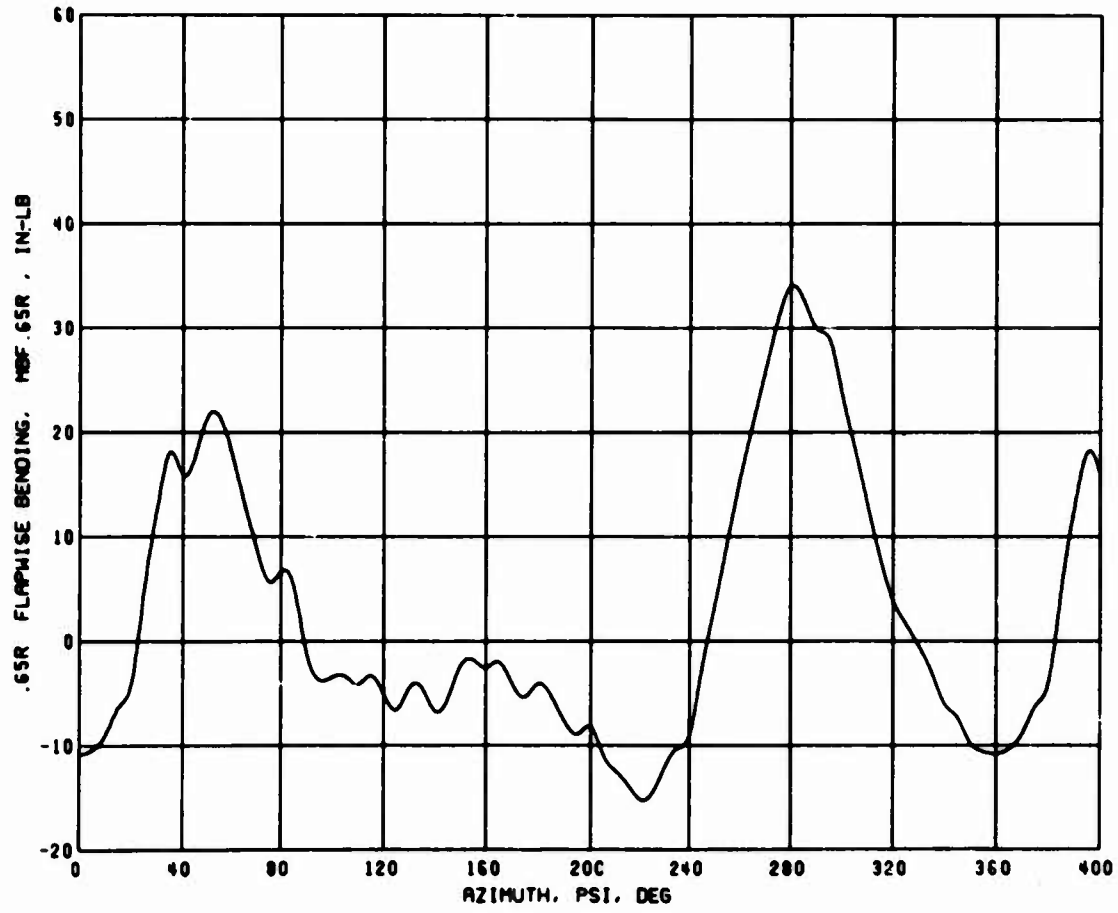

(c) Condition 49, $\mu = 0.502$, $C_L/\sigma = 0.0822$, $C_D/\sigma = 0.00474$

Figure 38. Concluded.

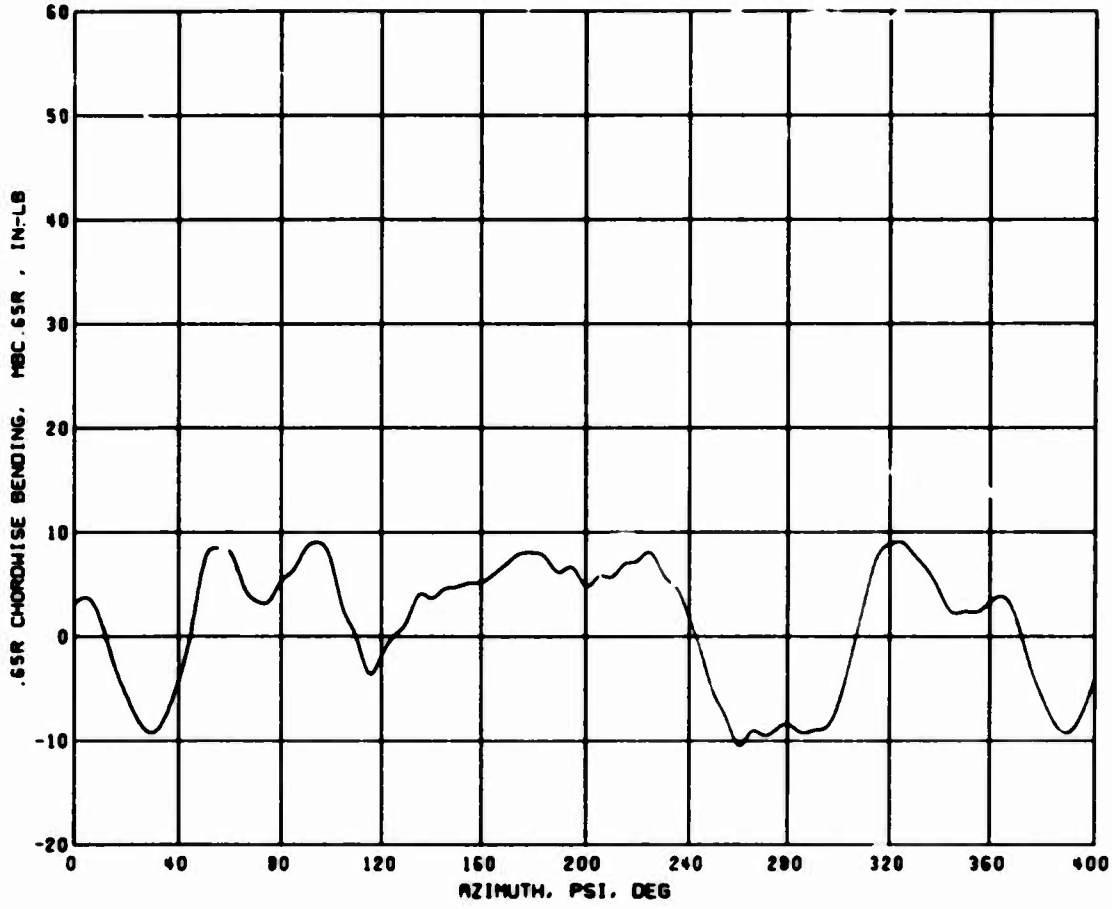

(a) Condition 34, $\mu = 0.352$, $C_L/\sigma = 0.0790$, $C_D/\sigma = 0.00222$

Figure 39. Average Revolution Time History Data; .65R Chordwise Bending, $\theta_1 = 0$ deg, $\delta_F = 0$ deg, $S_E = 1$.

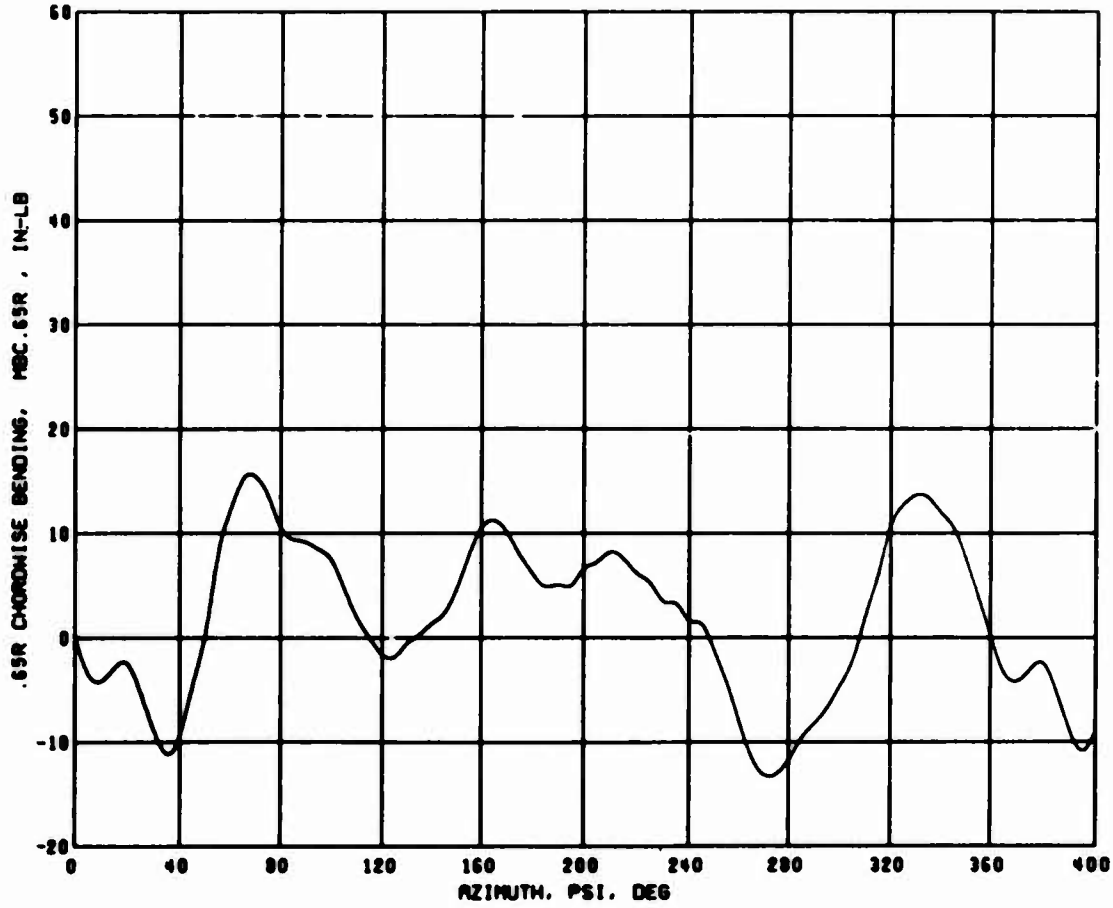

(b) Condition 25, $\mu = 0.40$, $C_L/\sigma = 0.0789$, $C_D/\sigma = -0.00113$

Figure 39. Continued.

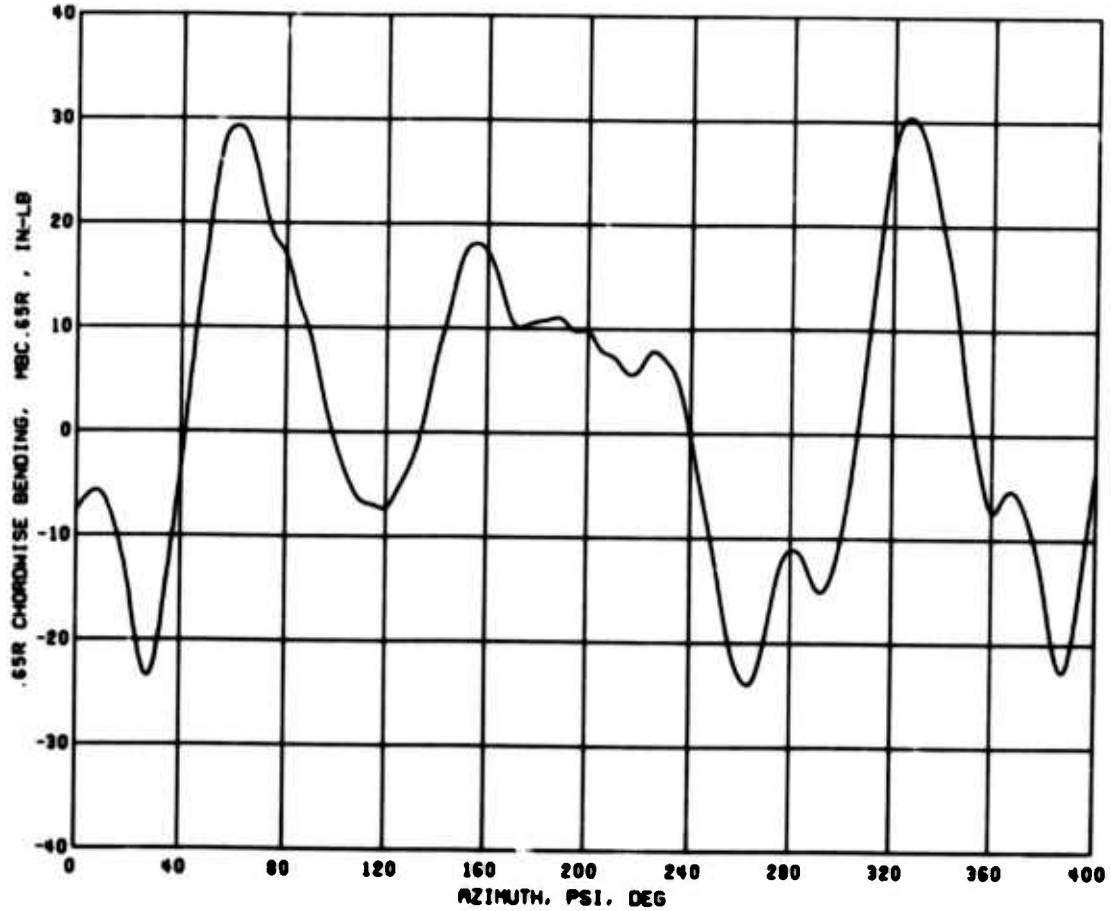

(c) Condition 49, $\mu = 0.50$, $C_L/\sigma = 0.0835$, $C_D/\sigma = 0.00445$

Figure 39. Concluded.

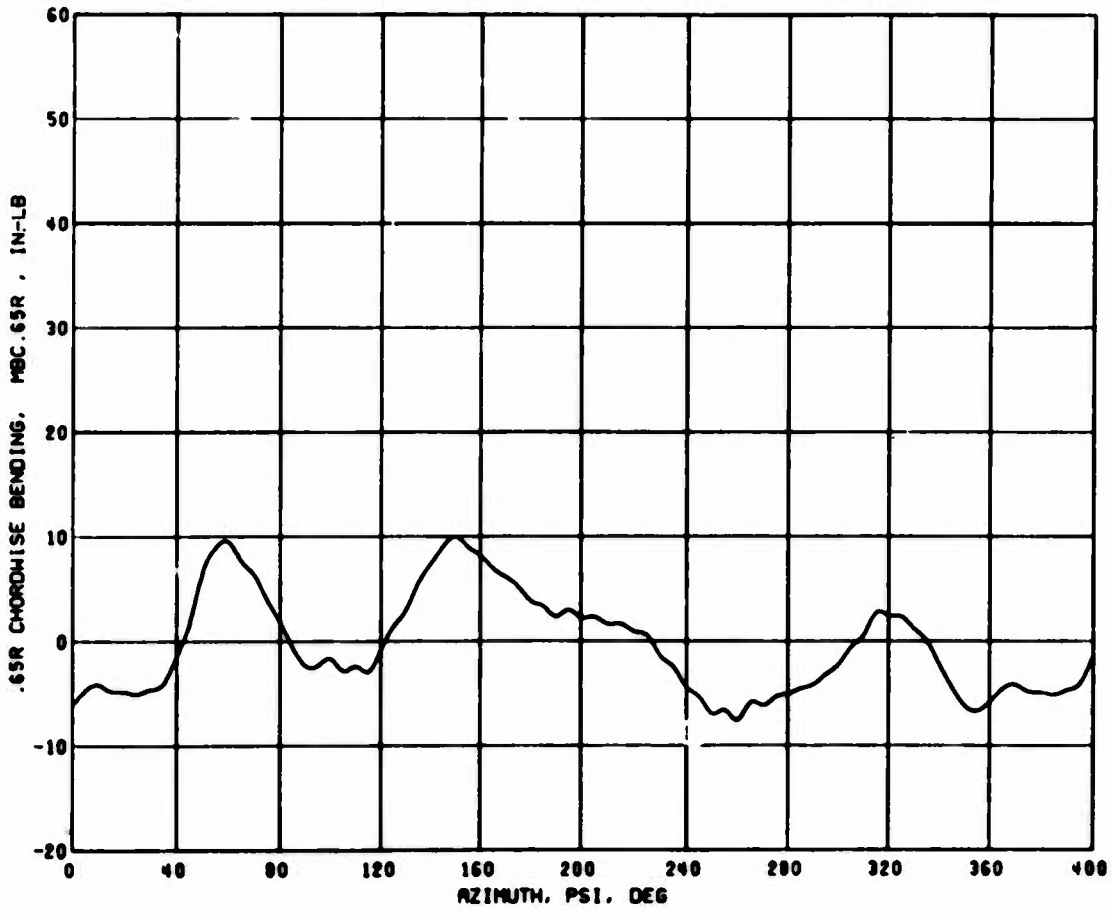

(a) Condition 34, $\mu = 0.352$, $C_L/\sigma = 0.0796$, $C_D/\sigma = 0.00328$

Figure 40. Average Revolution Time History Data; .65R Chordwise Bending, $\theta_1 = -8$ deg, $\delta_F = 0$ deg, $S_E = 1$.

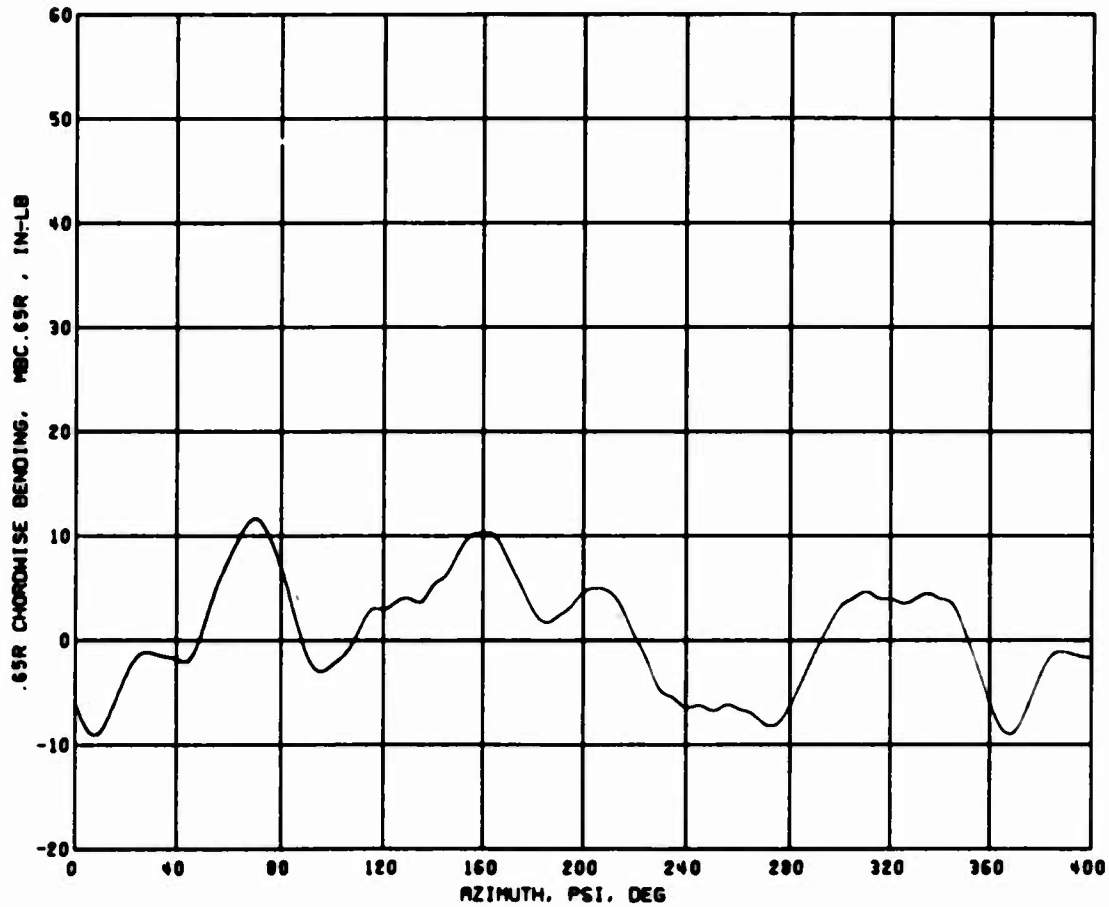

(b) Condition 25, $\mu = 0.399$, $C_L/\sigma = 0.0794$, $C_D/\sigma = -0.00096$

Figure 40. Continued.

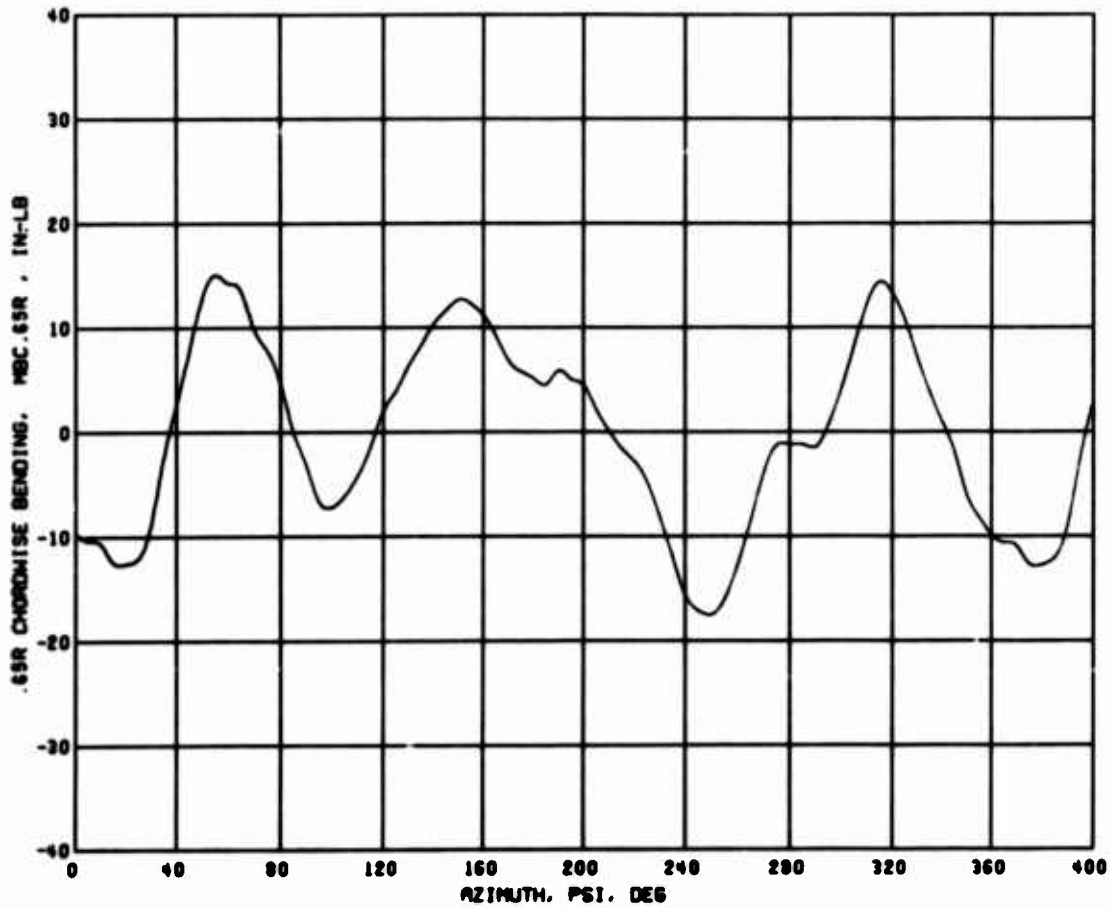

(c) Condition 49, $\mu = 0.502$, $C_L/\sigma = 0.0810$, $C_D/\sigma = 0.00433$

Figure 40. Concluded.

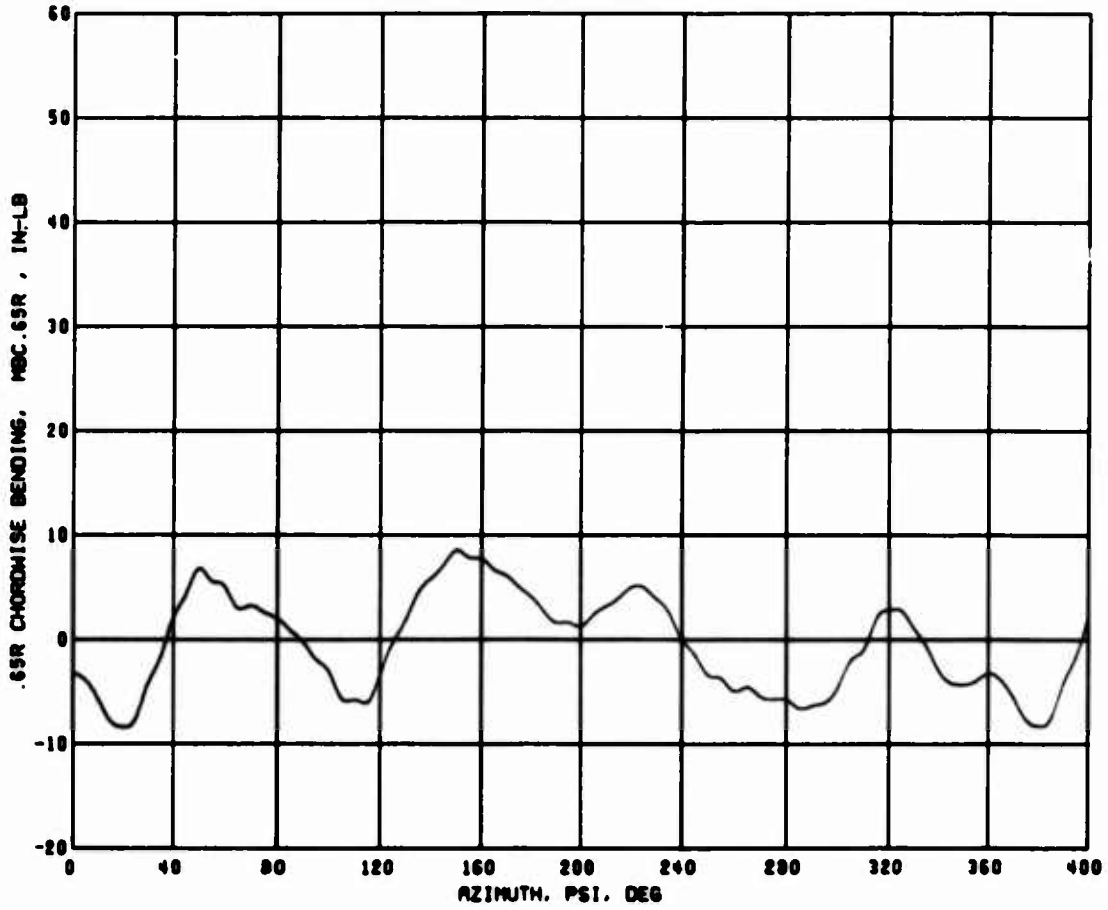

(a) Condition 34, $\mu = 0.352$, $C_L/\sigma = 0.0795$, $C_D/\sigma = 0.00131$

Figure 41. Average Revolution Time History Data; .65R Chordwise Bending, $\theta_1 = 0$ deg, $\delta_F = 5$ deg, $S_E = 1$.

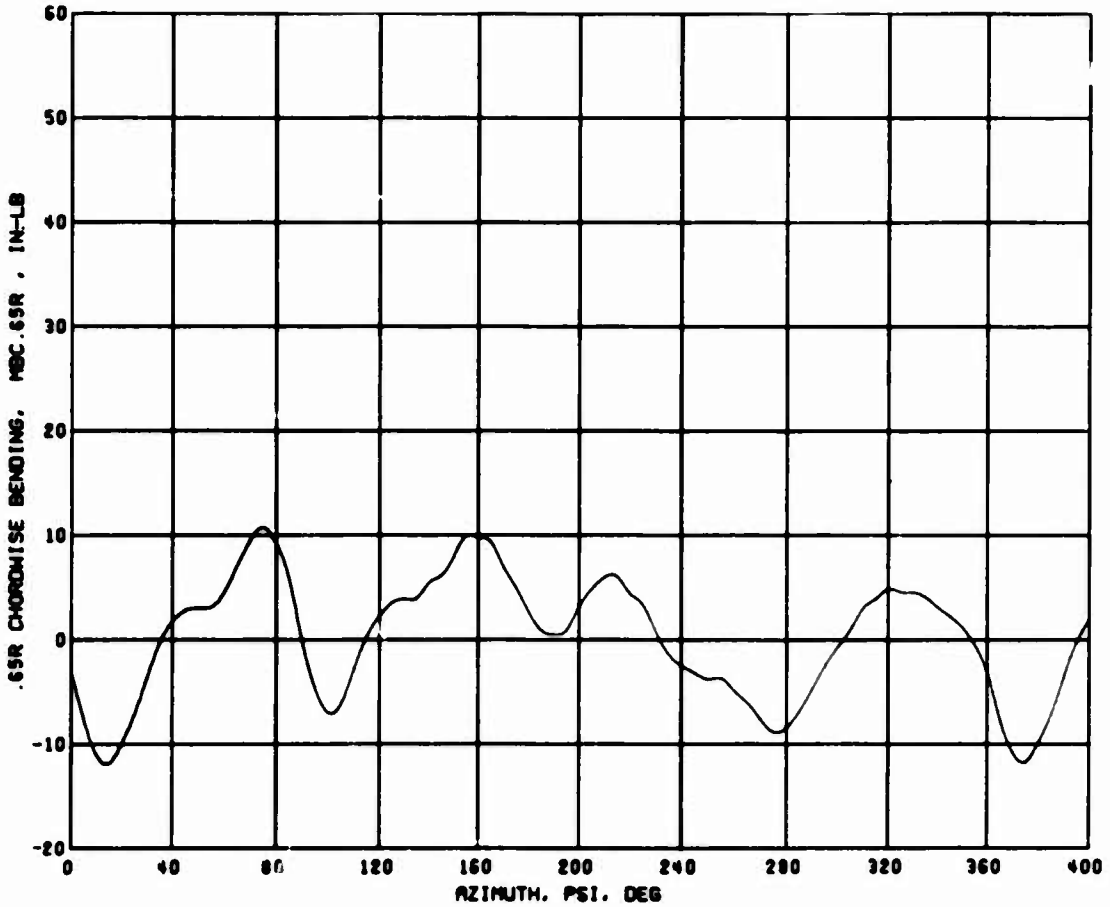

(b) Condition 25, $\mu = 0.399$, $C_L/\sigma = 0.0824$, $C_D/\sigma = -0.00142$

Figure 41. Continued.

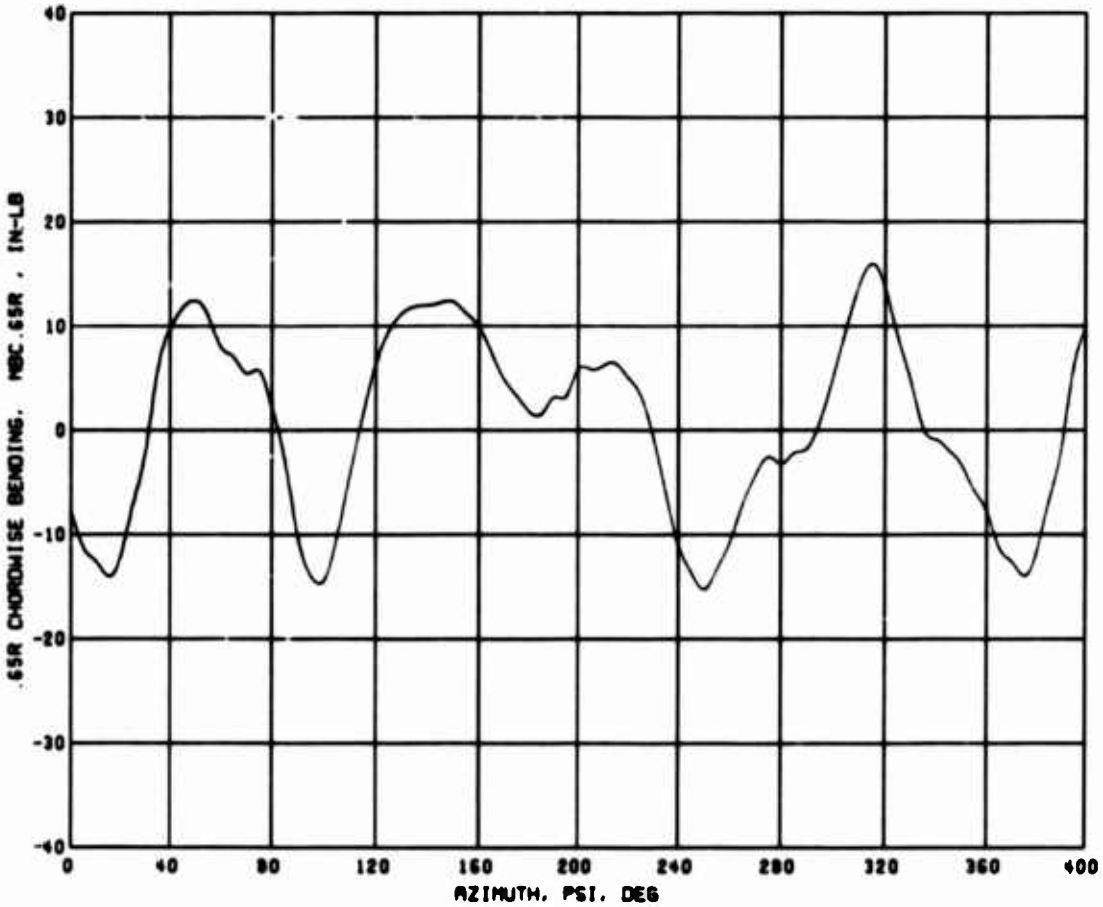

(c) Condition 49, $\mu = 0.502$, $C_L/\sigma = 0.0826$, $C_D/\sigma = 0.00545$

Figure 41. Concluded.

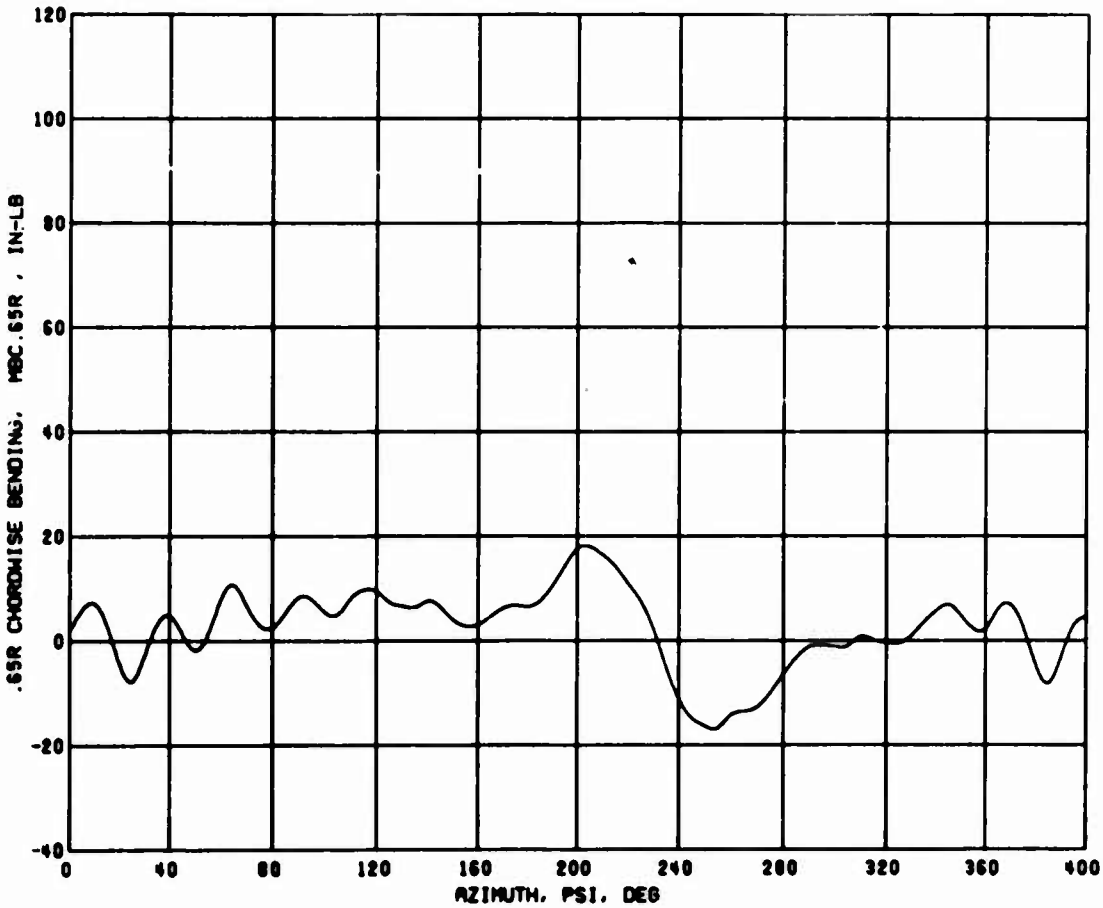

(a) Condition 34, $\mu = 0.352$, $C_L/\sigma = 0.0775$, $C_D/\sigma = 0.00157$

Figure 42. Average Revolution Time History Data; .65R Chordwise Bending, $\theta_1 = 0$ deg, $\delta_F = 0$ deg, $S_E = 3$.

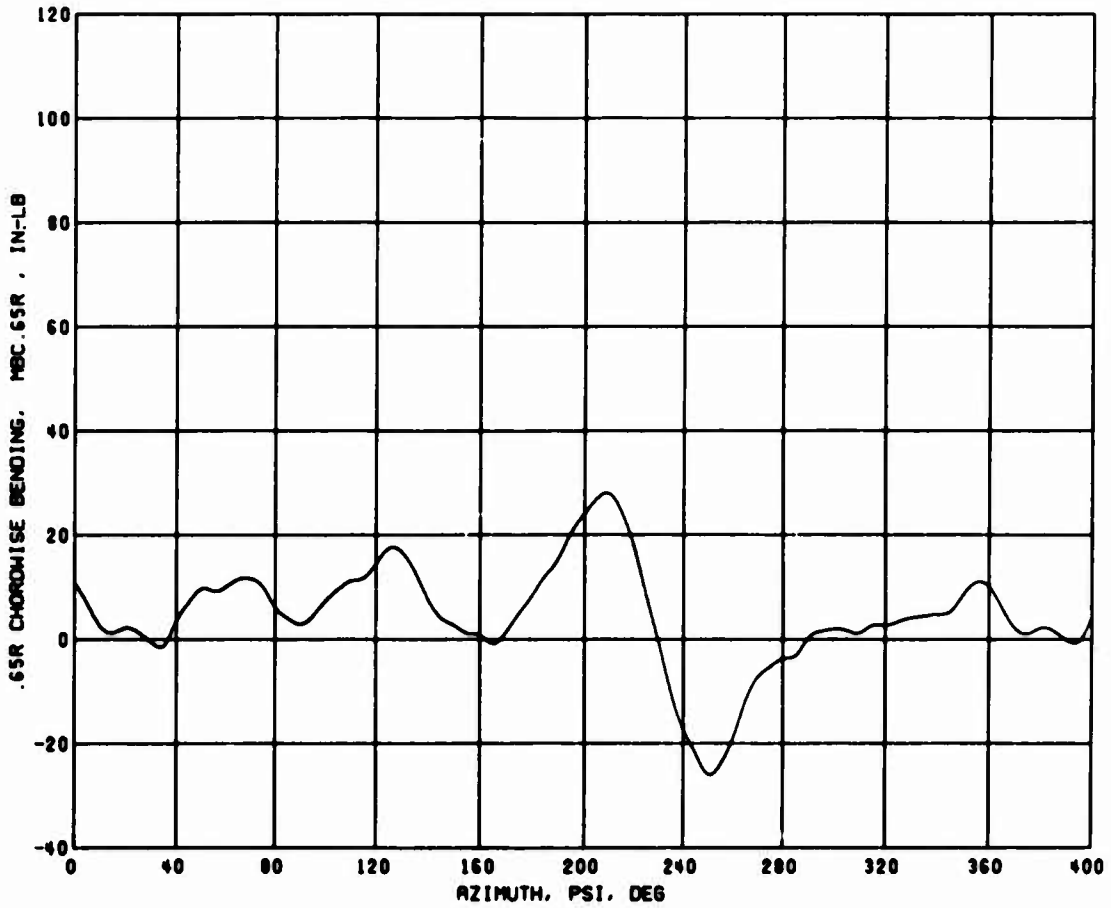

(b) Condition 25, $\mu = 0.399$, $C_L/\sigma = 0.0752$, $C_D/\sigma = -0.00153$

Figure 42. Continued.

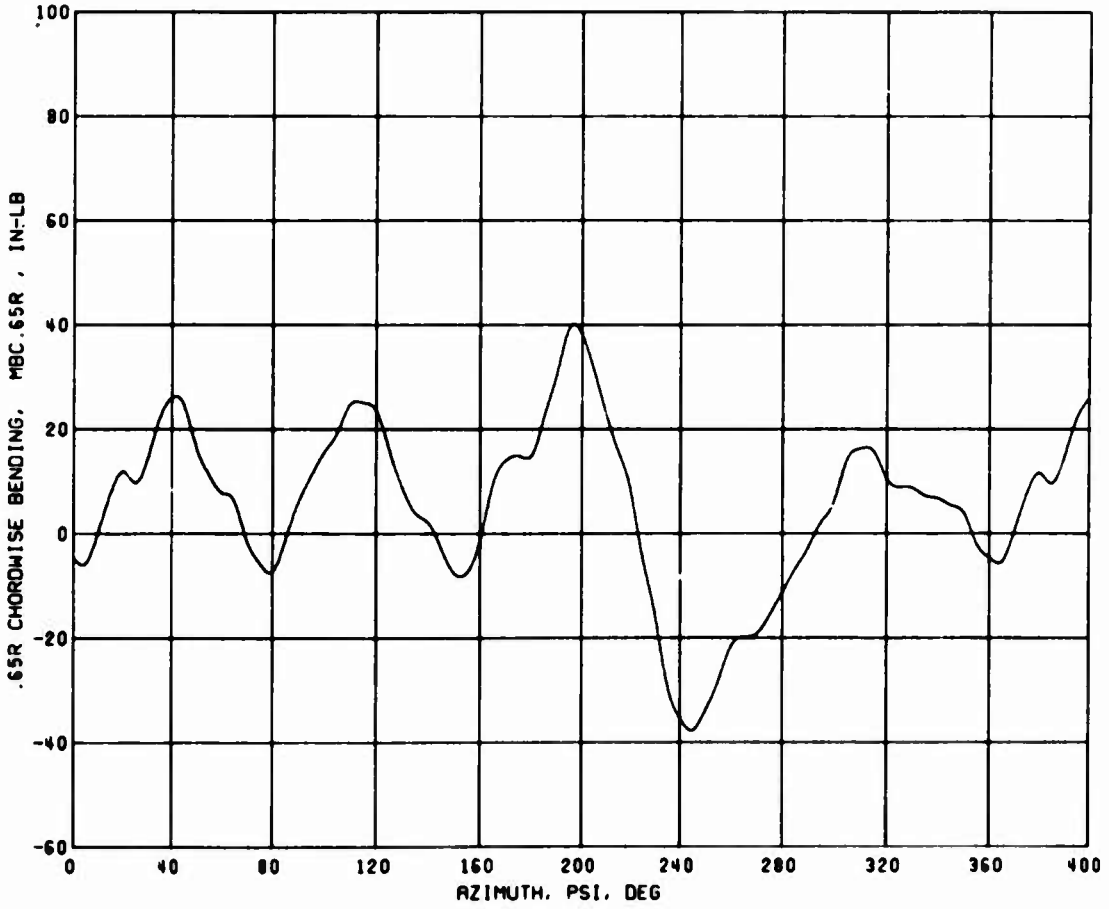

(c) Condition 49, $\mu = 0.502$, $C_L/\sigma = 0.0822$, $C_D/\sigma = 0.00474$

Figure 42. Concluded.

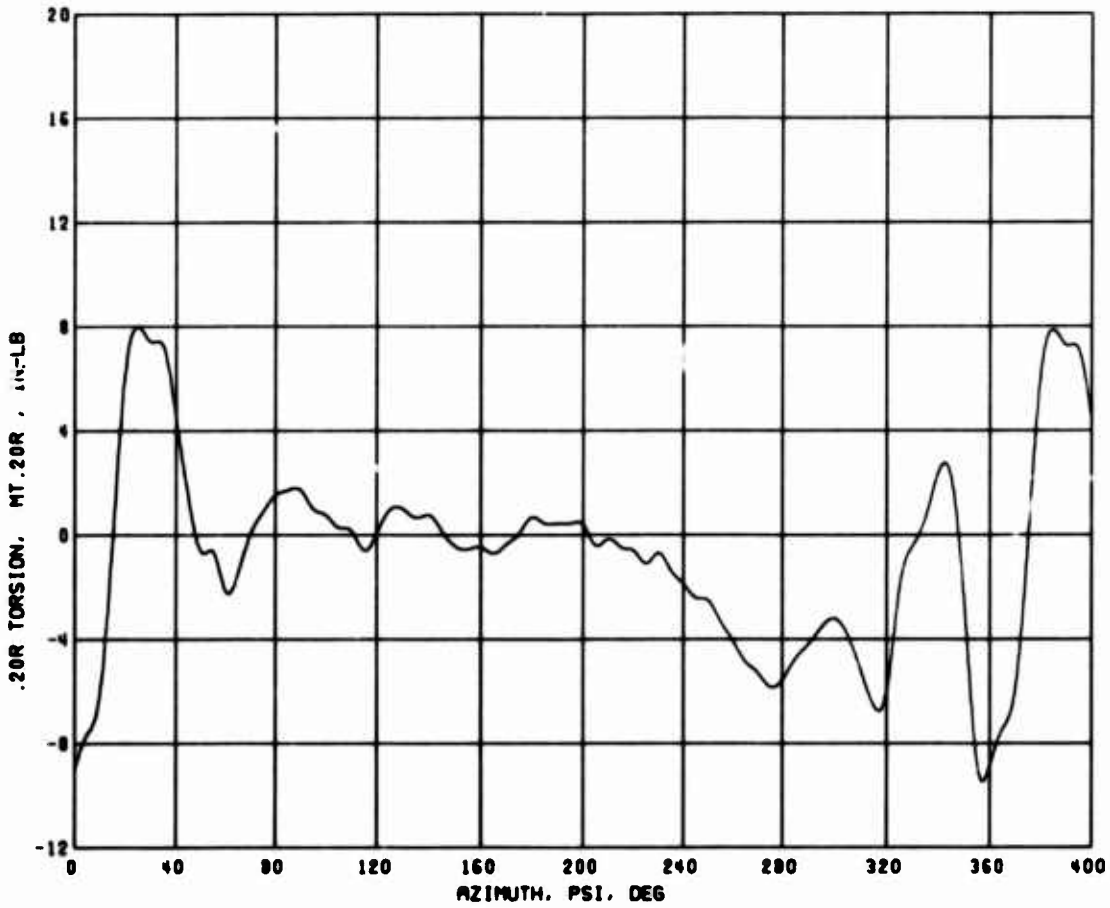

(a) Condition 34, $\mu = 0.352$, $C_L/\sigma = 0.0790$, $C_D/\sigma = 0.00222$

Figure 43. Average Revolution Time History Data; .20R Torsion, $\theta_1 = 0$ deg, $\delta_F = 0$ deg, $S_E = 1$.

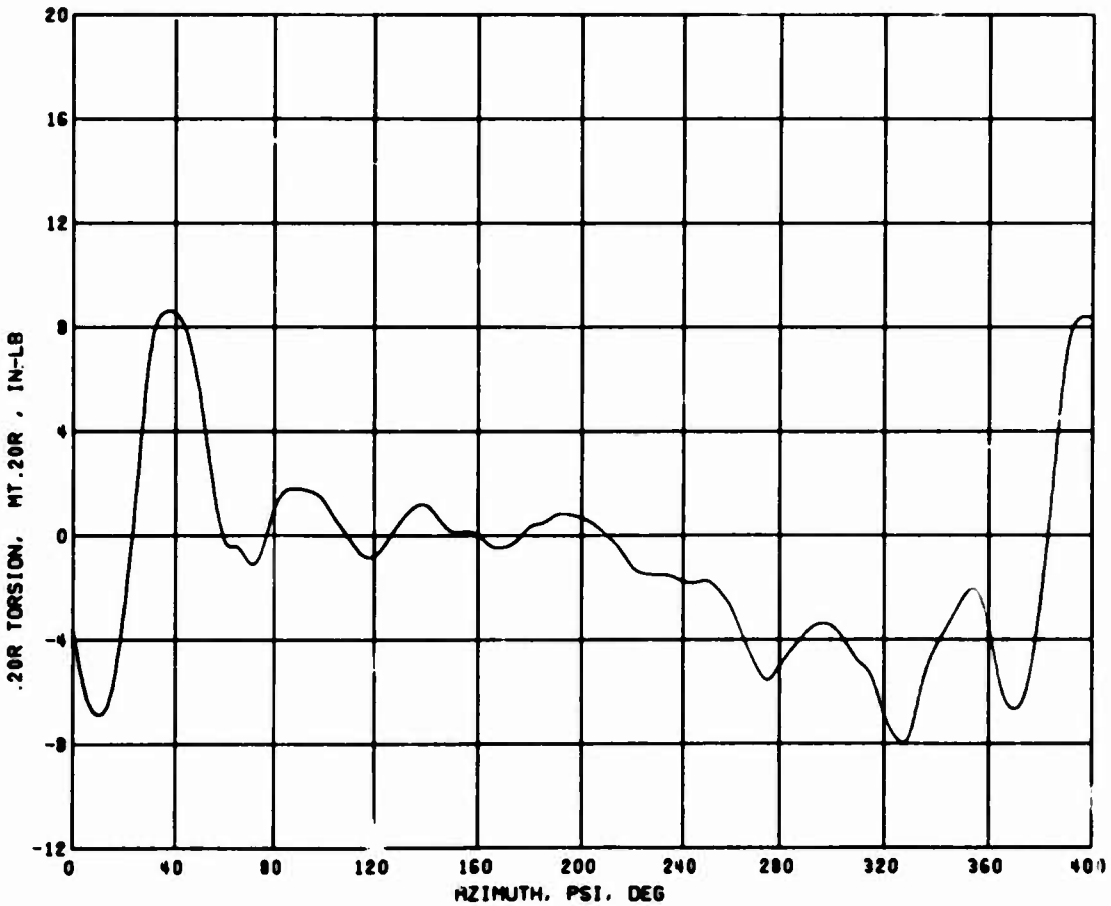

(b) Condition 25, $\mu = 0.40$, $C_L/\sigma = 0.0789$, $C_D/\sigma = -0.00113$

Figure 43. Continued.

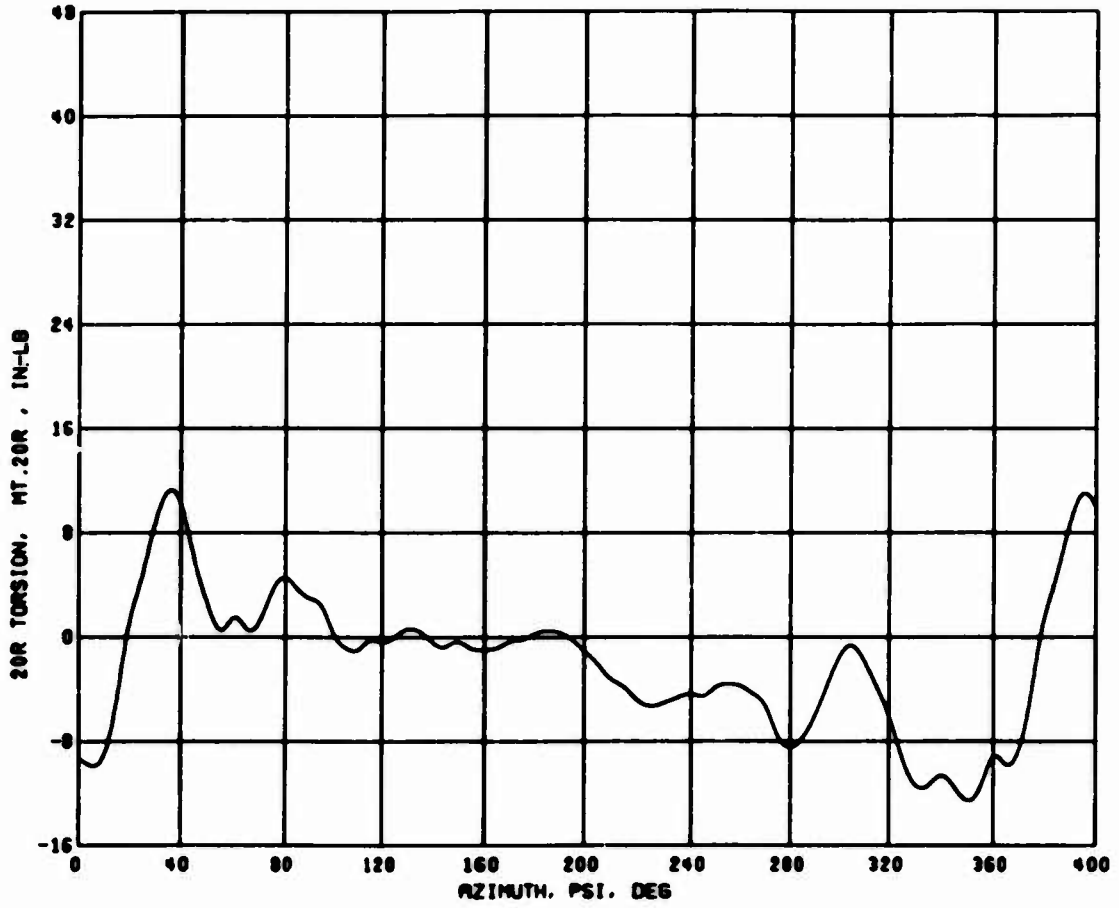

(c) Condition 49, $\mu = 0.50$, $C_L/\sigma = 0.0835$, $C_D/\sigma = 0.00445$

Figure 43. Concluded.

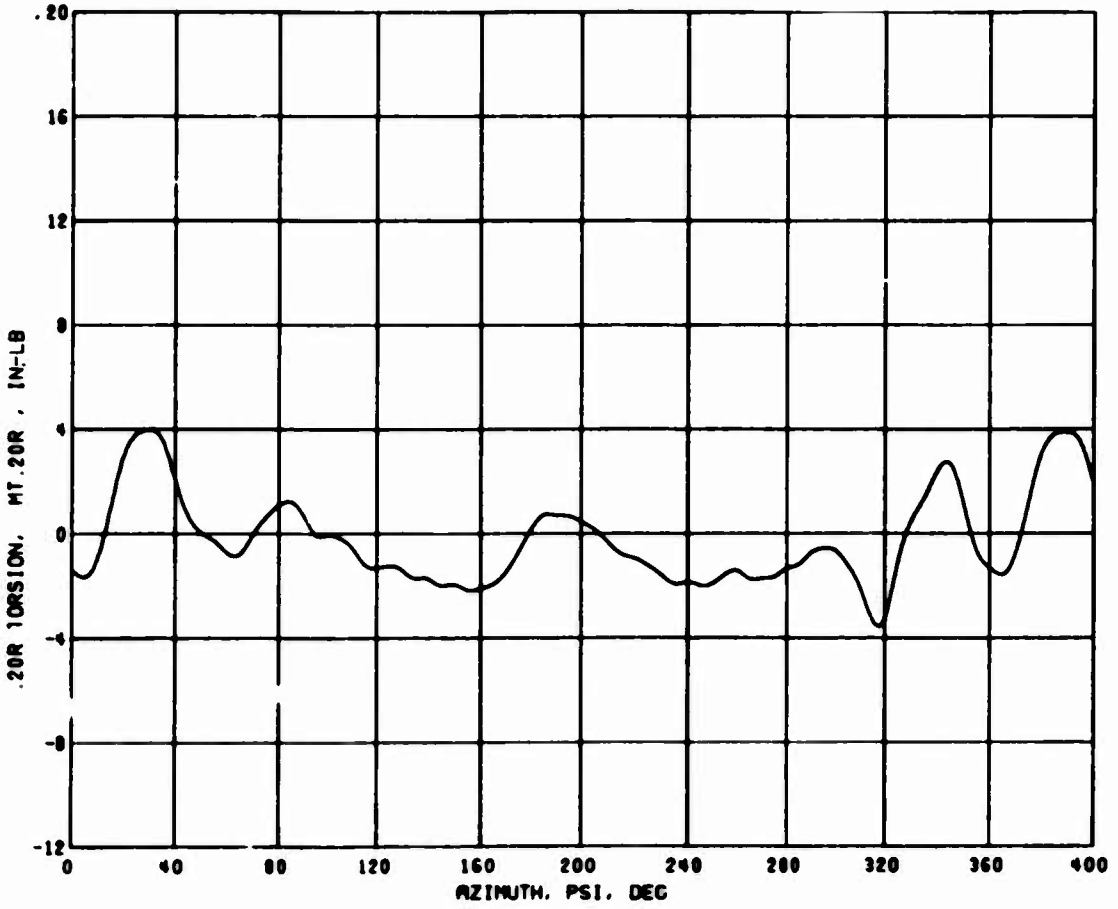

(a) Condition 34, $\mu = 0.352$, $C_L/\sigma = 0.0796$, $C_D/\sigma = 0.00328$

Figure 44. Average Revolution Time History Data; .20R Torsion, $\theta_1 = -8$ deg, $\delta_F = 0$ deg, $S_E = 1$.

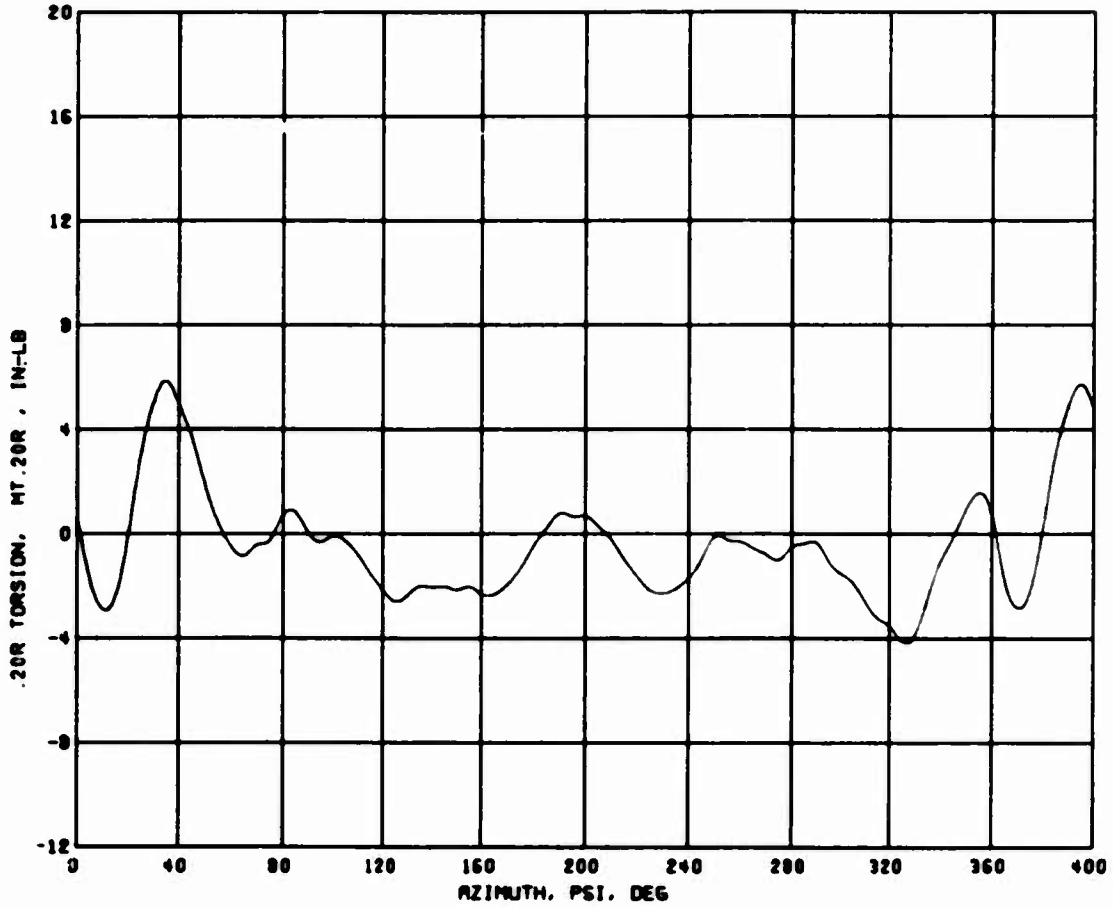

(b) Condition 25, $\mu = 0.399$, $C_L/\sigma = 0.0794$, $C_D/\sigma = -0.00096$

Figure 44. Continued.

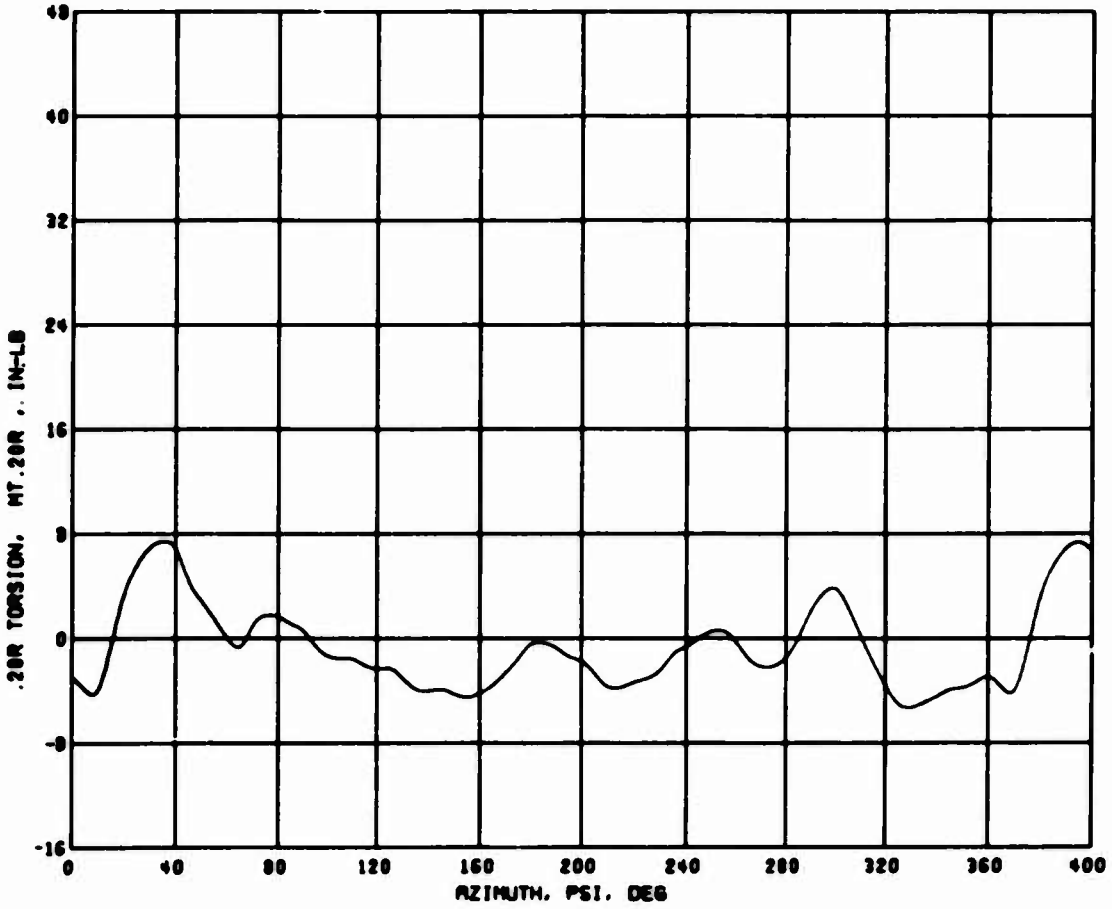

(c) Condition 49, $\mu = 0.502$, $C_L/\sigma = 0.0810$, $C_D/\sigma = 0.00433$

Figure 44. Concluded.

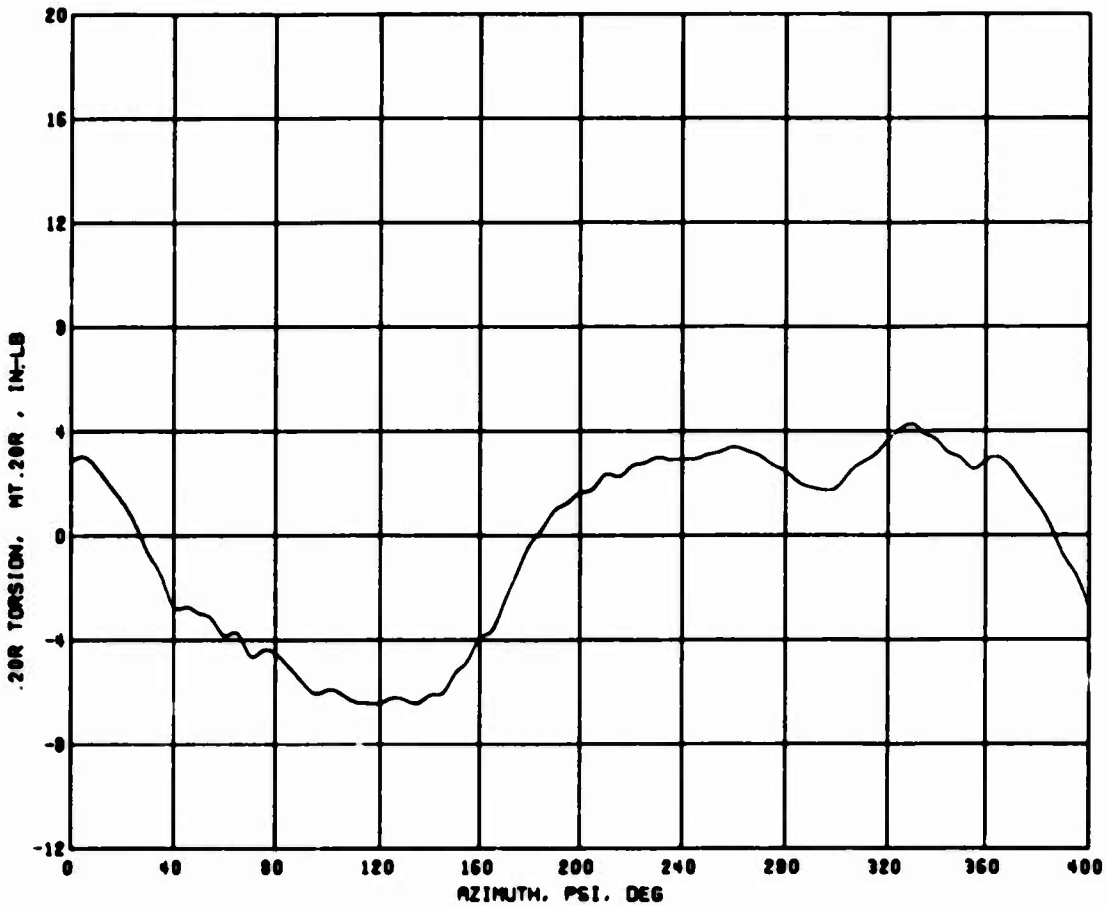

(a) Condition 35, $\mu = 0.352$, $C_L/\sigma = 0.0795$, $C_D/\sigma = 0.00131$

Figure 45. Average Revolution Time History Data; .20R Torsion, $\theta_1 = 0$ deg, $\delta_F = 5$ deg, $S_E = 1$.

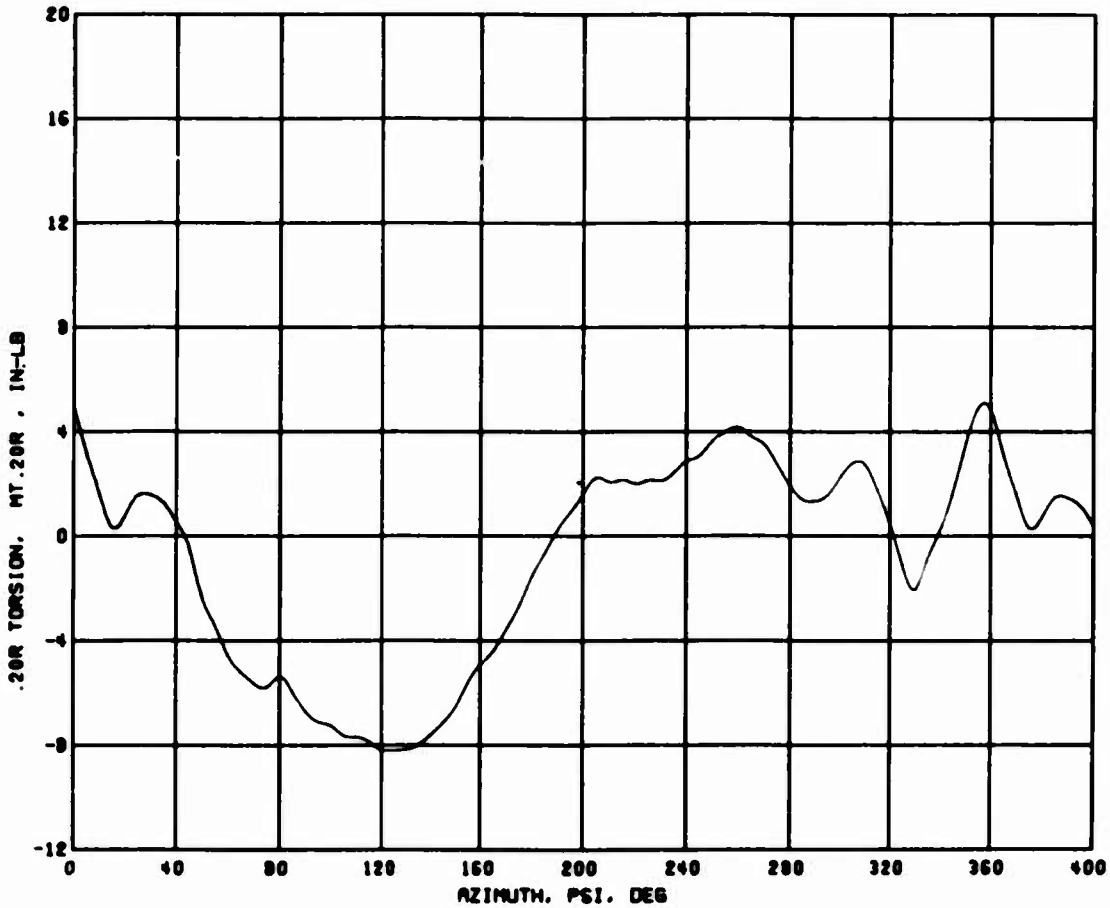

(b) Condition 25, $\mu = 0.399$, $C_L/\sigma = 0.0824$, C_D/σ -0.00142

Figure 45. Continued.

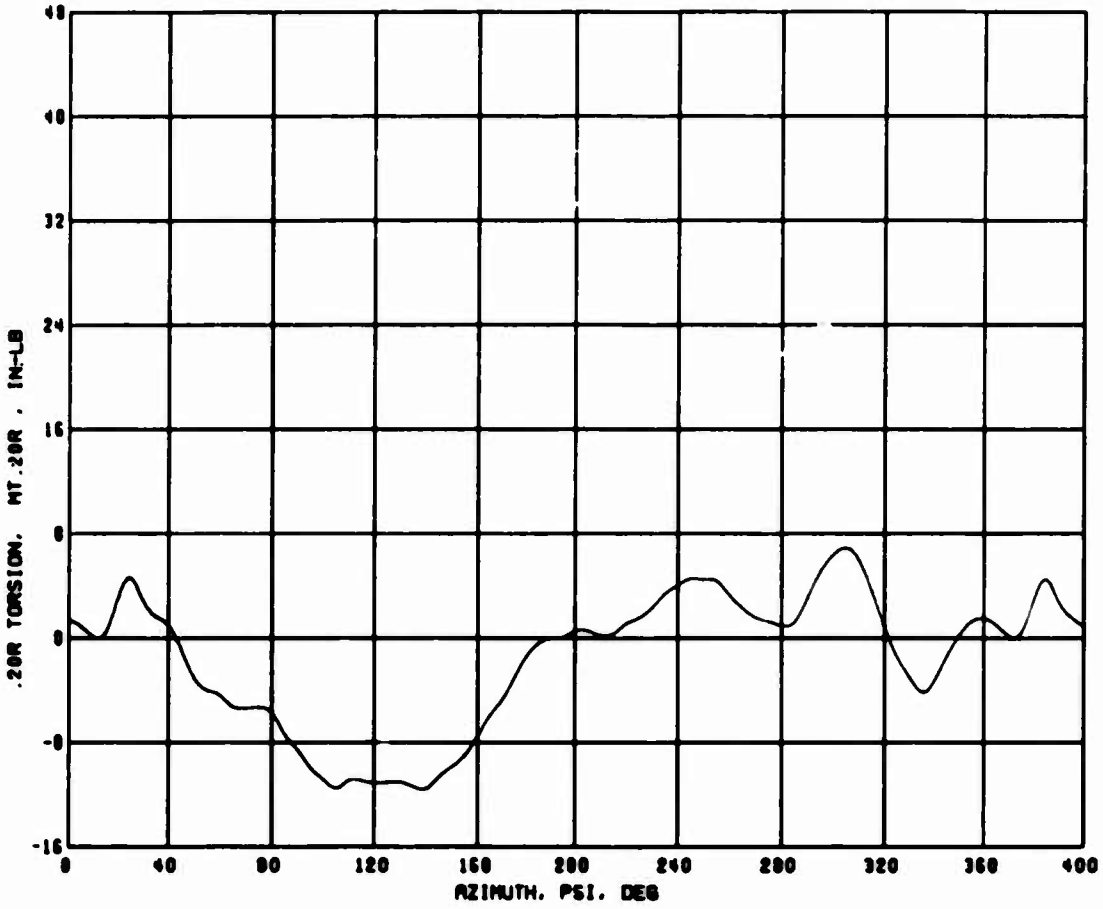

(c) Condition 49, $\mu = 0.502$, $C_L/\sigma = 0.0826$, $C_D/\sigma = 0.00545$

Figure 45. Concluded.

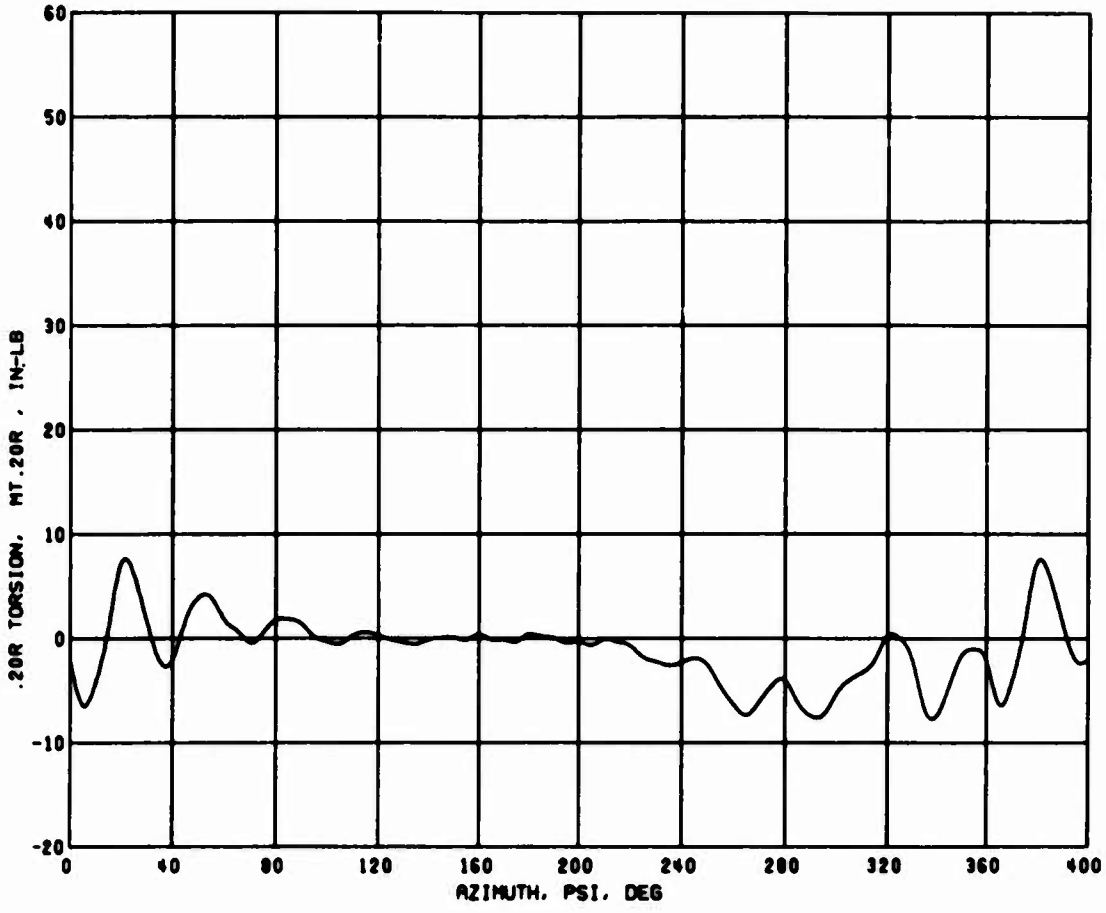

(a) Condition 34, $\mu = 0.352$, $C_L/\sigma = 0.0775$, $C_D/\sigma = 0.00157$

Figure 46. Average Revolution Time History Data; .20R Torsion, $\theta_1 = 0$ deg, $\delta_F = 0$ deg, $S_E = 3$.

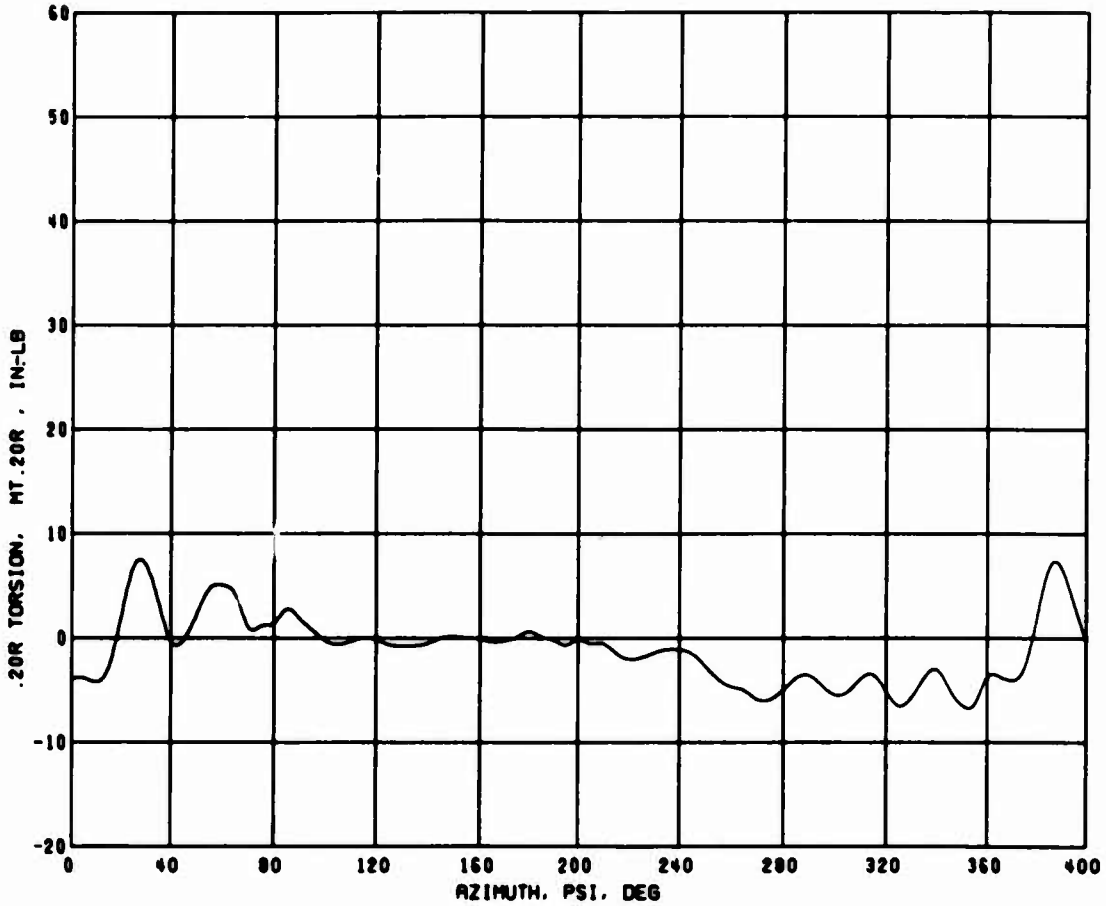

(b) Condition 25, $\mu = 0.399$, $C_L/\sigma = 0.0752$, $C_D/\sigma = -0.00153$

Figure 46. Continued.

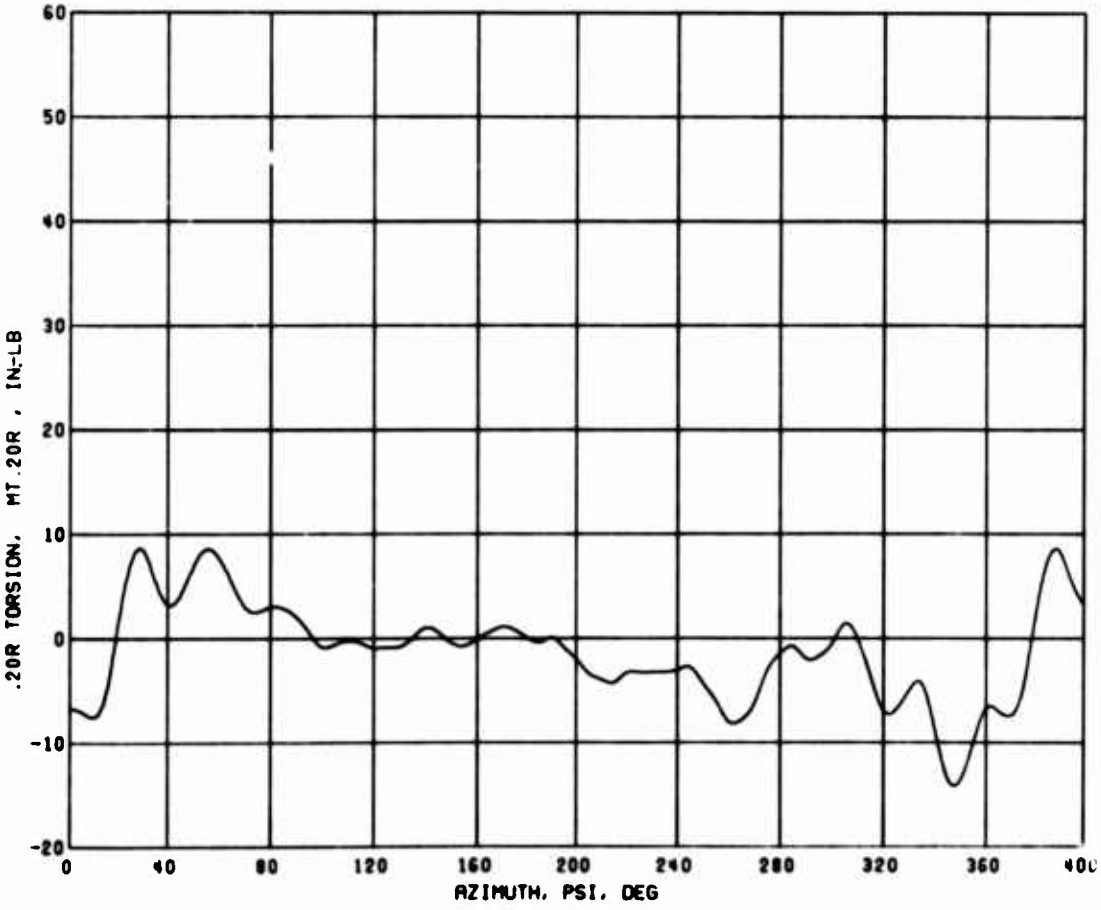

(c) Condition 49, $\mu = 0.502$, $C_L/\sigma = 0.0822$, $C_D/\sigma = 0.00474$

Figure 46. Concluded.

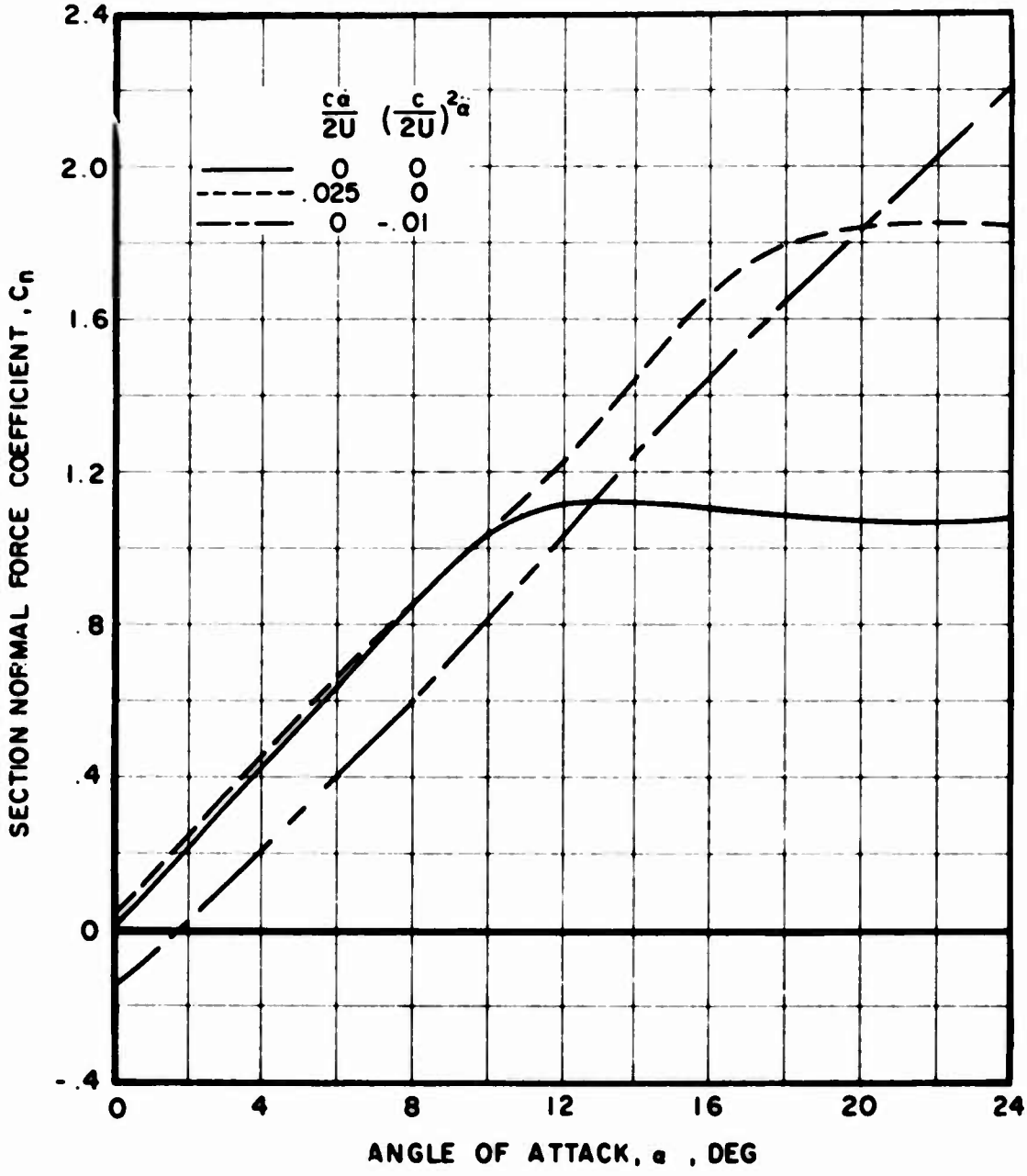

(a) Normal Force Coefficient

Figure 47. Effect of Pitching Velocity and Acceleration on Variation of Aerodynamic Coefficients With Angle of Attack.

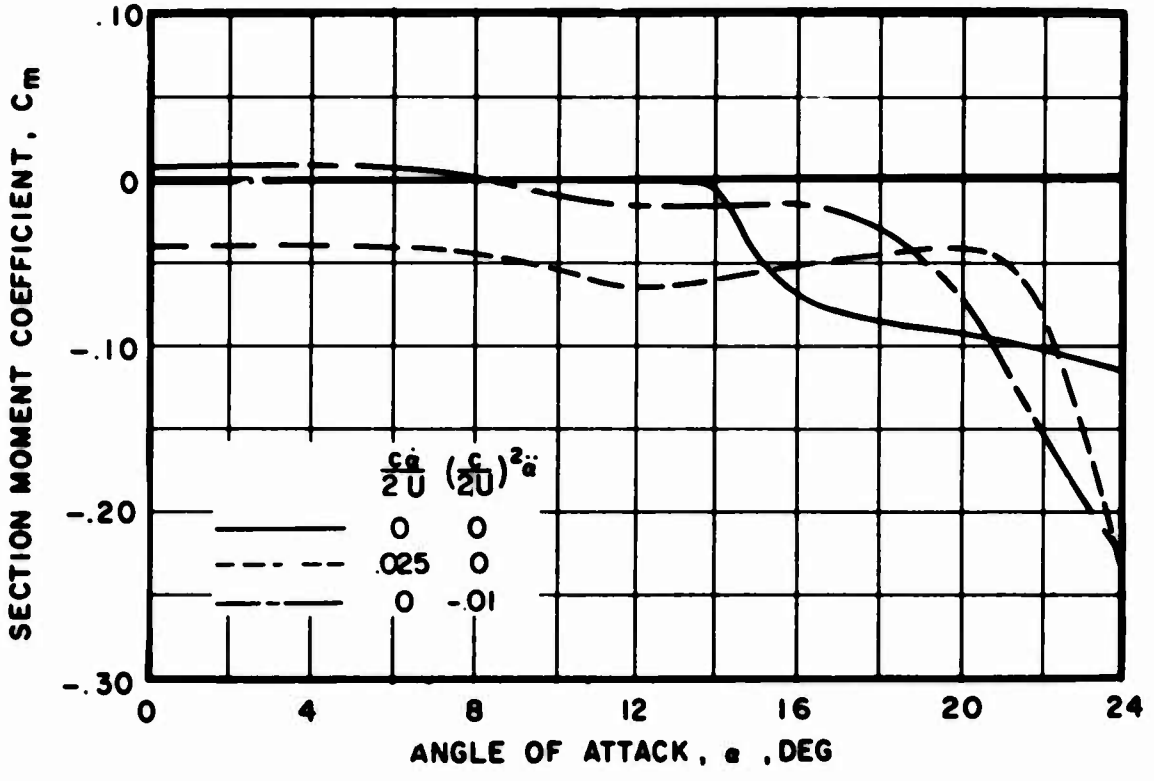

(b) Moment Coefficient

Figure 47. Concluded.

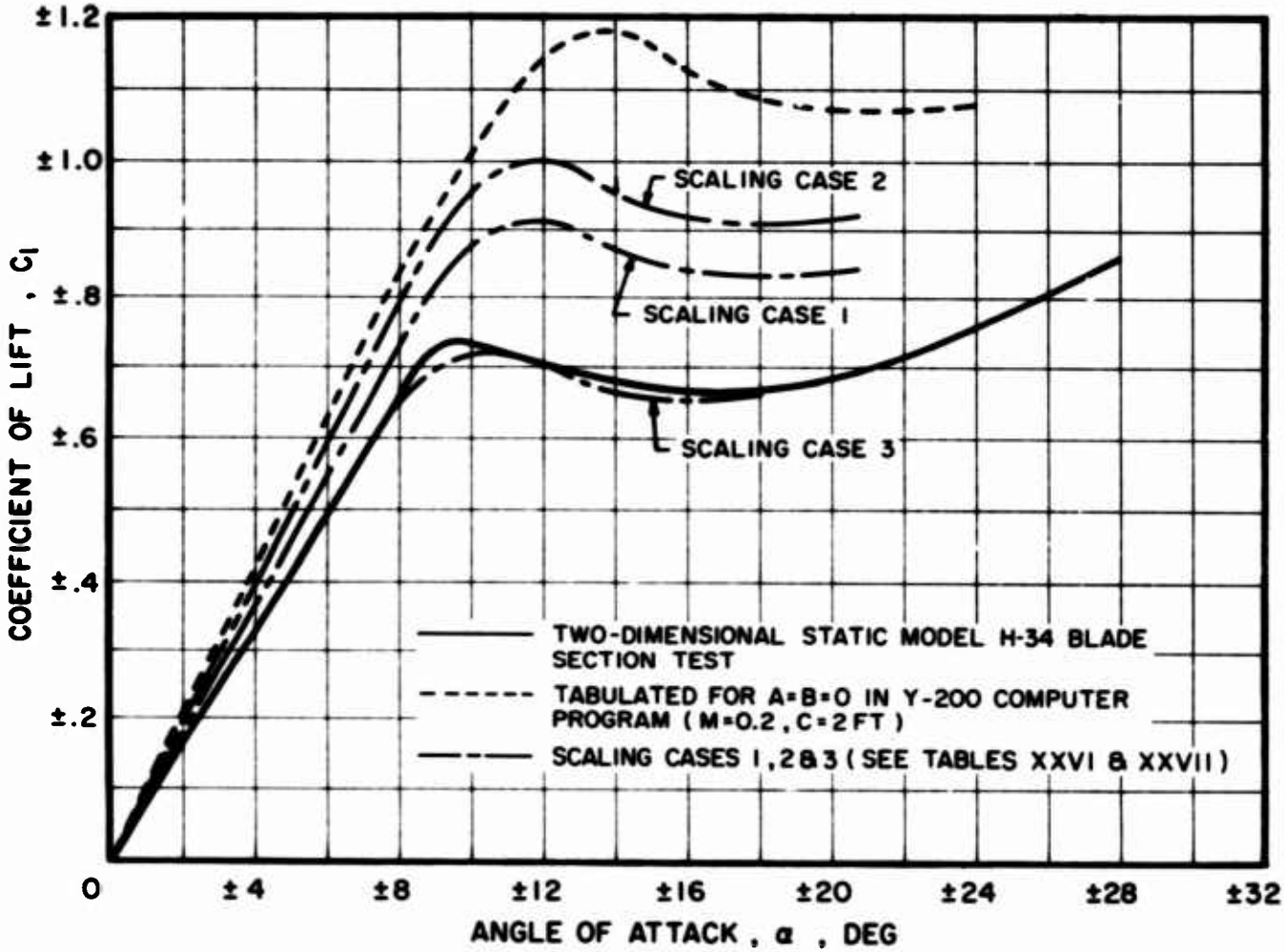

(a) M = 0.10

Figure 48. Comparison of Scaled Lift Coefficient Versus Angle of Attack With Static Full-Scale and Model Data.

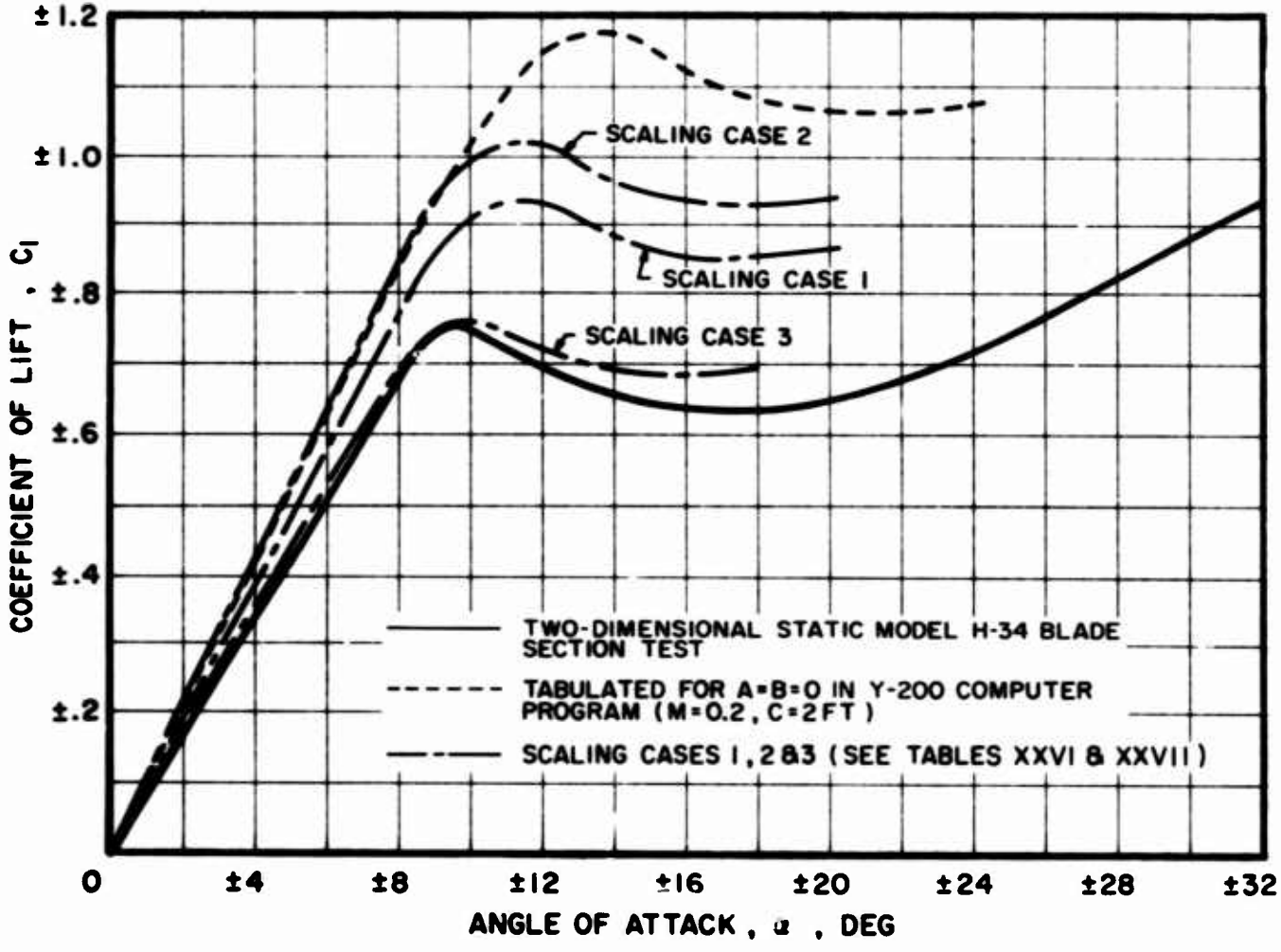

(b) M = 0.18

Figure 48. Continued.

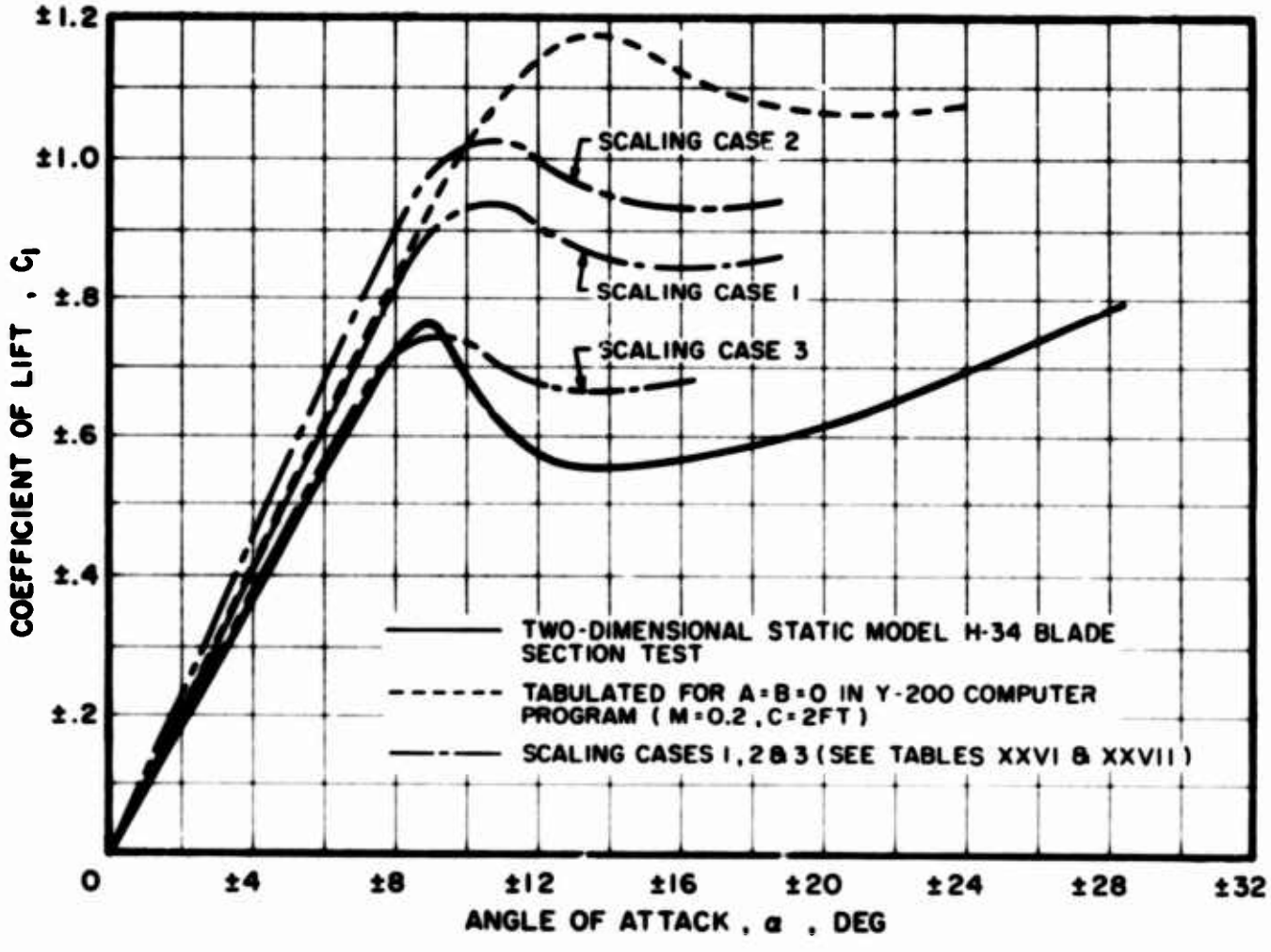

(c) M = 0.33

Figure 48. Continued.

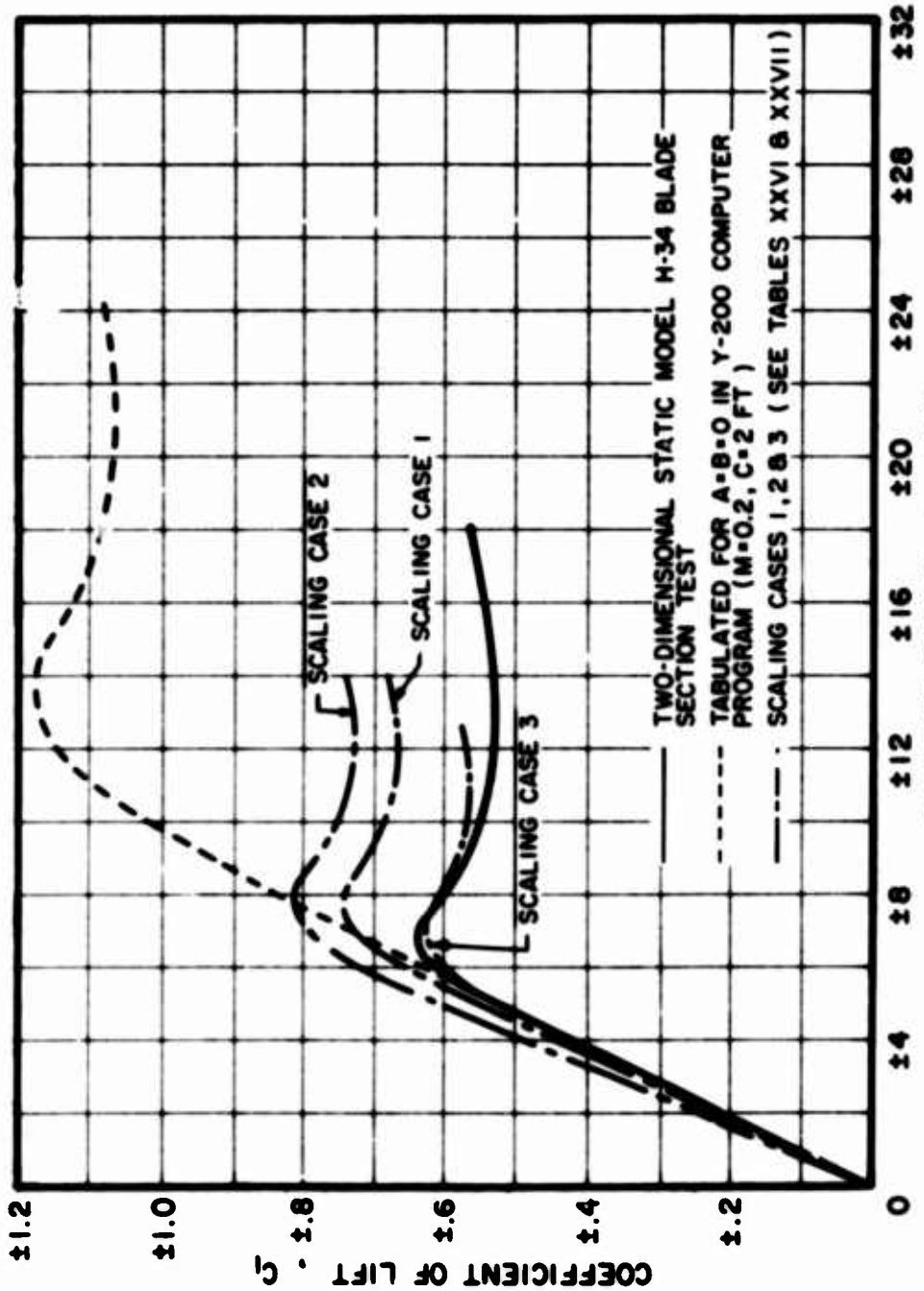

(d) M = 0.47

Figure 48. Continued.

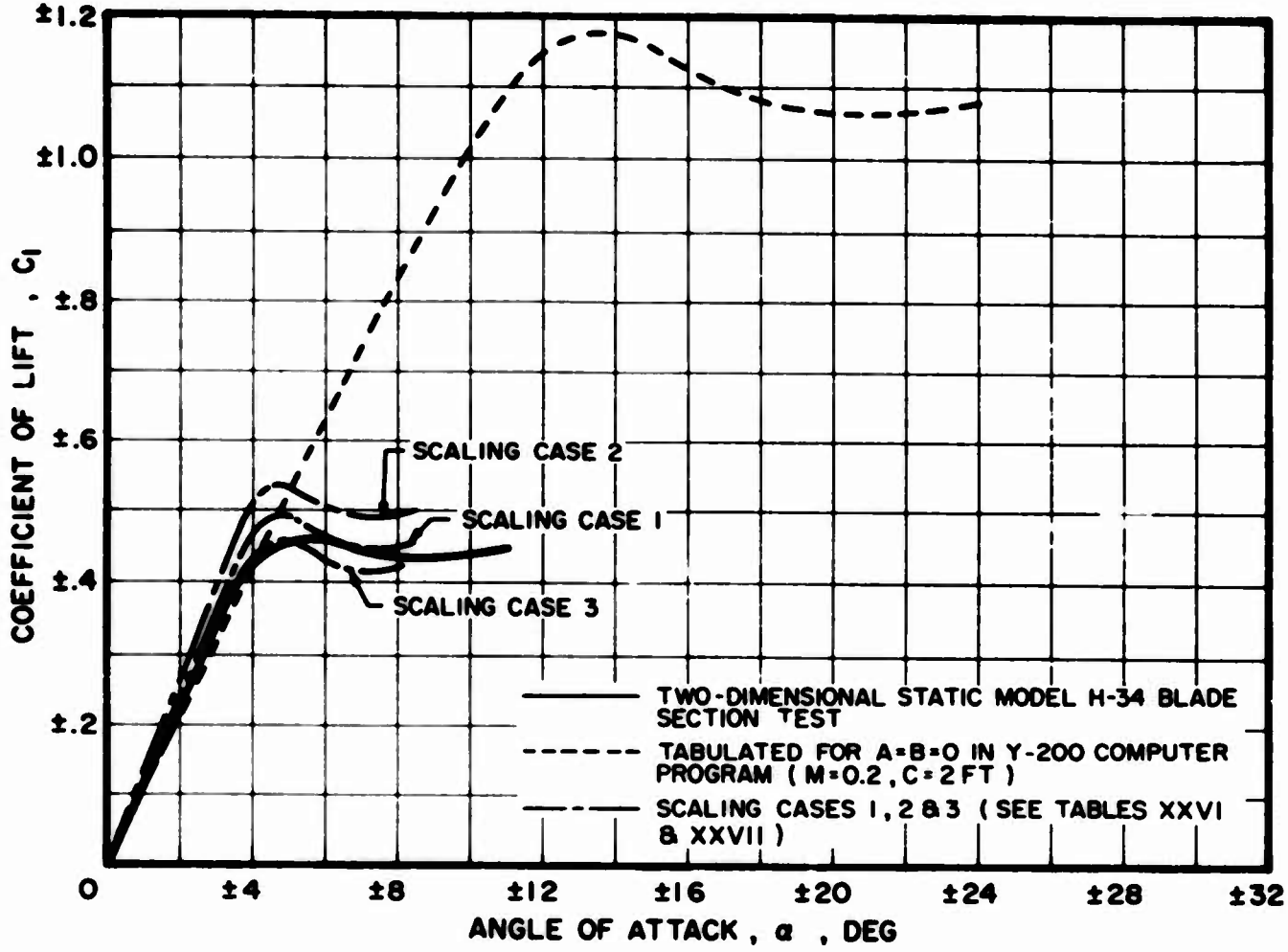

(e) M = 0.56

Figure 48. Concluded.

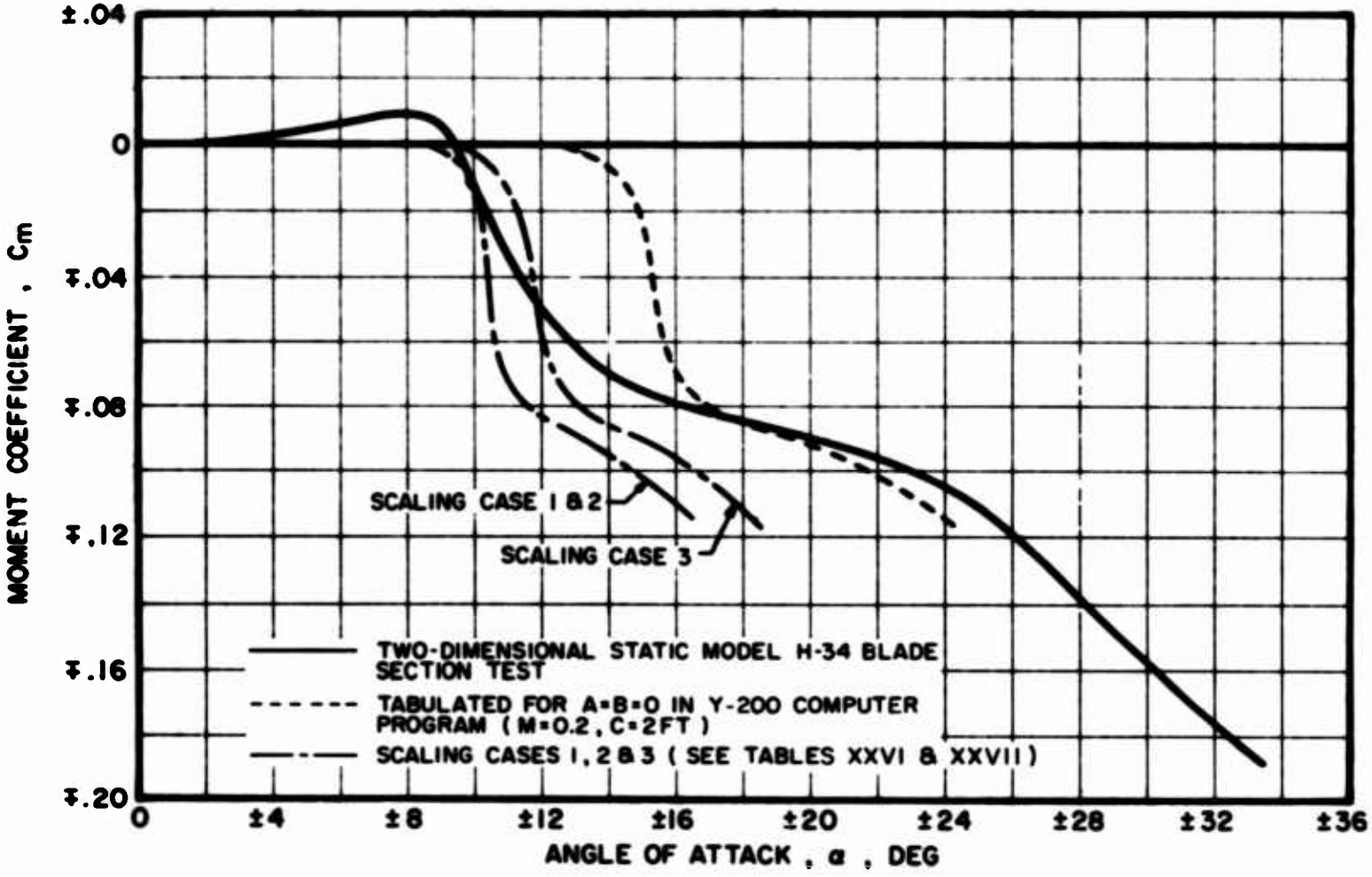

(a) M = 0.10

Figure 49. Comparison of Scaled Moment Coefficient Versus Angle of Attack With Static Full-Scale and Model Data.

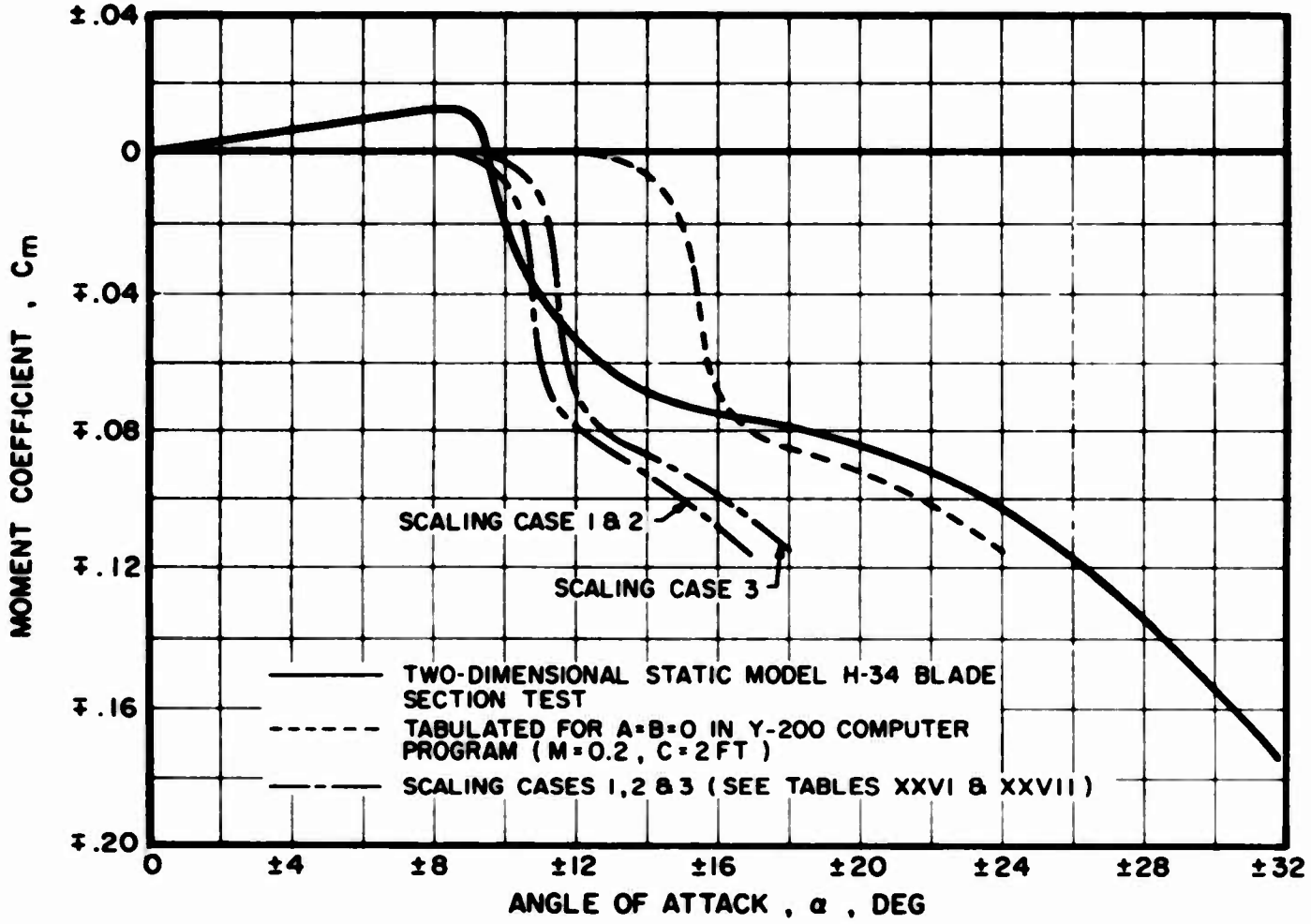

(b) M = 0.18

Figure 49. Continued.

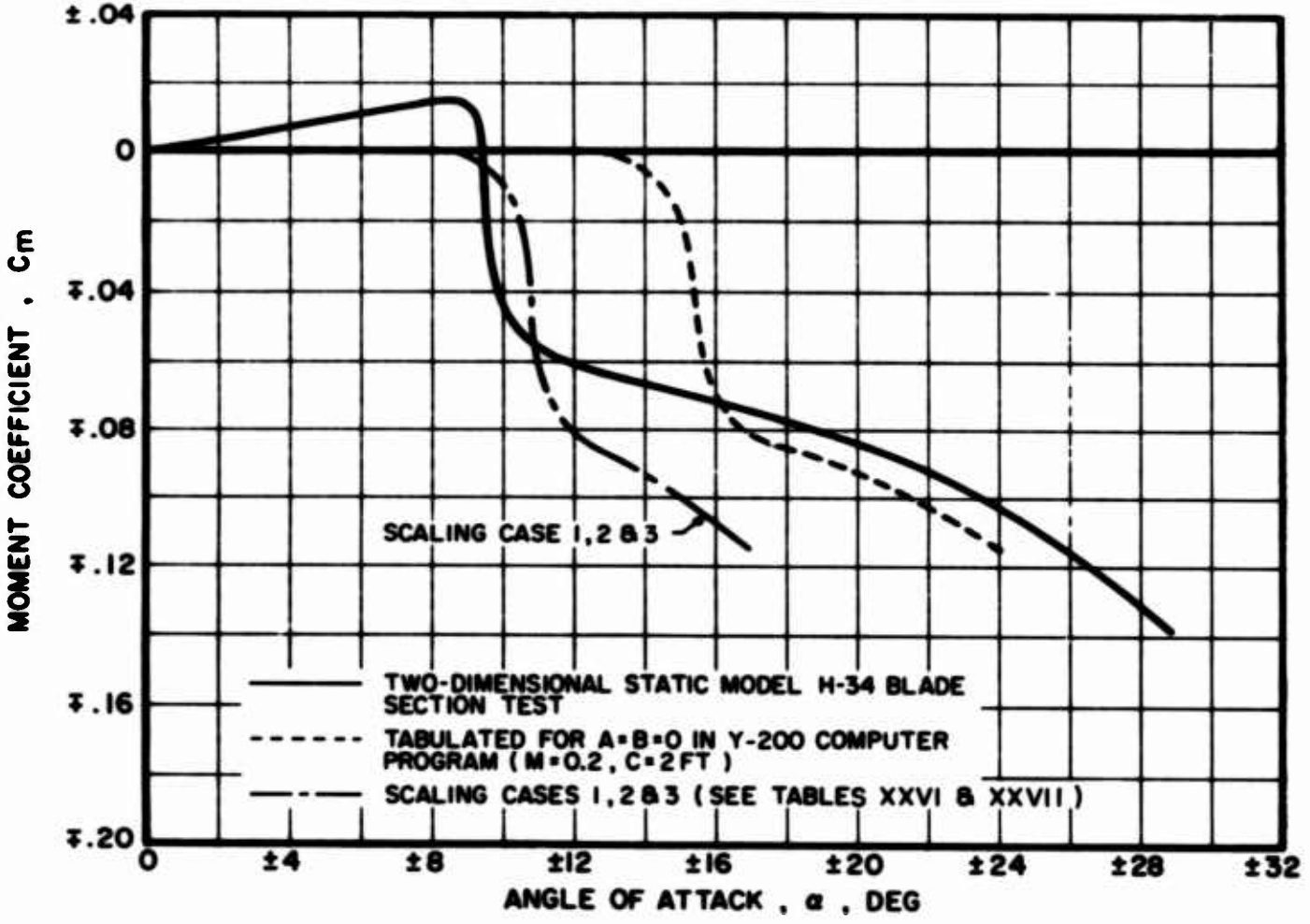

(c) M = 0.33

Figure 49. Continued.

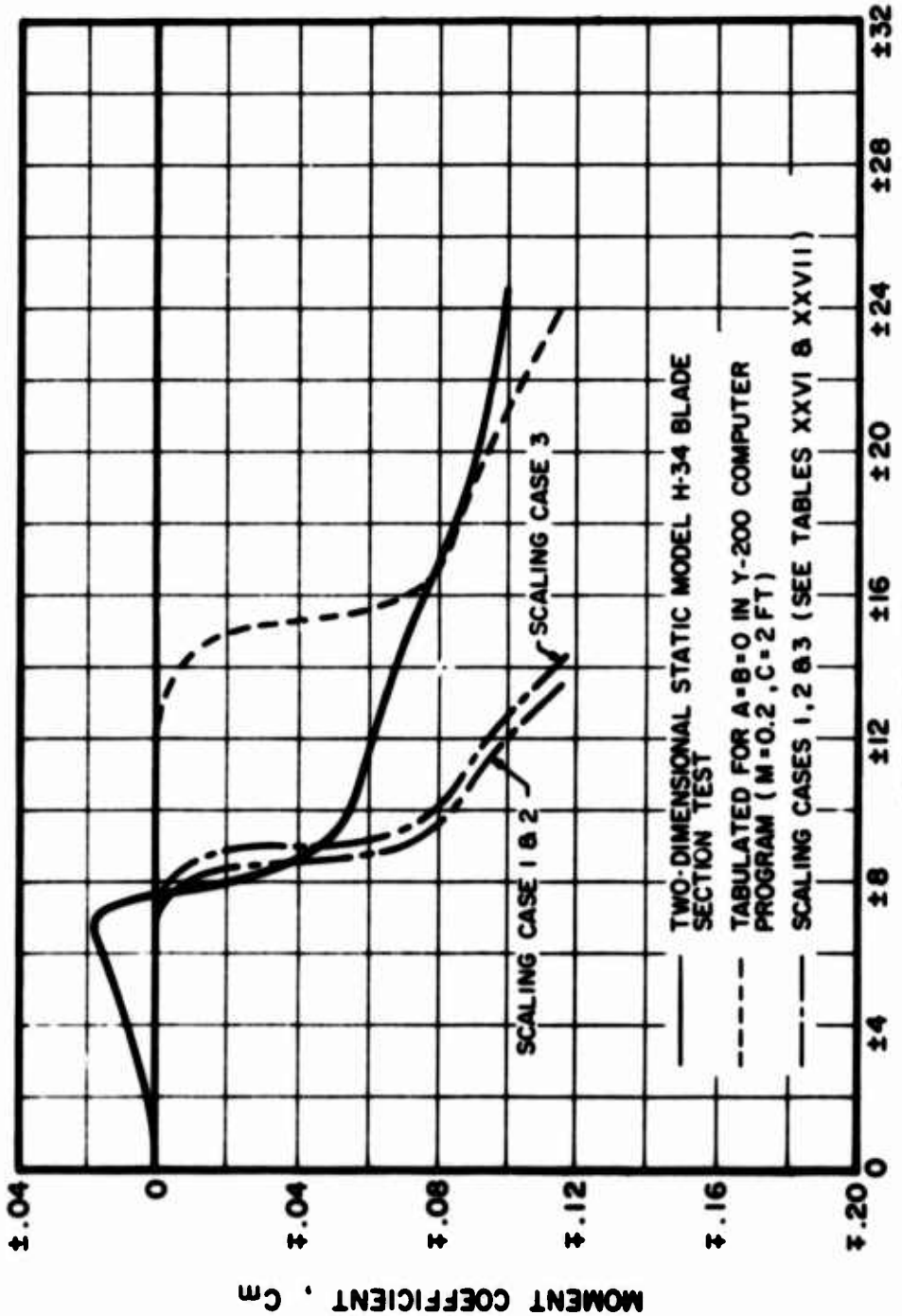

(d) M = 0.47

Figure 49. Continued.

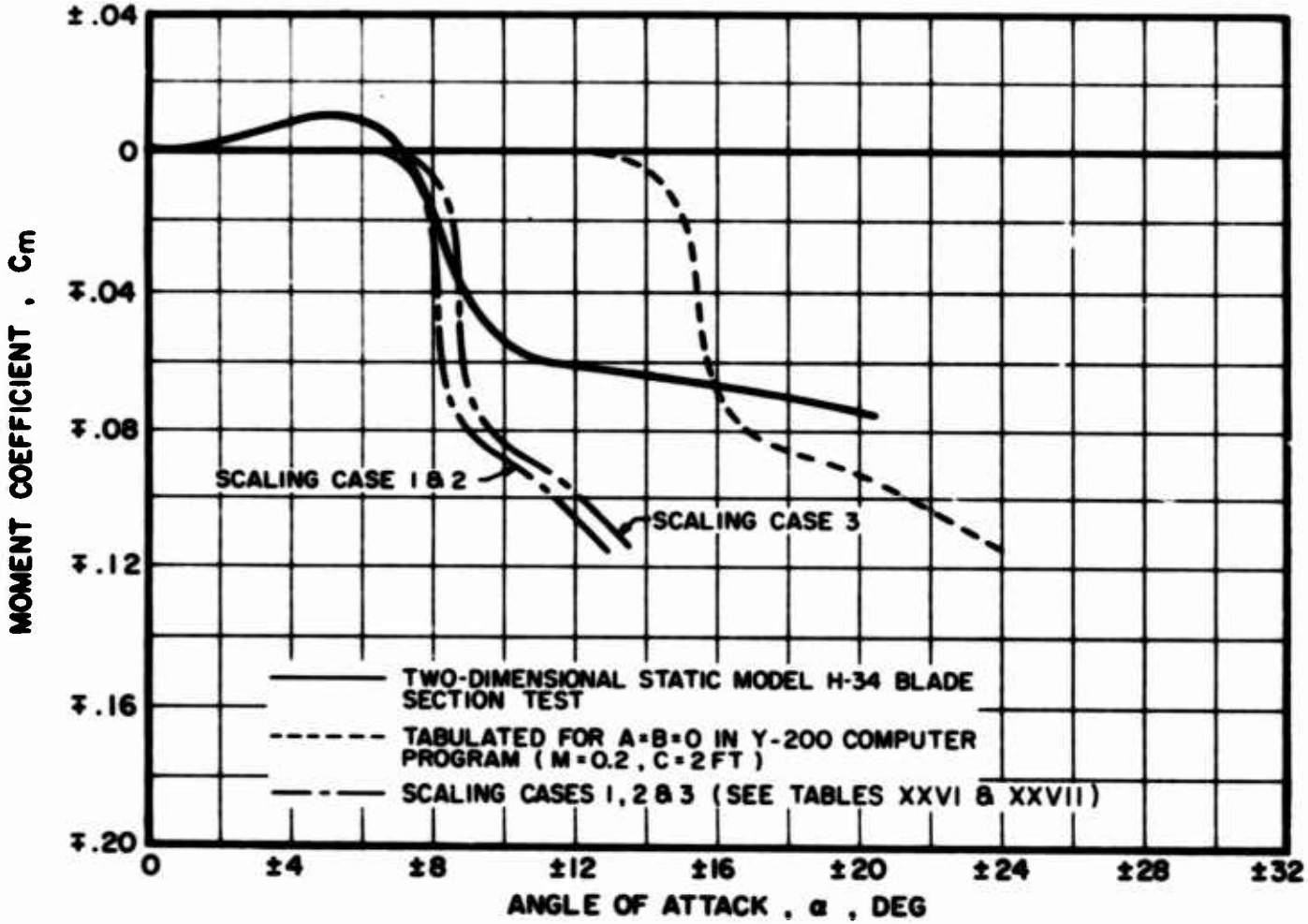

(e) M = 0.56

Figure 49. Concluded.

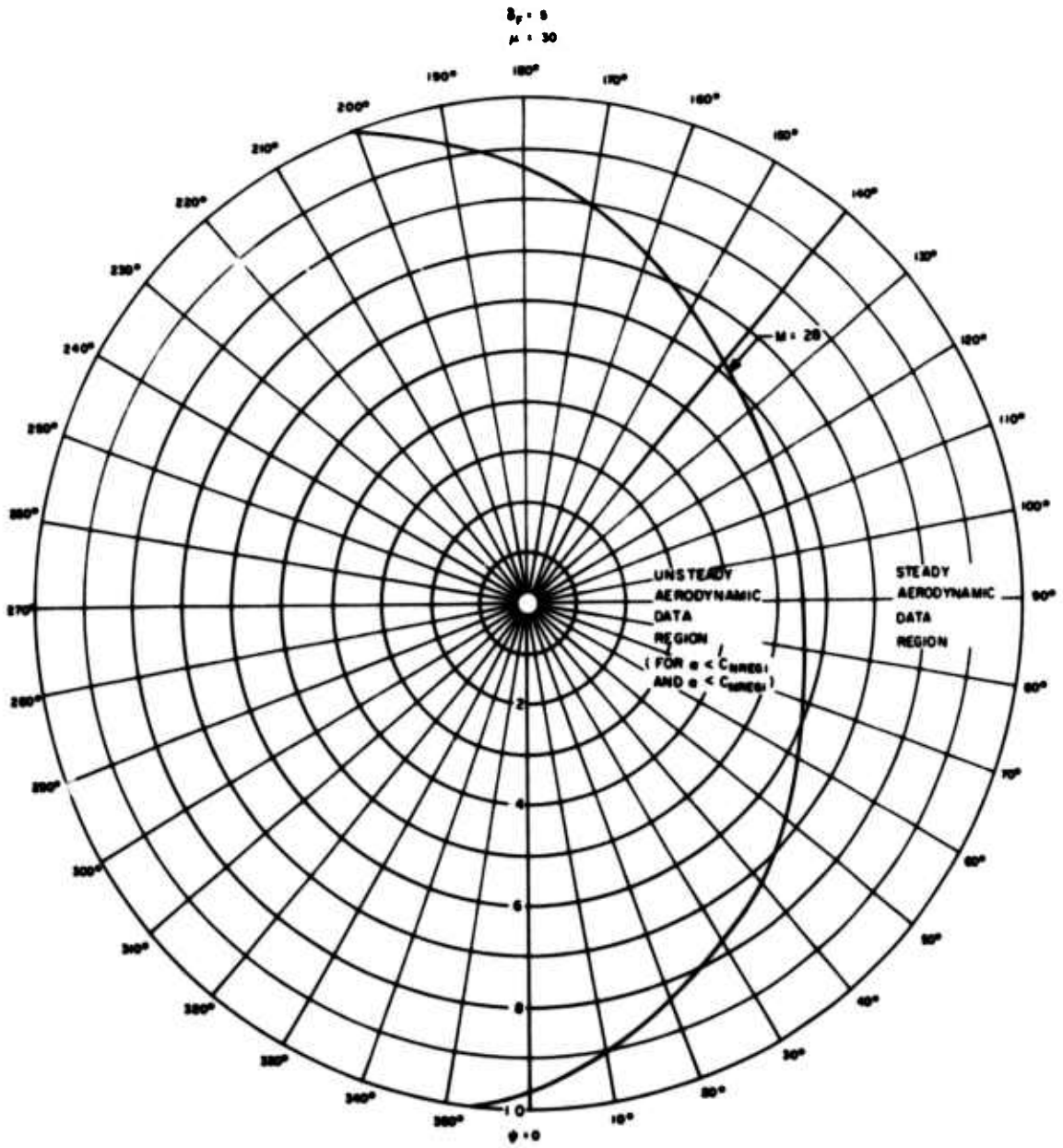

Figure 50. Sample of Steady and Unsteady Aerodynamic Regions of Application for the Flapped Blade.

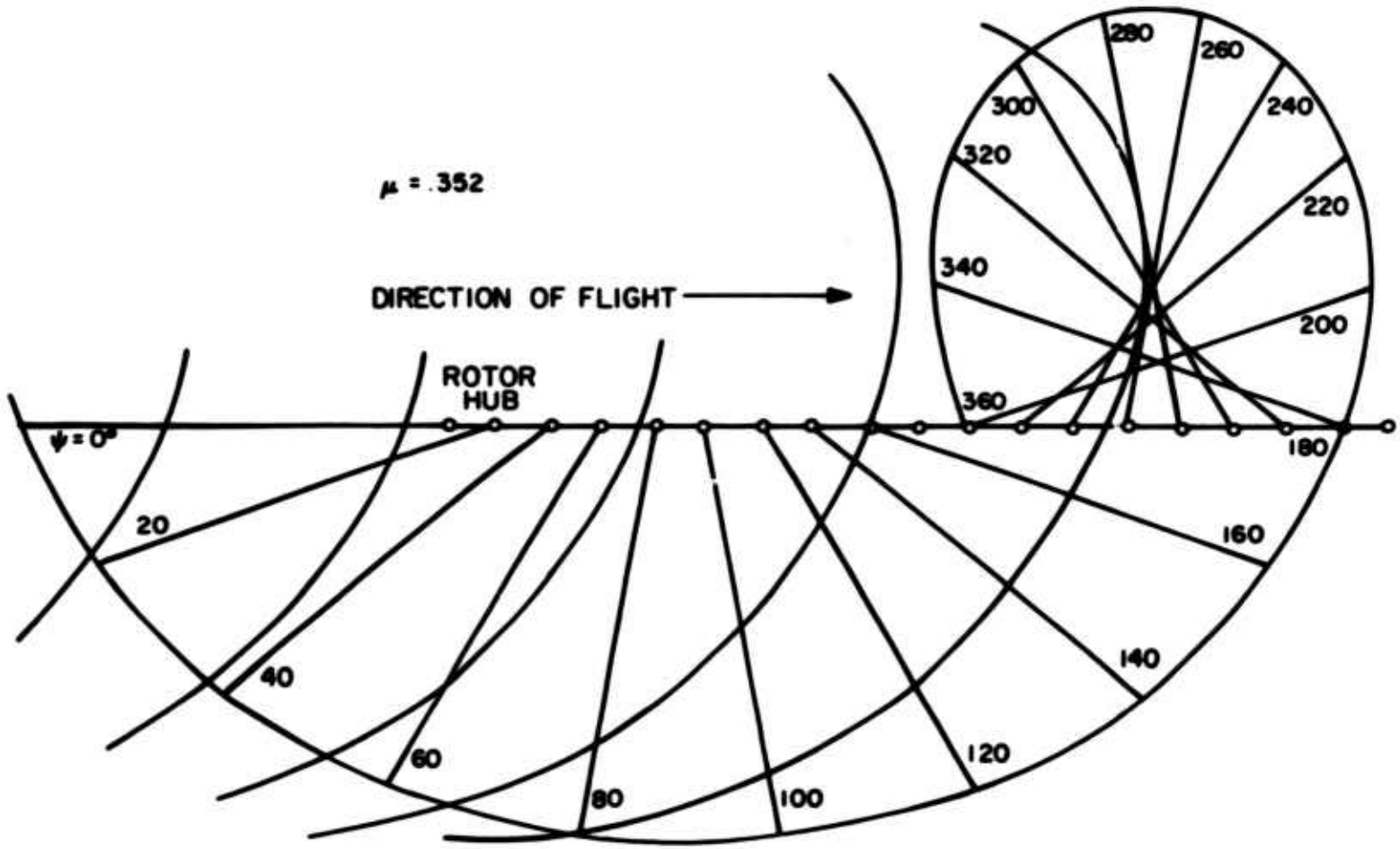

Figure 51. Blade and Tip Vortex Proximity.

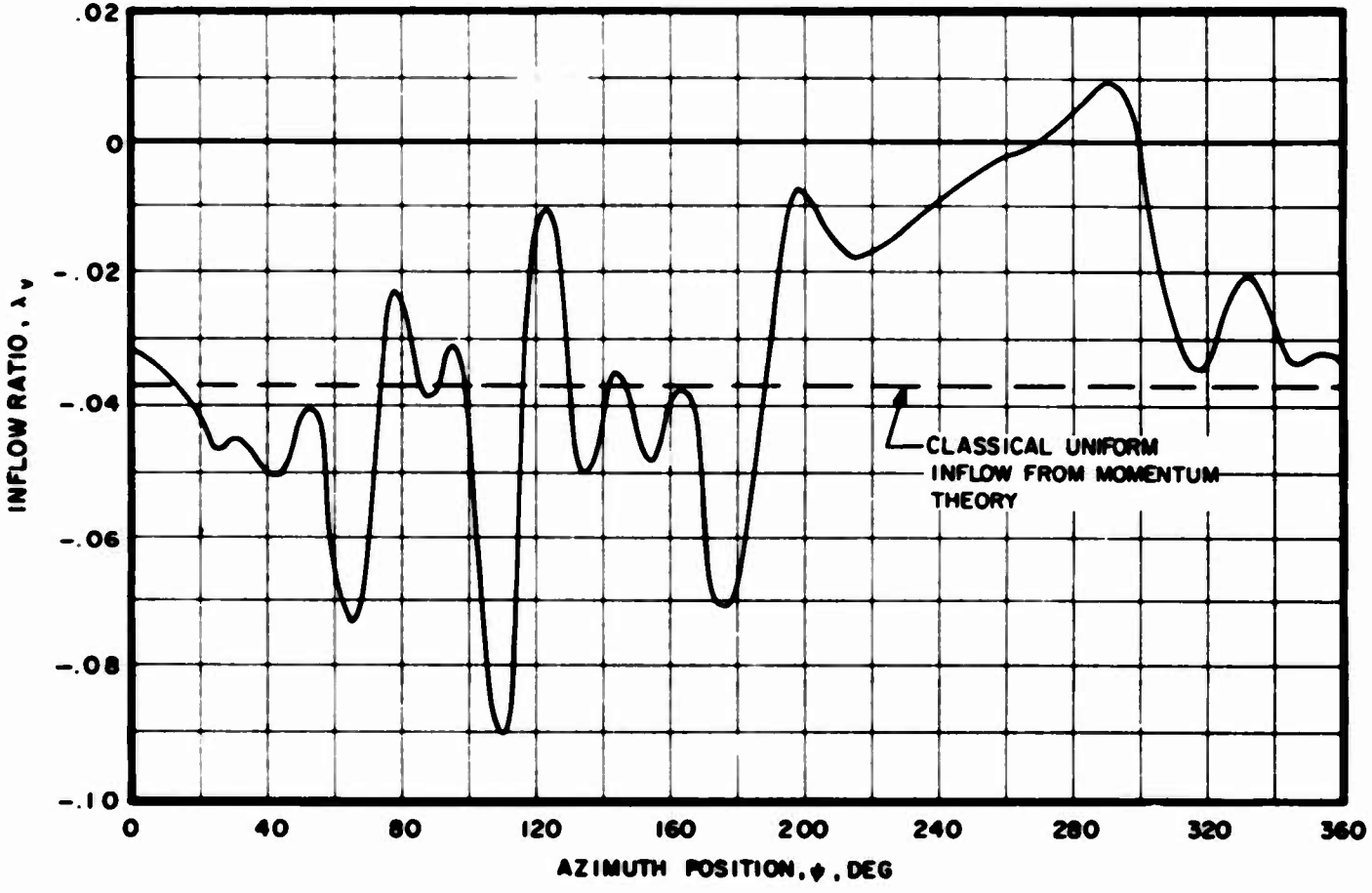

(a) Radius = 0.45 R

Figure 52. Sample of Variable Inflow From Prescribed Wake Calculation; $\mu = 0.352$, $C_L/\sigma = 0.070$, $\alpha_s = -5$ deg, $a_{1s} = 3.6$ deg, $b_{1s} = 0$ deg.

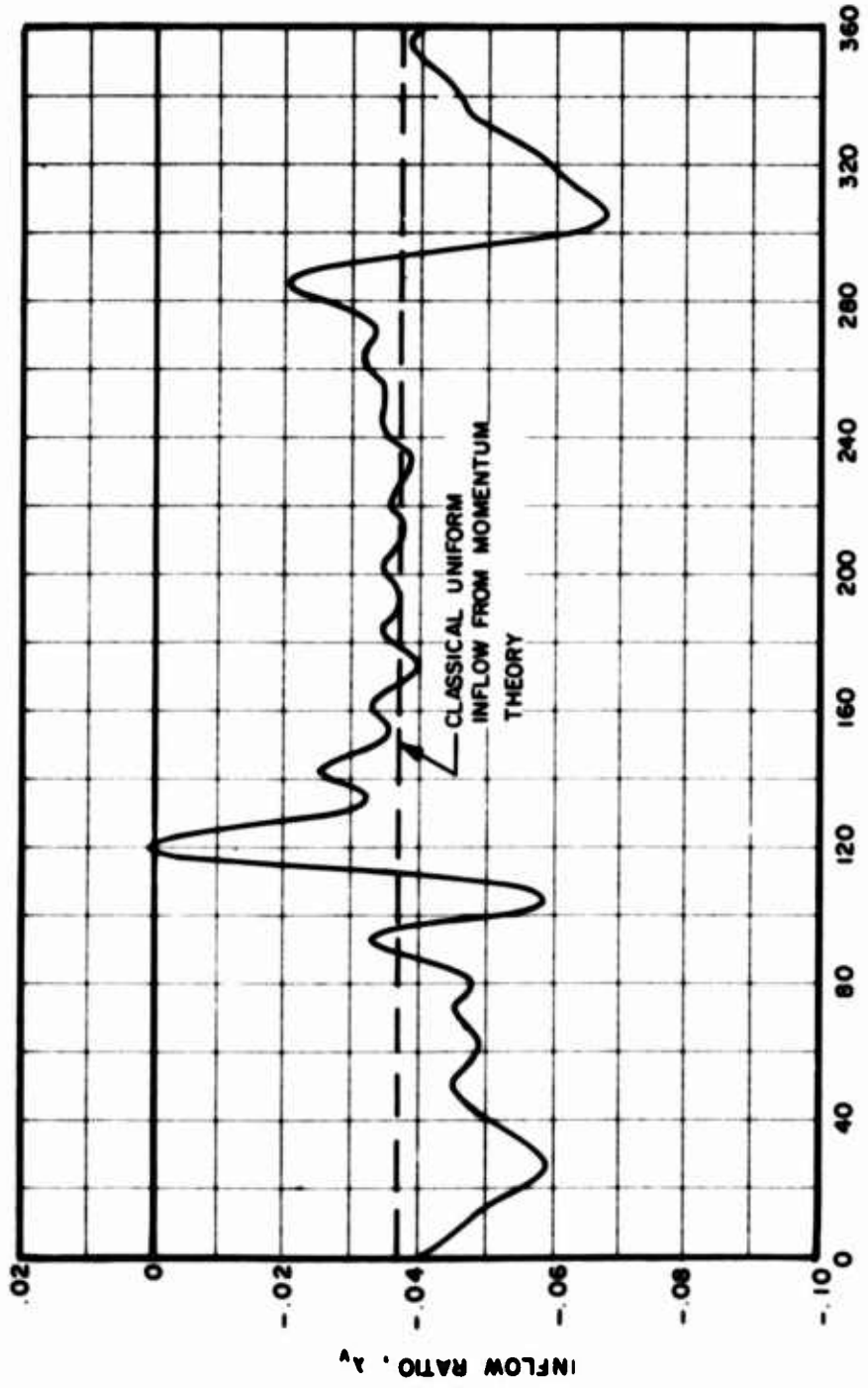

(b) Radius = 0.80 R

Figure 52. Continued.

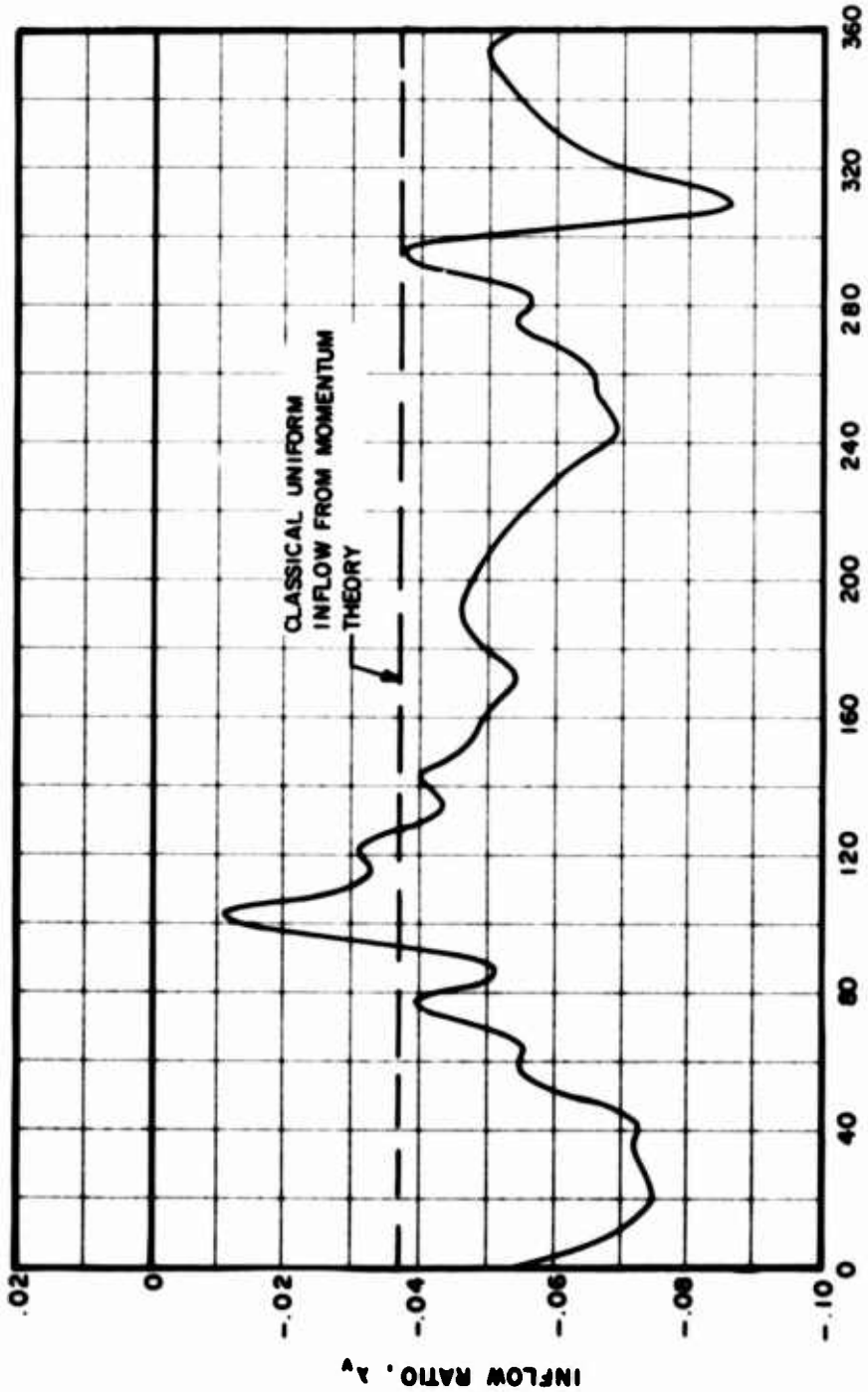

(c) Radius = 0.93 R

Figure 52. Concluded.

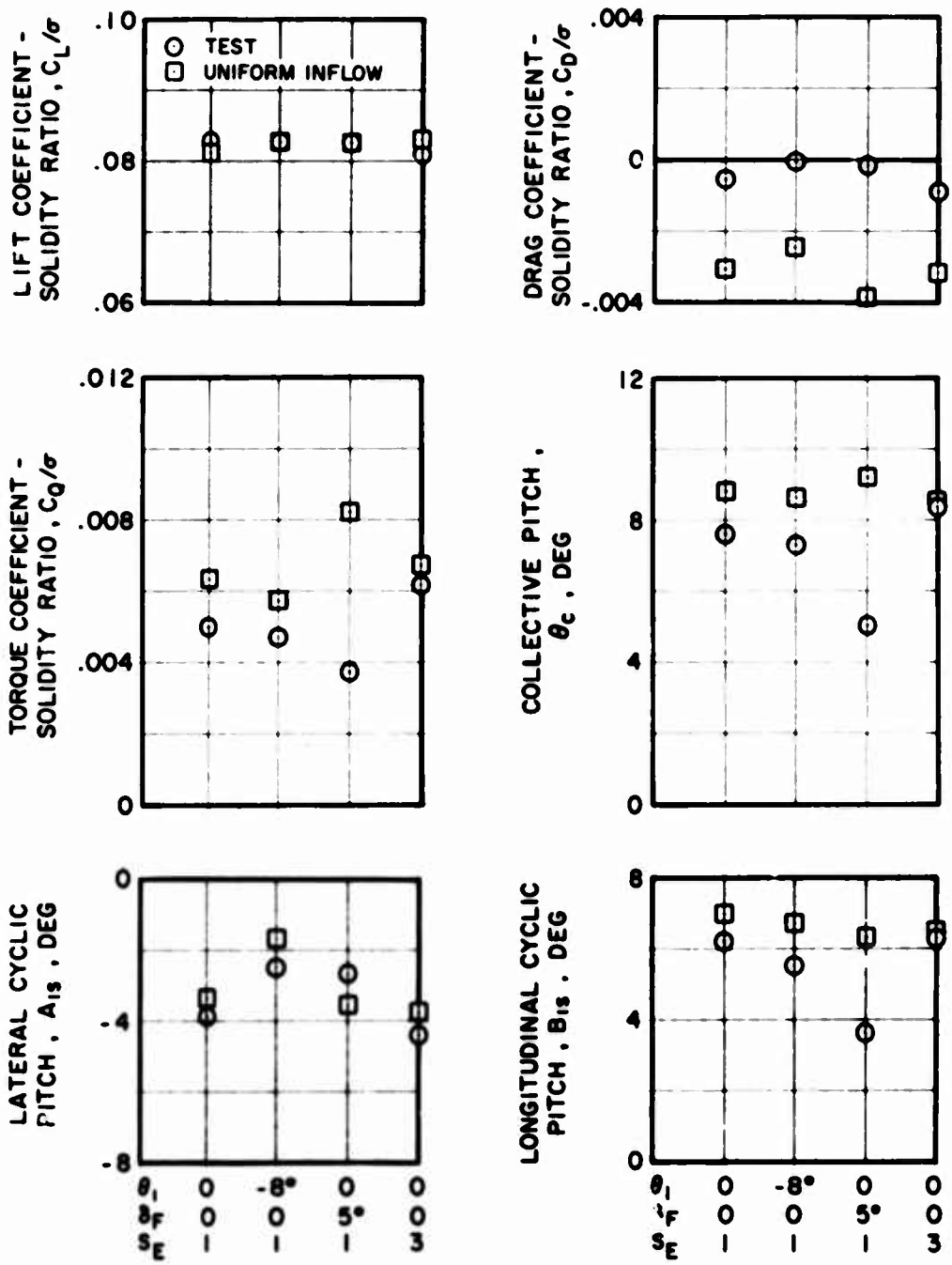

Figure 53. Correlation of Test and Calculated Data for Condition 7; V_s = 124 kn, μ = 0.30, α_s = 0 deg, $a_{1s} = b_{1s}$ = 0 deg.

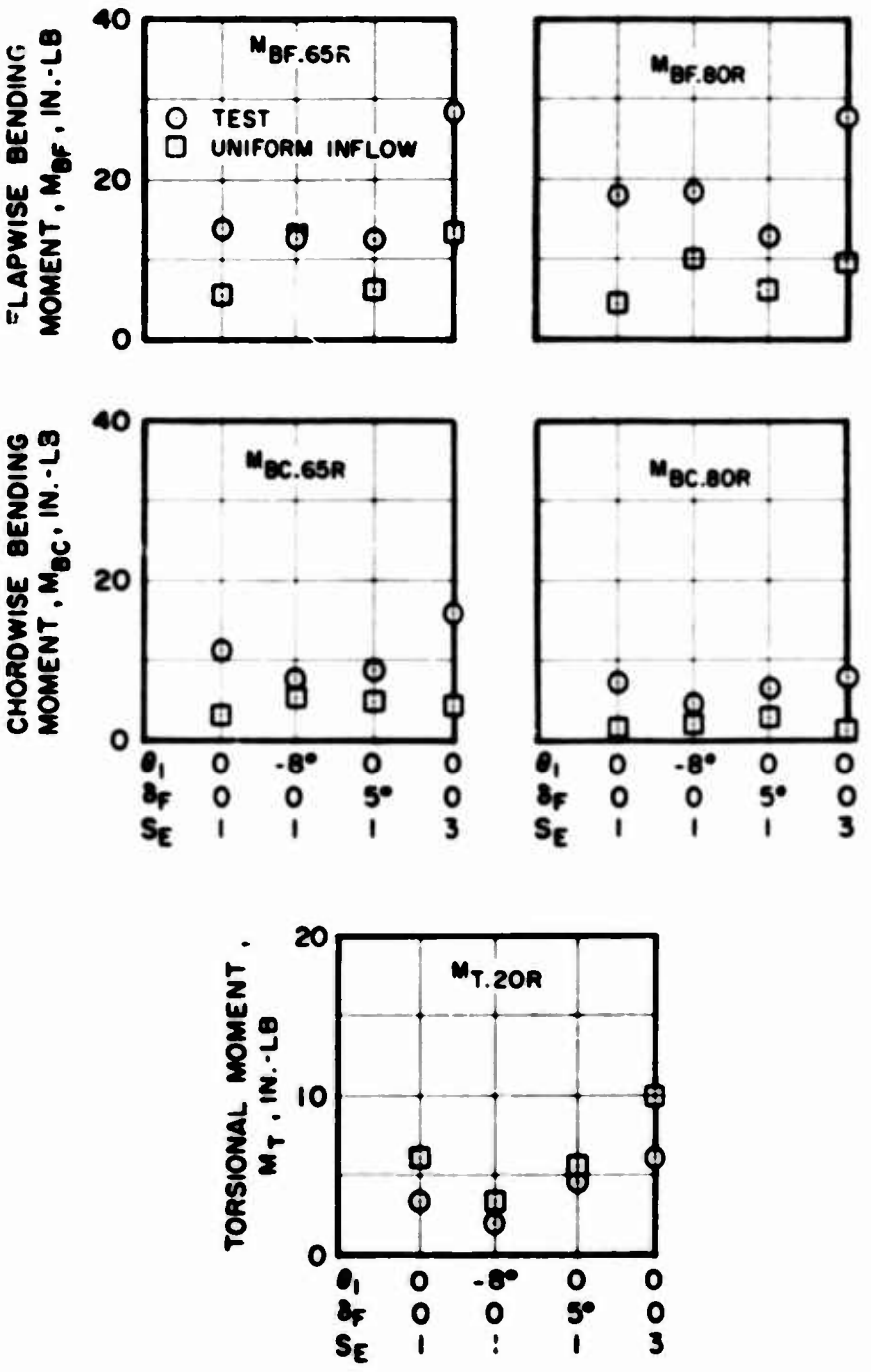

Figure 53. Concluded.

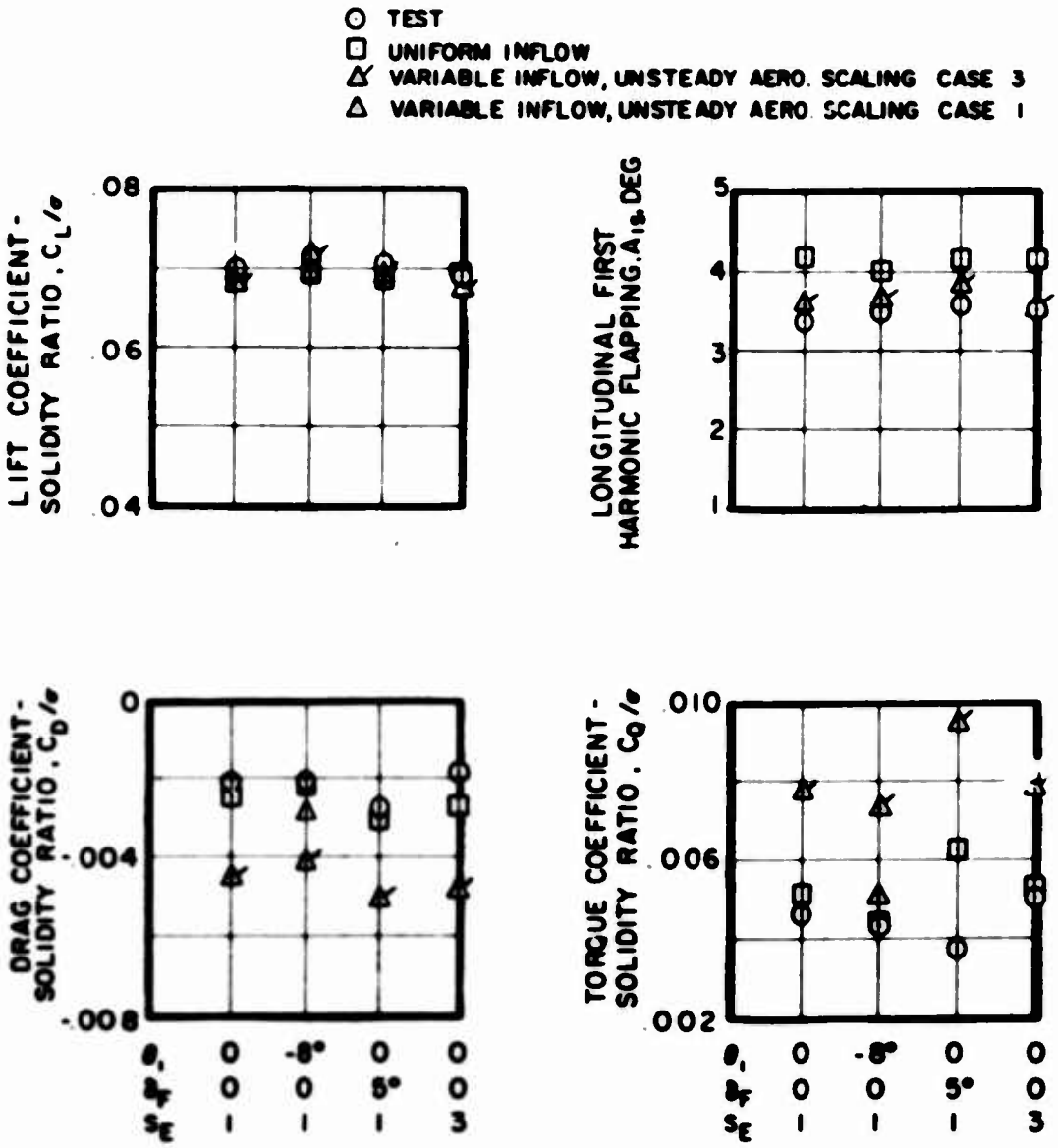

Figure 54. Correlation of Test and Calculated Data for Condition 36; V_s = 146 kn, μ = 0.35, α_s = -5 deg, a_{1s} = 3.6 deg, b_{1s} = 0 deg.

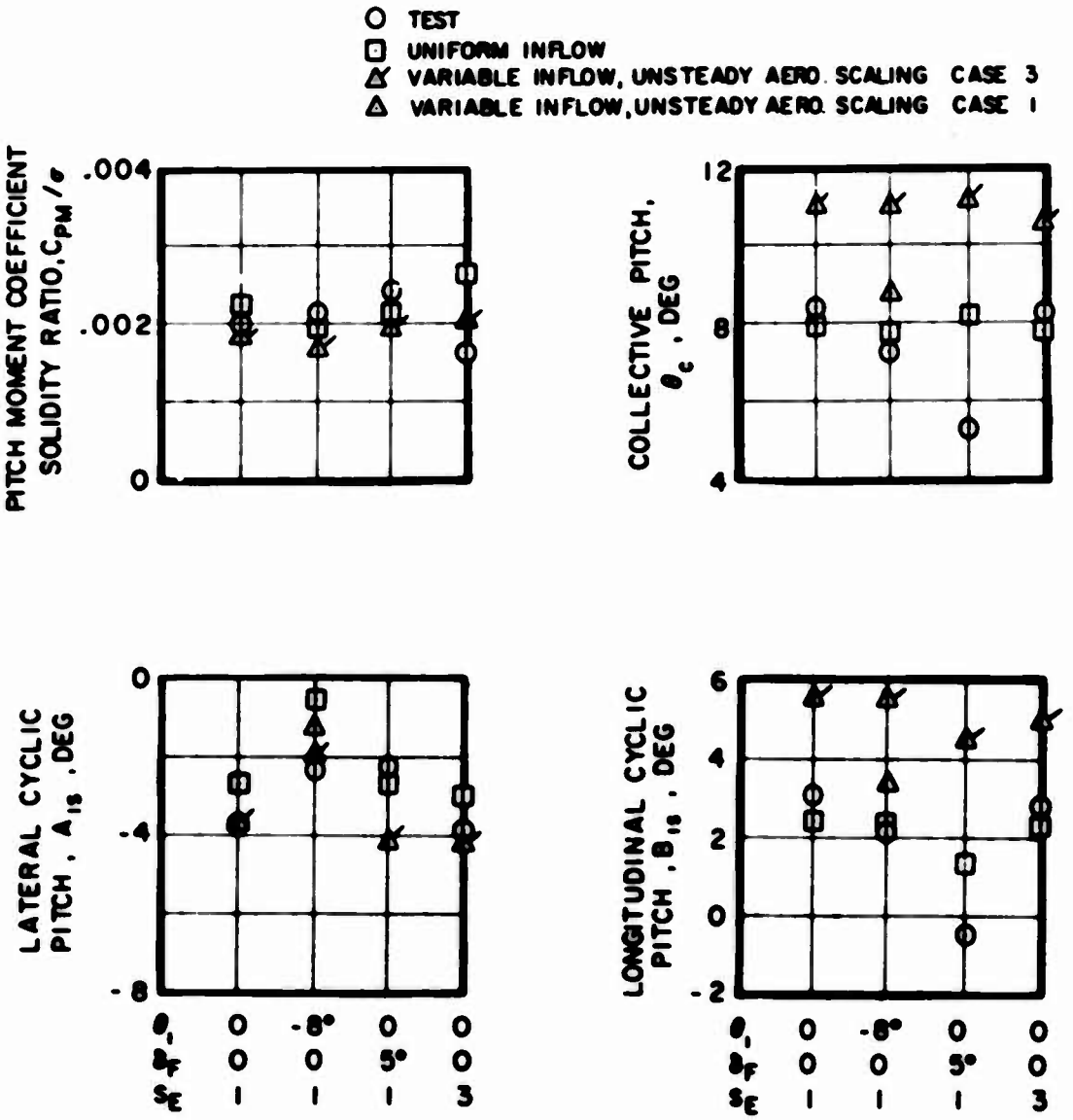

Figure 54. Continued.

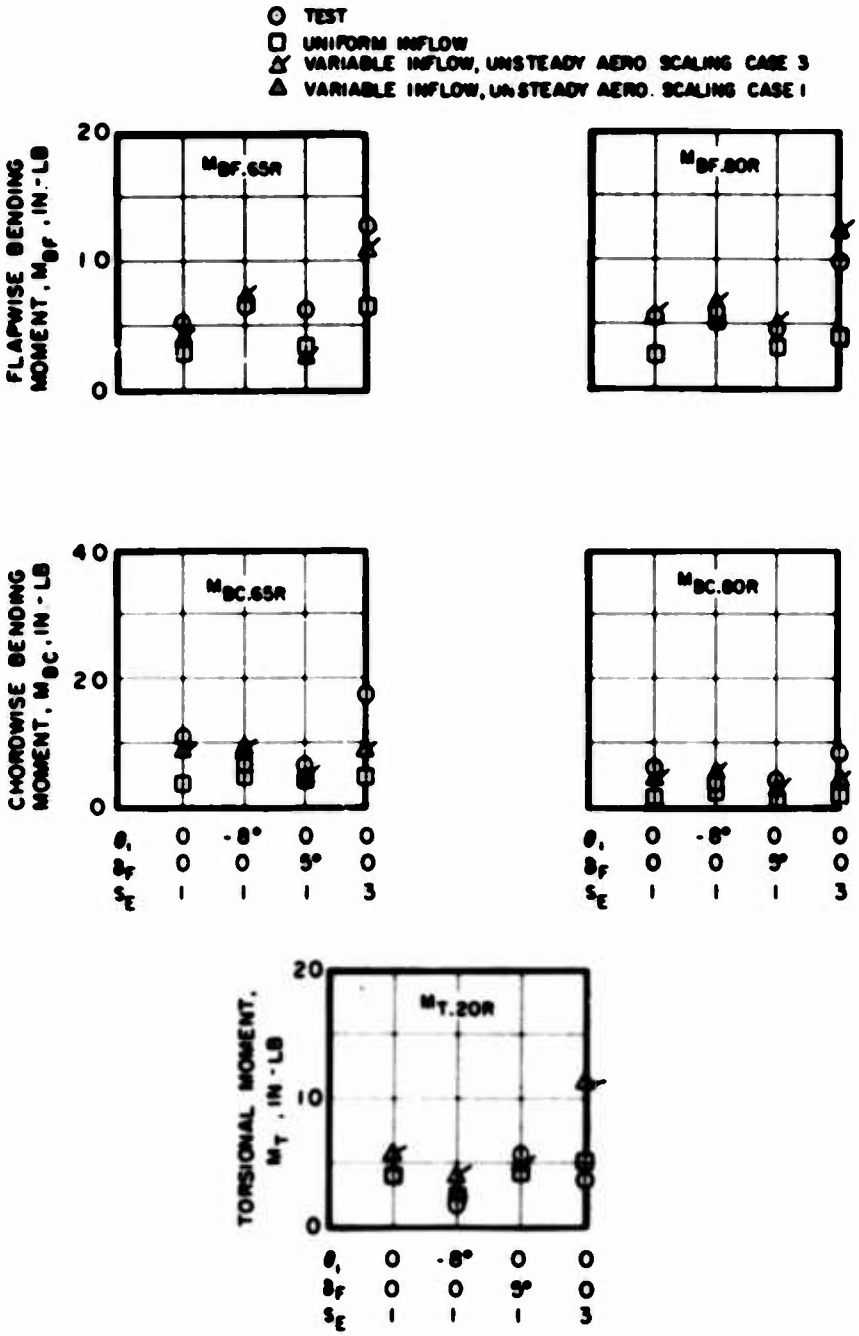

Figure 54. Concluded.

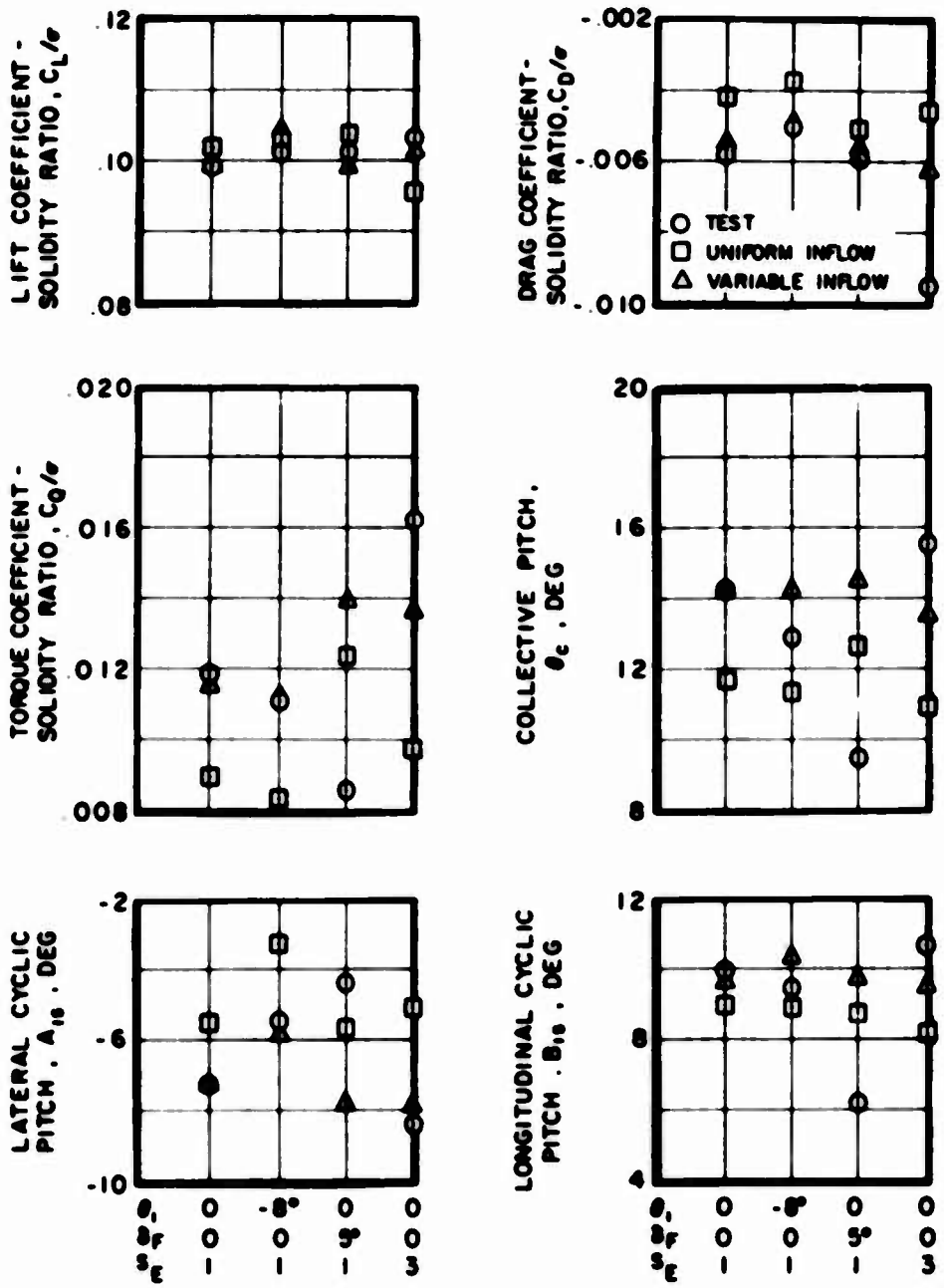

Figure 55. Correlation of Test and Calculated Data for Condition 71; V_s = 124 kn, μ = 0.30, α_s = 0 deg, $a_{1s} = b_{1s}$ = 0 deg.

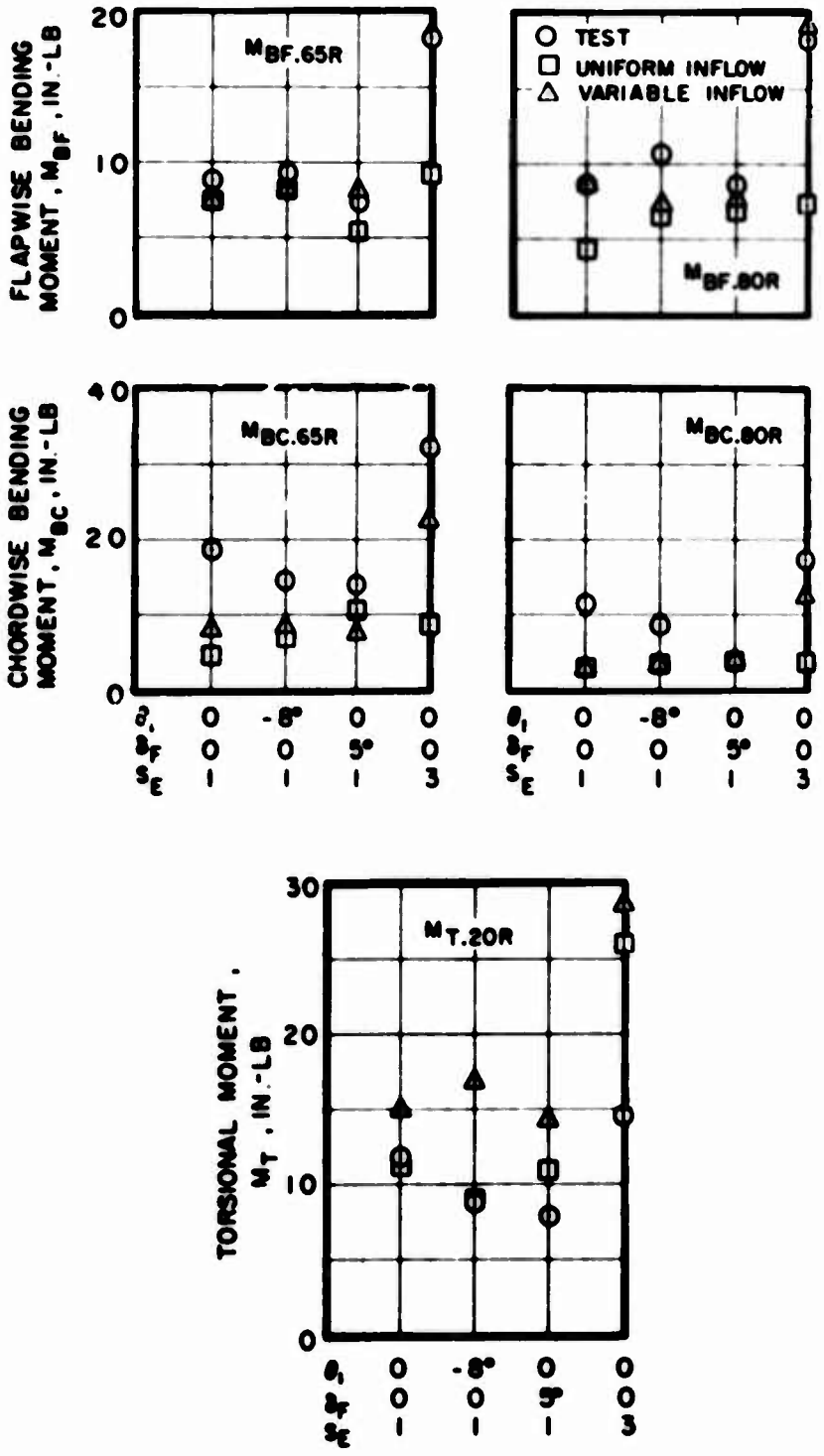

Figure 55. Concluded.

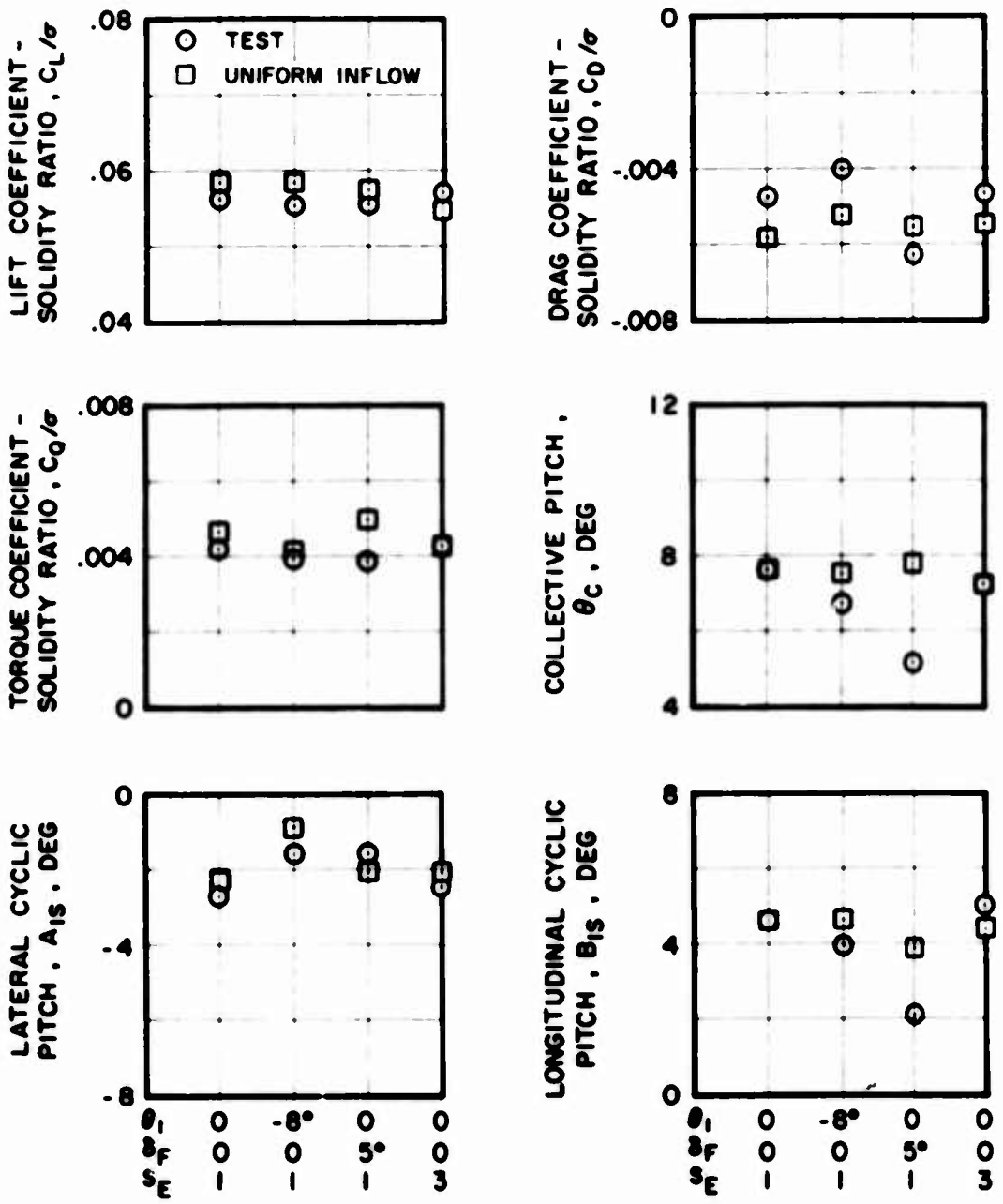

Figure 56. Correlation of Test and Calculated Data for Condition 80; V_s = 124 kn, μ = 0.30, α_s = -5 deg, a_{1s} = b_{1s} = 0 deg.

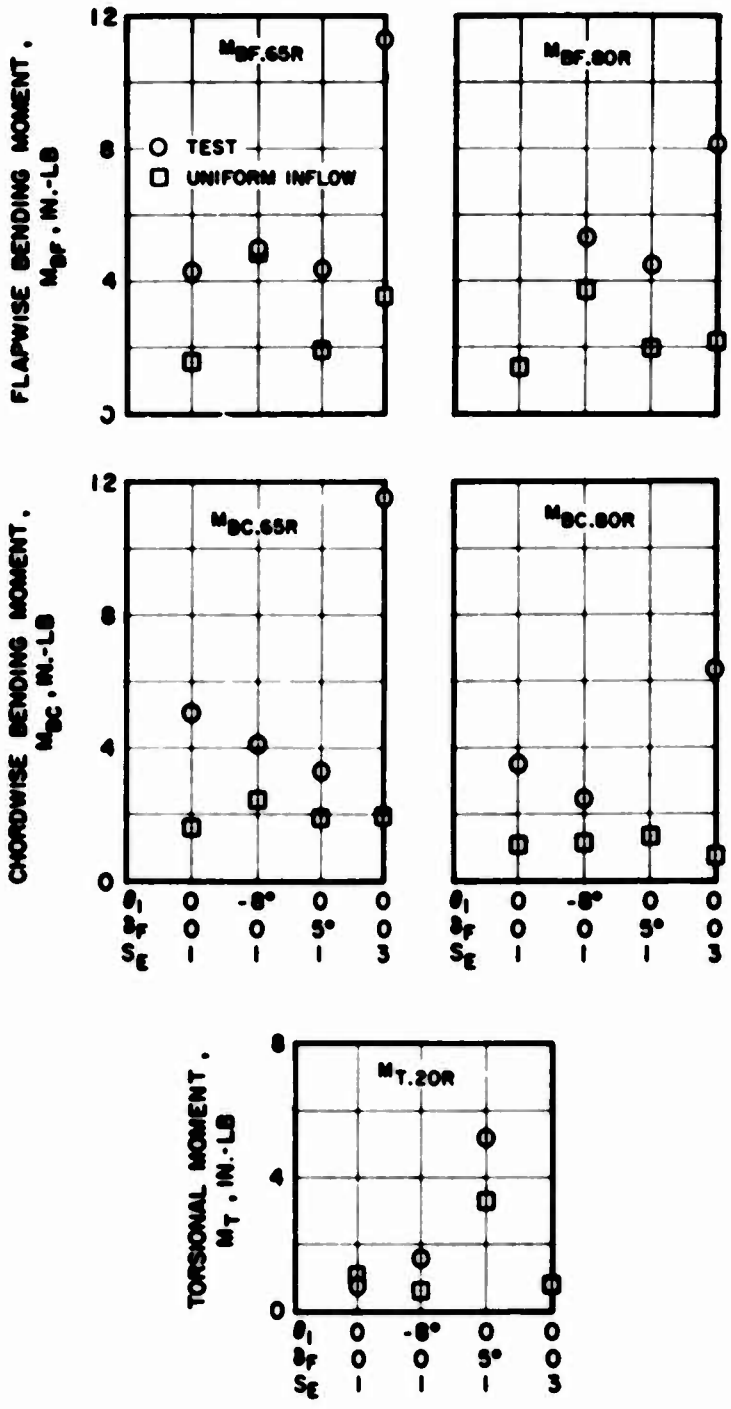

Figure 56. Concluded.

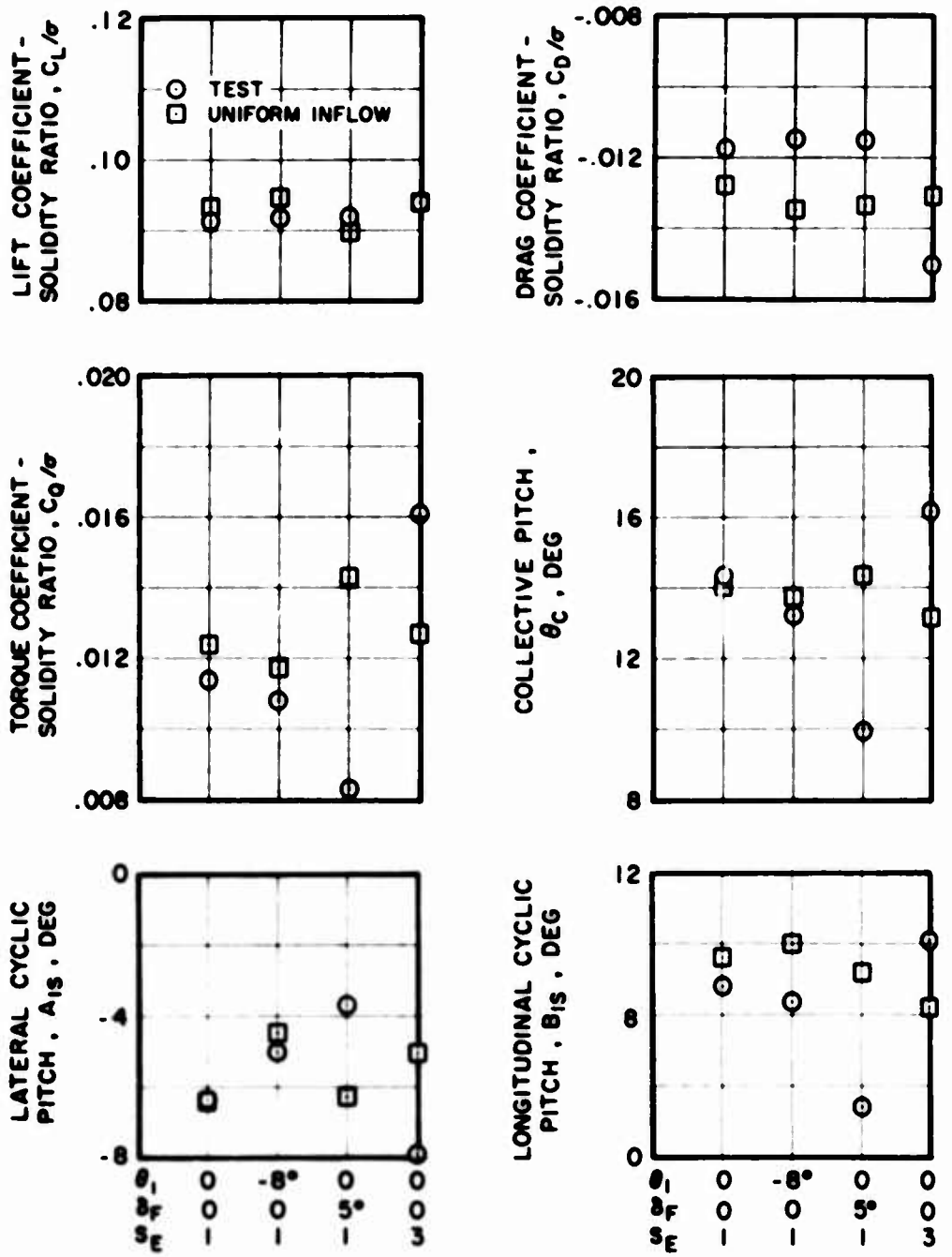

Figure 57. Correlation of Test and Calculated Data for Condition 82; V_s = 124 kn, μ = 0.30, α_s = -5 deg, a_{1s} = b_{1s} = 0 deg.

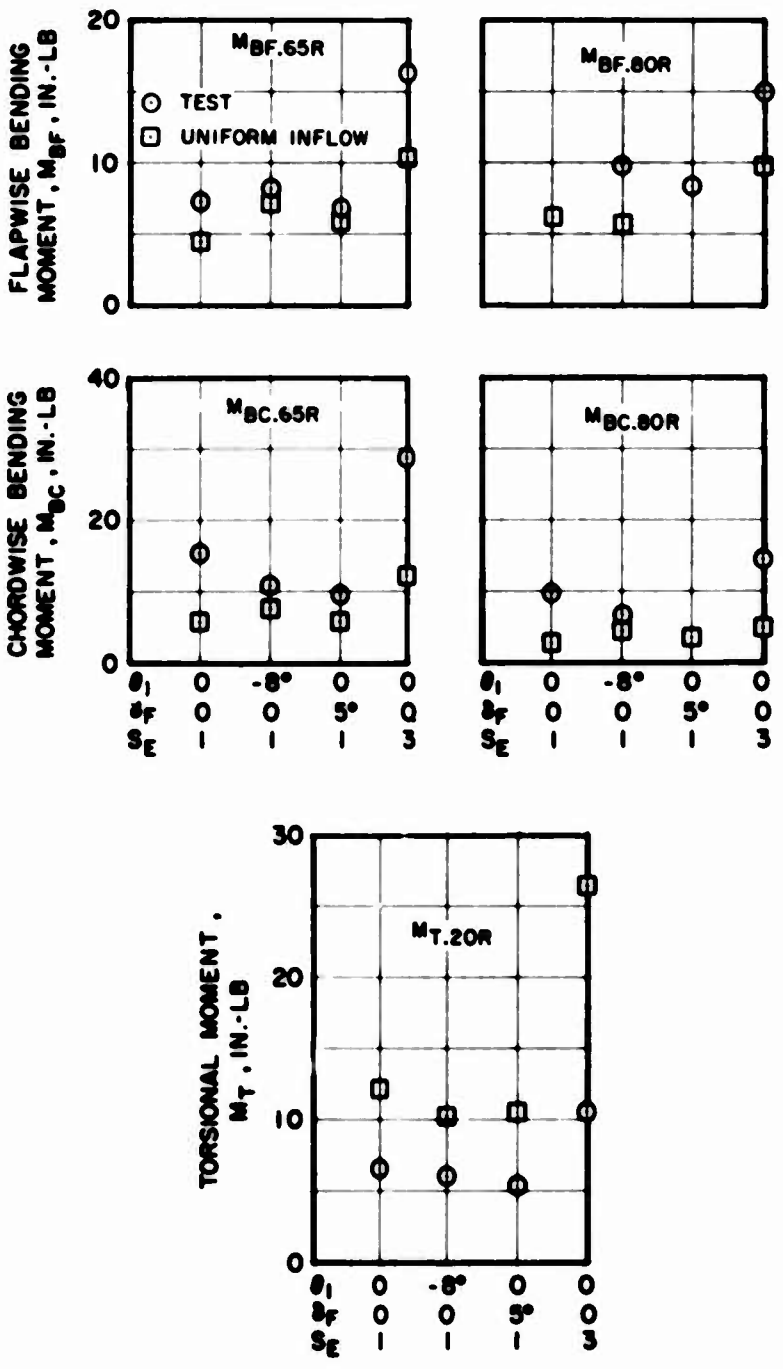

Figure 57. Concluded.

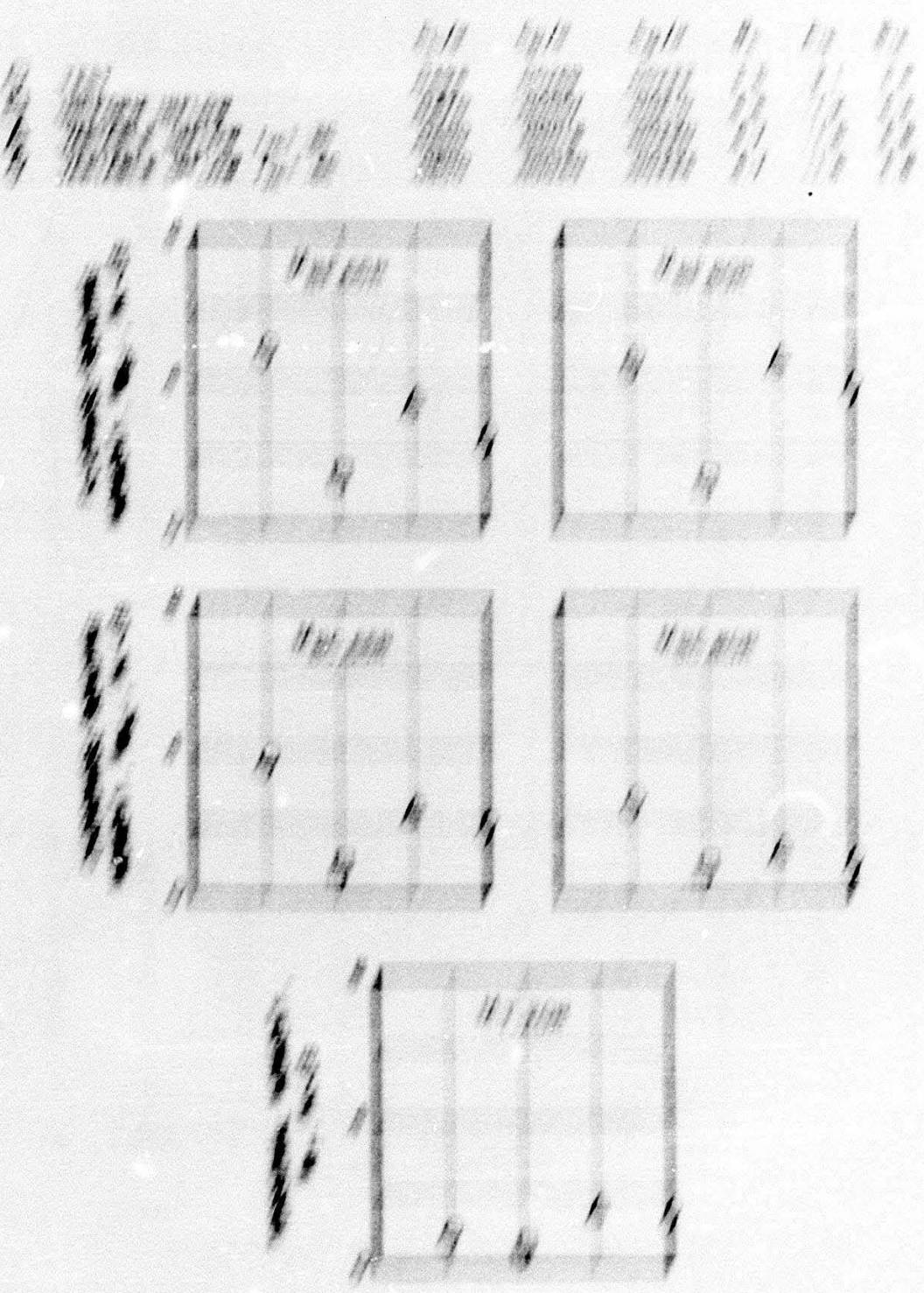

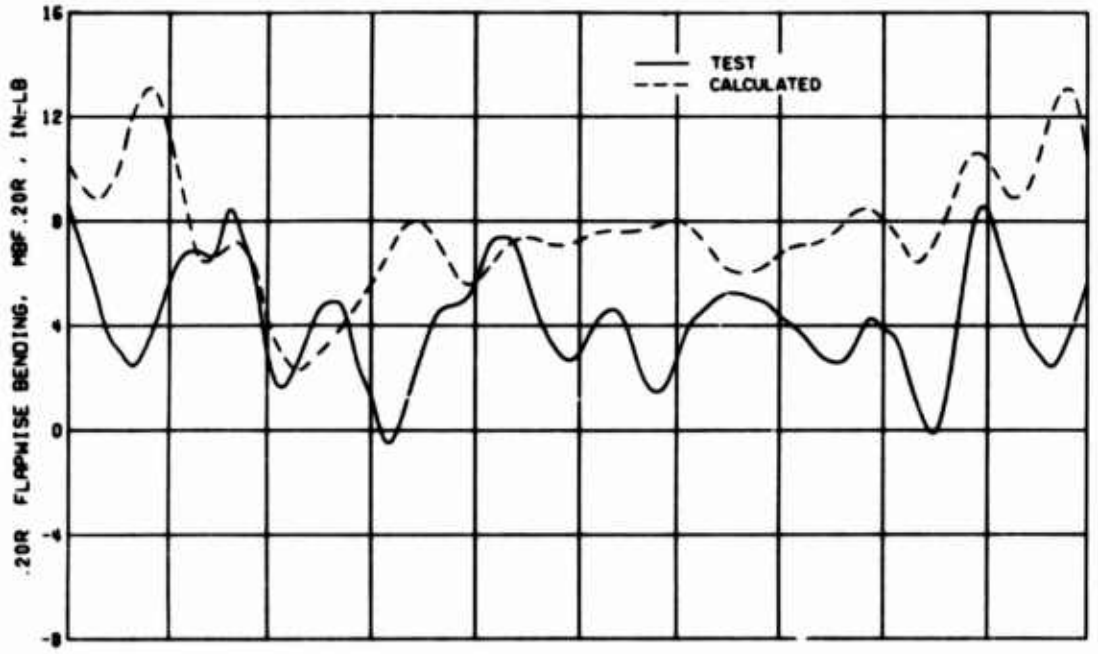

(a) .20R Flapwise Bending, Condition 7

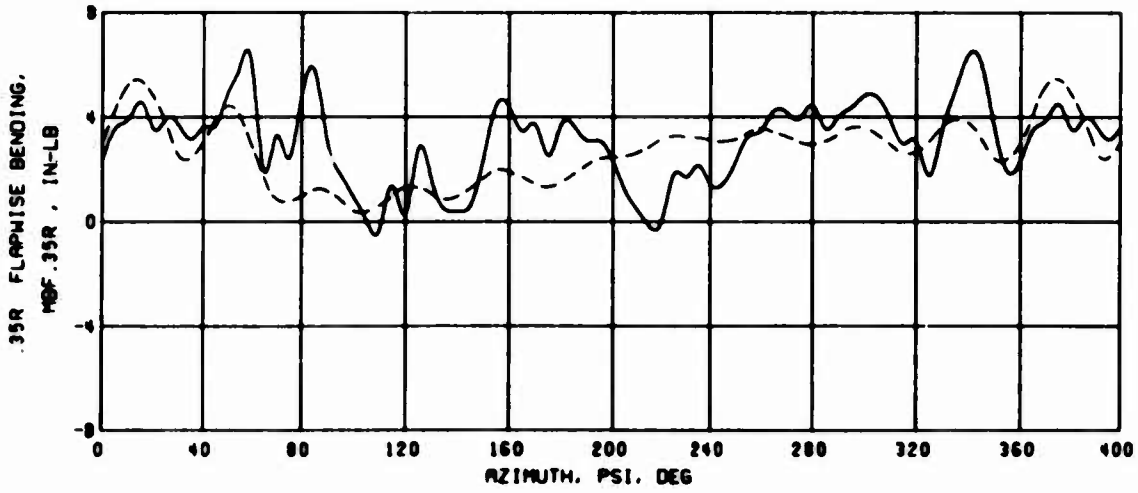

(b) .35R Flapwise Bending, Condition 7

Figure 59. Correlation of Test and Calculated Flapwise Bending With Uniform Inflow; θ_1 = 0 deg, δ_F = 0 deg, S_E = 1.

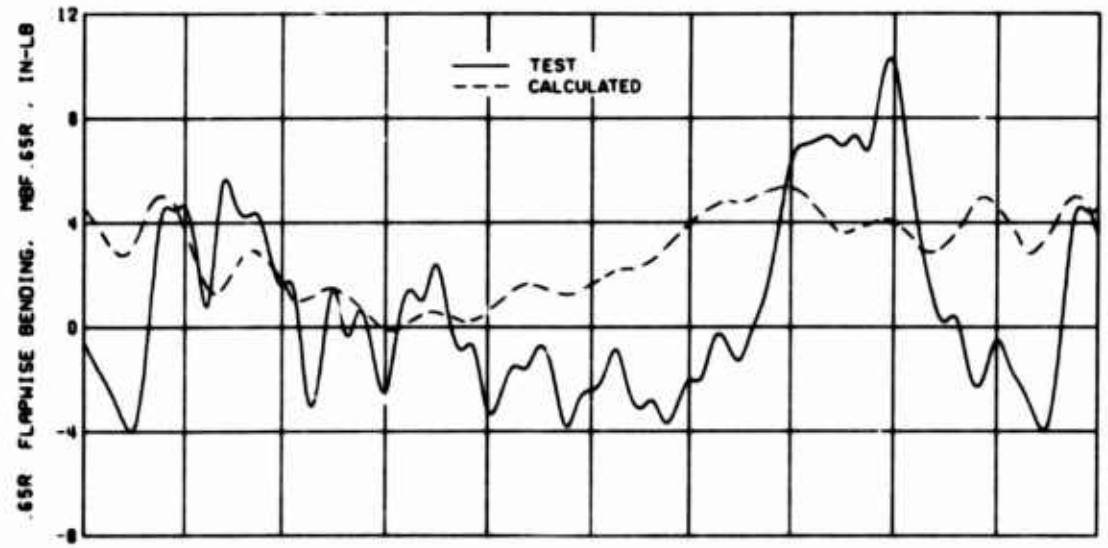

(c) .65R Flapwise Bending, Condition 7

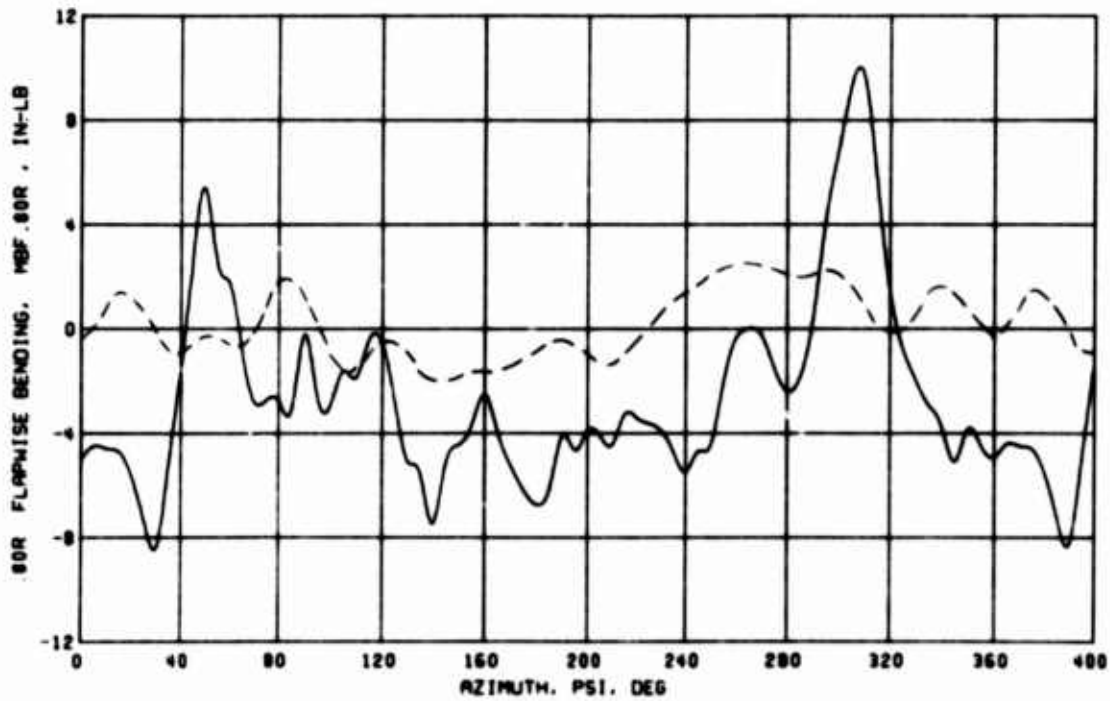

(d) .80R Flapwise Bending, Condition 7

Figure 59. Continued.

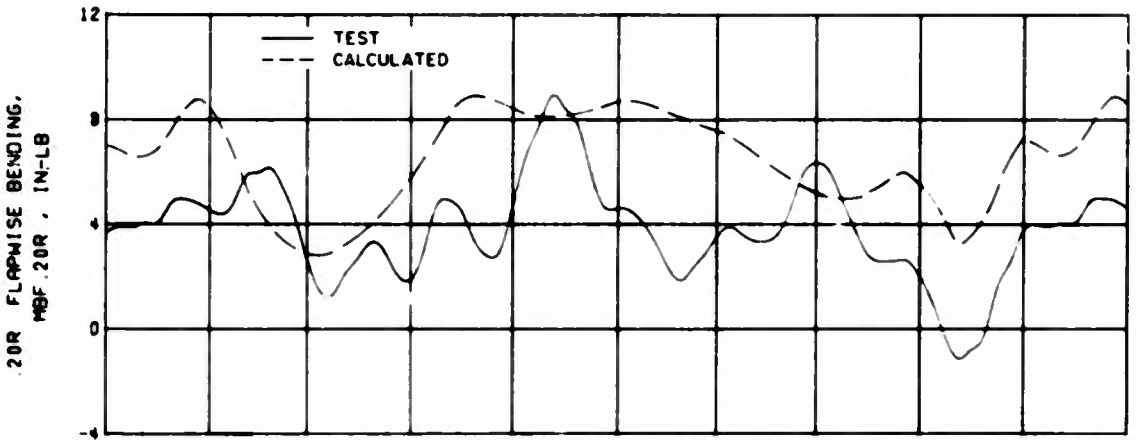

(e) .20R Flapwise Bending, Condition 36

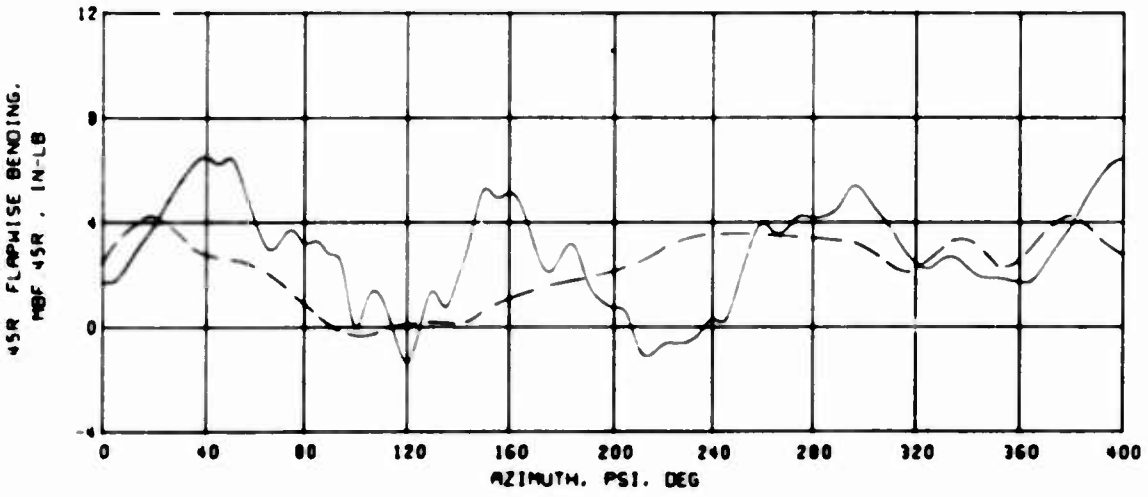

(f) .45R Flapwise Bending, Condition 36

Figure 59. Continued.

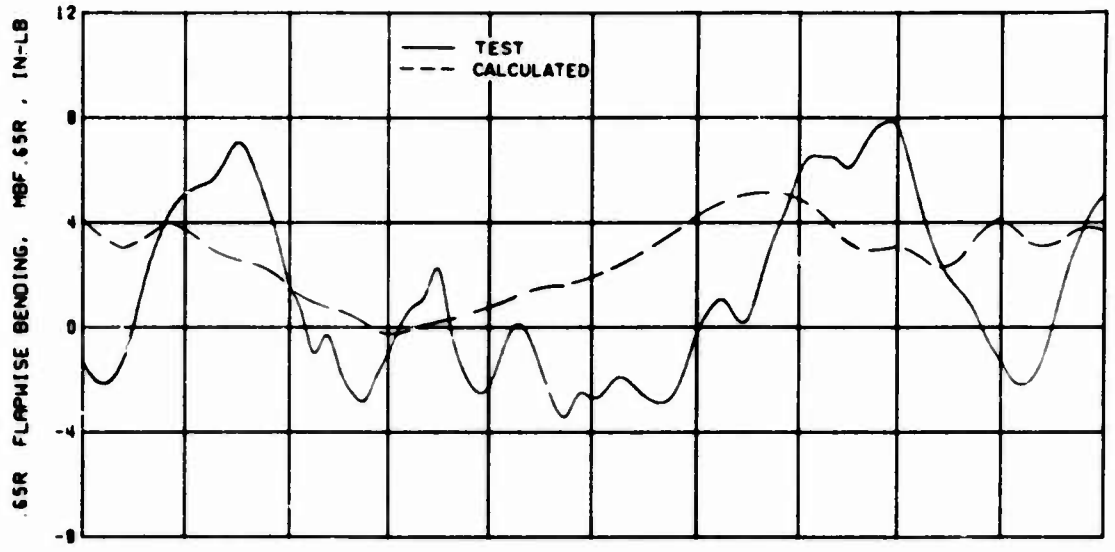

(g) .65R Flapwise Bending, Condition 36

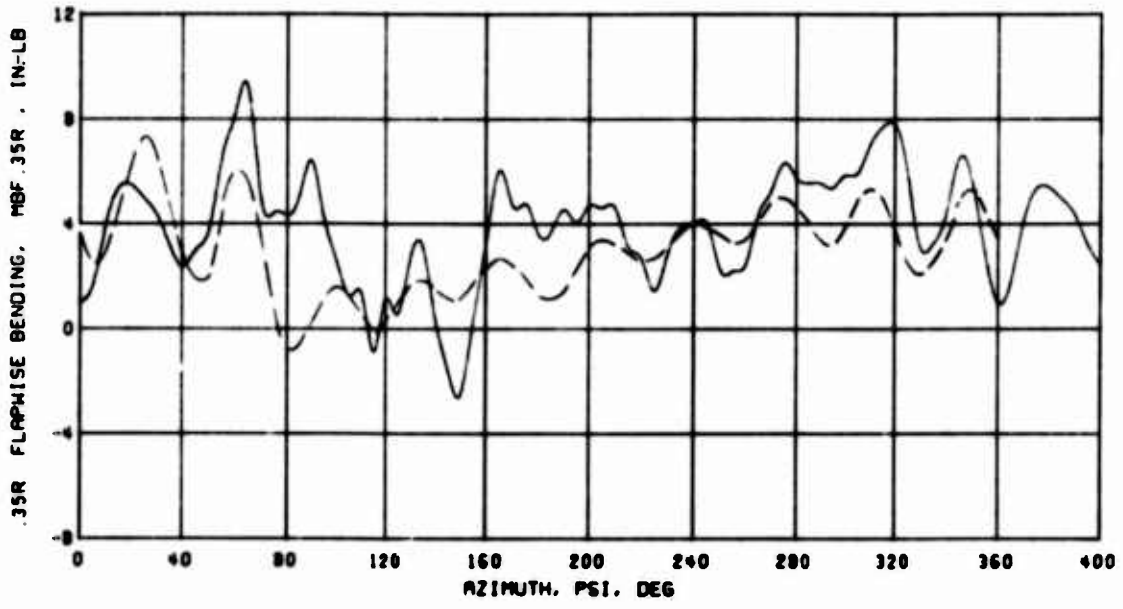

(h) .35R Flapwise Bending, Condition 71

Figure 59. Continued.

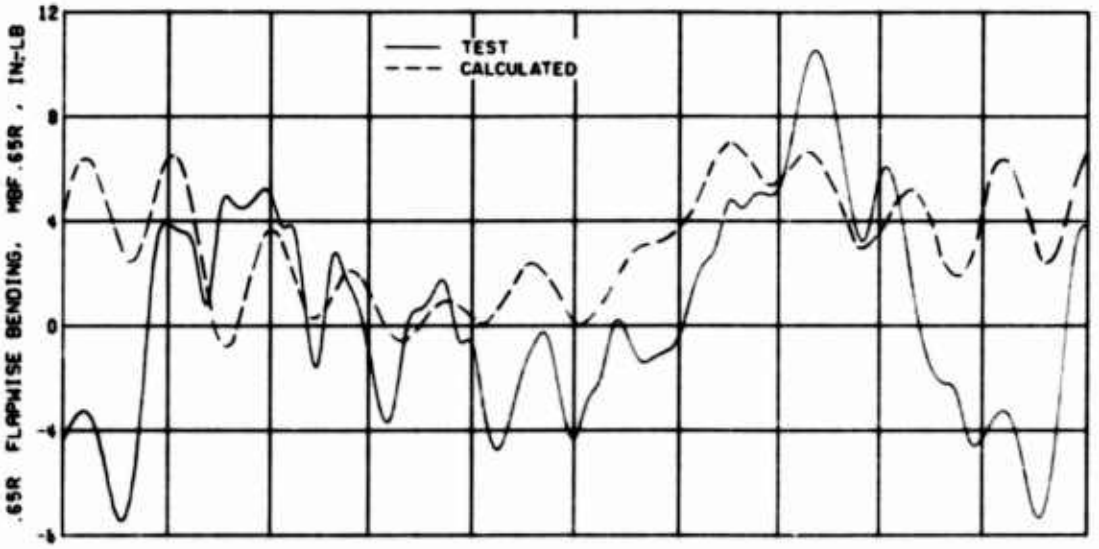

(i) .65R Flapwise Bending, Condition 71

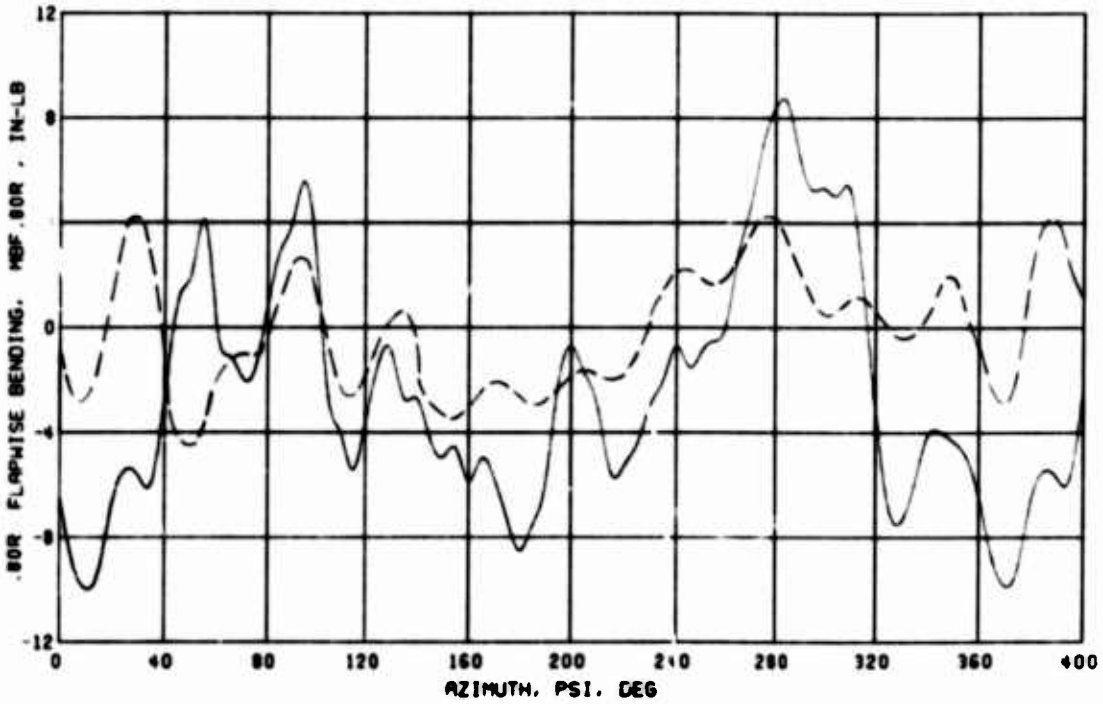

(j) .80R Flapwise Bending, Condition 71

Figure 59. Continued.

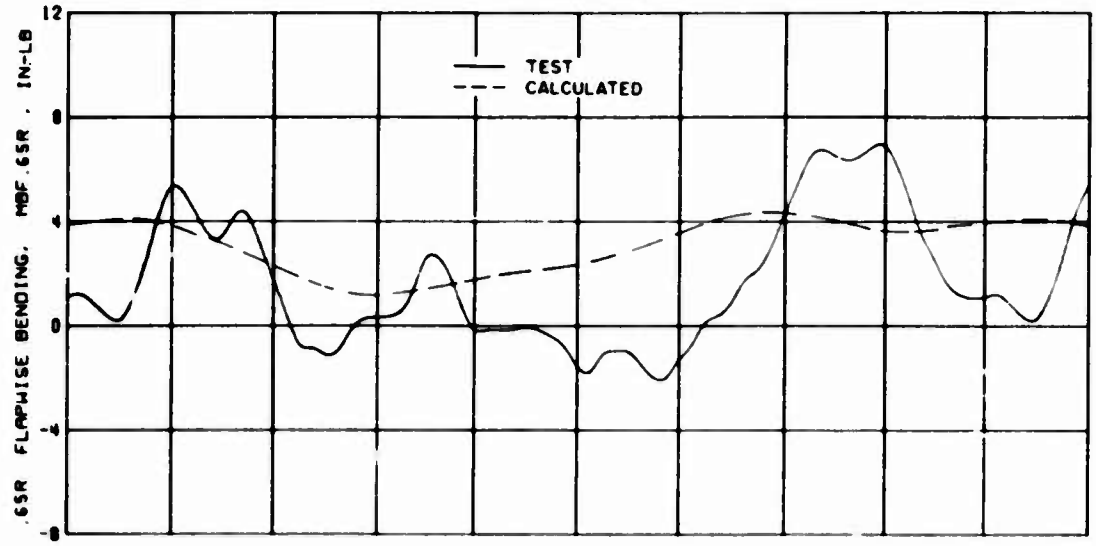

(k) .65R Flapwise Bending, Condition 80

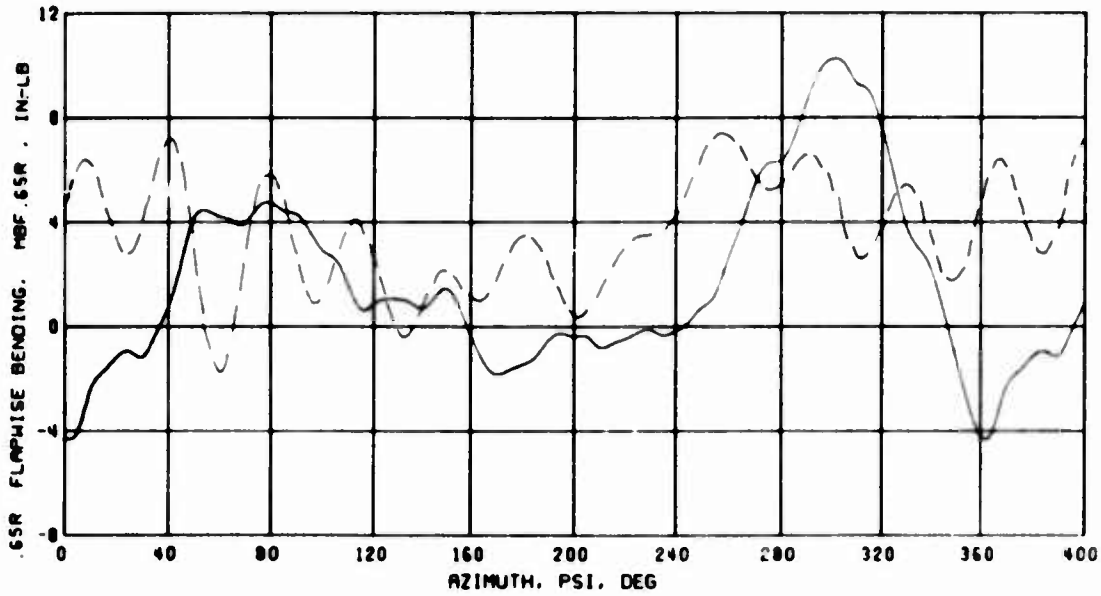

(l) .65R Flapwise Bending, Condition 82

Figure 59. Concluded.

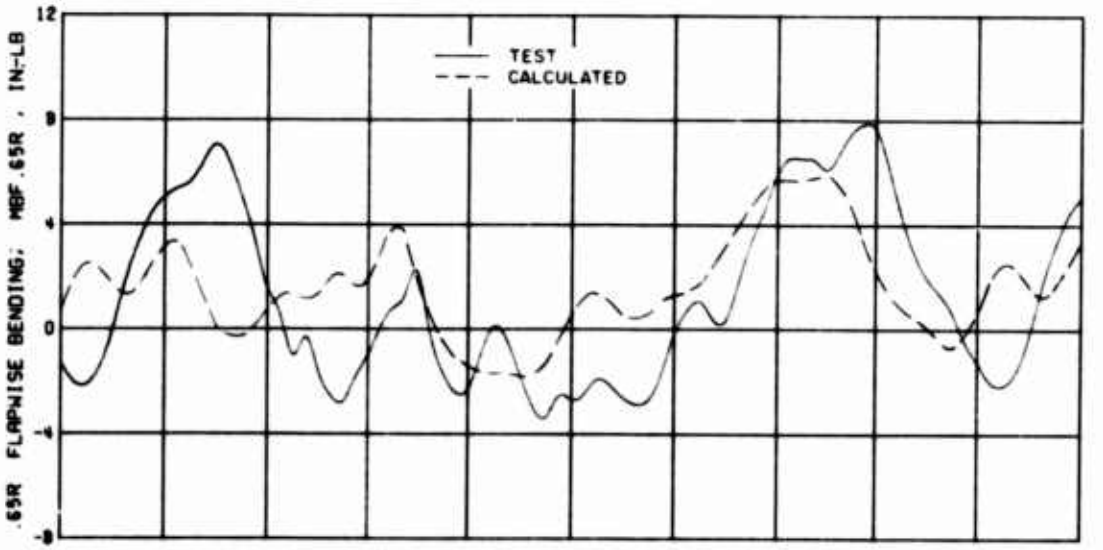

(a) .65R Flapwise Bending, Condition 36

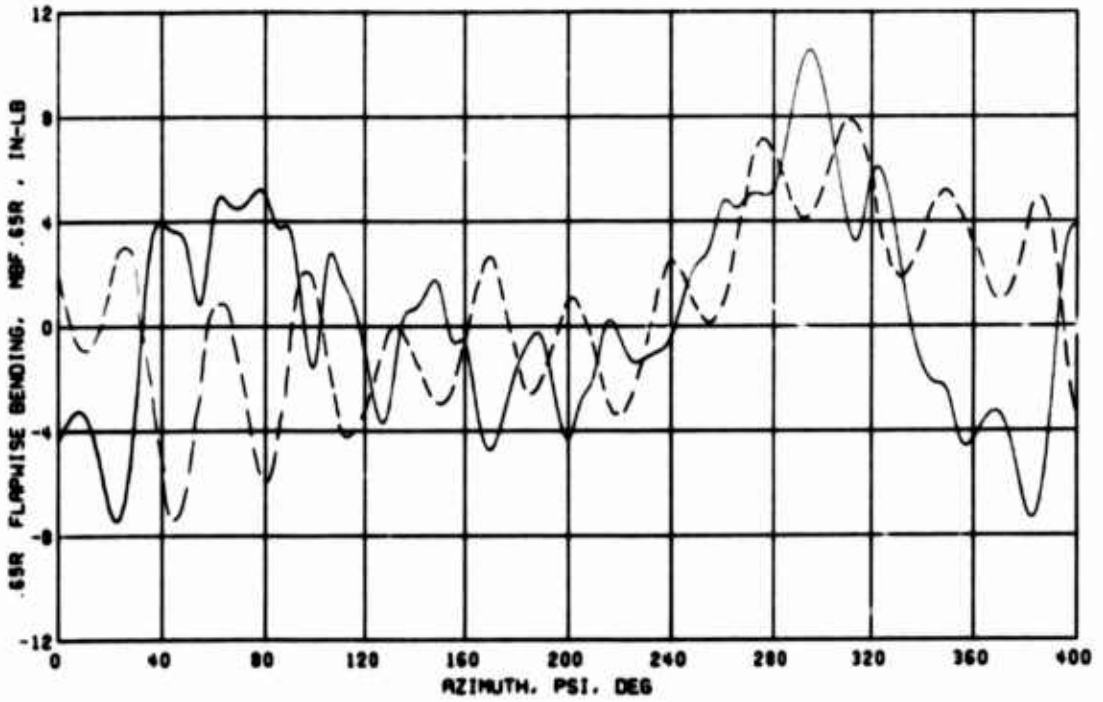

(b) .65R Flapwise Bending, Condition 71

Figure 60. Correlation of Test and Calculated Flapwise Bending With Variable Inflow; θ_1 = 0 deg, δ_F = 0 deg, S_E = 1.

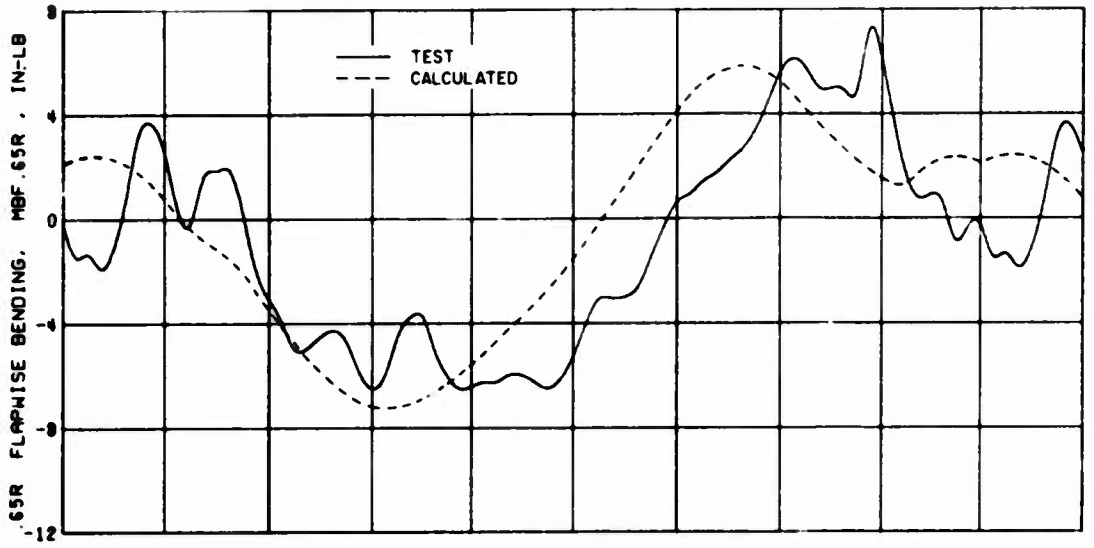

(a) .65R Flapwise Bending, Condition 7

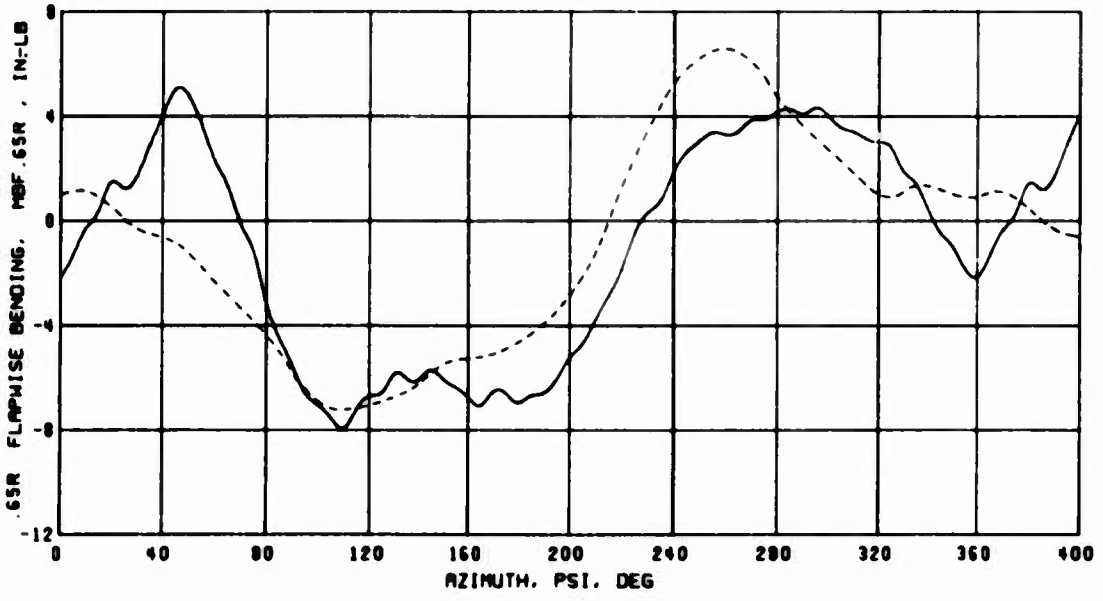

(b) .65R Flapwise Bending, Condition 36

Figure 61. Correlation of Test and Calculated Flapwise Bending With Uniform Inflow; θ_1 = -8 deg, δ_F = 0 deg, S_E = 1.

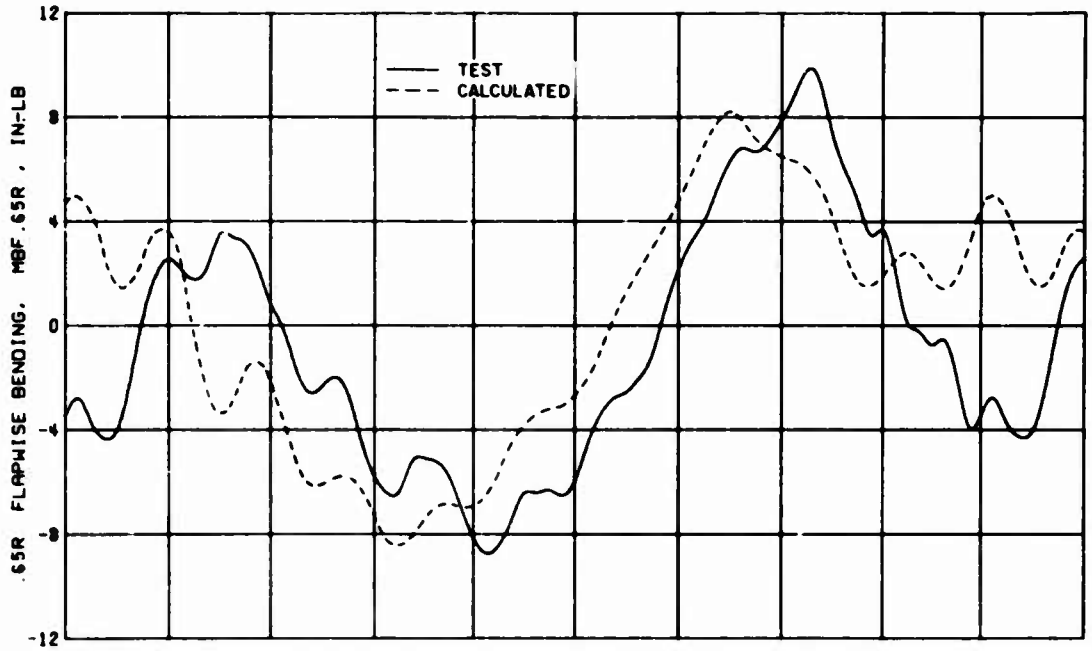

(c) .65R Flapwise Bending, Condition 71

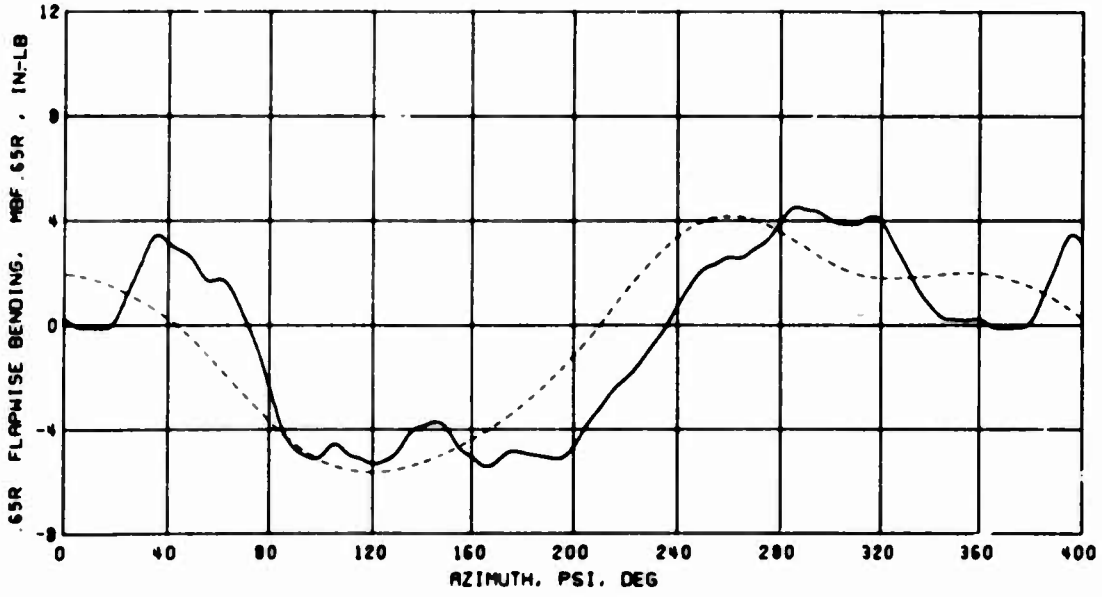

(d) .65R Flapwise Bending, Condition 80

Figure 61. Continued.

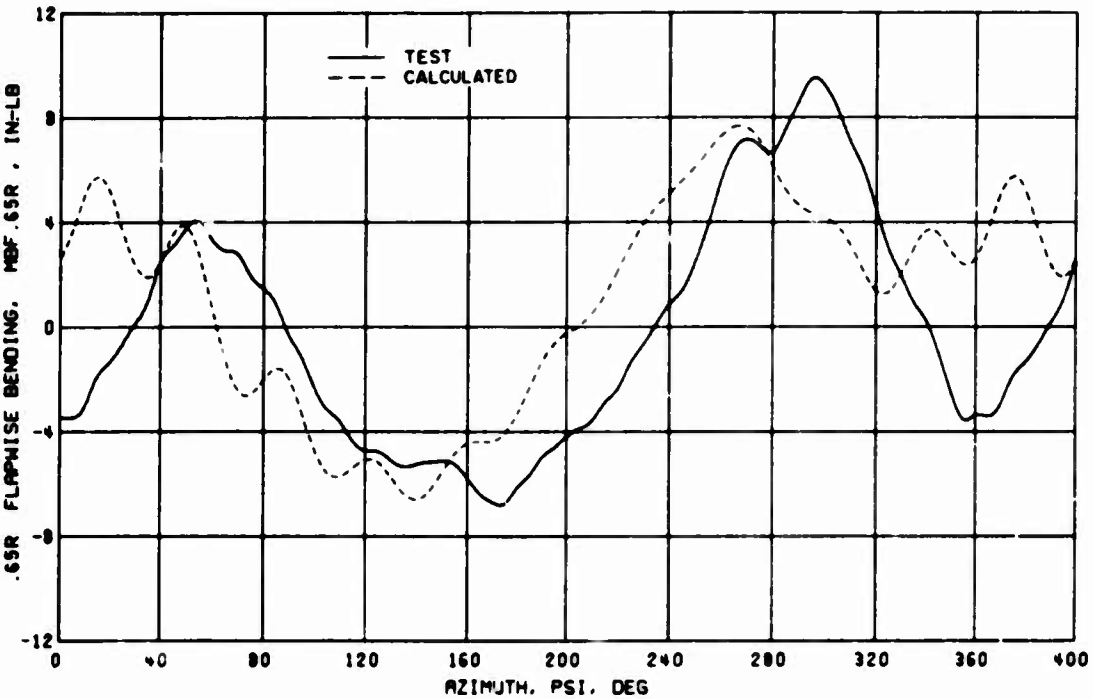

(e) .65R Flapwise Bending, Condition 82

Figure 61. Concluded.

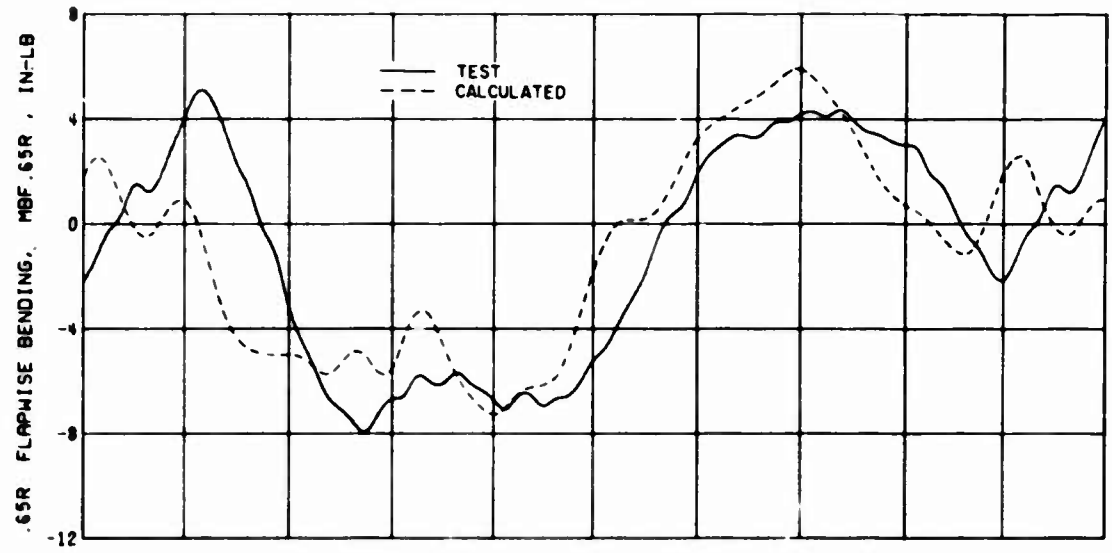

(a) .65R Flapwise Bending, Condition 36, Unsteady Aerodynamic Scaling Case 3

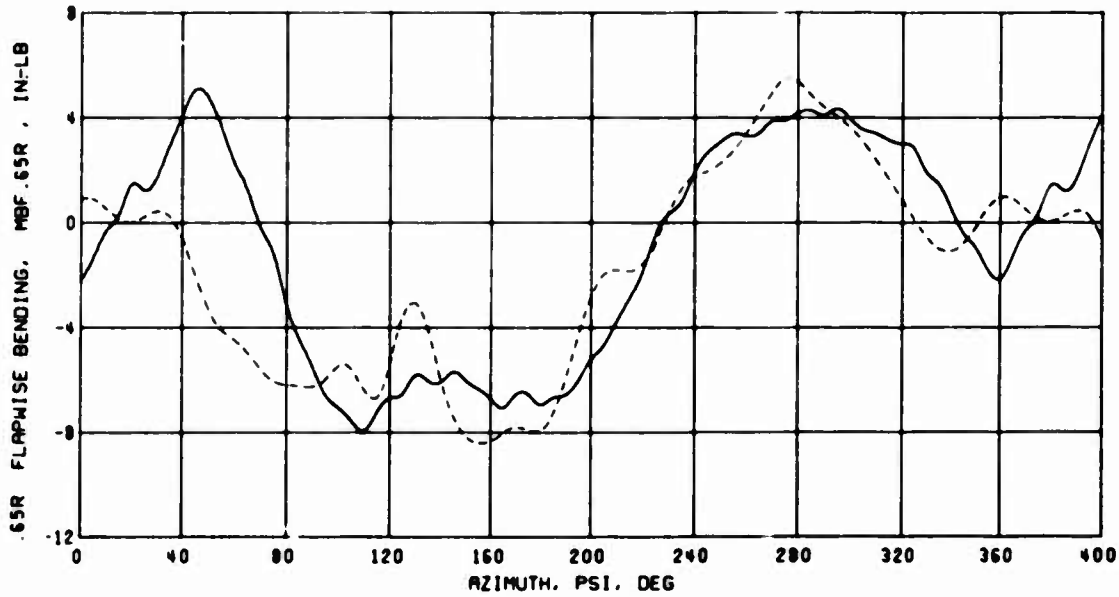

(b) .65R Flapwise Bending, Condition 36, Unsteady Aerodynamic Scaling Case 1

Figure 62. Correlation of Test and Calculated Flapwise Bending With Variable Inflow; θ_1 = -8 deg, δ_F = 0 deg, S_E = 1.

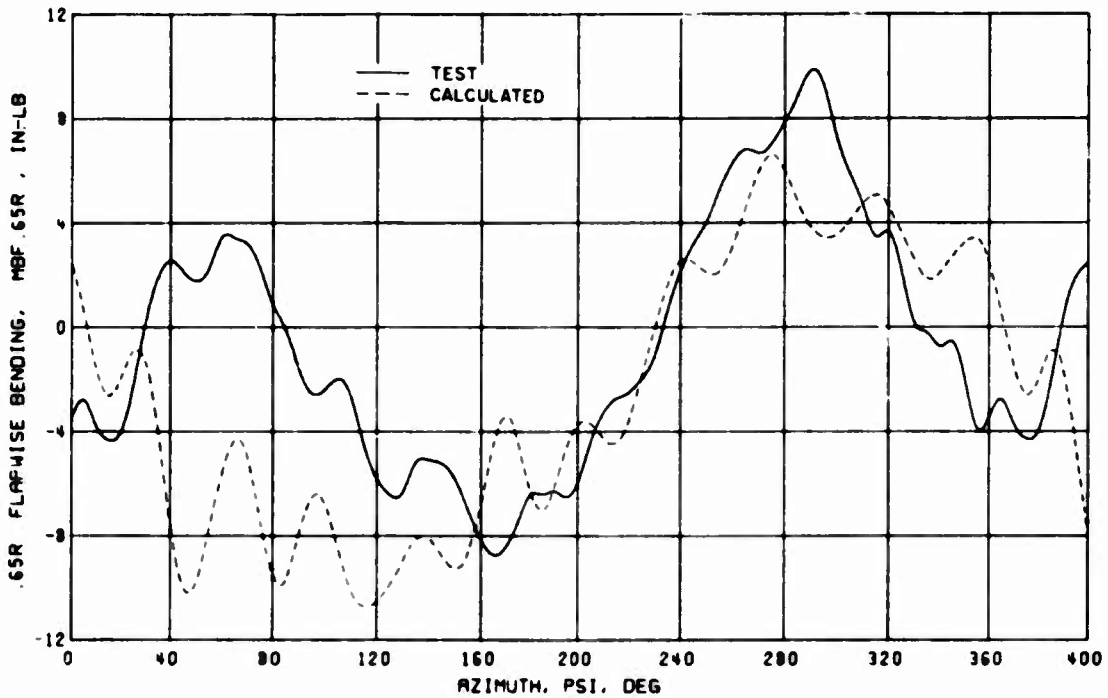

(c) .65R Flapwise Bending, Condition 71, Unsteady Aerodynamic Scaling Case 1

Figure 62. Concluded.

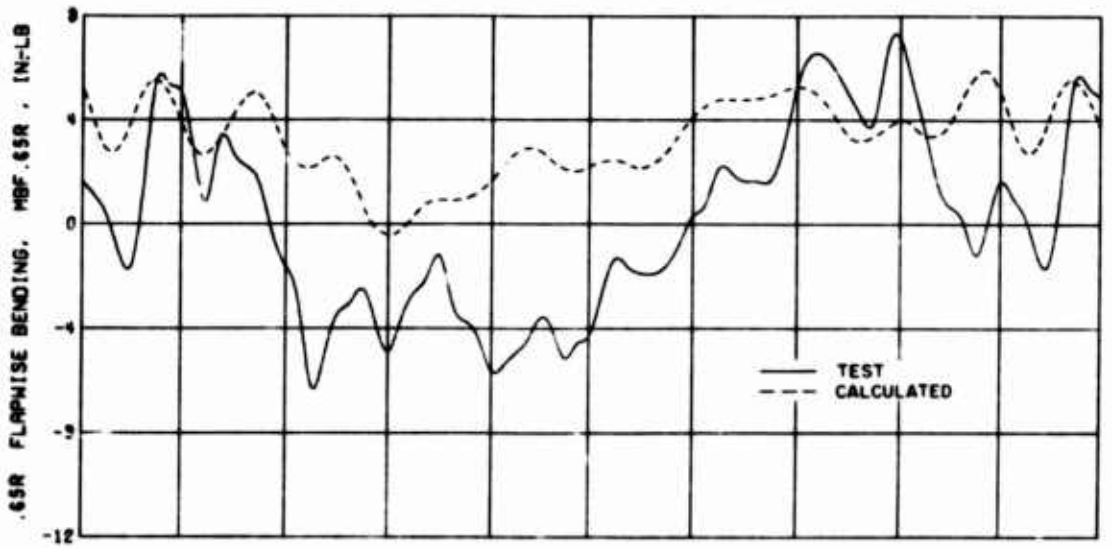

(a) .65R Flapwise Bending, Condition 7

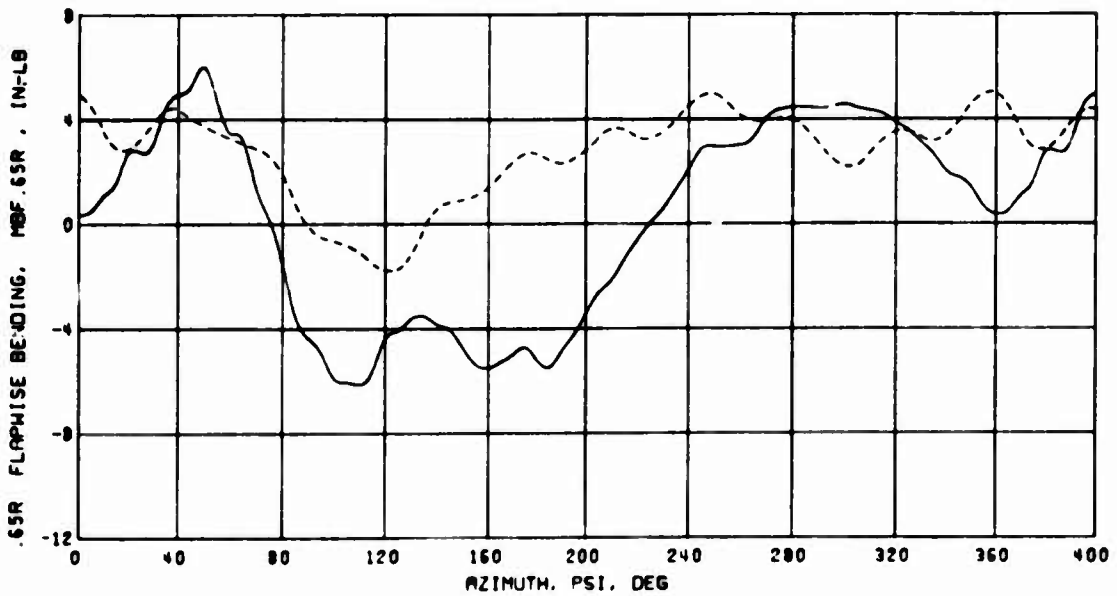

(b) .65R Flapwise Bending, Condition 36

Figure 63. Correlation of Test and Calculated Flapwise Bending With Uniform Inflow; θ_1 = 0 deg, δ_F = 5 deg, S_E = 1.

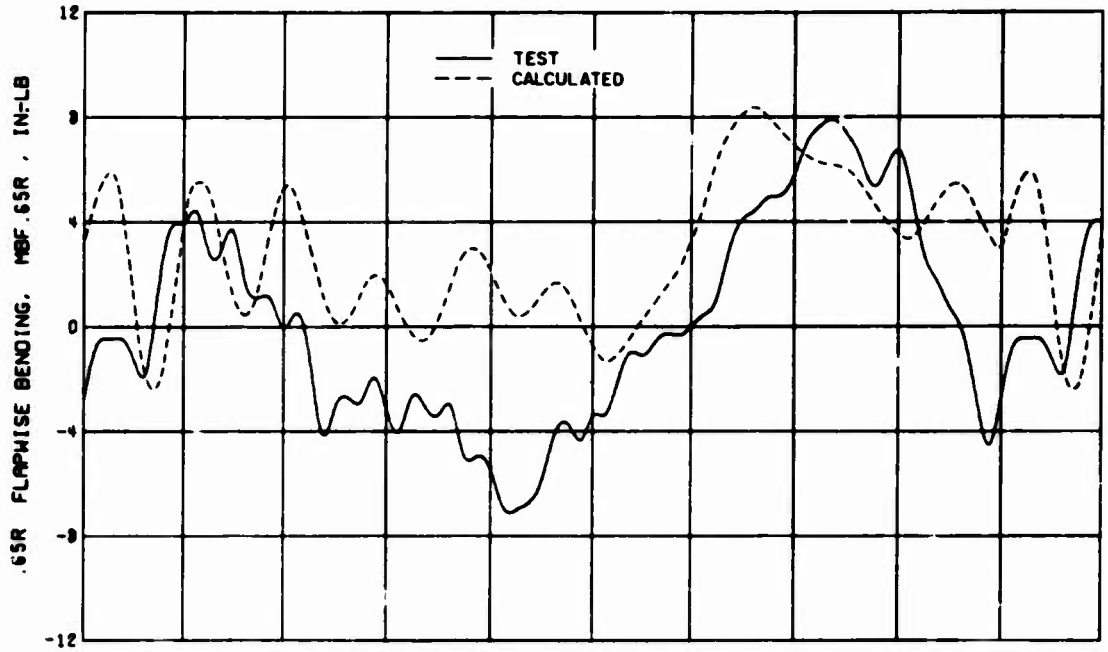

(c) .65R Flapwise Bending, Condition 71

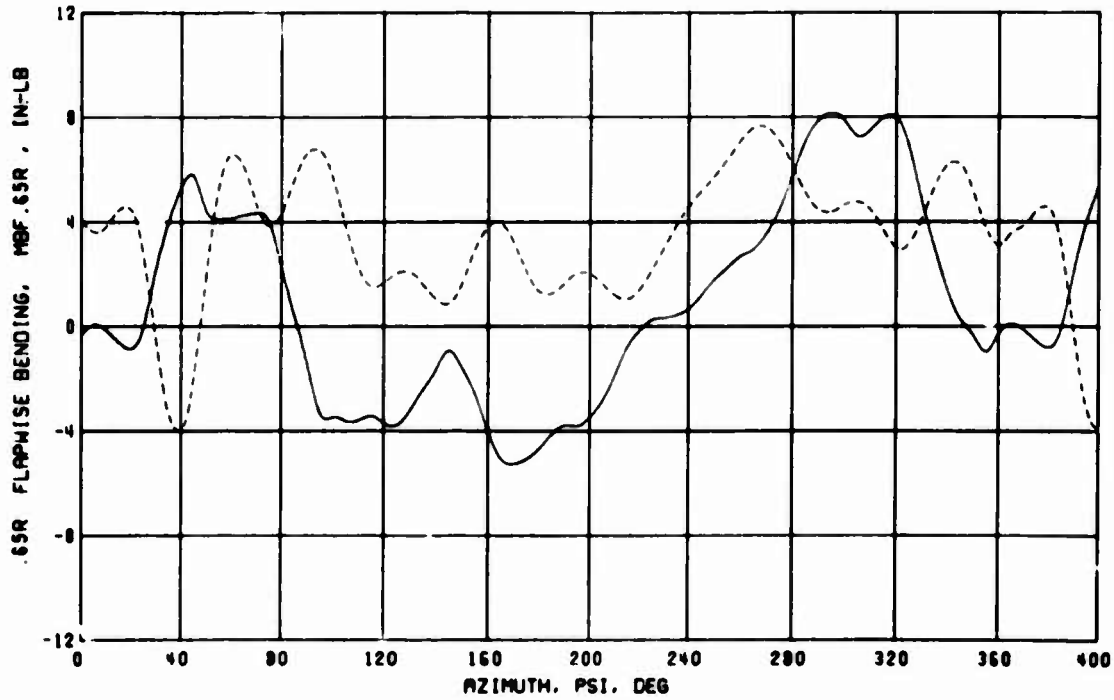

(d) .65R Flapwise Bending, Condition 82

Figure 63. Concluded.

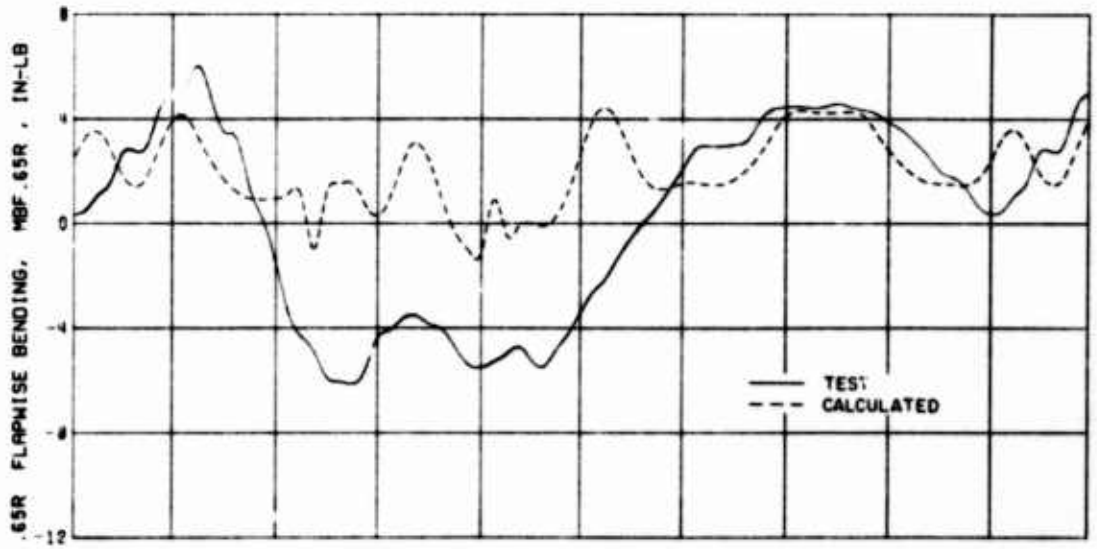

(a) .65R Flapwise Bending, Condition 36

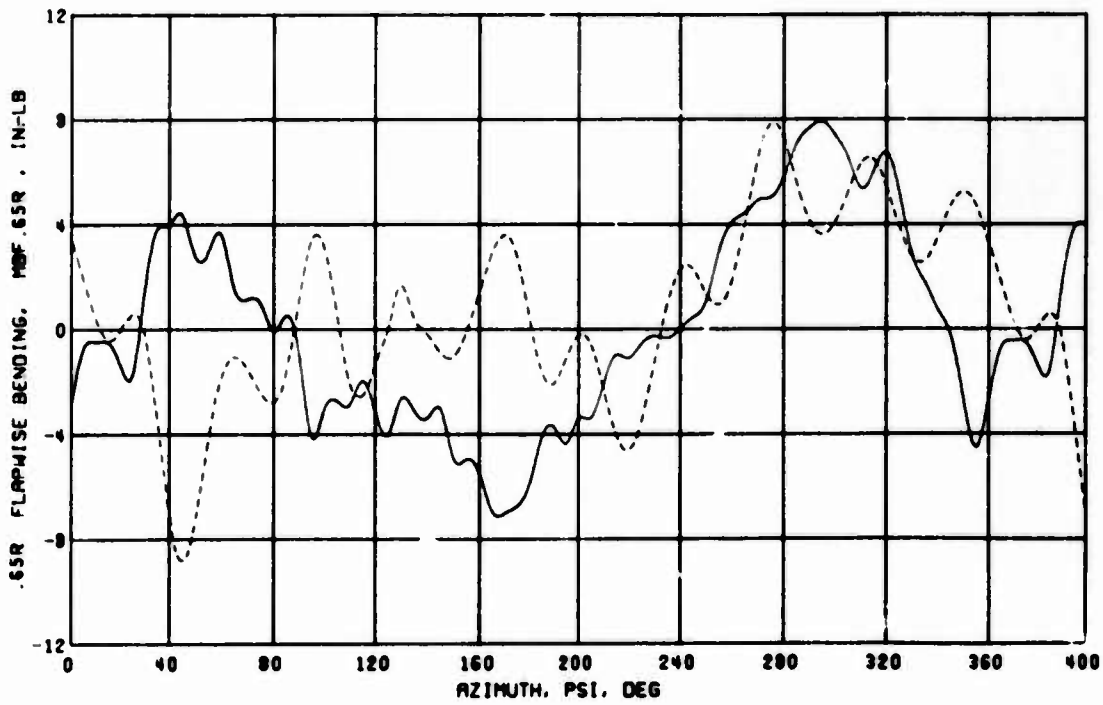

(b) .65R Flapwise Bending, Condition 71

Figure 64. Correlation of Test and Calculated Flapwise Bending With Variable Inflow; θ_1 = 0 deg, δ_T = 5 deg, S_E = 1.

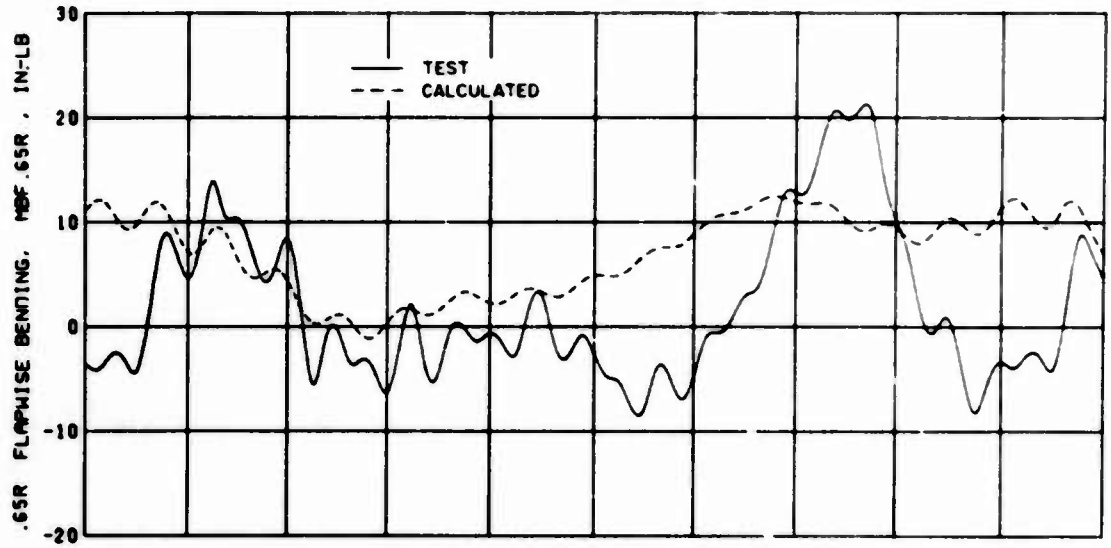

(a) .65R Flapwise Bending, Condition 7

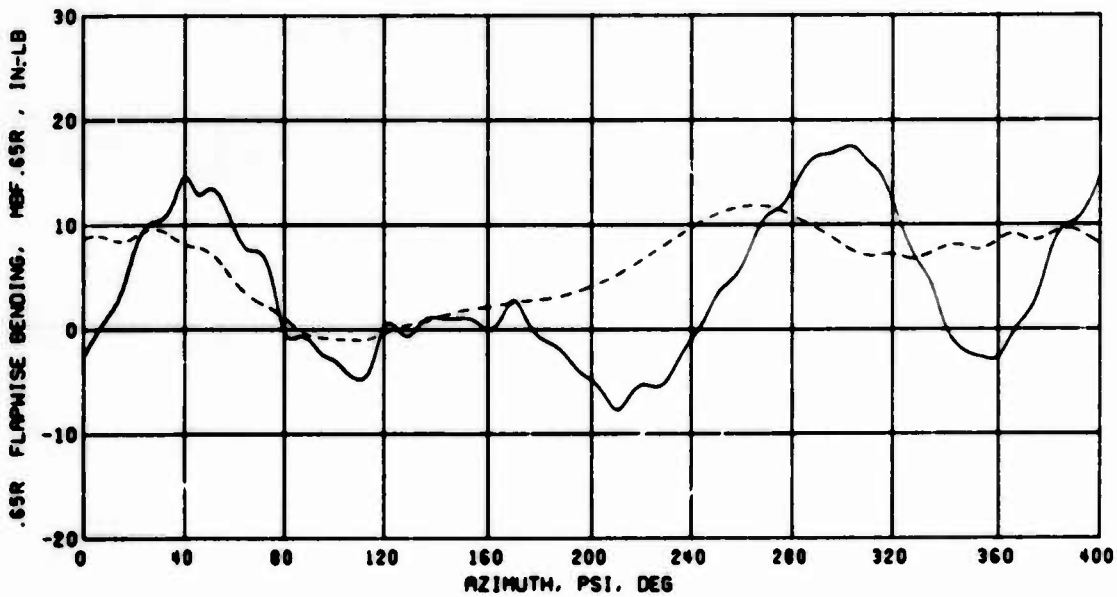

(b) .65R Flapwise Bending, Condition 36

Figure 65. Correlation of Test and Calculated Flapwise Bending with Uniform Inflow; θ_1 = 0 deg, δ_F = 0 deg, S_E = 3.

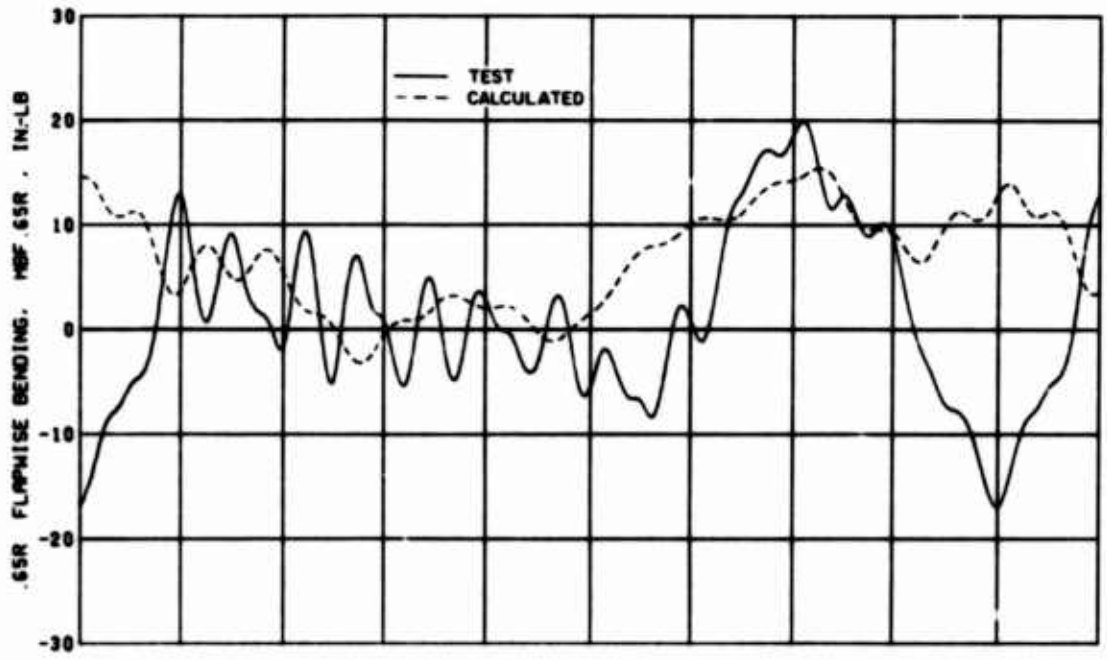

(c) .65R Flapwise Bending, Condition 71

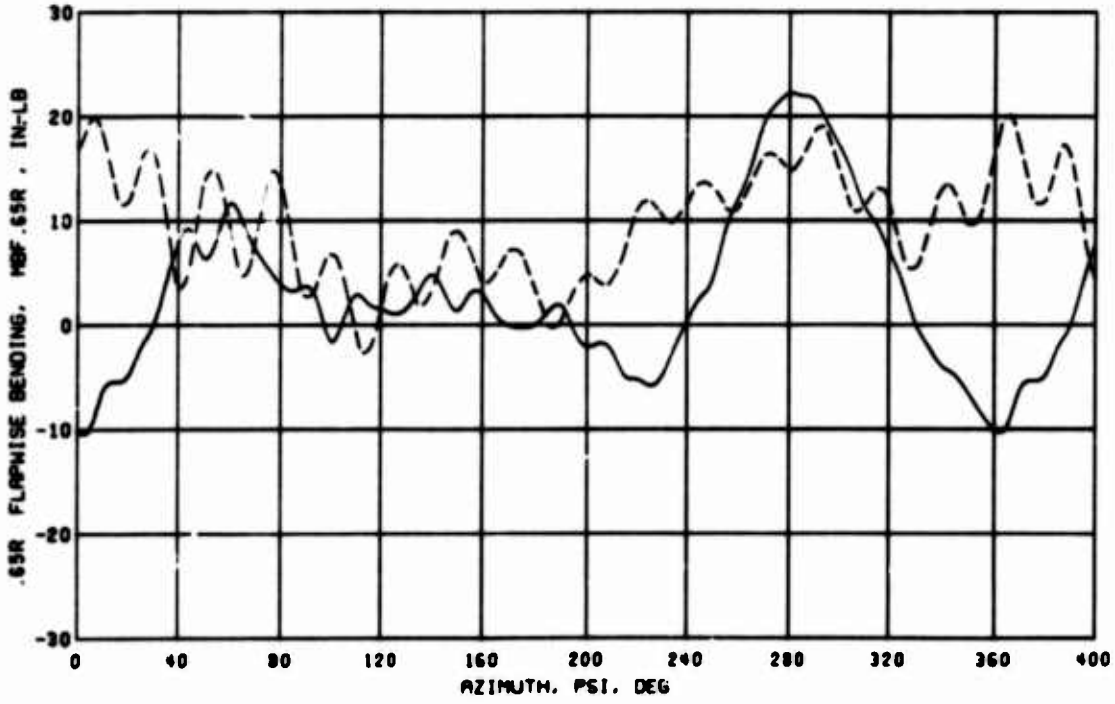

(d) .65R Flapwise Bending, Condition 82

Figure 65. Concluded.

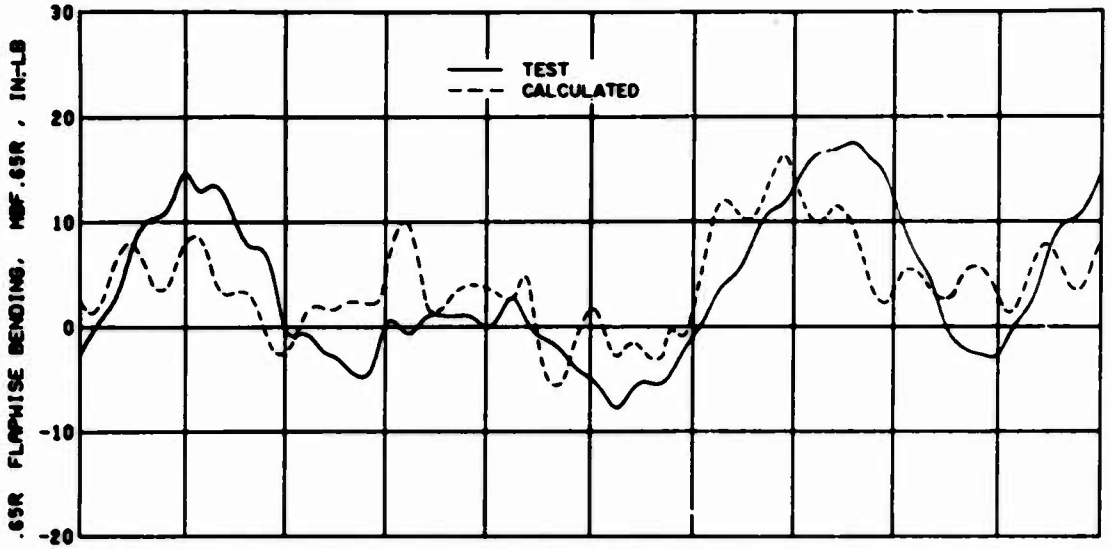

(a) .65R Flapwise Bending, Condition 36

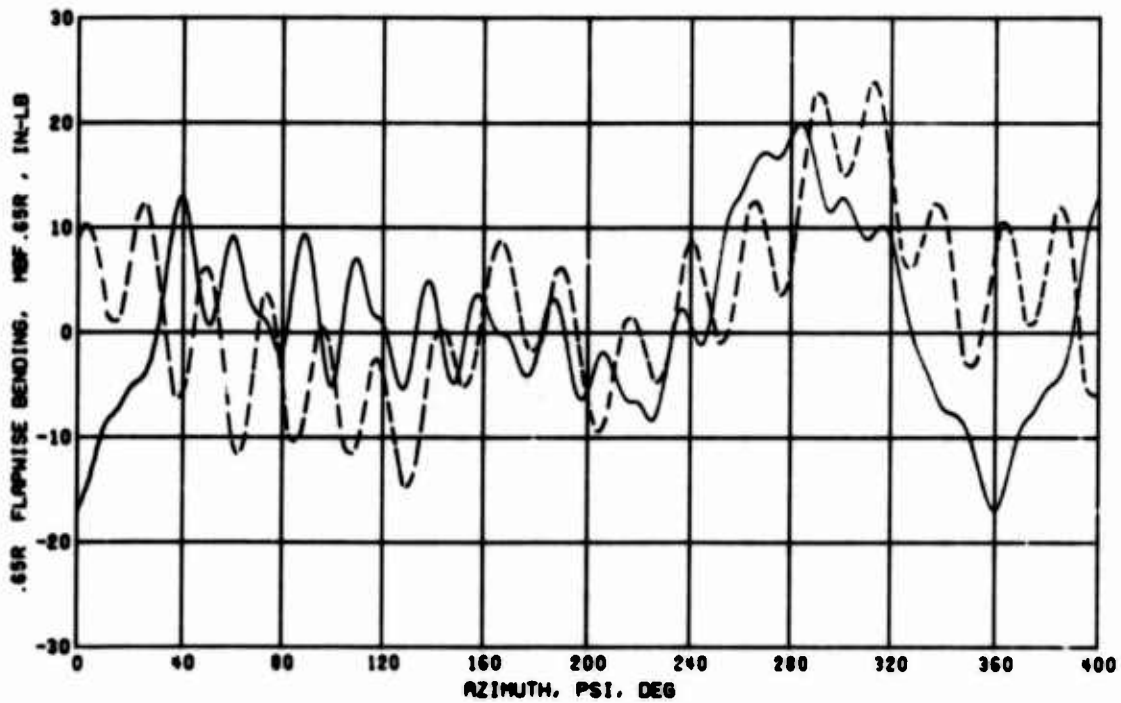

(b) .65R Flapwise Bending, Condition 71

Figure 66. Correlation of Test and Calculated Flapwise Bending With Variable Inflow; θ_1 = 0 deg, δ_F = 0 deg, S_E = 3.

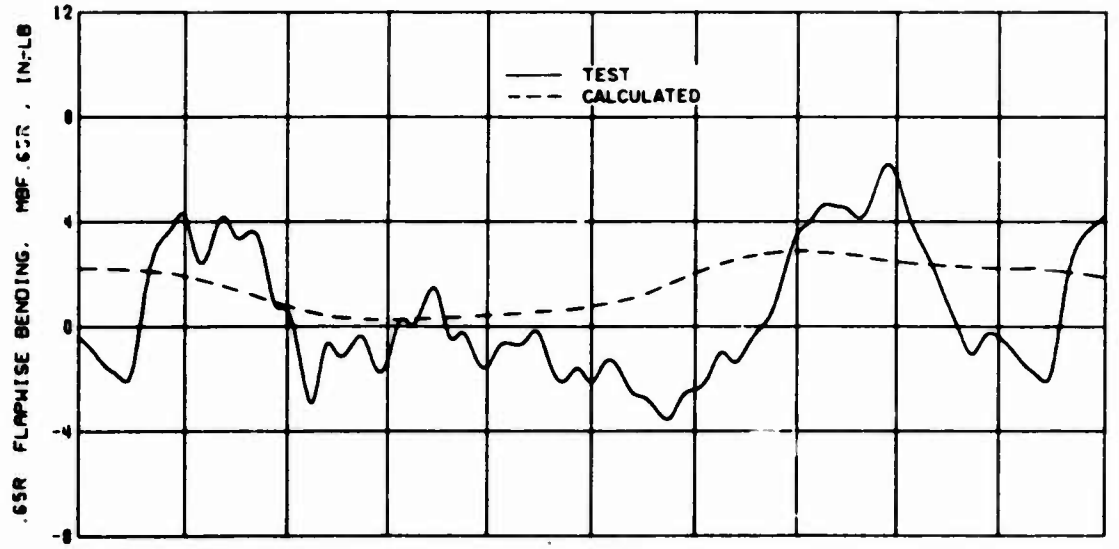

(a) Uniform Inflow

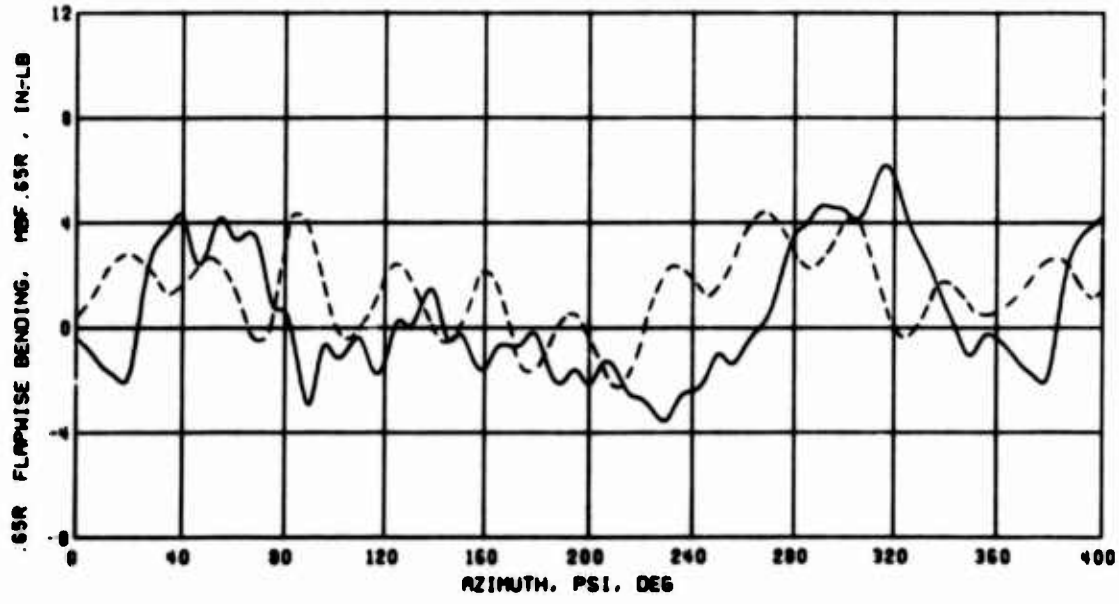

(b) .3 Chord Vortex Core Size

Figure 67. Effect of Variable Inflow Vortex Core Size Assumption on Correlation of Test and Calculated .65R Flapwise Bending; θ_1 = 0 deg, δ_F = 0 deg, S_E = 1, Condition 1.

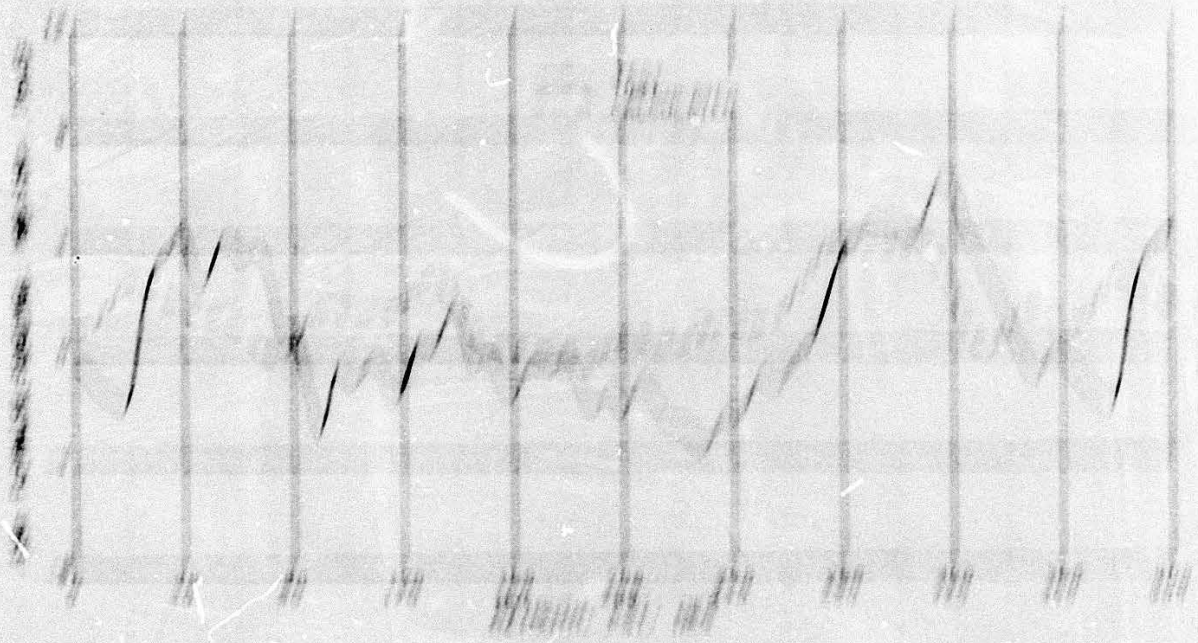

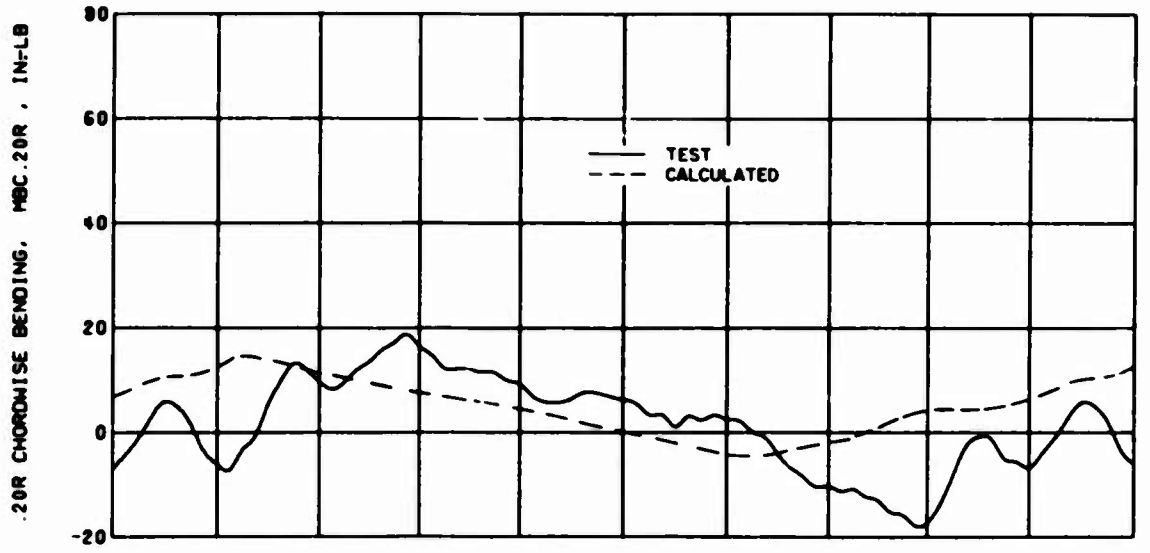

(a) .20R Chordwise Bending, Condition 7

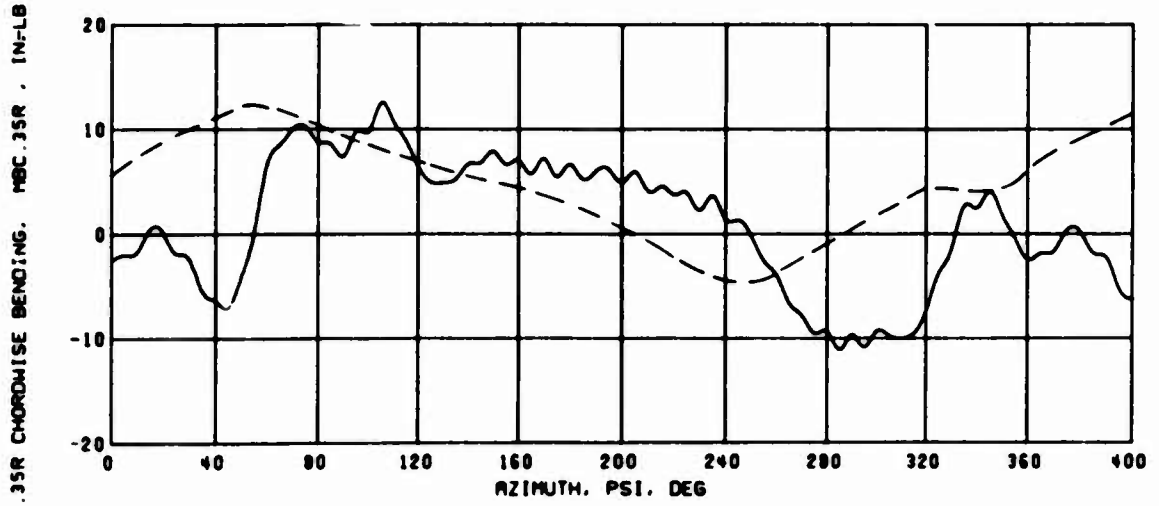

(b) .35R Chordwise Bending, Condition 7

Figure 68. Correlation of Test and Calculated Chordwise Bending With Uniform Inflow; θ_1 = 0 deg, δ_F = 0 deg, S_E = 1

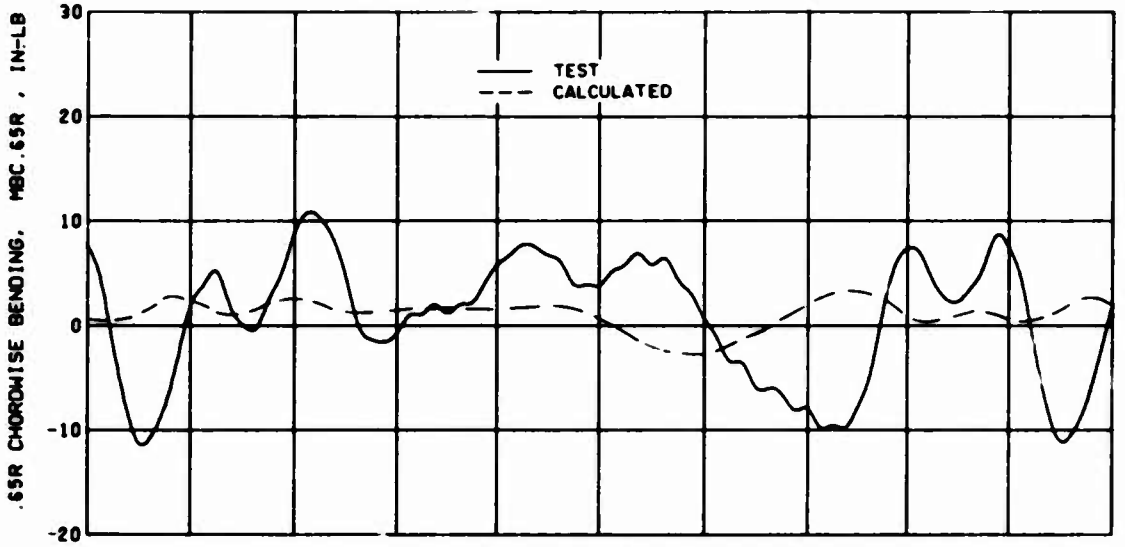

(c) .65R Chordwise Bending, Condition 7

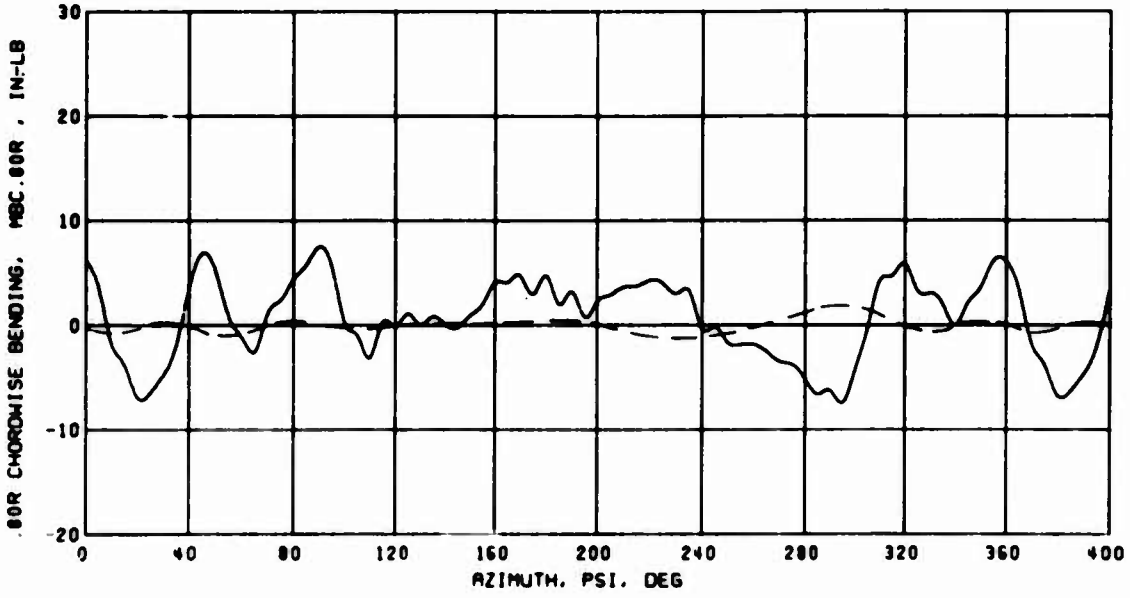

(d) .80R Chordwise Bending, Condition 7

Figure 68. Continued.

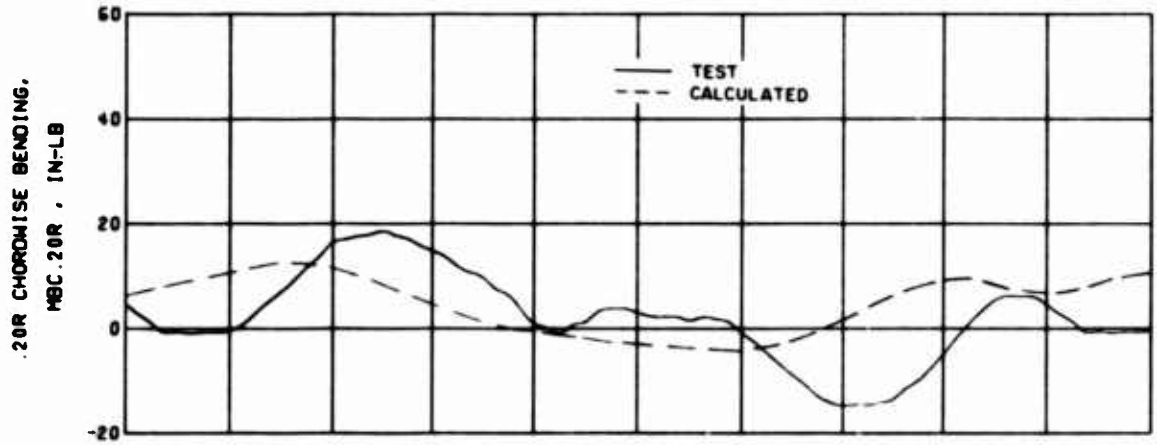

(e) .20R Chordwise Bending, Condition 36

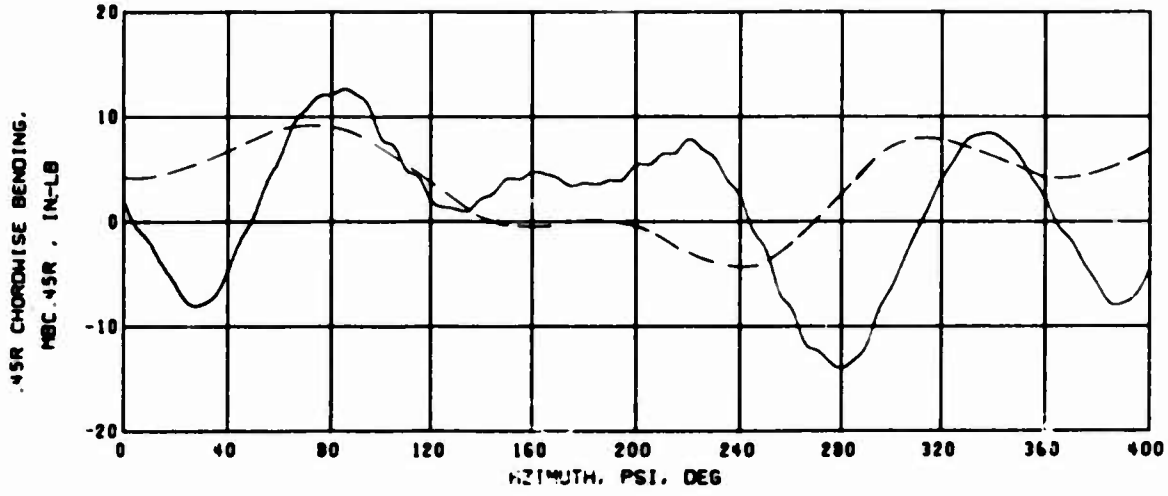

(f) .45R Chordwise Bending, Condition 36

Figure 68. Continued.

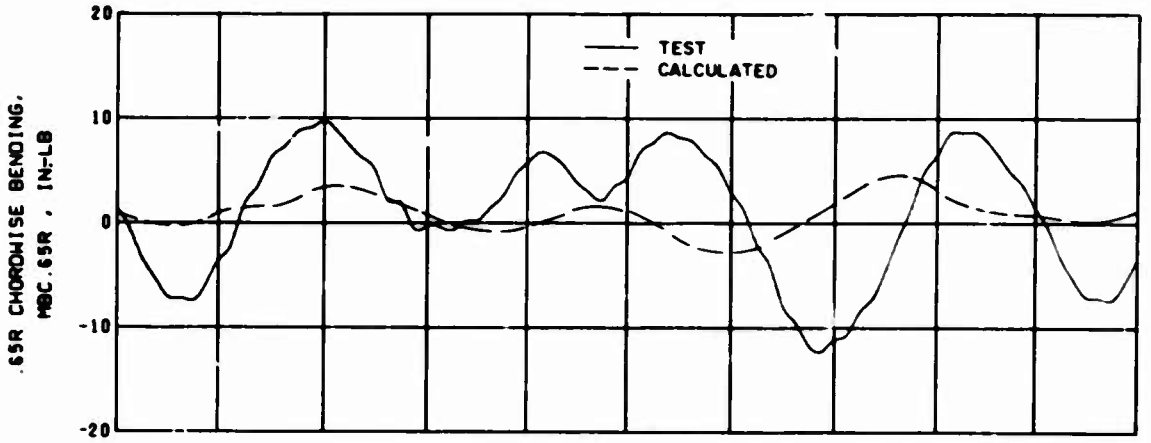

(g) .65R Chordwise Bending, Condition 36

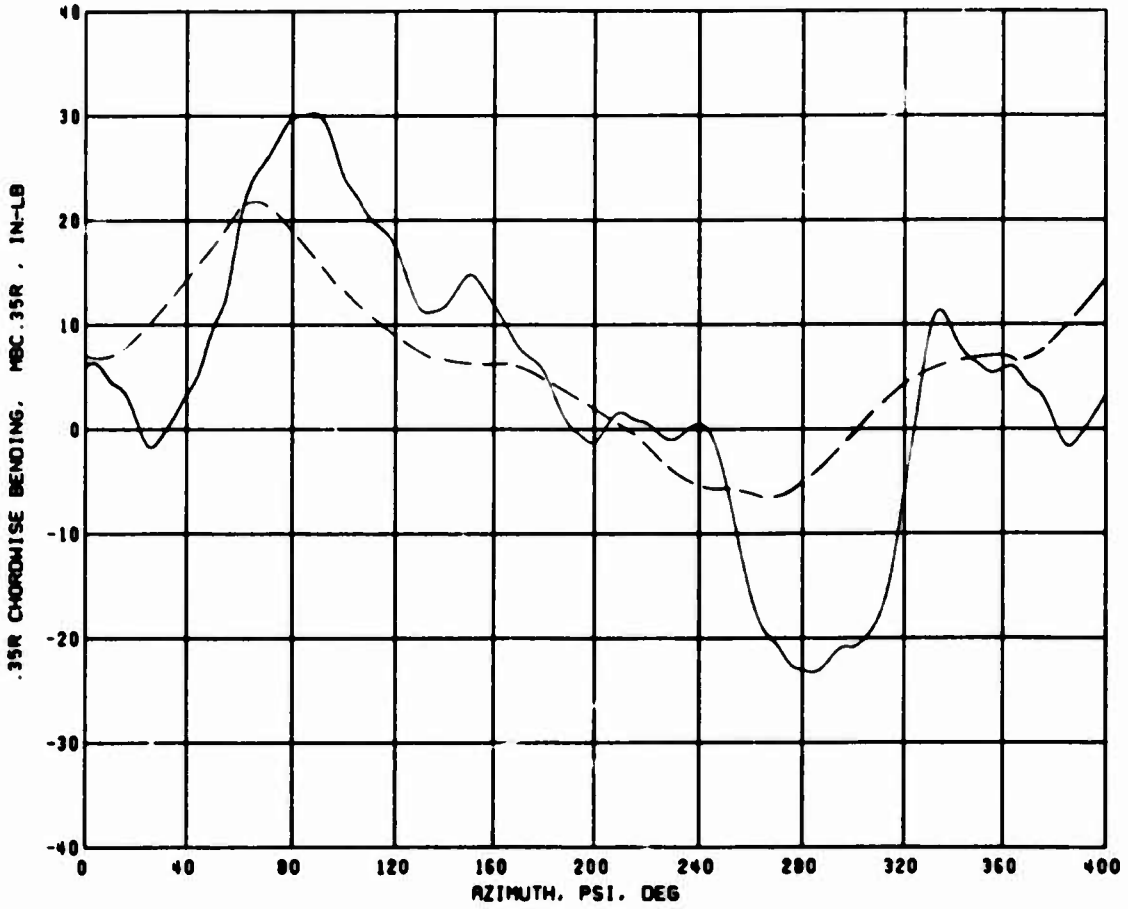

(h) .35R Chordwise Bending, Condition 71

Figure 68. Continued.

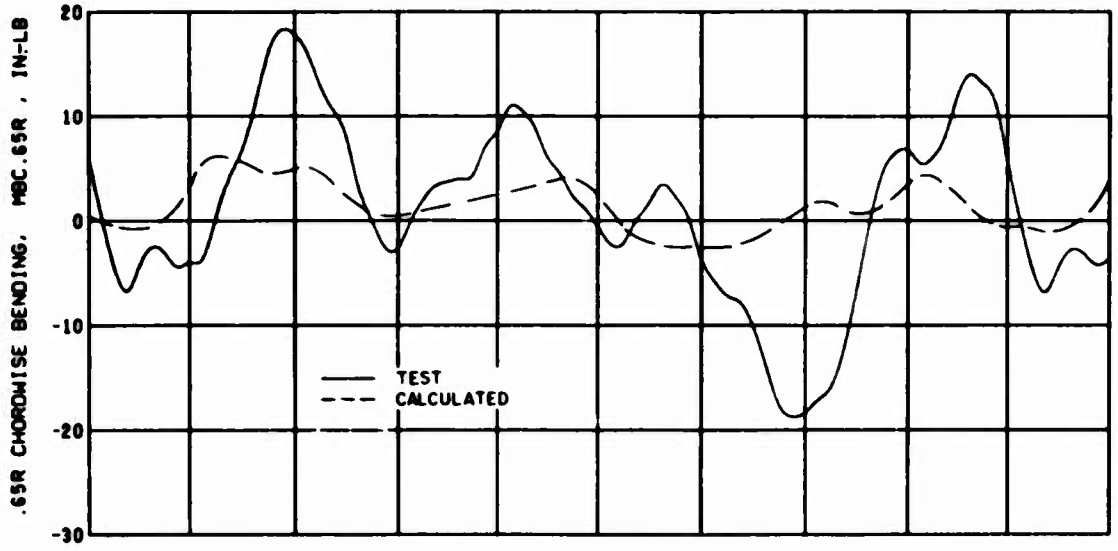

(i) .65R Chordwise Bending, Condition 71

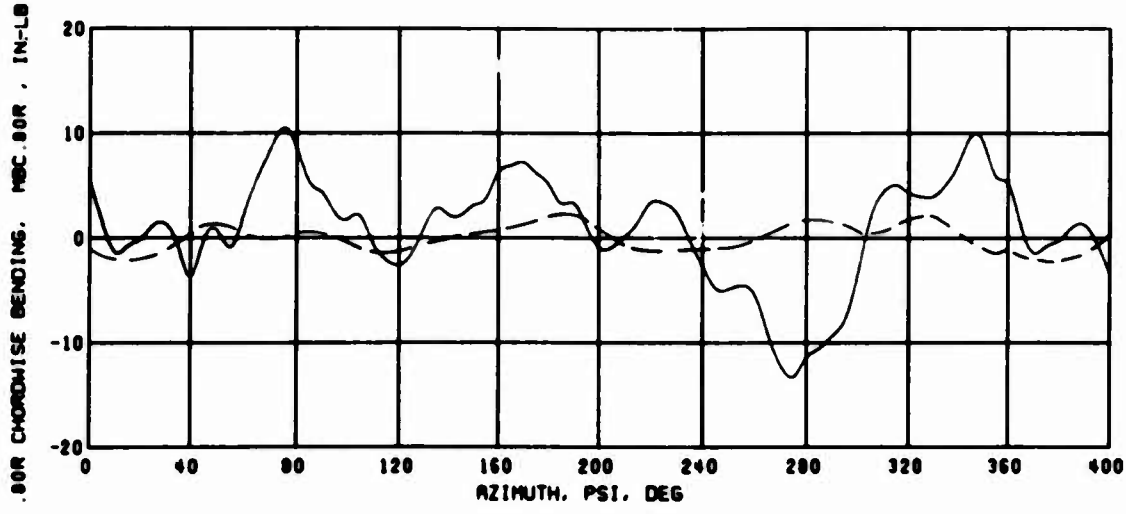

(j) .80R Chordwise Bending, Condition 71

Figure 68. Continued.

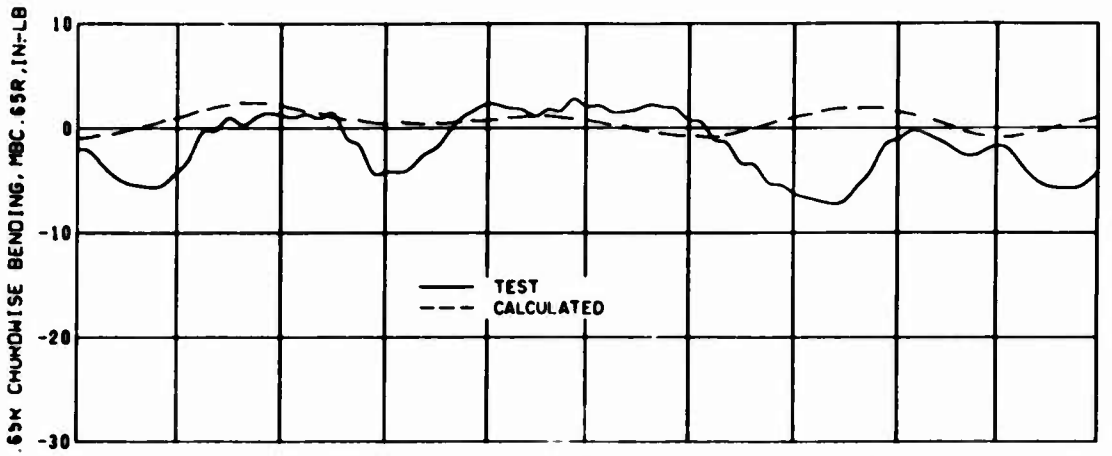

(k) .65R Chordwise Bending, Condition 80

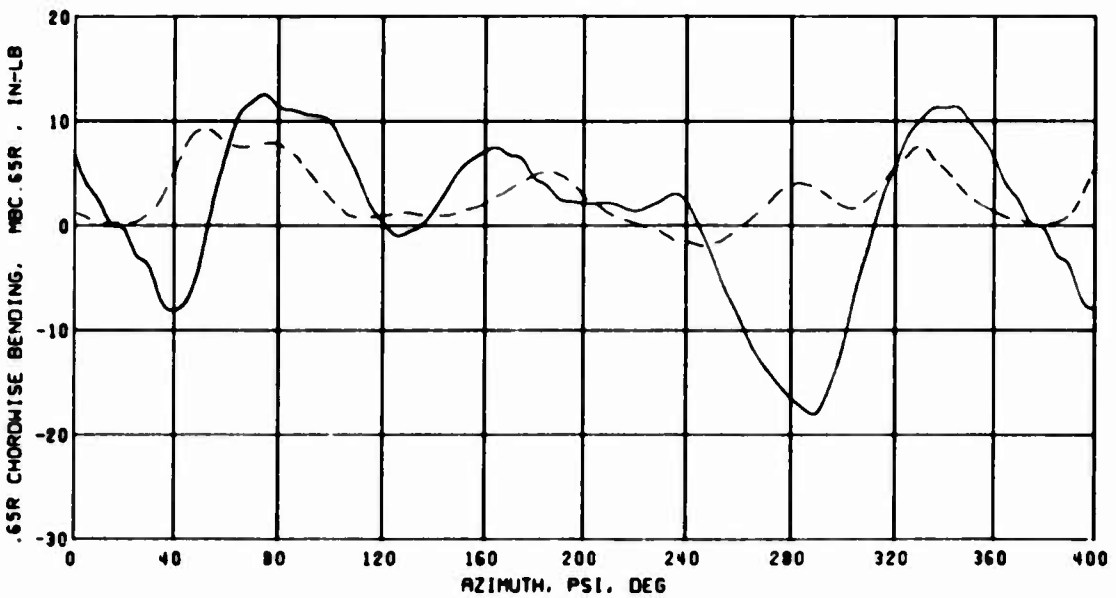

(l) .65R Chordwise Bending, Condition 82

Figure 68. Concluded.

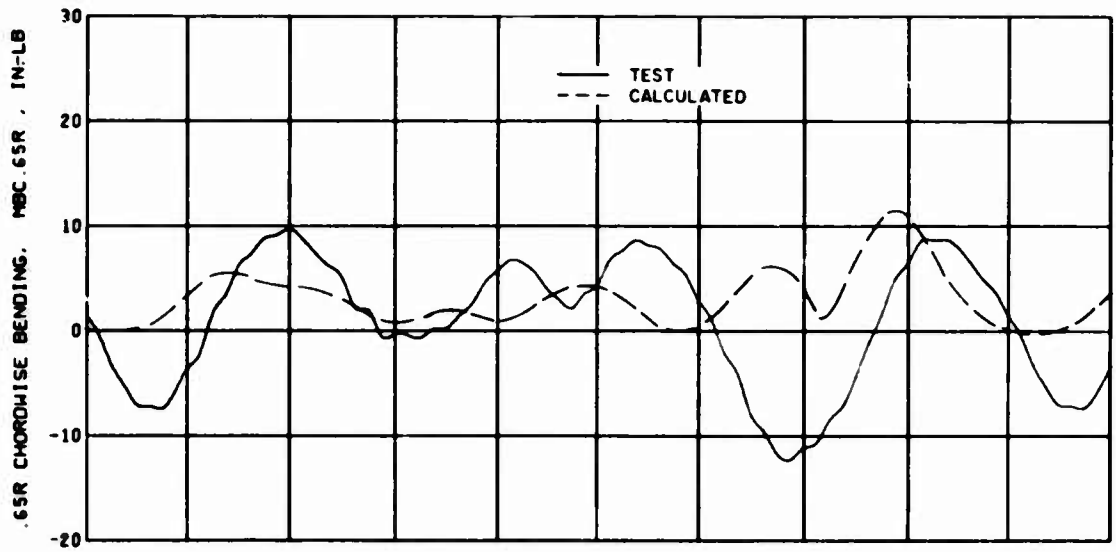

(a) .65R Chordwise Bending, Condition 36

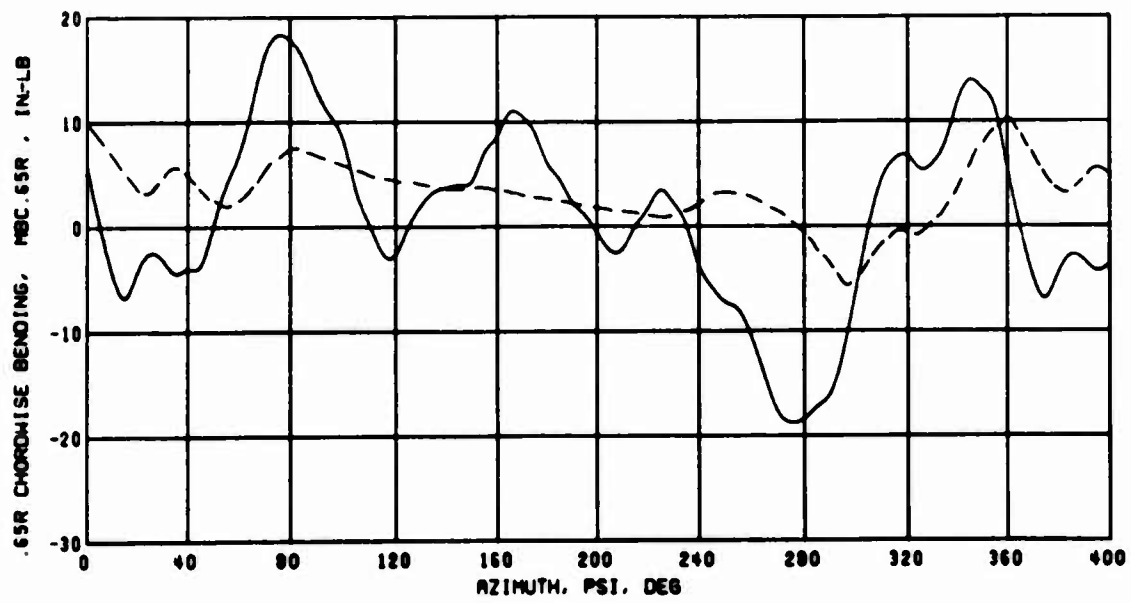

(b) .65R Chordwise Bending, Condition 71

Figure 69. Correlation of Test and Calculated Chordwise Bending With Variable Inflow; θ_1 = 0 deg, δ_F = 0 deg, S_E = 1.

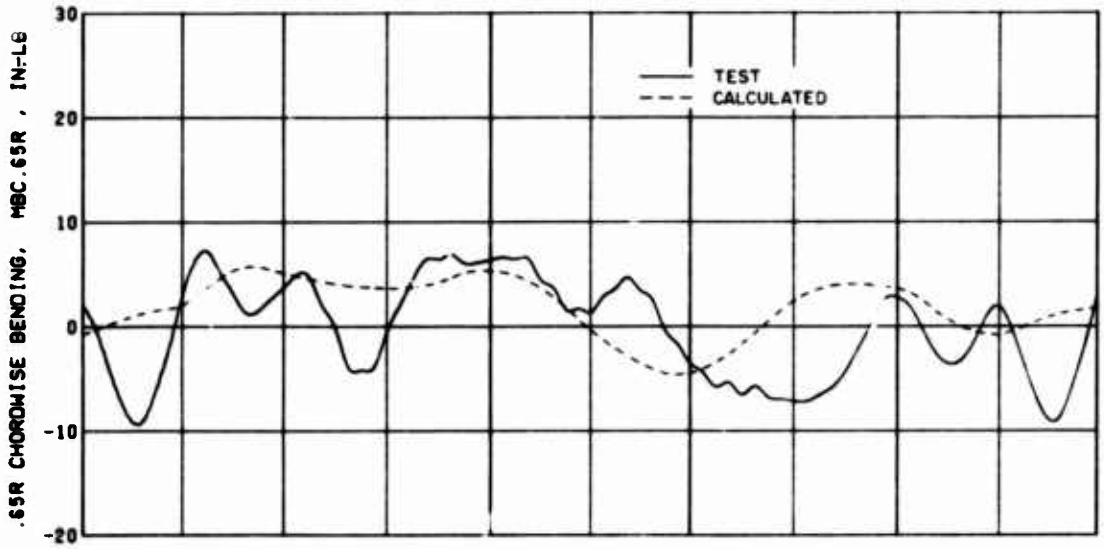

(a) .65R Chordwise Bending, Condition 7

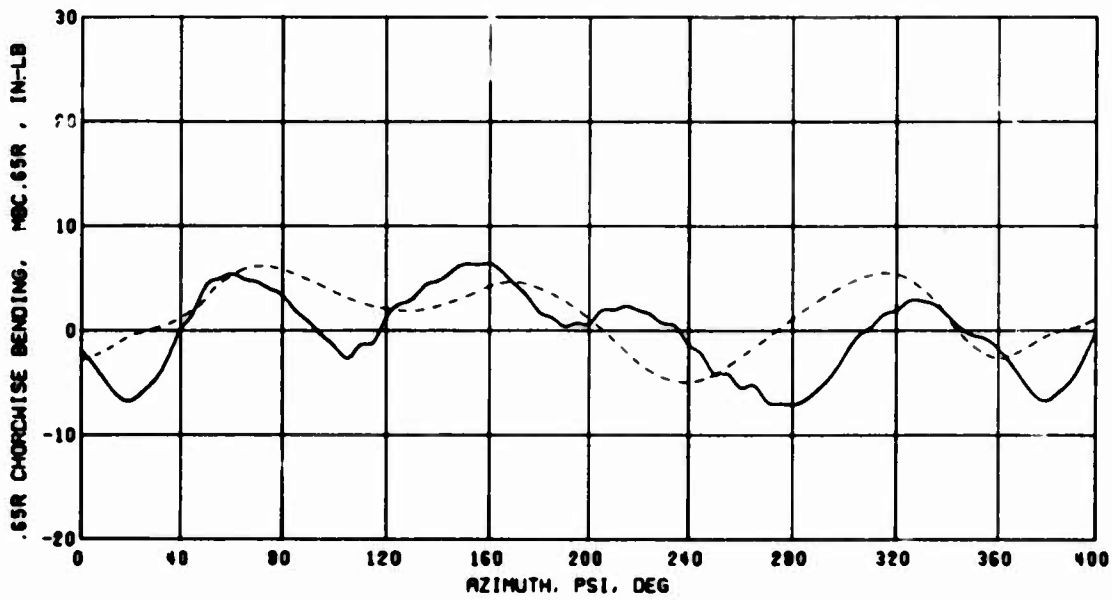

(b) .65R Chordwise Bending, Condition 36

Figure 70. Correlation of Test and Calculated Chordwise Bending With Uniform Inflow; $\theta_1 = -8$ deg, $\delta_F = 0$ deg, $S_E = 1$.

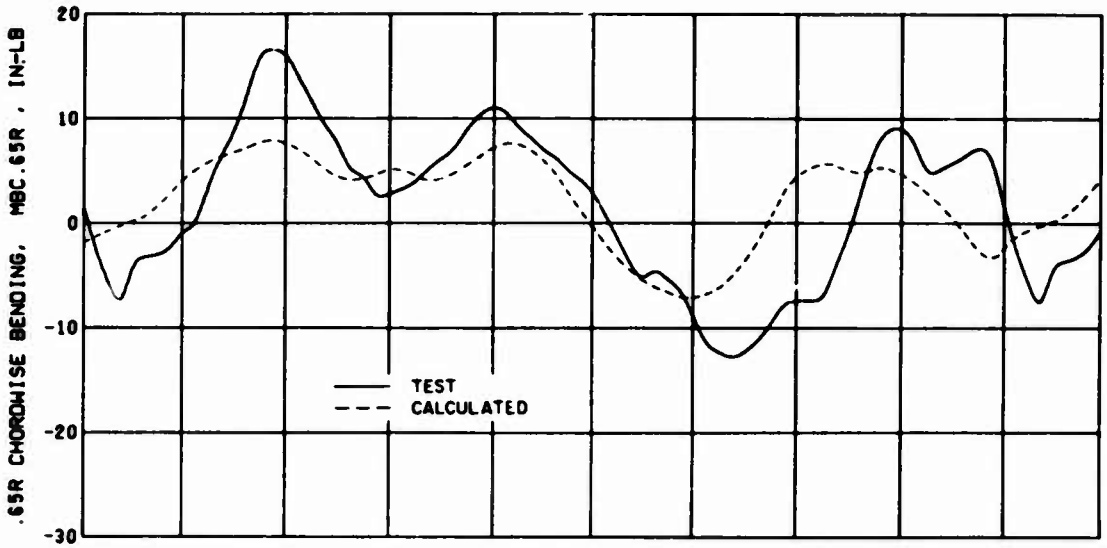

(c) .65R Chordwise Bending, Condition 71

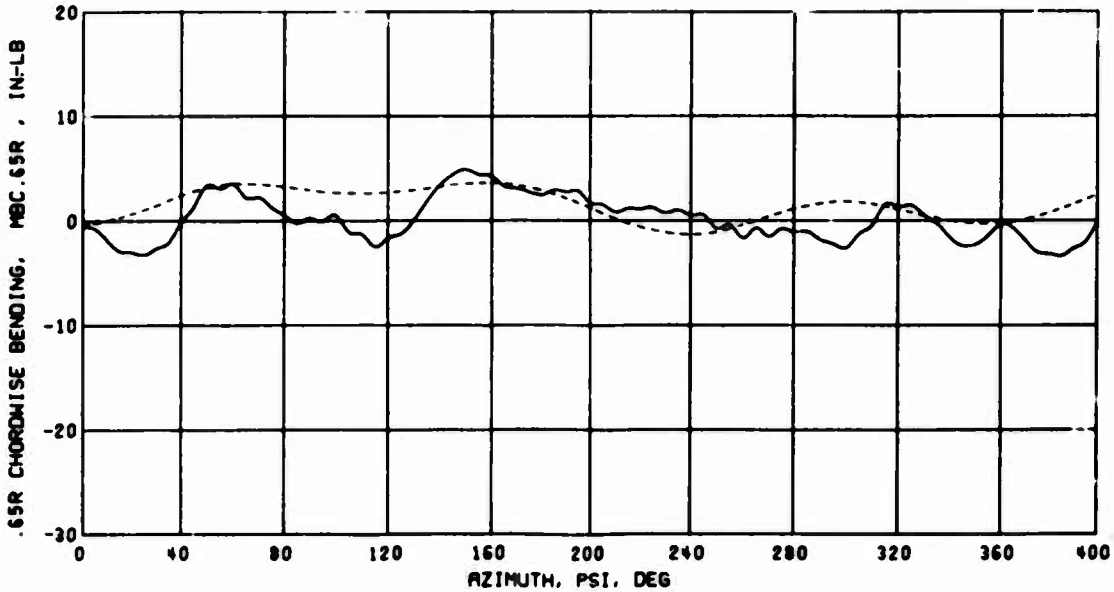

(d) .65R Chordwise Bending, Condition 80

Figure 70. Continued.

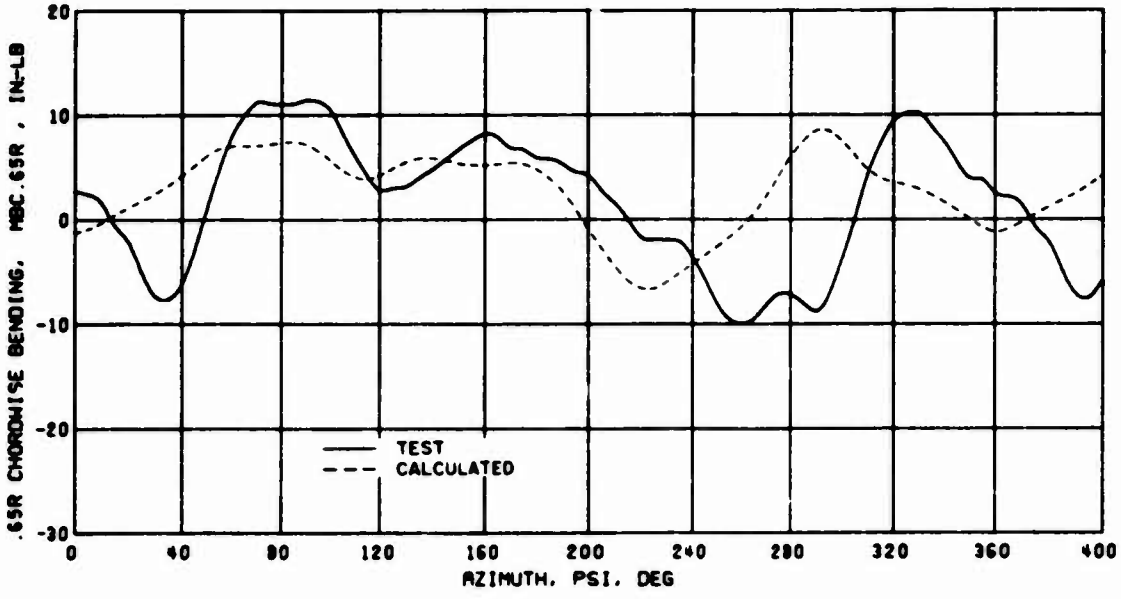

(e) .65R Chordwise Bending, Condition 82

Figure 70. Concluded.

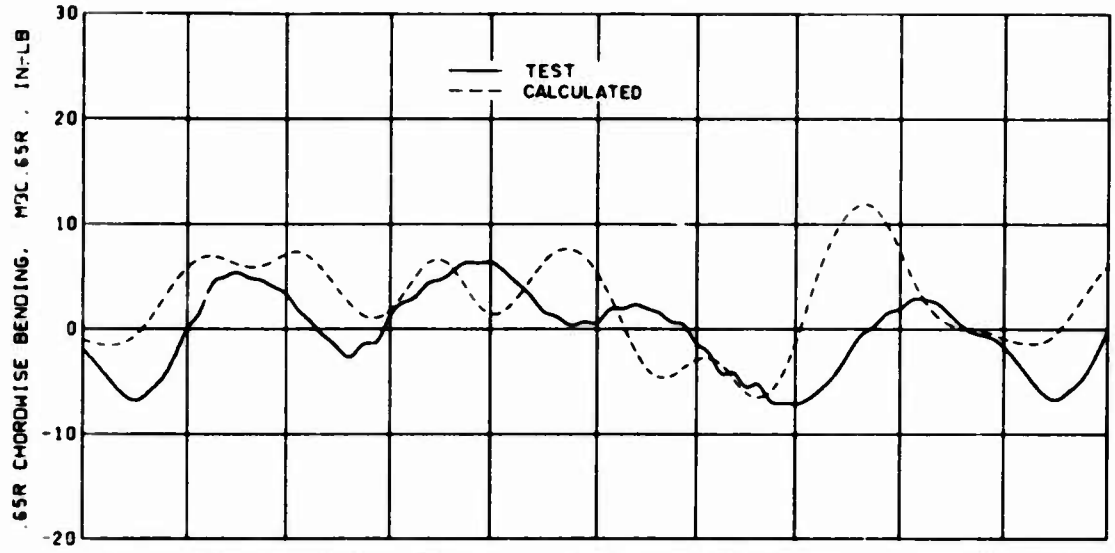

(a) .65R Chordwise Bending, Condition 36, Unsteady Aerodynamic Scaling Case 3

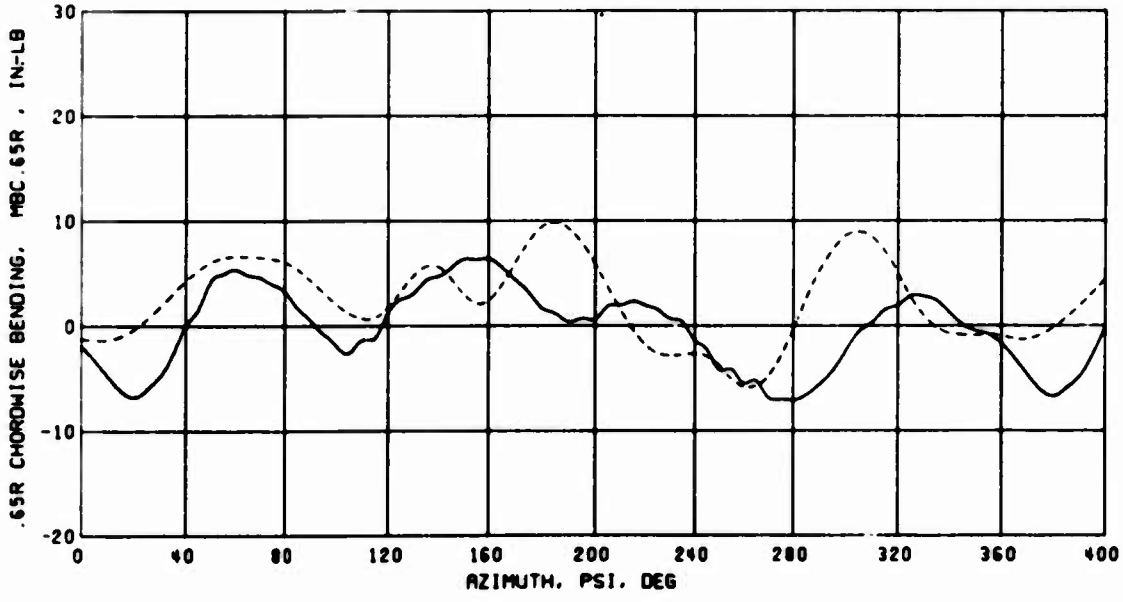

(b) .65R Chordwise Bending, Condition 36, Unsteady Aerodynamic Scaling Case

Figure 71. Correlation of Test and Calculated Chordwise Bending With Variable Inflow; $\theta_1 = -8$ deg, $\delta_F = 0$ deg, $S_E = 1$.

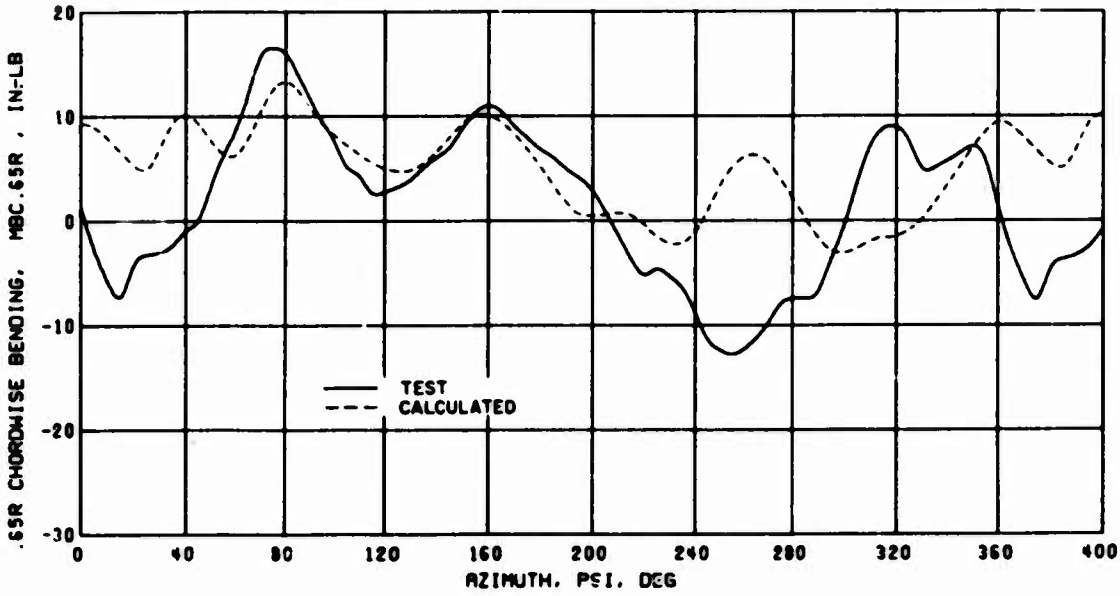

(c) .65R Chordwise Bending, Condition 71, Unsteady Aerodynamic Scaling Case 1

Figure 71. Concluded.

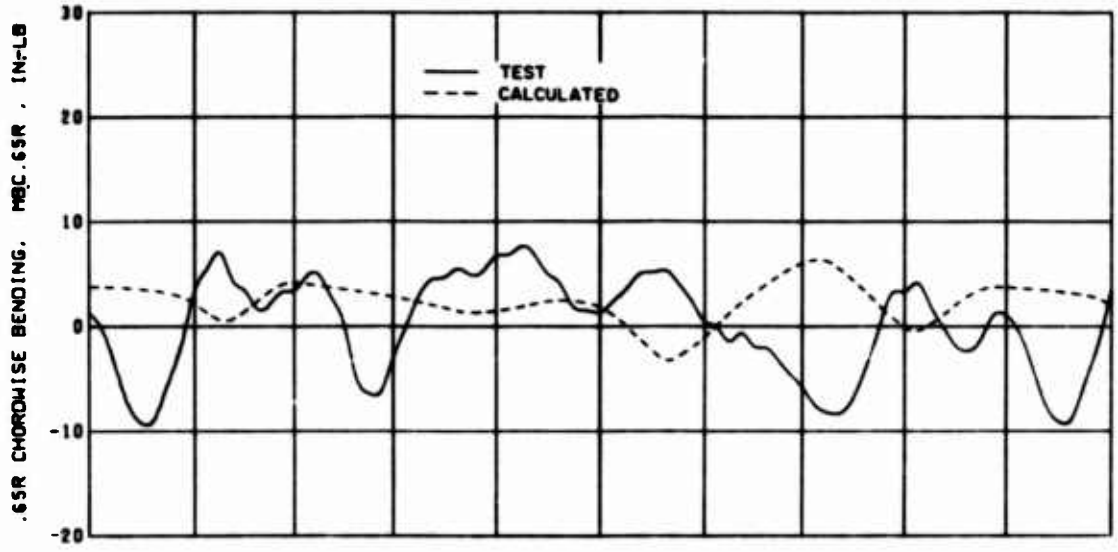

(a) .65R Chordwise Bending, Condition 7

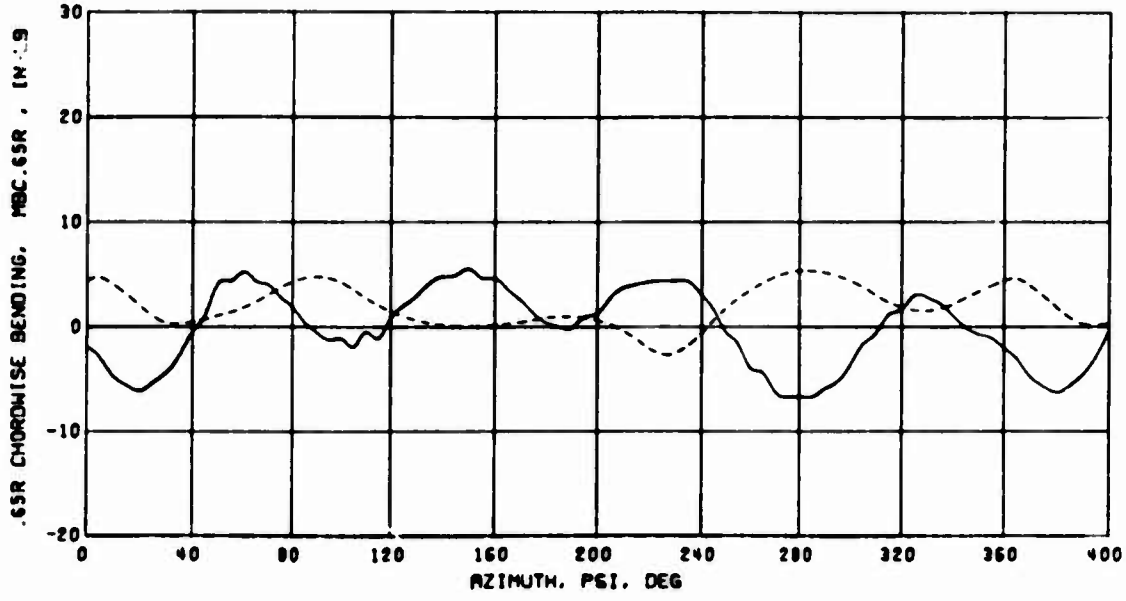

(b) .65R Chordwise Bending, Condition 36

Figure 72. Correlation of Test and Calculated Chordwise Bending With Uniform Inflow; θ_1 = 0 deg, δ_F = 5 deg, S_E = 1.

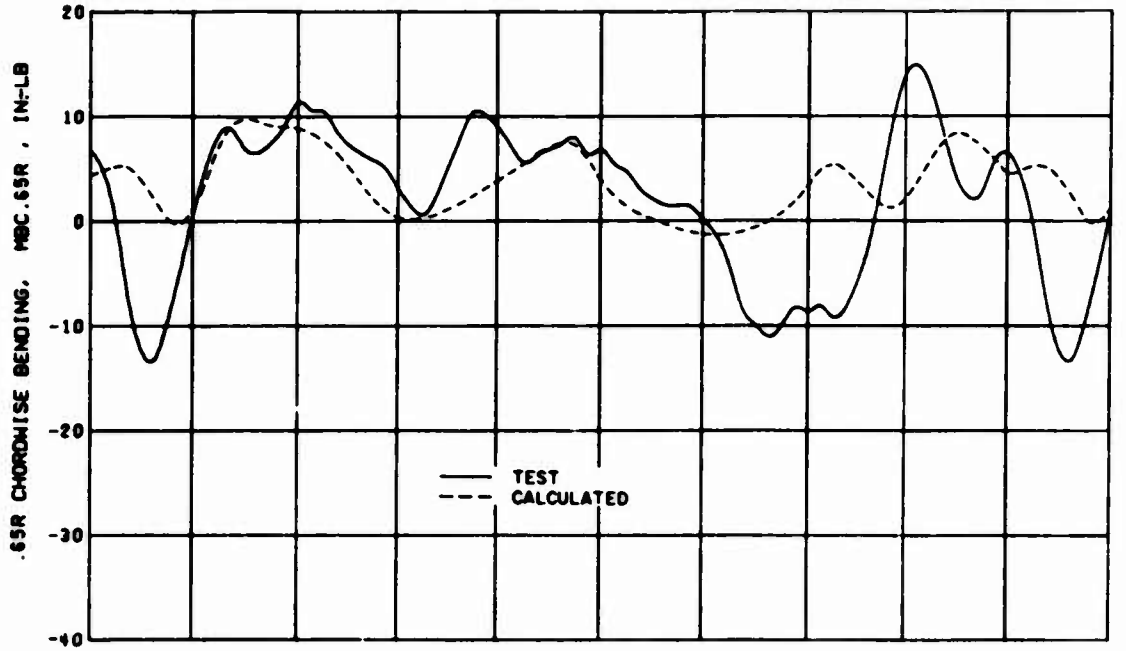

(c) .65R Chordwise Bending, Condition 71

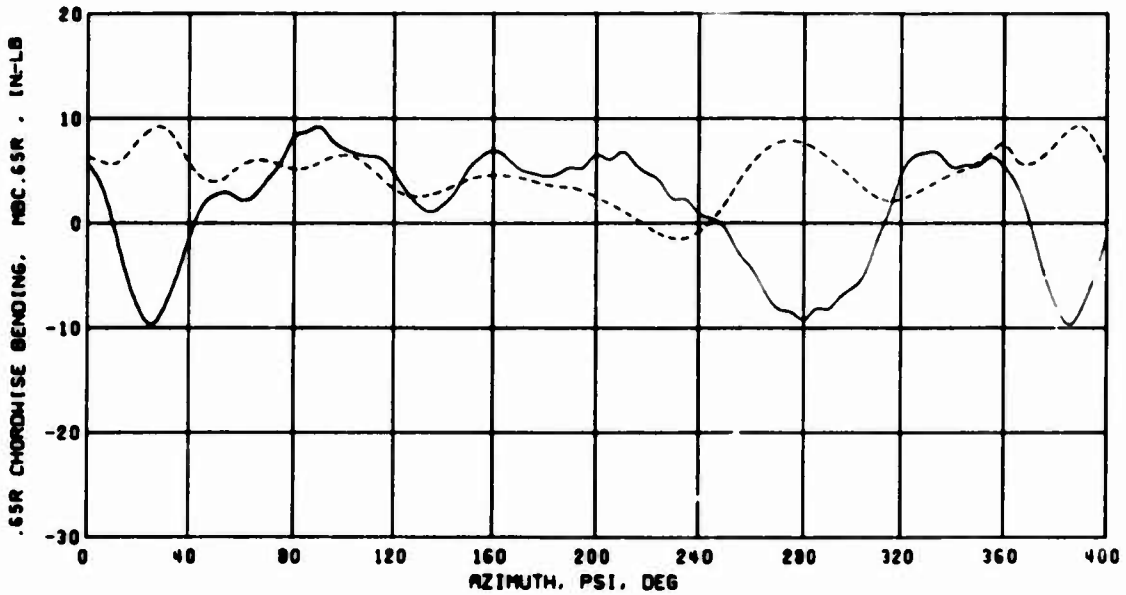

(d) .65R Chordwise Bending, Condition 82

Figure 72. Concluded.

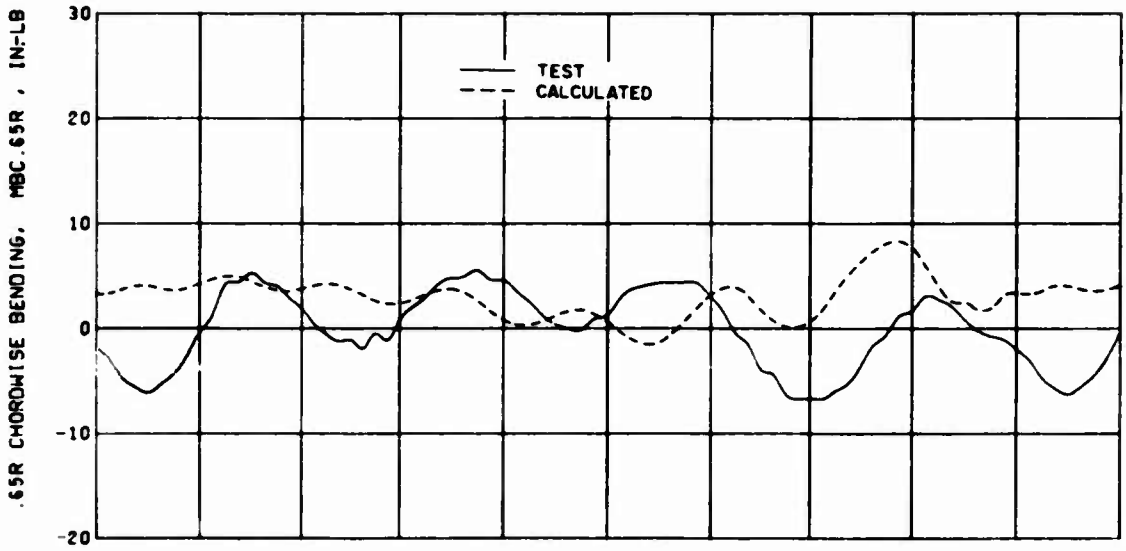

(a) .65R Chordwise Bending, Condition 36

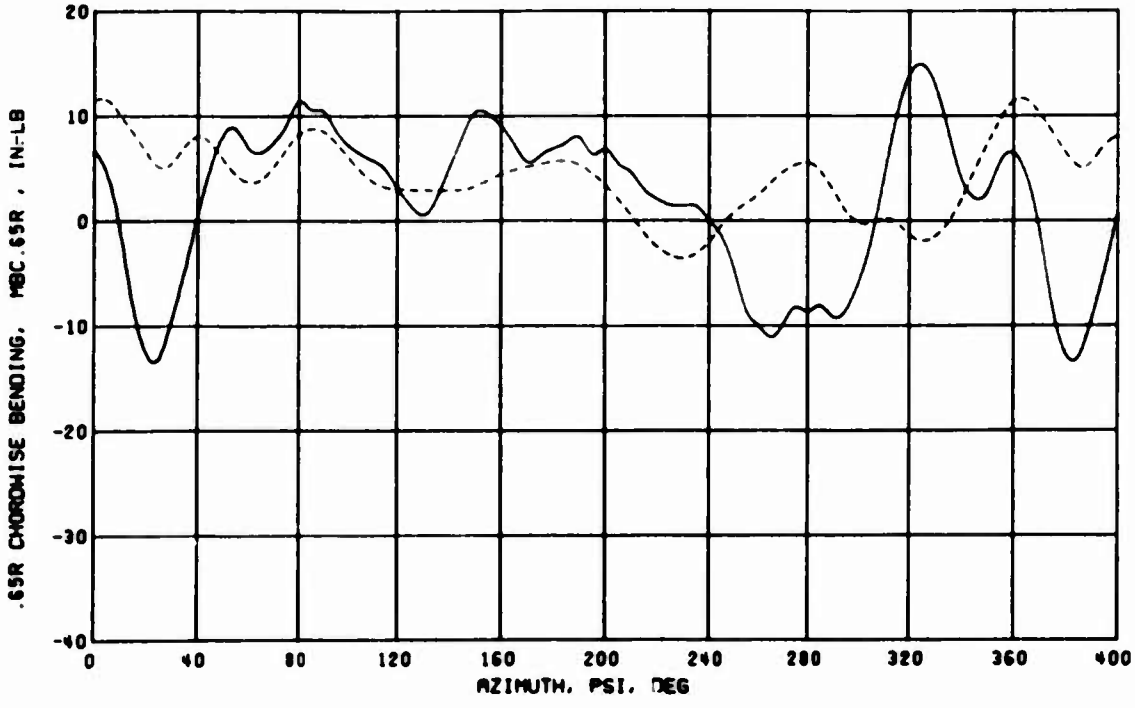

(b) .65R Chordwise Bending, Condition 71

Figure 73. Correlation of Test and Calculated Chordwise Bending With Variable Inflow; θ_1 = 0 deg, δ_F = 5 deg, S_E = 1.

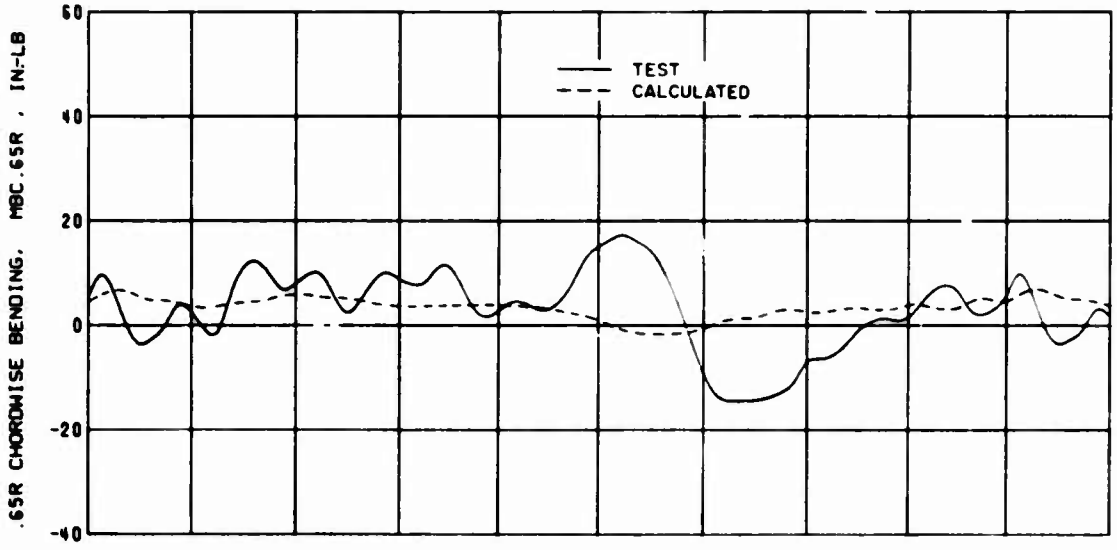

(a) .65R Chordwise Bending, Condition 7

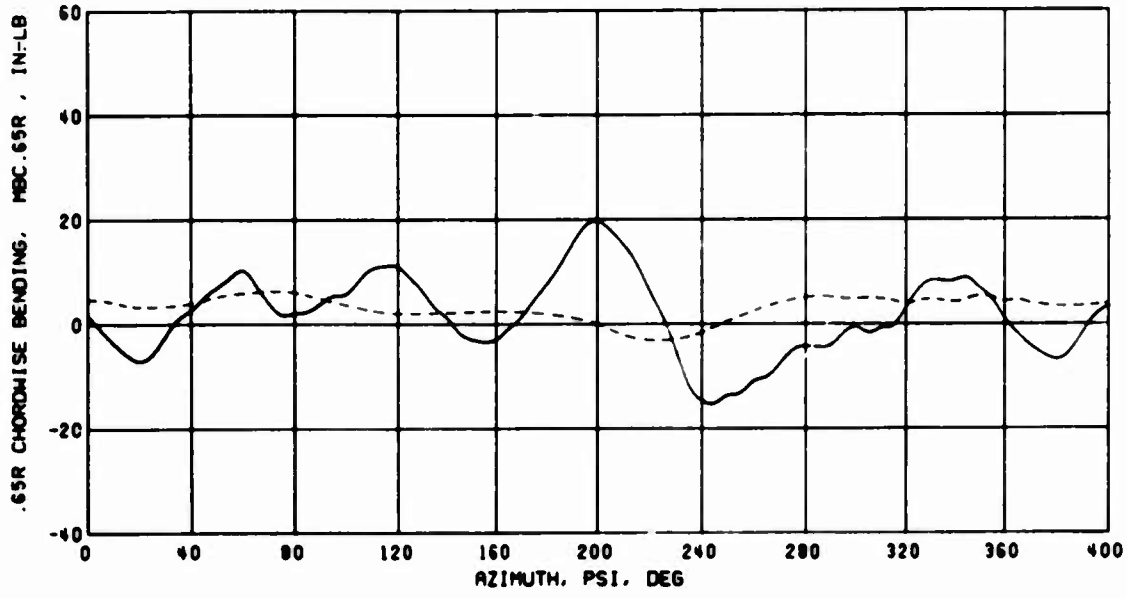

(b) .65R Chordwise Bending, Condition 36

Figure 74. Correlation of Test and Calculated Chordwise Bending With Uniform Inflow; θ_1 = 0 deg, δ_F = 0 deg, S_E = 3.

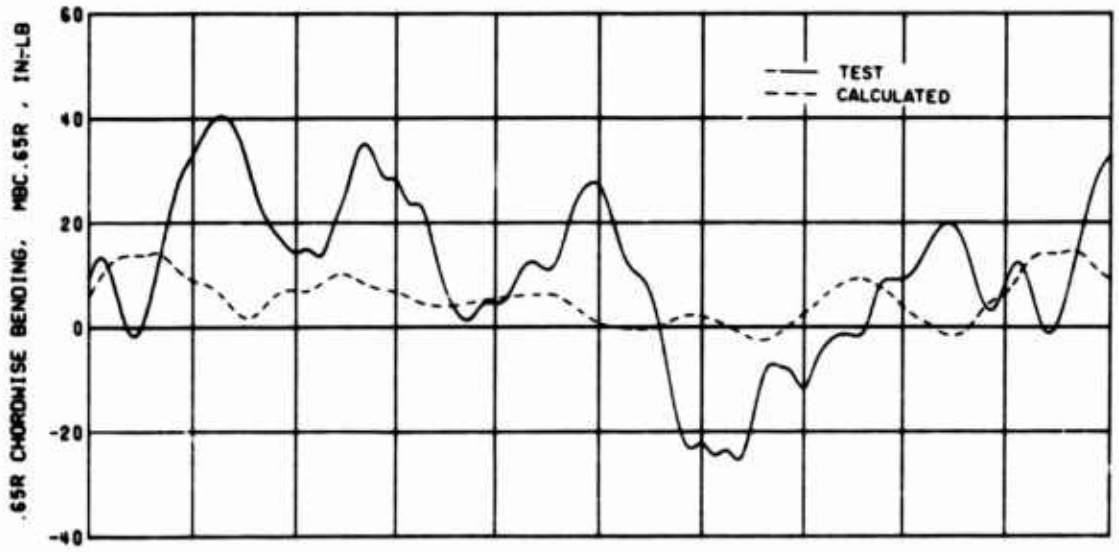

(c) .65R Chordwise Bending, Condition 71

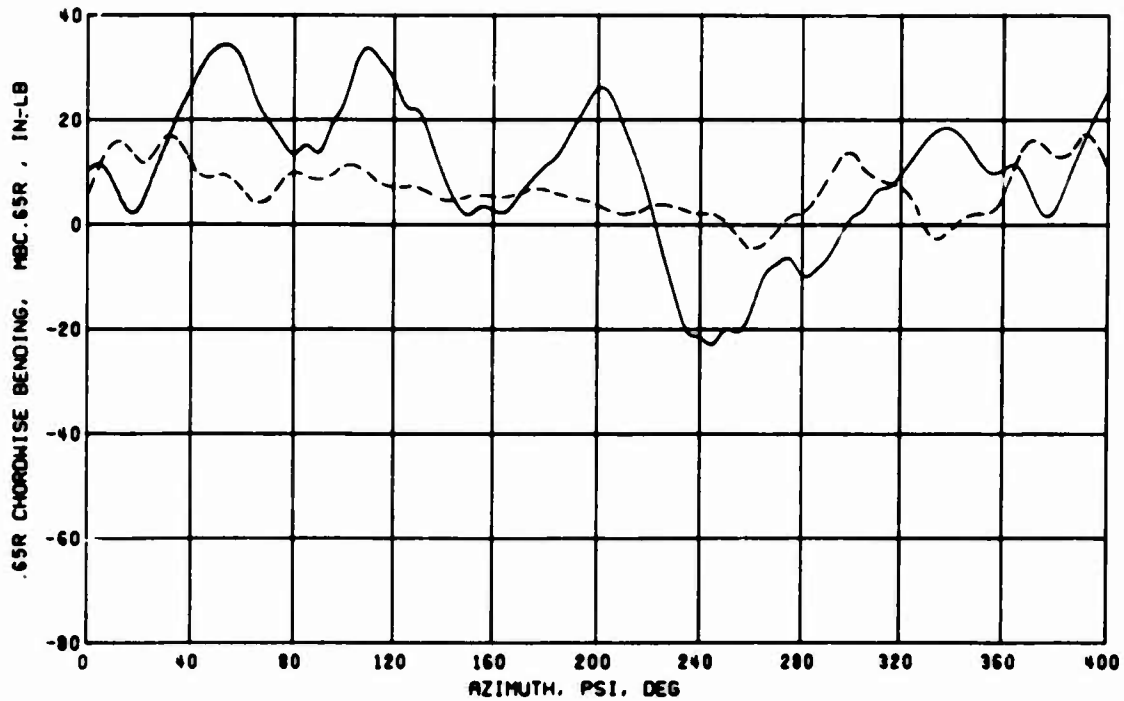

(d) .65R Chordwise Bending, Condition 82

Figure 74. Concluded.

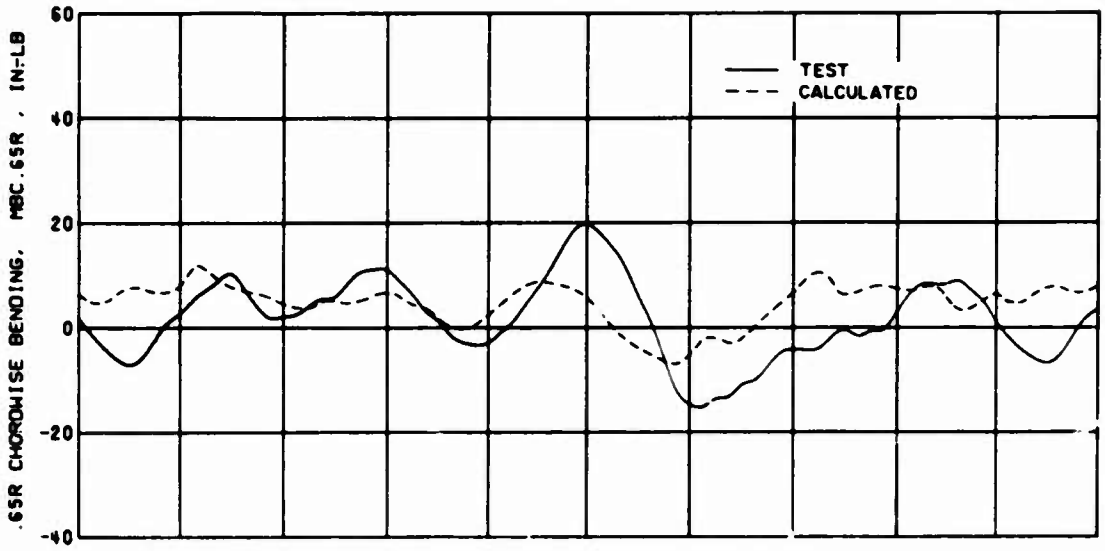

(a) .65R Chordwise Bending, Condition 36

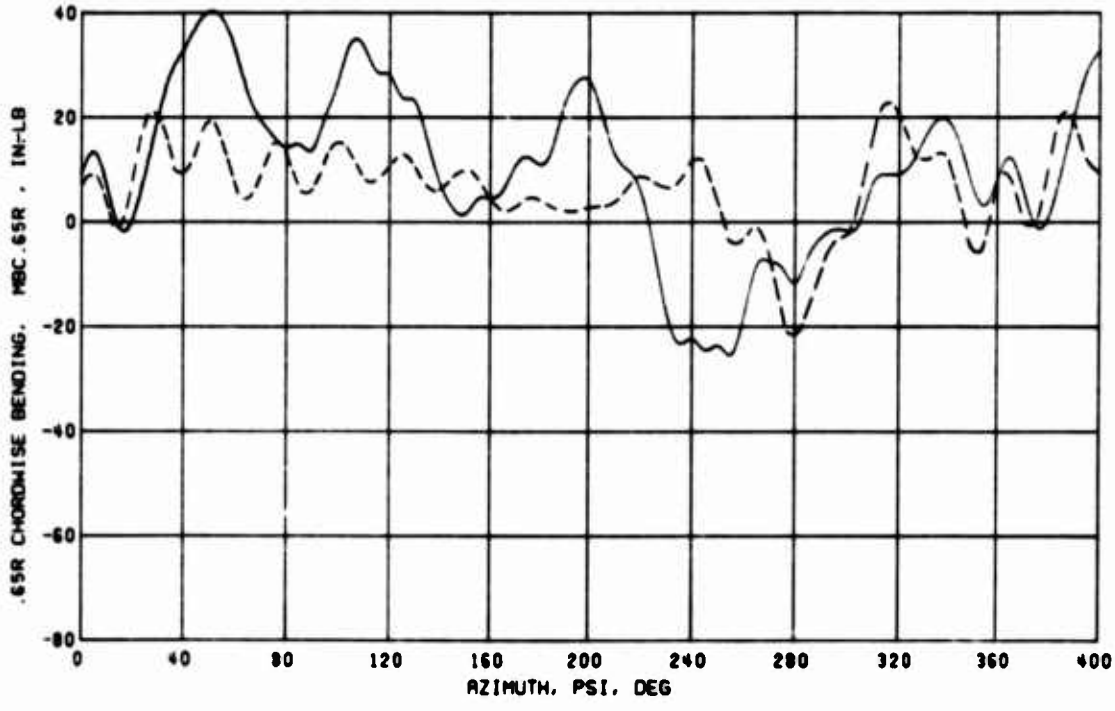

(b) .65R Chordwise Bending, Condition 71

Figure 75. Correlation of Test and Calculated Chordwise Bending With Variable Inflow; θ_1 = 0 deg, δ_F = 0 deg, S_E = 3.

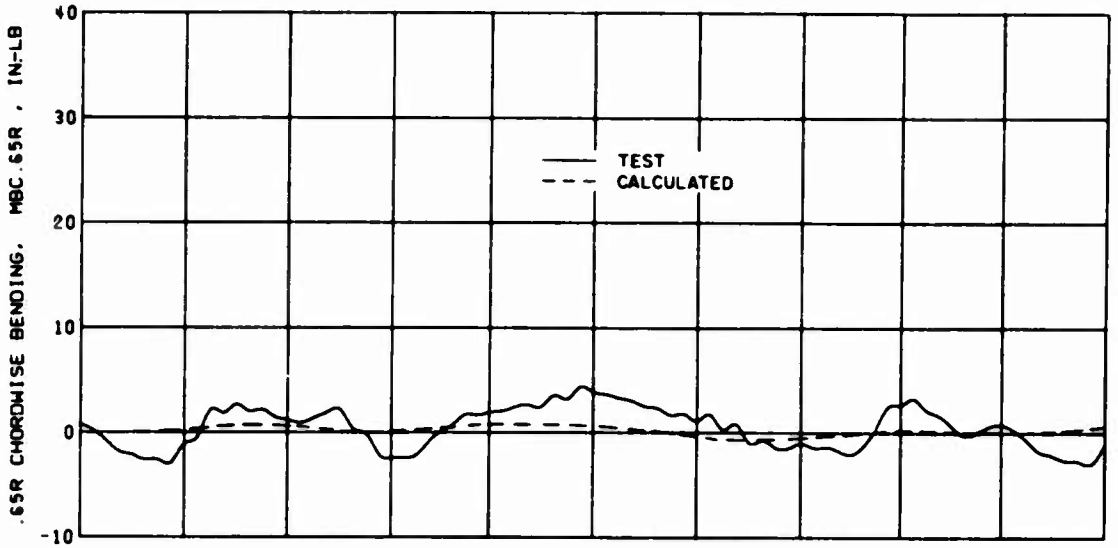

(a) Uniform Inflow

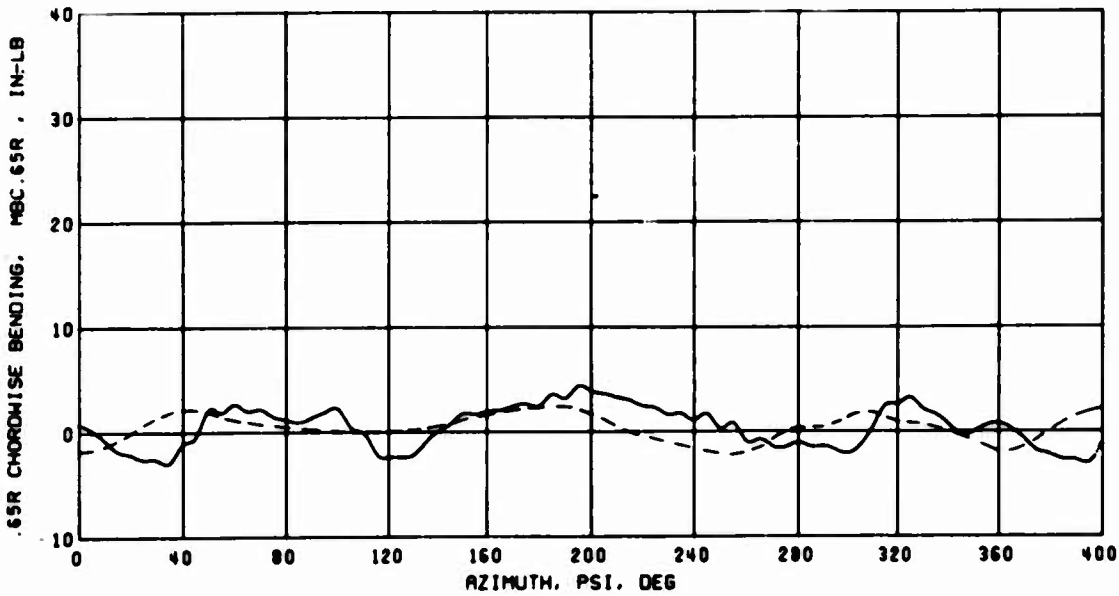

(b) .3 Chord Vortex Core Size

Figure 76. Effect of Variable Inflow Vortex Core Size Assumption on Correlation/Test and Calculated .65R Chordwise Bending; θ_1 = 0 deg, δ_F = 0 deg, S_E = 1, Conditionl.

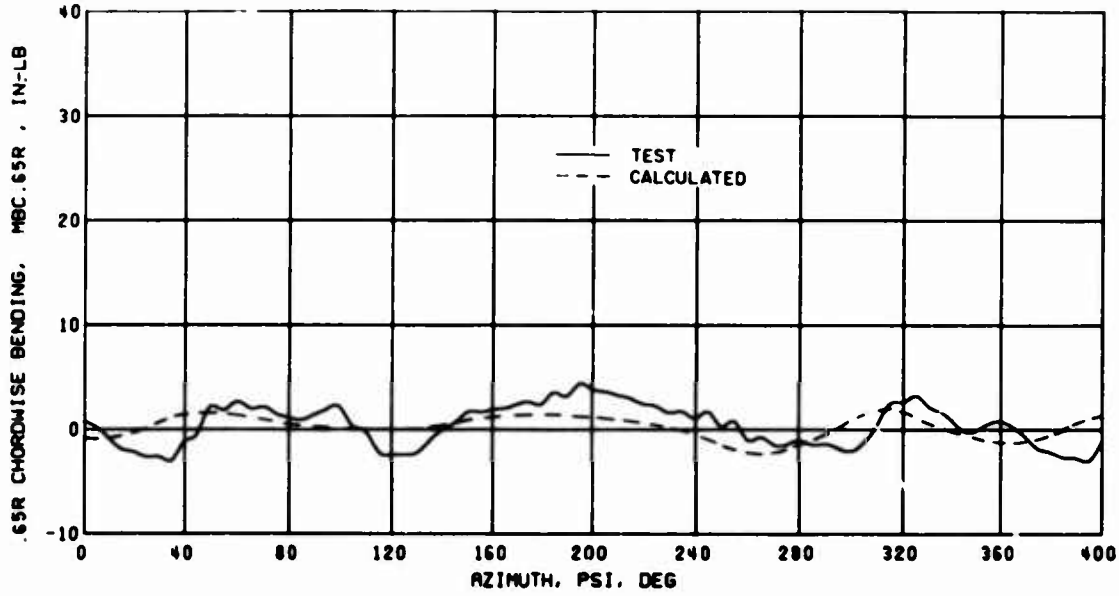

(c) .6 Chord Vortex Core Size

Figure 76. Concluded.

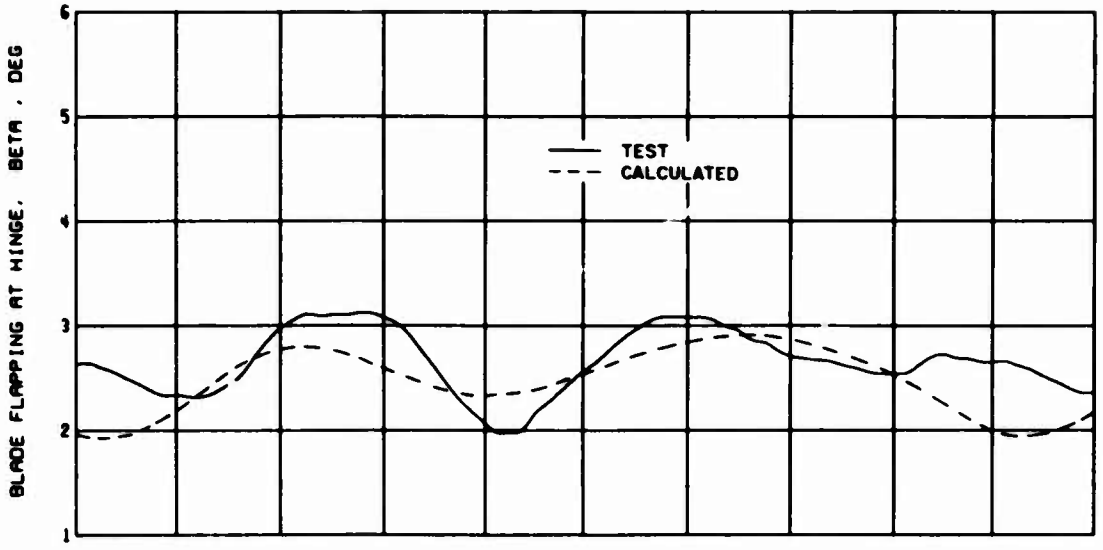

(a) Blade Flapping at Hinge, Condition 1

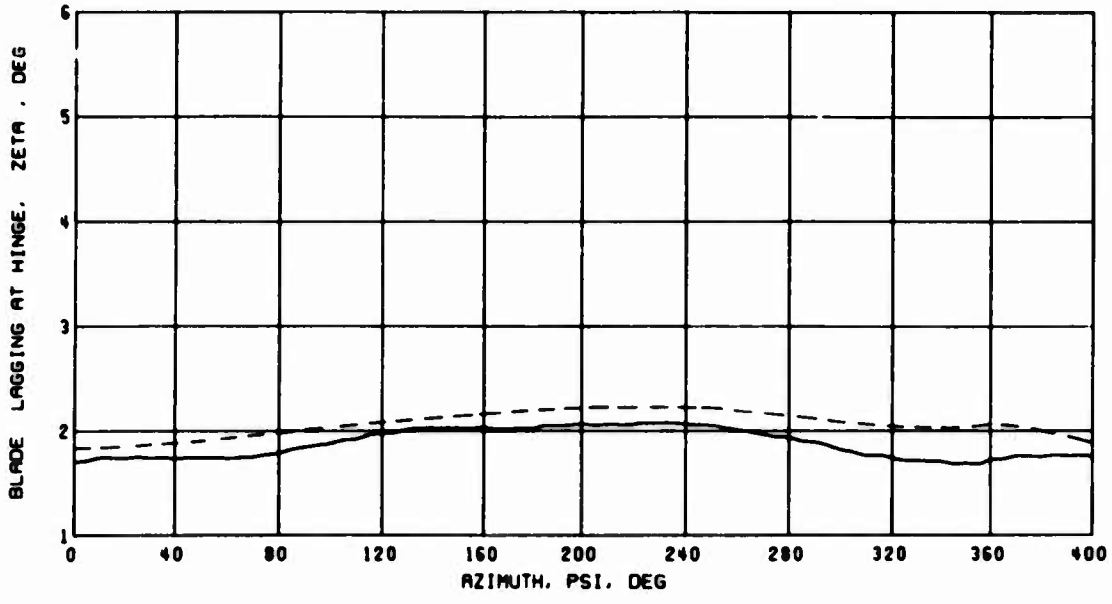

(b) Blade Lagging at Hinge, Condition 1

Figure 77. Correlation of Test and Calculated Blade Hinge Motions With Uniform Inflow; $\theta_1 = 0$ deg, $\delta_F = 0$ deg, $S_E = 1$.

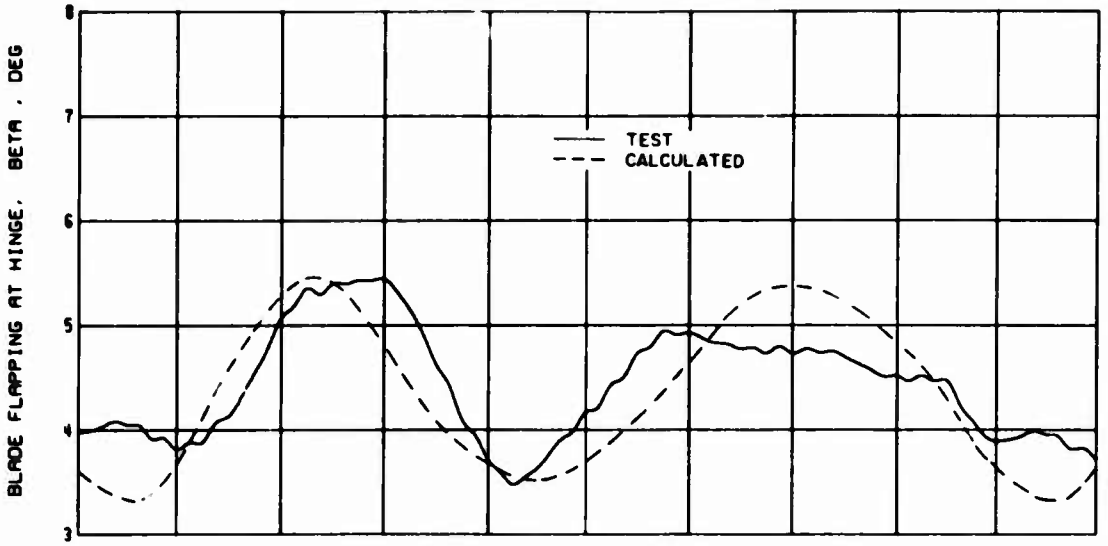

(c) Blade Flapping at Hinge, Condition 7

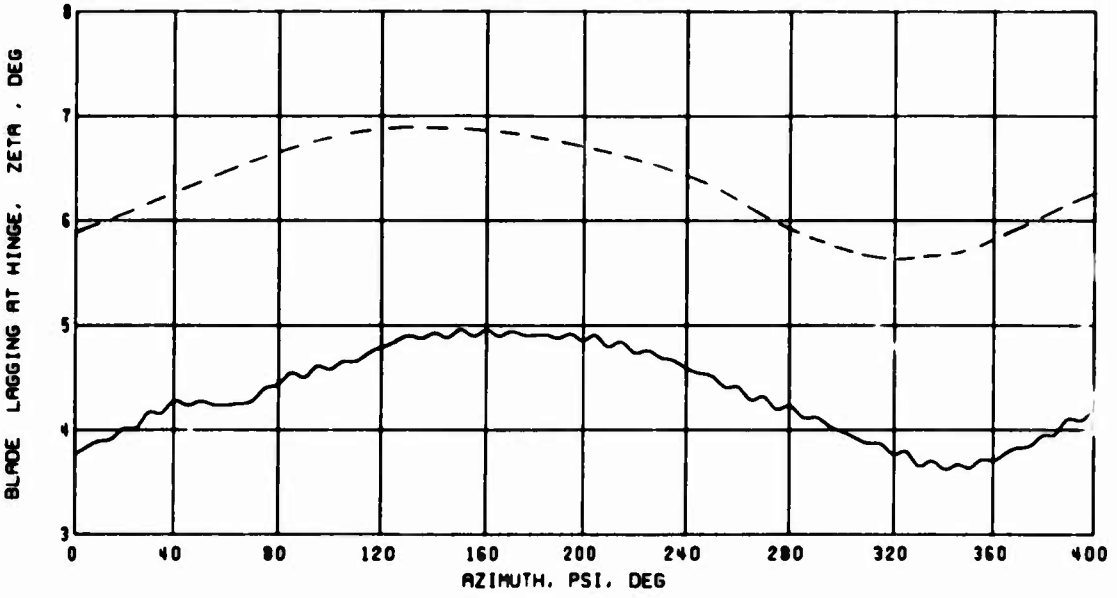

(d) Blade Lagging at Hinge, Condition 7

Figure 77. Continued.

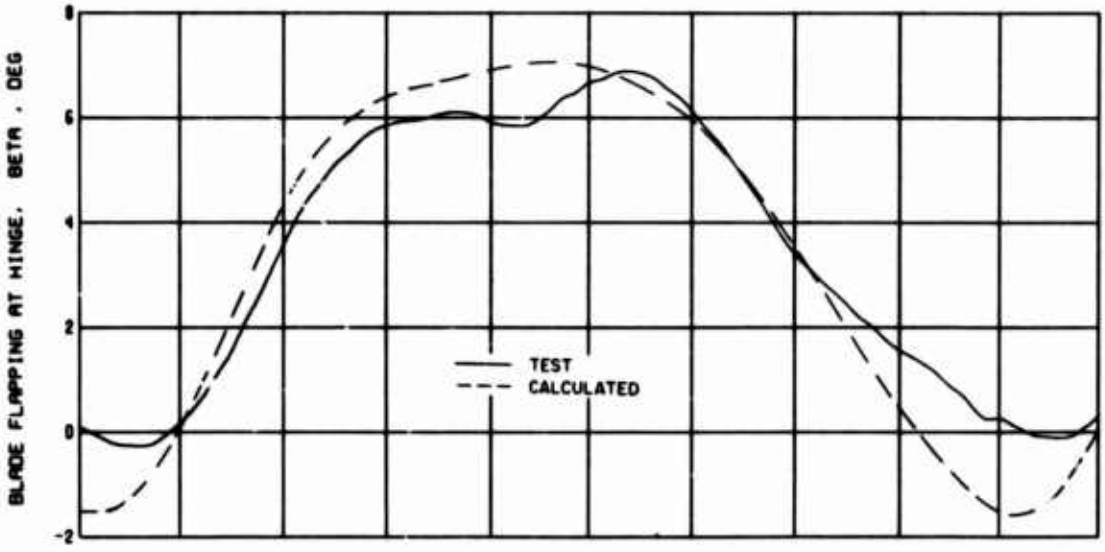

(e) Blade Flapping at Hinge, Condition 36

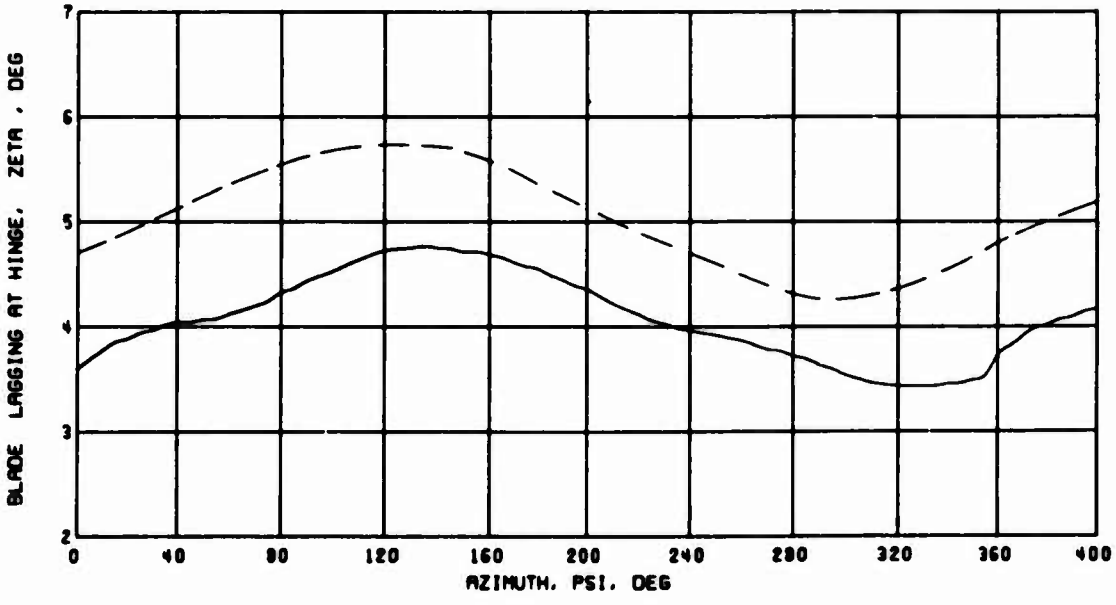

(f) Blade Lagging at Hinge, Condition 36

Figure 77. Continued.

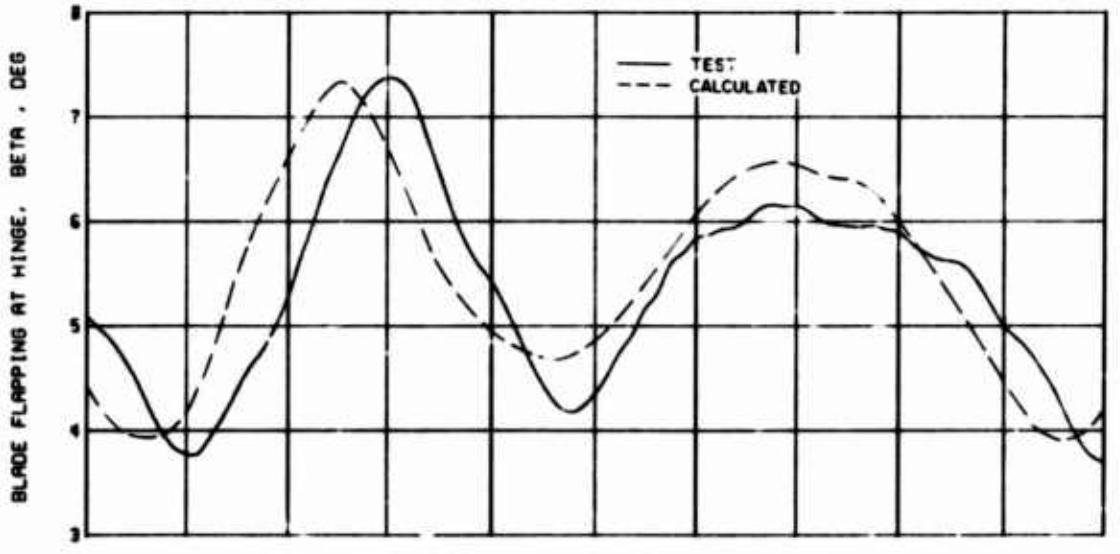

(g) Blade Flapping at Hinge, Condition 71

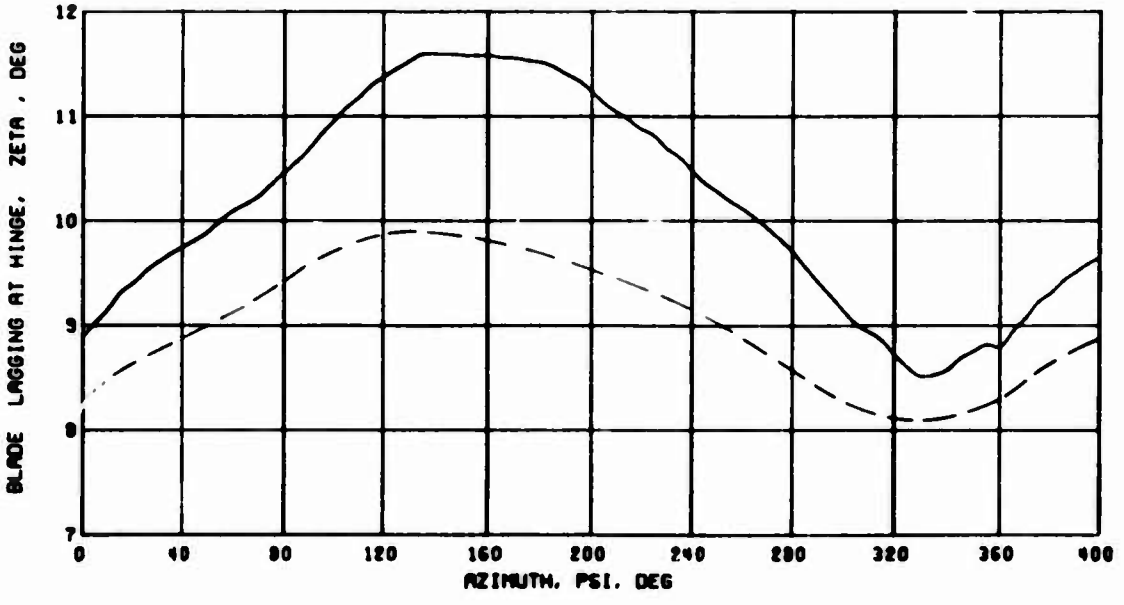

(h) Blade Lagging at Hinge, Condition 71

Figure 77. Continued.

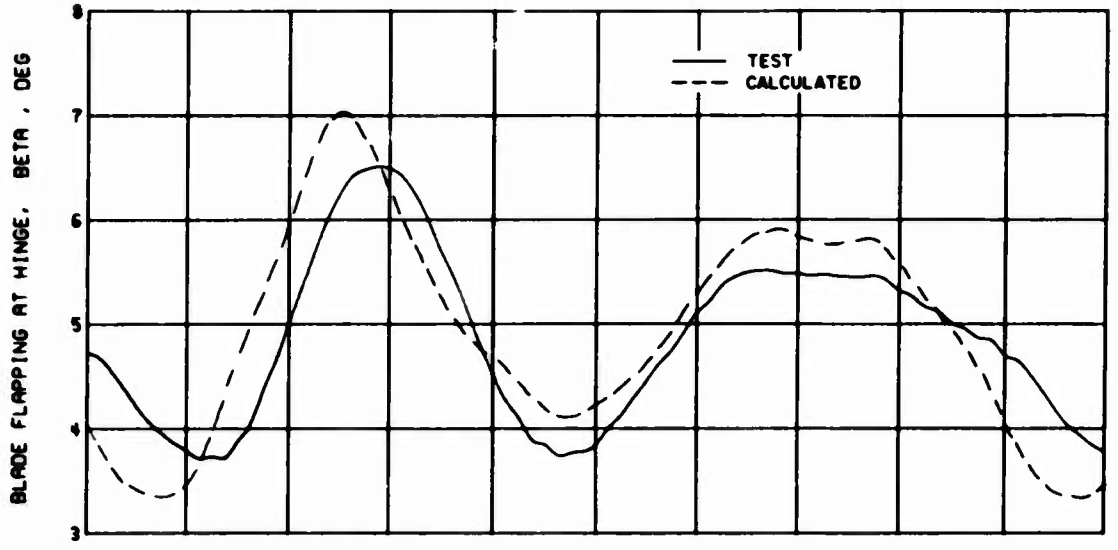

(i) Blade Flapping at Hinge, Condition 82

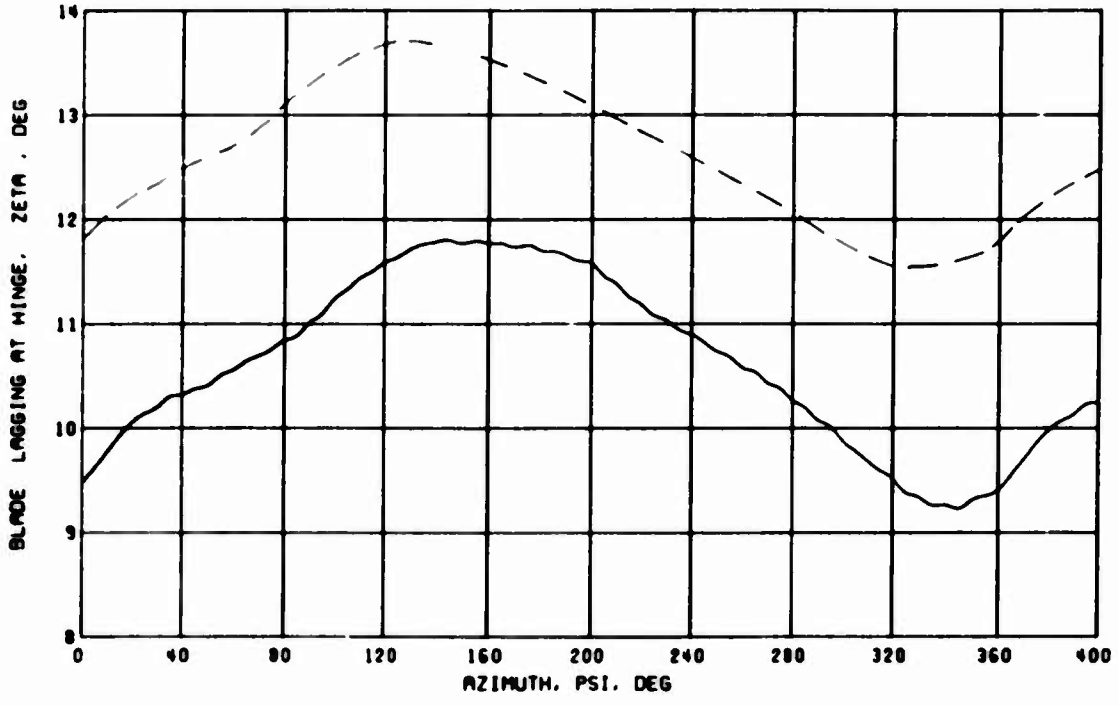

(j) Blade Lagging at Hinge, Condition 82

Figure 77. Concluded.

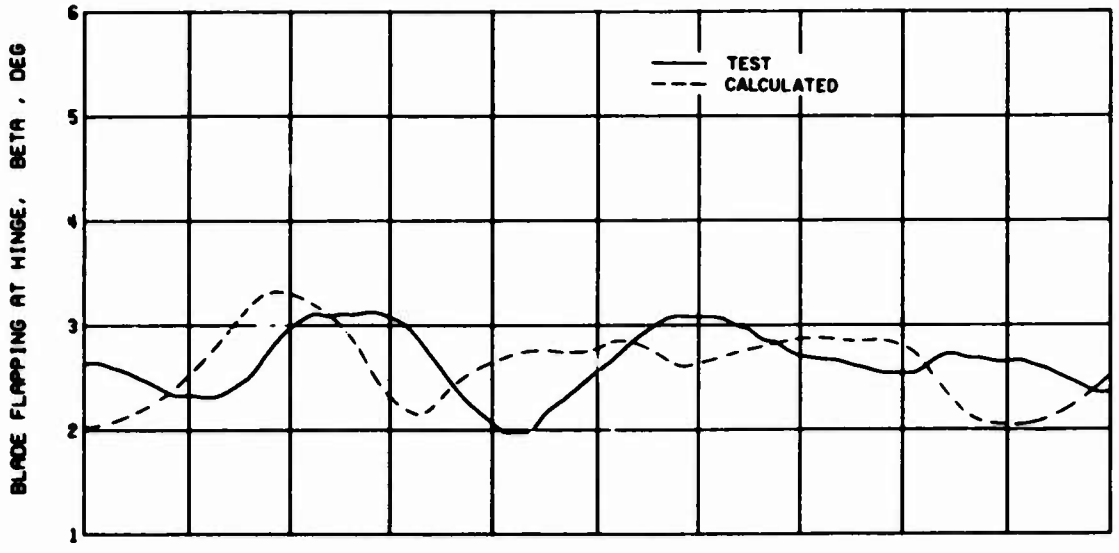

(a) Blade Flapping at Hinge, Condition 1

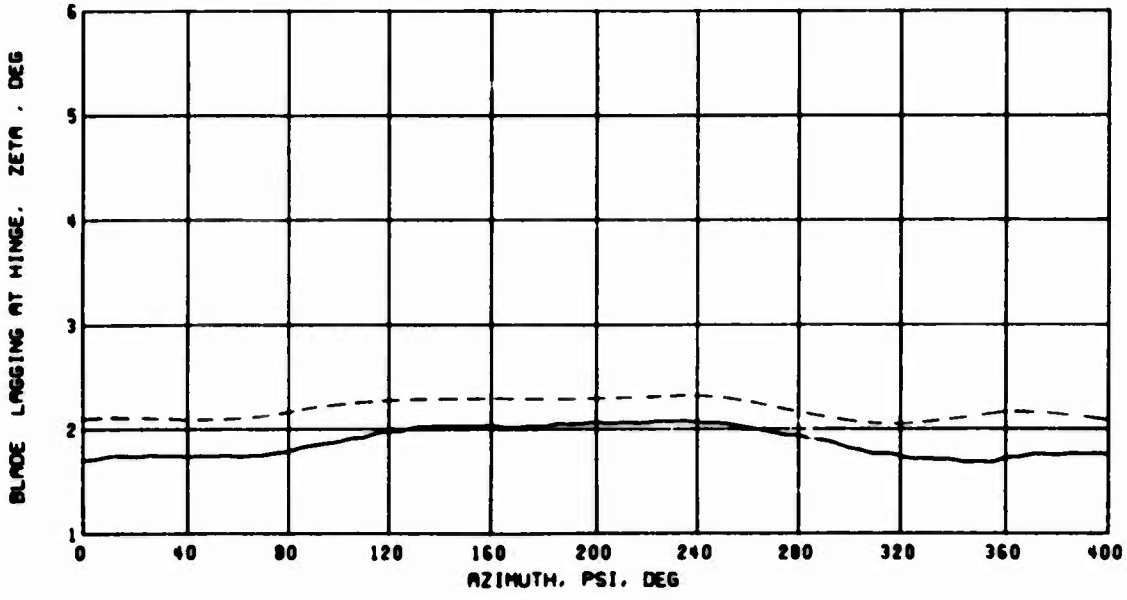

(b) Blade Lagging at Hinge, Condition 1

Figure 78. Correlation of Test and Calculated Blade Hinge Motions With Variable Inflow; θ_1 = 0 deg, δ_F = 0 deg, S_E = 1.

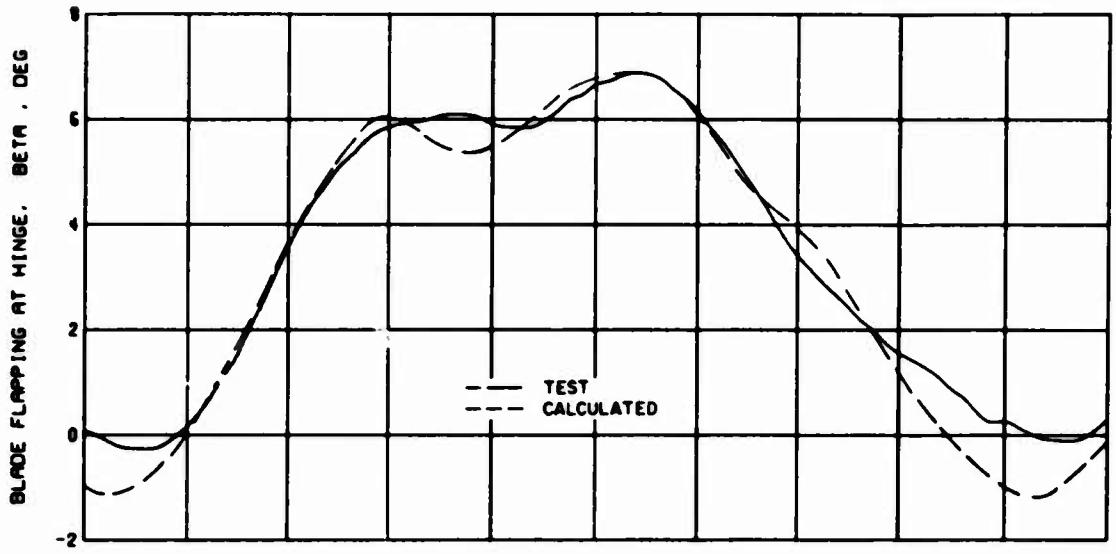

(c) Blade Flapping at Hinge, Condition 36

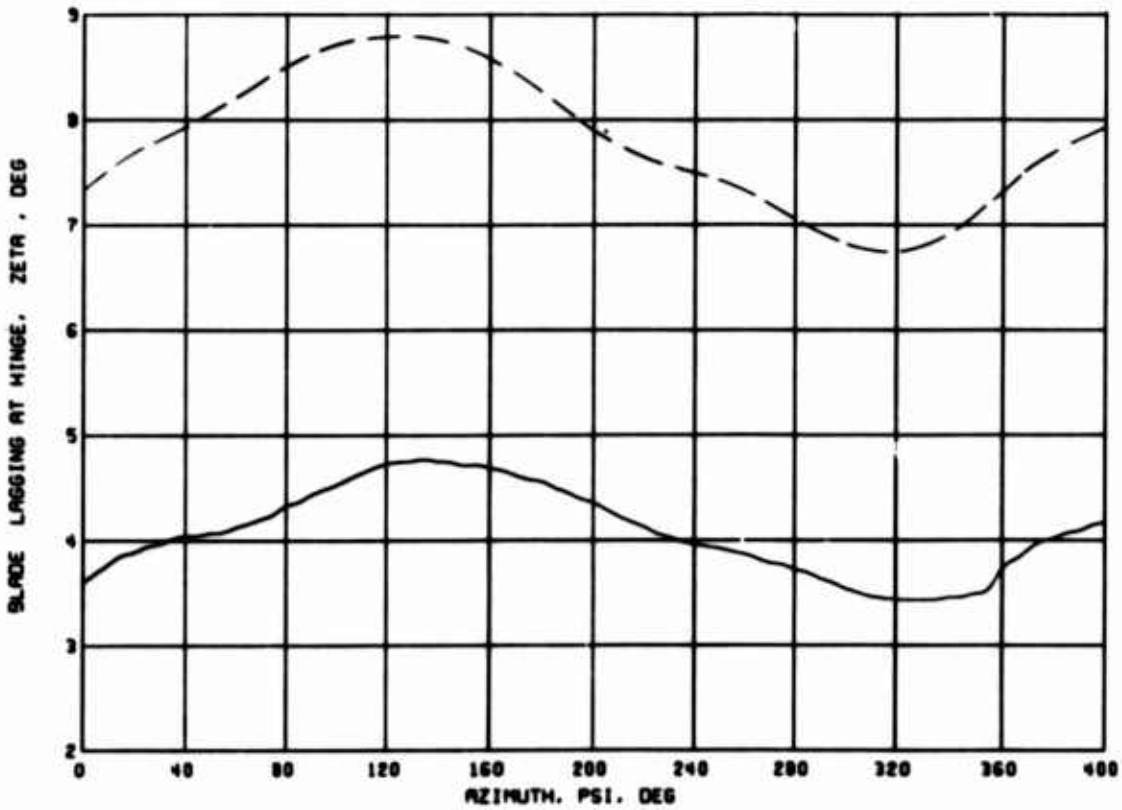

(d) Blade Lagging at Hinge, Condition 36

Figure 78. Continued.

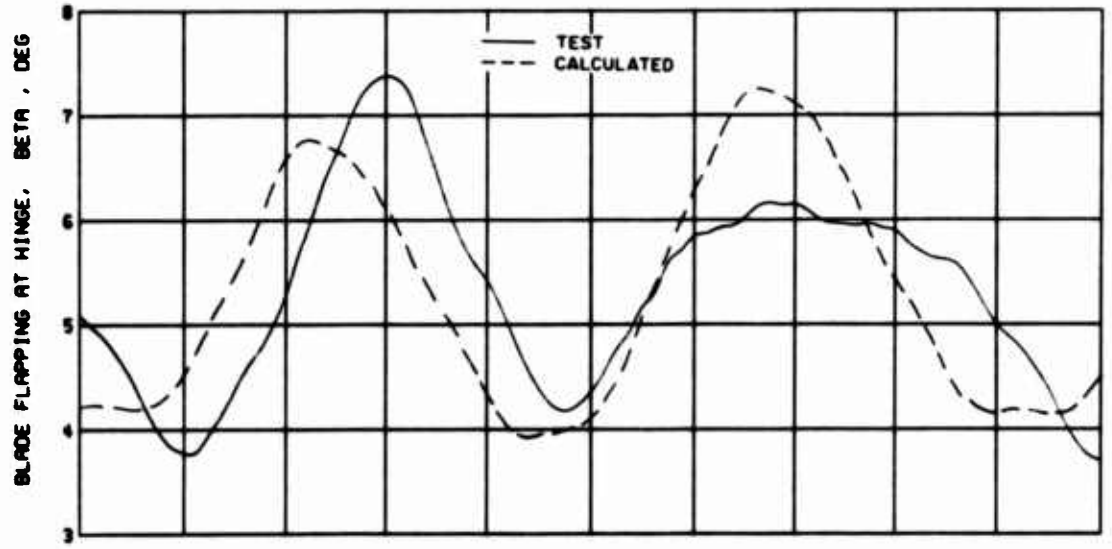

(e) Blade Flapping at Hinge, Condition 71

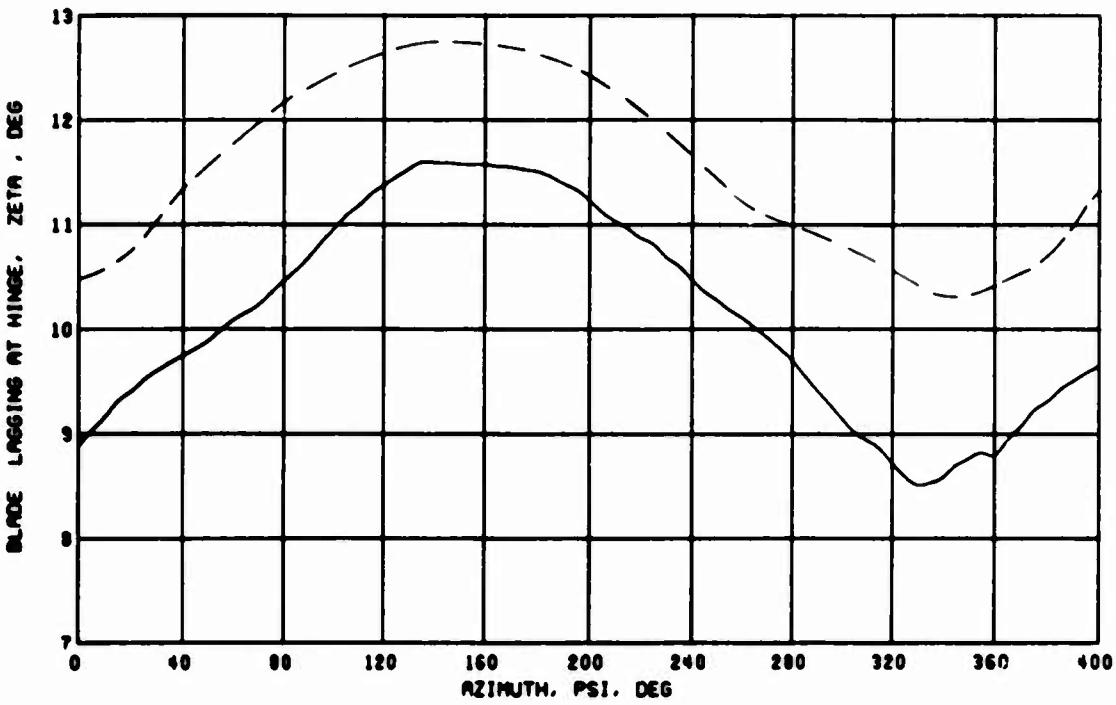

(f) Blade Lagging at Hinge, Condition 71

Figure 78. Concluded.

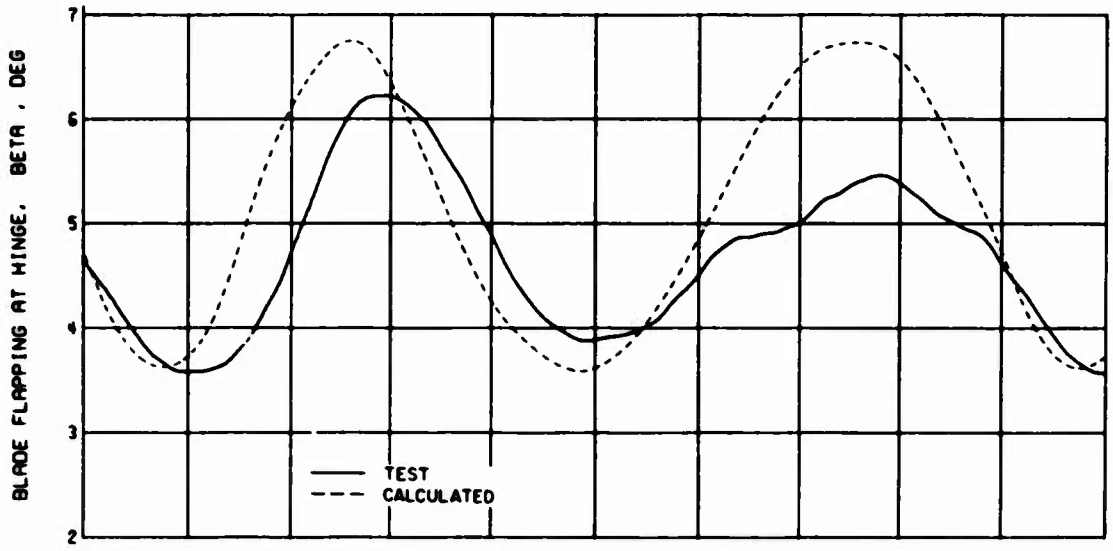

(a) Blade Flapping at Hinge, Condition 82

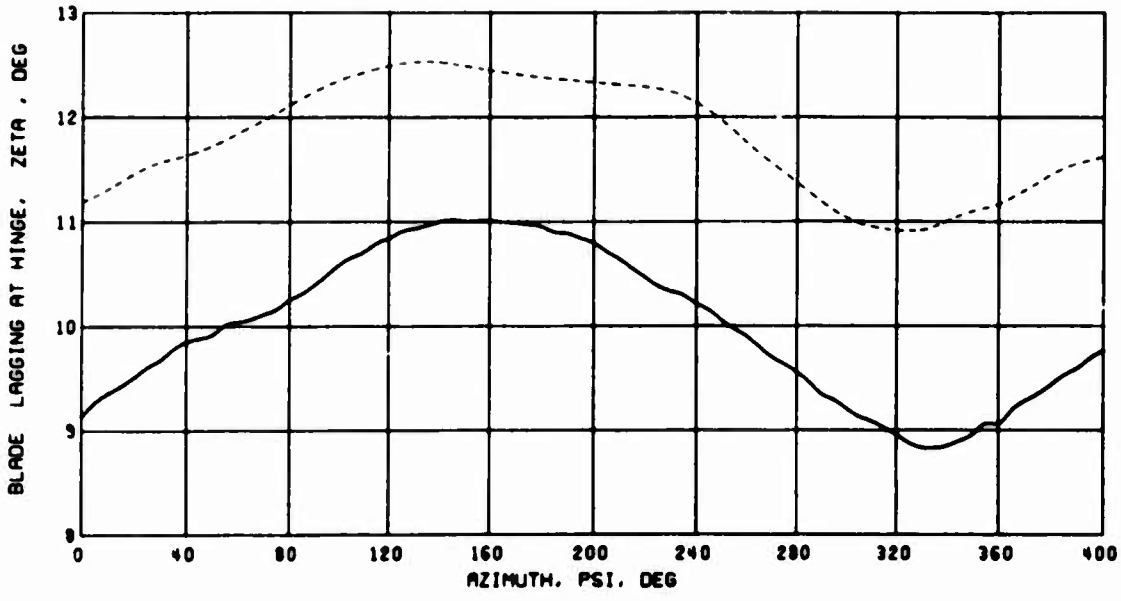

(b) Blade Lagging at Hinge, Condition 82

Figure 79. Correlation of Test and Calculated Blade Hinge Motions With Uniform Inflow; $\theta_1 = -8$ deg, $\delta_F = 0$ deg, $S_E = 1$.

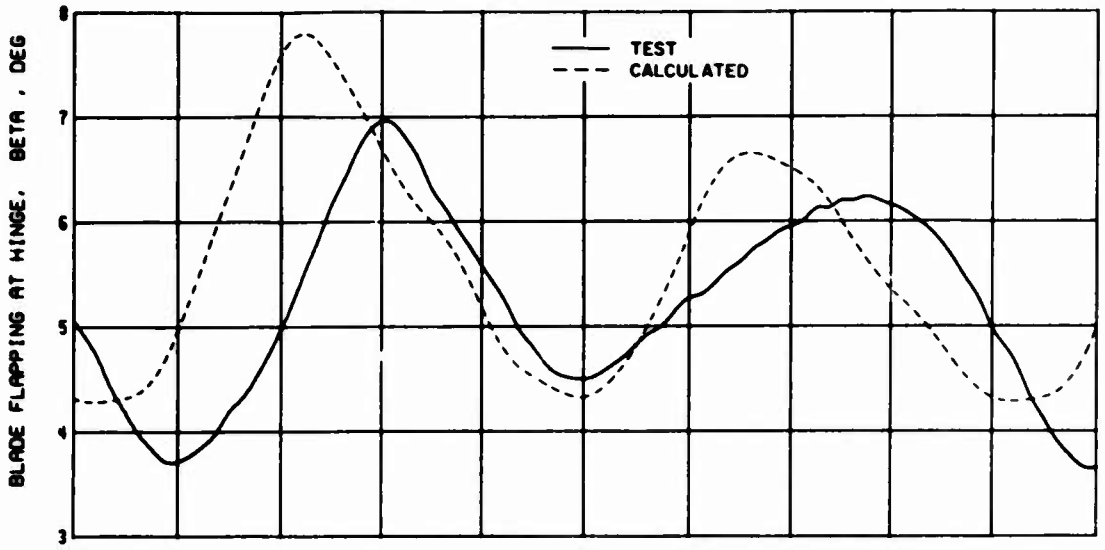

(a) Blade Flapping at Hinge, Condition 71

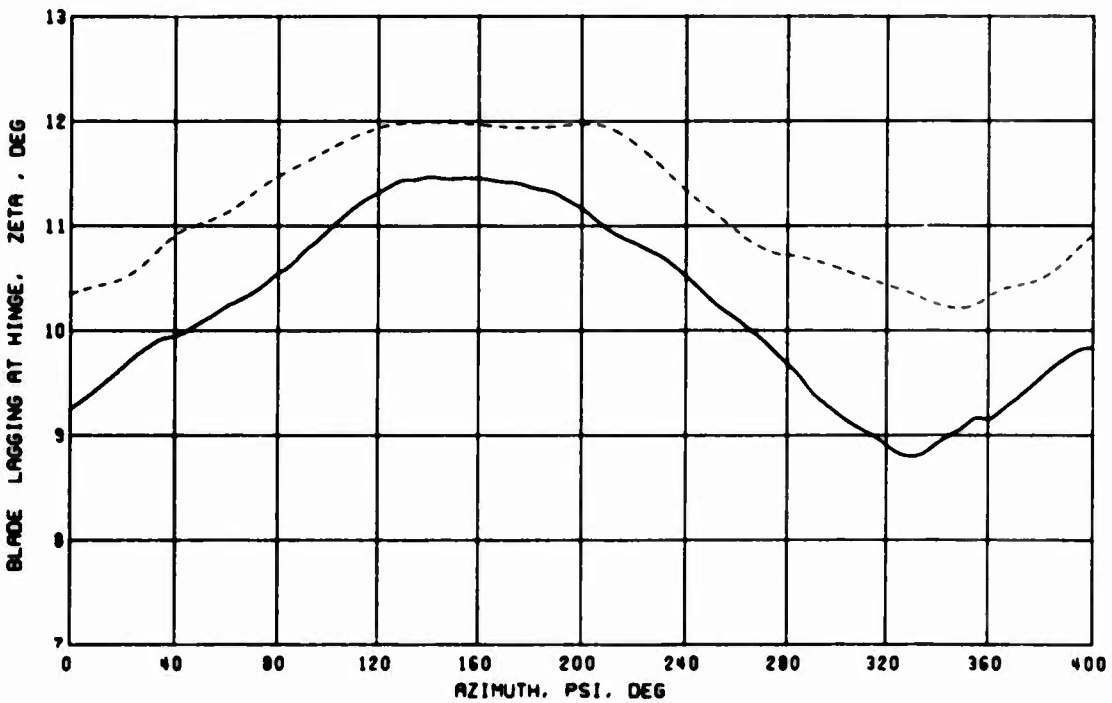

(b) Blade Lagging at Hinge, Condition 71

Figure 80. Correlation of Test and Calculated Blade Hinge Motions With Variable Inflow: $\theta_1 = -8$ deg, $\delta_F = 0$ deg, $S_E = 1$.

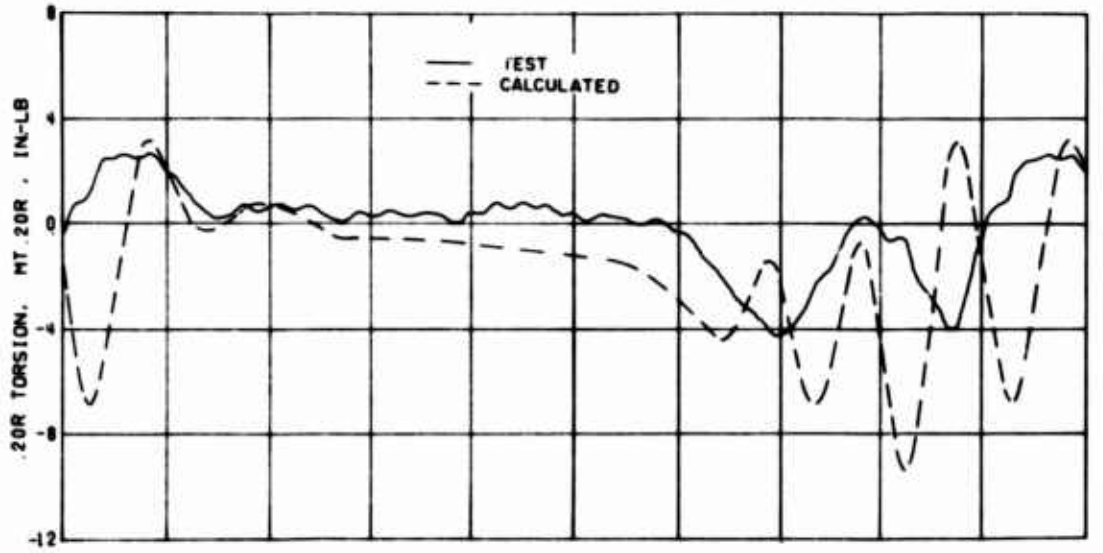

(a) .20R Torsion, Condition 7

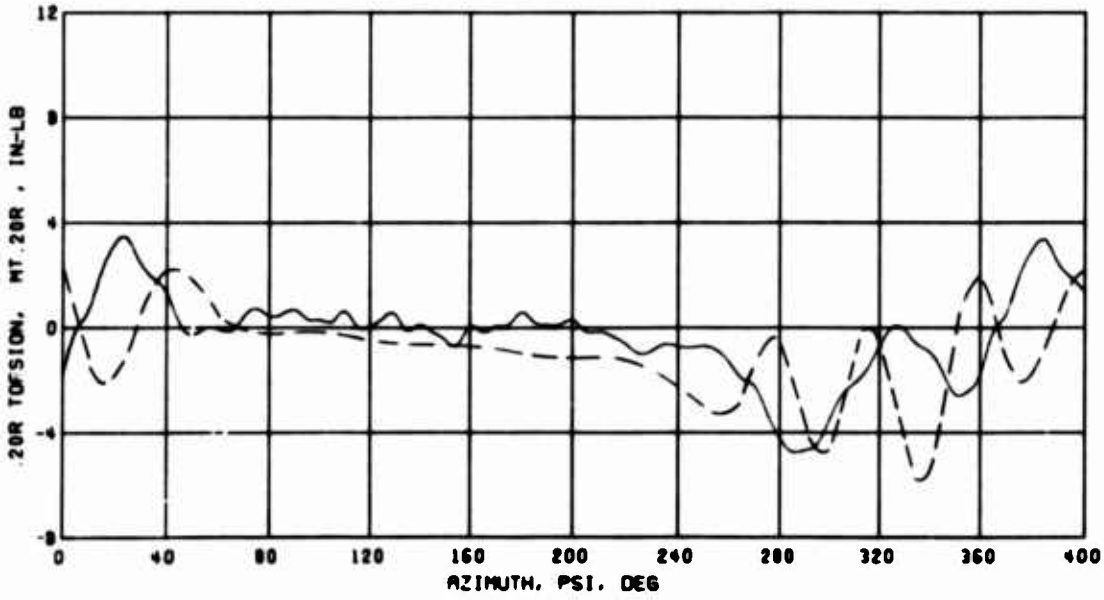

(b) .20R Torsion, Condition 36

Figure 81. Correlation of Test and Calculated Torsion With Uniform Inflow; θ_1 = 0 deg, δ_F = 0 deg, S_E = 1.

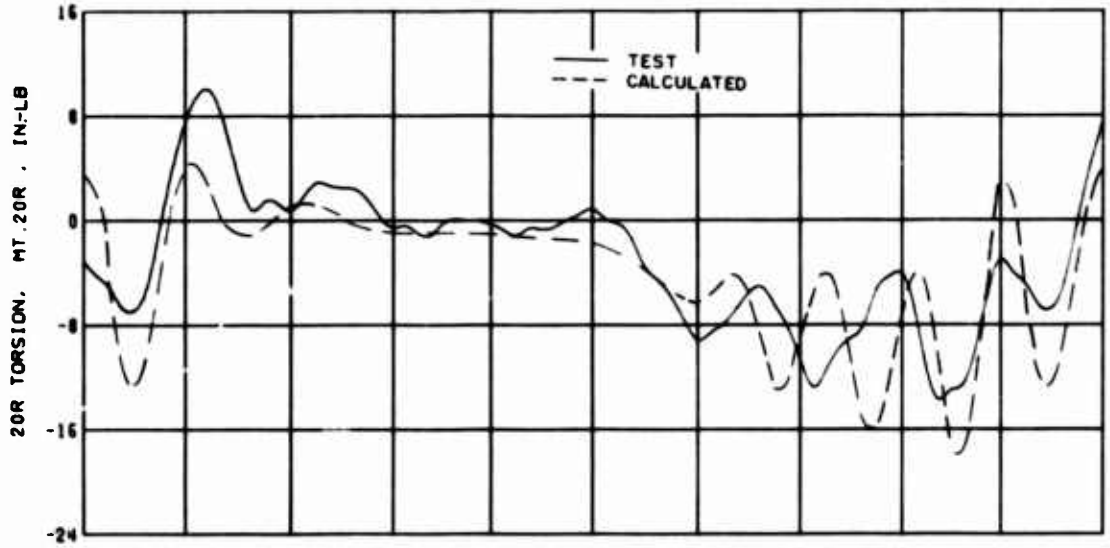

(c) .20R Torsion, Condition 71

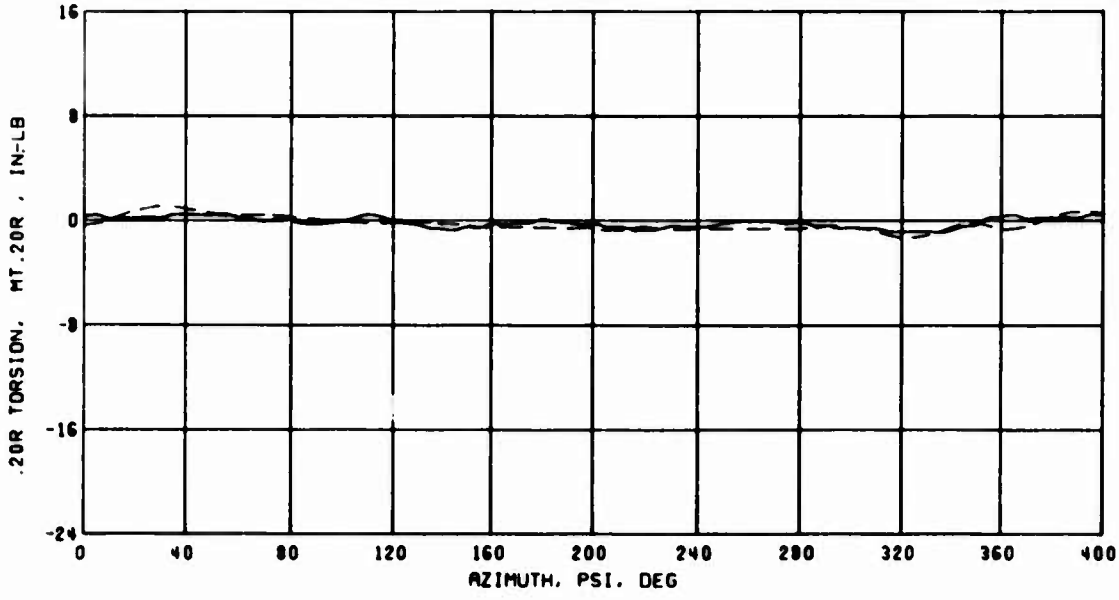

(d) .20R Torsion, Condition 80

Figure 81. Continued.

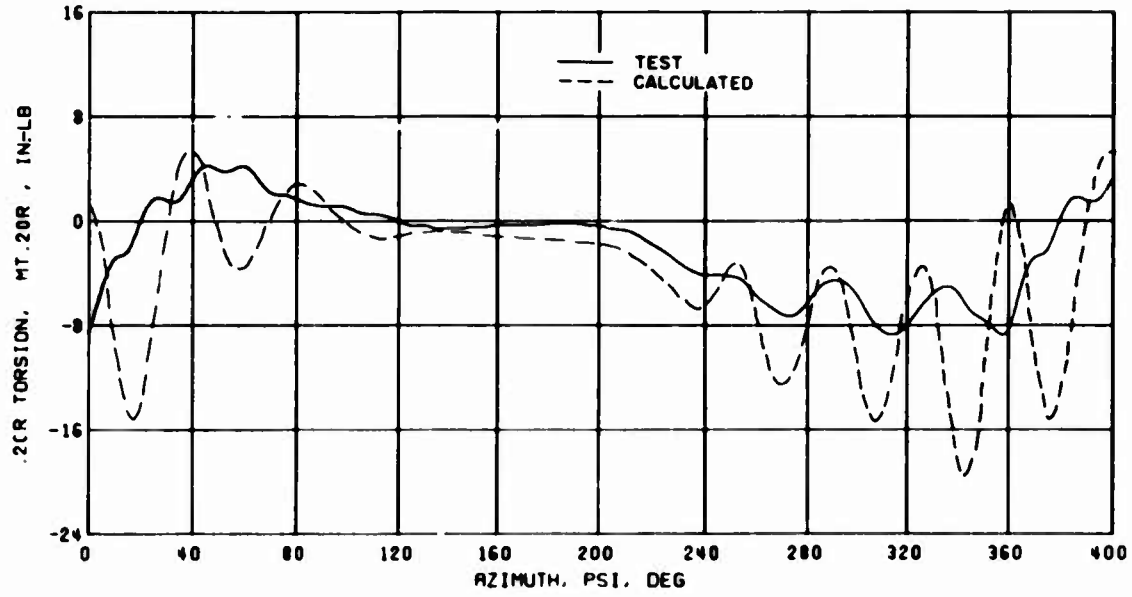

(e) .20R Torsion, Condition 82

Figure 81. Concluded.

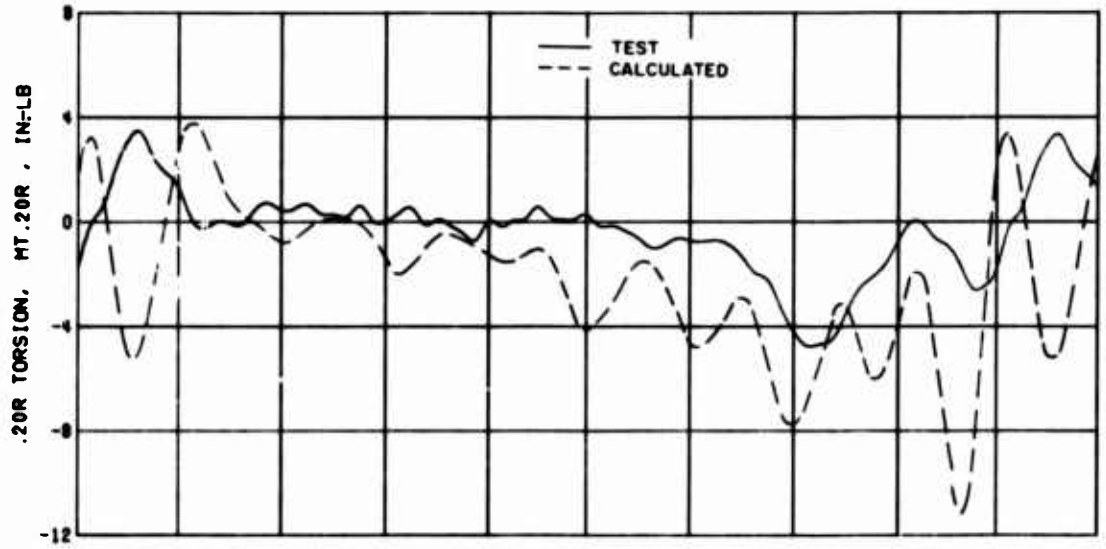

(a) .20R Torsion, Condition 36

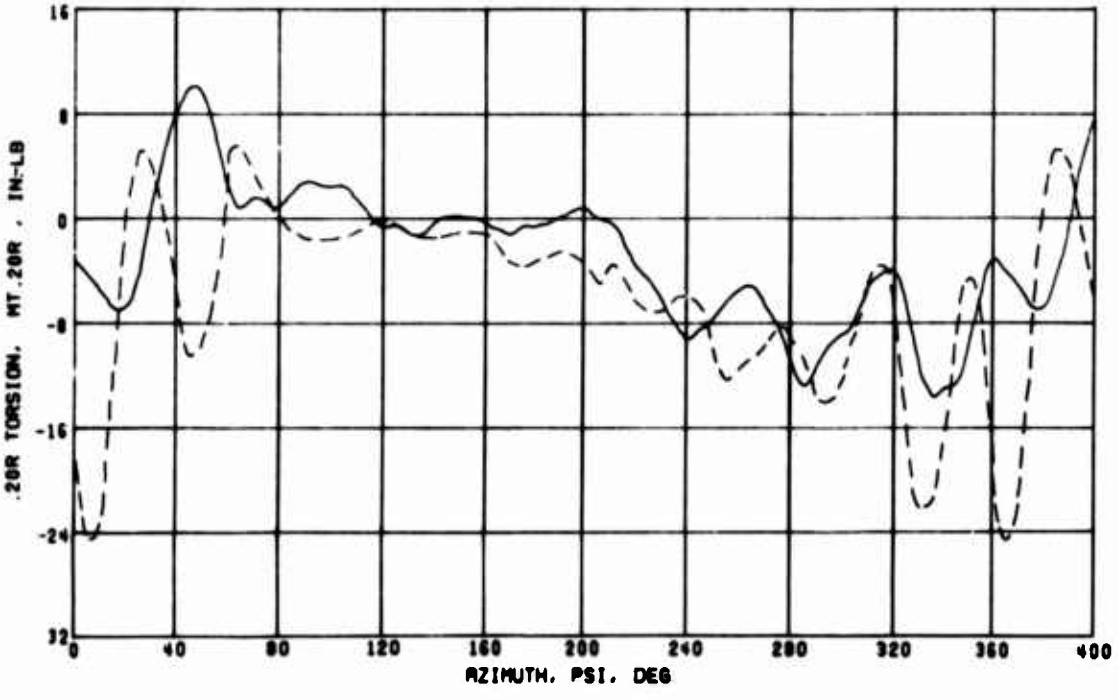

(b) .20R Torsion, Condition 71

Figure 82. Correlation of Test and Calculated Torsion With Variable Inflow; θ_1 = 0 deg, δ_F = 0 deg, S_E = 1.

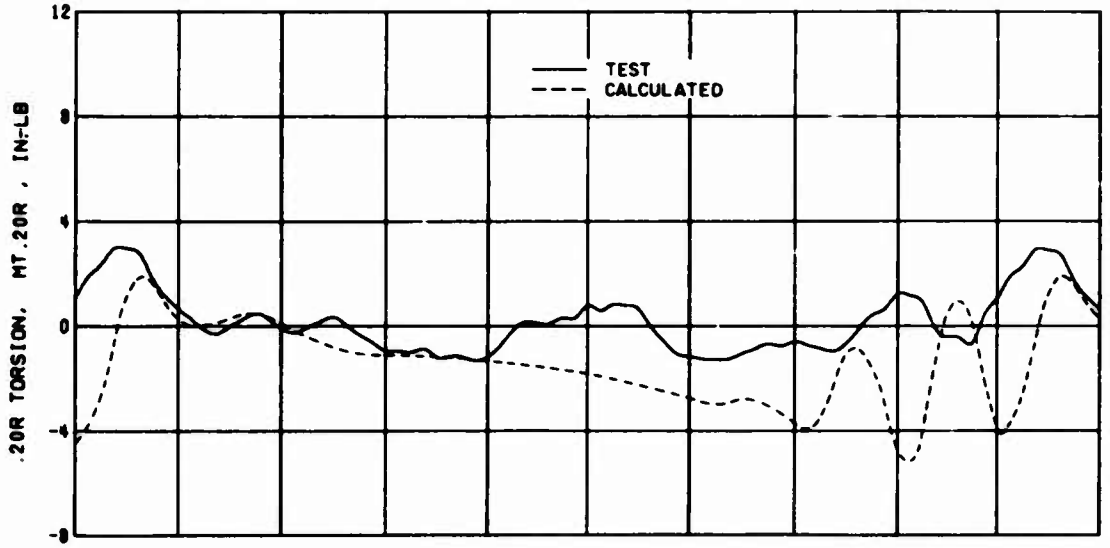

(a) .20R Torsion, Condition 7

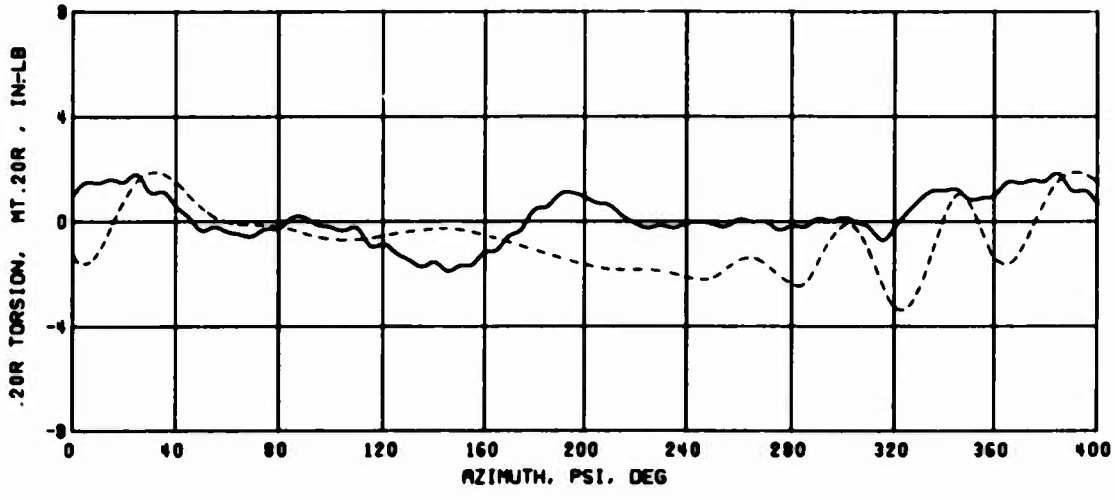

(b) .20R Torsion, Condition 36

Figure 83. Correlation of Test and Calculated Torsion With Uniform Inflow; θ_1 = -8 deg, δ_F = 0 deg, S_E = 1.

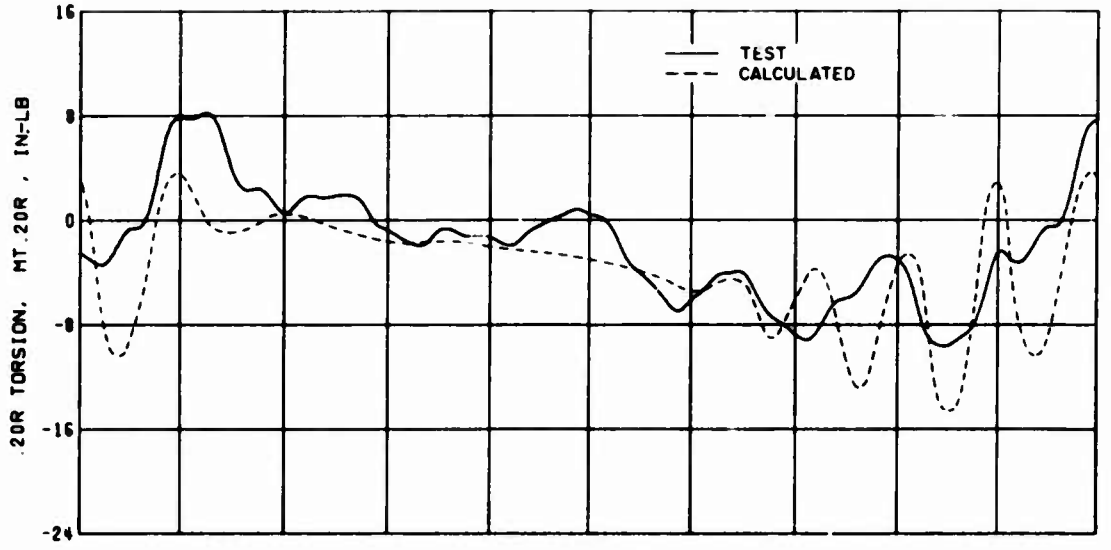

(c) .20R Torsion, Condition 71

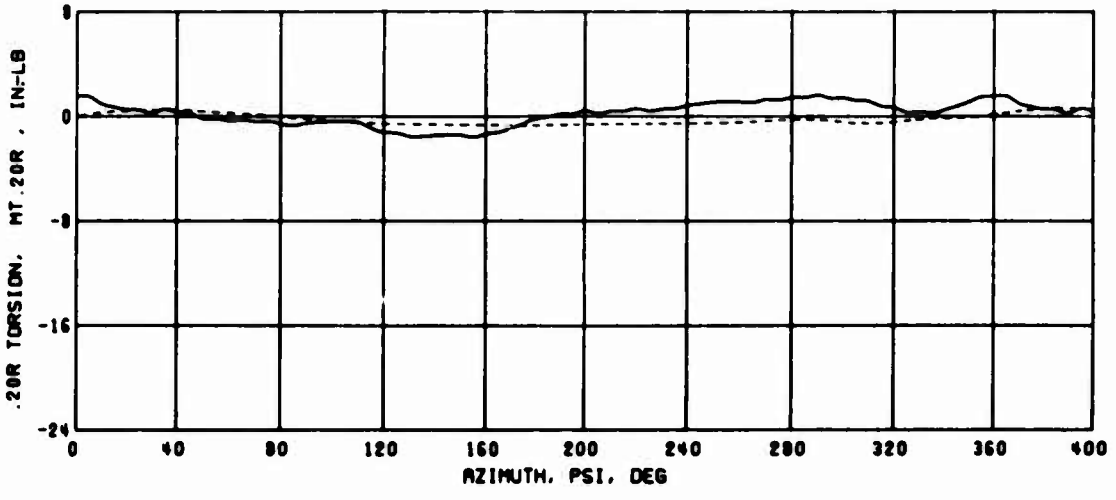

(d) .20R Torsion, Condition 80

Figure 83. Continued.

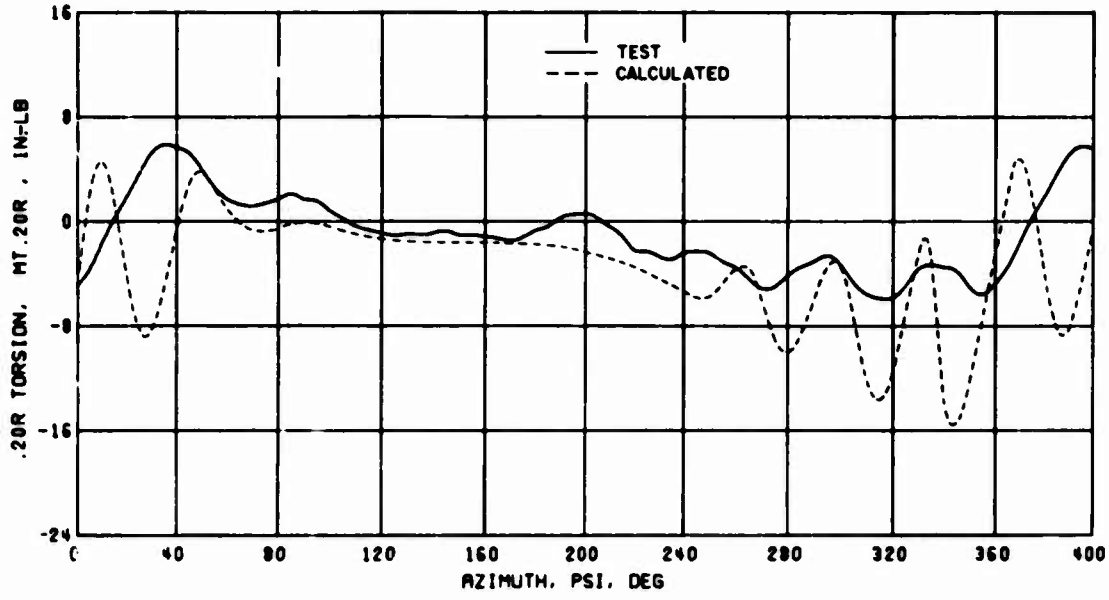

(e) .20T Torsion, Condition 82

Figure 83. Concluded.

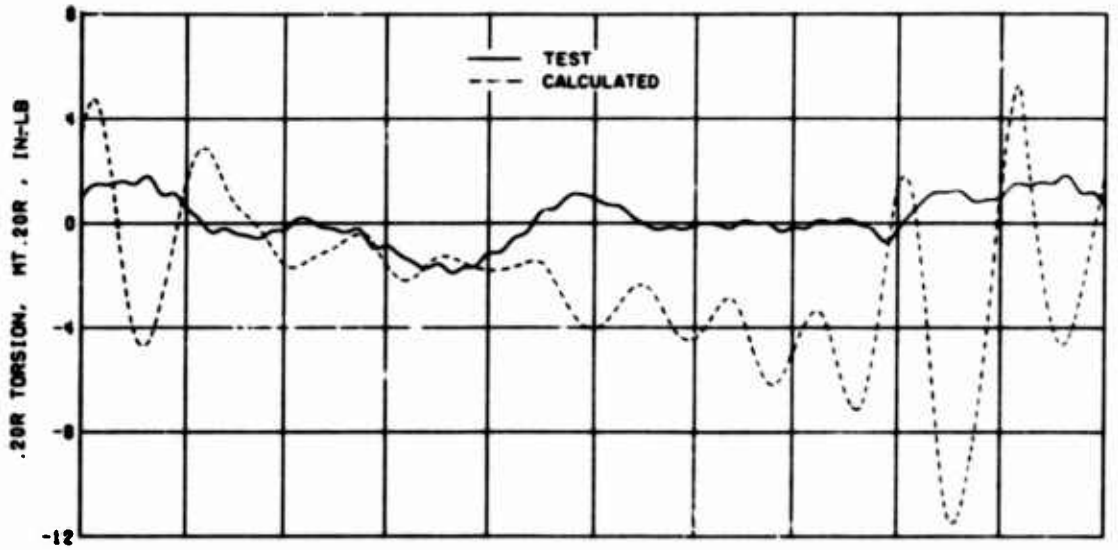

(a) .20R Torsion, Condition 36, Unsteady Aerodynamic Scaling Case 3

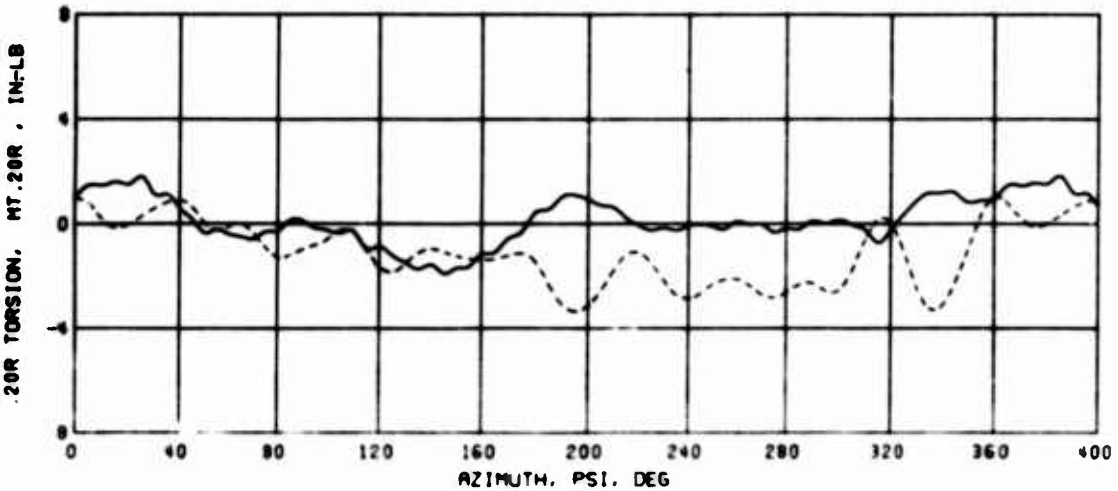

(b) .20R Torsion, Condition 36, Unsteady Aerodynamic Scaling Case 1

Figure 84. Correlation of Test and Calculated Torsion With Variable Inflow; θ_1 = -8 deg, δ_F = 0 deg, S_E = 1.

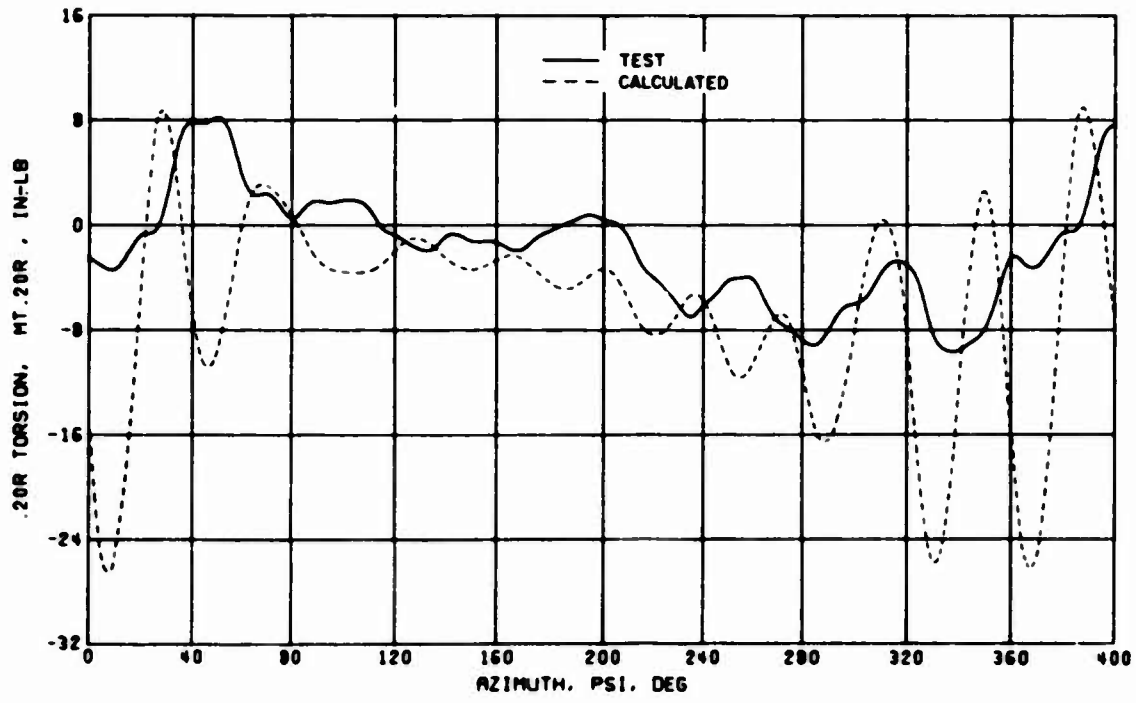

(c) .20R Torsion, Condition 71, Unsteady Aerodynamic Scaling Case 1

Figure 84. Concluded.

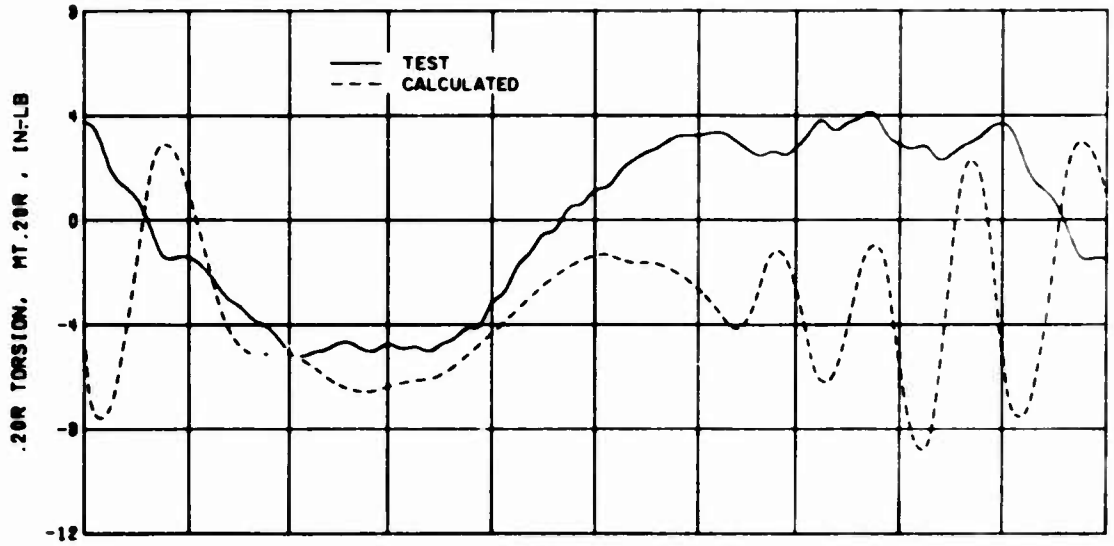

(a) .20R Torsion, Condition 7

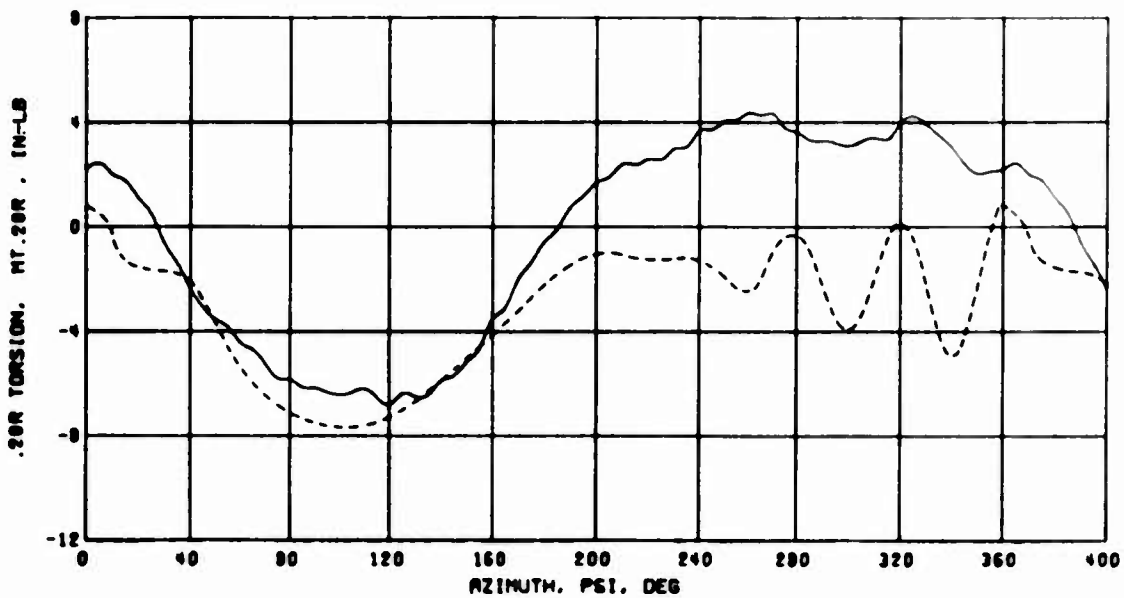

(b) .20R Torsion, Condition 36

Figure 85. Correlation of Test and Calculated Torsion With Uniform Inflow; θ_1 = 0 deg, δ_P = 5 deg, S_E = 1.

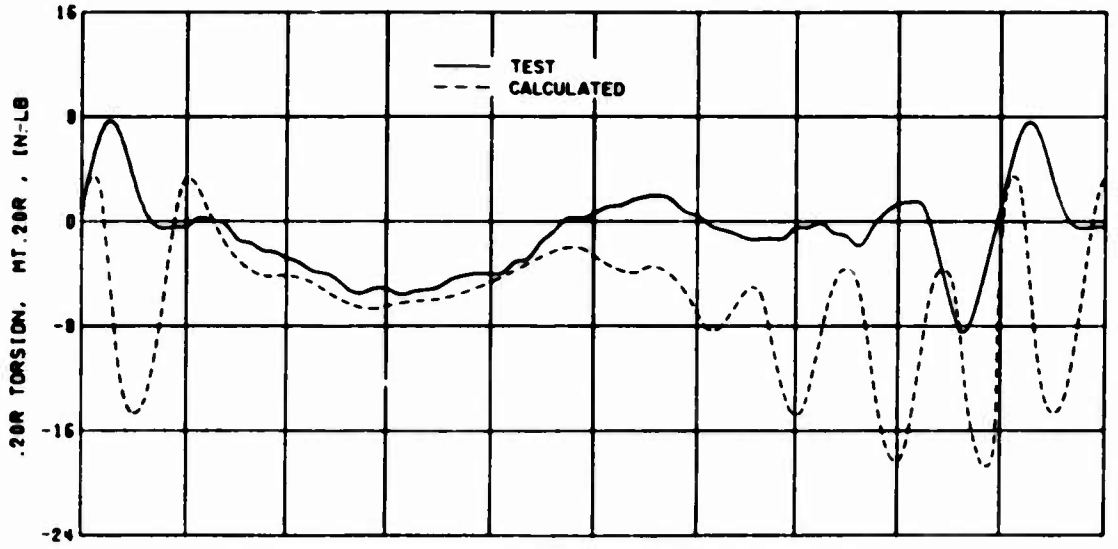

(c) .20R Torsion, Condition 71

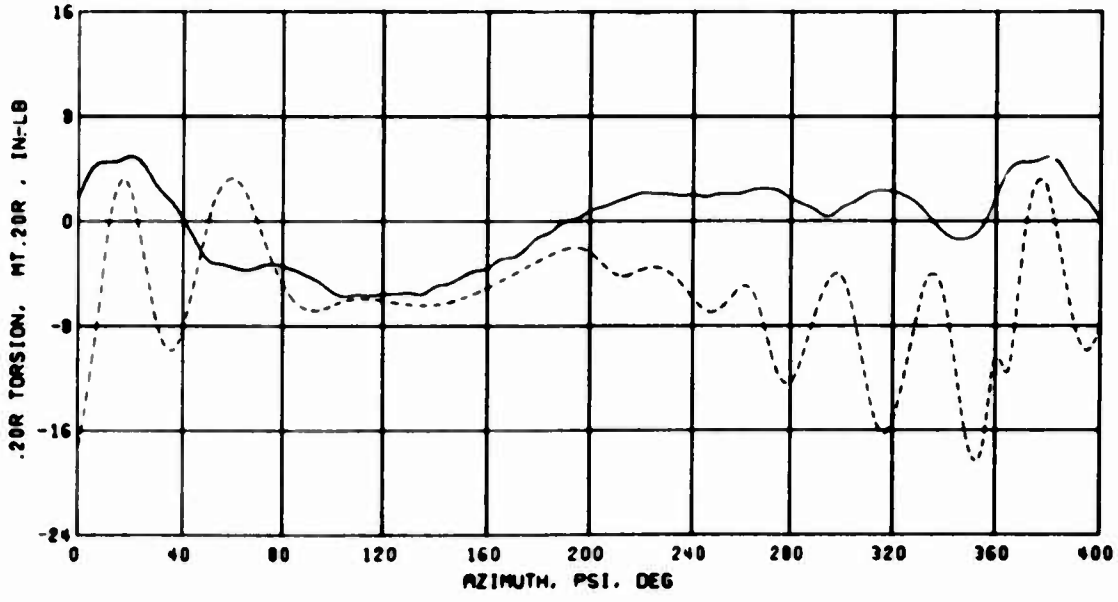

(d) .20R Torsion, Condition 82

Figure 85. Concluded.

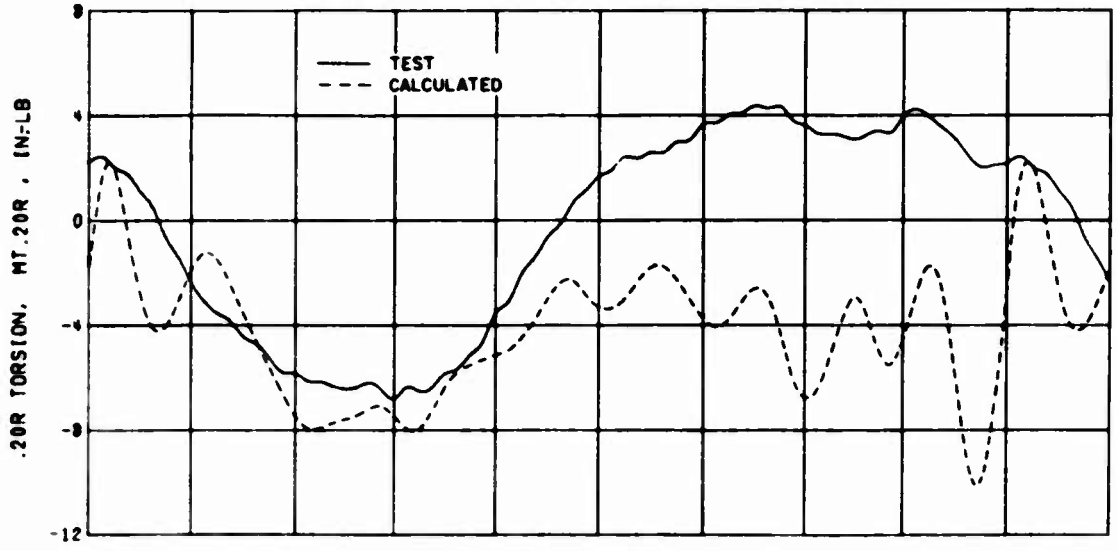

(a) .20R Torsion, Condition 36

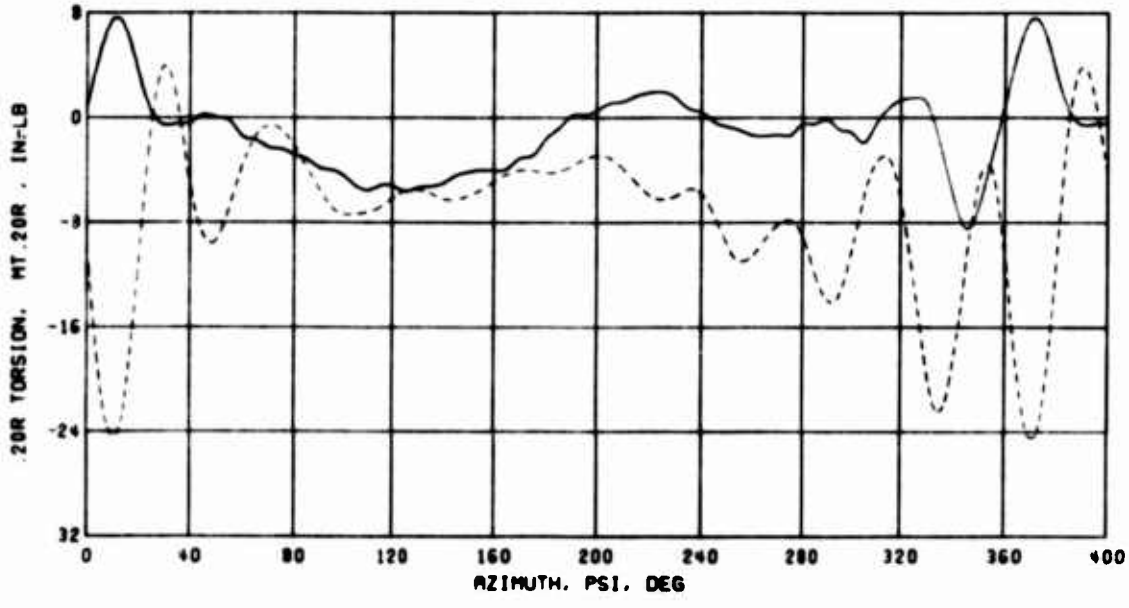

(b) .20R Torsion, Condition 71

Figure 86. Correlation of Test and Calculated Torsion With Variable Inflow; θ_1 = 0 deg, δ_P = 5 deg, S_E = 1.

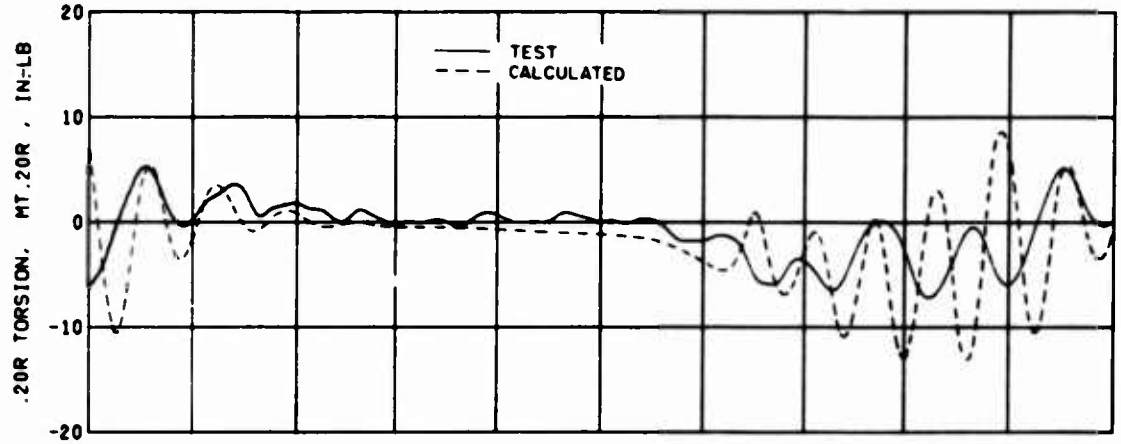

(a) .20R Torsion, Condition 7

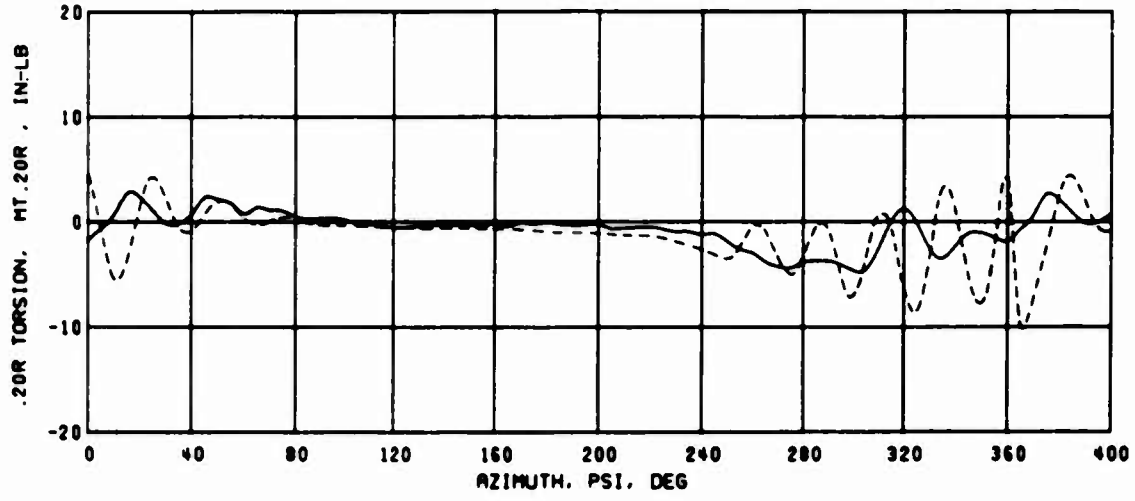

(b) .20R Torsion, Condition 36

Figure 87. Correlation of Test and Calculated Torsion With Uniform Inflow; θ_1 = 0 deg, δ_F = 0 deg, S_E = 3.

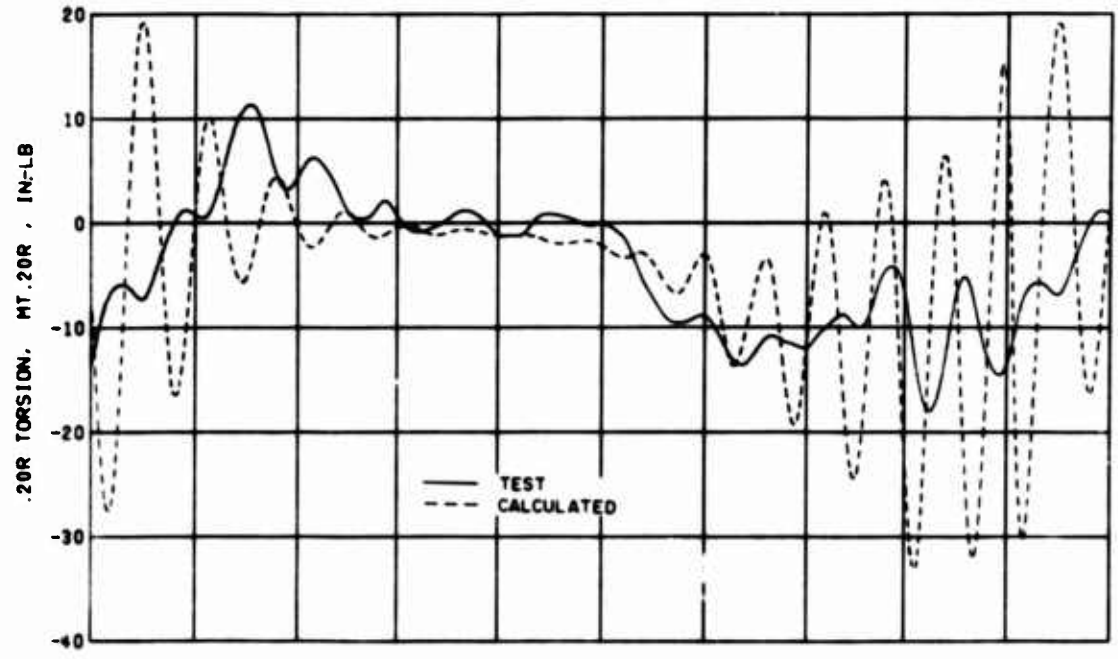

(c) .20R Torsion, Condition 71

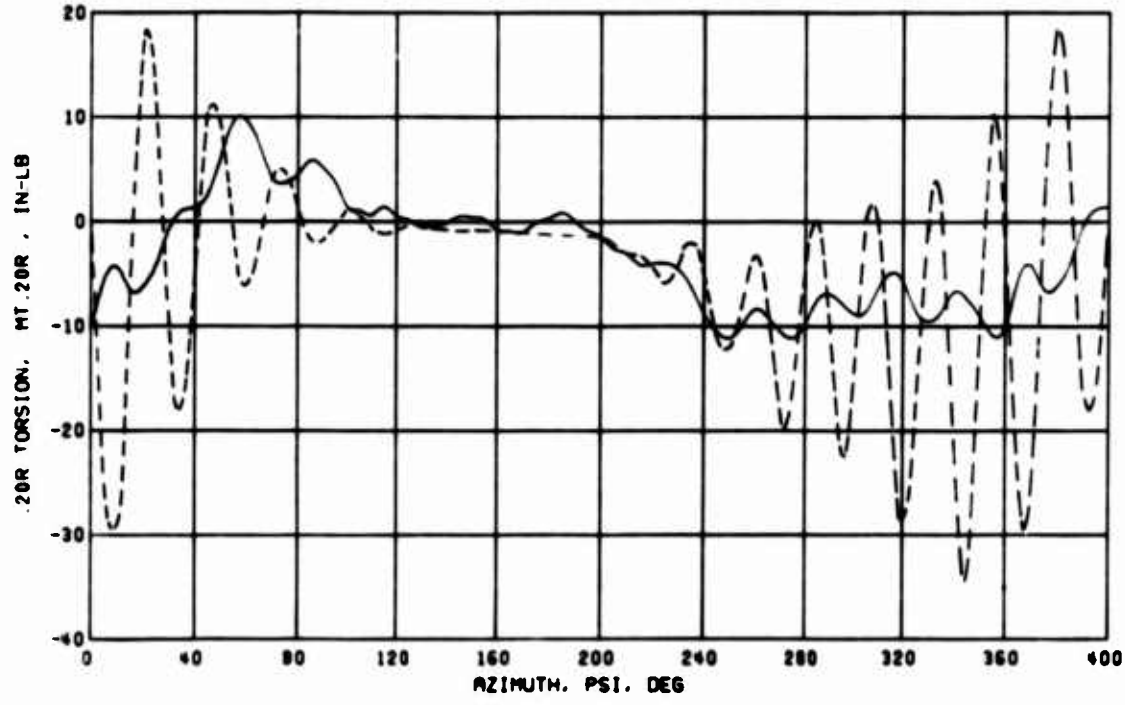

(d) .20R Torsion, Condition 82

Figure 87. Concluded.

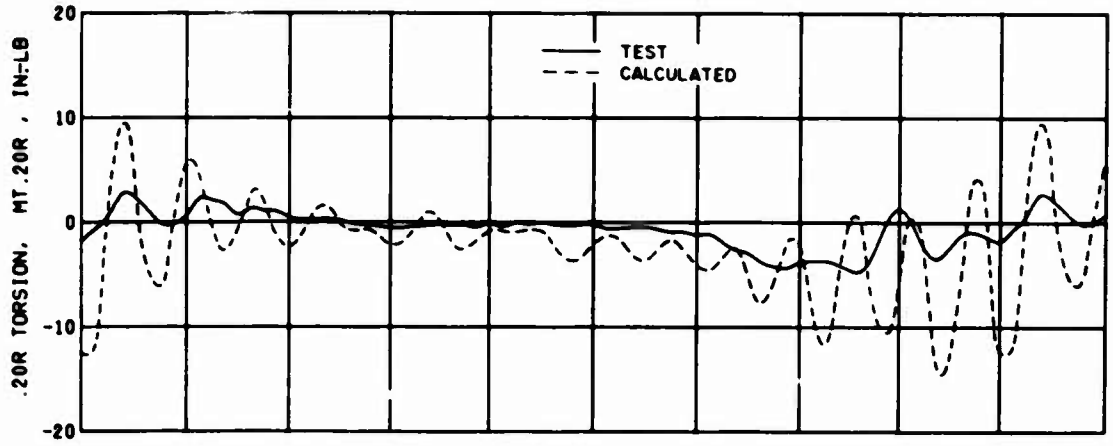

(a) .20 Torsion, Condition 36

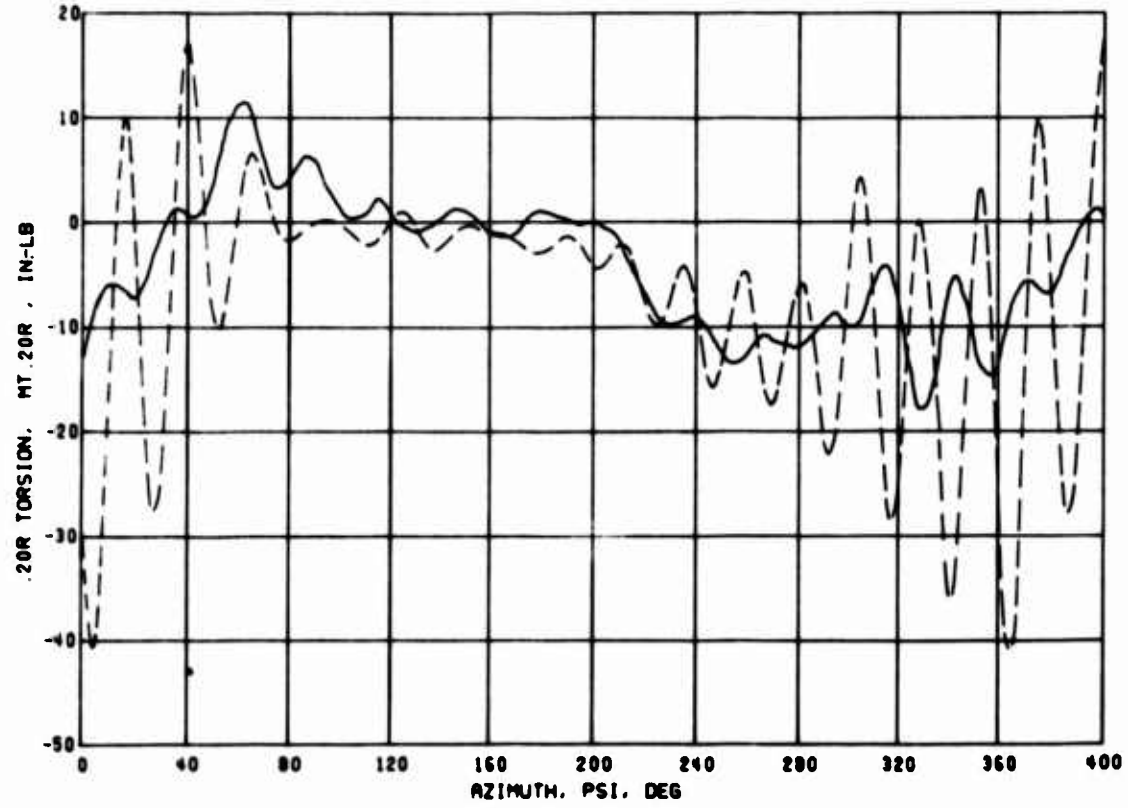

(b) .20 Torsion, Condition 71

Figure 88. Correlation of Test and Calculated Torsion With Variable Inflow; θ_1 = 0 deg, δ_F = 0 deg, S_E = 3.

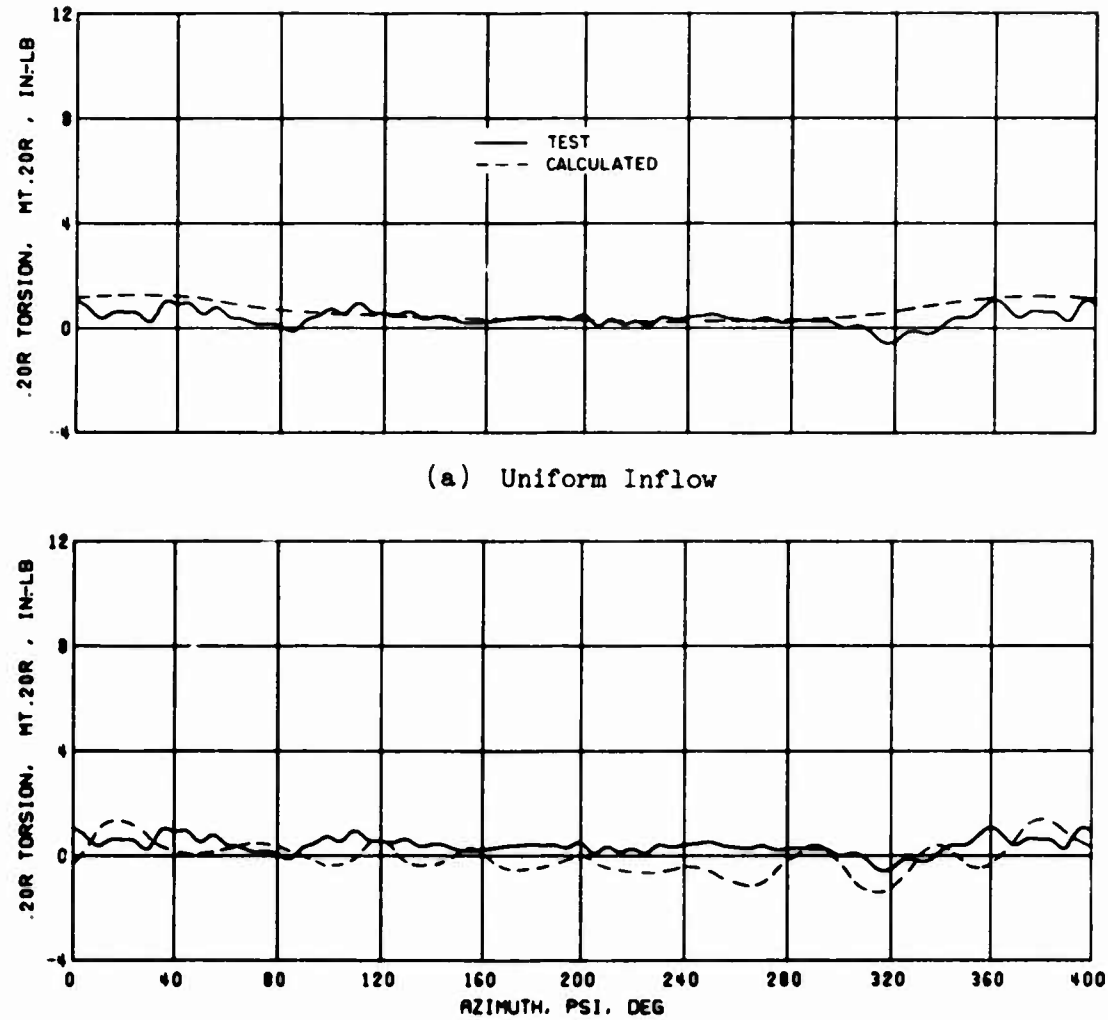

(a) Uniform Inflow

(b) .3 Chord Vortex Core Size

Figure 89. Effect of Variable Inflow Vortex Core Size Assumption on Correlation of Test and Calculated .20R Torsion; θ_1 = 0 deg, δ_F = 0 deg, S_E = 1, Condition 1.

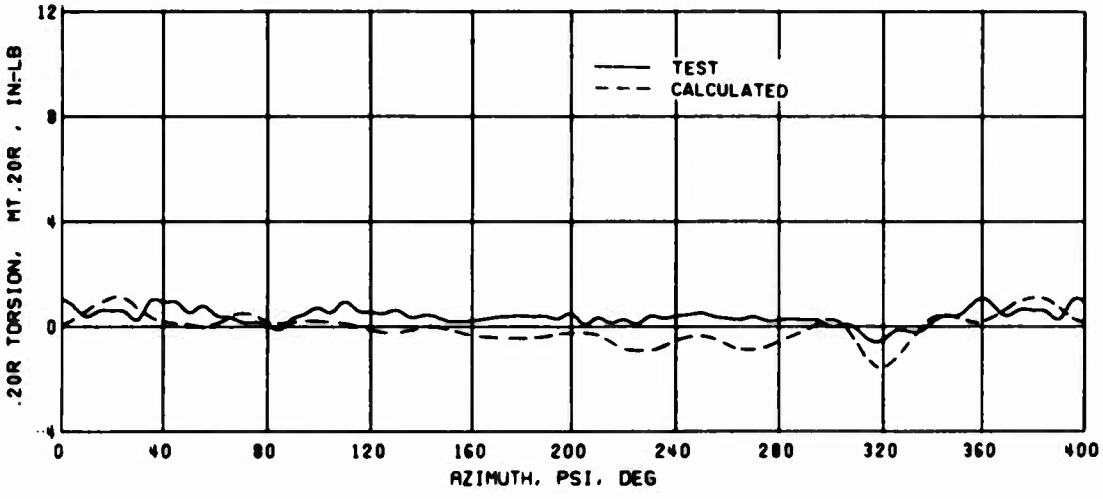

(c) .6 Chord Vortex Core Size

Figure 89. Concluded.

APPENDIX I

FULL-SCALE H-34 BLADE DATA

TABLE XLIX. H-34 MAIN ROTOR BLADE MISCELLANEOUS DATA

PARAMETER	VALUE	UNITS
Airfoil section NACA 0012		
Airfoil chord	16.4	in.
Radial location of airfoil inboard end	53.7	in.
Elastic axis location aft of leading edge (for radial stations outboard of 54 in.)	3.9	in.
Rotor radius	336.0	in.
Flapping and lead-lag hinge radial location	12.0	in.
Young's modulus (E)	10×10^6	$lb/in.^2$
Shear modulus (G)	4×10^6	$lb/in.^2$
Feathering axis location aft of leading edge	4.1	in.

TABLE L. H-34 MAIN ROTOR BLADE DISTRIBUTED WEIGHT, CHORDWISE CENTER-OF-GRAVITY POSITION, AND TORSIONAL INERTIA (STANDARD BLADE)

Δr (in.)	r_{in} (in.)	r_{out} (in.)	w (lb/in.)	Y_{CG}* (in.)	I_θ (lb-sec^2)
1.0	12.0	13.0	9.0	0.0	0.270
11.0	13.0	24.0	5.50	0.0	0.129
4.0	24.0	28.0	4.75	0.0	0.068
4.0	28.0	32.0	1.64	0.0	0.043
2.0	32.0	34.0	1.57	0.0	0.034
2.0	34.0	36.0	1.29	0.0	0.024
2.0	36.0	38.0	1.07	0.0	0.015
3.0	38.0	41.0	0.45	0.0	0.008
13.0	41.0	54.0	0.30	0.0	0.005
23.0	54.0	77.0	0.35	-0.55	0.012
1.0	77.0	78.0	0.40	0.20	0.016
239.0	78.0	317.0	0.45	0.20	0.016
6.0	317.0	323.0	0.55	-0.27	0.018
4.0	323.0	327.0	0.80	-0.01	0.028
2.0	327.0	329.0	0.95	-0.01	0.034
2.0	329.0	331.0	0.45	-0.97	0.016
2.0	331.0	333.0	0.90	0.0	0.031
2.0	333.0	335.0	0.15	-7.3	0.005
1.0	335.0	336.0	0.25	-2.3	0.008

* Distance of center of gravity forward of feathering axis.

TABLE LI. H-34 MAIN ROTOR BLADE DISTRIBUTED WEIGHT, CHORDWISE CENTER-OF-GRAVITY POSITION, AND TORSIONAL INERTIA (AS INSTRUMENTED FOR PRESSURE MEASUREMENTS)

Δr (in.)	r_{in} (in.)	r_{out} (in.)	w (lb/in.)	Y_{CG}* (in.)	I_θ (lb-sec^2)
1.00	12.00	13.00	9.00	0.00	0.270
11.00	13.00	24.00	5.50	0.00	0.129
4.00	24.00	28.00	4.75	0.00	0.068
4.00	28.00	32.00	1.64	0.00	0.043
2.00	32.00	34.00	1.57	0.00	0.034
2.00	34.00	36.00	1.29	0.00	0.024
2.00	36.00	38.00	1.07	0.00	0.015
3.00	38.00	41.00	0.45	0.00	0.008
13.00	41.00	54.00	0.30	0.00	0.005
23.00	54.00	77.00	0.35	-0.55	0.012
1.00	77.00	78.00	0.40	0.20	0.014
2.00	78.00	80.00	0.50	0.20	0.018
3.00	80.00	83.00	0.45	0.20	0.016
7.00	83.00	90.00	0.55	0.20	0.018
36.00	90.00	126.00	0.45	0.20	0.016
13.00	126.00	139.00	0.55	0.20	0.018
35.00	139.00	174.00	0.45	0.20	0.016
12.00	174.00	186.00	0.55	0.20	0.019
60.00	186.00	246.00	0.45	0.20	0.016
11.00	246.00	257.00	0.55	0.20	0.019
24.00	257.00	281.00	0.45	0.20	0.016
24.00	281.00	305.00	0.55	0.20	0.019
12.00	305.00	317.00	0.45	0.20	0.016
6.00	317.00	323.00	0.55	-0.27	0.018
4.00	323.00	327.00	0.80	-0.01	0.028
2.00	327.00	329.00	0.95	-0.01	0.034
2.00	329.00	331.00	0.45	-0.97	0.016
2.00	331.00	333.00	0.90	0.0	0.031
2.00	333.00	335.00	0.15	-2.3	0.0050
1.00	335.00	336.00	0.25	-2.3	0.0080

* Distance of center of gravity forward of feathering axis.

TABLE LII. H-34 MAIN ROTOR BLADE STRUCTURAL AREA AND MOMENTS OF INERTIA

Δr (in)	r_{in} (in.)	r_{out} (in.)	A_s (in^2)	I_{chd} (in^4)	I_{flp} (in^4)
1.50	12.00	13.50	78.33	84.76	7.80
2.50	13.50	16.00	55.00	50.00	7.80
2.00	16.00	18.00	55.00	17.80	50.00
8.00	18.00	26.00	53.13	46.20	50.00
1.50	26.00	27.50	47.50	29.20	29.20
1.50	27.50	29.00	26.77	9.20	11.14
3.50	29.00	32.50	16.30	3[illegible].00	23.10
2.50	32.50	35.00	14.70	30.35	15.83
1.00	35.00	36.00	12.90	26.33	10.87
4.00	36.00	40.00	5.59	23.66	7.07
4.00	40.00	44.00	3.59	18.34	1.90
9.00	44.00	53.00	3.45	17.91	1.85
24.00	53.00	77.00	3.21	17.18	1.71
259.00	77.00	336.00	2.92	15.94	1.47

TABLE LIII. H-34 MAIN ROTOR BLADE STRUCTURAL AREA TORSIONAL RADIUS OF GYRATION

Δr (in)	r_{in} (in)	r_{out} (in)	r_{GS} (in)
1.00	12.00	13.00	3.41
11.00	13.00	24.00	3.02
4.00	24.00	28.00	2.35
4.00	28.00	32.00	3.20
2.00	32.00	34.00	2.88
2.00	34.00	36.00	2.71
2.00	36.00	38.00	2.35
3.00	38.00	41.00	2.50
13.00	41.00	54.00	2.41
23.00	54.00	77.00	2.43
1.00	77.00	78.00	2.46
2.00	78.00	80.00	2.46
3.00	80.00	83.00	2.45
7.00	83.00	90.00	2.37
36.00	90.00	126.00	2.45
13.00	126.00	139.00	2.37
178.00	139.00	317.00	2.45
6.00	317.00	323.00	2.37
13.00	323.00	336.00	2.45

TABLE LIV. H-34 MAIN ROTOR BLADE TORSIONAL STIFFNESS

Δr (in.)	r_{in} (in.)	r_{out} (in.)	JG_2 (lb-in.^{2})x10^{-6}	J (JG÷4x10^6)
16.00	12.00	28.00	11.90	2.950
12.00	28.00	40.00	45.22	11.305
14.00	40.00	54.00	22.42	5.605
20.00	54.00	74.00	20.52	5.130
7.00	74.00	81.00	19.00	4.750
249.50	81.00	330.50	17.67	4.418
5.50	330.50	336.00	17.67	4.418

APPENDIX II

COMPUTER PROGRAM DOCUMENTATION

USER'S INSTRUCTIONS FOR DATA RETRIEVAL AND DISPLAY PROGRAM

(Refer to the report section "TEST DATA OBTAINED", p.30.

Input

A. Tape for one of the blade configurations
B. Input Cards

(1) First Card

Field	Columns	Input Item:
1	1-4	Operating condition number
2	5-8	Physical measurement (channel) number
3	9-12	First revolution number in a time history sample
4	13-16	Last revolution number in a time history sample
5	17-20	First revolution in a time history sample for frequency analysis
6	21-24	Last revolution in a time history sample for frequency analysis
7	25-34	Lowest frequency component in analysis
8	35-44	Frequency increment in analysis
9	45-48	Number of frequencies in analysis
10	49-52	Control word for summary option (mean, rms, max, min)
11	53-56	Control word for azimuth-averaged revolution time history
12	57-60	Number of harmonics in harmonic analysis
13	61-64	Harmonic table control number

Fields 7 and 8 are real positive decimal numbers. All other fields are right-adjusted integers. Fields 3 and 5 must be numbers from 1 to 40 to exercise the corresponding options. Fields 4 and 6 must be equal to or greater than 3 and 5 respectively, and no greater than 40 to exercise the corresponding options. Fields 10, 11 and 13 must be 1, 2 or 3 to exercise those options. If, on the first card, any of the fields 3, 5, 10, 11, 12, 13 contain 999 or are blank, the corresponding option will not be exercised for that condition-channel combination. The options may be turned on for succeeding condition-channel combinations by inputs in those fields.

(2) Succeeding Cards

The format is the same as the first card format. If any fields are 0 or blank, the inputs will remain as they were for the preceding card. If any of fields 3, 5, 10, 11, 12, and 13 contain 999, that option will not be exercised.

If condition number 9999 is input, the body of data to be retrieved is considered to be complete.

Input for a new body of data can now be entered, otherwise the computer run will be terminated.

A maximum of 100 request cards can be input for each body of data. If more are desired in a computer run, 9999 can be entered as a condition number, and a new body of data started.

Output

Time history sampling will be carried out in response to legal entries in fields 3 and 4. The indicated revolutions will be tabulated in vertical columns. The table heading will contain the blade configuration description, condition number, and rotor operating parameters. A one-page printer plot of the time history data will appear for each revolution. The condition number and rotor operating parameters will be printed beside the plot.

Frequency analysis will be carried out in response to proper entries in fields 5, 6, 7, 8, and 9. The amplitude components A_i, B_i, and R_i will be tabulated and plotted for each frequency. The nonharmonic analysis frequencies should range between .15 and 15. cycles per revolution if all 40 revolutions of data are used. An input of 1, 2, or 3 in field 10 will print out average, root-mean-square about the average, maximum value, and minimum value in the data for that condition and channel. The tabulation is continued by specifying additional conditions and/or channels on succeeding cards. If 1 is input in field 10, the tabulation will proceed by channels for a condition. The tables will be output in ascending condition number. The channels will appear in the same order as they appeared in the input deck for the specified body of data. If 3 is input in field 10, the tabulation will proceed by conditions for a channel. The tables will be output in ascending channel number. The conditions will appear in the same order as they were entered in the input deck. If 2 is input in field 10, both table types will be output.

An input in field 11 will print out average revolution time histories. The tabulation of similar data for succeeding channels and conditions will proceed by channels for a condition if 1 is placed in field 11. The tabulation will proceed by conditions for a channel if 3 is placed in field 11. A 2 in field 11 will cause the printing of both table types. Time history printer plots of each average revolution will also be printed.

Similarly, inputs in fields 12 and 13 provide a harmonic analysis which is tabulated by channels for a condition if a 1 is input in field 13, by conditions for a channel if 3 is input, and both tables if 2 is input.

LIST OF SYMBOLS

A	nondimensional pitch rate
$[A]$	flexibility matrix
$A_{(i)}$	indicated angle of attack for test point (i), deg
A_j	even (cosine) part of frequency component from numerical frequency analysis, engineering units
A_{NH}	cosine part of nonharmonic amplitude component, engineering units
A_S	blade spar structural crossection area, $in.^2$
A_T	tunnel test section crossectional area, ft^2
A_{ls}	lateral cyclic pitch, blade pitch down over tail, deg
A_{lsR}	indicated value of A_{ls}, deg
a_i	cosine part of ith modal response to unit cosine force, in.
$a(\omega_j)$	analytical counterpart of A_j
a_{ls}	longitudinal first-harmonic flapping component, blade down over tail, deg
B	nondimensional pitch acceleration
B_j	odd (sine) part of frequency component from numerical frequency analysis, engineering units
B_{NH}	sine part of nonharmonic amplitude component, engineering units
B_{ls}	longitudinal cyclic pitch, blade pitch down over right (advancing) side, deg
B_{lsR}	indicated value of B_{ls}, deg
b	number of rotor blades
b_i	sine part of ith modal response to unit cosine force, in.
b_{ls}	lateral first-harmonic flapping component, blade down over right side, deg
$b(\omega_j)$	analytical counterpart of B_j
C_d	section coefficient of drag

$C_{d(i)}$	corrected coefficient of drag at the ith two-dimensional test point
$C_{dR(i)}$	uncorrected coefficient of drag at the ith two-dimensional test point
C_D/σ	rotor drag coefficient - solidity ratio, $D_R/\rho\pi\Omega^2R^4\sigma$
C_{DP}	coefficient of pth viscous damper
C_{EFF}	effective rotor head damping
C_{EFFT}	torsional damping coefficient, in.-lb-sec
C_{EFFV}	vertical damping coefficient, lb-sec/in.
C_{EFFX}	fore-aft damping coefficient, lb-sec/in.
C_{EFFY}	lateral damping coefficient, lb-sec/in.
$C_{(i)}$	indicated chordwise force at test point (i), lb
C_l	section coefficient of lift
$C_{l(i)}$	coefficient of lift at the ith two-dimensional test point
C_L	rotor coefficient of lift
C_L/σ	rotor lift coefficient-solidity ratio, $L_R/\rho\pi\Omega^2R^4\sigma$
C_m	section coefficient of pitching moment
$C_{m(i)}$	corrected coefficient of pitching moment at the ith two-dimensional test point
$C_{mR(i)}$	uncorrected coefficient of pitching moment at the ith two-dimensional test point
C_{mn}	balance conversion matrix elements
CMREG1	upper limit of local angle of attack at which unsteady aerodynamic pitching moment data is used in blade response calculation, deg
CMREG2	lower limit of local angle of attack at which steady aerodynamic pitching moment data is used in blade response calculation, deg
C_{mt}	value of C_m in unsteady aerodynamic data table
C_n	section normal force coefficient

CNREG1	upper limit of local angle of attack at which unsteady aerodynamic pitching moment data is used in blade response calculation, deg
CNREG2	lower limit of local angle of attack at which steady aerodynamic pitching moment data is used in blade response calculation deg,
$C_{nss}(M)$	value of steady state C_n at Mach number M and $\alpha_{sn}(M)$
C_{nsst}	value of steady state C_n at α_{snt} in unsteady aerodynamic data table
C_{nt}	value of C_n in unsteady aerodynamic data table
C_{PM}/σ	rotor pitching moment coefficient-solidity ratio, $M_S/\rho\pi\Omega^2R^5\sigma$
C_Q/σ	rotor torque coefficient-solidity ratio, $-N_S/\rho\pi\Omega^2R^5\sigma$
C_{RM}/σ	rotor rolling moment coefficient - solidity ratio $L_S/\rho\pi\Omega^2R^5\sigma$
C_T	rotor thrust coefficient, $-Zs/\rho\pi\Omega^2R^4$
C_Y/σ	rotor side-force coefficient - solidity ratio, $Y_S/\rho\pi\Omega^2R^4\sigma$
c	airfoil chord, in. or ft
$[D]$	physical damping matrix
$[D_G]$	generalized damping matrix
D_R	rotor drag force, lb
$D_{R(i)}$	indicated drag force at test point (i), lb
E	Young's modulus, $lb/in.^2$
F_c	arbitrary offset constant, physical units
F_n	rotor force factor, lb
$(F_{RQ})_J$	jth analysis frequency, cycles/rev
F_s	initial analysis frequency, cycles/rev
f_{BCi}	experimental nonrotating natural frequency for the ith chordwise mode, cps
f_{BFi}	experimental nonrotating natural frequency for the ith flapwise mode, cps
f_{Ti}	experimental nonrotating natural frequency for the ith torsional mode, cps

G	shear modulus, $lb/in.^2$
$G_{A(i)}$	angle of attack transducer reading at ith two-dimensional test point, gage units
G_{AE}	angle of attack transducer end zero, gage units
G_{AO}	angle of attack transducer average zero, gage units
G_{AS}	angle of attack transducer start zero, gage units
G_{DE}	balance drag component end zero, gage units
$G_{D(i)}$	balance drag component reading at ith two-dimensional test point, gage units
G_{DO}	balance drag component average zero, gage units
G_{DS}	balance drag component start zero, gage units
G_{LE}	balance lift component end zero, gage units
$G_{L(i)}$	balance lift component at ith two-dimensional test point, gage units
G_{LO}	balance lift component average zero, gage units
G_{LS}	balance lift component start zero, gage units
G_{ME}	balance pitch moment component end zero, gage units
$G_{M(i)}$	balance pitch moment component at ith two-dimensional test point, gage units
G_{MO}	balance pitch moment component average zero, gage units
G_{MS}	balance pitch moment component start zero, gage units
H	total pressure, lb/ft^2
H_L	aerodynamic plus gravity tare moment in L_{BAC} direction, gage units
H_M	aerodynamic plus gravity tare moment in M_{BAC} direction, gage units
H_N	aerodynamic plus gravity tare moment in N_{BAC} direction, gage units
H_x	aerodynamic plus gravity tare force in X_{BAC} force direction, gage units

H_Y	aerodynamic plus gravity tare force Y_{BAC} force direction, gage units
H_Z	aerodynamic plus gravity tare force in Z_{BAC} force direction, gage units
$\{I\}$	unit column matrix
$[I]$	unit diagonal matrix
I_{chd}	chordwise blade bending stiffness area moment of inertia, $in.^4$
I_{flp}	flapwise blade bending stiffness area moment of inertia, $in.^4$
I_{mch}	chordwise mass moment of inertia of blade per unit span, $lb\text{-}sec^2$
I_{mfl}	flapwise mass moment of inertia of blade per unit span, $lb\text{-}sec^2$
I_θ	torsional mass moment of inertia of blade per unit span, $lb\text{-}sec^2$
J	blade torsional stiffness constant, $in.^4$
K	number of digital data values in a time history segment for frequency analysis
$[K]$	stiffness matrix
K_A	angle of attack transducer conversion constant, deg^{-1}
K_{EFF}	effective stiffness, lb/in.
K_{EFFT}	torsional spring constant, in.-lb
K_{EFFV}	vertical spring constant, lb/in.
K_{EFFX}	fore-aft spring constant, lb/in.
K_{EFFY}	lateral spring constant, lb/in.
K_{MN}	pressure transducer conversion constant, lb/ft^2
L_{BAC}	indicated right side down rolling moment in rotor shaft axis system, gage units
L_0	static offset correction for L_{BAC}, gage units
L_R	rotor lift force, lb
$L_{R(i)}$	indicated lift force at ith two-dimensional test point, lb
L_S	rotor right side down rolling moment in shaft axis system, ft-lb
M	Mach number

$[M]$	mass matrix
$M_{A(i)}$	aerodynamic pitching moment for the ith test point, in.-lb or ft-lb
M_{BAC}	indicated nose-up pitching moment in rotor shaft axis system, gage units
$M_{BC.XR}$	chordwise bending at .X radius, leading edge in tension, in.-lb
$M_{BF.XR}$	upward flapwise bending at .X radius, in.-lb
M_C	fiber glass model chordwise bending moment, in.-lb
$M_{CB(i)}$	pitch moment correction at ith two-dimensional test point for normal force and chordwise deflection, in.-lb
M_{CFS}	full-scale chordwise bending moment, in.-lb
M_{CRM}	replica model chordwise bending moment, in.-lb
M_{EFF}	effective mass, lb-sec^2/in.
M_{EFFT}	torsional inertia, in.-lb-sec^2
M_{EFFV}	vertical inertia, lb-sec^2/in.
M_{EFFX}	fore-aft inertia, lb-sec^2/in.
M_{EFFY}	lateral inertia, lb-sec^2/in.
M_F	fiber glass model flapwise bending moment, in.-lb
M_{FFS}	full-scale flapwise bending moment, in.-lb
M_{FRM}	replica model flapwise bending moment, in.-lb
$M_{(i)}$	Mach number at ith two-dimensional test point
M_{Gi}	generalized mass of the ith natural mode
$M_{NB(i)}$	pitch moment correction at ith two-dimensional test point for normal deflection, in.-lb
$M_{NW(i)}$	pitch moment correction at ith two-dimensional test point for airfoil weight and normal deflection, in.-lb
M_o	static offset correction for M_{BAC}, gage units
$M_{R(i)}$	indicated pitch moment at the ith two-dimensional test point, in.-lb

M_T	fiber glass model torsion moment, in.-lb
M_{TFS}	full-scale torsion moment, in.-lb
M_{TRM}	replica model torsion moment, in.-lb
$M_{T.XR}$	torsion moment at .X radius nose up, in.-lb
$M_{UW(i)}$	pitch moment correction at ith two-dimensional test point for airfoil static unbalance, in.-lb
$M_{1,90}$	blade tip Mach number at 90° azimuth
N_O	static offset correction for N_{BAC}, gage units
N_{BAC}	indicated nose right yawing moment in rotor shaft axis system, gage units
N_{FD}	arbitrary constant for discontinuity detection
N_{FE}	ending revolution for time history segment for frequency analysis
N_{FS}	starting revolution for time history segment for frequency analysis
$N_{(i)}$	indicated normal force at ith two-dimensional test point, lb
N_{PRV}	digital time history data values per revolution
N_S	rotor nose right yawing moment about shaft, ft-lb
N_{SFL}	scale factor for L_{BAC}, gage units/lb
N_{SFM}	scale factor for M_{BAC}, gage units/lb
N_{SFN}	scale factor for N_{BAC}, gage units/lb
N_{SFX}	scale factor for X_{BAC}, gage units/lb
N_{SFY}	scale factor for Y_{BAC}, gage units/lb
N_{SFZ}	scale factor for Z_{BAC}, gage units/lb
P	static pressure, lb/ft^2
q	dynamic pressure, lb/ft^2
$\{qm\}$	column matrix of modal amplitudes
q_{vj}	amplitude of jth chordwise mode

q_{wi}	amplitude of ith flapwise mode
R	rotor radius, ft
R_c	physical equivalent of electrical calibration signal, engineering units
R_G	parameter for compressible adiabatic flow equations, $^oF\text{-}sec^2/ft^2$
R_j	resultant frequency component from numerical frequency analysis, engineering units
RN	Reynolds number
R_{NH}	resultant of nonharmonic amplitude component, engineering units
r_{GS}	radius of gyration of blade spar structural crossection, in.
r_{in}	radial distance of inboard end of blade segment from center of rotation, in.
r_{out}	radial distance of outboard end of blade segment from center of rotation, in.
r_{vc}	vortex core size, ft
$r(\omega_j)$	analytical counterpart of R_j
S	airfoil span, in.
S_E	ratio of blade elastic stiffness to dynamically scaled value
S_s	geometric scale factor
T	kinetic energy, in.-lb
T_{SC}	wind tunnel stagnation temperature, ^oF
t	time, sec
U	resultant velocity with respect to blade, ft/sec
V	flow velocity, ft/sec or kn
$V_{A(i)}$	angle of attack transducer net output at test point (i)
$V_{D(i)}$	balance drag component net output at test point (i), gage units
$V_{L(i)}$	balance lift component net output at test point (i), gage units
$V_{M(i)}$	balance moment component net output at test point (i), gage units

V_s	simulated full-scale equivalent speed, ft/sec or kn
v	momentum theory induced inflow velocity, ft/sec
W_D	digital data value, computer units
W_E	blade response data value in engineering units
W_M	weight of airfoil for two-dimensional test, lb
W_o	average data value on tape in zero reference condition, computer units
W_R	average data value on tape in "RCAL" records, computer units
$(W_T)_k$	kth digital value in selected time history segment for frequency analysis
W_Z	average data value on tape in "ZCAL" records, computer units
w	blade weight per unit span, lb/in.
X_{BAC}	indicated longitudinal force normal to rotor shaft on model internal balance, gage units
X_H	column of modal deflections at head in direction of force
X_J	Jth data value in a time history record
$\overline{X}_J$	interpolated quantity for Jth data value
X_O	static offset correction for X_{BAC}, gage units
X_S	rotor longitudinal force forward normal to shaft, lb
X_{UA}	resultant of head response to unit cosine force or moment, in. or rad
X_{UI}	sine part of head response to unit cosine force or moment, in. or rad
X_{UR}	cosine part of head response to unit cosine force or moment, in. or rad
Y_{BAC}	indicated side force to right and normal to rotor shaft on model internal balance, gage units
Y_{CG}	distance of mass center of gravity of blade section aft of the feathering axis, in.
Y_O	static offset correction for Y_{BAC}, gage units

Y_S	rotor side force to right normal to shaft, lb
Z_{BAC}	indicated vertical force downward along rotor shaft, gage units
Z_O	static offset correction for Z_{BAC}, gage units
Z_S	rotor thrust force down along shaft, lb
α	corrected angle of attack, deg
α_c	rotor control angle of attack, $\alpha_s - B_{ls}$
(α_{fr})	indicated model fuselage nose up angle of attack, deg
$\alpha_{G(i)}$	airfoil midspan geometric angle of attack at the ith test point, deg
α_o	start and end angle of attack, deg
α_s	corrected rotor shaft nose up angle of attack, deg
$\alpha_{sm}(M)$	angle of attack for pitching moment stall at Mach number M, deg
α_{smt}	angle of attack for pitching moment stall in unsteady aerodynamic data table, deg
$\alpha_{sn}(M)$	angle of attack for normal force stall at Mach number M, deg
α_{snt}	angle of attack for normal force stall in unsteady aerodynamic data table, deg
α_T	angle of attack for unsteady aerodynamic data table look-up, deg
β	blade upward flapping at hinge, deg
γ	specific heat ratio parameter for compressible adiabatic flow equations
γ_{Dpi}	deflection of the pth viscous damper in the ith mode
$\{\gamma_m\}$	mode shape column matrix
γ_{wi}	ith flapwise mode shape
γ'_{wi}	slope of ith flapwise mode shape
γ''_{wi}	curvature of ith flapwise mode shape
γ''_{vj}	curvature of jth chordwise mode shape

ΔF_{RQ}	frequency increment, cycles/rev
ΔP	pressure transducer output for total minus static pressure, gage units
Δr	radial length of segment along blade, in.
Δa	wall effect correction to fuselage angle of attack, deg
δ_F	plain flap downward deflection, deg
ζ	blade lag in drag direction at hinge, deg
ζ_{BCi}	experimental structural damping for the nonrotating ith chordwise natural mode, percent of critical
ζ_{BFi}	experimental structural damping for the nonrotating ith flapwise natural mode, percent of critical
ζ_{Ti}	experimental structural damping for the nonrotating ith torsional natural mode, percent of critical
η	structural damping coefficient
θ_c	collective pitch at 75% radius
θ_e	elastic blade torsional deflection, rad or deg
$\theta_{(i)}$	airfoil midspan torsional elastic deflection, deg
θ_l	built-in blade linear twist, from axis of rotation to blade tip, deg
λ	ratio of inflow velocity to ΩR
λ_v	ratio of inflow velocity to ΩR from prescribed wake calculation
μ	rotor advance ratio, $V/\Omega R$
ρ	air density in flow, slugs/ft^3
ρ_o	air density at zero velocity, slugs/ft^3
σ	rotor solidity, $bc/\pi R$
σ_C	full-scale chordwise bending stress, lb/in.^{2}
σ_{CFS}	fiber glass model chordwise bending full-scale equivalent stress, lb/in.^{2}
σ_F	full-scale flapwise bending stress, lb/in.^{2}

σ_{FFS}	fiber glass model flapwise bending full-scale equivalent stress, lb/in.^{2}
σ_T	full-scale torsion stress, lb/in.^{2}
$\sigma_{T.15R}$	full-scale torsion stress at 15% rotor radius, lb/in.^{2}
σ_{TFS}	fiber glass model torsional full-scale equivalent stress, lb/in.^{2}
$\sigma_{TFS.15R}$	fiber glass model torsional full-scale equivalent stress at 15% rotor radius, lb/in.^{2}
ϕ_{UA}	rotor head phase response to unit vibratory force, deg
ψ	azimuth angle, deg
ψ_{SP}	swashplate phase angle, deg
Ω	rotor rotational speed, rad/sec
Ω_S	simulated full-scale rotor rotational speed, rad/sec
ω_F	forcing frequency, cycles or rad/sec
ω_J	ratio of analysis frequency to rotational frequency
ω_n	natural frequency, cycles or rad/sec
ω_{NH}	nonharmonic frequency, cycles/rev
ω_{ni}	natural frequency of ith natural mode, cycles or rad/sec

DERIVATIVE NOTATION

$\dot{}$	$\frac{d}{dt}$
$\ddot{}$	$\frac{d^2}{dt^2}$

6047-74